Vitalii Ivanov · Ivan Pavlenko ·
Oleksandr Liaposhchenko ·
José Machado · Milan Edl   *Editors*

Advances in Design, Simulation and Manufacturing III

Proceedings of the 3rd International Conference on Design, Simulation, Manufacturing: The Innovation Exchange, DSMIE-2020, June 9–12, 2020, Kharkiv, Ukraine – Volume 2: Mechanical and Chemical Engineering

Springer

Lecture Notes in Mechanical Engineering

Vitalii Ivanov · Ivan Pavlenko ·
Oleksandr Liaposhchenko ·
José Machado · Milan Edl
Editors

Advances in Design, Simulation and Manufacturing III

Proceedings of the 3rd International Conference on Design, Simulation, Manufacturing: The Innovation Exchange, DSMIE-2020, June 9–12, 2020, Kharkiv, Ukraine – Volume 2: Mechanical and Chemical Engineering

Editors
Vitalii Ivanov
Sumy State University
Sumy, Ukraine

Oleksandr Liaposhchenko
Sumy State University
Sumy, Ukraine

Milan Edl
University of West Bohemia
Pilsen, Czech Republic

Ivan Pavlenko
Sumy State University
Sumy, Ukraine

José Machado
University of Minho
Guimaraes, Portugal

Preface

This volume of Lecture Notes in Mechanical Engineering contains selected papers presented at the 3rd International Conference on Design, Simulation, Manufacturing: The Innovation Exchange (DSMIE-2020), held in Kharkiv, Ukraine, during June 9–12, 2020. The conference was organized by the Sumy State University, National Technical University "Kharkiv Polytechnic Institute," and International Association for Technological Development and Innovations, in partnership with Technical University of Kosice (Slovak Republic), Kielce University of Technology (Poland), University of West Bohemia (Czech Republic), Poznan University of Technology (Poland), and Association for Promoting Innovative Technologies—Innovative FET (Croatia).

DSMIE-2020 is the international forum for fundamental and applied research and industrial applications in engineering. The conference focuses on a broad range of research challenges in the fields of manufacturing, materials, mechanical, and chemical engineering, addressing current and future trends in design approaches, simulation techniques, computer-aided systems, software development, ICT tools, and Industry 4.0 strategy implementation for engineering tasks solving. DSMIE-2020 brings together researchers from academic institutions, leading industrial companies, and government laboratories located around the world for promoting and popularization of the scientific fundamentals of manufacturing.

DSMIE-2020 received 161 contributions from 28 countries around the world. After a thorough peer-review process, the Program Committee accepted 93 papers written by authors from 23 countries. Thank you very much to the authors for their contribution. These papers are published in the present book, achieving an acceptance rate of about 58%. Extended versions of selected best papers will be published in scientific journals: Management and Production Engineering Review (published by De Gruyter and indexed by ISI/ESCI, Scopus), Archives of Mechanical Technology and Materials (Poland), and Journal of Engineering Sciences (Ukraine).

We would like to thank members of the Program Committee and invited external reviewers for their efforts and expertise in contributing to reviewing, without which it would be impossible to maintain the high standards of peer-reviewed papers.

Program Committee members and invited external reviewers devoted their time and energy for peer-reviewing manuscripts. Our reviewers come from all over the world and represent 29 countries and affiliated with 63 institutions.

Thank you very much to keynote speakers: Erwin Rauch (Italy), Dagmar Caganova (Slovak Republic), Mateusz Barczewski (Poland), Arun Nagarajah (Germany), Domenico Guida (Italy) and Alex Enrich Prast (Sweden) for sharing their knowledge and experience.

The book "Advances in Design, Simulation and Manufacturing III" was organized into two volumes according to the main conference topics: Volume 1—Manufacturing and Materials Engineering and Volume 2—Mechanical and Chemical Engineering. Each volume is devoted to research in design, simulation, and manufacturing in the areas of (1) manufacturing engineering, (2) materials engineering, (3) mechanical engineering, and (4) chemical engineering.

This volume consists of five parts. The first part is aimed at recent developments in the mechanics of solids and structures. It includes studies in the fields of identification of car dynamic models, liquid sloshing in cylindrical shells, the cavitational wearing of modified ceramics, shock waves in foam materials, movement of particles in spiral gutters and swirling flow in a confuser, up-to-date approaches in mathematical modeling and designing the hydraulic and mechatronic systems, as well as in estimating operating characteristics of automatic balancing devices for centrifugal pumps, and ensuring the reliability of lever-blade shock absorbers.

The second part includes studies in the field of numerical simulation of coupled problems, including wearing, compression, detonation, and collision. Mainly, it presents computer means for simulation of wearing process, friction interaction, and corrosion, as well as the research of energy state of the alloys. It additionally includes computer means for carrying out numerical simulations for gas turbine, aircraft, and other industrial applications.

The third part is devoted to chemical process technology, including ultrasonic technology, capillary rising process, pneumatic classification, membrane electrolysis, and absorption process. Cooling process intensification for granular mineral fertilizers and substantiation of energy parameters of vibroextraction for solid–liquid systems are also presented in this part.

The fourth part is based on recent developments in the field of heat and mass transfer. It presents the studies in the development of high-pressure stages for steam turbines, improvement of heating supply systems, and improvement of cooling and air conditioning systems. Experimental research of the operating processes in gas boilers and aerothermopressors is also included in this part.

The fifth part is aimed at energy-efficient technologies and industrial ecology. Particularly, ways for increasing the efficiency of water treatment, as well as for the development of eco-friendly bio-utilization processes and improvement of their production techniques, are proposed. Additionally, this part is devoted to decreasing gas emissions, as well as at the development of biofuels.

We appreciate the partnership with Springer, StrikePlagiarism, EasyChair, and our sponsors for their essential support during the preparation of DSMIE-2020.

Thank you very much for DSMIE Team. Their involvement and hard work were crucial to the success of the DSMIE-2020 conference.

DSMIE's motto is "Together we can do more for science, technology, engineering, and education."

June 2020   Vitalii Ivanov
                                                                                              Ivan Pavlenko
                                                                                 Oleksandr Liaposhchenko
                                                                                              José Machado
                                                                                                 Milan Edl

Organization

Steering Committee

General Chair

Vitalii Ivanov — Sumy State University, Ukraine

Co-chair

Andriy Marchenko — National Technical University "Kharkiv Polytechnic Institute," Ukraine

Members

Olena Avdieieva — National Technical University "Kharkiv Polytechnic Institute," Ukraine

Yevheniia Basova — National Technical University "Kharkiv Polytechnic Institute," Ukraine

Sergey Dobrotvorskiy — National Technical University "Kharkiv Polytechnic Institute," Ukraine

Oleksandr Gusak — Sumy State University, Ukraine

Oleksandr Liaposhchenko — Sumy State University, Ukraine

Olena Naboka — National Technical University "Kharkiv Polytechnic Institute," Ukraine

Ivan Pavlenko — Sumy State University, Ukraine

Alexander Permyakov — National Technical University "Kharkiv Polytechnic Institute," Ukraine

Oleksandr Usatyi — National Technical University "Kharkiv Polytechnic Institute," Ukraine

Vitalii Yepifanov — National Technical University "Kharkiv Polytechnic Institute," Ukraine

Program Committee (in alphabetical order)

Gabriel Abba	University of Lorraine, France
Jean-Francois Antoine	University of Lorraine, France
Katarzyna Antosz	Rzeszow University of Technology, Poland
Peter Arras	KU Leuven, Belgium
Michal Balog	Technical University of Kosice, Slovak Republic
Shahzad Barghi	University of Western Ontario, Canada
Jozef Bocko	Technical University of Kosice, Slovak Republic
Glen Bright	University of KwaZulu-Natal, South Africa
Sajid Ullah Butt	National University of Sciences and Technology, Pakistan
Dagmar Caganova	Slovak University of Technology, Slovak Republic
Emilia Campean	Technical University of Cluj-Napoca, Romania
Robert Cep	VSB-Technical University of Ostrava, Czech Republic
Vasile George Cioata	Polytechnic University of Timisoara, Romania
Olaf Ciszak	Poznan University of Technology, Poland
Oguz Colak	Eskisehir Technical University, Turkey
Ronnie II Concepcion	University of Perpetual Help System DALTA, Philippines
Marcela Contreras	Autonomous University of Occidente, Mexico
Radu Cotetiu	Technical University of Cluj-Napoca, Romania
Alina Crisan	University of Agricultural Sciences and Veterinary Medicine, Romania
Predrag Dasic	University Union "Nikola Tesla," Serbia
Oleksandr Derevianchenko	Odessa National Polytechnic University, Ukraine
Mihai Dragomir	Technical University of Cluj-Napoca, Romania
Milan Edl	University of West Bohemia, Czech Republic
Mathieu Gautier	University Lyon, France
Renata Gnatowska	Czestochowa University of Technology, Poland
Mihaly Gorbe	John von Neumann University, Germany
Domenico Guida	University of Salerno, Italy
Oleksandr Gusak	Sumy State University, Ukraine
Mikulas Hajduk	Technical University of Kosice, Slovak Republic
Michal Hatala	Technical University of Kosice, Slovak Republic
Siamak Hoseinzadeh	University of Pretoria, South Africa
Ihor Hurey	Lviv Polytechnic National University, Ukraine
Vitalii Ivanov	Sumy State University, Ukraine
Maryna Ivanova	National Technical University "Kharkiv Polytechnic Institute," Ukraine
Bozena Kaczmarska	Kielce University of Technology, Poland
Lydmila Kalafatova	Donetsk National Technical University, Ukraine
Lucia Knapcikova	Technical University of Kosice, Slovak Republic

Oldrych Kodym	College of Logistics, Czech Republic
Peter Krizan	Slovak University of Technology, Slovak Republic
Jan Krmela	Alexander Dubcek University of Trencin, Slovak Republic
Dmytro Kryvoruchko	Sumy State University, Ukraine
Ivan Kuric	University of Zilina, Slovak Republic
Piotr Kurylo	University of Zielona Gora, Poland
Oleksandr Liaposhchenko	Sumy State University, Ukraine
Slawomir Luscinski	Kielce University of Technology, Poland
Jose Mendes Machado	University of Minho, Portugal
Arun Mathew	Vellore Institute of Technology, India
Mykola Melnychuk	Lutsk National Technical University, Ukraine
Ronald L. Mersky	Widener University, USA
Ievgen Mochalin	Zhejiang Normal University, China
Marek Ochowiak	Poznan University of Technology, Poland
Daniela Onofrejova	Technical University of Kosice, Slovak Republic
Oleh Onysko	Ivano-Frankivsk National Technical University of Oil and Gas, Ukraine
Vitalii Pasichnyk	National Technical University of Ukraine "KPI named after I. Sikorskyi," Ukraine
Justyna Patalas-Maliszewska	University of Zielona-Gora, Poland
Ivan Pavlenko	Sumy State University, Ukraine
Dragan Perakovic	University of Zagreb, Croatia
Marco Perisa	University of Zagreb, Croatia
Oleksandr Permiakov	National Technical University "Kharkiv Polytechnic Institute," Ukraine
Jan Pitel	Technical University of Kosice, Slovak Republic
Grigore Marian Pop	Technical University of Cluj-Napoca, Romania
Oleksandr Povstyanoy	Lutsk National Technical University, Ukraine
Erwin Rauch	Free University of Bolzano, Italy
Michal Rogalewicz	Poznan University of Technology, Poland
Andrii Rogovyi	Kharkiv National Automobile and Highway University, Ukraine
Yiming Rong	Southern University of Science and Technology, China
Saad Nahi Saleh	Tikrit University, Iraq
Michal Sasiadek	University of Zielona Gora, Poland
Vira Shendryk	Sumy State University, Ukraine
Robert Sika	Poznan University of Technology, Poland
Amarjit Singh	National Institute of Technology Hamirpur, India
Lesya Shkitsa	Ivano-Frankivsk National Technical University of Oil and Gas, Ukraine
Vsevolod Sklabinskyi	Sumy State University, Ukraine

Volodymyr Sokolov V.	Dahl East Ukrainian National University, Ukraine
Dusan N. Sormaz	Ohio University, USA
Marcin Sosnowski	Jan Długosz University of Częstochowa, Poland
Michael Storchak	University of Stuttgart, Germany
Vadym Stupnytskyi	Lviv Polytechnic National University
Antoni Swic	Lublin University of Technology, Poland
Yuliia Tarasevych	AGH University of Science and Technology, Poland
Volodymyr Tonkonogyi	Odessa National Polytechnic University, Ukraine
Justyna Trojanowska	Poznan University of Technology, Poland
Michael Tseitlin	National Technical University "Kharkiv Polytechnic Institute," Ukraine
Lela Turmanidze	Batumi Shota Rustaveli State University, Georgia
Leonid Ulyev	National Technical University "Kharkiv Polytechnic Institute," Ukraine
Nicolae Ungureanu	Technical University of Cluj-Napoca, Romania
Leonilde Rocha Varela	University of Minho, Portugal
Yana Vasilchenko	Donbass State Engineering Academy, Ukraine
Joachim Venus	Leibniz Institute for Agricultural Engineering and Bioeconomy, Germany
Josef Voldrich	University of West Bohemia, Czech Republic
George-Christopher Vosniakos	National Technical University of Athens, Greece
Djordje Vukelic	University of Novi Sad, Serbia
Christian Willberg	German Aerospace Center, Germany
Jerzy Winczek	Czestochowa University of Technology, Poland
Oleg Zabolotnyi	Lutsk National Technical University, Ukraine
Jozef Zajac	Technical University of Kosice, Slovak Republic
Viliam Zaloga	Sumy State University, Ukraine
Volodymyr Zavialov	National University of Food Technologies, Ukraine
Jan Zdebor	University of West Bohemia, Czech Republic
Lianyu Zheng	Beihang University, China

Invited External Reviewers (in alphabetical order)

Volodymyr Atamanyuk	Lviv Polytechnic National University, Ukraine
Jan Awrejcewicz	Lodz University of Technology, Poland
Jose Manoel Balthazar	Institute of Aeronautics and Space, Brazil
Paulo Jorge Bartolo	University of Manchester, UK
Kristina Berladir	Sumy State University, Ukraine
Vladimira Binasova	University of Zilina, Slovak Republic
Frantisek Botko	Technical University of Kosice, Slovak Republic

DSMIE Team (in alphabetical order)

Olena Avdieieva	National Technical University "Kharkiv Polytechnic Institute," Ukraine
Yevheniia Basova	National Technical University "Kharkiv Polytechnic Institute," Ukraine
Kristina Berladir	Sumy State University, Ukraine
Maryna Demianenko	Sumy State University, Ukraine
Ludmyla Dobrovolska	National Technical University "Kharkiv Polytechnic Institute," Ukraine
Vitalii Ivanov	Sumy State University, Ukraine
Maryna Ivanova	National Technical University "Kharkiv Polytechnic Institute," Ukraine
Kateryna Kostyk	National Technical University "Kharkiv Polytechnic Institute," Ukraine
Oleksandr Liaposhchenko	Sumy State University, Ukraine
Ivan Pavlenko	Sumy State University, Ukraine
Oleksandr Starynskyi	Sumy State University, Ukraine

Contents

Numerical Simulation of Coupled Problems

Chemical Process Technology

Heat and Mass Transfer

Mechanics of Solids and Structures

Liquid Sloshing in Circular Toroidal and Coaxial Cylindrical Shells

Artem Karaiev[1(✉)] and Elena Strelnikova[1,2]

[1] V.N. Karazin, Kharkiv National University,
4, Svobody Square, Kharkiv 61022, Ukraine
`a.karaiev@karazin.ua`
[2] A. Pidgorny Institute of Mechanical Engineering Problems of the National
Academy of Sciences of Ukraine, 2/10, Pozhars' koho Street,
Kharkiv 61046, Ukraine

Abstract. Free liquid vibrations in circular toroidal and coaxial cylindrical shells are considered. The liquid is supposed to be an ideal and incompressible one, and its flow inside the reservoirs is irrotational. In these assumptions, there exists a velocity potential that satisfies the Laplace equation. The mixed boundary value problem to determine this potential and liquid pressure are formulated for the Laplace equation and further reduced to solving the system of one-dimensional singular integral equations. For its numerical implementation, the boundary element method is used taking into account the ring shape of the free surface. The effective numerical procedures are proposed to accurate calculations of singular integrals containing elliptical integrals in their kernels. Numerical simulations are provided for both circular toroidal and coaxial cylindrical shells for different filling levels and various widths of gaps. The analytical solution is received for coaxial cylindrical shells, including a limit case of the infinitesimal gap. This solution can be considered as a benchmark test and allows us to validate the proposed numerical method.

Keywords: Free liquid vibrations · Circular toroidal and coaxial cylindrical shells · Boundary element method

1 Introduction

Toroidal and coaxial cylindrical shells are widely used in various engineering applications, such as airspace, agricultural machinery, transportation, automobile and piping industries, pressure and fusion reactor vessels, fuel tanks, and neutron accelerators. Problems of liquid sloshing in such containers are of great significance for developing advanced computational techniques to reduce structures weights and sizes, to estimate dynamic influences, as well as vibrations level at the design stage.

The field experiments to testify the equipment are very expensive, and sometimes they lead to the destruction of equipment items. Numerical simulation so can be considered as a useful and reliable tool for virtual experiments. At the design stage, this numerical research makes it possible to find different parameters of reservoirs and tune out the structure under consideration from unwanted resonant frequencies.

2   Literature Review

Thorough reviews of the sloshing phenomenon, including analytical and experimental results, were done in the works of Ibrahim [1] and Zingoni [2]. Since analytic methods are not acceptable for reservoirs with complicated geometrical shapes, and due to the impossibility of carrying out the expensive field experiments, numerical methods are expensively developed for solutions of linear boundary value problems of liquid sloshing.

Dynamic analysis of fluid-filled shell structures is often performed by using finite and boundary element programs [3–5]. Despite numerous practical applications of toroidal and coaxial cylindrical fluid-filled shells, the scientific literature in this area is not so considerable. In [6], the vibrations of empty toroidal shells are under consideration. Future development of methods for estimating free and forced vibrations of partially filled toroidal tanks is achieved in [7–9].

The problems of stability and vibrations of coaxial circular cylindrical reservoirs of finite length are studied in [10–12], assuming the region between the cylindrical shells is partially filled with an ideal and incompressible liquid.

It would be noted that both analytical and numerical methods have experienced difficulties and even failed accuracy when radii of free surfaces become primarily small. For example, there are well known analytical solutions for almost filled tanks with small radii of the free surface, the solutions of so-called "ice fishing problems". Here one has to consider an infinitely comprehensive and deep ocean covered with ice, with a small round hole for fishing. Sloshing in such "containers" was first studied by McIver [13]. Here the approximation of this infinite case was made using the spherical tank with the small round hole on its top. Sloshing in spherical tanks for liquefied natural gas carriers, including small radii of the free surface by analytical approach, was studied by Faltinsen and Timokha in [14] and for water supply towers by Curadelli et al. [15]. Different approximate methods [14, 16] for estimating the natural sloshing frequencies were starting with famous works by Budiansky [17] and McIver [13]. Considering toroidal and coaxial cylindrical shells, one can observe that a similar problem is appearing, when radii of the free surface are sufficiently small. For toroidal shells, it corresponds to almost fully-filled reservoirs, whereas for coaxial cylindrical shells, it assumes that the width of the gap is minimal. A similar problem was considered by Gnitko in [18], where vibrations of the liquid-filled fuel tank with cylindrical and spherical compartments were studied using the boundary element method (BEM).

The present paper is devoted to further development of BEM concerning the liquid sloshing in reservoirs with ring free surfaces of arbitrary widths.

3   Research Methodology

3.1   Problem Statement

In this paper, we consider sloshing problems in fluid-filled rigid shells of revolution. Suppose that the liquid is an ideal and incompressible one, and its flow inside containers is non-vortex. In these assumptions, there exist a velocity potential $\mathbf{v} = \nabla\varphi$. Assume also that the only external load acting on the system is the gravity force

$\mathbf{F} = \rho_l \mathbf{g}$, with $\mathbf{g}$ as the gravity acceleration, and ρ_l for the liquid density. Then Euler's system of equations for the ideal fluid [19] is transformed to

$$\Delta\varphi = 0, \quad \nabla\left(\frac{\partial\varphi}{\partial t} + \frac{1}{2}|\nabla\varphi|^2 + \frac{1}{\rho_l}p - (\mathbf{g},\mathbf{r})\right) = 0. \tag{1}$$

Here $\mathbf{r}$ is for radii-vectors of points inside the fluid domain, p is for liquid pressure. Supposing that liquid displacements are sufficiently small, we obtain the following linearized form of the Bernoulli equation:

$$p = -\rho_l\left(\frac{\partial\varphi}{\partial t} + gz\right) + p_0, \tag{2}$$

where z is the vertical coordinate of the point inside the fluid domain, p_0 is atmospheric pressure.

The governing equation of the fluid motion is Laplace's equation in (1) for potential φ. Receiving the solution of this equation, one can obtain both the fluid velocity $\mathbf{v}$ as the gradient of a function φ, and the pressure p from Bernoulli's Eq. (2). So it is necessary to formulate the boundary value problem for Laplace's equation.

We consider the problems of liquid vibrations in toroidal and coaxial cylindrical shells. The distinguishing feature of such shells of revolution is the ring shape of their free surfaces, as shown in Fig. 1a).
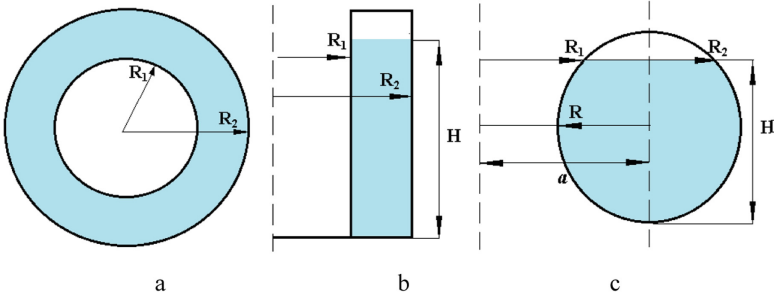
Fig. 1. Free surface sketch (a) and cross-sectional geometry of coaxial cylindrical (b) and circular toroidal shells (c).

Here R_1 and R_2 are inner and outer radii of the free surface, H is the filling level, R is the radius of the toroidal shell, a is the distance between the axis of rotation of circular toroidal shell and center of the revolving circle.

On the wetted surfaces of the shells denoted by S_1, we set the boundary impermeability condition as follows [3]:

$$\left.\frac{\partial\varphi}{\partial\mathbf{n}}\right|_{S_1} = 0, \tag{3}$$

where $\mathbf{n}$ is an outward unit normal to the considered wetted surface. On the free surface, the following dynamic and kinematic boundary conditions are satisfied [3]:

$$\frac{\partial \varphi}{\partial \mathbf{n}}\bigg|_{S_0} = \frac{\partial \zeta}{\partial t}; \quad p - p_0|_{S_0} = 0, \tag{4}$$

where an unknown function ς describes the shape and position of the free surface. Thus, for the velocity potential φ and the function ς the following boundary-value problem is formulated:

$$\Delta \varphi = 0, \frac{\partial \varphi}{\partial \mathbf{n}}\bigg|_{S_1} = 0, \frac{\partial \varphi}{\partial \mathbf{n}}\bigg|_{S_0} = \frac{\partial \zeta}{\partial t}, \quad p - p_0|_{S_0} = 0. \tag{5}$$

The dynamic condition in (5) using relation (2) is transformed into

$$\frac{\partial \varphi}{\partial t} + g\zeta = 0. \tag{6}$$

It is evident that zero eigenvalues exist for problem (5)–(6), but they will be excluded using the following orthogonality condition:

$$\iint\limits_{S_0} \frac{\partial \varphi}{\partial \mathbf{n}} dS_0 = 0. \tag{7}$$

3.2   Mode Decomposition Method

Consider the velocity potential φ as the following series:

$$\varphi = \sum_{k=1}^{M} \dot{d}_k \varphi_k. \tag{8}$$

For functions φ_k introduced above the next boundary value problems are considered:

$$\Delta \varphi_k = 0, \frac{\partial \varphi_k}{\partial \mathbf{n}}\bigg|_{S_1} = 0, \frac{\partial \varphi_k}{\partial \mathbf{n}}\bigg|_{S_0} = \frac{\partial \varsigma}{\partial t}, \quad \frac{\partial \varphi_k}{\partial t} + g\zeta = 0, \iint\limits_{S_0} \frac{\partial \varphi_k}{\partial \mathbf{n}} dS_0 = 0. \tag{9}$$

Let differentiate the fourth equation in the relationship (9) with respect to t and substitute there the expression for ς'_t from the third one of Eqs. (9). Suppose hereinafter that

$$\varphi_k(t, x, y, z) = e^{i\chi_k t}\varphi_k(x, y, z). \tag{10}$$

It leads to the sequence of eigenvalue problems with following conditions on the free surface for each primary function φ_k:

$$\frac{\partial \varphi_k}{\partial \mathbf{n}} = \frac{\chi_k^2}{g}\varphi_k \tag{11}$$

with their own values $\lambda_k = \chi_k^2/g$.

It follows from Eq. (8), and third of relations (9) that unknown function ζ can be received in the form

$$\zeta = \sum_{k=1}^{M} d_k \frac{\partial \varphi_k}{\partial \mathbf{n}}. \tag{12}$$

The effective numerical procedure to solve these eigenvalue problems using the boundary element method was proposed in [3, 5].

3.3 System of Singular Boundary Integral Equations

To define unknown basic functions $\varphi_k (k = 1, 2...M)$, the direct formulation of the boundary element method is in use as it was proposed by C. Brebbia in [20]. Dropping index k the basic integral relation is received in the following manner:

$$2\pi\varphi(P_0) = \iint_S q\frac{1}{|P - P_0|}dS - \iint_S \varphi\frac{\partial}{\partial\mathbf{n}}\frac{1}{|P - P_0|}dS, \tag{13}$$

where $S = S_1 \cup S_0$; points P and P_0 belong to surface S. By $|P - P^0|$ we denote the Cartesian distance between points P and P^0. In (13) the function φ, defined on the surface S_1, is the pressure on the moistened shell surface, and the function q, defined on the free surface S_0, presents the flux.

Using boundary conditions from (9) and (11), one can obtain the system of singular integral equations as in [3, 5]

$$\begin{cases} 2\pi\varphi_1 + \int_{S_1}\varphi_1\frac{\partial}{\partial\mathbf{n}}\left(\frac{1}{r}\right)dS_1 - \frac{\chi_k^2}{g}\int_{S_0}\varphi_0\frac{1}{r}dS_0 + \int_{S_0}\varphi_0\frac{\partial}{\partial z}\left(\frac{1}{r}\right)dS_0 = 0, \\ -\int_{S_1}\varphi_1\frac{\partial}{\partial\mathbf{n}}\left(\frac{1}{r}\right)dS_1 - 2\pi\varphi_0 + \frac{\chi_k^2}{g}\int_{S_0}\varphi_0\frac{1}{r}dS_0 = 0. \end{cases} \tag{14}$$

Here for convenience, the potential values are denoted by φ_0 on the free surface, and by φ_1 on the shell walls.

3.4   Reducing to the System of One-Dimensional Integral Equations

There exist two types of kernels in the integral operators introduced above in (14). Namely, they are

$$A(S, \sigma)\psi = \iint_S \psi \frac{\partial}{\partial \mathbf{n}} \frac{1}{|P - P_0|} dS; \quad B(S, \sigma)\psi = \iint_S \psi \frac{1}{|P - P_0|} dS; \quad P_0 \in \sigma. \quad (15)$$

If in formulae (15) the surfaces S and σ coincided then integrals over S are singular ones, and their numerical treatment has to take into account not only the presence of this singularity but also the strongly non-uniform distribution of integrands over the singular boundary element. Standard quadratures failed in evaluations of these integrals.

Considering the axisymmetric case, we reduce surface integrals to curve integrals using integration by the angle variable [21]. Singular operators, integrated by the angle variable, are expressed in terms of complete elliptic integrals of the first and second kind [21] are the following:

$$\iint_{S_k} \frac{\partial}{\partial \mathbf{n}} \left(\frac{1}{|\mathbf{r}_k - \mathbf{r}|}\right) dS_k = \int_{\Gamma_k} \Theta(\mathbf{r}_k, \mathbf{r})\rho(z)d\Gamma_k, \iint_{S_k} \frac{1}{|\mathbf{r}_k - \mathbf{r}|} dS_k = \int_{\Gamma_k} \Phi(\mathbf{r}_k, \mathbf{r})\rho(z)d\Gamma_k,$$

$$(16)$$

where

$$\Theta(\mathbf{r}_k, \mathbf{r}) = \frac{4}{\sqrt{a+b}} \left\{ \frac{1}{2r} \left[\frac{\rho^2 - \rho_k^2 + (z_k - z)^2}{a - b} E(m) - K(m) \right] n_r + \frac{z_k - z}{a - b} E(m)n_z \right\},$$

$$\Phi(\mathbf{r}_k, \mathbf{r}) = \frac{4}{\sqrt{a+b}} K(m), \mathrm{E}(k) = \int_0^{\pi/2} \sqrt{1 - k^2 \sin^2 \theta} d\theta, K(m) = \int_0^{\pi/2} \frac{d\theta}{\sqrt{1 - m^2 \sin^2 \theta}}$$

$$a = \rho^2 + \rho_k^2 + (z - z_k)^2, \quad b = 2\rho\rho_k, m^2 = \frac{2b}{a+b}.$$

The second kind complete elliptic integral $K(m)$ is received near singular points as follows:

$$K(m) = \frac{2}{\pi} \ln\frac{1}{m'} + \frac{4}{\pi} \int_0^1 \frac{1}{\sqrt{(1 - x^2)(1 - m'^2 x^2)}} \ln\frac{1}{x} dx, m'^2 = 1 - m^2, \quad (17)$$

To treat with obtained logarithmic singularity, the quadrature formulas with nodes as the roots of orthogonal polynomials with the logarithmic weight [20] are in use, and technique described in [5] is applied.

4 Results

4.1 Analytical Benchmark Test

The general solution of the axisymmetric Laplace equation in cylindrical coordinates can be represented as follows

$$\varphi(\rho,z) = (AJ_0(\lambda\rho) + BY_0(\lambda\rho))(C \sinh(\lambda z) + D \cosh(\lambda z)).$$

Unknown constants and eigenvalues can be found from the boundary conditions. To determine the normal derivative, the partial derivatives of the velocity potential are received.

$$\begin{cases} \frac{\partial\varphi}{\partial\rho} = -\lambda(AJ_1(\lambda\rho) + BY_1(\lambda\rho))(C \sinh(\lambda z) + D \cosh(\lambda z)) \\ \frac{\partial\varphi}{\partial z} = -\lambda(AJ_0(\lambda\rho) + BY_0(\lambda\rho))(C \cosh(\lambda z) + D \sinh(\lambda z)) \end{cases}$$

As the normal derivative of the velocity potential should be zero at any point on the lateral surface, we choose three points, namely, the extreme lower, left and right ones. These conditions lead to the following system considering $C = 0$ due to the boundary condition on the bottom:

$$\begin{cases} AJ_1(\lambda a) + BY_1(\lambda a) = 0 \\ AJ_1(\lambda(a+d)) + BY_1(\lambda(a+d)) = 0 \end{cases}$$

For the non-trivial solution of this system its determinant must be equal to zero, i.e.

$$J_1(\lambda(a+d))Y_1(\lambda a) - J_1(\lambda a)Y_1(\lambda(a+d)) = 0$$

Eigenvalues λ are determined precisely from this equation. Then the velocity potential for coaxial cylindrical shells became:

$$\varphi(\rho,z) = (Y_1(\lambda(a+d))J_0(\lambda\rho) - J_1(\lambda a)Y_1(\lambda\rho)) \cosh(\lambda z)$$

Next, we determine the own frequencies ω. To do this, we substitute the found potential into the kinematic boundary condition. Then the following formula is received.

$$\frac{\omega^2}{g} = \lambda \tanh(\lambda H)$$

The resolving equation for the eigenvalues can be written in the following form:

$$J_1(\lambda(a+d))Y_1(\lambda a) - J_1(\lambda a)Y_1(\lambda(a+d)) = 0 \tag{17}$$

where a is the radius of the inner wall of the hollow cylinder, and d is the width of the gap between the inner and outer radius.

4.2 Axisymmetric Liquid Vibrations in Coaxial Cylindrical Shells

The liquid vibrations in coaxial cylindrical shells are considered using the boundary element method. The sketch of this shell structure is given in Fig. 1, b. The shell structure is referred to as the cylindrical coordinate system (x, θ, z). To testify the developed here method the analytical benchmark test is considered. Axisymmetric liquid sloshing in coaxial cylindrical shells with different R_2 and R_1, and $H = 2$ m is considered.

The following Table 1 gives the values of liquid frequencies for different gaps between the cylindrical shells.

Table 1. Liquid frequencies for different coaxial cylindrical shells.

R_1, m	R_2, m	$n = 1$	$n = 2$	$n = 3$	$n = 4$	$n = 5$
1	2	3.2014	6.3241	9.4668	12.6174	15.7742
1	1.5	6.3454	12.647	18.977	25.317	31.6718
1	1.25	16.664	28.76	41.687	54.0281	66.856
1	1.125	33.286	57.493	83.392	107.769	133.31
1	1.0625	66.671	114.08	165.47	213.872	265.15

Differences between analytical and numerical solutions are e-4 for $R_2 \in [1.125, 2]$, and e-3 for $R_2 = 1.0625$. In all variants, we use the equal number of boundary elements on free surfaces. For such a small radius as $R_2 = 1.0625$ it is necessary to increase the number of elements to archive the same accuracy.

Analyzing obtained results, one can conclude that decreasing the gap between the cylindrical shells leads to increasing the sloshing frequencies by analogy with "ice-fishing problem" [13].

Figure 2 demonstrates the three first modes of liquid vibrations in coaxial cylindrical shells with $R_1 = 1$ m, $R_2 = 2$ m, and $H = 2$ m.

The modes are of Bessel-like behavior.

Fig. 2. The axisymmetric mode shapes of liquid vibrations in coaxial cylindrical shells.

The numbers of boundary elements are $N_1 = 100$ $N_2 = 100$ $N_3 = 100$ along vertical walls, bottom, and free surface, respectively. Further increasing of these numbers does not lead to accuracy changing.

4.3   Axisymmetric Liquid Vibrations in Circular Toroidal Shells

The liquid vibrations in toroidal shells are considered using the proposed boundary element method. The sketch of this shell is given in Fig. 1, c. The radius of toroidal shell R is equal to 1 m for all considered cases. The filling level is different; the small values of the ring surface width are considered.

Table 2 below presents the values of liquid frequencies for toroidal shells with different parameters.

Table 2. Liquid frequencies for different circular toroidal shells.

a, m	b, m	$n = 1$	$n = 2$	$n = 3$	$n = 4$	$n = 5$
2	0.5	2.1555	3.9436	5.7753	7.57592	9.4084
2	−0.5	2.2132	4.0300	5.8605	7.66795	9.4965
2	0.5	4.3579	7.8623	11.579	15.1308	18.807
2	−0.9	4.4665	7.9844	11.668	15.2224	18.881
2	0.9	1.9650	3.5381	5.1208	6.6845	8.2670

The results of numerical simulations show that frequencies are mostly dependent on the width of the free surface's ring and are similar for both low and high filling levels.

5   Conclusion

The boundary element method is extended to the problems of sloshing in circular toroidal and coaxial cylindrical shells. The distinguishing feature of such shells of revolution is the ring shape of their free surfaces. The method elaborated allows us to carry out numerical simulation of free liquid vibrations both for different ring widths and various filling levels. The analytical solution is obtained for free fluid vibrations in coaxial cylindrical shells. Special attention is paid for the limit case of the infinitesimal gap. The comparison is made of analytical and numerical results that validated the efficiency of the proposed computational approach.

References

1. Ibrahim, R.A.: Liquid Sloshing Dynamics. Theory and Applications. Cambridge University Press, Cambridge (2005)
2. Zingoni, A.: Liquid-containment shells of revolution. A review of recent studies on strength, stability and dynamic. Thin-Walled Struct. **87**, 102–114 (2015)
3. Gnitko, V., Degtyariov, K., Naumenko, V., Strelnikova, E.: BEM and FEM analysis of the fluid-structure Interaction in tanks with baffles. Int. J. Comput. Methods Exp. Meas. **5**(3), 317–328 (2017)
4. Spyros, A.K., Papaprokopiou, D., Platyrracho, M.A.: Finite element analysis of sloshing in horizontal-cylindrical industrial vessels under earthquake. J. Press. Vessel Technol. Trans. ASME **131**, 05130101–05130111 (2009)
5. Gnitko, V., Marchenko, U., Naumenko, V., Strelnikova, E.: Forced vibrations of tanks partially filled with the liquid under seismic load. In: Proceedings of XXXIII Conference Boundary elements and other mesh reduction methods, WITPress, Transaction on Modeling and Simulation, vol. 52, pp. 285−296 (2011)
6. Wang, X.H., Redekop, D.: Natural frequencies analysis of moderately-thick and thick toroidal shells. Procedia Eng. **14**, 636–640 (2011)
7. Enoma, N., Egware, H.O., Itoje, H.J., Unueroh, U.G.: Membrane solutions for circular toroidal shells under internal hydrostatic pressure. J. Multidiscip. Eng. Sci. Technol. **2**(10), 2895–2901 (2015)
8. Zua, L., Koussiosb, S., Beukersb, A.: A novel design solution for improving the performance of composite toroidal hydrogen storage tanks. Int. J. Hydrog. Energy **37**, 14343–14350 (2012)
9. Zingoni, A., Mokhothu, B., Enoma, N.: A theoretical formulation for the stress analysis of multi-segmented spherical shells for high-volume liquid containment. Eng. Struct. **87**, 21–31 (2015)
10. Jeong, K.-H.: Natural frequencies and mode shapes of two coaxial cylindrical shells coupled with bounded fluid. J. Sound Vib. **215**(1), 105–124 (1998)
11. Bochkarev, S.A., Lekomtsev, S.V., Matveenko, V.P.: Numerical modeling of spatial vibrations of cylindrical shells partially filled by liquid. Comput. Technol. **18**(2), 12–24 (2013)
12. Mikilyan, M., Marzocca, P.: Vibration and stability of coaxial cylindrical shells with a gap partially filled with liquid. J. Aerosp. Eng. **32**(6), 12–26 (2019)
13. McIver, P.: Sloshing frequencies for cylindrical and spherical containers filled to an arbitrary depth. J. Fluid Mech. **201**, 243–250 (1989)
14. Faltinsen, O.M., Timokha, A.N.: Sloshing. Cambridge University Press, Cambridge (2009)
15. Curadelli, O., Ambrosini, D., Mirasso, A., Amani, M.: Resonant frequencies in an elevated spherical container partially filled with water: FEM and measurement. J. Fluids Struct. **26**(1), 148–159 (2010)
16. Kulczycki, T., Kwaśnicki, M., Siudeja, B.: The shape of the fundamental sloshing mode in axisymmetric containers. J. Eng. Math. **99**(1), 157–193 (2016)
17. Budiansky, B.: Sloshing of liquid in circular canals and spherical tanks. J. Aerosp. Sci. **27**(3), 161–172 (1960)
18. Gnitko, V.V., Degtyariov, K.G., Naumenko, V.V., Strelnikova, E.A.: Coupled BEM and FEM analysis of fluid-structure interaction in dual compartment tanks. Int. J. Comput. Methods Exp. Meas. **6**(6), 976–988 (2018)
19. Landau, L.D., Lifshits, E.M.: Fluid Dynamics. Pergamon Press, Oxford (1987)

20. Brebbia, C.A., Telles, J.C.F., Wrobel, L.C.: Boundary Element Techniques. Springer, Heidelberg and New York (1984). https://doi.org/10.1007/978-3-642-48860-3
21. Gnitko, V.I., Degtyariov, K.G., Karaiev, A.O., Strelnikova, E.A.: Singular boundary method in a free vibration analysis of compound liquid-filled shells. WIT Trans. Eng. Sci. **126**, 189–200 (2019)

Experimental Identification of a Car Dynamic Model Using the Numerical Algorithms for Subspace State-Space System Identification

Antonio Lettieri[1] and Carmine Maria Pappalardo[2(✉)]

[1] MEID4 Academic Spin-Off of the University of Salerno, Fisciano, Italy
[2] University of Salerno, 132, via Giovanni Paolo II,
84084 Fisciano, Salerno, Italy
`cpappalardo@unisa.it`

Abstract. In this paper, a system identification numerical procedure is used to perform an experimental work based on the System Identification Toolbox available in MATLAB. This work aims to show the possibility of identifying a mathematical model of a car using low-cost sensors. The instrumentation used to reach this goal is composed of an Arduino Mega2560, a GPS receiver module, and an inertial measurement unit. The Arduino is used to handle the sensors and to save the measured data. The inertial platform is used to get the linear acceleration and angular rates of the system, while the GPS is used to get the trajectory of the car. By employing the N4SID algorithm, a discrete state-space model of the system can be identified and used to predict the behavior of the car system. It is also possible to obtain a continuous model from the discrete one and to identify the natural frequencies and the system damping factors. The results show the possibility to easily identify a mathematical model of a complex system using a limited set of experimental data.

Keywords: Applied system identification · Car dynamics · State-space representation · Numerical Algorithms for Subspace State-Space System Identification (N4SID)

1 Introduction

The goal of this paper is to show the possibility of using a system identification numerical procedure to develop a black-box mathematical model of a car. In this section, the background information about the problem at hand and the organization of the manuscript are given. Firstly, the system identification theory allows for developing a mathematical model of a real dynamic system using available experimental data. The experimental data can be used to develop the relationships which describe the behavior of the system using an iterative procedure to obtain the most accurate model. For a black-box model, the experiment design is of primary importance because the results of this phase are the basis of the model. An inaccurate data set will result in a poor model unable to properly describe the system dynamical behavior. This obvious aspect is indeed the main challenge encountered in addressing system identification problems.

The sensors used in this investigation to estimate the model of the car are an inertial platform, which is composed of a three-axis accelerometer and three angular rate sensors, and a GPS receiver. The sensors are connected to the ArduinoMega2056 controller, which is connected through a serial port to a personal computer. Using Arduino and a program developed in MATLAB by the authors, the data can be acquired and processed to perform the system identification. By doing so, the numerical results found showed good repeatability.

The remaining part of this manuscript is structured as follows. Section 2 reports a brief literature review on the topic presented in the paper. In Sect. 3, the methodology and the procedure used to identify the car model are explained in detail. Section 4 shows the results of the model obtained. Section 5 presents a summary of the work and the conclusions reached.

2 Literature Review

Analyzing the behavior of a mechanical system excited by externally applied forces can be a critical issue. Particular attention must be paid to the uncertainties in the modeling process [1–3], and different techniques can be used according to the different fields of mechanics and physics, such as studies on friction and noise [4, 5], terra-mechanics [6–9], energy [10, 11] and biomedical engineering [12]. Complex systems can be modeled using the multibody approach, which is well described in the literature [13, 14]. By using the multibody technique, a wide range of mechanical systems can be analytically described, and different kinds of studies can be done in this direction [15–28]. When experimental data are available, on the other hand, it is possible to use the system identification theory. Interesting references are the works of Ljung [29] and Juang [30]. The system identification theory is based on the use of experimental data to identify a mathematical model, and this paper focuses in particular on the subspace system identification approach [31, 32]. An interesting overview of the different identification methods is presented by Chu et al. [33]. A focus on the state-of-the-art about the subspace methods is provided by Favoreel et al. in [34]. In particular, the algorithm used in this paper is the N4SID (Numerical Algorithms for Subspace State-Space System Identification) originally developed by Van Overschee and De Moor [35]. The state-space representation is a powerful tool that can be used to analyze different problems. Many applications can be found in the field of civil engineering. For instance, in [36], Astroza et al. studied the variation of the modal properties of a building. In [37], Garcia-Illescas et al. monitored the vibration frequencies of a metro line in Mexico City. In [38], Nord et al. identified the modal parameters of a lighthouse during ice-structure interaction. In [39], Colucci and De Simone used a subspace model to tune a Tuned Liquid Damper (TLD). Another important field of application is control engineering where the subspace models are used to define control strategies [40–44]. Other applications can be found in the study of gas turbines, machine tools, space manipulators, and multibody mechanical systems in general [45–50].

3   Research Methodology

In this section, the basic aspects related to the system identification and the state-space theory are presented. The system identification theory allows developing a dynamic model starting from experimental data. The method used in this work is based on the N4SID (Numerical Algorithms for Subspace State-Space System Identification), which allows obtaining a state-space model by starting directly from the experimental measurements.

The system identification procedure can be divided into three principal phases. In the first phase, the design of experiments must be defined to choose what to measure and how to do it. It is important to recognize the most important quantities, to collect and to measure them as well as possible. The quality of the collected data is the basis on which an accurate model is defined. In the second phase, the structure of the model and the model itself can be found using the experimental data set. In this stage, the quality of the model can be evaluated by trying to reproduce the known outputs of the system. The last phase is the validation of the model. The purpose of this last phase is to understand if the model is good enough for its applications. If the model is reliable, it can be used to predict the behavior of the system of interest, otherwise, a new identification procedure becomes necessary. In some cases, the experimental data can be not appropriate to describe the system and, therefore, another set of experiments is requested.

Using the System Identification Toolbox available in MATLAB, it is possible to properly organize the experimental data to realize an input-output system identification and finally obtain a discrete state-space model of the mechanical system of interest. The equations of motion relative to a linear dynamical system are given by:

$$\mathbf{M}\ddot{\mathbf{q}}(t) + \mathbf{R}\dot{\mathbf{q}}(t) + \mathbf{K}\mathbf{q}(t) = \mathbf{F}(t) \tag{1}$$

where the vector of generalized displacements, velocities, and accelerations are respectively denoted with the vectors $\mathbf{q}(t)$, $\dot{\mathbf{q}}(t)$, and $\ddot{\mathbf{q}}(t)$ of dimension n_q, while $\mathbf{M}$, $\mathbf{R}$, and $\mathbf{K}$ are respectively the mass, damping, and stiffness matrices of dimension $n_q \times n_q$, whereas the external forcing function is indicated with $\mathbf{F}(t)$. On the other hand, defining the output vector $\mathbf{y}(t)$ of dimension n_y, the output equations can be written using the following matrix form:

$$\mathbf{y}(t) = \mathbf{C}_a\ddot{\mathbf{q}}(t) + \mathbf{C}_v\dot{\mathbf{q}}(t) + \mathbf{C}_d\mathbf{q}(t) \tag{2}$$

where $\mathbf{C}_a$, $\mathbf{C}_v$, and $\mathbf{C}_d$ are the output influence matrices for the generalized accelerations, velocities, and displacements, respectively. Defining the state vector of the system $\mathbf{z}(t)$ of dimension $n_z = 2n_q$ as:

$$\mathbf{z}(t) = \begin{bmatrix} \mathbf{q}(t) \\ \dot{\mathbf{q}}(t) \end{bmatrix} \tag{3}$$

and defining $\mathbf{u}(t)$ as the input vector of dimension n_u, the state-space equations of motion and the set of the output equations can be written as:

$$\begin{cases} \dot{\mathbf{z}}(t) = \mathbf{A}_c\mathbf{z}(t) + \mathbf{B}_c\mathbf{u}(t) \\ \mathbf{y}(t) = \mathbf{C}\mathbf{z}(t) + \mathbf{D}\mathbf{u}(t) \end{cases} \tag{4}$$

where $\mathbf{A}_c$ is the continuous-time state matrix of dimension $n_z \times n_z$, $\mathbf{B}_c$ is the continuous-time input influence matrix having a dimension $n_z \times n_u$, $\mathbf{C}$ is the output influence matrix of dimension $n_y \times n_z$, and $\mathbf{D}$ is the direct transmission matrix having a dimension $n_y \times n_u$. These matrices can be readily assembled as follows:

$$\mathbf{A}_c = \begin{bmatrix} \mathbf{O} & \mathbf{I} \\ -\mathbf{M}^{-1}\mathbf{K} & -\mathbf{M}^{-1}\mathbf{R} \end{bmatrix}, \mathbf{B}_c = \begin{bmatrix} \mathbf{0} \\ -\mathbf{M}^{-1}\mathbf{B}_f \end{bmatrix} \tag{5}$$

$$\mathbf{C} = \begin{bmatrix} \mathbf{C}_d & -\mathbf{C}_a\mathbf{M}^{-1}\mathbf{K}\mathbf{C}_v & -\mathbf{C}_a\mathbf{M}^{-1}\mathbf{R} \end{bmatrix}, \mathbf{D} = \mathbf{C}_a\mathbf{M}^{-1}\mathbf{B}_f \tag{6}$$

where $\mathbf{O}$ is the zero matrix, $\mathbf{0}$ is the zero vector, $\mathbf{I}$ is the identity matrix, and $\mathbf{B}_f$ is an influence matrix which defines the location and the type of inputs in accordance with the following equation:

$$\mathbf{F}(t) = \mathbf{B}_f\mathbf{u}(t) \tag{7}$$

The previous state-space representation is valid in the continuous-time domain, but the experimental data are discrete values. Thus, by using the identification procedure, one can obtain a discrete-time state-space model of the system. In general, a discrete state-space model has the following structure:

$$\begin{cases} \mathbf{z}(k+1) = \mathbf{A}_d\mathbf{z}(k) + \mathbf{B}_d\mathbf{u}(k) \\ \mathbf{y}(k) = \mathbf{C}\mathbf{z}(k) + \mathbf{D}\mathbf{u}(k) \end{cases} \tag{8}$$

where k represents the discrete-time, $\mathbf{z}(k)$ is the discrete-time state vector, $\mathbf{u}(k)$ is the discrete-time input vector, $\mathbf{y}(k)$ is the discrete-time output vector, $\mathbf{A}_d$ is the discrete-time state matrix, and $\mathbf{B}_d$ is the discrete-time input influence matrix. The identification method based on the N4SID algorithm reformulates the system state-space model in the following form:

$$\begin{cases} \mathbf{Y}_p = \mathbf{\Gamma}_i\mathbf{Z}_p + \mathbf{H}_i\mathbf{U}_p \\ \mathbf{Y}_f = \mathbf{\Gamma}_i\mathbf{Z}_f + \mathbf{H}_i\mathbf{U}_f \\ \mathbf{Z}_f = \mathbf{A}^i\mathbf{Z}_p + \mathbf{\Delta}_i\mathbf{U}_p \end{cases} \tag{9}$$

where $\mathbf{Y}_p$ and $\mathbf{Y}_f$ are, respectively, the Hankel matrices of past and future outputs, $\mathbf{U}_p$ and $\mathbf{U}_f$ are, respectively, the Hankel matrices of past and future inputs, $\mathbf{Z}_p$ and $\mathbf{Z}_f$ are, respectively, the past and future state vectors, $\mathbf{H}_i$ is the Toeplitz matrix, $\mathbf{\Gamma}_i$ is the observability matrix, and $\mathbf{\Delta}_i$ is the controllability matrix. By properly manipulating the equations, it is possible to identify the state-space model of the system, as it is demonstrated in this work using numerical experiments.

4   Results

In this section, the numerical results of the system identification process based on experimental measurements are shown. The method used for the identification is based on the N4SID algorithm, which gives the matrices that represent the discrete-time state-space model as outputs. The inputs of the system under study are the longitudinal acceleration, the lateral acceleration, and the yaw rate of the car employed as an experimental test rig. On the other hand, the outputs of the system are the data of the GPS receiver. Thus, the experimental measurements shown in Fig. 1 are processed by the N4SID numerical procedure to obtain the following set of discrete-time matrices $\mathbf{A}_d$, $\mathbf{B}_d$, $\mathbf{C}$, and $\mathbf{D}$:

$$\mathbf{A}_d = \begin{bmatrix} 0.9918 & -0.0024 & -0.0057 & 0.0001 \\ 0.0226 & 0.9872 & -0.0156 & -0.0696 \\ 0.0261 & 0.0057 & 1.0030 & -0.0071 \\ 0.0517 & 0.0487 & -0.208 & 0.9301 \end{bmatrix} \tag{10}$$

$$\mathbf{B}_d = \begin{bmatrix} 0 & 0 & 0 \\ -0.0006 & 0.0041 & -0.0019 \\ 0.0059 & -0.0021 & -0.0018 \\ 0.0106 & 0.0086 & -0.0043 \end{bmatrix} \tag{11}$$

$$\mathbf{C} = \begin{bmatrix} 649.4 & 3.1 & -1.9 & -0.1 \\ 1099 & -11.3 & -3.0 & 0.6 \end{bmatrix} \tag{12}$$

while $\mathbf{D}$ is a null matrix. The dynamical system is identified using the experimental data obtained during a test where the car is following a straight path at a constant velocity. After the system identification, the model is tested using the data obtained from another test performed following the same path but at a different velocity to validate the identified model. The inputs used to identify the model are shown in Figs. 1-a), b), and c). These are the car's longitudinal acceleration denoted with $\ddot{y}$, the car's lateral acceleration denoted with $\ddot{x}$, and the car's yaw rate denoted with $\dot{\psi}$. The comparison between the numerical results obtained from the system identification procedure is represented in Fig. 1-d). Furthermore, the identified model is also employed to predict the behavior of the system using the inputs of a different test shown in Fig. 2. In this case, the numerical results are reported in Fig. 2-d), while the inputs are reported in Figs. 2-a), b), and c).

a) Lateral acceleration

b) Longitudinal acceleration

c) Yaw rate
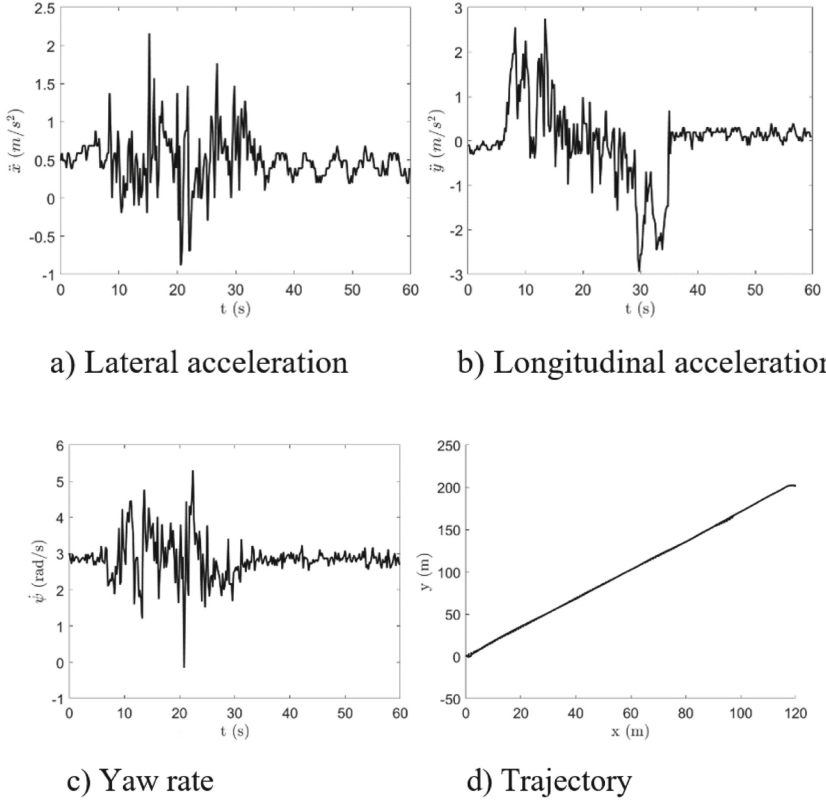
d) Trajectory

Fig. 1. Identification of the dynamical model. In figure a)-c), the inputs of the model are respectively reported: lateral acceleration, longitudinal acceleration, and yaw rate. In figure d), the solid line represents the experimental trajectory, while the dashed line indicates the model results.

From the identified discrete model, it is possible to obtain the continuous one and then evaluate the undamped angular frequencies of the system denoted with $\omega_{n,i}$ and the damping ratios of each mode denoted with ξ_i. By doing so, the following numerical parameters are found:

$$\begin{cases} \omega_{n,1} = 0.3459 \,(rad/s) \\ \omega_{n,2} = 0.0447 \,(rad/s) \end{cases}, \begin{cases} \xi_1 = 0.6142(-) \\ \xi_2 = 0.0967(-) \end{cases} \tag{13}$$

The numerical results found are acceptable and are useful for predicting the dynamical behavior of the identified car model.

a) Lateral acceleration   b) Longitudinal acceleration

c) Yaw rate   d) Trajectory
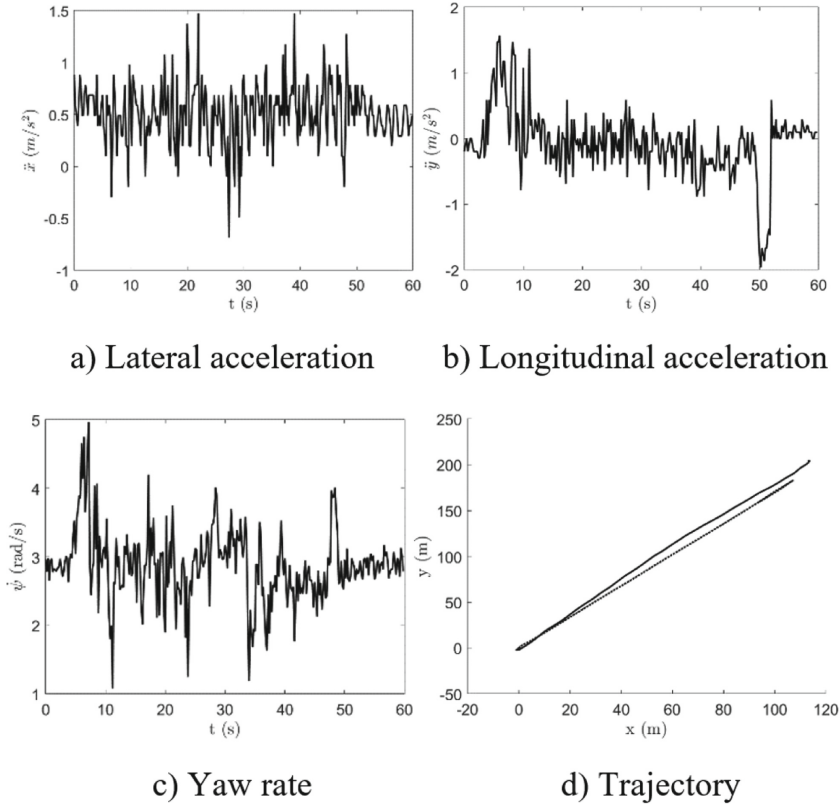
Fig. 2. Validation of the dynamical model. In figure a)-c), the inputs of the model are respectively reported: lateral acceleration, longitudinal acceleration, and yaw rate. In figure d), the solid line represents the experimental trajectory, while the dashed line indicates the model output.

5 Conclusions

This work is aimed at identifying a state-space model of a car using a simple set of sensors. Despite the complexity of the system and the simplicity of the sensors used, the identification procedure showed some interesting results. For a smooth trajectory, the model can predict the behavior of the system with reasonable precision. Even if there are some practical issues related to the acquisition system that could be resolved in future studies, the system identification procedure once more showed the possibility of describing a complex system in a relatively simple way, bypassing the physical description of the system. In future works, to improve the quality of the identified model, the signals could be filtered to enhance the quality of the dataset fed to the numerical procedure based on the N4SID algorithm. Another improvement could be the use of a more stable GPS device, as well as increasing the number of accelerometers and gyroscopes, to have a more accurate description of the car system. Future research works will be devoted to the analysis of more complex vehicle systems.

References

1. Villecco, F.: On the evaluation of errors in the virtual design of mechanical systems. Machines **6**(3), 36 (2018)
2. Zhang, Y., Li, Z., Gao, J., Hong, J., Villecco, F., Li, Y.: A method for designing assembly tolerance networks of mechanical assemblies. Math. Probl. Eng. **2012**, 26 (2012)
3. Villecco, F., Pellegrino, A.: Evaluation of uncertainties in the design process of complex mechanical systems. Entropy **19**(9), 475 (2017)
4. De Simone, M.C., Guida, D.: Modal coupling in presence of dry friction. Machines **6**(1), 8 (2018)
5. De Simone, M.C., Rivera, Z.B., Guida, D.: Finite element analysis on squeal-noise in railway applications. FME Trans. **46**(1), 93–100 (2018)
6. Formato, A., Ianniello, D., Romano, R., Pellegrino, A., Villecco, F.: Design and development of a new press for grape marc. Machines **7**(3), 51 (2019)
7. Formato, G., Romano, R., Formato, A., Sorvari, J., Koiranen, T., Pellegrino, A., Villecco, F.: Fluid-structure interaction modeling applied to peristaltic pump flow simulations. Machines **7**(3), 50 (2019)
8. Formato, A., Ianniello, D., Pellegrino, A., Villecco, F.: Vibration-based experimental identification of the elastic moduli using plate specimens of the olive tree. Machines **7**(2), 46 (2019)
9. Naviglio, D., Formato, A., Scaglione, G., Montesano, D., Pellegrino, A., Villecco, F., Gallo, M.: Study of the grape cryo-maceration process at different temperatures. Foods **7**(7), 107 (2018)
10. Ghomshei, M., Villecco, F.: Energy metrics and Sustainability. In: International Conference on Computational Science and Its Applications, vol. 5592, pp. 693–698. Springer, Berlin, Heidelberg (2009)
11. Cattani, C., Mercorelli, P., Villecco, F., Harbusch, K.: A theoretical multiscale analysis of electrical field for fuel cells stack structures. In: International Conference on Computational Science and Its Applications, vol. 3980, pp. 857–864. Springer, Berlin, Heidelberg (2006)
12. Sena, P., Attianese, P., Carbone, F., Pellegrino, A., Pinto, A., Villecco, F.: A fuzzy model to interpret data of drive performances from patients with sleep deprivation. Comput. Math. Methods Med. **2012**, 868410 (2012)
13. Shabana, A.A.: Dynamics of Multibody Systems, 4th edn. Cambridge University Press, Cambridge (2013)
14. Nikravesh, P.E.: Computer-Aided Analysis Of Mechanical Systems. Prentice-Hall Inc, Upper Saddle River (1988)
15. Concilio, A., De Simone, M.C., Rivera, Z.B., Guida, D.: A new semi-active suspension system for racing vehicles. FME Trans. **45**(4), 578–584 (2017)
16. Rivera, Z.B., De Simone, M.C., Guida, D.: Unmanned ground vehicle modelling in Gazebo/ROS-based environments. Machines **7**(2), 42 (2019)
17. Guida, R., De Simone, M.C., Dašić, P., Guida, D.: Modeling techniques for kinematic analysis of a six-axis robotic arm. IOP Conf. Ser.: Mater. Sci. Eng. **568**(1), 12115 (2019)
18. Pappalardo, C.M., Patel, M.D., Tinsley, B., Shabana, A.A.: Contact force control in multibody pantograph/catenary systems. Proc. Inst. Mech. Eng. Part K: J. Multi-Body Dyn. **230**(4), 307–328 (2016)
19. Pappalardo, C.M., Patel, M., Tinsley, B., Shabana, A.A.: Pantograph/catenary contact force control. In: ASME 2015 International Design Engineering Technical Conferences and Computers and Information in Engineering Conference. American Society of Mechanical Engineers Digital Collection (2015)

20. Kulkarni, S., Pappalardo, C.M., Shabana, A.A.: Pantograph/catenary contact formulations. J. Vib. Acoust. **139**(1), 011010 (2017)
21. Patel, M.D., Pappalardo, C.M., Wang, G., Shabana, A.A.: Integration of geometry and small and large deformation analysis for vehicle modelling: chassis, and airless and pneumatic tyre flexibility. Int. J. Veh. Perform. **5**(1), 90–127 (2019)
22. Pappalardo, C.M.: A natural absolute coordinate formulation for the kinematic and dynamic analysis of rigid multibody systems. Nonlinear Dyn. **81**(4), 1841–1869 (2015)
23. Cossalter, V., Lot, R., Massaro, M.: An advanced multibody code for handling and stability analysis of motorcycles. Meccanica **46**(5), 943–958 (2011)
24. Pappalardo, C.M., Zhang, Z., Shabana, A.A.: Use of independent volume parameters in the development of new large displacement ANCF triangular plate/shell elements. Nonlinear Dyn. **91**(4), 2171–2202 (2018)
25. Pappalardo, C.M., Wang, T., Shabana, A.A.: Development of ANCF tetrahedral finite elements for the nonlinear dynamics of flexible structures. Nonlinear Dyn. **89**(4), 2905–2932 (2017)
26. Pappalardo, C.M., Wang, T., Shabana, A.A.: On the formulation of the planar ANCF triangular finite elements. Nonlinear Dyn. **89**(2), 1019–1045 (2017)
27. Pappalardo, C.M., Wallin, M., Shabana, A.A.: A new ANCF/CRBF fully parameterized plate finite element. J. Comput. Nonlinear Dyn. **12**(3), 031008 (2017)
28. Pappalardo, C.M., Yu, Z., Zhang, X., Shabana, A.A.: Rational ANCF thin plate finite element. J. Comput. Nonlinear Dyn. **11**(5), 051009 (2016)
29. Ljung, L.: System Identification Theory for the user, 2nd edn. PTR Prentice Hall, Upper Saddle River (1999)
30. Juang, J., Phan, M.: Identification and Control of Mechanical Systems. Cambridge University Press, Cambridge (2001)
31. Van Overschee, P., De Moor, B.: Subspace Identification for Linear Systems: Theory—Implementation—Applications. Springer, Berlin (2012)
32. Katayama, T.: Subspace Methods for System Identification – A Realization Approach. Springer, Berlin (2006)
33. Chu, J., Yuan, L., Hu, Y., Pan, C., Pan, L.: Comparative analysis of identification methods for mechanical dynamics of large-scale wind turbine. Energies **12**(18), 3429 (2019)
34. Favoreel, W., De Moor, B., Van Overschee, P.: Subspace state space system identification for industrial processes. J. Process Control **10**(2–3), 149–155 (2000)
35. Van Overschee, P., De Moor, B.: N4SID: subspace algorithms for the stochastic systems. Automatica **30**(1), 75–93 (1994)
36. Astroza, R., Hernandez, F., Dìaz, P., Gutierrez, G.: System identification of a five-story building using seismic strong-motion data. In: Dynamics of Civil Structures, vol. 2, pp. 181–189. Springer (2020)
37. García-Illescas, M.Á., Murià-Vila, D., Alvarez-Icaza, L.: Monitoring and identification of vibration frequencies on a portion of México City Metro Line 12. Adv. Civil Eng. **2019**, 4128320 (2019)
38. Nord, T.S., Petersen, Ø.W., Hendrikse, H.: Stochastic subspace identification of modal parameters during ice–structure interaction. Philos. Trans. R. Soc. A **377**(2155), 20190030 (2019)
39. Colucci, F., De Simone, M.C., Guida, D.: TLD design and development for vibration mitigation in structures. In: Karabegović, I. (ed.) New Technologies, Development and Application II. NT 2019. LNNS, vol 76, pp. 59–72. Springer, Cham (2019)
40. De Simone, M.C., Guida, D.: Identification and control of an unmanned ground vehicle by using Arduino. UPB Sci. Bull. Ser. D. **80**, 141–154 (2018)

41. Sharifzadeh, M., Pisaturo, M., Senatore, A.: Real-time identification of dry-clutch frictional torque in automated transmissions at launch condition. Proc. Inst. Mech. Eng. Part D: J. Automob. Eng. (2019). https://doi.org/10.1177/0954407019857268
42. De Simone, M.C., Guida, D.: Control design for an under-actuated UAV model. FME Trans. **46**(4), 443–452 (2018)
43. De Simone, M.C., Rivera, Z., Guida, D.: Obstacle avoidance system for unmanned ground vehicles by using ultrasonic sensors. Machines **6**(2), 18 (2018)
44. Quatrano, A., De, S., Rivera, Z.B., Guida, D.: Development and implementation of a control system for a retrofitted CNC machine by using Arduino. FME Trans. **45**(4), 565–571 (2017)
45. Jiang, Y., Xue, N., Lu, S., Song, X.: Vibration suppression of a cantilevered piezoelectric laminated composite plate subjected to hygrothermal loads. IOP Conf. Ser.: Mater. Sci. Eng. **531**(1), 012035 (2019)
46. Hu, Y.C., Chen, P.J., Chang, P.Z.: Thermal-feature system identification for a machine tool spindle. Sensors **19**(5), 1209 (2019)
47. Costa, A.G., Maldonado, J.L.B., Romero, F.A., Sanmartín, J.C., Valarezo, M., Castillo, H.: N4SID method applied to obtain a discrete-time linear state space system as a mathematical model of a jaw crusher prototype. In: 2017 CHILEAN Conference on Electrical, Electronics Engineering, Information and Communication Technologies (CHILECON), pp. 1–6 (2017)
48. Ni, Z., Liu, J., Wu, Z., Shen, X.: Identification of the state-space model and payload mass parameter of a flexible space manipulator using a recursive subspace tracking method. Chin. J. Aeronaut. **32**(2), 513–530 (2019)
49. Liu, X., Yang, X., Zhu, P., Xiong, W.: Robust identification of nonlinear time-delay system in state-space form. J. Franklin Inst. **356**(16), 9953–9971 (2019)
50. Holcomb, C., De Callafon, R.: Subspace identification for disturbance rejection control design in gas turbines. In: 2015 European Control Conference ECC, pp. 842–847. IEEE, Linz (2015)

Cavitational Wearing of Modified Ceramics

Aleksandr Litvinenko[1] , Yuriy Boyko[1] , Bohdan Pashchenko[1] ,
Yuriy Sukhenko[2] , and Evhenii Shtefan[3(✉)]

[1] National University of Food Technologies,
68, Volodymyrska Street, Kiev 01033, Ukraine
hoykke@gmail.com
[2] National University of Life and Environmental Sciences of Ukraine,
15, Heroiv Oborony Street, Kiev 03041, Ukraine
[3] National Technical University of Ukraine "Igor Sikorsky
Kyiv Polytechnic Institute", 37, Peremohy Avenue, Kiev 03056, Ukraine
shtefanevgenii@gmail.com

Abstract. The results of studies of cavitation resistance of modified ceramics
are presented. ZrO_2 was inserted into the matrix based on Al_2O_3 in the amount
of 2% by weight. The experiments were carried out under the action of ultra-
sound, which was generated by oscillations of a magnetostrictive vibrator. The
frequency of cavitation effect 22 and 44 kHz was used. The intensity of wear of
the specimens was evaluated by the losses of their mass. It was shown that the
insertion of ZrO_2 into the Al_2O_3 ceramic matrix increases the resistance of
ceramics. The nature of dependencies shows a similar pattern of wear of the
specimens. The increase in the content of Al_2O_3 in the structure of the material
and the addition of the small dispersed ZrO_2 increases the viscosity of ceramics.
The shock waves after the collapse of cavitation bubbles are quenched in
ceramics and increased its durability. The process of wearing of ceramics is
cyclical. It is accompanied by the separation of the micro-particles. The
destruction of the material occurs along the grain boundaries of Al_2O_3, internal
defects, and glass-visible phase. The wear rates are similar for the tested spec-
imens. The cyclical nature of ceramic wear is identical to metal wearing. This
allows the use of known approaches for the analysis of results. The study of the
rate of mass losses of ceramic specimens demonstrated the similarity with the
hydro abrasive wearing of metals.

Keywords: Modified ceramics · Vibration · Cavitation wearing

1 Introduction

Technological equipment in various industries implements the processing of products
mainly in a liquid-phase state. At the same time, special conditions of flow appear in
the equipment units (fittings, pump seals, diffusers, confuser, Venturi nozzles). These
conditions include cavitation. It causes intensive wearing of equipment. Its reliability
and durability are reduced under such circumstances. Thus, a rational choice of
appropriate materials is relevant. One of these materials is ceramics.

Studies of its cavitation-erosion resistance and patterns of wearing are of great practical importance. Physics, mechanical, chemical and operational properties of technical ceramics based on aluminum oxide are determined by [1]:

– the content of Al_2O_3 and the ratio of phase components, impurities and binders;
– the rate of the defining crystalline phases;
– the size, shape, and nature of the distribution of phase components;
– the structure and porosity of the specimen;
– pore size and its density, their shape and placement;
– the nature, properties, and temperature of the environment.

The plastic deformation is entirely absent in brittle materials. The fragile nature of its destruction is the most typical. Ceramics relate to such materials. Hooke's law is fair for most ceramic materials. They are evaluated by the value of the bending strength, modulus of elasticity, shear, and separate other indicators, which are characteristic for the research of metallic materials. The behavior of ceramic materials during cavitation wearing is similar to metal structural materials. Known dependencies can be used for them [2].

2   Literature Review

The data of cavitation wearing of these materials are limited in the scientific and technical literature.

The literature has some information about their properties under certain operating conditions [3, 4]. In ceramic materials, elastic deformations are founded to arise as a result of the shock wave action of cavitation bubbles. They cause the appearance of surface cracks on the surface and their gradual destruction [5–7]. Experimental research of cavitation wear of specimens of ceramic materials due to their destruction by ultrasonic cavitation is conducted. They show that ceramic materials are not inferior to traditional structural materials in terms of wear resistance [7, 8].

The manufacturing of structural elements from practically pure Al_2O_3 is known from [9]. Ceramics are used for valves of homogenizers [10] and pipes for transporting corrosive-active media with a solids content of up to 20% [11] and loaded small parts [5] (Fig. 1).

Fig. 1. Specimens of ceramic products.

Ceramics is comparable by durability with corrosion-resistant steels. However, the operational properties of ceramics can be improved. This is achieved by introducing modifying components into their composition, for example, ZrO_2.

The addition of chemically inert ZrO_2 in ceramics inhibits the growth of corundum crystals. For example, the addition of 0.5–1.0% ZrO_2 contributes to the formation of crystals no more than 15 μm [12]. Submicron ZrO_2 and Al_2O_3 interlayers appear at the corundum grain boundaries. The crystals have a smaller size and are better isometrically at the same time.

The insertion of modifying additives to the composition of ceramics changes not only its operational characteristics. This fact may change its cavitation resistance.

Wearing different types of based on Al_2O_3 ceramics under cavitation conditions was studied in [13].

It has been revealed that elastic deformations occur in ceramic materials due to the mechanical action of cavitation. They lead to the formation of surface cracks and their growth. The concentration of stresses leads to the cleavage of the microscopic volumes of the material, and the process of mechanical action repeats cyclically.

The cavitation resistance of the modified ceramic materials was actively investigated in [10, 14–16].

Information about the ceramic cavitation wear at various intensities of mechanical shock is limited. That's why the research for new scientific and practical results must be continuous.

3   Research Methodology

The authors present the research of the cavitation resistance of specimens of modified ceramics based on the matrix Al2O3 with the addition of ZrO2 up to 2% by mass.

Specimens were made from grinded alumina of α, β, γ modifications by pressing and sintering at temperature 1500 °C. The Al_2O_3 grain size was 15…30 μm.

Their main characteristics are shown in Table 1.

Table 1. The main characteristics of the specimens of modified ceramics.

Properties	Number of specimens	
	1	2
Content of components, % mass	$Al_2O_3 - 98$ $ZrO_2 - 2$	$Al_2O_3 - 95$ $Si\ O_2 - 3$ $Zr\ O_2 - 2$
Density, g/sm^3	4,1	3,9
Elastic modulus, E·10^2, MPa	3,4…3,6	3,0…4,2
Impact strength, κJ/m^3	340…650	280…400

The resistance of the specimens was determined by the action of ultrasonic cavitation, which was generated by oscillations of a magnetostrictive vibrator with a frequency 22 and 44 kHz. The vibrator amplitude −20 μm. Specimens were placed at the distance of 0.5 mm under the vibrator. The indicator of the wearing resistance of the specimens was the loss of their mass. It was determined by the gravimetric method at fixed time intervals. The electronic scales "Radwag WAA 210" with measurement accuracy 10^{-4} g was used.

The mechanisms of cavitation impact on the material of ultrasonic and hydrodynamic cavitation are identical. The use of ultrasonic cavitation is preferable for speeding up the experiments. This approach allows for obtaining a comparative assessment of the wear resistance of materials.

4 Results

The results are presented in Figs. 2 and 3, which characterize the loss of mass by the specimens at the frequency of vibrator – 22 and 44 kHz, respectively.

Obviously, that the specimen № 2 is the least resistant to cavitation effects. The graph of mass losses (Fig. 2) shows that up to 160 min, there is an accumulation of internal deformations. After this, the micro-volume of the substance takes off. This effect is most pronounced for the specimen № 2.

After that, the process of mass losses is stabilized. The specimen № 1 wears out less intensively for all the time of the research. The mass losses of two specimens are approximately the same, with an increase in the oscillation frequency up to 44 kHz. The wearing kinetics is explained by specimen surface layer defects. There is a tendency for the rise of mass loss with the continuation of the experiment.

The comparative data of the experiments are presented in Table 2.
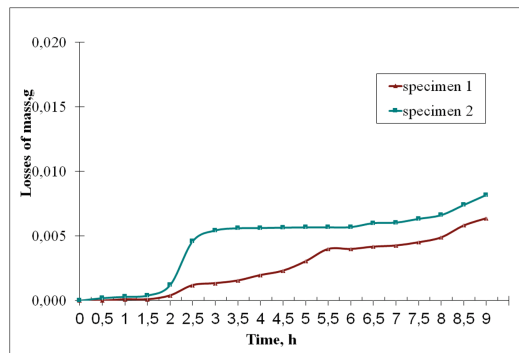
Fig. 2. The dependence of the mass losses of the specimens at a frequency of 22 kHz on time.
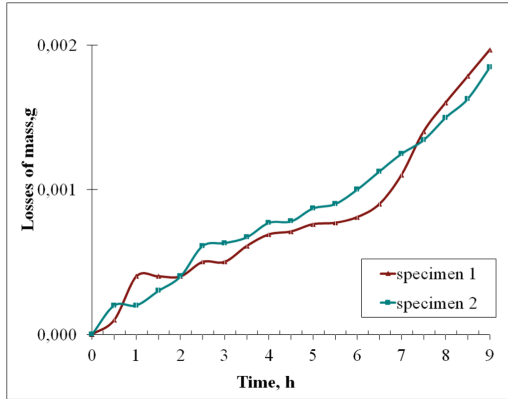
Fig. 3. The dependence of the mass losses of the specimens at a frequency of 44 kHz on time.

Table 2. The comparative results of the experiments.

Time, h.	Losses of mass, g			
	The oscillation frequency 22 kHz		The oscillation frequency 44 kHz	
	Specimen 1	Specimen 2	Specimen 1	Specimen 2
1	0,0001	0,0003	0,0002	0,0004
3	0,0014	0,0054	0,0006	0,0005
6	0,0040	0,0057	0,0010	0,0008
9	0,0064	0,0082	0,0018	0,0020

The wear resistance of the specimens with different oscillation frequencies is determined by the intensity of the mechanical impact on them [17].

This is confirmed by the graph of the rate of mass losses of the specimens (Fig. 4 and 5). The cyclical pattern of wearing is most pronounced at the frequency of 44 kHz. Mechanical impact on the surface of the specimens causes an intensive formation of micro-cracks. They are formed at the boundaries of internal defects or large grains of Al_2O_3. The authors obtain a similar result when researching the ceramics without modifying additives [13]. The additives of SiO_2 form the glassy phase between grains of Al_2O_3. It weakens the structure of the specimens and is a source of cracking. The cavitation resistance of the specimen № 2 is explained by the hanging content of Al_2O_3 and by the introduction of fine-grained ZrO_2 into the composition of the specimen.

This allows increasing the viscosity of ceramics. The shock waves after the collapse of cavitation bubbles are absorbed by the structure of the material. This contributes to reducing the resistance of ceramics under conditions of cavitation. In this case, the tensile-compression forces are distributed in each specimen surface layer. Constant surface updating is associated with the accumulation of fatigue cracks and the ceramics micro-volumes sharp separation.
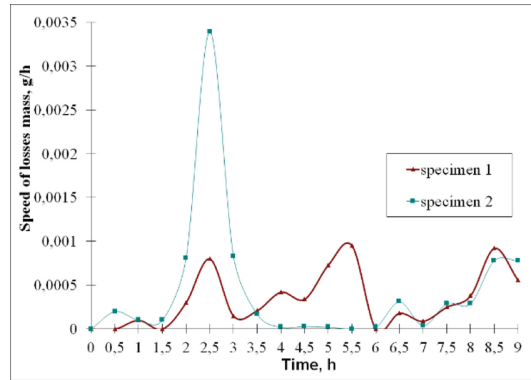
Fig. 4. The rate of mass losses of the specimens at an oscillation frequency of 22 kHz.
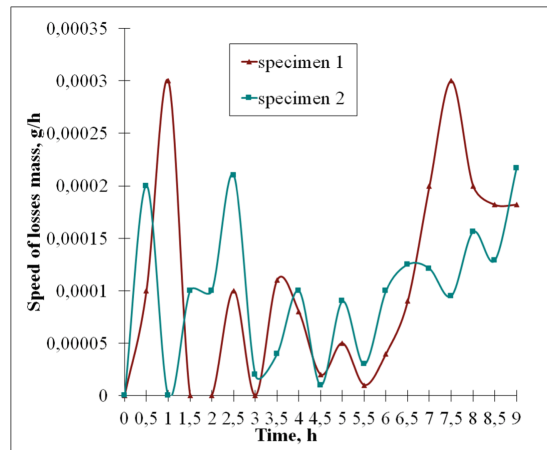
Fig. 5. The rate of mass losses of the specimens at an oscillation frequency of 44 kHz.

Ceramics do not have plastic deformation. The brittle fracture nature of its destruction is the most typical. Hooke's law is valid for most types of ceramics. Their characteristics are evaluated by the values of flexural strength, Young's modulus and other indicators. These indicators are typical for research of metal. It can be assumed that the behavior of ceramic materials during cavitation wear is similar to metals. Therefore, traditional approaches can be used for the research of ceramics. That is why the cyclical nature of the destruction of ceramics can be compared with hydro-abrasive wear of metals.

5 Conclusions

The introduction of the modifier of ZrO_2 into the Al_2O_3 ceramic matrix allows the significant increase of its wear resistance. The wear of materials is determined by the intensity of the cavitation effect and the phase ratio of components. The mechanism of wear of ceramics has a cyclical nature, which is similar to the hydro-abrasive wear of metals. To assess the wear of ceramics, it is possible to use the approach similar to that one used for the assessment of the wear of metals. The use of modified ceramics is recommended for equipment elements that are operated under cavitation and water jet wearing conditions. The chemical ceramics inertness is useful for working in aggressive technological environments.

References

1. Hees, M.: Verwirbelungen Halten Keramik Sauber. Ernahrungsindustrie **6**, 64–65 (2001)
2. Lukasik, K.: The Comparison of a selected material for homogenizing valves. In: Problems and Prospects for Creating and Implementing of the New Resource and Energy Saving Technologies Equipment in the Food and Processing Industries, vol. 3, p. 94. USUFT (2000)
3. Meltser, A., Ananevskyi, I., Kyrychenko, I.: New control valve for waterjet environments. Armature Constr. **3**(42), 26–28 (2006)
4. Caccese, V., Berube, K.A., Light, K.H.: Cavitation erosion resistance of various material systems. Ships Offshore Struct. **1**(4), 309–322 (2006)
5. Niebuhr, D.: Cavitation erosion behavior of ceramics in aqueous solutions. Wear **263**(1), 295–300 (2007)
6. Borek, W., Tanski, T., Krol, M.: Cavitation: Selected Issues. London Intech, London (2018)
7. Moussatov, A., Granger, C., Dubus, B.: Cone-like bubble formation in ultrasonic cavitation field. Ultrason. Sonochem. **10**, 191–195 (2003)
8. Moussatov, A., Granger, C., Dubus, B.: Ultrasonic cavitation in thin liquid layers. Ultrason. Sonochem. **12**, 415–422 (2005)
9. Kang, S.-J.L.: Sintering: Densification. Grain Growth and Microstructure. Elsevier, Amsterdam (2005)
10. Garcia-Atance, F.G., Hadfield, M., Tabeshfar, K.: Pseudoplastic deformation pits on polished ceramics due to cavitation erosion. Ceram. Int. **37**, 1919–1927 (2011)
11. Grimm, A., Bast, S., Tillmanns, R., Schumacher, M.: Keramik Leichtbautiele. Keram. Z. **58**(1), 8–11 (2006)
12. Medvedovski, E.: Wear-resistant engineering ceramics. Wear **249**(9), 821–828 (2001)
13. Litvinenko, A., Boyko, Yu., Pashchenko, B., Sukhenko, Yu.: Effect of phase composition on cavitation resistance of ceramics. In: Ivanov, V. et al. (eds.) Advances in Design, Simulation and Manufacturing. DSMIE-2018. LNME, pp. 299–305. Springer, Cham (2019). https://doi.org/10.1007/978-3-319-93587-4_31
14. Lua, J., Zum Gahr, K.-H., Schneider, J.: Microstructural effects on the resistance to cavitation erosion of ZrO, ceramics in water. Wear **265**, 1680–1686 (2008)
15. Pedzich, Z., Jasionowski, R., Ziabka, M.: Cavitation Wear of structural oxide ceramics and selected composite materials. J. Eur. Ceram. Soc. **34**, 3351–3356 (2014)

16. Pędzich, Z., Jasionowski, R., Ziąbka, M.: Cavitation wear of ceramics - part I. Mechanisms of cavitation wear of alumina and tetragonal zirconia sintered polycrystals. Compos. Theory Pract. **13**(4), 288–292 (2013)
17. Bovsunovskii, A.: Efficiency of crack detection based on damping characteristics. Eng. Fract. Mech. **214**, 464–473 (2019)

Influence of Weak Shock Wave
on the Dynamic Stress State of Foam Materials

Olena Mikulich[(✉)] , Lyudmila Samchuk , and Yulia Povstiana

Lutsk National Technical University, 75, Lvivska Street, Lutsk 43018, Ukraine
shyprao@gmail.com

Abstract. This paper proposes the technique for the analysis of weak shock wave influence on the dynamic stress state of foam materials with negative and positive Poisson's ratio. The investigation of the dynamic behavior of foam materials under the action of weak shock waves is performed in the framework of couple stress elasticity, where one can account for the influence of shear rotation deformation in structurally inhomogeneous media. For the solution of the non-stationary problem, Fourier transforms are used. The calculation of transforms of dynamic stresses in the foam medium is performed by using the boundary integral equation method and the theory of complex variable functions in the framework of couple stress elasticity. The numerical implementation of the developed algorithm is based on the method of mechanical quadrature and collocation technique. For calculation of originals of dynamic stresses discrete, Fourier transform is used. The distribution of dynamic hoop stresses in a positive and negative Poisson's ratio foam medium with tunnel cavities under the action of a weak shock wave is investigated. The algorithm is effective in the analysis of the dynamic behavior of the foam media with tunnel defects of various cross-sections.

Keywords: Auxetic · Couple stress elasticity · Time domain problem

1 Introduction

The development of modern technologies for the production of foam materials makes it possible to obtain suitable materials with rigidity, hardness, and density. Therefore, foam materials and products made of them have a wide application today. Among them, there are products made of both flexible and rigid foam types.

Besides, the technologies of obtaining foam materials with negative Poisson's ratio have expanded. These materials are also called auxetics. For obtaining such materials, the foam with low rigidity is used. Methods of obtaining auxetic materials are described in the works of Lakes R.S. [1], Grimma J. [2] and others.

Thus, in the work of Lakes R.S. [1], the method of creating synthetic materials with negative Poisson's ratio was based on the triaxial compression and heat treatment of as-received foam for converting to negative Poisson's ratio foam. Furthermore, Grima J. [2] presented an alternative method converting the open-cell polyurethane foam into the auxetic foam, which was based on using a novel chemo-mechanical process.

Most studies of the effects of different types of loads on such materials are experimental [3–5]. Therefore, the problem of developing theoretical methods of investigation of time-variable load influence on the stress state of foam materials with defects is very important.

Numerical experiments show that using classical elasticity theory for studying such materials produces significant errors since classical elasticity has no length scale. For the effective evaluation of the influence of non-stationary load on such materials with an accounting of their internal structure for a solution to this problem, the micropolar elasticity must be used. In the framework of micropolar elasticity, one can account for rotations of points and a length scale.

Therefore, the investigation of the dynamic behavior of foam materials in this paper is performed in the framework of couple stress elasticity.

2 Literature Review

When the action of all applied to the body, forces are determined by force stresses, the stress-strain state is symmetric, and it describes in the framework of classical elasticity theory. However, using the equations of symmetric elasticity theory cannot be described with the necessary precision of the phenomenon and the effects which are observed in foam media and structures under the action of time-changed load.

For the structural inhomogeneous materials, the action of all forces on the body needs to be determined by not only force stresses but also couple stresses. In addition, accounting for the couple stresses, one must assume that the internal microstructure exists in an infinitesimal amount of material.

Such questions are considered within the framework of the micropolar theory of elasticity or Cosserat elasticity [6, 7]. Here, every material point has the properties of a rigid body. This point has six degrees of freedom, which are characterized by the position in space and its orientation. Within the Cosserat continuum, there are additional physical parameters, which characterize the linear size, the moment of inertia of the parts, and the properties of the parts relative to the rotation. The study of the interaction of particles of the micropolar body is carried out not only accounting for the force (ordinary) stresses but also the moment (couple) stresses.

For the obtaining of correct values of dynamic stresses and deformations of auxetic foams (which are related to structural inhomogeneous materials) under the action of non-stationary load, the investigation of stress-strain state of such materials must be performed within the Cosserat elasticity [7], where one can account for the influence of shear-rotation deformations of microparticles of the medium.

Among the methods of exploration of the mechanical behavior of foam media with negative Poisson's ratio, one can be distinguished numerical approaches and analytical methods.

There are a few publications, which present results of numeric modelling of influence different types of load on stress and deformation distribution in auxetic foam media. Among them is [8], where the effect of the adhesive properties on the overall auxeticity of a rod consisting of two concentrically aligned cylindrical isotropic foams with Poisson's ratio of opposite signs under torsional loads is investigated. In [9], the

wave propagation problem of auxetic cellular structures and compared with conventional cellular materials are analyzed.

Based on the finite element analysis, the displacement and stress fields in locally heated three dimensional auxetic and cubic structures are compared in [5]. The optimization method of honeycomb and re-entrant honeycomb structures of a two-phase composite material is shown in [10].

Accounting for the effect of shear-rotational deformations significantly complicated the equation of motion of structural inhomogeneous media, so in the closed-form analytical solutions for only some classes of static problems were obtained. In the framework of couple stress elasticity equality of the vectors, macro and micro-rotations were accepted. Using such assumption simplified the motion equation of medium. Besides, such an assumption gave the opportunities for obtaining analytical solutions for some types of static and time-harmonic problems in series form.

Thus, in [12], the solutions of some types of static and time-harmonic problems for the Cosserat continuum with constrained micro-rotations are built using the series method. The fundamental functions for the static problem linear isotropic size-dependent couple stress elasticity with using the boundary element method are derived in [13]. However, [13] did not describe the application of obtained fundamental functions to the investigation of stresses and deformation in the case of the existence of different types of defects in the body. Thus, the obtained results were only theoretical.

In [14], the development of the boundary integral equation method to solving time-domain problems of couple stress elasticity is presented. The numerical implementation of the proposed approach is performed in [14] for the case of the second exterior dynamic problem.

Therefore, the aim of the paper is an analysis of the dynamic stress state of foam media with positive and negative Poisson's ration on the base of comparing of hoop dynamic stresses on the boundary of tunnel defects constant cross-section the under the action of time-variable loads in form of the weak shock wave in the framework of couple stress elasticity.

3 Research Methodology

3.1 Statement of the Problem

Consider medium with the tunnel cavity, which is under conditions of plane deformation (Fig. 1). The boundary of a cross-section of the cavity is denoted by L. The center of gravity in case of plane deformation is placed at the origin of a Cartesian coordinate system $x_1Ox_2x_3$.
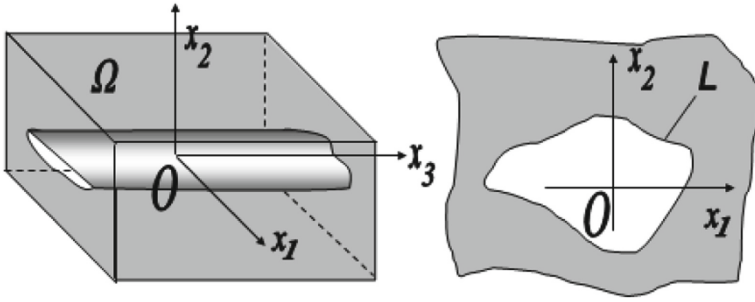
Fig. 1. The model of the research object.

The problem is in the determination of the hoop and radial dynamic stresses in the foam medium with tunnel cavity under the action of weak shock waves.

The representation of the potential of a weak shock wave is written in the form [15]:

$$\phi_1(\mathbf{x}, t) = \begin{cases} \phi_0 f\left(\frac{\mathbf{x}}{a} - c_1 \frac{t}{a}\right), & t \geq 0; \\ 0, & t < 0, \end{cases} \quad \phi_2(\mathbf{x}, t) = 0, \tag{1}$$

where ϕ_0 is a constant, a is a length characteristic, $c_1 = \sqrt{\frac{\lambda + 2\mu}{\rho}}$ is the speed of expansion wave, ρ is the density of a material, μ, λ are Lame parameters, $\mathbf{x} = \{x_1; x_2\}$, t is the time.

The boundary conditions of the problem are written as:

$$\sigma_n|_L = \Phi_1(x, t), \quad \tau_n|_L = \Phi_2(x, t), \tag{2}$$

where $\Phi_1(\mathbf{x}, t)$, $\Phi_2(\mathbf{x}, t)$ are given at the boundary functions which are determined by the potential of weak shock wave (1), $\overrightarrow{n}$ is normal to the boundary of the cavity.

The analysis of deformations in the foam medium under the action of external load confirms the possibility of presenting these deformations as the summation of the translational and rotational displacements of microparticles. Each micro-rotation of the particles of the medium is associated with their translational displacement. Besides, microparticles of a foam medium cannot make micro-rotations without translational displacements. This is due to the structure of the foam material. Therefore, for the foam materials, the macro-rotation vector of medium depends on the micro-rotation vector of microparticles [16].

For solving the non-stationary problem as to the investigation of weak shock wave influence on the stress state of the foam media with tunnel defects, the apparatus of couple stress elasticity is chosen. In the framework of couple stress, elasticity vectors of micro-rotation and macro-rotation are the same. The motion equations of couple stress

elasticity account for the internal momentum of the quantity motion of the micropar-
ticles. It is assumed that:

$$\varpi = \frac{\text{rot}(\mathbf{u})}{2},$$

(3)

where $\mathbf{u}$ is the displacement vector, ϖ is the rotation vector. Functions $\mathbf{u}$ and ϖ are
continuous functions.

3.2   Wave Speeds in the Couple Stress Elasticity

The motion equation of the couple stress elasticity is written as [12]:

$$(\lambda + 2\mu)\text{grad}(\text{div}(\mathbf{u})) + \text{rot}\left(\text{rot}\left(\frac{B}{4}\Delta \mathbf{u} - \mu \cdot \boldsymbol{u}\right)\right) = \rho \frac{\partial^2 \mathbf{u}}{\partial t^2},$$

(4)

where $\mathbf{u}(\mathbf{x},t) = \{u_j(\mathbf{x},t)\}, j = 1,2$ is a vector of displacements, B is the constant of the
microstructure of a material, Δ is Laplace operator. The Eq. (4) is obtained by the
substitution of the formula (3) to the motion equations of Cosserat elasticity [17].

We write the displacement vector $\mathbf{u}(\mathbf{x},t)$ as the sum of the potential $\varphi(\mathbf{x},t)$ and
vortex $\psi(\mathbf{x},t)$ functions:

$$\mathbf{u}(\mathbf{x},t) = grad(\varphi) + rot(\psi),$$

and substitute it in Eq. (4). We obtain two equations of the hyperbolic and parabolic
types:

$$\Delta\varphi - \frac{1}{c_1^2}\frac{\partial^2 \varphi}{\partial t^2} = 0, \quad \ell^2\Delta\Delta\psi - \Delta\psi - \frac{1}{c_2^2}\frac{\partial^2 \psi}{\partial t^2} = 0,$$

(5)

where ℓ is a scale factor which has a dimension of the length and depends on the
microstructure of the material, $\ell = \sqrt{\frac{B}{4\mu}}$, $c_2 = \sqrt{\frac{\mu}{\rho}}$ is the speed of the shear wave.

The last of Eqs. (5) shows that shear and transverse rotation waves have dispersion
properties. Applying the Fourier transforms to Eqs. (5) and using representation for
vortex functions and using representation for vortex function $\psi(\mathbf{x},t)$ in the form:

$$\psi = \Psi + \Phi,$$

we obtain:

$$\Delta\widehat{\varphi} + \frac{\omega^2}{c_1^2}\widehat{\varphi} = 0, \quad \Delta\widehat{\Psi} + \frac{\omega^2}{c_3^2}\widehat{\Psi} = 0, \quad \Delta\widehat{\Phi} - \frac{\omega^2}{c_4^2}\widehat{\Phi} = 0,$$

(6)

where ω is the frequency, $\widehat{\varphi}, \widehat{\Phi}, \widehat{\Psi}$, are Fourier transforms of according functions.

The speeds of shear-rotation waves in couple stress elasticity are defined in the form:

$$c_3 = \sqrt{\frac{c_2}{2}\left(\sqrt{c_2^2 + 4\ell^2\omega^2} + c_2\right)}, c_4 = \sqrt{\frac{c_2}{2}\left(\sqrt{c_2^2 + 4\ell^2\omega^2} - c_2\right)}.$$

Equations (6) show that the speed of the expansion wave does not affect the couple stresses. When $\ell \to 0$ the first speed of the waves c_3 tends to the speed c_2. The second speed of the waves c_4 disappears with an imaginary wave number $\frac{i\omega}{c_4}$.

In this case, the obtained solutions coincide with the solutions for the classic theory of elasticity.

3.3 The Solution of the Problem

Applying the Fourier transforms to the motion Eq. (4) one can obtain the equation which is equivalent to the equation of the time-harmonic motion with cyclic frequency ω. For constructing the solution in the field of Fourier transforms, we use the approach proposed in [14]. The Fourier transforms of displacements is written as:

$$\widehat{u}_i = \int_L p_j \cdot U_{ij}^{(coupl)*} dL, \tag{7}$$

where $U_{ij}^{(coupl)*}$ are the fundamental functions that are obtained in [14] in the framework of couple stress elasticity, p_j are unknown functions, L is the boundary of a cross-section of the cavity.

Satisfying of Fourier transforms of boundary conditions (2), we obtain the system of integral equations:

$$\frac{\mathrm{Re}(q)}{2} + PV\int_L \left(f_1(\mathbf{x}, \mathbf{x}^0)qd\zeta + f_2(\mathbf{x}, \mathbf{x}^0)\overline{q}d\overline{\zeta}\right) = \widehat{\Phi}_1(\mathbf{x}, t), \tag{8}$$

$$\frac{\mathrm{Im}(q)}{2}v_1 + PV\int_L \left(g_1(\mathbf{x}, \mathbf{x}^0)qd\zeta + g_2(\mathbf{x}, \mathbf{x}^0)\overline{q}d\overline{\zeta}\right) = \widehat{\Phi}_2(\mathbf{x}, t), \tag{9}$$

where we separate the singularities in the integration functions f_m, g_m for the small value of argument and apply Plemelj-Sokhotski formulas for the limit transition. Here $pdL = -iqd\zeta$, $p = p_1 + ip_2$ is the unknown complex function, $\zeta = x_1^0 + ix_2^0$, $v_1 = 1 - \frac{B\rho\omega^2}{2\mu^2}$ is the constants. Here, the integrals are understood in the sense of Cauchy principal value.

3.4 Defined of the Dynamic Stress

For the numerical solving of the system of integral Eqs. (8)–(9), the algorithm [18] is applied, which is based on the mechanical quadrature method and collocation method.

Using the numerical implementation developed in [18], one can lead the determining of unknown functions on the boundary of cavity cross-section based, which are the solutions of the system of singular integral Eqs. (8)–(9) to the solving of a system of linear equations. In this case, the solution of the linear equation system is the values of the unknown functions in the collocation points on the cavity boundary.

For defining the transforms of hoop stresses, we are applying the approach, which was proposed in [14]. According to the approach developed in [14], we build analytical representation in integral form for determining corresponding stresses in framework couple stress elasticity:

$$\widehat{\sigma}_\theta(\mathbf{x}, \omega) = \frac{\mathrm{Re}(q)}{2} \upsilon_2 + PV \int_L \left(h_1(\mathbf{x}, \mathbf{x}^0) q d\zeta + h_2(\mathbf{x}, \mathbf{x}^0) \overline{q} d\overline{\zeta} \right) + \widehat{\sigma}_\theta^{refl}(\mathbf{x}, \omega), \quad (10)$$

where $h_k = h_k(\mathbf{x}, \mathbf{x}^0)$ are known functions [14], υ_2 is the constant [14], $\widehat{\sigma}_\theta^{refl}(\mathbf{x}, \omega)$ are the stresses which arise from the action of reflected from the boundary of the cavity wave.

For numerical calculations of transforms of hoop stresses, we substitute the obtained solutions of the system of integral Eqs. (8)–(9) to the formulas for determining of hoop stresses (10). The values of originals of the dynamic hoop stresses are calculated based on the discrete Fourier transform.

4   Results

Using the developed approach, we investigate the effect of the weak shock wave on the dynamic stress state of a negative and positive Poisson's ratio medium with the tunnel cavity. The function that describes the changing intensity of the load over time is chosen in the form [14].

Let the wave is placed at the centre of the Cartesian coordinate system at time moment $t = 0$. The wave moves in the direction of the axis Ox_1. Along the path of the wave, the defect in the form of a tunnel cavity is circular is placed. The centre of cavity cross-section is shifted on distance $4R$ relative to the origin Cartesian coordinate system (Fig. 2).
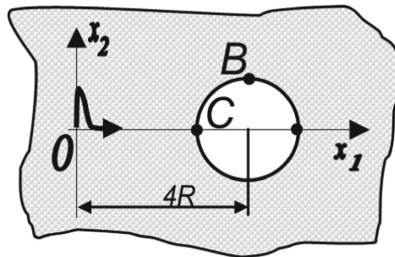
Fig. 2. 2D model.

For numerical calculations, we use the elastic constants, which are obtained in [5], required to describe isotropic Cosserat elastic solid. The auxetic foam was obtained at full compression from the Scott Industrial polyurethane foam [5].

The as-received foam of the initial density is $\rho = 30$ kg/m^3, Poisson's ratio is $v = 0.3$, the shear modulus is $G = 45$ kPa, length characteristic of couple stress elasticity is $\ell = 3$ mm. For the negative Poisson's ratio foam, the density of foam specimens is $\rho = 96$ kg/m^3, Poisson's ratio is $v = -0.63$, the shear modulus is $G = 16$ kPa, length characteristic of couple stress elasticity is $\ell = 1.8$ mm.

The investigation of a dynamic stress state is performed for the case when the impulse of a weak shock wave is given in form [14] with dimensionless time duration $t_* = 8$.

Figure 3 shows the distribution of the normalized hoop stresses on the boundary of the circular cavity of radius $R = 10$ mm in positive (a) and negative (b) Poisson's ratio media.
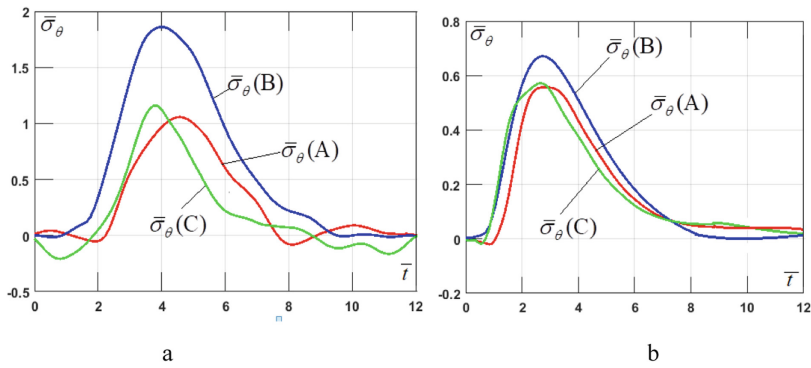
Fig. 3. Normalized hoop stresses on the boundary of the circular cavity in positive (a) and negative (b) Poisson's ratio media.

Comparing the curves of Fig. 3 shows that the maximum values of normalized hoop stresses at the boundary of the cavity is smaller in 2.4 times in materials with a negative Poisson's ratio than in material with positive Poisson's ratio. However, the distribution of hoop stresses along the boundary of the cavity is substantially different for materials with a negative and positive Poisson's ratio.

In negative Poisson's ratio foam, the dynamic stresses have almost the same values in all points of boundary. For the foam materials with positive Poisson's ratio, these values are varied in different points of the boundary. This is because the re-entrant structures of auxetic are less rigidly and have greater microrotations of the medium particles than in honeycomb cell structures with a positive Poisson's ratio.

5   Conclusions

Numerical calculations confirm that analysis of the dynamic stress state of foam media with positive and negative Poisson's ratio needs to investigate with accounting for the influence of microstructure of the material, especially under the action of time-variable loads.

Based on the numerical calculation results, one can conclude that the dynamic stress state of structurally inhomogeneous materials depends on not only the physical characteristics of the medium (such as the density, Young's modulus, etc.) but also on the internal structure, which influence is determined by the Poisson's ratio.

The study of the dynamic interaction of a weak shock wave with a defect in the form of a tunnel cavity in the foam medium with negative and positive Poisson's ratio based on comparing the distribution of dynamic hoop stresses in the boundary of the cavity showed that the stress states of such materials differ significantly not only in numerical values of stresses but also in their distribution.

Thus, the developed approach, which is modified in the work, allows investigating the weak shock wave effect in structurally inhomogeneous media with the negative and positive Poisson's ratio.

References

1. Lakes, R.S.: Experimental micro mechanics methods for conventional and negative poisson's ratio cellular solids as cosserat continua. J. Eng. Mater. Tech. **113**, 148–155 (1991)
2. Grima, J., Attard, D., Gatt, R., Cassar, R.: A novel process for the manufacture of auxetic foams and for their re-conversion to conventional form. Adv. Eng. Mater. **11**(7), 533–535 (2009)
3. Lakes, R.S.: Physical meaning of elastic constants in cosserat, void, and microstretch elasticity. J. Mech. Mater. Struct. **11**(3), 217–229 (2016)
4. Li, D., Dong, L., Lakes, R.: A unit cell structure with tunable poisson's ratio from positive to negative. Mater. Lett. **164**, 456–459 (2016)
5. Rueger, Z., Lakes, R.S.: Cosserat elasticity of negative poisson's ratio foam: experiment. Smart Mater. Struct. **25**, 1–8 (2016)
6. Altenbach, H., Eremeyev, V.: Cosserat media. In: Generalized Continua from the Theory to Engineering Applications, vol. 541, pp. 65–130 (2013)
7. Hassanpour, S., Heppler, G.: Micropolar elasticity theory: a survey of linear isotropic equations, representative notations, and experimental investigations. Math. Mech. Solids **12**, 1–19 (2015)
8. Lim, T-Ch.: Auxeticity of concentric auxetic-conventional foam rods with high modulus interface adhesive. Materials **11**(2), 223–235 (2018)
9. Hou, X., Deng, Z., Zhou, J.: Simplistic analysis for the wave propagation properties of conventional and auxetic cellular structures. Int. J. Numer. Anal. Model. **2**(4), 298–314 (2011)
10. Strek, T., Jopek, H., Idczak, E., Wojciechowski, K.: Computational modelling of structures with non-intuitive behaviour. Materials **10**, 1386–1402 (2017)
11. Hadjesfandiari, A.R., Dargush, G.F.: Couple stress theory for solids. Int. J. Solid Struct. **48**(18), 2496–2510 (2011)

12. Savin, G.N., Shulga, N.A.: Dynamic plane problem of the moment theory of elasticity. Appl. Mech. **3**(6), 216–221 (1967)
13. Hadjesfandiari, A.R., Dargush, G.F.: Fundamental solutions for isotropic size-dependent couple stress elasticity. Int. J. Solid Struct. **50**(9), 1253–1265 (2013)
14. Mikulich, O., Shvabyuk, V., Pasternak, Ia., Andriichuk, O.: Modification of boundary integral equation method for investigation of dynamic stresses for couple stress elasticity. Mech. Res. Commun. **91**, 107–111 (2018)
15. Tabak, E.G., Rosales, R.R.: Focusing of weak shock waves and the von Neumann paradox of oblique shock reflection. Phys. Fluids **6**(5), 1874–1892 (1994)
16. Wang, Y., Gioia, G., Cuitiño, A.: The deformation habits of compressed open-cell solid foams. J. Eng. Mater. Tech. **122**, 376–378 (2000)
17. Nowacki, W.: The Linear Theory of Micropolar Elasticity. Springer, New York (1974)
18. Mikulich, O., Shvabyuk, V., Sulym, H.: Dynamic stress concentration at the boundary of an incision at the plate under the action of weak shock waves. Acta Mechanica et Automatica **11**(3), 217–221 (2017)

Design of Hydraulic Mechatronic Systems with Specified Output Characteristics

Anatolii Panchenko[1(✉)] , Angela Voloshina[1] , Olena Titova[1] ,
Igor Panchenko[1] , and Anatoly Caldare[2]

[1] Tavria State Agrotechnological University,
18, B. Khmelnitsky Avenue, Melitopol 72310, Ukraine
tia_tgatu@ukr.net
[2] Joint Stock Company "HIDROINPEX",
118A, V. Stroescu Street, 3000 Soroca, Moldova

Abstract. Current trends in expanding the scope of mechatronic systems with a hydraulic drive of active working bodies of self-propelled vehicles require the development of new approaches to solve the problem of improving the output characteristics of hydraulic drives of mechatronic systems with rotary hydraulic machines. It is established that for the drive of active working bodies and running systems of self-propelled equipment, the orbital and planetary hydraulic machines are mostly used. When designing mechatronic systems, much attention is paid to ensuring the specified output characteristics of the actuators of the designed system. A methodology for designing hydraulic mechatronic systems with the elements of multi-criteria optimization has been developed, which allows designing a mechatronic system with specified output characteristics. The optimization parameters of the controls of the mechatronic system with a hydraulic drive of the active working bodies of self-propelled vehicles have been substantiated. This technique involves five stages: the choice of the mechatronic system parameters; substantiation of optimized control parameters; development of a mechatronic system model; optimization of selected parameters of the mechatronic system; analysis of optimization results. The parameters of optimization of controls of a mechatronic system with a hydraulic drive for active working bodies and running systems of self-propelled vehicles have been substantiated. As a result of the studies, the optimal settings of the safety valve of the mechatronic system have been established, providing deviations of the pressure and angular velocity of the actuators from the set ones with an error of 0.17% and 0.67%, respectively.

Keywords: Mechatronic system · Planetary hydraulic motor · Optimization criterion · Integral quadratic estimate

1 Introduction

A natural tendency to expand the scope of mechatronic systems with a hydraulic drive of the active working bodies of self-propelled vehicles makes it necessary to create a new generation of rotary-action hydraulic machines. Accelerating the growth rate of

requirements for the technical level of hydraulic machines leads to an increase in research and the complexity of design work.

It is possible to speed up the stage of development of new models of hydraulic machines for hydraulic drives of mechatronic systems of self-propelled equipment by developing and introducing more advanced design methods based on modern achievements in the field of calculation and modeling.

It is known that for drives of active working bodies and running systems of self-propelled vehicles, orbital [1–4] and planetary [5–8] hydraulic motors are mostly used. It should be noted that in previous studies, insufficient attention was paid to the problems of calculating and designing the elements of mechatronic systems [9] with given output characteristics, the proposed mathematical models did not cover all nodes of the hydraulic motor and their interconnections, and a number of assumptions introduced to simplify the calculations reduced the accuracy of the obtained indicators.

Thus, current trends in expanding the scope of mechatronic systems with a hydraulic drive of active working bodies of self-propelled vehicles require the development of new approaches to solving the problem of improving the output characteristics of hydraulic drives with rotary hydraulic machines.

2   Literature Review

Currently, much attention is paid to the study of superchargers used in hydraulic systems [10]. Similarity criteria were determined and verified by numerical studies [11] considering the ratio of three main similarity factors: geometric dimensions, the pressure of the active stream at the device inlet, and density of the working medium. A reasonable assessment of the efficiency of hydrodynamic machines by dissipative power is presented [12]. Mathematical modeling of the flow using the SST-model of turbulence is proposed [13]. The implementation of a mathematical model of rotor vibrations for a multistage centrifugal compressor is considered [14]. The rotor dynamics of multistage centrifugal machines are studied [15]. A procedure for calculating elastic strains has been developed. The adequacy of the proposed method is confirmed by the calculation results [16]. However, the works did not address the issues related to the calculation, modeling, and design of rotary-action hydraulic machines.

An analysis of the studies [1, 2] related to the design of rotary action hydraulic machines allows us to conclude that they were carried out without due regard for a number of important factors allowing developing a more complete mathematical model and make more efficient use of modern mathematical optimization methods, computer technology, and software tools.

Geometrical [17], mathematical [4, 5, 7], and hydrodynamic models [18] are proposed, theoretical studies of the influence of the geometric parameters of the flow parts of the gerotor pump on its output characteristics are performed. Much attention is paid to the distribution of the working fluid [6] and the influence of the geometric parameters of the distribution systems on the output characteristics of planetary hydraulic machines [5, 7]. The relationship between the design features of hydraulic machines, the output characteristics and the flow of the working fluid has not been investigated.

A computational [19] and experimental model [20] of the hydraulic system are proposed. A universal model of a mechatronic system with a hydraulic drive is developed [4, 5]. The relationship between the elements of the mechatronic system and the working fluid, as a whole, is not considered.

The multi-criteria choice of the optimal configuration was considered [21]. Optimizing hydrodynamic profiling was performed [22]. The results of optimizing the geometric parameters of centrifugal pumps using mathematical models of spatial flows of an incompressible fluid are presented [23]. However, the issues related to the design methodology of orbital and planetary hydraulic motors with elements of multi-criteria optimization have not been considered in the works.

3   Research Methodology

Mechatronic systems with planetary hydraulic motors in their output characteristics are developed for the use in drives of active working bodies and running systems of road, construction, agricultural, and other self-propelled machinery. Therefore, the design of a mechatronic system with predetermined output characteristics is one of the main stages in the general chain of issues that arise in the design of self-propelled equipment and its elements.

To ensure the given output characteristics when designing a mechatronic system with a hydraulic drive of active working bodies and running systems of self-propelled vehicles, a design methodology has been developed. The developed methodology involves five stages: a selection of the mechatronic system parameters that affect its output characteristics; substantiation of the optimized parameters of the controls of the mechatronic system; development of a mechatronic system model with the possibility of optimizing its output characteristics; optimization of selected parameters of the mechatronic system; analysis of optimization results.

4   Results

The Choice of Mechatronic System Parameters Affecting Its Output Characteristics. When designing a mechatronic system, for example, for drives of active working bodies of self-propelled agricultural equipment (as the most popular), it is necessary to take into account the specific operating conditions of this equipment. For almost all drives of self-propelled agricultural machinery, the acceleration of the mechatronic system should be carried out at almost full load of the working body (90…95%). In this case, the acceleration time should not exceed 2…3 s. Based on this, the main parameters of the mechatronic system affecting its output characteristics (torque and speed of the working body) are the change in pressure p and angular velocity ω.

Justification of the Optimized Parameters of the Controls of the Mechatronic System. Studies of the dynamics of the mechatronic system have established [5] that the acceleration process is determined by the closing time of the safety valve. Therefore, as the optimized parameters of the safety valve– the spring stiffness of the working

dispenser C_x, its preliminary compression x_z, and the positive overlap of the working dispenser x_0 are selected.

Development of a Mechatronic System Model With the Possibility of Optimizing Its Output Characteristics. When optimizing the parameters that determine the output characteristics of the mechatronic system, we use the integral quadratic estimate adopted in the theory of automatic control as an optimality criterion [5, 24]. Having the curves of the optimized pressure parameters $p(t)$ and the angular velocity $\omega(t)$), as well as the theoretical (given) curves of the same parameters $p_{theor}(t)$ and $\omega_{theor}(t)$, we calculate their difference at any time relative to $p(t)$ and $\omega(t)$, respectively.

Moreover, the optimization criterion I is determined from the expression [5, 24]:

$$
I_p = \int_0^{T_{t.p}} \frac{[p(t) - p_{theor}(t)]^2}{[p(t)]^2} \, dt,
$$
$$
I_\omega = \int_0^{T_{t.p}} \frac{[\omega(t) - \omega_{theor}(t)]^2}{[\omega(t)]^2} \, dt;
\tag{1}
$$

where $T_{t.p}$ – time the transition process; $p(t)$, $\omega(t)$ – are the dependences of the curves transition process, determined from the optimized parameters of the safety valve C_x, x_z and x_0; $p_{theor}(t)$, $\omega_{theor}(t)$ – theoretical (given) curves of the transition process.

In the optimization process, criterion I tends to the minimum value, and the curves $p(t)$, $\omega(t)$ and $p_{theor}(t)$, $\omega_{theor}(t)$, reflecting the acceleration process, approach each other. As a given trajectory for the curves $p_{theor}(t)$ and $\omega_{theor}(t)$) during the operation of the mechatronic system, we consider the exponent [5, 24]:

$$
p_{theor}(t) = p_0 \cdot \left[1 - e^{-\frac{t}{T}}\right] = 20,9 \cdot \left[1 - e^{-\frac{t}{0,035}}\right],
$$
$$
\omega_{theor}(t) = \omega_0 \cdot \left[1 - e^{-\frac{t}{T}}\right] = 70 \cdot \left[1 - e^{-\frac{t}{0,85}}\right];
\tag{2}
$$

where T – is the time constant; p_0, ω_0 – are the specified values of pressure and angular velocity during acceleration, respectively.

When optimizing the parameters characterizing the process of changing pressure and angular velocity during acceleration of the hydraulic drive of the mechatronic system, the following initial conditions are formulated: the pressure value should not exceed the maximum value of the working pressure of the planetary hydraulic motor p_{max} = 21 MPa; the magnitude of the pressure peaks during start-up should not exceed 32 MPa; the system acceleration time (until the safety valve closes) must not exceed two seconds ($T_{t.p}$ = 2 s); The initial values of the optimized parameters of the safety valve are C_x = 200 N/cm, x_z = 0.53 cm and x_0 = 0.125 cm.

When developing a model for optimizing the output characteristics of the mechatronic system, we take the mathematical model of the mechatronic system with a planetary hydraulic motor [6], implemented using the Vissim simulation package, and expressed as a structural-functional diagram (Fig. 1).

To perform the optimization, the proposed mathematical model and the structural-functional diagram of the mechatronic system (Fig. 1) are supplemented by expressions that allow determining the optimality criterion (1) and the trajectory of a given theoretical curve (2).
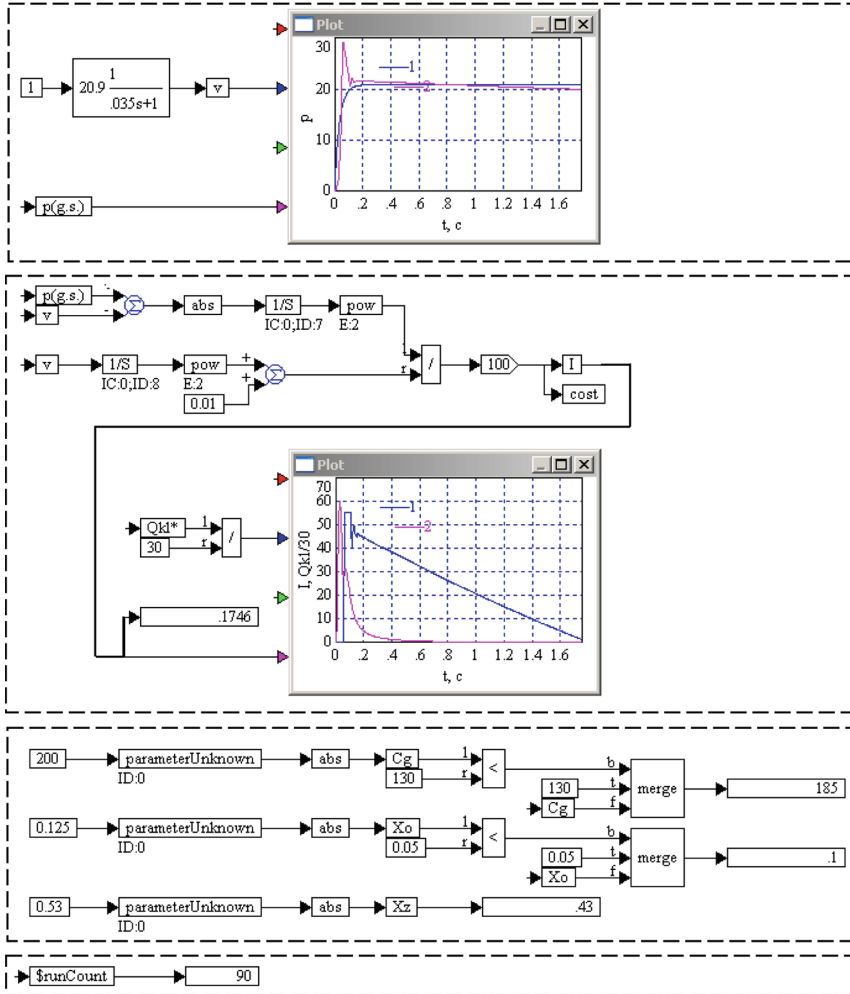
Fig. 1. The structural and functional scheme for optimizing the output characteristics of a mechatronic system with a planetary hydraulic motor.

Block 1 reflects the start of the mechatronic system, where curve 1 changes exponentially, and curve 2 characterizes the change in pressure $p(t)$ (angular velocity $\omega(t)$) in the mechatronic system (Fig. 1) with varying optimized parameters. Block 2 allows determining the optimization criterion I, which tends to a minimum. Block 3 allows varying the optimization parameters. The number of iterations is reflected in block 4.

Justification of the Optimization Method. The standard Vissim simulation package allows for the optimization of using three methods: Powell, Polac Ribiere, Fletcher Reeves. The results of setting the parameters of the safety valve (C_x, x_0, and x_z) when optimizing the output characteristics of the hydraulic mechatronic system of the active working body of a mobile agricultural machine and optimization criterion I are given in Table 1.

Table 1. Results of adjusting the safety valve parameters during the optimization by various methods.

Indicators	Optimization methods					
	Powell		Polac Ribiere		Fletcher Reeves	
	p	ω	p	ω	p	ω
Number of iterations	49	26	334	72	334	72
C_x	185	195	199.9	199.9	199.9	199.9
x_0	0.1	0.09	0.15	0.43	0.15	0.43
x_z	0.43	0.45	0.28	$5.7 \cdot 10^{-3}$	0.28	$5.7 \cdot 10^{-3}$
I	0.17	0.67	6.24	13.19	6.24	13.19

An analysis of the results shows that more accurate settings of the safety valve parameters while optimizing the output characteristics of the mechatronic system were obtained using the optimization method – Powell; the use of optimization methods Polac Ribiere and Fletcher Reeves is impractical since it gives a large error.

Analysis of Optimization Results. Optimization of the parameters of the controls of the mechatronic system involves the determination of parameters that affect its output characteristics, as well as the determination of output characteristics at the optimal values of the parameters of the controls.

The analysis of the given dependencies (Fig. 2a) shows that at the initial values of the safety valve parameters, the process of pressure change $p(t)$ (curve 2) differs significantly from the given $p_{theor}(t)$ (curve 1). The excess pressure is above the set by 15%, and the pressure during acceleration exceeds the set by 24%.

The noted discrepancies (Fig. 2b) of the real $p(t)$ and given $p_{theor}(t)$ pressure curves are characteristically represented by the dependence of the dynamics of changes in the optimization criterion $I_p(t)$ (curve 2). The value of the pressure optimization criterion is $I_p(t) = 9.12\%$.

It should be noted (Fig. 2c) that the change in the angular velocity $\omega(t)$ during the acceleration (curve 2) also differs significantly from the given $\omega_{theor}(t)$ (curve 1). The noted discrepancies (Fig. 2d) of the real $\omega(t)$ and given $\omega_{theor}(t)$ curves of the change in angular velocity are represented by the dependence $I_\omega(t)$ (curve 2). Moreover, the value of the optimization criterion for angular velocity is $I_\omega = 2.83\%$.
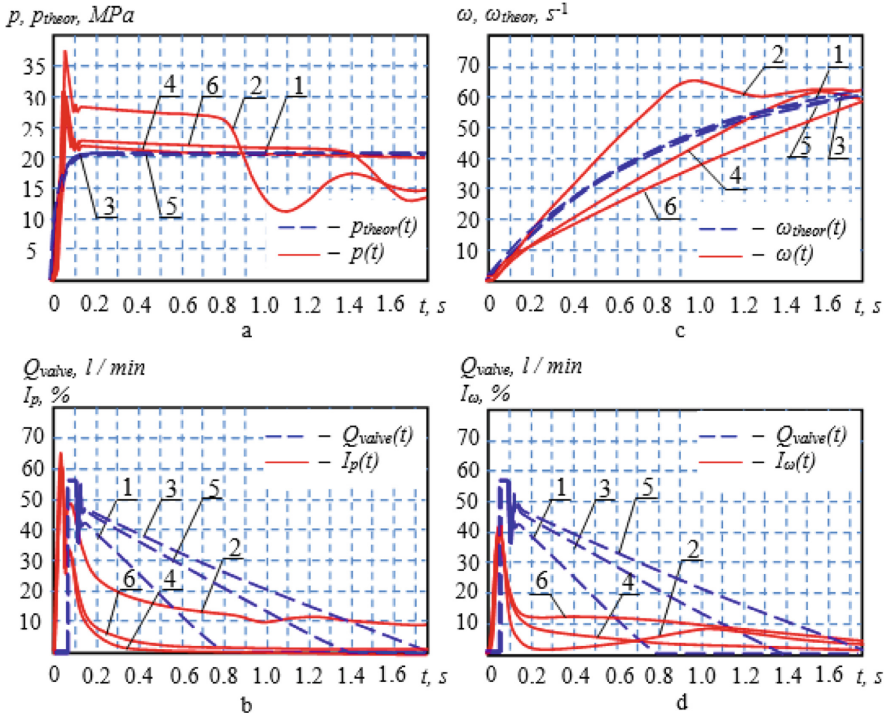
Fig. 2. The characteristics of the acceleration process of the hydraulic drive of the mechatronic system at the initial values of the optimized valve parameters: a – pressure change; b – change in the optimization criterion for pressure; c – change in angular velocity; d – change in the optimization criterion for angular velocity; curves 1 and 2 correspond to the valve settings for pressure – $C_x = 200$ N/cm, $x_z = 0.53$ cm, $x_0 = 0.125$ cm and angular velocity – $C_x = 200$ N/cm, $x_z = 0.53$ cm, $x_0 = 0.125$ cm; curves 3 and 4 correspond to the valve settings for pressure – $C_x = 185$ N/cm, $x_z = 0.43$ cm, $x_0 = 0.1$ cm and angular velocity – $C_x = 195$ N/cm, $x_z = 0.45$ cm, $x_0 = 0.09$ cm; curves 5 and 6 correspond to the valve settings for pressure – $C_x = 195$ N/cm, $x_z = 0.45$ cm, $x_0 = 0.09$ cm and angular velocity – $C_x = 185$ N/cm, $x_z = 0.43$ cm, $x_0 = 0.1$ cm.

The duration of the acceleration process (Fig. 2b and d – curves 1) is $T_{t.p} = 0.8$ s, which is quite acceptable.

An analysis of the given dependences of the pressure and the angular velocity changes during the acceleration of the mechatronic system (Fig. 2) shows that when optimizing the parameters of the safety valve ($C_x = 185$ N/cm, $x_z = 0.43$ cm, $x_0 = 0.1$ cm), the process of changing the pressure $p(t)$ in the mechatronic system (Fig. 2a, curve 4) is practically the same given $p_{theor}(t)$ (curve 1). In this case, the pressure drop is less than the set by 6%, and the pressure values during acceleration do not exceed the set.

Slight discrepancies (Fig. 2b) of the real $p(t)$ and the given $p_{theor}(t)$ pressure curves are represented by the dependence $I_p(t)$ (curve 4). The value of the optimization criterion for pressure is $I_p = 0.17\%$.

It should be noted (Fig. 2c) that the change in the angular velocity $\omega(t)$ when optimizing the parameters of the safety valve ($C_x = 195$ N/cm, $x_z = 0.45$ cm, $x_0 = 0.09$ cm) during the acceleration (curve 4) is already slightly different from the given $\omega_{theor}(t)$ (curve 3). The noted discrepancies in $\omega(t)$ and $\omega_{theor}(t)$ are represented by the dependence (Fig. 2d) of the dynamics of changes in $I_\omega(t)$ (curve 4). Moreover, the value of the optimization criterion for the angular velocity is $I_\omega = 0.67\%$.

The duration of the acceleration process (Fig. 2b and d curves 3) is now different and amounts to $T_{t.p} = 1.75$ s for the pressure and $T_{t.p} = 1.39$ s for the angular velocity, respectively.

As a result of the studies, it was found that the optimal settings of the safety valve provide a deviation of $p(t)$ from $p_{theor}(t)$ during acceleration of the hydraulic actuator $I_p = 0.17\%$ and $\omega(t)$ from $\omega_{theor}(t)$ are $I_\omega = 0.67\%$.

To establish the best optimum, another virtual experiment was conducted to determine the change in the output parameters of a mechatronic system with a hydraulic drive.

An analysis of the given dependencies (Fig. 2a) shows that, when optimizing the parameters of the safety valve ($C_x = 195$ N/cm, $x_z = 0.45$ cm, $x_0 = 0.09$ cm), the process of changing $p(t)$ (curve 6) partially differs from the given $p_{theor}(t)$ (curve 5). In this case, the pressure deviation during the acceleration is insignificant (up to 7%).

Slight discrepancies (Fig. 2b) of the real $p(t)$ and the given $p_{theor}(t)$ pressure curves are represented by the dependence of the dynamics of the change in $I_p(t)$ (curve 6). The value of the optimization criterion for the pressure is $I_p = 1.45\%$.

It should be noted (Fig. 2c) that the change in the angular velocity $\omega(t)$ when optimizing the parameters of the safety valve ($C_x = 185$ N/cm, $x_z = 0.43$ cm, $x_0 = 0.1$ cm) during acceleration (curve 5) differs significantly from the given $\omega_{theor}(t)$ (curve 6). The noted discrepancies between the real $\omega(t)$ and given $\omega_{theor}(t)$ curves of the change in the angular velocity (Fig. 2d) are represented by the dependence $I_\omega(t)$ (curve 6). The value of the optimization criterion is $I_\omega = 3.11\%$.

The duration of the acceleration process (Fig. 2b and d – curves 5) is also different and amounts to $T_{t.p} = 1.39$ s for the pressure and $T_{t.p} = 1.75$ s for the angular velocity, respectively.

As a result of the studies, the following statements can be made: the optimal settings of the safety valve: $C_x = 185$ N/cm, $x_z = 0.43$ cm, $x_0 = 0.1$ cm provide deviations of the pressure change $p(t)$ in the mechatronic system with a hydraulic drive active working bodies of the self-propelled equipment, from given $p_{theor}(t)$ with an error of $I_p = 0.17\%$. Deviations of the angular velocity $\omega(t)$ from the given $\omega_{theor}(t)$ with an error of $I_\omega = 0.67\%$ are provided by the settings of the safety valve: $C_x = 195$ N/cm, $x_z = 0.45$ cm, $x_0 = 0.09$ cm.

5   Conclusions

As a result of the research, a technique was developed with elements of multi-criteria optimization that allows designing a hydraulic mechatronic system with specified output characteristics. The optimization parameters of the controls of the mechatronic system with a hydraulic drive of the active working bodies of self-propelled vehicles are substantiated.

The analysis of optimization criteria shows that the optimal settings of the safety valve provide deviations of the pressure change with an error of 0.17% and the angular velocity – 0.67% of the set. For pressure, the optimal settings of the safety valve are: C_x = 185 N/cm, x_0 = 0.1 cm and x_z = 0.43 cm, and for the angular velocity – C_x = 195 N/cm, x_z = 0.45 cm and x_0 = 0.09 cm.

References

1. Stryczek, J., Bednarczyk, S., Biernack, K.: Strength analysis of the polyoxymethylene cycloidal gears of the gerotor pump. Arch. Civil Mech. Eng. **14**(4), 647–660 (2014). https://doi.org/10.1016/j.acme.2013.12.005
2. Stryczek, J., Bednarczyk, S., Biernack, K.: Gerotor pump with POM gears: design, production technology, research. Arch. Civil Mech. Eng. **14**(3), 391–397 (2014). https://doi.org/10.1016/j.acme.2013.12.008
3. Panchenko, A., Voloshina, A., Milaeva, I., Panchenko, I., Titova, O.: The Influence of the form error after rotor manufacturing on the output characteristics of an orbital hydraulic motor. Int. J. Eng. Technol. **7**(4.3), 1–5 (2018). https://doi.org/10.14419/ijet.v7i4.3.19542
4. Panchenko, A., Voloshina, A., Kiurchev, S., et al.: Development of the universal model of mechatronic system with a hydraulic drive. East.-Euro. J. Enterp. Technol. **4**(7(94)), 51–60 (2018). https://doi.org/10.15587/1729-4061.2018.139577
5. Panchenko, A.I., Voloshina, A.A.: Planetary Rotary Hydraulic Motors, Calculation and Designing. Publishing and Printing Center "Lux", Melitopol (2016)
6. Voloshina, A., Panchenko, A., Boltyansky, O., Panchenko, I., Titova, O.: Justification of the kinematic diagrams for the distribution system of a planetary hydraulic motor. Int. J. Eng. Technol. **7**(4.3), 6–11 (2018). https://doi.org/10.14419/ijet.v7i4.3.19544
7. Panchenko, A., Voloshina, A., Boltyansky, O., et al.: Designing the flow-through parts of distribution systems for the PRG series planetary hydraulic motors. East.-Eur. J. Enterp. Technol. **3**(1(93)), 67–77 (2018). https://doi.org/10.15587/1729-4061.2018.132504
8. Voloshina, A., Panchenko, A., Boltyansky, O., Titova, O.: Improvement of manufacture workability for distribution systems of planetary hydraulic machines. In: Ivanov, V. et al. (eds.) Advances in Design, Simulation and Manufacturing II. DSMIE 2019. LNME, pp. 732–741. Springer, Cham (2019). https://doi.org/10.1007/978-3-030-22365-6_73
9. Gamez-Montero, P., Codina, E., Castilla, R.: A review of gerotor technology in hydraulic machines. Energies **12**, 2423 (2019). https://doi.org/10.3390/en12122423
10. Rogovyi, A.: Energy performances of the vortex chamber supercharger. Energy **163**, 52–60 (2018). https://doi.org/10.1088/1757-899x/233/1/012011
11. Rogovyi, A., Khovanskyy, S.: Application of the similarity theory for vortex chamber superchargers. IOP Conf. Ser.: Mater. Sci. Eng. **233** (2017). https://doi.org/10.1088/1757-899x/233/1/012011
12. Fesenko, A., Basova, Y., Ivanov, V., Ivanova, M., Yevsiukova, F., Gasanov, M.: Increasing of equipment efficiency by intensification of technological processes. Periodica Polytech. Mech. Eng. **63**(1), 67–73 (2019). https://doi.org/10.3311/PPme.13198
13. Rogovyi, A., Khovanskyy, S., Grechka, I., Pitel, J.: The wall erosion in a vortex chamber supercharger due to pumping abrasive mediums. In: Design, Simulation, Manufacturing: The Innovation Exchange, pp. 682–691 (2019)

14. Pavlenko, I., Simonovskiy, V., Ivanov, V., Zajac, J., Pitel, J.: Application of artificial neural network for identification of bearing stiffness characteristics in rotor dynamics analysis. In: Ivanov, V. et al. (eds.) Advances in Design, Simulation and Manufacturing. DSMIE-2018. LNME, pp. 325–335. Springer, Cham (2019). https://doi.org/10.1007/978-3-319-93587-4_34

15. Pavlenko, I.V., Simonovskiy, V.I., Demianenko, M.M.: Dynamic analysis of centrifugal machine rotors supported on ball bearings by combined using 3D and beam finite element models. IOP Conf. Ser.: Mater. Sci. Eng. **233**(1) (2017). https://doi.org/10.1088/1757-899x/233/1/012053

16. Gaydamaka, A., Kulik, G., Frantsuzov, V., et al.: Devising an engineering procedure for calculating the ductility of a roller bearing under a no-central radial load. East.-Eur. J. Enterp. Technol. **3**(7(99)), 6–10 (2019). https://doi.org/10.15587/1729-4061.2019.168145

17. Altare, G., Rundo, M.: Computational fluid dynamics analysis of gerotor lubricating pumps at high-speed: geometric features influencing the filling capability. J. Fluids Eng. **38**(11) (2016). https://doi.org/10.1115/1.4033675

18. Chiu-Fan, H.: Flow characteristics of gerotor pumps with novel variable clearance designs. J. Fluids Eng. **137**(4) (2015). https://doi.org/10.1115/1.4029274

19. Van de Ven, J.D.: On fluid compressibility in switch-mode hydraulic circuits. Part I: modeling and analysis. J. Dyn. Syst. Meas. Control **135**(2) (2012). https://doi.org/10.1115/1.4023062. 021013-021013-13

20. Van de Ven, J.D.: On fluid compressibility in switch-mode hydraulic circuits. Part II: experimental results. J. Dyn. Syst. Meas. Control **135**(2) (2012)., https://doi.org/10.1115/1.4023063. 021014-021014-7

21. Karpus, V.E., Ivanov, V.A.: Choice of the optimal configuration of modular reusable fixtures. Russ. Eng. Res. **32**(3), 213–219 (2012). https://doi.org/10.3103/S1068798X12030124

22. Liaposhchenko, O.O., Sklabinskyi, V.I., Zavialov, V.L., Pavlenko, I.V., Nastenko, O.V., Demianenko, M.M.: Appliance of inertial gas-dynamic separation of gas-dispersion flows in the curvilinear convergent-divergent channels for compressor equipment reliability improvement. IOP Conf. Ser.: Mater. Sci. Eng. **233**(1), 012025 (2017). https://doi.org/10.1088/1757-899X/233/1/012025

23. Syomin, D., Rogovyi, A.: Features of a working process and characteristics of irrotational centrifugal pumps. Procedia Eng. **39**, 231–237 (2012). https://doi.org/10.1016/j.proeng.2012.07.029

24. Strutinsky, V.B., Kolot, O.V.: Simulation mathematical modeling of dissipative characteristics of hydromechanical systems. Ind. Hydraul. Pneum. **2**, 63–68 (2003)

Mathematical Modeling of the Operating Process in LS Hydraulic Drive Using MatLab GUI Tools

Oleksandr Petrov[(✉)] , Andrii Slabkyi , Inna Vishtak ,
and Leonid Kozlov

Vinnytsia National Technical University,
95, Khmel'nyts'ke Hwy, Vinnytsia 21021, Ukraine
`petrovov@vntu.edu.ua`

Abstract. The main objective of this research is to describe the LS hydraulic drive based on a multimode directional control valve, for the most important operation of the hydraulic drive, to develop a mathematical model, to describe the developed mathematical model in the MATLAB system, to develop a software module in the MATLAB system for conducting theoretical studies of the mathematical model of the hydraulic drive. The subject of research is working processes in the LS hydraulic drive, a mathematical model of the LS hydraulic drive. Methods of mathematical modelling of differential equations of a nonlinear mathematical model, development of software module analytical methods were used in the research. The result of the research is the mathematical model of the LS hydraulic drive in the form of a system of differential equations and the scheme in the MATLAB Simulink system, which provided the solution of mathematical model equations and obtaining graphs of transients in a hydraulic drive. The algorithm for data exchange in the MATLAB Simulink system and the GUI graphical interface program, which implements data exchange, allows us to investigate the influence of the parameters of a load-sensitive hydraulic drive on the amount of overregulation by the pressure of the hydraulic pump in the hydraulic drive.

Keywords: Matlab Simulink · Mathematical model · Load-sensing · Hydraulic drive · Modeling of working process

1 Introduction

Construction and agricultural machinery is mainly equipped with hydraulic drives of constant consumption, which, in comparison with load-sensing (LS) hydraulic drives, are characterized by a significant loss of power while regulating the speed of working engines [1, 2]. The development and introduction of new energy-saving systems of load-sensing hydraulic drives for replacing outdated traditional hydraulic drive systems are possible based on the results of ground-breaking studies [3, 4]. Today, such studies are conducted based on information and computer systems. But work with such systems of research requires a high level of qualification, which in the conditions of production requires

specially trained personnel. Besides, the pace of production requires quick research, to reduce the time between the project and the batch production [5, 6].

The purpose of the paper is to develop specialized programs that will allow a quick theoretical analysis of product quality without any additional research.

The following tasks must be solved:

1. developing of a mathematical model for modeling the working processes in the hydraulic drive based on the well-known hydraulic-driven load-sensing system;
2. developing of the algorithm for data exchange, which will allow communication of the input parameters of the mathematical model, with the output - transient process in the hydraulic drive sensitive to loading;
3. developing a program of the data exchange interface, which will allow investigating the influence of hydraulic-driven parameters of a load-sensitive load on the characteristics of the hydraulic drive.

2   Literature Review

Hydraulic drive based on cylinder and the proportional directional valve is a nonlinear dynamic system with unknown parameters that depend on valve producing technology [7]. Nevertheless, a comparison between experimental researches and modelling results demonstrates that using experimental static flow characteristics allows obtaining the mathematical model of drive. This model describes the drive at frequency up to 5 Hz with enough accuracy for engineering design tasks. Modelling of the drive at higher frequency requires taking into account elasticity and dissipative properties of system elements such us high-pressure hose, pipe, connection socket, etc. and dynamic characteristic of a hydraulic power station.

A retrofitted electro-hydraulic proportional system for hydraulic excavator was introduced firstly [8]. According to the principle and characteristic of the load-independent flow distribution (LUDV) system, taking a boom hydraulic system as an example and ignoring the leakage of hydraulic cylinder and the mass of oil in it, a force equilibrium equation and a continuous equation of hydraulic cylinder were set up. Based on the flow equation of the electro-hydraulic proportional valve, the pressure passing through the valve and the difference of pressure were tested and analyzed. The results show that the difference in pressure does not change with load, and it approximates to 2.0 MPa. And then, assume the flow across the valve is directly proportional to spool displacement and is not influenced by the load, a simplified model of the electro-hydraulic system was put forward. At the same time, by analyzing the structure and load-bearing of boom instrument, and combining the equivalent moment equation of manipulator with rotating law, the estimation methods and equations for such parameters as equivalent mass and bearing force of hydraulic cylinder were set up.

Variable pump driving variable motor (VPDVM) is the future development trend of the hydraulic transmission of an unmanned ground vehicle [9]. VPDVM is a dual-input single-output nonlinear system with coupling, which is difficult to control. High-pressure automatic variables bang-bang (HABB) was proposed to achieve the desired

motor speed. First, the VPDVM nonlinear mathematic model was introduced. Then linearized by feedback linearization theory, and the zero-dynamic stability was proved. The HABB control algorithm was proposed for VPDVM, in which the variable motor was controlled by high-pressure automatic variables and the variable pump was controlled by bang-bang. Finally, the simulation of VPDVM controlled by HABB was developed. Simulation results demonstrate the HABB can implement the desired motor speed rapidly and has strong robustness against the variations of desired motor speed, load and pump speed [10].

The electro-hydraulic driving system of the load-sensitive electro-hydraulic robot designed and can satisfy the work of multiple actuators without interference at the same time, it has to load sensitive function in pressure, saves energy and responds quickly [11]. The constant pressure valve mainly affects the stability of the continuous pressure variable pump, even the whole system through the spool displacement, so it is important to ensure the stability of the spool displacement. By analyzing the different damping values between the two-way flow control valve and the main valve control chamber in the main valve block, it provides a reference for the optimization and improvement of the load sensing proportional multiplex valve [12].

The paper [13] deals with the solution of a scientific task consisting of development and research of a new hydraulic drive circuit providing highly efficient operation of the hydraulic drive control system and the necessary dynamic and static. A circuit of the load-sensing (LS) hydraulic drive based on a multimode directional control valve for the mobile working machine has been developed. A non-linear mathematical model of the LS hydraulic drive based on the multimode directional control valve has been elaborated. Theoretical research was conducted based on the mathematical model using the MATLAB software package. It was determined that the design parameters of the pressure relief valve of the multimode directional control valve, realizing the feedback, influence the dynamic and static characteristics of the LS hydraulic drive. Such values of the pressure relief valve parameters have been found which provide minimal values of stabilization error, regulation time and excessive control [14].

3   Research Methodology

The authors have developed an LS hydraulic drive with a multimode directional control valve, which provides a smaller loss of power, in different operating modes of the hydraulic drive, compared with analogues. In particular, in the hydraulic drive the constant value of the balancing pressure difference is provided in the mode of unloading of the hydraulic pump 0,3–0,4 MPa, and in the mode of adjustment of the consumption of the hydraulic motor – 0,7–0,8 MPa [15]. To research, the characteristics of the LS hydraulic drive developed its design scheme (Fig. 1).

The scheme includes (Fig. 1): a hydraulic pump 1, a multimode directional control valve 25, a hydraulic cylinder 3, working lines 28 and 31, and a tank 28. A multimode hydraulic directional control valve 25 consists of a safety-overflow Section 4 and a work Section 24. The safety-overflow Section 4 contains overflow valve 5, the safety valve 10, throttle 23, pressure hydraulic line 15, control line 12 and drainage line 16. The overflow valve 5 comprises a spool 6 with radial openings 13, a plunger 7, springs

8 and 9, auxiliary throttle 26, overflow 33 and supplemental 14 cameras. The safety valve 10 consists of a spool and a spring 11. The working section of the multimode directional control valve contains a distributive spool 2, a logic valve 17 connected to channels 29 and 30, a pressure hydraulic line 15, a control line 12, a drainage line 17, and two-way drainage folding from the pusher 18, balls 19 and 21, springs 20 and 22. The hydraulic drive works in four modes: unloading of the hydraulic pump, controlling the flow rate of the hydraulic engine, the maximum consumption of the hydraulic engine and overload protection.
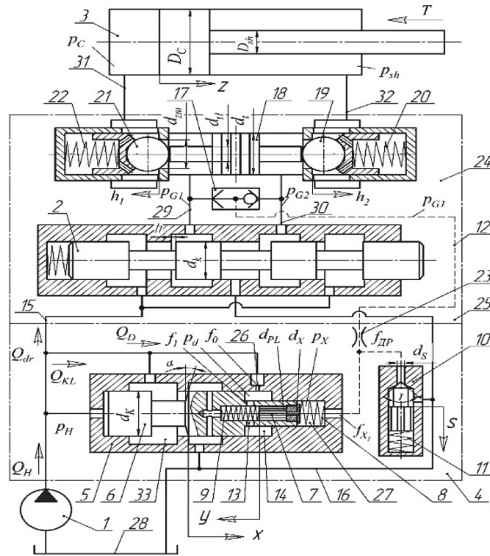
Fig. 1. Scheme of the LS hydraulic drive with a multimode directional control valve.

In the mode of unloading of the hydraulic pump at the neutral position of the distributor spool 2, working fluid is not supplied to the hydraulic cylinder. In this case, balls 19 and 21 close the drain from the chambers of the hydraulic cylinder. In the safety-overflow section, the working fluid is drained into the tank through the overflow chamber 33 due to the displacement of the spring-loaded spool 6 to the right. Also, the drain of the working fluid is closed through the auxiliary throttle 26, auxiliary chamber 14, radial holes 13 of spool 6. In this case, the radial openings 13 are opened as a result of finding the plunger 7 in the extreme right position under the action of the spring 9.

In the mode of controlling the flow rate of the hydraulic engine, the distribution spool 2 is shifted by a value h. In this case, the working fluid from the hydraulic pump 1 enters the ball of the hydraulic lock 21 through passage 29. Under the pressure of the p_H, the ball 21 is shifted to the left, and the working fluid enters the piston chamber of the hydraulic cylinder 3, where the pressure is p_C corresponding to the load T on the rod of the hydraulic cylinder 3. When this pusher 18 displaces the ball 19, providing a drain of the working fluid from the rod chamber of the hydraulic cylinder 3 through the

passage 30 and the drain line 16 into the tank. Since the pressure of the working liquid in the channel 29 exceeds the pressure in the channel 30, the logic valve 17 connects the channel 29 and the control line 12. The pressure of the control of the p_G in the control line 12 will correspond to the pressure p_C. The pressure fluid p_G flows through the control line 12 and moves the plunger 7 to the extreme left position. The plunger 7 overlaps the radial holes 13 of the spool 6 of the overflow valve 5 by stopping the working fluid drain through the auxiliary throttle 26 and auxiliary chamber 14. In this case, the working liquid from the hydraulic pump 1 enters the overflow chamber 33 and the left end of the spool 6, as well as the auxiliary chamber 14 through auxiliary choke 26. In the overflow chamber 33, the pressure of the p_H is set, and in the auxiliary chamber 14 – p_d, where $p_H = p_d$. Spool 6 will be under the action of forces formed by the pressure of p_H, p_d, p_G, and strength of spring 8. In this operating mode, with the help of the overflow valve 5, a constant equalizing pressure drop Δp is formed on the working window of the directional control valve spool. In neglecting the loss of pressure in the injection line, the value of Q_{dr} through the working window of the distributing spool to the hydraulic cylinder 3 will depend on the magnitude of the working window of the distributing spool 2 and the difference in pressure of the $p_H - p_G$ and will be maintained stable, regardless of the value of the load T on the rod of the hydraulic cylinder 3. With the unchanged position of the distributing spool and increase (or decrease) of the value of the load T on the rod of the hydraulic cylinder 3, the pressure of the hydraulic pump will be equal to $p_H = \Delta p + p_G$, where $p_G = p_C$ and the flow of the working fluids Q_{dr} remain stable.

According to the scheme (Fig. 1), a mathematical model is compiled with the following assumptions:

1. The parameters of the hydraulic drive elements are concentrated.
2. The temperature of the working fluid was considered constant.
3. The volume of lines during the transition process does not change.
4. The coefficients of flow through the throttling and spool elements are constant.
5. The mode of operation in the hydraulic drive is non-cavitational.
6. Losses of pressure in hydraulic lines were not taken into account.
7. The compliance coefficient of the gas-liquid mixture and the rubber-metal sleeves were taken into account as average values for the considered pressure ranges.
8. Wave processes in the hydraulic drive and its elements were not considered.

The mathematical model of an LS hydraulic drive based on a multimode directional control valve has the form:

$$\frac{dp_{G1}}{dt} = \frac{1}{\beta \cdot W_{G1}} \cdot \left(0,43 \cdot h - \frac{6,3}{p_H - p_{G1}} - 6,9 \cdot 10^{-4} \right) - \frac{\mu \cdot f_{zm}}{\beta \cdot W_{G1}} \cdot \sqrt{\frac{2 \cdot (p_{G1} - p_C)}{\rho}}$$

$$- \frac{\mu \cdot f_{dr}}{\beta \cdot W_{G1}} \cdot \sqrt{\frac{2 \cdot (p_{G1} - p_S)}{\rho}};$$

(1)

$$\frac{dp_H}{dt} = \frac{Q_H}{\beta \cdot W_H} - \frac{1}{\beta \cdot W_H} \cdot \left(0,43 \cdot h - \frac{6,3}{p_H - p_{G1}} - 6,9 \cdot 10^{-4}\right) - \frac{\mu \cdot \pi \cdot d_K \cdot x \cdot \sin\alpha}{\beta \cdot W_H} \cdot \sqrt{\frac{2 \cdot p_H}{\rho}}$$
$$- \frac{\mu \cdot f_0}{\beta \cdot W_H} \cdot \sqrt{\frac{2 \cdot (p_H - p_D)}{\rho}}; \tag{2}$$

$$\frac{dp_C}{dt} = \frac{dz}{dt} \cdot \frac{\pi \cdot D_C^2}{4 \cdot \beta \cdot W_C} - \frac{\mu \cdot f_{zm}}{\beta \cdot W_C} \cdot \sqrt{\frac{2 \cdot (p_{G1} - p_C)}{\rho}}; \tag{3}$$

$$\frac{dp_{sh}}{dt} = \frac{\mu \cdot f_{zm}}{\beta \cdot W_{sh}} \cdot \sqrt{\frac{2 \cdot p_{sh}}{\rho}} - \frac{dz}{dt} \cdot \frac{\pi \cdot (D_C - D_{sh})^2}{4 \cdot \beta \cdot W_{sh}}; \tag{4}$$

$$\frac{dp_D}{dt} = \frac{\mu \cdot f_0}{\beta \cdot W_D} \cdot \sqrt{\frac{2 \cdot (p_H - p_D)}{\rho}} - \frac{\mu \cdot f_1}{\beta \cdot W_D} \cdot \sqrt{\frac{2p_D}{\rho}} - \frac{dx}{dt} \cdot \frac{\pi \cdot (d_K - d_X)^2}{4 \cdot \beta \cdot W_D}$$
$$- \frac{\pi \cdot d_K \cdot \varepsilon_1^3 \cdot p_D}{48 \cdot v \cdot \rho \cdot (l_1 - x) \cdot \beta \cdot W_D} - \frac{\pi \cdot d_{PL} \cdot \varepsilon_2^3 \cdot p_D}{48 \cdot v \cdot \rho \cdot l_2 \cdot \beta \cdot W_D}; \tag{5}$$

$$\frac{dp_S}{dt} = \frac{\mu \cdot f_{dr}}{\beta \cdot W_S} \cdot \sqrt{\frac{2 \cdot (p_{G1} - p_S)}{\rho}} - \frac{\mu \cdot f_S}{\beta \cdot W_S} \cdot \sqrt{\frac{2p_S}{\rho}} - \frac{\mu \cdot f_X}{\beta \cdot W_S} \cdot \sqrt{\frac{2 \cdot (p_S - p)}{\rho}}; \tag{6}$$

$$\frac{dV_C}{dt} = p_C \cdot \frac{\pi \cdot D_C^2}{4 \cdot m_C} - \frac{T}{m_C} + \frac{b_C}{m_C} \cdot \frac{dz}{dt} - p_{sh} \cdot \frac{\pi \cdot (D_C - D_{sh})^2}{4 \cdot m_C}; \tag{7}$$

$$\frac{dV_{h1}}{dt} = \frac{2 \cdot d_{zm} \cdot h_1 \cdot (p_{G1} - p_C)}{m_{zm}} - \frac{c_{zm} \cdot (H_{zm} + h_1)}{m_{zm}}; \tag{8}$$

$$\frac{dV_{h2}}{dt} = p_{G1} \cdot \frac{\pi \cdot (d_{sh} - d_{sh1})^2}{4 \cdot m_{zm}} - \frac{p_{sh} \cdot 2 \cdot d_{zm} \cdot h_2}{m_{zm}} - \frac{c_{zm} \cdot (H_{zm} + h_2)}{m_{zm}}; \tag{9}$$

$$\frac{dV_K}{dt} = p_H \cdot \frac{\pi \cdot d_K^2}{4 \cdot m_K} - p_X \cdot \frac{\pi \cdot d_X^2}{4 \cdot m_K} - p_D \cdot \frac{\pi \cdot (d_K - d_X)^2}{4 \cdot m_K} - \frac{c \cdot (H + x)}{m_K}$$
$$- \frac{1}{m_K} \cdot \left(17 + 17,7 \cdot \mu \cdot \pi \cdot d_K \cdot x \cdot \sin\alpha \cdot \sqrt{\frac{2 \cdot p_H}{\rho}} - \frac{3,1 \cdot 10^5}{x}\right) - \frac{(\rho \cdot v \cdot \pi \cdot d_K \cdot (l_1 - x))}{m_K}; \tag{10}$$

$$\frac{ds}{dt} = \frac{p_S \cdot \pi \cdot d_S \cdot s \cdot \sin(\gamma/2)}{b_S} - \frac{c_S \cdot (H_S + s)}{b_S}; \tag{11}$$

$$\frac{dy}{dt} = p_X \cdot \frac{\pi \cdot d_{PL}^2}{4 \cdot b_1} - \frac{c_1 \cdot (H_1 + y)}{b_1}. \tag{12}$$

The MATLAB program was used to solve mathematical model equations [16]. Direct access to mathematical, graphic and software MATLAB provides the Simulink module [17]. The Simulink module provides nonlinear simulation, which can be done either through the menu or through the command line [18]. The results of the simulation are displayed during the process, and you can change the parameters of the model, even at the time of the simulation [19, 20]. The mathematical model of the LS hydraulic drive in the MATLAB program has the form (Fig. 2).

Fig. 2. Model-scheme of solving mathematical model equations.

4 Results

The authors propose an algorithm for data exchange during the research of a mathematical model in the form of a program. The algorithm includes the steps of entering data, calculating and processing the results of mathematical modelling. Data entry for calculation is performed in the program environment using the appropriate interface. After entering the data, the program runs for execution, resulting in the data fall into the MATLAB Simulink environment. The developed block diagram of the solution of the equations of the mathematical model performs the calculation. It transmits the results of the calculation in the form of state variables, which may be pressure or displacement, in the environment of object-oriented programming. In this environment, with the help of the corresponding operators, the description of the variables, their processing and the formation of the result of the calculation is carried out. The generated results are transmitted to the program, where, with the help of the appropriate interface, the result is presented in the form of dependency charts and the calculated value of overregulation on the pressure of the hydraulic pump of the hydraulic actuator.

With the built-in MATLAB Editor Graphical User Interface (GUI), the graphical processing of the calculated results of the software «PROG» was executed. After filling in the fields for entering the initial data, the calculation and construction of the transition process graph are carried out. The «PROG» script is written as a PROG.m file run by the «PROG» command, in the MATLAB command line mode.

In Fig. 3 presents a developed program at the data entry stage, for mathematical modelling.
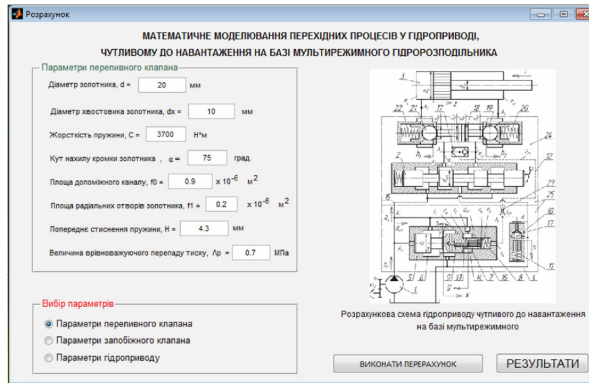
Fig. 3. The interface of the developed program (data entry).

The data are divided into three groups: the parameters of the overflow valve, the parameters of the safety valve and the parameters of the LS hydraulic drive. Parameters of overflow and safety valves include the value of their structural elements. The parameters of the LS hydraulic drive include the density and kinematic viscosity of the working oil, the coefficient of flow, the value of the diameter of the hydraulic cylinder of the hydraulic drive, etc. After entering the data, you must click the button Results.

The simulation results are presented in Fig. 4. The results are shown in the form of transients, reflecting the change in time of pressure in the hydraulic cylinder, in the hydraulic pump, moving the valve of the overflow valve and the piston of the hydraulic cylinder. Also, the program automatically calculates the amount of overregulation by the pressure of the hydraulic pump, which is presented at the bottom of the output window. Thus, in conditions of production of this hydraulic drive, it is possible to quickly investigate the influence of parameters of the components of the hydraulic drive on its characteristics without the need for additional research.
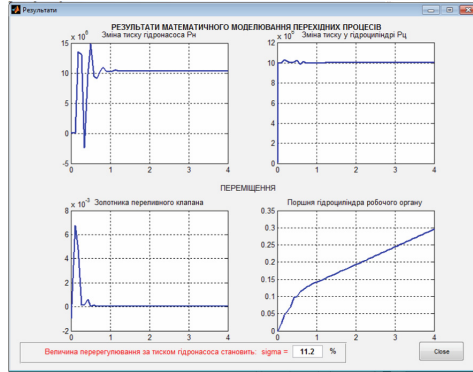
Fig. 4. The interface of the developed program (calculation results).

Implementation of the calculation of the value of the re-regulation of the pressure of the hydraulic pump in the MATLAB (GUI) system, represented by the script:

```
for i=4:1:533
x=(abs(Sigma.ans(2,i+1)-Date.ans(2,i))/Sigma.ans(2,i)*100)
if x>5
ind=i;
set(handles.hEd,'String',num2str(x,3));
set(handles.chPoint,'Enable','on');
set(handles.hEdX,'String',num2str(Sigma.ans(1,i)));
set(handles.hEdY,'String',num2str(Sigma.ans(2,i)));
set(handles.pbBuild,'Enable','off');
end
```

5   Conclusions

Based on the mathematical model of the LS hydraulic drive, a model-scheme was developed in the MATLAB Simulink environment, which ensured the solution of the equations of the mathematical model and obtaining graphs of the working processes in the hydraulic drive. The algorithm of data exchange is proposed, which using the object-oriented programming environment in MATLAB Simulink allows providing the connection of the input parameters of the mathematical model, with the outputs – the transient process in the LS hydraulic drive. Using Graphical User Interface Editor, a program has been developed in which the data exchange interface is implemented, which allows investigating the influence of parameters of an LS hydraulic drive e on the amount of overregulation by the pressure of the hydraulic pump in the hydraulic drive.

References

1. Siebert, J., Wydra, M., Geimer, M.: Efficiency improved load sensing system-reduction of system inherent pressure losses. Energies. **10**(7), 941 (2017). https://doi.org/10.3390/en10070941

2. Lovrec, D., Kastrevc, M., Ulaga, S.: Electro-hydraulic load sensing with speed-controlled hydraulic supply system on forming machines. Int. J. Adv. Manuf. Technol. **41**, 1066–1075 (2009). https://doi.org/10.1007/s00170-008-1553-y

3. Burennikov, Yu., Kozlov, L., Pyliavets, V., Piontkevych, O.: Mechatronic Hydraulic Drive with Regulator, Based on Artificial Neural Network. In: IOP Conference Series: Materials Science and Engineering, vol. 209, no. 1, p. 012071 (2017). https://doi.org/10.1088/1757-899x/209/1/012071

4. Kukhar, V., Grushko, A., Vishtak, I.: Shape indexes for dieless forming of the elongated forgings with sharpened end by tensile drawing with rupture. Solid State Phenom. **284**, 408–415 (2018). https://doi.org/10.4028/www.scientific.net/SSP.284.408

5. Obertyukh, R., Slabkyi, A., Marushchak, M., Koval, L., Baitussupov, D., Klimek, J.: Dynamic and mathematical models of the hydraulic-pulse device for deformation strengthening of materials. In: Proceedings Volume 10808, Photonics Applications in Astronomy, Communications, Industry and High-Energy Physics Experiments. Wilga, Poland (2018). https://doi.org/10.1117/12.2501519

6. Bosch Rexroth AG: Traktor-Hydraulik der nächsten Generation: Load-Sensing von Bosch Rexroth, Presseinformation PI042/17. Accessed 06 Sept 2017

7. Forental, V., Forental, M., Nazarov, F.: Investigation of dynamic characteristics of the hydraulic drive with proportional control. Procedia Eng. **129**, 695–701 (2015)

8. He, Q., Hao, P., Zhang, D.: Modeling and parameter estimation for hydraulic system of excavator's arm. J. Cent. South Univ. Technol. China **15**, 382–386 (2008). https://doi.org/10.1007/s11771-008-0072-1

9. Yan, Wang, Ze, Z., Xu-qing, Q.: Modeling and control for hydraulic transmission of unmanned ground vehicle. J. Central South Univ. **21**(1), 124–129 (2014)

10. Pavlenko, I., Trojanowska, J., Gusak, O., et al.: Estimation of the reliability of automatic axial-balancing devices for multistage centrifugal pumps. Periodica Polytechnica Mech. Eng. **63**(1), 52–56 (2019). https://doi.org/10.3311/PPme.12801

11. Zhang, C.Y., Chen, G.Z., Miao, C.W., Zhao, Y.F., Zhong, S.: Design and stability factors analysis of electro-hydraulic driving system for load-sensing electro-hydraulic robot. In: IOP Conference Series. Materials Science and Engineering, vol. 392, p. 062040 (2018). https://doi.org/10.1088/1757-899x/392/6/062040

12. Fesenko, A., Yevsiukova, F., Basova, Y., Ivanova, M., Ivanov, V.: Prospects of using hydrodynamic cavitation for enhancement of efficiency of fluid working medium preparation technologies. Periodica Polytechnica Mech. Eng. **62**(4), 269–276 (2018). https://doi.org/10.3311/PPme.11877

13. Pettersson, H., Krus, P., Jansson, A., Palmberg, J.O.: The design of pressure compensators for load sensing hydraulic systems. In: UKACC International Conference on Control 1996. IEE 427, p. 1456. University of Exeter, UK (1996)

14. Hagen, D., Pawlus, W., Ebbesen, M.K., Andersen, T.O.: Feasibility study of electrome-chanical cylinder drivetrain for offshore mechatronic systems. Model. Identif. Control A Nor. Res. Bull. **38**, 59–77 (2017)

15. Petrov, O., Kozlov, L., Lozinskiy, D., Piontkevych, O.: Improvement of the hydraulic units design based on CFD modeling. In: Lecture Notes in Mechanical Engineering XXII, pp. 653–660 (2019). https://doi.org/10.1007/978-3-030-22365-6_65

16. Luomaranta, M.: A stable electrohydraulic load sensing system based on a microcontroller. In: Proceedings of The Sixth Scandinavian International Conference on fluid Power. SICFP 1999, pp. 419–432. Tampere, Finland (1999)
17. Jędrzykiewicz, Z., Pluta, J., Stojek, J.: Application of the MATLAB-simulink package in the simulation tests on hydrostatic systems. Acta Montanistica Slovaca, Ročnik **3**(1), 29–36 (1998)
18. Lovrec, D., Ulaga, S.: Pressure control in hydraulic systems with variable or constant pumps. Exp. Tech. (Westport Conn.) **31**(2), 33–41 (2007). https://doi.org/10.1111/j.1747-1567.2007.00146.x
19. Berg, H., Ivantysynova, M.: Design and testing of a robust linear controller for secondary controlled hydraulic drive. Proc. Inst. Mech. Eng. Part I **213**, 375–386 (1999)
20. Čerkala, J., Jadlovska, A.: Methodology for experimental identification of the laboratory hydraulic system. Int. J. Eng. **3**, 33–40 (2014). Annals of Faculty Engineering Hunedoara

Gravitational Relief with Spiral Gutters, Formed by the Screw Movement of the Sinusoid

Sergiy Pylypaka[1] , Tatiana Volina[2(✉)] , Mikola Mukvich[3] ,
Galina Efremova[4] , and Olena Kozlova[5]

[1] National University of Life and Environmental Sciences of Ukraine,
15б Heroiv Oborony Street, Kiev 03041, Ukraine
[2] Sumy National Agrarian University, 160, Herasyma Kondratieva Street,
Sumy 40000, Ukraine
t.n.zaharova@ukr.netsu
[3] Separated Subdivision of National University of Life and Environmental
Sciences of Ukraine "Nizhyn Agrotechnical Institute",
10, Shevchenka Street, Nizhyn 16600, Ukraine
[4] Sumy Regional Institute of Postgraduate Pedagogical Education,
5, Rymskogo-Korsakova Street, Sumy 40007, Ukraine
[5] Sumy State Pedagogical University named after A.S. Makarenko,
87, Romens'ka Street, Sumy 40002, Ukraine

Abstract. The differential equations of the particle movement along a rough screw surface formed by the screw motion of a sinusoid under the action of the force of its weight are composed in the article. The sinusoid is located on a vertical plane and is an axial cross-section of the helical surface. The equations are solved by numerical methods and trajectories of a particle movement along a helical surface are constructed. Graphs of changing particle velocity and its distance from the surface axis were also received. The conditions of the stabilization of the particle movement are found. It is shown that in the general case, as a result of acceleration, the particle moves away from the surface axis and stops in one of its gutters. The changing of constant coefficients can control the depths and density of the gutters. In the particular case at zero depth of the gutter, a sinusoid becomes a straight line and the particle moves along the surface of the screw conoid.

Keywords: Axial cross-sectional curve · Friction coefficient · Particle · Movement trajectory · Differential equations

1 Introduction

To begin with, screw surfaces are widely spread in technology. It is the working bodies of many machines. For example, devices with a vertical screw gutter, which are called screw separators, are used in the mining industry for the enriching of minerals [1, 2]. It is a well-known fact, that screw gutters can have a different shape. The nature of the movement of the technological material along the helical surface depends on it.

The shape of the gutter depends on its axial cross-section curve. To accurately describe the movement of a body along a helical surface, it is necessary to take into account additional inertia forces from its rotation, which is extremely difficult to do. Therefore, in many cases, these forces are neglected if body sizes or angular velocities of its rotation are small [3, 4], such as, for example, when they are moved using hoisting-and-transport machines [5].

2   Literature Review

It is clear, that the particles of material constantly contact with the surfaces of the working bodies in working machines. In agricultural production, this applies to tillage tools [6] or tools for cleaning manure [7]. When a material is separated, particles move along an oscillating surface [8, 9]. A great deal is being written and said about the fact, that particles of material in contact with the surface may have a different origin: particles in a moving stream, mechanical particles, particles of a liquid or a gas [10, 11]. The movement of particles that are in contact with moving spiral working bodies, considered in the articles [12, 13]. Furthermore, the motion of particles on the surface of a rotating vertical helicoid is studied in [14]. In many cases, to simplify calculations, it is customary to consider the body as a material particle. Against this background, the research is aimed at ensuring the reliable mathematical model of particle motion in a helical surface with a given curve of its axial cross-section, namely: a sinusoid. The resulting surface consists of identical gutters located at different distances from the axis of the surface.

3   Research Methodology

Let us start with the fact that the sinusoid, which is taken as the axial cross-sectional curve of the helical surface, is given by parametric equations in the vertical plane. In the coordinate system x0z (see Fig. 1, a), the sinusoid equations in the function of the independent variable ρ are:

$$x = \rho; \qquad z = c \sin a\rho, \tag{1}$$

where a and c are constants, specifying the amplitude and period of the sinusoid; ρ is an independent variable that characterizes the distance from the current point of the sinusoid to the 0z axis (see Fig. 1, a).

Clearly, for the creation of a helical surface, it is essential to rotate uniformly the plane with the sinusoid (1) around the 0z axis while moving it along this axis, that is, to give the plane a screw motion. The set of curve positions in such a motion will describe a helical surface. Mathematically, such a surface is described by parametrical equations:

$$X = \rho \cos \alpha; \qquad Y = \rho \sin \alpha \qquad z = c \sin a\rho + b\alpha, \tag{2}$$

where b is a screw parameter. It is a constant value that specifies the lead of the helix (the lead is H = 2πb);

α is the second independent variable of the surface (the angle of rotation of the plane in which the sinusoid is located, around the vertical axis OZ).

In Fig. 1, the vertical axis is indicated by the lowercase letter "z", and for the axes of the surface (2), the capital "Z" is used. To distinguish the equations of the surface and the lines (in particular, the lines on the surface, when their equations are completely equal), the capital letters "X", "Y", "Z" are used to designate the axes and equations of the surface, and for the axes and equations of the lines – lowercase "x", "y", "z".

In Fig. 1, a the arc of a sinusoid is constructed at a = 3, c = 0.4 and the changing of the distance ρ is within the limits ρ = 0.2π…1.5π, and in Fig. 1, b – the corresponding screw surface within one lead at b = 0.5.
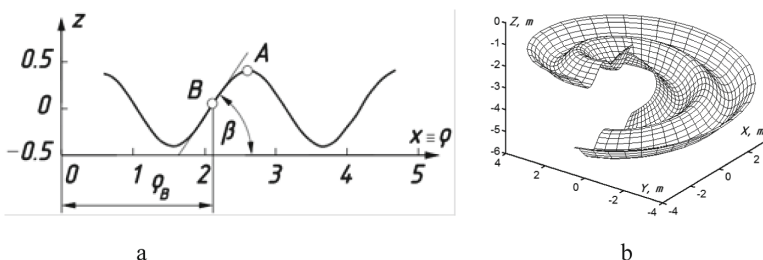
Fig. 1. To the formation of a helical surface, when the axial cross-section curve is a sinusoid: a) axial cross-section curve (1) with a = 3, c = 0.4; b) screw surface within one lead.

The differential equation of particle motion along a helical surface (2) is composed in the form $m\overline{w} = \overline{F}$, where m is the mass of the particle, $\overline{w}$ is the acceleration vector, $\overline{F}$ is the resulting vector of forces applied to the particle. These forces are the particle weight force mg (g = 9.81 m/s^2), the surface reaction R and the friction force f·R resisting the particle sliding on the surface (f is the friction coefficient). It is necessary to write the reduced vector equation in projections on the coordinate axes. As a result, one obtains a system of three differential equations.

To compose the equations, it is essential to know the unit vectors defining the direction of the applied forces. Firstly, the weight force of the particle mg is directed downwards, that is, in the opposite direction to the direction of the OZ axis, therefore its unit vector is:

$$\{0; \; 0; \; -1\} \tag{3}$$

Secondly, the reaction force R is directed along the normal to the surface. The coordinates of the surface normal vector $\overline{N}$ are found as the vector product of two vectors tangent to the coordinate lines. The projections of these vectors are partial first-order derivatives of the surface (2):

$$\begin{aligned} \dot{X}_\rho &= \cos\alpha; & \dot{Y}_\rho &= \sin\alpha; & \dot{Z}_\rho &= ac\cos a\rho; \\ \dot{X}_\alpha &= -\rho\sin\alpha; & \dot{Y}_\alpha &= \rho\cos\alpha; & \dot{Z}_\alpha &= b. \end{aligned} \tag{4}$$

The subscript denotes the variable by which differentiation is made. The direction of the surface normal vector is reversed if the rows in the vector multiplication determinant (4) are interchanged. Therefore, it is necessary to ensure that the projection onto the OZ axis of the obtained vector is positive, which corresponds to the physical essence of the process. Let us find the vector product of the tangent vectors (4):

$$\overline{N} = \begin{vmatrix} X & Y & Z \\ \dot{X}_\rho & \dot{Y}_\rho & \dot{Z}_\rho \\ \dot{X}_\alpha & \dot{Y}_\alpha & \dot{X}_\alpha \end{vmatrix} = \left\{ \begin{array}{c} b\sin\alpha - ac\rho\cos a\rho\cos\alpha; \\ -b\cos\alpha - ac\rho\cos a\rho\sin\alpha; \\ \rho. \end{array} \right\} \tag{5}$$

Here is the normal vector (5) to a unit one, after which its projections are:

$$N_x = \frac{b\sin\alpha - ac\rho\cos a\rho\cos\alpha}{\sqrt{b^2 + \rho^2(1 + a^2c^2\cos^2 a\rho)}}; N_y = -\frac{b\cos\alpha + ac\rho\cos a\rho\sin\alpha}{\sqrt{b^2 + \rho^2(1 + a^2c^2\cos^2 a\rho)}};$$
$$N_z = \rho/\sqrt{b^2 + \rho^2(1 + a^2c^2\cos^2 a\rho)}. \tag{6}$$

Finally, the friction force is directed tangentially to the particle trajectory in the opposite direction of the velocity vector. If the independent variables ρ and α of the surface are connected by a certain dependence, then one obtains the equations of one variable, that is, lines on the surface. Let us associate the variables ρ and α using a new variable – time t. As a result, we obtain two new dependences $\rho = \rho(t)$ and $\alpha = \alpha(t)$, which define the assumed trajectory of the particle. They are unknown functions. So, it is necessary to find it.

Let us find the projections of the particle velocity using differentiating of Eqs. (2), assuming that these equations are the trajectory equations depending on one variable—time t:

$$\dot{x} = \dot{\rho}\cos\alpha - \rho\dot{\alpha}\sin\alpha; \quad \dot{y} = \dot{\rho}\sin\alpha + \rho\dot{\alpha}\cos\alpha; \quad \dot{z} = ac\dot{\rho}\cos a\rho + b\dot{\alpha}. \tag{7}$$

Then the value of the velocity V of the particle motion:

$$V = \sqrt{\dot{x}^2 + \dot{y}^2 + \dot{z}^2} = \sqrt{\dot{\rho}^2 + \rho^2\dot{\alpha}^2 + (ac\dot{\rho}\cos a\rho + b\dot{\alpha})^2}. \tag{8}$$

The unit velocity vector is found by dividing the projections (7) by the value of the speed (8):

$$T_x = (\dot{\rho}\cos\alpha - \rho\dot{\alpha}\sin\alpha)/\sqrt{\dot{\rho}^2 + \rho^2\dot{\alpha}^2 + (ac\dot{\rho}\cos a\rho + b\dot{\alpha})^2};$$
$$T_y = (\dot{\rho}\sin\alpha + \rho\dot{\alpha}\cos\alpha)/\sqrt{\dot{\rho}^2 + \rho^2\dot{\alpha}^2 + (ac\dot{\rho}\cos a\rho + b\dot{\alpha})^2}; \tag{9}$$
$$T_z = (ac\dot{\rho}\cos a\rho + b\dot{\alpha})/\sqrt{\dot{\rho}^2 + \rho^2\dot{\alpha}^2 + (ac\dot{\rho}\cos a\rho + b\dot{\alpha})^2}.$$

Acceleration of a particle in the projections on the coordinate axes can be found by differentiating the speed expressions (7):

$$\ddot{x} = (\ddot{\rho} - \rho\dot{\alpha}^2)\cos\alpha - (\rho\ddot{\alpha} + 2\dot{\rho}\dot{\alpha})\sin\alpha;$$
$$\ddot{y} = (\ddot{\rho} - \rho\dot{\alpha}^2)\sin\alpha + (\rho\ddot{\alpha} + 2\dot{\rho}\dot{\alpha})\cos\alpha; \qquad (10)$$
$$\ddot{z} = ac(\ddot{\rho}\cos a\rho - a\dot{\rho}^2\sin a\rho) + b\ddot{\alpha}.$$

Let us decompose the vector equation $m\overline{w} = \overline{F}$ in the projections on the coordinate axes OXYZ taking into account that the friction force acts along the velocity vector in the opposite direction:

$$m\ddot{x} = -fRT_x + RN_x; \quad m\ddot{y} = -fRT_y + RN_y; \quad m\ddot{z} = -fRT_z + RN_z - mg. \qquad (11)$$

Actually, after substituting into (11) the directional cosines (6) and (9) receive:

$$m\ddot{x} = -\frac{fR\,(\dot{\rho}\cos\alpha - \rho\dot{\alpha}\sin\alpha)}{\sqrt{\dot{\rho}^2 + \rho^2\dot{\alpha}^2 + (ac\dot{\rho}\cos a\rho + b\dot{\alpha})^2}} + R\frac{b\sin\alpha - ac\rho\cos a\rho\cos\alpha}{\sqrt{b^2 + \rho^2(1 + a^2c^2\cos^2 a\rho)}};$$

$$m\ddot{y} = -\frac{fR\,(\dot{\rho}\sin\alpha + \rho\dot{\alpha}\cos\alpha)}{\sqrt{\dot{\rho}^2 + \rho^2\dot{\alpha}^2 + (ac\dot{\rho}\cos a\rho + b\dot{\alpha})^2}} - R\frac{b\cos\alpha + ac\rho\cos a\rho\sin\alpha}{\sqrt{b^2 + \rho^2(1 + a^2c^2\cos^2 a\rho)}};$$

$$m\ddot{z} = -\frac{fR\,(ac\dot{\rho}\cos a\rho + b\dot{\alpha})}{\sqrt{\dot{\rho}^2 + \rho^2\dot{\alpha}^2 + (ac\dot{\rho}\cos a\rho + b\dot{\alpha})^2}}$$
$$+ R\frac{\rho}{\sqrt{b^2 + \rho^2(1 + a^2c^2\cos^2 a\rho)}} - mg. \qquad (12)$$

Besides, after substituting the second derivatives (10) into Eqs. (12), one obtains a system of differential equations describing the motion of a particle. Having solved it relatively to unknown functions $\ddot{\alpha} = \ddot{\alpha}(t)$, $\ddot{\rho} = \ddot{\rho}(t)$ and R = R (t), we receive:

$$\ddot{\alpha} = \frac{2\dot{\alpha}\dot{\rho}}{A}\left[\frac{\dot{\alpha}fb}{V} - \frac{\rho}{A}\left(1 + a^2c^2\cos^2 a\rho\right)\right] - \frac{1}{A}\left(\frac{\dot{\alpha}f\rho}{V} + \frac{b}{A}\right)\left(\dot{\alpha}^2\rho ac\cos a\rho - \dot{\rho}^2 a^2 c\sin a\rho + g\right);$$

$$\ddot{u} = \frac{\dot{\alpha}^2\rho}{A}\left[\frac{\rho^2 + b^2}{A} - \frac{\dot{\rho}\rho acf\cos a\rho}{V}\right] + \frac{1}{A}\left(\frac{f\dot{\rho}}{V} + \frac{\rho ac\cos a\rho}{A}\right)\left(2b\dot{\alpha}\dot{\rho} - g\rho + \dot{\rho}^2 a^2 c\sin a\rho\right);$$

$$R = \frac{m}{A}\left[\dot{\alpha}^2\rho^2 ac\cos a\rho - 2b\dot{\alpha}\dot{\rho} + \rho\left(g - \dot{\rho}^2 a^2 c\sin a\rho\right)\right].$$

$$(13)$$

One should not forget that in differential Eqs. (13), the symbol V denotes the particle velocity, the expression of which is induced in (8). In addition, another character A is introduced, replacing the repeating expression:

$$A = \sqrt{a^2 c^2 \rho^2 \cos^2 a\rho + \rho^2 + b^2} \,. \tag{14}$$

Finally, for finding the dependences $\alpha = \alpha(t)$ and $\rho = \rho(t)$, it suffices to solve the system of the first two Eqs. (13), because they are interconnected, and the reaction of the surface R is determined from these solutions. To solve the system, it is essential to use numerical methods.

4   Results

Let the axial cross-section of the helical surface be the sinusoid presented in Fig. 1, a. The particle falls to point A (see Fig. 1, a), that is, to the top of the ridge, which corresponds to the initial value of the distance $\rho_A = 2.6$ m. The initial speed is set in the radial direction (from the axis and to the axis of the helical surface), there is $\dot{\rho}_A = \pm 1$ m/s. When $\dot{\rho}_A = -1$ m/s, the particle begins to move from point A to the axis of the surface and moves down into the gutter, where continues downward movement (see Fig. 2, a). When $\dot{\rho}_A = 1$ m/s, the particle begins to move from point A from the axis of the surface and having made a certain path, stops. This is also seen on the graph of the velocity V changing (see Fig. 2, b).
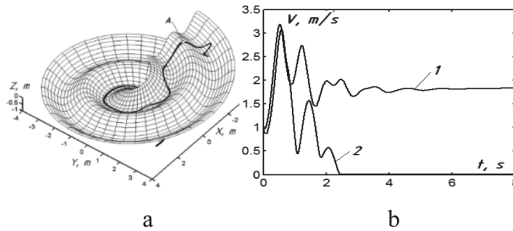
Fig. 2. Graphic illustrations of particle movement along a helical surface (motion time t = 8 s, friction coefficient f = 0.3): a) the trajectory of the particle, starting at the point A; b) the graph of the changing in the movement speed V.

In the first case, the speed stabilizes (the curve in the graph is indicated by the number 1) and approaches to a constant value of about 2 m/s. After stabilization, the trajectory of movement is a helix on the surface. In the second case (the curve in the graph is numbered 2), the particle stops after 2.5 s of movement. This is explained by the fact that as the distance from the axis increases, the angle of inclination of the helixes (probable trajectories of motion) decreases. When the angle of inclination of the helix of the gutter bottom becomes less than the angle of friction, movement becomes impossible. This angle can be found using the well-known formula $\varphi = \text{arctg}(b/\rho)$. For our case, $\rho = 3.7$ m, that is $\varphi = \text{arctg}(0.5/3.7) = 7.7°$. This is significantly less than the friction angle $\varphi_f = \text{arctg} f = \text{arctg}\ 0.3 = 16.7°$. In the first case, the angle φ exceeds the friction angle, namely, for $\rho = 1.5$ m (see Fig. 1, a), it is 18.4°.
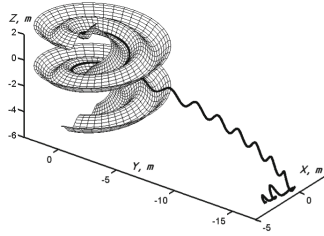
Fig. 3. The trajectory of the particle with the friction coefficient f = 0.1.

Let us consider how the trajectory of the particle changes with decreasing friction coefficient f. In Fig. 3, the trajectory of a particle with a friction coefficient f = 0.1 is constructed, which begins to move from the bottom of the gutter at ρ = 1.5 m and the initial velocity V_0 = 0.

Moreover, by analyzing the trajectory, it can be concluded that the particle accelerates along the channel to such an extent that its further movement continues from the axis of the surface, overcoming a certain number of channels and ends in the last gutter. This is confirmed by the graph of the particle velocity changing (see Fig. 4, a).

a

b
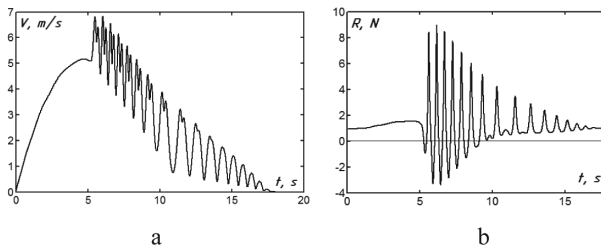
Fig. 4. Graphs of changing of the particle motion characteristics (motion time t = 18 s, friction coefficient f = 0.1): a) the graph of the movement speed V changing; b) the graph of the changing of the reaction force R for a particle of mass m = 0.1 kg.

When a particle moves along a trajectory close to the helix for a period of 5 s (see Fig. 4, b), the reaction force is a positive value. When a particle makes a wavelike motion while overcoming gutters (the surface is conventionally not shown in Fig. 3 for this part of the trajectory), the reaction of the surface R changes accordingly, taking negative values. These dependencies are derived from the mathematical condition that the particle is always on the surface. This would be true if the particle were between two equidistant surfaces, the reactions of which alternated depending on the sign. Since the surface is one, it means separation of the particle from it at the moment of the changing of the reaction sign from positive to negative. In this regard, the wave-like part of the trajectory of the particle can differ from the real one.
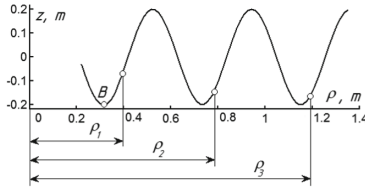
Fig. 5. Sinusoid is the axial cross-section of the helical surface for given constants a = 15, c = 0.2.

A decrease in the sinusoid period leads to a decreasing in the difference in the distance ρ between the lower helix lines of the adjacent surface gutters. As a result, the difference between their angles of inclination decreases. One can assume that this will change the nature of the movement of particles with the different friction coefficient and allow them to move along different gutters without stopping.

In Fig. 5 a sinusoid is constructed at a = 15 and c = 0.2, that is, the period is reduced by 5 times (the amplitude is reduced by 2 times, which also affects the character of the particle motion). The screw parameter of the surface is b = 35 m. Particles with a zero initial velocity and different friction coefficients were fed to the screw surface constructed from these data to the same lower point B close to the axis of the gutter surface (see Fig. 5).

This point corresponds to the distance ρ = 0.31 m. As the particle accelerates, it moves away from the axis, that is, the distance ρ increases for some time, and then the movement stabilizes (approximately 5 s later, which follows from Fig. 6, a). In Fig. 6, a) graphs of changing of the distance ρ for particles with different friction coefficients are constructed. It shows that particles with different friction coefficients f, after stabilization, move at different distances from the surface axis. At f = 0.4 the distance ρ is 0.4 m. This distance is indicated in Fig. 5 as ρ_1 and indicates the point on the sinusoid through which the helix passes – the trajectory of the particle. For particles with a friction coefficient f = 0.3 and f = 0.2, these distances are denoted as ρ_2 and ρ_3. Figure 5 shows that the trajectory of the particle passes above the gutter bottom. Researches have shown that it can not be higher than point B (see Fig. 1a). This point is the inflection point of the sinusoid and after it, the angle β begins to decrease (see Fig. 1a). The trajectory of the particle during the transition period can be above point B, remaining within the gutter, and after stabilization, it moves along a helix located below point B.

In Fig. 6b, a graph of changing of the particle motion velocity with different friction coefficients is constructed. After stabilization of the motion, the speeds become constant and differ a little from each other.
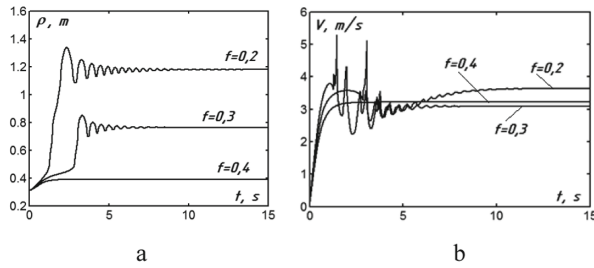
Fig. 6. Graphs of changing of the particle motion characteristics (motion time t = 15 s, particle feed distance to the gutter bottom ρ = 0.31 m): a) the graph of the changing of the distance ρ from the surface axis; b) the graph of the changing of movement speed V.

In Fig. 7, trajectories of particle motion with different friction coefficients were constructed. The lower part of Fig. 7a, b shows that the particle moves in different channels. For clarity Fig. 7 shows the horizontal projection of the trajectory without a surface. It shows how the distance ρ changes and how it begins to stabilize after a particle fall in the second gutter, approaching the mark of 0.8 m, which corresponds to Fig. 6a.

It should be noted that when a = c = 0, the surface (2) turns into a screw conoid. Then the system of Eq. (13) is greatly simplified. The result of its solution is presented in Fig. 8. It shows that the particle initially accelerates to speeds above 2 m/s while moving away from the axis of the surface, then its movement slows down due to a decrease of the surface angle. Approximately 2.5 s after the start of the movement, the particle stops.
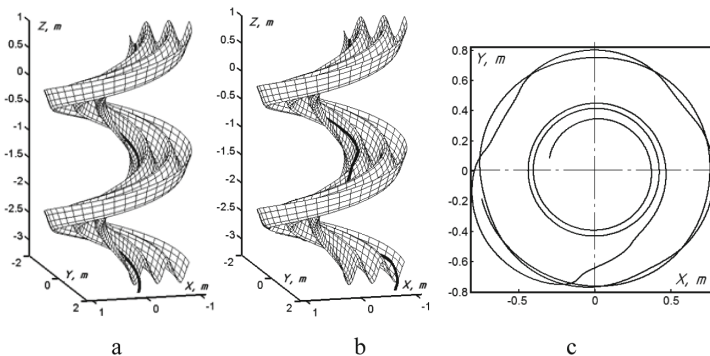
Fig. 7. Trajectories of a particle with different friction coefficient: a) the trajectory on the surface at f = 0.4; b) the trajectory on the surface at f = 0.2; c) the horizontal projection of the trajectory at f = 0.3.
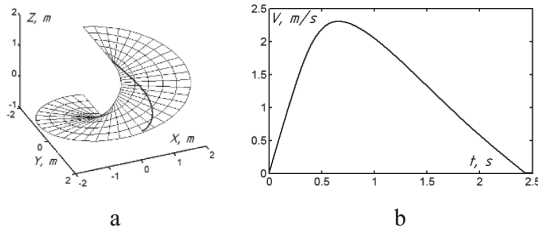
Fig. 8. Graphic illustrations of the particle motion on the surface of the screw conoid (the motion time t = 2.5 s, b = 0.35 m, f = 0.3): a) the trajectory of movement; b) a graph of the changing of movement speed V.

5   Conclusions

The obtained differential equations allow describing the particle motion along a helical surface with a sinusoid like an axial cross-section curve. The numerical solution of a system of differential equations makes it possible to study the nature of the particle motion along such a surface under the action of its weight force. When particles with different friction coefficients fall in the same point on the surface, their trajectories during subsequent movement differ from each other. It is possible to choose the constructive parameters of the surface in such a way that after stabilization of the motion of a group of particles with a practically equal friction coefficient will move along individual gutters. As the friction coefficient decreases, the distance to the gutter, along which the groups of particles move, increases. Doubtless, that this makes it possible to increase the efficiency of technological material separation by the fractions according to the friction characteristics in comparison with the existing separators with one gutter. In a particular case, the sinusoidal axial cross-section curve of the surface becomes a straight line. Then the surface is a helical conoid for which motion stabilization is impossible. Thus, after the initial acceleration, the particle stops at some distance from its axis. The received accuracy of results is quite acceptable for practice.

References

1. Chernenko, V.: Calculation of Means of Continuous Transport. Politehnika, SP (2011)
2. Matveev, A., Lebedev, I., Nikiforova, L., Yakovlev, B.: Simulation of the motion of particles in a screw pneumatic separator. Mountain Inf. Anal. Bull. (Sci. Tech. J.) **10**, 172–178 (2014)
3. Batluk, V., Basov, M., Klymets, V.: Mathematical model for motion of weighted parts in curled flow. Int. Q. J. **2**(3), 17–24 (2013)
4. Liaposchenko, O., Pavlenko, I., Nastenko, O.: The model of crossed movement and gas-liquid flow interaction with captured liquid film in the inertial-filtering separation channels. Sep. Purif. Technol. **173**, 240–243 (2017). https://doi.org/10.1016/j.seppur.2016.08.042
5. Loveikin, V., Romesevych, Yu.: Dynamic optimization of a mine winder acceleration mode. Naukovyi Visnyk Natsionalnoho Hirnychoho Universytetu **4**, 81–87 (2017)

6. Prem, M., Prem, R., Dabhi, K., Baria, A., Lepcha, P.: Use of different tillage tools for minimizing number of passes in secondary tillage operations. Int. J. Current Microbiol. Appl. Sci. **6**(12), 3109–3116 (2017). https://doi.org/10.20546/ijcmas.2017.612.363
7. Golub, G., Lukach, V., Ikalchyk, M., Tesliuk, V., Chuba, V.: Experimental study into energy consumption of the manure removal processes using scraper units. Eastern-Eur. J. Enterp. Technol. **4**(1), 20–26 (2018)
8. Pylypaka, S., Klendii, M., Zaharova, T.: Movement of the particle on the external surface of the cylinder, which makes the translational oscillations in horizontal planes. Lect. Not. Mech. Eng. **F2**, 336–345 (2019)
9. Pylypaka, S., Klendii, M., Kremets, T., Klendii, O.: Particle motion over the surface of a cylinder, which performs translational oscillations in a vertical plane. Eng. J. **22**(3), 83–92 (2018)
10. Golub, G., Szalay, K., Kukharets, S., Marus, O.: Energy efficiency of rotary digesters. Progr. Agricult. Eng. Sci. **13**(1), 35–49 (2017)
11. Kobets, A.S., Ponomarenko, N.O., Kharytonov, M.M.: Construction of centrifugal working device for mineral fertilizers spreading. INMATEH Agricult. Eng. **51**(1), 5–14 (2017)
12. Isaev, YuM, Semashkin, N.M., Nazarova, N.N.: Justification of the process of seed movement by a spiral-helical working organ. Bull. Ulyanovsk State Agricult. Acad. **1**, 97–99 (2011)
13. Adamchuk, V.V.: Investigation of the general case of dispersal of mineral fertilizers by a centrifugal dispersing body. Bull. Agrarian Sci. **12**, 51–57 (2003)
14. Pavlenko, I., Liaposhenko, A., Ochowiak, M., Demyanenko, M.: Solving the stationary hydroaeroelasticity problem for dynamic deflection elements of separation devices. Vib. Phys. Syst. **29**, 2018026 (2018)

Development of an Energy Recovery Device Based on the Dynamics of a Semi-trailer

Massimo Sicilia[1] and Marco Claudio De Simone[2(✉)]

[1] MEID4 Academic Spin-Off of the University of Salerno,
Via Giovanni Paolo II, 132, 84084 Fisciano, Salerno, Italy
[2] Department of Industrial Engineering, University of Salerno,
Via Giovanni Paolo II, 132, 84084 Fisciano, Salerno, Italy
`mdesimone@unisa.it`

Abstract. A semi-trailer is a vehicle without a power unit, whose purpose is to carry goods and materials; semi-trailers differ one from another based on the type and weight of the transported goods. In this work, we analyzed the motion dynamics of a generic articulated vehicle and developed a rigid multibody model. First, we analyzed mathematical models from literature to understand the vehicle's dynamic; secondly, we created a 3D model, based on theoretical background and typical constructive solutions; finally, we launched multibody simulations in a multi-domain environment SimScape. The results were used to evaluate the obtainable electric energy harvesting part of semi-trailer wheels' rotational kinetic energy; finally, the electric power would be stored into a battery. Having an energy recovery system mounted directly on the semi-trailer would result in great benefits both for the costs and for the environmental impact: since every utility needs the engine to be always active, with an electric source we could power every utility of the semi-trailer without using the engine so that we could avoid the unnecessarily introduction of pollutants into the atmosphere.

Keywords: Heavy vehicle · Dynamics · Vehicle · Multibody · Fuel economy

1 Introduction

A *semi-trailer* is an unpowered vehicle, typically trained by a powerful vehicle for transporting goods and materials [1]. In contrast to the classic trailer, the semi-trailer is partially supported by the motor unit, so that it can carry heavier loads [2]. As mentioned before, the semi-trailer does not have any power unit [3], which means that every movement or electric consumption must be supplied by the engine of the power vehicle [4]. It can be interesting to have an electric generator installed on the semi-trailer so that fuel is not consumed unnecessarily [5]; the electric generator will convert some kinetic rotational energy of the wheels into electric energy, so we need to understand the impact of having another resistant torque in overall vehicle's dynamics [6].

In the case of heavy vehicles, pneumatic suspension springs are used instead of conventional steel springs. An electric air pump or a motor compressor pumps the air into flexible bellows, usually in reinforced rubber. Air pressure inflates the bellows and

lifts the frame off the pin [7]. Due to the heavyweights, many possible solutions are available based on the kind of load [8]. The most used solution is the hydro-elastic axle suspension [9], which we have considered when studying the problem: this type of suspensions allows us to carry heavy loads, ensuring good stability [10, 11]. The stability of the vehicle is affected by many factors, such as the road profile or due to dynamical instabilities [12, 13]. When articulated vehicles are modelled, they are usually treated as a system of single bodies connected in various ways [14]. The natural way of dealing with such complex systems is to divide the vehicle into several rigid and flexible elements [15, 16].

Furthermore, the dynamic behavior of an articulated vehicle is also complex [17, 18]. Some significant problems need to be solved or simplified to study this mechanical problem [19, 20]. Such issues are:

- Many degrees of freedom
- Big distributions of mass
- The presence of two vehicles connected with a pin

Dynamic analysis can be carried out using mathematical models, among which the quarter car model [21] and half car model [22, 23] are the best known in the literature. These models are mainly used to study the motion of the suspended mass due to various road profiles: having well-calibrated suspension parameters allows us to absorb most of the vibrations coming from the road profile's variations, and it avoids amplification [24, 25]. Another type of analysis can be done following a multibody approach [26]: the dynamics of the entire vehicle are easier to study using multibody models [27], and the vibrational analysis can be done using a multibody model as well [28, 29].

2 Literature Review

In literature, it is possible to find many mathematical models, more or less complex, to describe the dynamics of a generic vehicle [30]. The *half-car model* is useful to describe the pitch-and-bounce dynamic of the vehicle.

The mathematical model is useful to analyze vibrations of the system because a relation between longitudinal velocity and road profile (the real cause of vibrations) can always be found.

As mentioned before, a multibody model was preferred to simulate the dynamic behavior of the articulated vehicle [31]. The multibody approach foresees to describe the dynamic of the single body with the system of equations written in the following form:

$$\mathbf{M}(\mathbf{q})\ddot{\mathbf{q}} - \mathbf{Q_v} + \mathbf{C_q^T}\boldsymbol{\lambda} = \mathbf{F} \tag{1}$$

$$\mathbf{C}(\mathbf{q}, \dot{\mathbf{q}}) = 0 \tag{2}$$

The multibody approach allows managing much more DOF than any other mathematical model thanks to its structure [32]. The kinematic constraints and joints, limit

the possible DOFs the multibody system can have, so it is possible to study more complex systems (compared to mathematical models) without significant simplifications [33]. Also, a multibody model is easier to implement and to manage in the calculator; there is a lot of software that simulates the dynamic behavior of the vehicles using a multibody approach [34, 35].

3 Research Methodology

The half-car model is typically referred to a single vehicle (Fig. 1a), but it can be easily extended like reported in Fig. 1b, while in Fig. 2, a possible decomposition of a truck is shown: it is easy to see that, based on the decomposition, the final model of the mechanical system will be more or less complex. The software used in this work named SimScape allows performing multibody analysis of any mechanical system [36]. It requires a 3D model that can be created using any 3D modeling software, so we created a 3D model of a truck using SolidWorks [37, 38].
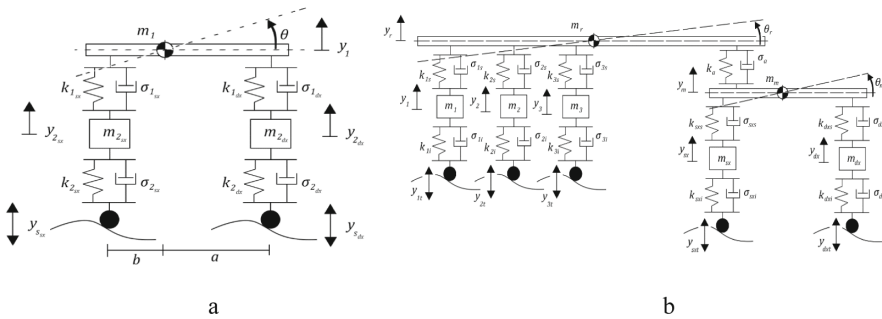
Fig. 1. Half car model scheme: classic scheme (a); half car applied to the semitrailer-truck system (b).
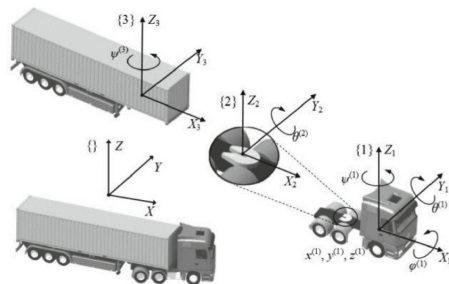
Fig. 2. A multibody decomposition of an articulated vehicle.

Considering that the focus of this work is the semi-trailer, the 3D model of the motor unit is downloaded on the net, while the semi-trailer is fully designed by the authors [39, 40]. The model is simplified, but every mechanical system needed for motion is included [41, 42]. SimScape outputs a Simulink scheme that can be used to perform simulations [43]. The final Simulink scheme is shown in Fig. 3. The solver used for the simulation is the ode45, based on an explicit Runge-Kutta (4,5) formula. In this scheme, the bodies and the kinematic constraints defined in the 3D model are present and fully editable, so that every mechanical behavior can be modelled and added to the simulation. In Simulink, the following was developed:

- A contact model between tires and road
- The behavior for the semitrailer's suspensions
- An electric machine model for energy recovery
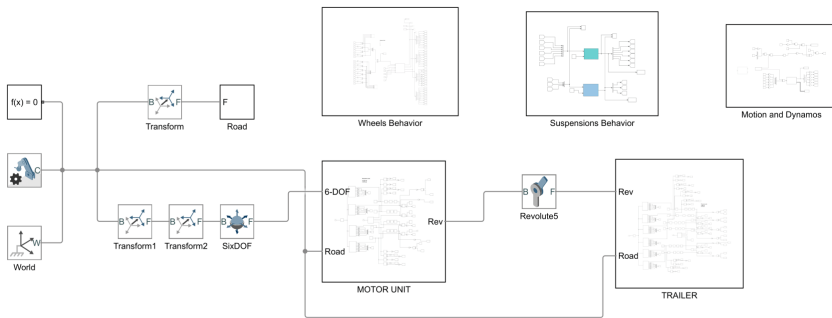
Fig. 3. SimScape multi-domain environment.

The interaction between a single tire and the road is decomposed in three fundamental components: a *normal reaction* based on the sinking of the wheel [44]; a *longitudinal reaction* based on the contact point's longitudinal velocity between the road and the tire; a *lateral reaction* introduced only to prevent every unwanted lateral motion.

$$F_n = -ky_r - \sigma\dot{y}_r, y_r < 0 \qquad (3)$$
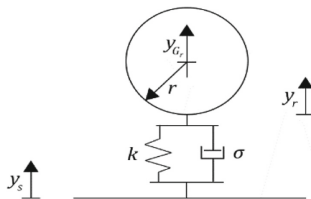
Fig. 4. Wheel schematization.

The normal reaction is shown in Eq. (3) and respects the reference systems shown in Fig. 4.

$$F_a = F_n \mu_d (v_p) \tag{4}$$

The longitudinal reaction is modeled as a friction force [45] as shown in (4), depending on the contact point's velocity between the road and the wheel.

$$F_l = -\sigma_l \dot{z}_r \tag{5}$$

This lateral reaction is introduced only to avoid every unwanted motion since that in the simulations the vehicle will follow a straight path [46]. The Eq. (5) shows the mathematical model of such force.

The semi-trailer's suspensions consist of a spring element, typically a pneumatic element [49], and a damper element, typically an oil damper [50]. To simplify, the suspensions are modelled with a torsional spring and a translational damper with their proportionality constants. This displacement is shown in Fig. 5.
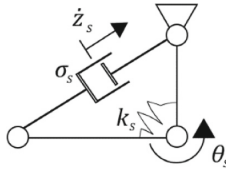
Fig. 5. Scheme of the suspension system.

The mathematical models of these two reactions are shown in Eqs. (6), (7).

$$T_s = k_s (\theta_{eq} - \theta_s) \tag{6}$$

$$F_s = -\sigma_s \dot{z}_s \tag{7}$$

To evaluate the obtainable electric energy, we added a simple DC machine model to every tire. This model needs the rotational velocity of the rotor ω (in this case, the rotational velocity of the wheel) as input and outputs electromechanical resistant torque and generated current. The machine is connected to an electric load and a battery model to store the electric energy. The DC machine follows the electromechanical Eq. (8), with ω angular velocity of the wheels.

$$J \frac{d\omega}{dt} = T_e - T_L - B_m \omega - T_f \tag{8}$$

In Table 1, the parameters used for the numerical activity are shown: these values were taken from the manuals of manufacturers of suspension for heavy trucks. The overall mass of the semitrailer complete with its load was supposed to be 30 tons, as found in the relevant regulations.

Table 1. Suspension parameters used for the simulations.

Parameters	Value
Ground stiffness coefficient k	10^8 N/m
Ground damping coefficient σ	10^4 N·s/m
Longitudinal dynamic friction coefficient μ_d	1 -
Lateral damping coefficient σ_l	10^5 N·s/m
Suspensions stiffness coefficient k_s	$2*10^6$ N·m/rad
Suspensions damping coefficient σ_s	$5*10^3$ N·s/m

We structured the model in main object blocks in which the necessary physics data is measured, while in the behavior blocks, we modeled the dynamics of the problem with the physics data collected before. The road profile was supposed to be flat for simplicity. This work aimed to test the effectiveness of an energy recovery device to be mounted on semi-trailers from an energy point of view. For this reason, we presumed to mount the current generator directly on the wheel axle.

4   Results

The purpose of the simulations was to test the effect of the additional resistant torque on the dynamics of the truck, due to the presence of the generator. Furthermore, we wanted to evaluate the amount of energy harvested during the motion. The following figures show the behavior of the vehicle at various supposed speeds and the corresponding energy accumulated by the device. For all simulations, we decided to activate the device once the cruising speed was reached.
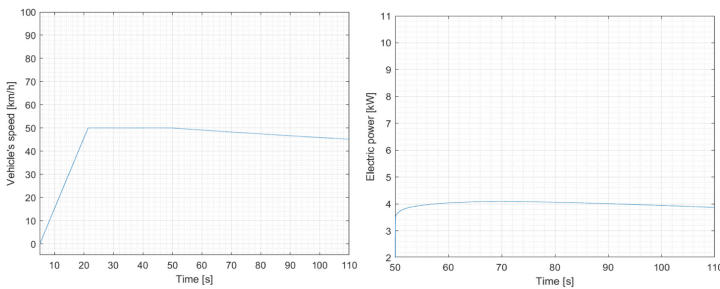
Fig. 6. Vehicle's speed profile (left); electric power generated (right) – 50 km/h target.

The first simulation is shown in Fig. 6. The impact of the devices barely affects the velocity of the vehicle, but the generated electric power is not so high.
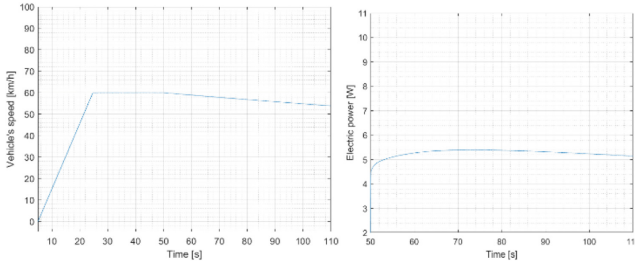
Fig. 7. Vehicle's speed profile (left); electric power generated (right) – 60 km/h target.

In Fig. 7, it can be seen how the deceleration increases with velocity. The electric power generated starts to be interesting and seems to have an approximately constant trend.
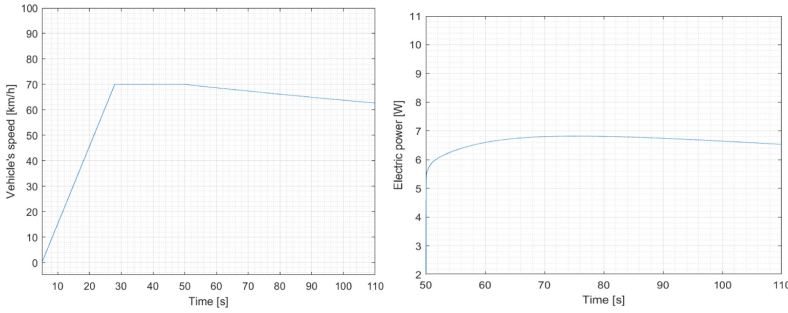
Fig. 8. Vehicle's speed profile (left); electric power generated (right) – 70 km/h target.
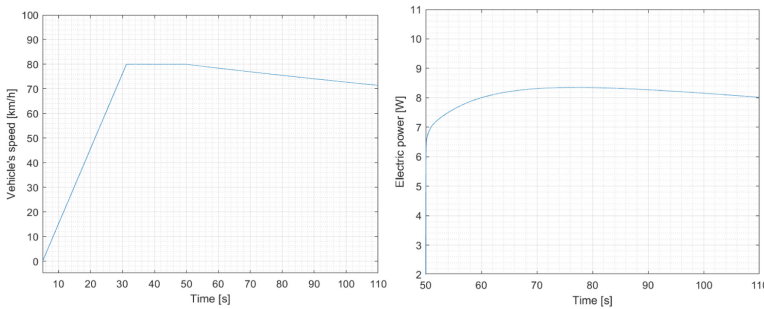
Fig. 9. Vehicle's speed profile (left); electric power generated (right) – 80 km/h target.

In Fig. 8, the deceleration of the vehicle starts to be significant, together with electric power that increases with velocity.

The final simulation reported, shown in Fig. 9 since most semi-trailers have a speed limit of 80 km/h. The electric power is enough to power many utilities on the semi-trailer, while the deceleration is now consistent: this means that the energy recovery phase can be used as regenerative braking without using regular brakes.

5 Conclusions

In this paper, the authors wanted to evaluate the feasibility of using a generator to harvest energy during the motion of a heavy vehicle. The idea is to generate electricity to power the on-board services, especially in the various stops to which the vehicles are bound by law, avoiding having to turn on the heat engine. This problem is particularly notable for refrigerated trailers, which are obliged to maintain a certain temperature for the proper conservation of the load. For this reason, a multibody model of a semi-trailer has been created, paying particular attention to the suspension system of the towed vehicle. The aim is to evaluate the forces between the wheels and the road surface, evaluating, therefore, the losses due to the presence of the generator. The simulation was conducted with the Simulink software in the Simscape multi-domain environment. For this first study, a simple DC motor was used to test the effectiveness of such an idea. The results for various speed targets reached to evaluate the electric energy at various operating conditions were reported and made it possible to conclude that:

- An electrical machine on every wheel does not affect the vehicle's overall stability;
- At low speed, the resistant electromechanical torques of the devices are neglectable;
- The electric power at high vehicle's speed is considerable.

In conclusion, we can affirm that the use of such a device onboard can have a positive influence on the reduction of fuel consumption by reducing emissions and transport costs.

References

1. Naviglio, D., Formato, A., Scaglione, G., Montesano, D., Pellegrino, A., Villecco, F., Gallo, M.: Study of the grape cryo-maceration proceedings at difference temperatures. Foods **7**(107) (2018)
2. Gao, L., Ma, F., Jin, C.: A model-based method for estimating the attitude of underground articulated vehicles. Sensors **19**(23), 5245 (2019)
3. Rivera, Z.B., De Simone, M.C., Guida, D.: Unmanned ground vehicle modelling in Gazebo/ROS-based environments. Machines **7**(2), 42 (2019)
4. Pappalardo, C.M., Wang, T., Shabana, A.A.: On the formulation of the planar ANCF triangular finite elements. Nonlinear Dyn. **89**, 1019–1045 (2017)
5. De Simone, M.C., Rivera, Z.B., Guida, D.: Obstacle avoidance system for unmanned ground vehicles by using ultrasonic sensors. Machines **6**, 18 (2018)
6. Bai, G., Meng, Y., Liu, L., Luo, W., Gu, Q., Li, K.: A new path tracking method based on multilayer model predictive control. Appl. Sci. **9**(13), 2649 (2019)
7. De Simone, M.C., Guida, D.: Identification and control of a unmanned ground vehicle by using arduino. UPB Sci. Bull. Ser. D **80**, 141–154 (2018)

8. De Ruiter, A.: Optimal design of a hydro-elastic rear axle suspension for heavy trucks. Technische Unversiteit Eindhoven (1997)
9. Pappalardo, C.M., Yu, Z., Zhang, X., Shabana, A.A.: Rational ANCF thin plate finite element. J. Comput. Nonlinear Dyn. **11**, 051009 (2016)
10. Sena, P., Attianese, P., Carbone, F., Pellegrino, A., Pinto, A., Villecco, F.: A fuzzy model to interpret data of drive performances from patients with sleep deprivation. Comput. Math. Methods Med. 868410 (2012)
11. De Simone, M.C., Guida, D.: Control design for an under-actuated UAV model. FME Trans. **46**, 443–452 (2018)
12. Concilio, A., De Simone, M.C., Rivera, Z.B., Guida, D.: A new semi-active suspension system for racing vehicles. FME Trans. **45**, 578–584 (2017)
13. Sena, P., D'Amore, M., Pappalardo, M., Pellegrino, A., Fiorentino, A., Villecco, F.: Studying the influence of cognitive load on driver's performances by a fuzzy analysis of lane keeping in a drive simulation. IFAC Proc. **2013**(46), 151–156 (2013)
14. Gögen, E., Emre Özcan, K.: The effect of dolly suspension parameters to the european modular system vehicle combination. Eur. Mech. Sci. **2**(4), 128–132 (2018)
15. Stoerkle, J.: Lateral dynamics of multiaxle vehicles. Diss. Master thesis, Institute for Dynamic Systems and Control, Swiss Federal Institute of Technology, Zürich, Switzerland **14**(2) (2013)
16. Pappalardo, C.M.: A natural absolute coordinate formulation for the kinematic and dynamic analysis of rigid multibody systems. Nonlinear Dyn. **81**, 1841–1869 (2015)
17. Sena, P., Attianese, P., Pappalardo, M., Villecco, F.: FIDELITY: fuzzy inferential diagnostic engine for on-line support to physicians. In: International Conference on the Development of Biomedical Engineering in Vietnam, pp. 396–400 (2012)
18. Spivey, C.: Analysis of ride quality of tractor semi-trailers. Clemson University All Theses, vol. 123 (2007)
19. Stoner, W. J.: Dynamic Simulation Methods for Evaluating Vehicle Configuration and Roadway Design, University of Iowa (1991)
20. Adamiec-Wójcik, I., Warmas, K.: Modelling articulated vehicles with a flexible semi-trailer. Arch. Mech. Eng. **80**(3), 389–407 (2013)
21. Nordberg, A.: Simulation of a complete truck and trailer assembly: multi body dynamics. Luleå tekniska universitet Institutionen för teknikvetenskap och matematik (2018)
22. Kushairi, S., Schmidt, R., Rahman Omar, A., Azlan Mat Isa, A., Hudha, K.: Tractor-trailer modelling and validation. Int. J. Heavy Veh. Syst. **21**(1), 64–82 (2014)
23. Salaani, M.K., Heydinger, G.J., Grygier, P.A.: Heavy tractor-trailer vehicle dynamics modeling for the national advanced driving simulator. SAE Technical Papers (2003)
24. Cheng, C., Evangelou, S.A.: Series active variable geometry suspension robust control based on full-vehicle dynamics. J. Dyn. Syst. Measur. Control Trans. ASME **141**(5), 051002 (2019)
25. Sastry, D.V.A.R., Ramana, K.V., Rao, N.M., Pruthvi, P., Santhosh, D.U.V.: Analysis of MR damper for quarter and half car suspension systems of a roadway vehicle. Int. J. Veh. Struct. Syst. **9**(1), 17–22 (2017)
26. Colucci, F., De Simone, M.C., Guida, D.: TLD design and development for vibration mitigation in structures. Lect. Not. Networks Syst. **76**, 59–72 (2020)
27. Pappalardo, C.M., Guida, D.: Development of a new inertial-based vibration absorber for the active vibration control of flexible structures. Eng. Lett. **26**(3), 372–385 (2018)
28. Liu, Q., Zhang, N., Feng, F.: Handling performance of tractor-semitrailers equipped with hydraulically interconnected suspension. Proc. Inst. Mech. Eng. Part D J. Automob. Eng. **233**(12), 3098–3111 (2019)

29. Pappalardo, C.M., Wallin, M., Shabana, A.A.: A new ANCF/CRBF fully parameterized plate finite element. J. Comput. Nonlinear Dyn. **12**, 031008 (2017)
30. Li, H.: Vibration and handling stability analysis of articulated vehicle with hydraulically interconnected suspension. J. Vib. Control **25**(13), 1899–1913 (2019)
31. Guida, R., De Simone, M.C., Dašić, P., Guida, D.: Modeling techniques for kinematic analysis of a six-axis robotic arm. In: IOP Conference Series: Materials Science and Engineering, vol. 568, no. 1, p. 012115 (2019)
32. Pappalardo, C.M., Zhang, Z., Shabana, A.A.: Use of independent volume parameters in the development of new large displacement ANCF triangular plate/shell elements. Nonlinear Dyn. **91**, 2171–2202 (2018)
33. Shastry, P., El-Gindy, M., Nguyen, N.: Pickup truck and trailer gross vehicle weight study, SAE Technical Papers (2019)
34. de Saxe, C., Cebon, D.: Estimation of trailer off-tracking using visual odometry. Veh. Syst. Dyn. **57**(5), 752–776 (2019)
35. Genta, G.: Meccanica dell'autoveicolo. Levrotto & Bella (2000)
36. Pappalardo, C.M., Guida, D.: A time-domain system identification numerical procedure for obtaining linear dynamical models of multibody mechanical systems. Arch. Appl. Mech. **88** (8), 1325–1347 (2018)
37. Villecco, F.: On the evaluation of errors in the virtual design of mechanical systems. Machines **6**, 36 (2018)
38. Formato, A., Ianniello, D., Romano, R., Pellegrino, A., Villecco, F.: Design and development of a new press for grape marc. Machines **7**, 51 (2019)
39. De Simone, M.C., Rivera, Z.B., Guida, D.: Finite element analysis on squeal-noise in railway applications. FME Trans. **46**, 93–100 (2018)
40. Lucet, E., Micaelli, A.: Stabilization of a road-train of articulated vehicles. Rob. Auton. Syst. **114**, 106–123 (2019)
41. Zhang, Y., Li, Z., Gao, J., Hong, J., Villecco, F., Li, Y.: A method for designing assembly tolerance networks of mechanical assemblies. Math. Probl. Eng. **2012**, 513958 (2012)
42. Villecco, F., Pellegrino, A.: Evaluation of uncertainties in the design process of complex mechanical systems. Entropy **19**, 475 (2017)
43. Quatrano, A., De Simone, M.C., Rivera, Z.B., Guida, D.: Development and implementation of a control system for a retrofitted CNC machine by using Arduino. FME Trans. **45**, 565–571 (2017)
44. Patel, M.D., Pappalardo, C.M., Wang, G., Shabana, A.A.: Integration of geometry and small and large deformation analysis for vehicle modelling: chassis, and airless and pneumatic tyre flexibility. Int. J. Veh. Perform. **5**, 90–127 (2019)
45. Formato, G., Romano, R., Formato, A., Sorvari, J., Koiranen, T., Pellegrino, A., Villecco, F.: Fluid–Structure Interaction Modeling Applied to Peristaltic Pump Flow Simulations. Machines **7**(50) (2019)
46. De Simone, M.C., Guida, D.: Modal coupling in presence of dry friction. Machines **6**(8) (2018)
47. Kulkarni, S., Pappalardo, C.M., Shabana, A.A.: Pantograph/catenary contact formulations. J. Vib. Acoust. **139**, 011010 (2017)
48. Sun, Q., Sun, J., Jin, Z., Sun, S.: Mode selection of tractor-and-semitrailer swap transport for ro-ro shipping under land-sea combined transportation. Maritime Policy Manag. **46**(8), 995–1010 (2019)

49. Pappalardo, C.M., Patel, M., Tinsley, B., Shabana, A.A.: Pantograph/catenary contact force control. In: ASME 2015 International Design Engineering Technical Conferences and Computers and Information in Engineering Conference. American Society of Mechanical Engineers Digital Collection, Boston, Massachusetts, USA, 2–5 August 2015, pp. 1–11 (2015)
50. Formato, A., Ianniello, D., Pellegrino, A., Villecco, F.: Vibration-based experimental identification of the elastic moduli using plate specimens of the olive tree. Machines **7**(46) (2019)

Studies of the Swirling Submerged Flow Through a Confuser

Andrii Rogovyi[1](✉) ⓘ, Serhii Khovanskyi[2] ⓘ, Iryna Hrechka[3] ⓘ,
and Anatoly Gaydamaka[3] ⓘ

[1] Kharkiv National Automobile and Highway University,
25, Yaroslava Mudrogo Street, Kharkiv 61002, Ukraine
`asrogovoy@ukr.net`
[2] Sumy State University, 2, Rymskogo-Korsakova Street, Sumy 40007, Ukraine
[3] National Technical University "Kharkiv Polytechnic Institute",
2, Kyrpychova Street, Kharkiv 61002, Ukraine

Abstract. In vortex devices, it is often required to conserve part of the energy of the swirl flow to be dispersed. One of the most rational ways to save energy is to use a confuser. The characteristic of the confuser on a swirling flow has been little studied. It was performed a numerical simulation of the operating characteristics of the confuser. To validate the mathematical model, a comparison is made with the experimental data on the expiration of a swirling jet. Validation of the results was made by comparing with the experimental results not only qualitatively, but also quantitatively in terms of velocities at characteristic points of the flow. A comparison of the flow patterns shows a fairly accurate description of the flow pattern, the attenuation of rotation, and the velocity values in different sections by a mathematical model. A comparison of the use of the SST turbulence model to the effects of streamline curvature and system rotation is presented. The application of the RANS approach using the adjusted SST turbulence model allows quickly determining all the main characteristics of the swirl flow using medium-power computers. An analysis of the operation mode of confusers of different angles on a swirling flow shows that an increase in the average speed and pressure at the outlet from the confuser with a large angle leads to the possibility of saving most of the swirling flow energy and using it in the future.

Keywords: Swirling flows · Confuser · Numerical simulation · Turbulence · Submerged flow

1 Introduction

Swirling flows are among the most common in nature. They are found in some natural phenomena: tornado and cyclone [1]. Often swirling flows are used in technology: hydrocyclones, dust collectors, fuel combustion, vortex valves, ejectors, mixers and centrifuges [2, 3]. Unlike classical swirl-free flows, which in most cases can be calculated using fairly simple equations, swirl flows require calculations using the Navier-Stokes equations, or significant simplifications for asymptotic solutions [4]. In the practice of designing vortex devices, it is often to face with swirling submerged flows [5, 6].

2   Literature Review

Unlike a direct-flow flooded jet, for which there are dependencies for calculating the main parameters, for a swirling jet, it is necessary to undertake new calculations each time taking into account the degree of swirl [7]. To this date, a lot of experimental and numerical studies of such a flow have been carried out and many dependencies have been obtained that can help researchers evaluate the main parameters [8–11]. But, if at least one of the parameters goes beyond the scope of those studied in these works, then it is necessary to conduct independent calculations or experiments. This requires the development of adequate algorithms and methods for calculating swirling jets with the ability to qualitatively evaluate parameters with minimal computing resources.

In many hydraulic devices, it becomes necessary to use the energy of a swirling jet: vortex chamber superchargers [12], turbines [13], pumps [14, 15], cyclones. Most often, the swirling flow is either thrown out or is not fully used with the help of guide vanes. On the other hand, the use of classical flow direction methods has drawbacks when being used for swirling flows. Even, the use of confuser leads to the appearance of a "vortex effect of confuser". Similar problems are also encountered in the design of mechatronic hydraulic drive systems, where swirling flows arise in pumps, engines, and equipment components and the task of preserving their energy for further use is posed [16–19]. There are two approaches to the study of swirling flows: experimental and calculated using computational fluid dynamics (CFD) [20, 21]. To this date, there is a huge number of studies of coherent vortex structures that occur during the expiration of swirling jets. However, there is still no clear understanding of the features of their rotation and their quantity, depending on the swirl number.

In addition, it is rather complicated to apply the results of these studies, often obtained using modern methods of experimental and numerical research (PIV techniques, Direct Numerical Simulation (DNS) and Large Eddy Simulation (LES) methods of numerical analysis) for engineering purposes. Therefore, it becomes relevant to a search for procedures of adequate numerical calculation and their application in engineering analysis, especially when external flow parts, such as diffusers and confusers, are entered into a rotating flow.

When optimizing flow parameters, CFD calculations are the best way, with further verification of the adequacy by experimental researches [22–25].

The work is aimed at studying the work of the confuser on swirling flows. The influence of the main parameters of the flooded swirling jet on the possibility of conserving the energy of the swirling flow and its use in the future was determined.

3   Research Methodology

The research was carried out in two stages. First, a swirling flooded jet was investigated and the flow parameters were compared with experimental data. When calculating the jet, the most suitable number of elements, the turbulence model and corrections to it were analyzed. After it was confirmed that the use of the mathematical model leads to adequate results of the calculation of the characteristics of the swirling flow, the operation of the confuser was studied. The calculations were carried out in the OpenFoam open-source CFD software.

4   Results

4.1   Computational Model

To this date, there is a fairly large number of software systems for CFD calculations, which include many different turbulence models on a paid and free basis [26]. The use of these complexes involves preliminary preparation of the geometry of the flow part using 3D geometry modeling packages [27–29], as well as structural strength calculations if necessary [30–34]. Many authors conclude that the free OpenFoam system is one of the best for such calculations. In addition, one of the best turbulence models is a modified two-layer "$k − \omega$" model of Menter's shear stress transfer turbulence (SST model [35–37]), which takes into account the features of the flow near solid walls and in the external flow. At the same time, the use of DNS and LES, as well as hybrid models, can lead to more accurate solutions [38], however, this often leads to hard to overcome computational costs now.

The system of equations of the SST model adjusted for the effects of streamline curvature and system rotation is as follows [12, 37]:

$$
\begin{aligned}
\frac{\partial(\rho k)}{\partial t} + \frac{\partial}{\partial x_j}\left(\rho u_j k\right) &= \frac{\partial}{\partial x_j}\left(\mu_{ef}\frac{\partial k}{\partial x_j}\right) + P_k - \beta * \rho k\omega; \\
\frac{\partial(\rho\omega)}{\partial t} + \frac{\partial}{\partial x_j}\left(\rho u_j\omega\right) &= \frac{\partial}{\partial x_j}\left(\mu_{ef}\frac{\partial \omega}{\partial x_j}\right) - \rho\beta\omega^2 + Cd_\omega + \alpha\frac{\rho}{\mu_t}P_k,
\end{aligned}
\tag{1}
$$

where x_j – Cartesian coordinates; u_j – Cartesian velocity components; ρ – density; $\mu_{ef} = \mu + \mu_t$ – effective viscosity; μ_t – turbulent viscosity; μ – molecular viscosity; t – time; k – the kinetic energy of turbulent pulsations; P_k – production of turbulence kinetic energy; Cd_ω – cross-diffusion term in SST model; α, β, β^* – empirical constants of the SST model; ω – turbulence eddy frequency.

Constants and details relating to Eqs. (1) can be found in [37].

Mathematical modeling of the flow was carried out with the following boundary conditions: on the wall – no-slip wall $\overline{V}\big|_b = 0$, the value of two velocity components was set in the inlet section: axial V_z and tangential $V_\tau = \omega r$, in the output channels, the pressure was equal to zero $p\big|_b = 0$. The calculation was carried out in a steady-state setting for an incompressible fluid – water.

The standard OpenFoam solver was used based on the control volume method and the PISO algorithm. The calculation continued until the residuals of all equations were reduced to values 10^{-5}. To estimate the required number of grid elements, three grids were selected, consisting of tetragonal and prismatic elements near walls. The coarse grid was with the number of elements of 1 million, the normal - 6 million and the fine - 12.5 million. The results of calculations on the normal and fine mesh showed a discrepancy of not more than 3%, which led to the conclusion that the normal mesh partition was sufficient for research with the 6 million numbers of elements. All grid partitions provided the parameter $y^+ < 2$.

4.2   Model Verification

To confirm the possibility of using the above mathematical model in the class of problems solved in the study, the calculation results were compared with experimental data [39].
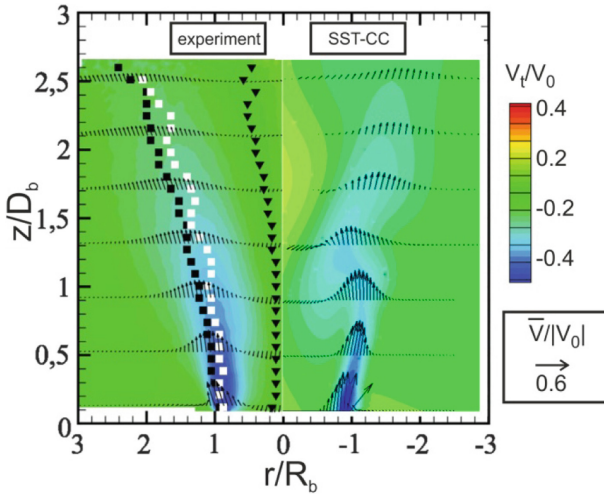
Fig. 1. Velocity decay. Contours of normalized tangential velocity (level of color) for experimental data (left) and calculating data (right) flows. $V_0 = 13$ m/s.

A comparison of the experimental results (Fig. 1 and 2 on the left) with the calculation (Fig. 1 and 2 on the right) was performed with the same swirl number $S = 1, 4$. It required a few calculations and the choice of the one for comparison in which $S = 1, 4$. The experimental data were obtained using the stereo-PIV technique, the features of which can be found in the article [39], where the experimental results were taken from. The nozzle exit diameter was selected $D_b = 38$ mm.

Figure 1 and 2, the tangential and axial velocities are related to the maximum absolute velocity of the swirling flow at the exit of the nozzle (V_0). Analyzing the figures, we can conclude that the mathematical model adequately describes the flow of a swirling jet, especially in the longitudinal plane. In cross-sections, there is a lack of the necessary reverse flow, which is associated with a lack of the necessary determination of the vacuum pressure near the axis of the swirling flow. This drawback of RANS models in general and SST models, in particular, are known and described in many works [9, 12, 23, 37]. To minimize this effect, a correction of the turbulence model was applied to take into account the rotation and curvature of streamlines. However, the possibilities of such adjustment are also limited and did not lead to a complete coincidence of experimental and calculated data.
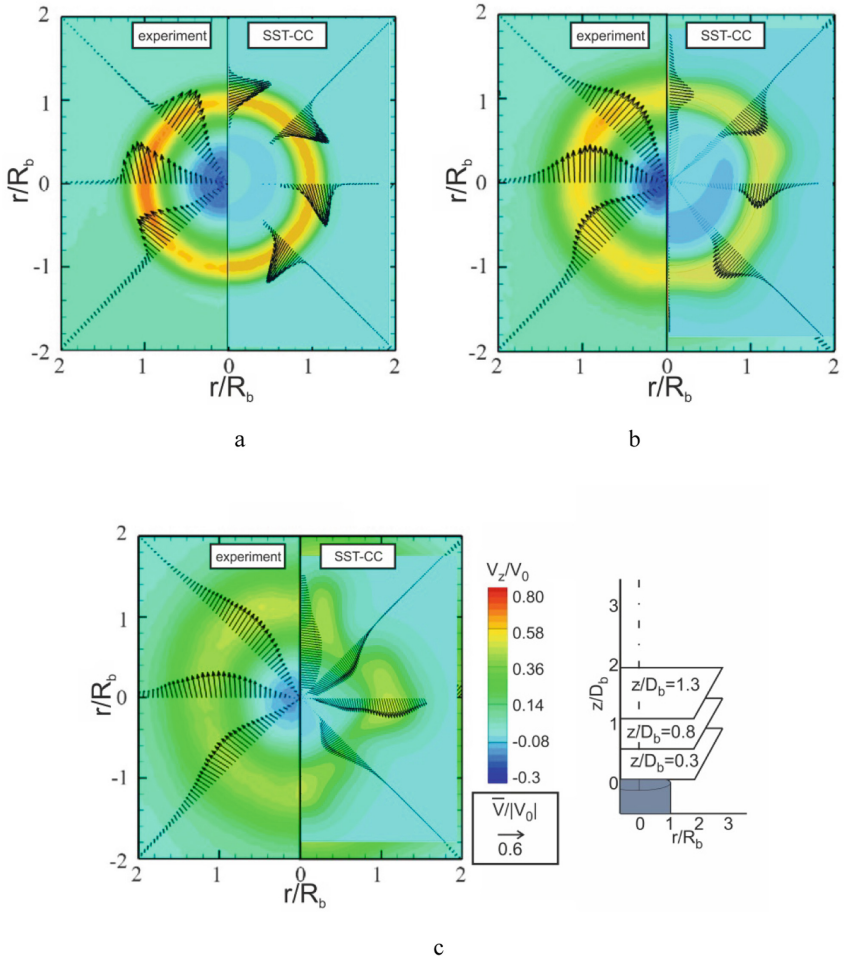
Fig. 2. Contours of normalized axial velocity (level of color) for experimental data (left) and calculating data (right) flows in three transverse planes: a) $z/D_b = 0,3$; b) $z/D_b = 0,8$; c) $z/D_b = 1,3$. $V_0 = 13$ m/s.

On the other hand, a comparison of flow patterns (Fig. 1) shows that the model describes the flow shape, the magnitude of the attenuation of rotation, and the velocity values in different sections quite correctly. Thus, we can conclude that it is possible to use the selected mathematical model for studying the behavior of a swirling flooded jet.

4.3   The Flow of a Swirling Jet Through the Confuser

By definition, a confuser is a pressure pipe that tapers downstream. For direct flows, the movement of fluids in the confuser is accompanied by an increase in velocity and a drop in pressure. The resistance of the confuser with equal geometric proportions is always less than in the confuser. The swirling flow significantly affects the above conclusions, due to a change in pressure in the cross-section and the occurrence of a decrease in pressure near the axis, as well as an increase in it at the periphery, which is a consequence of the action of centrifugal force. The degree of centrifugal force influence can be estimated using the swirl number.

In this study, it was considered the use of two confusers with different opening angles for the direction of a swirling flooded jet, with a degree of swirl similar to that, which occurs in vortex chamber superchargers [3, 5, 12, 35].
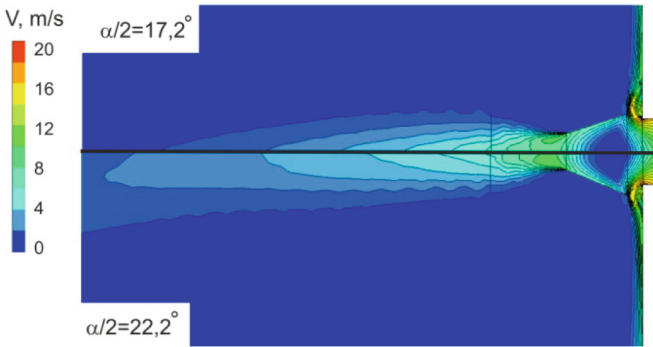
Fig. 3. Contours of the velocity of a swirling jet in the confusers of different angles.

Figure 3 shows the velocity fields for the flow of a submerged swirling jet passing through confusers with angles $\alpha/2 = 17,2°$ and $22,2°$. An increase in the average flow velocity is observed when using a confuser with an angle $\alpha/2 = 22,2°$, which leads to the possibility of preserving most of the energy of the swirling flow. Figure 3 illustrates an increase in the region of decay of the jet velocity in the case of the passage of the confuser $22,2°$, which confirms, at a qualitative level, the conclusion about an increase in the stored energy in such a confuser. A similar conclusion can be reached when studying the pressure distributions shown in Fig. 4.
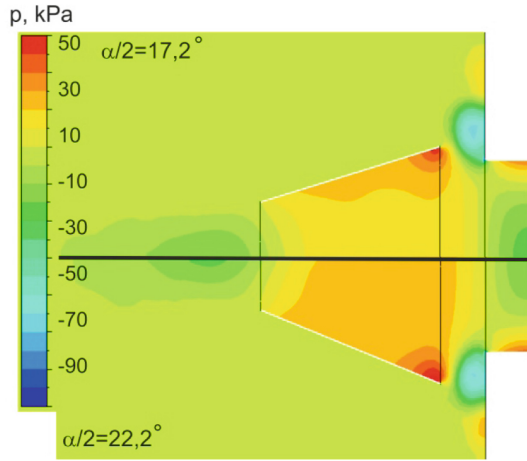
Fig. 4. Contours of the static pressure of a swirling jet in the confusers of different angles.

At an angle of confuser $22, 2°$, the average pressure in the confuser is higher than for a confuser with an angle $17, 2°$.
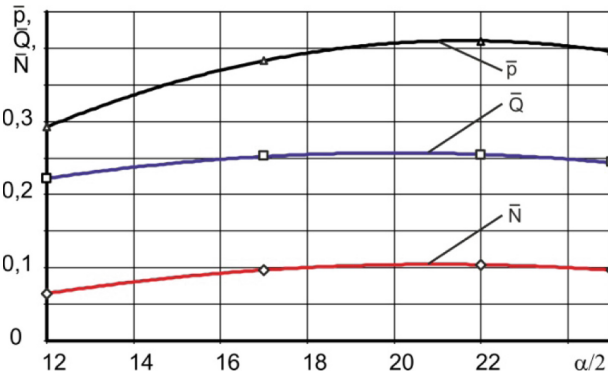
Fig. 5. The effect of the confuser angle on the parameters of the jet.

The effect of the confuser angle on the pressure, flow rate and power of the jet at the outlet of the confuser is shown in Fig. 5. All parameters are related to the parameters of the jet at the inlet to the computational domain. It can be concluded that the optimum confuser angle is 20–22° for a given swirl number ($S = 0, 74$) and its location from the outlet of the swirling jet from the nozzle ($\bar{x} = x/D = 0, 23$).

5   Conclusion

In vortex devices, it is often required to conserve part of the energy of the swirl flow to be dispersed. One of the most rational ways to save energy is to use a confuser. First, a swirling flooded jet was investigated, and the flow parameters were compared with experimental data. Since the use of the mathematical model led to adequate results, the operation of the confuser has studied.

1. A comparison of the flow patterns shows a fairly accurate prediction of the flow pattern, the amount of damping of rotation, and the velocity values in different sections.
2. The application of the RANS approach using the adjusted SST turbulence model allows quickly determining all the main characteristics of the swirl flow using medium-power computers.
3. An analysis of the operation of different confusers in a swirling flow showed that an increase in the average velocity and pressure at the outlet of the confuser with a large angle leads to the possibility of saving most of the swirling flow energy and using it in the future.
4. The optimum confuser angle is 20–22° for a given swirl number (S = 0,74) and its location from the outlet of the swirling jet from the nozzle ($\bar{x} = x/D = 0, 23$).

References

1. Varaksin, A.Y.: Air tornado-like vortices: Mathematical modeling (a review). High Temp. **55** (2), 286–309 (2017)
2. Liaposhchenko, O.O., Sklabinskyi, V.I., Zavialov, V.L., Pavlenko, I.V., Nastenko, O.V., Demianenko, M.M.: Appliance of inertial gas-dynamic separation of gas-dispersion flows in the curvilinear convergent-divergent channels for compressor equipment reliability improvement. In: IOP Conference Series: Materials Science and Engineering, vol. 233, no. 1, p. 012025 (2017). https://doi.org/10.1088/1757-899x/233/1/012025
3. Syomin, D., Rogovyi, A.: Features of a working process and characteristics of irrotational centrifugal pumps. Procedia Eng. **39**, 231–237 (2012)
4. Jawarneh, A.M., Sakaris, P., Vatistas, G.H.: Experimental and analytical study of the pressure drop across a double-outlet vortex chamber. J. Fluids Eng. **129**(1), 100–105 (2007)
5. Rogovyi, A., Khovanskyy, S.: Application of the similarity theory for vortex chamber superchargers. In: IOP Conference Series: Materials Science and Engineering, vol. 233, no. 1 (2017)
6. Mochalin, I., Zheng, S., Liu, J.: Improvement the performance of liquid purification by dynamic rotary filters. In: Design, Simulation, Manufacturing: The Innovation Exchange, pp. 633 − 642. Springer, Cham (2019)
7. Markovich, D.M., Abdurakipov, S.S., Chikishev, L.M., Dulin, V.M., Hanjalić, K.: Comparative analysis of low-and high-swirl confined flames and jets by proper orthogonal and dynamic mode decompositions. Phys. Fluids **26**(6), 065109 (2014)
8. Cozzi, F., Rohit, S., Solero, G.: Analysis of coherent structures in the near-field region of an isothermal free swirling jet after vortex breakdown. Exp. Thermal Fluid Sci. **109**, 109860 (2019)

9. Syred, N.: A review of oscillation mechanisms and the role of the precessing vortex core (PVC) in swirl combustion systems. Prog. Energy Combust. Sci. **32**(2), 93–161 (2006)
10. Cala, C.E., Fernandes, E., Heitor, M.V., Shtork, S.I.: Coherent structures in unsteady swirling jet flow. Exp. Fluids **40**(2), 267–276 (2006)
11. Alekseenko, S.V., Abdurakipov, S.S., Hrebtov, M.Y., Tokarev, M.P., Dulin, V.M., Markovich, D.M.: Coherent structures in the near-field of swirling turbulent jets: a tomographic PIV study. Int. J. Heat Fluid Flow **70**, 363–379 (2018)
12. Rogovyi, A.: Energy performances of the vortex chamber supercharger. Energy **163**, 52–60 (2018)
13. Tran, C. T., Long, X., Ji, B.: Vortical structures in the cavitating flow in the Francis-99 draft tube cone under off-design conditions with the new omega vortex identification method. In: Journal of Physics: Conference Series, vol. 1296, no. 1, p. 012011 (2019)
14. Voloshina, A., Panchenko, A., Boltyansky, O., Titova, O.: Improvement of Manufacture Workability for Distribution Systems of Planetary Hydraulic Machines. In: Ivanov, V., et al. (eds.) Advances in Design, Simulation and Manufacturing II. DSMIE 2019, pp., 732–741. Lecture Notes in Mechanical Engineering. Springer, Cham (2020)
15. Pavlenko, I.V., Simonovskiy, V.I., Demianenko, M.M.: Dynamic analysis of centrifugal machine rotors supported on ball bearings by combined using 3D and beam finite element models. In: IOP Conference Series: Materials Science and Engineering, vol. 233, no. 1, p. 012053 (2017). https://doi.org/10.1088/1757-899x/233/1/012053
16. Panchenko, A.,Voloshina, A., Kiurchev, S., Titova, O., Onopreychuk, D., Stefanov, V., Safoniuk, I., Pashchenko, V., Radionov, H., Golubok, M.: Development of the universal model of mechatronic system with a hydraulic drive. Eastern-Eur. J. Enterp. Technol. **4**,7 (94), 51–60 (2018)
17. Panchenko, A., Voloshina, A., Milaeva, I., Panchenko, I., Titova, O.: The influence of the form error after rotor manufacturing on the output characteristics of an orbital hydraulic motor. Int. J. Eng. Technol. **7**(4.3), 1–5 (2018)
18. Fesenko, A., Basova, Y., Ivanov, V., Ivanova, M., Yevsiukova, F., Gasanov, M.: Increasing of equipment efficiency by intensification of technological processes. Periodica Polytechnica Mech. Eng. **63**(1), 67–73 (2019)
19. Voloshina, A., Panchenko, A., Boltyansky, O., Panchenko, I., Titova O.: Justification of the kinematic diagrams for the distribution system of a planetary hydraulic motor. Int. J. Eng. Technol. **7**(4.3), 6–11 (2018)
20. Panchenko, A., Voloshina, A., Boltyansky, O., Milaeva, I., Grechka, I., Khovanskyy, S., Svynarenko, M., Glibko, O., Maksimova, M., Paranyak, N.: Designing the flow-through parts of distribution systems for the PRG series planetary hydraulic motors. Eastern-Eur. J. Enterp. Technol. **3**,1(93), 67–77 (2018)
21. Babenko, V.V., Blohin, V.A., Voskoboinick, A.V., Turick, V.N.: Velocity fluctuations in a swirling jet of a vortex chamber. Int. J. Fluid Mech. Res. **32**(2), 184–198 (2005)
22. Besagni, G., Inzoli, F.: Computational fluid-dynamics modeling of supersonic ejectors: screening of turbulence modeling approaches. Appl. Therm. Eng. **117**, 122–144 (2016)
23. Evdokimov, O.A., Piralishvili, S.A., Veretennikov, S.V., Guryanov, A.I.: CFD simulation of a vortex ejector for use in vacuum applications. In: Journal of Physics: Conference Series, vol. 1128, no. 1, p. 012127 (2018)
24. Pavlenko, I., Simonovskiy, V., Ivanov, V., Zajac, J., Pitel, J.: Application of artificial neural network for identification of bearing stiffness characteristics in rotor dynamics analysis. In: Ivanov, V., et al. (eds) Advances in Design, Simulation and Manufacturing. DSMIE 2018. Lecture Notes in Mechanical Engineering, pp. 325–335. Springer, Cham (2019). https://doi.org/10.1007/978-3-319-93587-4_34

25. Ivanov, V., Dehtiarov, I., Denysenko, Y., Malovana, N., Martynova, N.: Experimental diagnostic research of fixture. Diagnostyka **19**(3), 3–9 (2018)
26. He, P., Mader, C.A., Martins, J.R., Maki, K.J.: An aerodynamic design optimization framework using a discrete adjoint approach with OpenFOAM. Comput. Fluids **168**, 285–303 (2018)
27. Krol, O., Sokolov, V.: Modelling of spindle nodes for machining centers. In: Journal of Physics: Conference Series, vol. 1084, p. 012007 (2018)
28. Krol, O., Sokolov, V.: Parametric modeling of gear cutting tools. In: Advances in Manufacturing II. Lecture Notes in Mechanical Engineering, vol. 4, pp. 3–11 (2019)
29. Gaydamaka, A., Kulik, G., Frantsuzov, V., Hrechka, I., Khovanskyi, S., Rogovyi, A., Svynarenko, M., Maksimova, M., Paraniak, N.: Devising an engineering procedure for calculating the ductility of a roller bearing under a no-central radial load. Eastern-Eur. J. Enterp. Technol. **3**(7–99), 6–10 (2019)
30. Tkachuk, M., Bondarenko, M., Grabovskiy, A., Sheychenko, R., Graborov, R., Posohov, V., Lunyov, E., Nabokov, A., Vasiliev, A.: Thin-walled structures: analysis of the stressed-strained state and parameter validation. Eastern-Eur. J. Enterp. Technol. **1/7**(91), 18–29 (2018)
31. Tkachuk, M.M., Skripchenko, N., Tkachuk, M.A., Grabovskiy, A.: Numerical methods for contact analysis of complex-shaped bodies with account for non-linear interface layers. Eastern-Eur. J. Enterp. Technol. **5/7**(95), 22–31 (2018)
32. Tkachuk, M.: A numerical method for axisymmetric adhesive contact based on Kalker's variational principle. Eastern-Eur. J. Enterp. Technol. **3**(7–93), 34–41 (2018)
33. Tkachuk, M.M., Grabovskiy, A., Tkachuk, M.A., Hrechka, I., Ishchenko, O., Domina, N.: Investigation of multiple contact interaction of elements of shearing dies. Eastern-Eur. J. Enterp. Technol. **4**(100), 6–15 (2019)
34. Atroshenko, O., Tkachuk, M., Ustinenko, O., Bondarenko, O., Diomina, N.: A numerical analysis of non-linear contact tasks for the system of plates with a bolted connection and a clearance in the fixture. Eastern-Eur. J. Enterp. Technol. **1**(7), 24–29 (2016)
35. Rogovyi, A., Khovanskyy, S., Grechka, I., Pitel, J.: The wall erosion in a vortex chamber supercharger due to pumping abrasive mediums. In: Ivanov, V., et al. (eds.) Advances in Design, Simulation and Manufacturing. DSMIE-2018. Lecture Notes in Mechanical Engineering, pp. 682–691. Springer, Cham (2020)
36. Menter, F.R.: Two-equation eddy-viscosity turbulence models for engineering applications. AIAA J. **32**(8), 1598–1605 (1994)
37. Smirnov, P.E., Menter, F.R.: Sensitization of the SST turbulence model to rotation and curvature by applying the Spalart-Shur correction term. J. Turbomach. **131**(4), 041010 (2009)
38. Yin, J., Jiao, L., Wang, L.: Large eddy simulation of unsteady flow in vortex diode. Nucl. Eng. Des. **240**(5), 970–974 (2010)
39. Boushaki, T., Merlo, N., de Persis, S., Chauveau, C., Gökalp, I.: Experimental investigation of CH4-air-O2 turbulent swirling flames by Stereo-PIV. Exp. Thermal Fluid Sci. **106**, 87–99 (2019)

Operating Characteristics of Lever-Blade Shock Absorbers with the Extended Mechanical Structure

Ihor Sydorenko , Vladimir Tonkonogyi[(✉)] , Yuliia Babych ,
Yuliia Barchanova , and Zhang Yiheng

Odessa National Polytechnic University, 1, Shevchenko Avenue,
Odessa 65044, Ukraine
vmy47@ukr.net

Abstract. The torsion suspension is a widespread structure in today's transport machine engineering. Since the torsion bar represents just an elastic element, the problem of energy dissipation in suspensions is highly relevant for its application. Hydraulic absorbers with the movable element's reciprocating translational motion respectively to the housing or lever-type hydraulic shock absorbers of piston and vane types, with the movable element's rotational movement respectively to the housing, are currently used as a dissipation device in torsion suspension. These absorbers only implement throttle-valve type working characteristics, associated with these devices' functional capacities and depending on design constraints. The paper presents a synthesis of an innovative lever-blade absorber, whose performance is not related to the value of the working chamber's inner pressure. Their essential peculiarity relates to the presence of a mechanical control loop in the structure, that determines a close relationship between the performance and the value of the shock absorber movable element displacement relative to the body. In the process of synthesis, the appropriate methods, built based on technical systems' modeling with modified kinematic graphs, are tested. The synthesis results are shown in the form of structurally implemented samples. A comparative analysis of the samples with their basic performance determination is performed.

Keywords: Lever-Blade shock absorbers · Mechanical control loop · Shock absorber performance

1 Introduction

Currently, the use of a shock absorber with the translational or rotational movement of the working link does not always take into account the specific suspension design. So, in caterpillar propulsors with a torsion suspension, wide use has been gained by piston shock absorbers of various schemes, which are axial devices with the translational movement of the working link. However, the torsion bar suspension determines the angular displacement of its main element - the balancer, and the use of axial piston shock absorbers in its composition, in our opinion, can be considered irrational. This is since the cylinder of the axial-piston shock absorber and its rod are attached to the

machine body and the balancer with the help of ball joints. This decision is forced because the design features and the principle of operation of such a piston shock absorber do not provide for the action of bending moments on it. In addition, there is another, more serious problem. Namely, the attachment of the axial shock absorber to the machine body with the help of ball joints leads to a constant change of the external force system acting on the shock absorber, since in this case the cylinder and the rod of the shock absorber constantly change their position relative to the mover body during operation. In this case, the picture of real forces acting on the shock absorber may differ significantly from the calculated picture of forces, in accordance with which its operating characteristic is determined. A more natural solution for the suspension, the elements of which make angular movements, lies in the use of shock absorbers, the body of which is directly mounted on the housing of the mover, and the working body makes angular movements. Such devices include lever-piston and lever-blade shock absorbers. Considering the relative simplicity of lever-blade shock absorbers compared to lever-piston shock absorbers, their use as part of a torsion bar suspension can be considered more preferable (Fig. 1).
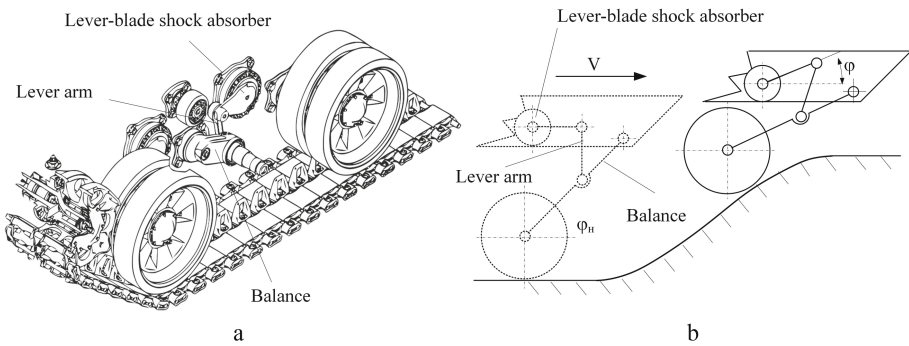
Fig. 1. Lever-blade shock absorber: application as part of a caterpillar mover (a); scheme of work when overcoming an obstacle (b).

In addition, there is a direct confirmation of the advantage of using lever-blade shock absorbers as part of torsion bar suspensions of a number of machines operating in difficult conditions compared to lever-piston shock absorbers. It has been established that their operating temperature (for example, when used in products T-72 and T-62) is significantly lower than that of piston shock absorbers operating under the same conditions (for example, in products T-80) [1, 2]. This is since the body of lever-blade shock absorbers constructively assumes close contact with the massive side of the machine, which ensures greater heat transfer. Due to their structural features, cases, axial piston shock absorbers cannot provide such contact, and as a result, their bodies are forced to be supplemented with cooling fins, the efficiency of which, given the operating conditions (dirt sticking, etc.) is very low. However, at the moment, a well-established technology for the production of axial piston shock absorbers, which determines their relatively low cost, provides the widespread use of these devices in

torsion suspensions. Increased requirements for the smooth movement of caterpillar movers, especially when driving on rough terrain at high speeds, have led to the fact that the operational characteristics of the shock absorbers used are ineffective.

Proceeding from this, the scientific and applied problem of synthesis and analysis, of the fundamentally new lever-blade shock absorbers, designed to work as part of torsion suspensions of caterpillar drives, whose performance characteristics exceed the performance characteristics of existing axial piston shock absorbers, should be considered relevant.

2 Literature Review

The solution to the problem of the synthesis of new lever shock absorbers with adjustable working characteristics led to the appearance of a large number of designs of such devices [3, 4]. In some of the proposed lever shock absorbers, some working characteristics are adjustable due to the simultaneous use of several chokes that are configured for a specific pressure [5, 6]. But in most cases, these devices are not considered independent but are only an element of an active suspension [7–9]. In this case, the lever shock absorbers, being part of the active system, have an external electromechanical or electro-hydraulic control [10–12]. For devices of this type, it is especially emphasized that their use is selective and justified only for expensive or special propulsion devices [13–15].

Given that passive systems are more preferable in terms of complexity and cost, the work was carried out using various methods for their structural optimization and synthesis, among which there are methods related to the application of the graph theory [16–18]. The results of studies related to the application of the modified kinematic graph method for structural analysis and synthesis of elastic and dissipative devices showed that, by adding additional mechanical structures to the structures of existing devices, their functionality can be significantly expanded [19, 20]. The result of applying this methodology for the structural analysis of an existing lever-blade shock absorber and the subsequent structural synthesis of a new device based on it is a fundamentally new design [20]. The close relationship between the basic and synthesized structures is determined by the fact that the designs of the devices under consideration have a set of elements that determine the same functional purpose (Fig. 2).

The devices consist of a housing 1, with radially-mounted partitions 2 with a rectangular throttle hole installed in its cylindrical hole. The shaft 3 with the blades is mounted coaxially in the cylindrical hole of the housing. Side washers 4 and flange covers with bearings 5 serve to orient the shaft 3 and create an internal airtight cavity.

The synthesized device has an additional mechanical structure in the form of a pivot-lever mechanism, which is represented by a lever 6 and a slider 7. One end of the lever is mounted for rotation on the shaft 3, and the other on the slider 7. The slider 4, partially moving in the radial direction along the partition 2, can partially or completely block the throttle hole. It is the presence of the presented mechanical structure that can significantly change the operating characteristic of the shock absorber since it determines the mechanical feedback between the displacement of the working body of the shock absorber and the area of the throttle hole.
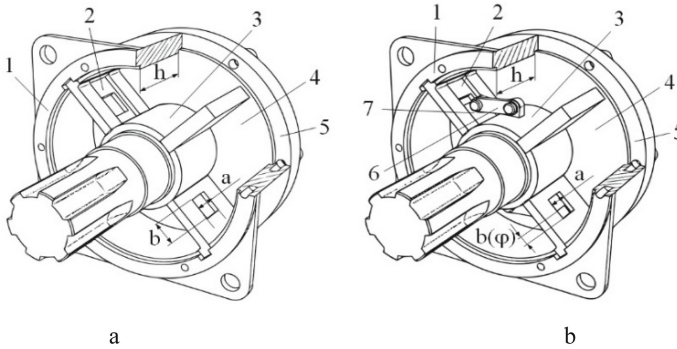
Fig. 2. Lever-blade shock absorber: base structure (a); with expanded structure (b).

3   Research Methodology

The problem of creating a mathematical model of the proposed device, which describes the range of its possible operating characteristics and their relationship with the geometric parameters of both the device itself and its control system, remains unresolved.

The aim of the study is an analytical study of the relationship between the mechanical characteristics of the control system of the proposed lever-blade damper and its operational characteristics.

To achieve this, we used a methodology for studying the characteristics of the shock absorber, based on the existing relationship between the volumetric flow rate of the working fluid Q passing through the throttle openings of the shock absorber blade (taking their area into account) and the pressure drop. This relationship is determined by the Torricelli formula [6].

$$Q = \mu A(p_1)\sqrt{2\frac{p_1}{\rho}} \tag{1}$$

where μ is the coefficient of discharge; A is the area of the throttle hole; p_1 is the pressure at the valve inlet; ρ is the density of the working.

4   Results

When conducting theoretical studies, both of the presented devices were considered, among which the main device is called sample A, and the synthesized device is called sample B. Structural diagrams of devices were made, in which the previously adopted numbering of the main elements was used (Fig. 3).
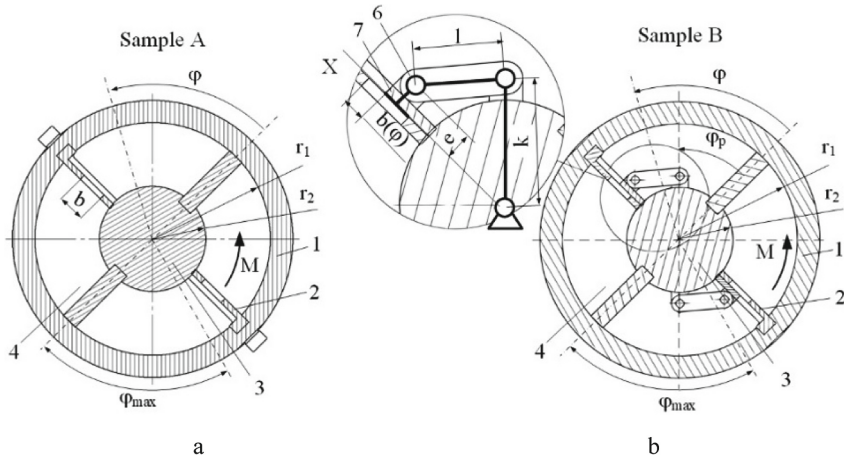
Fig. 3. Design schemes of the lever-blade shock absorbers for determining working diagrams: prototype with constant throttle holes (a); the proposed device with a structure extended by a pivot - lever mechanism (b).

During the research, the following assumptions were made: the basic geometric parameters of the devices are identical; at the initial moment, the angle φ between the blades of the shaft 3 and the jumpers 2 is 75 deg; in the initial position, the throttle hole is fully open. In the compression process, when an external load is applied to the shock absorber shaft in the form of a torque M and the working fluid flows from the working cavity I into the cavity II through the throttle hole in the partition. The volume, which is thus described by the blade of each of the presented shock absorbers per unit of time (flow rate) is equal to the volumetric flow rate of the fluid that flows through the throttle hole $Q = Q_h$. Given that the basic geometric parameters of the samples under consideration are equal, the volume that describes the blade of each of them per unit of time is calculated as the product of the speed of blade movement ω by its area

$$Q_h = \frac{\pi(r_1^2 - r_2^2)h}{2\pi} \cdot \frac{d\varphi}{dt} = \frac{(r_1^2 - r_2^2)h}{2} \cdot \omega, \qquad (2)$$

where r_1 is the radius of the inner cylindrical surface of the shock absorber body, r_2 is the radius of the outer surface of the shaft; h is the width of the housing; φ is the angle of rotation of the shaft with blades relative to the housing with partitions; ω is the speed of rotation.

Taking into account expressions (1) and (2), an expression is obtained, which determines the relationship between the geometric parameters of the device, the speed of the blade and the pressure in the working cavity I, which is true for both samples

$$\frac{(r_1^2 - r_2^2)h}{2}\omega = 2A_0\sqrt{2\frac{p_1}{\rho}}. \qquad (3)$$

Given that for sample A, the area of the throttle hole remains unchanged ($A_0 =$ const) over the entire range of the angle of rotation of the shaft with the blades, the solution of Eq. (3) with respect to pressure

$$p_{1A}(\omega) = \frac{h^2\omega^2(r_1^4 - 2r_1^2 r_2^2 + r_2^4)}{2(a \cdot b)^2 \mu^2 \rho}. \tag{4}$$

Let the rectangular throttle hole overlap as the angle of rotation of the shaft φ increases, then changing its area $A_0(\varphi) = a \cdot b(\varphi)$ with a constant value of the parameter a depends on the value of the movement of the slider $b(\varphi)$

$$b(\varphi) = b_n - \left[k \cdot \cos(\varphi) + 1 \cdot \cos\left(\arcsin\left(\frac{k \cdot \sin(\varphi) - e}{1} \right) \right) \right], \tag{5}$$

where b_n is the length of the rectangular throttle hole at the time taken as the initial one.

Then, taking into account expression (5) for sample B, the solution of Eq. (3) with respect to pressure p_1

$$p_{1B}(\omega, \varphi) = \frac{h^2\omega^2(r_1^4 - 2r_1^2 r_2^2 + r_2^4)}{2(a(b_n - b(\varphi))^2 \mu^2 \rho}. \tag{6}$$

To assess the effectiveness of the shock absorber, two of its interrelated indicators are used: a working diagram, which determines the pressure in the working cavity of the device depending on the movement of the working link $P(\varphi)$, and the actual working characteristic, which determines the strength (moment) of resistance on the working link of the device, depending on its speed is $M(\omega)$. When determining the parameters of the samples under consideration, certain values of their geometric parameters were adopted (Table 1).

Table 1. Geometric parameters of samples.

Name of the parameter, units measuring	Designation	Samples	
		A	B
The radius of the inner cylindrical surface of the body, mm	r_1	60	60
The radius of the outer surface of the shaft, mm	r_2	20	20
Shock absorber width, mm	h	40	40
The maximum angle of rotation of the shaft, deg	φ_{Max}	75	75
Throttle hole width, mm	a	15	15
Throttle bore length, mm	b_n	25	25
The distance from the axis of the device to the mounting point of the lever on the shaft, mm	k	–	25
Lever length, mm	l	–	20
The distance from the surface of the partition to the mounting point of the lever on the slider, mm	e	–	5

It should be noted that the magnitude and law of change of speed on the working link of the shock absorber has a significant impact on its working characteristic. When conducting analytical studies, it was assumed that the caterpillar mover moves through the obstacle in a sinusoidal form, which determines the full stroke (φ_{max} = 75 deg) of the shock absorber shaft. The impact on the obstacle occurs at time t = 2, while the frequency of rotation of the shock absorber shaft ω_{max} (taking into account the shape of the obstacle) has an extremum at t = 0,5 s. Given the large volume of mathematical calculations, the solutions obtained during the study are interpreted graphically for clarity.

For sample A, using expression (4) for given values of ω, we obtained a family of working diagrams (Fig. 4, a). The straight lines defining the working diagrams show that the pressure in the working cavity is completely independent of the position of the shaft with blades relative to the housing with partitions. Therefore, taking into account the relationship between displacement and speed (Fig. 4, b and Fig. 4, c), the working characteristic of sample A is a certain curve (Fig. 4, d) that determines the relationship between the moment on the shock absorber shaft M = ($p_1(r_2 − r_1)h)(r_1 + 0,5 (r_2 − r_1))$ in speed ω.
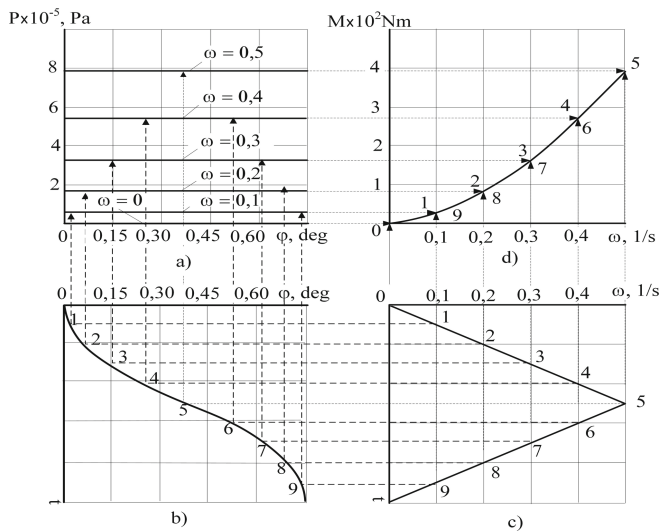
Fig. 4. Determination of the working characteristic of the lever-blade shock absorber (sample A): a family of working diagrams (a); the law of change in bias (b); law of change of speed (c); working characteristic (d).

Sample A accepted for comparison, is a well-known shock absorber, therefore the type of its working characteristic is known in the literature as progressive (throttle), and shows the relationship between three parameters: the force on the working link, the area of the throttle hole and the speed of movement of the working link [3, 4, 10].

For sample B, the graphical interpretation of the analytical studies is as follows. Calculations by expression (6) for given values of ω allow us to obtain a family of asymmetric working diagrams for a given sample (Fig. 5, a). The resulting family of working diagrams indicates that the pressure in the working cavity of the device depends not only on the speed of movement of the working link but also on its position in the range of the working stroke. Considering that, in the case under consideration, the working diagrams of sample B are asymmetric with respect to the middle of the working stroke, and also taking into account the relationship between movement and speed (Fig. 5, b and Fig. 5, c), we obtained a working characteristic of sample B, which is a loop (Fig. 5, d).
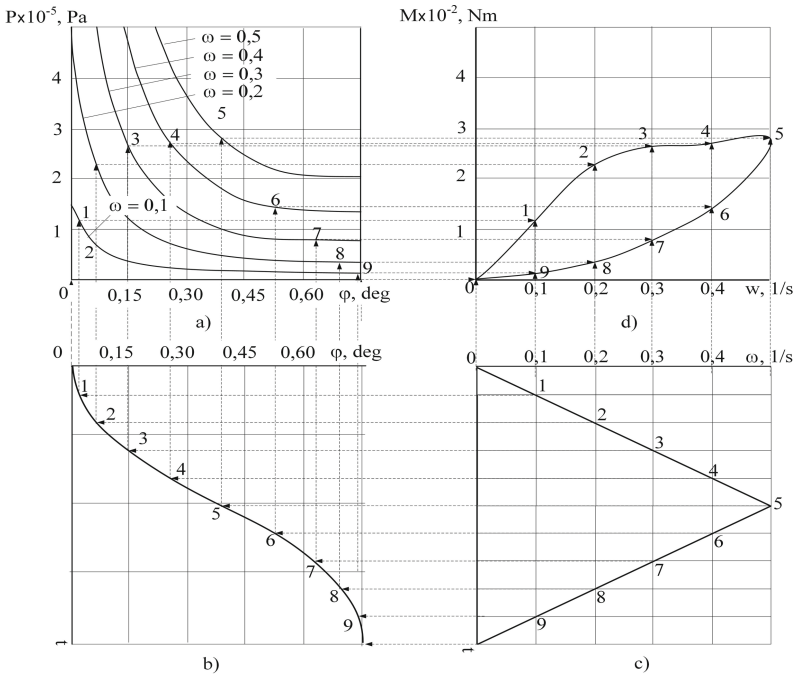
Fig. 5. Determination of the working characteristic of the lever-blade shock absorber (sample B): a family of working diagrams (a); the law of change in bias (b); law of change of speed (c); working characteristic (d).

The lower part of the loop, limited by points 0–5, defines a progressive (throttle) section. It is characterized by a relatively small change in the moment of resistance at the working link with an increase in the speed of the shock absorber in the first half of the stroke. The upper part of the loop, limited by points 5–9, 0, defines a deviating (valve) section. It is characterized by large values of the moment of resistance when the speed decreases in the second half of the stroke. The performance characteristic presented is not described in the literature, since it cannot be implemented in well-known shock absorber designs.

Further analytical studies have shown that when varying the easily changeable design parameters of the device, which include the shape, size, number, and location of the throttle holes on the partition, as well as the length of the lever 6, the shape and dimensions of the slide 7, sample B allows to implement various types of working characteristics, both symmetric and asymmetric.

5   Conclusions

The research results show that the proposed fundamentally new device automatically implements a performance that cannot be obtained using the well-known lever-blade shock absorbers.

It was found that the presence of a large number of easily variable design parameters determines a wide range of working characteristics of various types of non-linearity, which involves the synthesis of the target (required for one reason or another) working characteristics using the proposed device. Moreover, in our opinion, working characteristics that determine the different types of dissipation in individual sections of the working stroke of the shock absorber's working link can be of particular interest, which allows us to move on to solving rather complex problems of controlled dissipation. Such tasks, for example, include regulation of dissipation at the maximum displacement of the shock absorber's working body, which can prevent its "break-down"; regulation of dissipation with minimal displacement of the working body of the shock absorber to eliminate its "excessive rigidity" in the range of small displacements. The solution to these problems, in particular, will allow optimizing the suspension of the vehicle in general.

References

1. Chebitok, V.V.: Chassis of tanks. Suspen. Equip. Weapons **7**, 60–68 (2015)
2. Berezov, A.: Improving the security of armored vehicles abroad. Foreign Mil. Rev. **2**, 10–19 (2017)
3. Kotiev, G.O., Smirnov, A.A., Shilkin, V.P.: The Study of Working Processes in the Pneumohydraulic Devices of Suspension Systems for Tracked Vehicles. MSTU. N.E. Bauman, Moscow (2011)
4. Fuentes, R., Mineo, C., Pierce, S.G., Worden, K., Cross, E.J.: A probabilistic compressive sensing framework with applications to ultrasound signal processing. Mech. Syst. Signal Process. **117**, 383–402 (2019)
5. Pacejka, H.B.: Tire and Vehicle Dynamics. 2nd ed. Society of Automotive Engineers (2005)
6. Ryabov, I.M., Kovalev, A.M., Chernyshov, K.V.: Effect of types of road surface and the speed of the moving car on the oscillation amplitude its inertia mass of a dynamic vibration absorber of wheel. Automob. Ind. **7**, 18–19 (2013)
7. Emelyanov, R.: Modeling of the hydraulic drive working process with throttle regulation. Constr. Road Mach. **11**, 62–64 (2010)
8. Nikitin, O.: Hydraulics and Hydropneumatic Drive. MGTU Bauman, Moscow (2012)
9. Pozdeev, A.V., Novikov, V.V.: Adjustable pneumatic and pneumohydraulic springs of suspensions of vehicles. Volgograd State Technical University (2013)

10. Worden, K.: Uncertainty analysis in structural dynamics. Key Eng. Mater. **588**, 318–332 (2014)
11. Green, P.L., Worden, K.: Modelling friction in a nonlinear dynamic system via Bayesian inference. In: Conference Proceedings of the Society for Experimental Mechanics Series, vol. 6, pp. 543–553 (2013)
12. Siczek, K., Kuhar, M.: Researches on the amount of recuperated energy by electromagnetic shock absorber in small car. J. KONES Powertrain Transp. **20**(3), 367–374 (2013)
13. Lebedev, V., Tonkonogyi, V., Yakimov, A., Bovnegra, L., Klymenko, N.: Provision of the quality of manufacturing gear wheels in energy engineering. In: Advances in Design, Simulation and Manufacturing. DSMIE 2018. Lecture Notes in Mechanical Engineering, pp. 89–96. Springer, Cham (2019)
14. Dixon, J.: The Shock Absorber Handbook, 2nd edn. Wiley, Chichester (2007)
15. Worden, K., Green, P.L.: A machine learning approach to nonlinear modal analysis. Mechanical Systems and Signal Processing 84 (Part B), 34–53
16. Green, P.L., Worden, K., Sims, N.D.: On the identification and modelling of friction in a randomly excited energy harvester. J. Sound Vib. **332**(19), 4696–4708 (2013)
17. Taylor, D.: Energy Management Utilizing the Hydraulic Shock Absorber. Taylor Devices, Inc. (2016)
18. Usov, A.V., Tonkonogyi, V.M., Dašić, P.V., Rybak, O.V.: Modelling of temperature field and stress-strain state of the workpiece with plasma coatings during surface grinding. Machines **7**, 20 (2019)
19. Sydorenko, I.: Passive vibration isolation device with elements of active systems. Palmarium Academic Publishing, Saarbrücken (2011)
20. Sydorenko, I.: Analysis of the structure of the relaxation shock absorbers and modified the traditional kinematic. ASB Mech. Mach. Tools Mat. **1**(26), 88–91 (2014)

Estimation of Random Flow-Rate Characteristics of the Automatic Balancing Device Influence on Centrifugal Pump Efficiency

Yuliia Tarasevych[1]([⊠]) [iD], Ievgen Savchenko[2] [iD],
and Nataliia Sovenko[2] [iD]

[1] AGH University of Science and Technology,
30, Al. Mickiewicza, 30-059 Kraków, Poland
jtaras@agh.edu.pl
[2] Sumy State University, 2, Rymskoho-Korsakova St., Sumy 40007, Ukraine

Abstract. The main function of an automatic balancing device is to balance the axial force in multi-stage centrifugal pumps. The advantage of this method of axial force balancing is the self-regulation of the device parameters. This allows balancing the axial force at different pump operating modes. In classic designs, the static characteristic (dependence of the hydrodynamic axial force of the device on the face gap), as well as the flow rate characteristic of the balancing device, are substantially determined by the cylindrical gap geometry. A middle gap of the cylindrical throttle, as well as its conductivity, is a random function due to manufacturing tolerances and possible erosive wear of sealing surfaces under pump operation. The paper presents the method of calculating the flow rate characteristics of the device with the random changes in the middle gap during operation of the pump, as well as the influence of random changes in local hydraulic resistances and parameter taper of face gap. The analysis of the influence of each of the considered random factors is made. Probabilistic characteristics of the pump efficiency are determined.

Keywords: Cylindrical throttle · Face throttle · Flow-rate · Axial force · Probabilistic characteristics · Pump efficiency

1 Introduction

Support and sealing units are the most critical elements that determine the reliability, efficiency, and lifetime of any hydraulic system. These units should provide the necessary hermetic characteristics and stability under a long service life, not cause large friction and wear of moving parts and be operable in a wide temperature range and possible pressure drops thereby ensuring sufficiently high pump efficiency.

Automatic support and sealing systems are used in most high-pressure pumps for axial balancing of the rotor. A typical balancing device is shown in Fig. 1. Its d includes two sequentially arranged cylindrical *I* and face *II* throttle separated by a discharge chamber. The presence of this camera allows tracking the change in axial

force T acting on the pump rotor. Thus, the reliability of the pump is determined by the reliability of this device. Moreover, the overall efficiency of the pump is largely determined by the hermetic characteristic of the automatic device due to rather large values of leakage through the sealing channels of the device. An increase in device sealing, and, consequently, an increase in efficiency are possible due to a decrease in the cylindrical throttle gap value. With small gaps of the cylindrical and face throttle, the possibility of contact of the sealing surfaces increases. This leads to premature wear surfaces or in the worst case even to failure of the device.
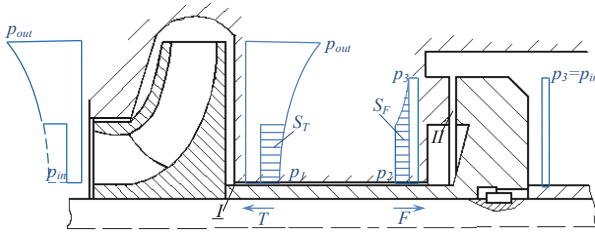
Fig. 1. Automatic balancing device.

Considering the possible wear of the surfaces of the cylindrical throttle, as well as random changes of its middle gap value caused by tolerances, is the aim of the work. Wear causes an increase in the cylindrical throttle gap and consequently a change in its resistance and flow rate. The operating characteristics of the automatic balancing device are determined by the flow rate balance on the cylindrical and face throttle. So, the flow rate and the gap of the face throttle also change, namely, increase. This leads to the disclosure of the face gap. An increase in flow rate, i.e. leakage through an automatic balancing device significantly reduces the total pump efficiency. Moreover, the resistance of the annular seal can become much less, and the pressure in the discharge chamber tends to the pumping pressure value (pressure before the annual seal) under some critical value of the cylindrical throttle gap. This can lead to the so-called disclosure of the balancing device associated with an unacceptable axial shift of the rotor and the pump stop, which subsequently leads to serious economic losses.

2   Literature Review

The general procedure of calculating the characteristics of the automatic balancing device is presented in a number of works [1–6]. The static characteristic of the balancing device is the dependence of the axial force on the gap of the face throttle. It is worth noting that these calculations are based on the results of theoretical and experimental studies of the hydrodynamic characteristics of cylindrical and face throttle [4, 8–10]. For an analytical description of this dependence, a number of assumptions are made regarding the throttles geometry. Namely, it does not take into account the change in the gap throttles values caused by eccentricity and shaft misalignment in the

annual seal, misalignment and force deformations in the face throttle [5–8]. The real shape of the cylindrical and face throttle is quite complex. The presence of eccentricity in a cylindrical throttle leads to an additional flow, and, consequently, to additional components of flow rate [1, 12]. The diffuser form of the face gap due to force deformations reduces the hydrostatic component, and, consequently, the total axial force [6]. These and some other geometric parameters determine the pressure value in the chamber of the unloading device, which determines the value of the axial force and flow rate.

It should be pointed out that the above-mentioned factors, namely eccentricity, deformations, local hydraulic resistance, middle radial gap and, in general, throttled pressure drop, are random variables [12, 13]. Consequently, the axial force value, the flow rate of the device as well as the pump efficiency are random variables or functions [12–14]. In previous works, the authors evaluated the influence of a random change in a number of parameters of the annual seal (inter-stage seals) and face throttle, due to manufacturing and installation errors on the static characteristics and pump efficiency. Namely, the random nature of the coefficients of local hydraulic losses, the middle radial gap of the cylindrical throttle and also the initial misalignment of the rotating and non-rotating disks are taken into account.

In this paper, the effects of changes in the middle gap of cylindrical throttle due to erosive wear of the sealing surfaces inclusive of a random change due to accepted manufacturing tolerances, local hydraulic resistances, and the axes misalignment parameter of the rotating and non-rotating discs on the unloading device flow rate, as well as the volumetric efficiency of the pump, are considered.

3   Research Methodology

Calculating scheme of eccentric cylindrical throttle [3] with immobile sleeve axis and rotating around sleeve axis with the non-zero frequency of precession axis of rotor is used to calculate the value of flow rate through the automatic balancing device. The elementary flow rate through the cylindrical throttle can be presented as $q = q_p + q_z + q_i$ based on Reynolds' equation for prevailing axial flow in the shot cylindrical throttle as well as averaged continuity equation with considering of non-stationary boundary conditions of velocities and local hydraulic resistances in pressure values. Here q_p is the so-called pressure component of elementary flow rate caused by throttled pressure, q_z is the component, caused by sealing surfaces moving (in the general case: rotation, precession and radial and angular oscillations), q_i is the inertia component, caused by the irregularity of velocity distribution in the cylindrical gap.

Value of q_z in the first approach does not depend on flow mode (laminar or turbulent) but can change through the throttle length.

Inertial component q_i nonlinearly depends on radial oscillations of the rotor in the general case. Moreover, the inertial component of the flow rate is non-zero only in conical throttles and under misalignment of sleeve and shaft axes. Inertial flow direction is largely determined by the parameter of taper: inertial flow reduces the value of total flow through the conical throttle and is directed as pressure flow in diffuser

throttle. Inertial component of flow rate increases with an increase in eccentricity. In this paper, the influence of the inertial properties of the liquid on the flow rate is not shown; this problem will be considered in further research.

Pressure component of the elementary flow-rate:

$$q_p = q_{p0}\left(1 + \frac{H\Delta\xi\varepsilon cos\varphi}{0.04l + 2H(\Delta\xi - 2\Theta\xi_m)}\right)(1 - \varepsilon cos\varphi)^{\frac{3}{2}},$$

here $q_{p0} = \left(\frac{4\Delta pH^3}{\rho\xi_c}\right)^{\frac{1}{2}}$ – flow-rate through the concentric cylindrical throttle, Δp – throttled pressure drop, H – the radial gap in the middle section along the throttle length, $\xi_c = \Delta\xi + \frac{Cl}{2H} - \Theta\xi_m$ common coefficient of resistance in conical throttle, Θ – relative angel of sleeve taper, $\Delta\xi = \xi_{11} - \xi_{12}$, $\xi_m = \xi_{11} + \xi_{12}$, ξ_{11} – coefficients of local hydraulic resistances at the inlet, ξ_{12}– at the outlet of the cylindrical throttle.

It is worth noting that the majority of research does not consider the influence of the tapered shape of the sleeve and eccentricity on flow-rate through the cylindrical throttle.

In this work, the flow rate through the cylindrical throttle is calculated under the constant value of the rotor frequency. The average resulting velocity of the pumping medium and its gradient along the gap thickness is changing with rotating frequency changing. Thus, the value of friction losses is also changing and this can influence the flow-rate value.

The total flow rate through the cylindrical throttle is determined by integration of elementary flow components on the circumference ($\varphi\,\varepsilon[0, 2\pi]$). Based on previous calculations [12] the value of the component q_z is two orders less than the flow rate due to the pressure flow, therefore, for further calculations, the expression of the flow rate of the pressure flow through a cylindrical throttle for the self-similar region of a turbulent flow is used

$$Q_c = g_c\sqrt{p_1 - p_{20}} = 2\pi r q_{p0}\left(1 + \frac{3}{4}\left(1 - \frac{\Delta\xi}{\xi_c}\right)\varepsilon_m^2\right). \tag{1}$$

The calculation scheme of the automatic balancing device is presented in Fig. 2.
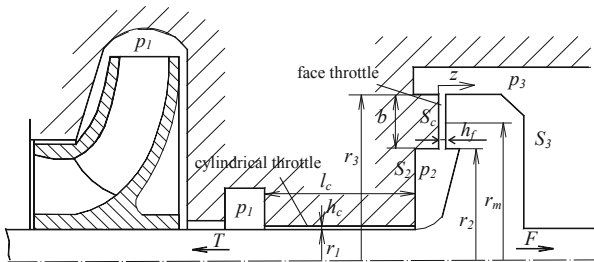
Fig. 2. Calculation scheme of the automatic balancing device.

The balance of fluid flow through the cylindrical and face throttle must be observed under the pump operation, therefore:

$$g_c \sqrt{p_1 - p_{20}} = g_f \sqrt{p_{20} - p_3}, \tag{2}$$

where g_c, g_f — conductivities of cylindrical and face throttle respectively.

Considering the last equation, if the conductivity values of the cylindrical and face throttle are known, as well as the pressure at the outlet of the pump and the inlet, the pressure in the chamber of automatic balancing device $-p_{20}$ can be determined.

Under the pump operation, the sealing surfaces of the front, as well as inter-stage annular seals and the cylindrical throttle of the automatic balancing device, are subject to erosive wear. The process of destruction of the surface layer of metal occurs as a result of electrochemical corrosion and the hydrodynamic effects of the pumped medium. This process leads to an increase in the middle radial gap of cylindrical throttle and, accordingly, to a change in the hydrodynamic characteristics of the automatic balancing device.

As shown in [14], an increase in the middle radial gap of cylindrical throttle by the action of steam-water mixtures can be modeled by an exponential dependence, which has its form for each specific material. For example, to evaluate changes in the middle radial gap of cylindrical throttle with a nominal gap value of 250 μm the following dependence for steel AISI 321 can be used.

$$H = 2.1 \cdot 10^{-4} \exp\left(4.507 \cdot 10^{-5} t\right) + 5.327 \cdot 10^{-13} t^2.$$

Figure 3 shows the time dependence of the middle radial gap of the cylindrical throttle for three grades of steel: AISI 321 (was taken as reference material), X20Cr13, X30Cr13.
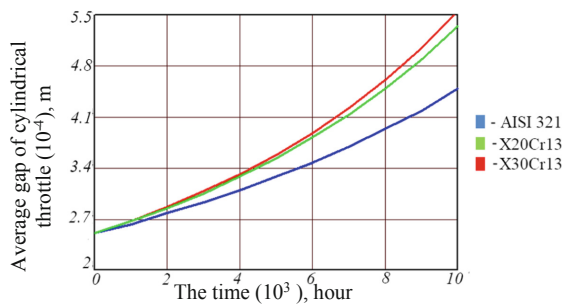
Fig. 3. The change of the middle gap of cylindrical throttle caused by the erosive wear for different grades of steel.

It should be noted that according to the operating data of the centrifugal pump type 300, the real values of the gaps of the annular seals of the impellers in some cases are 1.05–1.25 mm. Therefore, the dependencies are shown in Fig. 3 can be used to a rather

qualitative evaluation of the effect of changes in the cylindrical gap of the automatic balancing device on its characteristics. To make a quantitative evaluation, it is necessary to consider these dependencies as the main values of a random process characterizing the degree of wear of the surfaces, and the possible intervals of change should be set based on additional statistical data for at least each type of pump. Concurrently, such data are not presented in the available scientific and technical literature.

Due to the accepted tolerances in the design of the pump, the middle radial gap of the cylindrical throttle is a random variable, the distribution of which can be considered normal. The erosion wear process is a time depending on the process, therefore, the middle radial gap of a cylindrical throttle is a random function. The values of the wear approximating function can be set as a mean value of this random function for each moment. The flow rate through the face throttle and, consequently, the total flow rate through the automatic balancing device is also a random function with known probabilistic characteristics as it follows from the balance of fluid flow rates (2).

Leakages through annular seals of the running part and the automatic balancing device significantly affect the efficiency of the pump. Using the well-known equation for determining the efficiency of the pump.

$$\eta = \eta_{mech}\eta_{vol}\eta_{hydr},\tag{3}$$

where η_{mech} – mechanical efficiency, η_{vol} – volumetric efficiency, η_{hydr} – hydraulic efficiency of the pump.

Leakages through the cylindrical throttle determine the change in the volumetric efficiency, caused by a random changing the parameters of the cylindrical and face throttle and erosion of their surfaces. The volumetric efficiency can be defined by the formula:

$$\eta_{vol} = \frac{N_{hydr} - N_{vol}}{N_{hydr}} = \frac{\rho g Q_i H_t - \rho g Q_s H_t}{\rho g Q_i H_t} = \frac{Q}{Q + Q_s},\tag{4}$$

where $Q = Q_i - Q_s$; Q_s – the flow rate through the face throttle; Q_i – pump flow rate; $N_{hydr} = \rho g Q_i H_t$ – hydraulic power; H_t – theoretical pump head.

Pressure p_{20} in the automatic balancing device chamber, as shown above, depends on the middle radial gap and the overall hydraulic resistance of the cylindrical throttle, which are random parameters. To find the law of probability distribution of a pump's efficiency, one should know the multidimensional distribution of a system of random variables that determine the flow through the face throttle. The eccentricity, the middle radial gap, and the taper of the cylindrical throttle are independent random variables (the limits of eccentricity change are determined by the value of the radial gap). Therefore, the joint probability density can be written as [11]:

$$\begin{aligned}
f(\eta_{vol}) &= f\left(H, \varepsilon, \Theta, \xi_{11}, \xi_{12}, \xi_{11f}, \xi_{12f}, t\right) \\
&= f_1\left(H, t\right) f_2(\varepsilon|H) f_3(\Theta) f_5(\xi_{11}) f_6(\xi_{12}) f_7(\xi_{11f}) f_8(\xi_{12f}),
\end{aligned}\tag{5}$$

where $f_i(x_i)$ – probability density of corresponding random parameters, $f_2(\varepsilon|H)$ – probability density of eccentricity under condition $H = const$.

As it was made in [12] the normal law of distribution can be taken for appropriate random values (middle radial gap in the cylindrical throttle, caused by tolerances, coefficients of local hydraulic losses in cylindrical and face throttle, initial misalignment of rotating and non-rotating disks): $f(x_i) = \frac{1}{\sqrt{2\pi}\sigma_i} \exp\left[-\frac{(x_i - x_i)^2}{2\sigma_i^2}\right]$. Probabilistic characteristics of which is considered to be known. As mean values were taken deterministic values: $\langle h_c(t) \rangle = h_c(t)$, $\langle \overline{\beta} \rangle = \overline{\beta}$, $\langle \zeta_{if} \rangle = \langle \zeta_{ic} \rangle = 1.5$, $\langle \zeta_{of} \rangle = \langle \zeta_{oc} \rangle = 0.2 \langle \zeta_{if} \rangle$ and standard deviations were set as a percent deviation of values of the examined random values from its mean values, $\sigma_i = \Delta_i / 3$.

Based on the probability density of the volumetric efficiency (5), it is possible to calculate its probabilistic moments: mean values and standard deviations. It allows for obtaining the possible values of the volumetric efficiency of the pump with the required confidence probability.

4   Results

In Fig. 4a, the dependences of the fluid flow through the balancing device on the middle radial gap in the face throttle are determined for deterministic values of the main parameters for different values of the pump operating time and steel grades (a) and for different values of the eccentricity of the cylindrical throttle and its length (b).

a   b
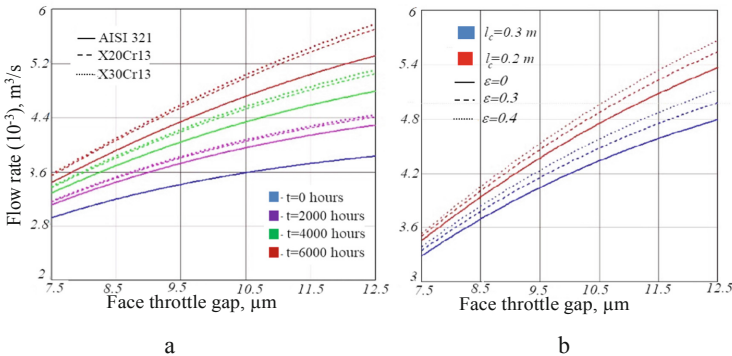
Fig. 4. Deterministic dependencies of the flow rate through the face throttle with considering an erosive change in the middle gap value of the cylindrical throttle.

Calculations are given for the following geometrical and regime parameters of the balancing device: $r_1 = 55$ mm, $r_2 = 77,5$ mm, $r_3 = 100$ mm, $h_c = 250$ mm, $l_1 = 210$ mm, $p_1 = 35 \cdot 10^6$ Pa, $p_3 = 3 \cdot 10^6 P$ a. The blue curve indicates the change in flow rate for the nominal value of the middle gap of the cylindrical throttle.

As it follows from the figure with an increase in the operating time of the balancing device, the flow rate increases. Moreover, the dependence for steel X20Cr13 of the flow rate on the middle face gap tends to linear.

Over time, blurring (increase) of the middle cylindrical throttle gap occurs. A corresponding decrease in the resistance of the cylindrical throttle leads to high pressures in the camera of the balancing device at the same value of the face gap. The value of the face gap at some value of the axial force due to blurring of the cylindrical gap will be greater and consequently the flow rate increases and the pump efficiency decreases (Fig. 4a).

As expected, the presence of eccentricity leads to an increase in flow rate which is also caused by the decrease in the hydraulic resistance of the cylindrical throttle and, consequently, an increase in pressure in the intermediate chamber. Obviously, the shorter the length of the cylindrical gap the lower its resistance and greater flow rate (Fig. 4b).

Figure 5 shows the change in the mean (main), the value of the flow rate through the balancing device from the middle face gap for the following operating time values: 2000, 6000 h.

As follows from the above graphs, the mean value of the flow rate through the balancing device differs from its deterministic value to the lower side within 1%. Such a difference is insignificant in engineering calculations, therefore, deterministic values obtained with considering the erosive change in the gap in time can be used as mean values. Also, note that the eccentricity gives a significant correction and for large of the face throttle gaps the difference increases.
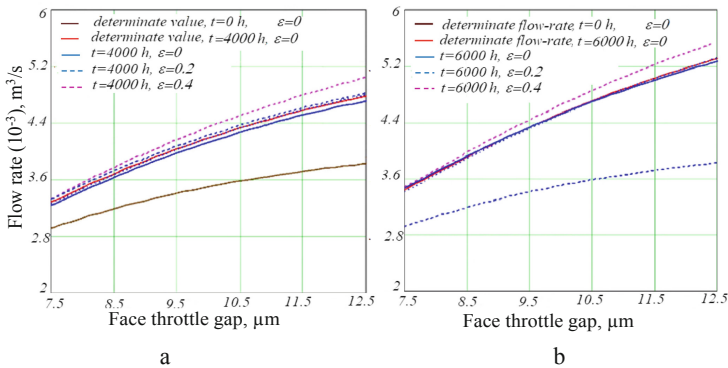
Fig. 5. The dependence of the mean value of the balancing device flow on the middle face gap for different operating times.

The probability densities of flow through the balancing device for the three values of the face gap are shown in Fig. 6.

The curves in Fig. 6 are obtained for a 10% deviation of the middle gap of cylindrical throttle due to manufacturing and installation tolerances. With an increase in the face gap value, the interval of possible values decreases. In addition, an increase in the face gap leads to an increase in the mean square deviations, and, accordingly, in the intervals of the possible flow rates through the balancing device for fixed time instants (lines of different colors but the same type).
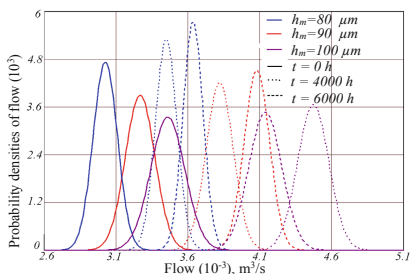
Fig. 6. The probability densities of flow through the balancing device.

Table 1. Standard deviations of the flow rate through the balancing device.

t, hours	Face gap, μm		
	80	90	100
0	$8.429 \cdot 10^{-5}$	$1.024 \cdot 10^{-4}$	$1.191 \cdot 10^{-4}$
4000	$7.521 \cdot 10^{-5}$	$9.452 \cdot 10^{-5}$	$1.149 \cdot 10^{-4}$
6000	$6.95 \cdot 10^{-5}$	$8.814 \cdot 10^{-5}$	$1.089 \cdot 10^{-4}$

Table 1 presents the standard deviations for different values of the face gap and different values of the operating time of the balancing device. From which it follows that with the same operating time under an increase in the face gap, possible deviations of the real flow from the calculated one will increase.

Under nominal operating, the value of the volumetric efficiency of the pump with a middle gap of cylindrical throttle $H = 250$ μm is $\eta_{vol} = 0,934$. After 6,000 h of pump operation, the gap increases to a value of $H = 347$ μm and $\eta_{vol} = 0.918$ for the face gap of 100 μm for the case where the deviation in the cylindrical gap value is 10% of the nominal. Thus, the decrease in pump efficiency due to tolerances and erosive wear of the sealing surfaces of the cylindrical throttle can reach 2.5%. With an increase in the relative deviation of the gap the volumetric efficiency of the pump decreases (Table 2).

Table 2. Volumetric efficiency of the pump.

t, hours	AISI 321	X20Cr13	X30Cr3
2000	0.929	0.928	0.928
4000	0.924	0.92	0.921
6000	0.918	0.913	0.914

5   Conclusions

When designing and calculating automatic balancing device, its geometric and operational parameters have a probabilistic nature. The operational characteristics of the pump and in particular automatic balancing device change under operation. For pumps pumping steam-water mixtures and contaminated liquids, this change is first of all caused by erosion wear of throttles. The erosion process has a pronounced probabilistic nature. The results obtained in the work confirm and also give a numerical estimation of the expected difference between the calculated (theoretical) and operational characteristics of the pump. The effect on the flow rate through the automatic balancing device and the value of the pump efficiency are analyzed with the consideration of a random change in the middle radial gap of the cylindrical throttle, random changing due to accepted tolerances, as well as random values of local hydraulic resistance and axial misalignment in the face throttle. As one would expect, the most significant deviation of the flow automatic balancing device characteristic gives an account of the possible change in the gap as a result of gap blurring. However, it should be noted that the neglect of some parameters, which in deterministic calculations have a negligible effect on the flow through the automatic balancing device under considering the probabilistic statement leads to an increase in the deviation of the flow characteristics from their nominal values. Since the flow rate through the automatic balancing device determines most of the pump losses and, consequently, its efficiency, it is not worth neglecting even these comparatively small corrections in analysis to increase the overall productivity and efficiency of the pump.

References

1. Marcinkovskij, V., Shevchenko, S.: Pumps of Nuclear Power Plants: Calculation, Design, Operation: Monograph. University book, Sumy (2018). [in Russian]
2. Pak, P., Belousov, A., Belousov, A.: Pumping Equipment for Nuclear Power Plants. Energoatomizdat, Moscow (2003). [in Russian]
3. Czegurko, L.: Centrifugal energy pumps, their malfunctions and tuning methods, Chelyabinsk (2002) [in Russian]
4. Korczak, A.: Investigation of balancing systems of axial thrust in multistage centrifugal pumps, Ed. Silesian University of Technology, Gliwice (2005) [in Polish]
5. Korczak, A., Martsynkovskyy, V., Peczkis, G., Zahorulko, A.: Diagnosis of the phenomenon of flow as an inspiration to inventions in the domain of constructing hydraulic machines. Procedia Eng. **39**, 286–302 (2012)
6. Korczak, A., Papierski, A.: The flow through the face clearance of disk relieving the axial force in multi-stage centrifugal pump. Trans. Inst. Fluid-Flow Mach. **N115**, 125–142 (2004)
7. Verbovyi, A., Neamtu, C., Sieryk, M., Vashyst, B., Pavlenko, V., Simonovskiy, V., Pavlenko, I.: Ensuring the vibration reliability of rotors connected by spline joints. J. Eng. Sci. **6**(2), D14–D19 (2019). https://doi.org/10.21272/jes.2019.6(2).d3
8. Jedral, W.: Turbulent fluid flow in hydraulically smooth transverse joints. Machine-building archive T. XXVIII, №1, pp. 39–53 (1981). [in Polish]
9. Jedral, W.: Methods for calculating longitudinal forces and unloading systems in vortex pumps, Scientific Works. Mechanics z 110, PW Publishing house (1988) [in Polish]

10. Karaskiewicz, K.: Investigation of Internal Flows in Pumps in Terms of Calculating Hydraulic Forces. Publishing house of the Warsaw University of Technology, Warsaw (2013). [in Polish]
11. Bolotin, V.V.: Methods of Probability Theory and Probability Theory in Calculations of Structures. Strojizdat, Moscow (1982). [in Russian]
12. Tarasevych, Y., Savchenko, I., Sovenko, N., Savchenko, A.: Research of influence of random change of annular seal parameters on efficiency of centrifugal pump. Eastern-Euro. J. Enterprise Technol. **6**(7(84)), 37–42 (2016)
13. Tarasevych, Y., Sovenko, N., Savchenko, I.: Influence of the stochastic nature parameters of throttle channels on characteristic of automatic balancing device of the centrifugal pump. In: Ivanov V., et al. (eds.) Advances in Design, Simulation and Manufacturing. DSMIE 2018. Lecture Notes in Mechanical Engineering. Springer, Cham (2019)
14. Tarasevych, Y., Sovenko, N.: Modeling the influence of cylindrical throttle erosion wear on characteristics of automatic balancing device. Tribologia **285**(3), 107–113 (2019)

Numerical Simulation of Coupled Problems

Simulation of Wearing Processes with High Sliding Speed

Aleksandr Dykha$^{(\boxtimes)}$, Ruslan Sorokatyi ,
and Volodymyr Dytyniuk

Khmelnytskyi National University, 11 Instytutska Street,
Khmelnytskyi 29016, Ukraine
`tribosenator@gmail.com`

Abstract. A calculation model of the wearing process under conditions of high-speed friction has been offered. The model is based on the thermokinetic theory of fracture. The determination of model parameters is based on a probabilistic-physical approach. The model is presented in discrete form and adapted for use by computer simulation methods using the Spatio-temporal discretization of the calculation algorithm. The analysis of the results showed that the prevailing factor that affects the stress-strain state of the tribosystem and the wearing processes is the rate of decrease of the friction coefficient from static to dynamic. It is proposed to use the rate of change of the friction coefficient to assess the effectiveness of using methods to increase the wear resistance of tribosystems under conditions of high-speed friction. As a result of the presented studies, an experimental analysis of the effect of changes in the coefficient of friction on the sliding velocity on wearing processes under conditions of high sliding velocities has been carried out. Experimental data confirm that the coefficient of change of the coefficient of friction is sensitive to the technology of the formation of the surface layer.

Keywords: Surface of friction · Markov chain · Tribological damage · Computer simulation · Laboratory test

1 Introduction

Calculation methods for analyzing the durability of tribosystems are preferred in conditions of extreme force and speed impacts. At the same time, experimental studies are difficult to implement and expensive. There is a number of difficulties in the development of methods for modeling the wear of friction units under high-speed friction. They are due to insufficient knowledge of the processes on the surfaces of the tribo-contact interaction, the probabilistic nature of external influences, and the influence of the operating conditions of the tribosystems. The characteristics of the stress fields of the friction nodes should be determined by taking into account dynamic effects under conditions of high sliding speeds and changes in the coefficient of friction as a function of sliding speed. When developing analysis methods, it is necessary to take into account that wearing processes are non-stationary random processes. Based on the features of the functioning of high-speed friction units, in most cases, computer

simulation methods are used to analyze the influence of the most significant factors on wearing processes. These methods involve the discretization of computational models in space and in time.

2 Literature Review

When modeling friction and wearing under conditions of high sliding speeds, it is necessary to take into account a number of specific factors of this process. First of all, we are talking about relative slip speeds of more than 80–100 m/s. And here the main feature is a significant decrease in the friction coefficient compared to the traditional operating conditions of the machines. The study of friction processes at high sliding speeds has been the subject of many scientific papers.

In [1] new routes to persistent superlubricity at the nanoscale the design of ultra-low dissipation nanomechanical devices may be guided. In the study [2] friction experiments are conducted to investigate dynamic slip resistance and time-resolved growth of metal films during dry metal-on-metal slip under extreme conditions.

The results of experimental studies of high-speed steel-steel friction have been presented. They show that the friction coefficient, in this case, can decrease to values of 0.0001. The determinants of the wearing elements of high-speed friction units [3–7] are the stress state, its dynamic nature, and temperature effects. In work [3], the effect of sliding friction processes on changes in the microstructure of materials was studied. This does not take into account the speed effect. In works [4, 5], an approach to the formation of components of surface contact stresses under the conditions of contact metal friction is studied. The geometric structure of the surface layer is also taken into account. In [6, 7] the influence of various technologies of surface hardening of steel on tribological parameters is considered: friction coefficient, wear, microstructure. At the same time, the mechanisms of fatigue wear of surfaces under sliding friction are not sufficiently considered.

Wearing as a result of the accumulation of tribological damage belongs to the class of cumulative damage. Basing on the processing of experimental material, the authors of [8, 9] have analyzed probabilistic models of the phenomenological processes of damage accumulation. It has been shown that models built based on random Markov processes with discrete time and states adequately describe the processes of cumulative damage.

3 Research Methodology

The first stage of building the model was the task of discretization of the wearing process. Using the impact model [8, 9], the wearing process is considered in discrete form. A number of assumptions have been made:

1. The process of interaction of the elements of the friction unit consists of repeating loading cycles. The loading cycle is the lifetime of the product during which tribological damage may accumulate and wearing may occur. The loading cycles

measure the time, which is discrete in this case. The assumption of the appearance of wearing only during the loading cycle does not distort the physical meaning of the model but gives significant advantages in the construction of design models.

2. The transition of the tribosystem from one state to another corresponds to the wearing of the surface layer by a certain amount. The states of wearing of the tribosystem are discrete and transient. The assumption of discreteness of wearing states is in good agreement with experimental data on the intermittent nature of the occurrence of disseminated damage in microvolumes.

3. The characteristics that determine the loading cycle remain unchanged within this cycle. This assumption postulates that the system of wearing is determined only at the beginning and at the end of the loading cycle. This condition is a condition for the Markov probability process. That is, wearing depends only on the loading cycle and the state of damage at its beginning.

4. To determine the probabilistic characteristics of the wearing process, it has been assumed that damage can occur only during the loading cycle. We denote w_{ii} is the probability that damage will not occur during the loading cycle. Then the probability of damage in this cycle is $1 - w_{ii}$, since the events form a complete group. If the wearing exceeds a critical value, the system will go into an absorbing state with a probability of exit from it equal to zero.

Thus, a model of the wearing process is obtained, which is described by a random Markov process with discrete states and time. The discrete model is embedded in the continuous physical wear process.

The parameters of the Markov chain are given if the vector of initial states and the matrix of transition probabilities are provided. In most cases, the components of the initial state vector $\pi_j(t = 0)$, are determined from the assumption that at the initial time, the system had no damage and was in the first state:

$$\left[\pi_j(t = 0)\right] = [1, 0, 0, \ldots, 0] \tag{1}$$

The probabilities of the states of the system at time $t > 1$ have been calculated as the product $\left[\pi_j(t - 1)\right]$ of the vector of unconditional probabilities at the time $(t - 1)$ and the transition probability matrix for the behaviour (если придерживаться британской версии англ.языка) of the tribosystem at time t:

$$\left[\pi_j(t)\right] = \left[\pi_j(t - 1)\right]\left[W_{ij}\right], i, j = 1, 2, \ldots, K_s \tag{2}$$

where $\left[\pi_j(t - 1)\right]$ is the vector of unconditional probabilities of finding the system in i - states ($i = 1, 2, \ldots, K_s$) at the time $(t - 1)$;
$\left[W_{ij}\right]$ is the matrix of transition probabilities;
K_s is the number of system states.

The transition probability matrix is given if the form is given and the components of the matrix w_{ij} are determined.

The authors of [8, 9] proved that the matrix of transition probabilities with single jumps up and the presence of an absorbing state most fully reflects the process of accumulation of tribological damage. The components of the transition probability matrix were identified through the correspondence between the parameters of the mathematical model and the physical characteristics of the wearing process under conditions of high-speed friction. Basing on the physical model of the wearing process, it has been assumed that transitions of the tribosystem from one state to another state occur under the influence of the wearing flow. When the wearing flow event occurs, the system transitions to the next state. In this case, the wearing flow event is understood as wearing a certain value of h. The wearing flow, according to the central limit theorem of flows, will be Poisson. That is, it has the properties of ordinariness and absence after the action, which does not violate the basic requirement of the Markov random process. Basing on the physical approach, the flux intensity $\lambda(t)$ is the average number of events per unit time. For the elementary region Δt adjacent to t [11], the intensity of the wearing flow $\lambda_I(t)$ at time t is defined as the wearing rate at time t divided by h.

$$\lambda_I(t) = \frac{V_I(t)}{h}, [1/\text{time}], \tag{3}$$

where $V_I(t)$ is the wearing rate at time t, (length/time, volume/time, mass/time); h is the value determined from the condition of the flow ordinary and having the dimension of length, mass, volume, depending on what wearing rate is used - linear, mass or volume.

The amount of wear h is selected from the following conditions. In one loading cycle, the probability of occurrence of a wearing value greater than h is very small.

To assess the wearing rate $V_I(t)$, the thermokinetic theory [10] is used. This theory makes it possible to study the combined effect of the stress state and temperature effects on tribological fracture.

The durability of the material under load σ according to [9]:

$$\tau = \tau_0 \exp\left(\frac{U_0 - \gamma\sigma}{kT}\right) \tag{4}$$

In [12], this dependence was specified considering the influence of the external environment in overcoming the energy barrier. Further, replacing the Boltzmann constant k with the gas constant R, we obtain:

$$\tau = \tau_0 \exp\left(\frac{U_0 - \gamma\sigma \pm \Delta G}{RT}\right), \tag{5}$$

where τ_0 is the time constant equal to the period of atomic vibrations in the body $10^{-13}...10^{-12}$ s;

T is the absolute temperature, K;
U_0 is the activation energy of the leading mechanism of destruction, J/mol;
γ is a structurally sensitive coefficient;
σ is the load;

ΔG is the coefficient taking into account the influence of the external environment ($\Delta G < 0$ - the external environment softens the layer, $\Delta G > 0$ - strengthens, and $\Delta G = 0$ - has a neutral effect).

Considering the cyclicity of the loading process, we represent the durability τ through the number of loading cycles N and the actual loading time per cycle t_c. We isolate the term $\sigma\gamma$ from the expression, which reflects that part of the work that the external influence performs in the destruction of the layer:

$$\sigma\gamma = U_0 - RT \, ln \left(\frac{N \cdot t_c}{\tau_0} \right) \pm \Delta G. \tag{6}$$

If we assume that the specific work of the friction forces A_f acts as the work of external forces, then we can write:

$$\sigma\gamma = \frac{A_f}{V_w}, \tag{7}$$

where V_w is the volume of the wear layer, mol.

Considering that $A_f = F_f L_S = f \cdot F_N \cdot L_S$, $V_w = (A_n \cdot h_w)/M$ and what attitude F_N/A_n represents contact pressure σ_N it can be written:

$$\sigma\gamma = \frac{f \cdot \sigma_N \cdot L_S \cdot M}{h_w}, \tag{8}$$

where f is the coefficient of friction;

F_N is the normal force, N;
L_S is the sliding friction path, m;
M is the molar volume, m^3/mol;
A_n is the nominal contact surface area, m^2;
h_w is the thickness of the wear layer, m.

Let us take as a friction model a generalized Coulomb-Amonton model taking into account the Stribeck effect, $f = f_d + (f_s - f_d) \cdot \exp(-\beta v_{sk})$. This model takes into account changes in the coefficient of friction as a function of sliding speed. As a result, expression (6) takes the form:

$$\tau = \tau_0 \exp \left(\frac{U_0 - \left[\frac{\sigma_N \cdot M \cdot L_S \cdot \left(f_d + (f_s - f_d) \cdot e^{(-\beta v_{sk})} \right)}{h_w} \right] \pm \Delta G}{RT} \right) \tag{9}$$

where f_d is the dynamic coefficient of friction;

f_s is the static coefficient of friction;
v_s is the relative slip velocity at the contact point;
β is the coefficient.

From the kinetic concept of fracture, durability is a fundamental characteristic of the mechanical strength of a material. It can be considered as a value inversely proportional to the average rate of the destruction process:

$$V_I(x, y, z, t) = \frac{1}{\tau}. \tag{10}$$

Then (3) takes the form:

$$\lambda_I(t) = \frac{1}{h\tau_0} \exp\left(-\frac{U_0 - \left[\frac{\sigma_N \cdot M \cdot L_S \cdot \left(f_d + (f_s - f_d) \cdot e^{(-\beta v_{sk})} \right)}{h_w} \right] \pm \Delta G}{RT(x, y, z, t)} \right), \tag{11}$$

where $V_I(x, y, z, t)$, $\sigma_N(x, y, z, t)$, $T(x, y, z, t)$ are the wearing rate, contact pressures, and temperature, respectively, at the point with coordinates (x, y, z) at time t.

Thus, through the function of the wearing rate, we can determine the main characteristic of the wearing flow, represented in the form of a Markov chain - the wearing flow intensity $\lambda_I(t)$, which determines the transitions of the system from one state to another.

The probability of the transition $w_{ij}(t)$ of the Markov chain from state i in which it was at time t to state j for an elementary time interval Δt is determined from the expression:

$$w_{ij}(t) \approx \lambda_I(t)\Delta t, \quad \text{for } i \neq j. \tag{12}$$

As $0 \leq w_{ij}(t) \leq 1$, $\lambda_I(t)\Delta t \leq 1$, $0 \leq \Delta t \leq 1/\lambda_I$.

The smaller Δt, the more accurately the probability of transition of the system from state to state will be determined [13]. Thus, using the probabilistic-physical approach, the parameters of the surface wear model under high-speed friction are obtained. It is described by a random Markov process with discrete states and time. The obtained model indicates that in estimating the wear rate of the layer, an important role is played by the coefficient ΔG, which takes into account the influence of the external environment. If $\Delta G < 0$ - the external environment increases the wear rate of the layer, $\Delta G > 0$ - reduces the wear rate of the layer, and $\Delta G = 0$ - has a neutral effect. In the case of wearing, the coefficient ΔG can be interpreted as a coefficient that takes into account the technology of formation of the surface layer and its effect on the activation energy of layer destruction processes. The proposed phenomenological model makes it possible to isolate and combine the main factors, distinguish their relationships and analyze the degree of influence on the wearing processes of friction units under conditions of high sliding speeds. The analysis of the obtained dependences shows that an increase in the sliding velocity, according to (11), leads to a decrease in the friction coefficient in the contact zone. However, the degree of influence will substantially depend on the value of the coefficient β. An increase in the sliding velocity will lead to an increase in temperature and dynamic loads in the contact zone. Accordingly, it will lead to a decrease in the activation energy and an increase in destructive processes in

the layer. At the same time, taking into account the weight coefficients at the indicated factors, contact pressures and temperature will have the prevailing effect on the wearing process. Using the presented model, it was possible to carry out a number of studies aimed at assessing the degree of influence of key factors on processes under high-speed friction. To confirm the conclusions drawn from the analysis of the model, an experimental analysis of the effect of changes in the coefficient of friction on the sliding velocity of the wearing processes under conditions of high sliding velocities has been carried out.

4   Results

The tests were carried out on a UMT-1 friction machine [14, 15] according to the disk – pin scheme (Fig. 1) with a maximum sliding speed of 60 m/s. A disk made of Stell 5140 with a diameter of 400 mm was used as a counter sample. The friction coefficient was determined by the moment of friction, which was fixed by the potentiometer of the friction machine for sliding speeds, respectively 5; 10; 20; 40; 60 m/s. Samples modified by various methods of chemical-thermal treatment were tested.
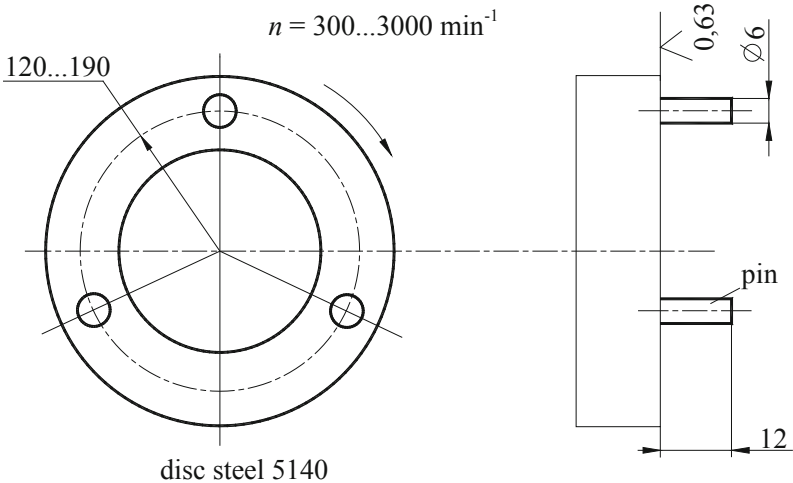
Fig. 1. Test scheme "disk - pin".

The experimental values of the friction coefficients for various slip velocities are presented in the Table 1.

Table 1. The results of determining the coefficient of friction.

Material	Sliding speed, ms^{-1}				
	5	10	20	40	60
A414 Grade A- Nitriding (N)	0.2	0.1	0.065	0.04	0.03
Stell 5140 - Nitriding (N)	0.2	0.088	0.058	0.035	0.026
A414 Grade A- Chemical-thermal treatment (CTT)	0.22	0.083	0.053	0.03	0.022
Stell 5120- Nitro carbonization (NC)	0.22	0.07	0.04	0.028	0.024
Stell 5140- Chemical-thermal treatment (CTT)	0.2	0.1	0.065	0.04	0.03

A graphical interpretation of the test results is presented in Fig. 2.

The analysis of the results indicates that in the entire range of the studied sliding velocities with increasing speed, a decrease in the coefficient of friction is observed from 0.2 (boundary, semi-dry friction) to 0.02 (friction through a liquid film). For some materials (Stell 5140 (CTT), Stell 5120 (NC)) stabilization of low values of the coefficient of friction takes place, starting from speeds of 40…50 m/s. Experimental data confirm the conclusion that the coefficient taking into account the rate of change of the coefficient of friction is sensitive to the technology of the formation of the surface layer.

1 - A 414 Grade A (N)
2 - Steel 5140 (N)
3 - A 414 Grade A (CTT)
4 - Steel 5120 (NC)
5 - Steel 5140 (CTT)
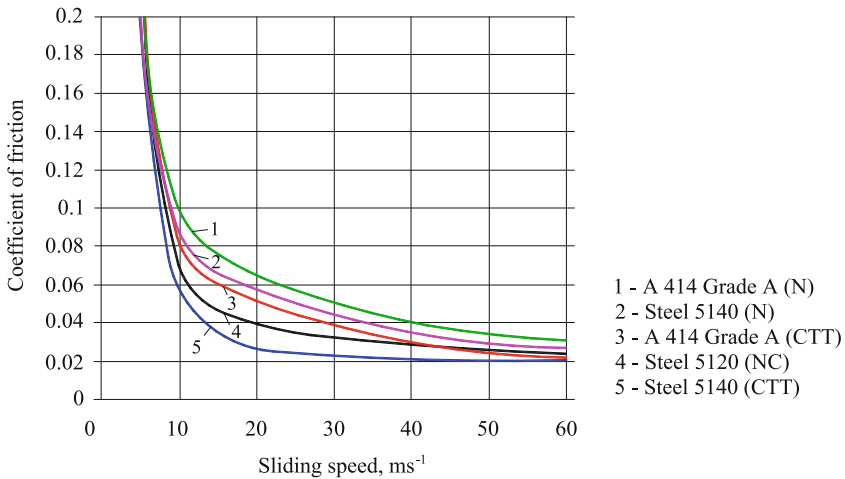
Fig. 2. The test results of samples of materials under conditions of high-speed friction.

In its turn, this recommends that the coefficient β should be used as a numerical criterion for evaluating the effectiveness of methods for increasing wear resistance at high sliding speeds.

5   Conclusions

1. A model of the wear process under conditions of high-speed friction is constructed. The model is based on the thermokinetic theory of fracture. It made it possible to unite the main factors and analyze their degree of influence on the wear of units operating in conditions of high sliding speed.

2. A generalized analysis of the results showed that the prevailing factor that affects the stress-strain state of the studied tribosystem and, accordingly, the wear processes, is the rate of decrease of the friction coefficient from static to dynamic.

3. As a criterion for evaluating the effectiveness of the use of materials, technological processes of coating, heat treatment, and other ways to increase the wear resistance of tribosystems under conditions of high-speed friction, the rate of change of the friction coefficient can be used. In this case, the coefficient β is taken as a quantitative assessment of the criterion.

References

1. Liu, Y., Grey, F., Zheng, Q.: The high-speed sliding friction of graphene and novel routes to persistent superlubricity. Sci. Rep. **4**, 4875 (2014). https://doi.org/10.1038/srep04875

2. Yuan, F., Liou, N., Prakash, V.: High-speed frictional slip at metal-on-metal interfaces. Int. J. Plastic. **25**(4), 612–634 (2009). https://doi.org/10.1016/j.ijplas.2008.12.006

3. Drozdov, Y.N., Yudin, E.G., Belov, A.I.: Applied Tribology (Friction, Wear, Lubrication). EkoPress, Moscow (2010)

4. Kindrachuk, M., Radionenko, O., Kryzhanovskyi, A., Marchuk, V.: The Friction mechanism between surfaces with regular micro under bondary lubrication. Aviation **18**(2), 64–71 (2014)

5. Kindrachuk, M.V., Vol'chenko, A.I., Vol'chenko, D.A., Zhuravlev, D.Y., Chufus, V.M.: Electrodynamics of the thermal contact friction interaction in metal-polymer friction couples. Mater. Sci. **54**(1), 69−77 (2018)

6. Sorokatyi, R., Chernets, M., Dykha, A., Mikosyanchyk, O.: Phenomenological model of accumulation of fatigue tribological damage in the surface layer of materials. In: Uhl, T. (eds.) Advances in Mechanism and Machine Science, vol. 73, pp. 3761−3769 (2019). https://link.springer.com/chapter/10.1007%2F978-3-030-20131-9_371

7. Kukhar, V.V., Vasylevskyi, O.V.: Experimental research of distribution of strains and stresses in work-piece at different modes of stretchforging with rotation in combined dies. Metall. Min. Ind. **3**, 71–78 (2014)

8. Kryshtopa, S., Kryshtopa, L., Bogatchuk, I., Prunko, I., Melnyk, V.: Examining the effect of triboelectric phenomena on wear-friction properties of metal-polymeric frictional couples. Eastern-Euro. J. Enterprise Technol. **1/5**(85), 40–45 (2017)

9. Banjac, M., Vencl, A., Otović, S.: Friction and wear processes – thermodynamic approach. Tribol. Ind. **36**(4), 341–347 (2014)

10. Dykha, A.V., Kuzmenko, A.G.: Solution to the problem of contact wear for four-ball wear-testing scheme. J. Frict. Wear **36**(2), 138–143 (2015)

11. Dykha, A., Sorokatyi, R., Makovkin, O., Babak, O.: Calculation-experimental modeling of wear of cylindrical sliding bearings. Eastern-Euro. J. Enterprise Technol. **5**(1(89)), 51–59 (2017). https://doi.org/10.15587/1729-4061.2017.109638

12. Etkin, V.A.: Thermokinetics (Synthesis of Heat Engineering Theoretical Grounds), Haifa (2010)
13. Ibatulin, I.D.: Kinetics of Fatigue Damage and Destruction of Surface Layers. Samara University, Samara (2008). (in Russian)
14. ASTM G 99 – Standard Test method for wear testing on a pin-on-disk test apparatus
15. Straffelini, G.: Friction and Wear, Methodologies for Design and Control. Springer, Berlin (2015)

Analysis of Frictional Interaction in a Couple "Billet – Crystallizer"

Oleg Khoroshylov[1]($\boxtimes$) , Oleg Podolyak[1] , Valentina Kuryliak[3] ,
Andrey Kipensky[2] , and Andrey Lomakin[1]

[1] Ukrainian Engineering Pedagogics Academy, 16, Universitetskaya Street,
Kharkiv 61003, Ukraine
`horol@i.ua`
[2] National Technical University "Kharkiv Polytechnic Institute", 2, Kirpicheva
Street, Kharkiv 61002, Ukraine
[3] Ukrainian Institute of Arts and Science, 14, Instytutska Street, Bucha 08292,
Kyiv, Ukraine

Abstract. The design of an experimental device (cold billet head) for deter-mining the forces of extraction from the mold of a continuous casting machine of copper alloy billets is proposed. The expediency of monitoring the temper-ature of the measuring element on which the base with strain gauges is made is shown. The temperature of the measuring element is controlled by a thermo-couple mounted on the axis of the cold billet head, which is the place for averaging the temperature over the cross-section of the temperature compensator and the measuring element. It is shown that at current levels of overcoming the frictional force of rest and the sliding friction force (graphite - bronze pair), the cross-sectional area of the base should be $5.33 \ 10^{-4}$ m^2. It is shown that the effort to overcome the static friction force exceeds the efforts to overcome the sliding friction force by 2.1–2.3 times.

Keywords: Continuous casting · Mold · Billet extraction force · Experimental cold billet head · Measuring element

1 Introduction

Continuous casting of billets in its efficiency in modern foundry is one of the leading places in the world. One of the most popular alloys in mechanical engineering (after iron-carbon) is non-ferrous alloys (in particular, we will consider BrO5TS5S5 bronze). The total global demand for copper, according to the World Bureau of Metal Statistics ("WBMS") for 2017, is estimated at 16.5 million tons [1]. Horizontal continuous casting machines billets (HCCMB) are used for the production of billets from copper alloys. Continuous casting of billets in its efficiency in modern foundry is one of the leading places in the world. From year to year, industrial enterprises of the machine-building complex increase the consumption of copper alloys and, at the same time, make demands on improving the quality of billets (mechanical properties). The increase in productivity of a continuous casting machine is directly related to linear productivity, i.e. with the speed of movement of the billet in the mold of a continuous

casting machine. One of the main reasons for the deterioration of the billet quality is dissipative processes due to an increase in its speed in the mold (the transition from the energy of disordered processes to the power of disordered non-linearly viscous part of the billet), which increases its damage. Therefore, to control the surface quality of the continuously cast billet, it is necessary to conduct a study of the influence of the speed of movement of the billet and the efforts of its extraction from the mold on the mechanical properties of the billets.

2   Literature Review

In modern mechanical engineering, continuous casting machines play an essential role in the manufacture of blanks of various sizes and brands with a suitable casting yield of 96%. A comparative analysis of the processes of continuous casting of hollow billets by centrifugal and continuous casting methods is presented in [2, 3]. One of the drawbacks of the continuous casting process is the relationship between the effort to extract the billet from the mold and the quality of the cast billet. A number of works have been published that are devoted to this issue [4–6]. In these works, it was shown that the effort to extract the billet causes stress in the billet, which significantly affects the damage to the billet.

In [7, 8], it is reported that on continuous casting machines with a swinging mold, it is not possible to determine how many components have the force to extract the billet from the mold. It was shown in work [6, 9] that, without taking into account the direction of movement of the billet at the beginning of the cycle, for three different modes of the basic cyclogram with cycle durations of 16, 12, and 8 s, the growth of the damage parameter is described by one addiction.

The popularity of the continuous casting process is based on the fact that the continuous casting machine has a significant advantage in both productivity and yield of casting compared to other billet production processes. So, for example, the yield of casting increases to 70% when casting in a chill mold and up to 96% when continuously casting [3].

On the basis of the obtained values of the rheological properties of copper alloys (creep), the authors of [4, 6] constructed models for determining the damageability and formation of cracks under tension depending on the efforts (stresses) and temperature in the billet. According to the author of [4], using the software package (simulation model), it is possible to determine the level of damage to the billet and the author [6] to predict the occurrence of cracks when the temperature distribution or other factors in the billet change.

So, modern researchers of the continuous casting process from many countries continue to study the processes of microcrack formation, both in copper and iron-carbon alloys. For example, the authors of [4, 10, 11] are involved in the processes of preventing surface cracks in both iron-carbon and non-ferrous alloys.

The publications provide a solution to various problems associated with the production of continuously cast billets, such as analysis of the rigidity of the segment for the frame of the continuous casting machine, depending on the efforts to extract the billet [12].

In [3] an experimental horizontal machine for continuous casting of blanks from copper alloys is shown (Fig. 1). Thus, one of the main reasons for the formation of microcracks on the surface of a cyclically moving billet is that, in most cases, software systems for calculating the damage parameter do not take into account the force to overcome the rest friction force (RFF). It was shown in [11] that the microcrack that occurred during the overcoming of the STF develops (deepens and expands) during the overcoming of the sliding friction force. It was shown in [13–15] that without taking rest friction force (RFF) efforts into account, it is impossible to build an automatic control system for the continuous casting process that could provide the expected quality of the billets (mechanical properties).
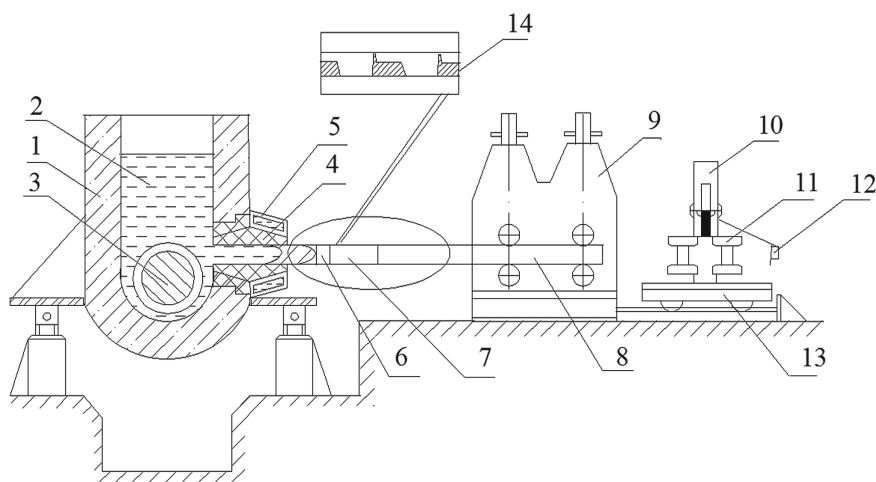
Fig. 1. 1 - Horizontal continuous casting machine of non-ferrous metal and alloy billets: 1 - housing metal; 2 - melt; 3 - mixer inductor for heating the melt; 4 - graphite mold sleeve; 5 - copper water-cooled crystallizer sleeve; 6 - cold billet head; 7 - measuring element with base; 8 - shank cold head billet; 9 - pulling stand; 10 - a flying circular saw; 11 - a device for clamping the billet before cutting; 12 - end switch; 13 - a trolley for moving a flying circular saw; 14 - force (or strain) station.

Therefore, our task is to more accurately determine the two-level effort when removing the billet (overcoming the rest friction force and sliding friction force in a pair: a graphite mold - bronze grade Br O5Ts5L5) for one cycle and determine their ratio 3.

3   Research Methodology

Our methodological task is to identify and compare two forces when removing billets from the crystallizer mold: it is the force to overcome the rest friction force and the force to overcome the sliding friction force. All operations to determine the effort to

extract the billet from the crystallizer were carried out on the machine shown in Fig. 1. All operations to assess the effort to remove the billet from the mold were carried out on a horizontal continuous casting machine of copper alloys, which was improved by installing a gearless drive with a rotating rotor [13, 15]. This drive has a lower rotation speed, which allows increasing the accuracy of control of the movement of the billet, which in turn increases the accuracy of determining the efforts to extract the billet.

Figure 1 presents the general scheme of the HCCMB, on which studies were carried out to determine the effort to extract the billet from the crystallizer during its cyclic motion.

The experimental device installed on the continuous casting machine includes: cold billet head 1, which is included in the threaded connection with temperature compensator 2;

- measuring element 2, on which the base 5 is made for installing strain gauges;
- ZetLab 410 signal amplifier and ZetLab 210 analog-to-digital and digital-to-analog conversion module;
- connecting wires.

At the beginning of the continuous casting process, a cold head with a shank is usually used. In our case, a measuring element with a base 6 was installed between the head and the shank for installing strain gauges (Fig. 2). The cold head shank is shown in Fig. 1 (pos 8).
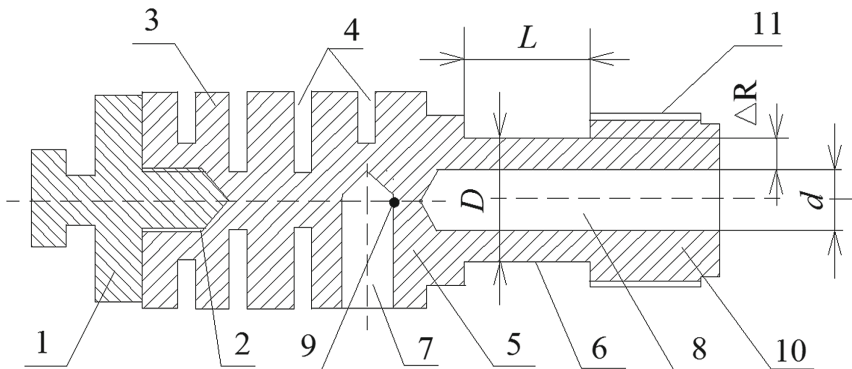
Fig. 2. An experimental device with a measuring element for determining the effort to extract the billet from the mold HCCMB: 1 - cold billet head; 2 - threaded connection; 3 - temperature compensator; 4 - annular thermal resistance; 5 - measuring element; 6 - the base surface of the measuring element for the installation of strain gauges; 7 8, - technological holes; 9 - thermocouple for monitoring the temperature of the measuring element; 10 - sleeve for connecting to the shank; 11 - threaded connection for attaching a shank cold head billet (not shown); L - is the length of the base of the measuring element; D, d - outer and inner diameters of the annular section of the base for calculating its cross-section; ΔR is the difference in the size of the outer and inner radii.

Before assembling the experimental device, the base L of the measuring element 5 is circular, and its cross-sectional area on the base L section is calculated. After that, load cells are glued on the outer surface of the base, and the wires are connected to the ZetLab 410 amplifier and the ZetLab 210 analog-to-digital and digital-to-analog conversion module. After that, the experimental device is calibrated.

To measure and record the force under load of the experimental device, wire strain gauges with a base of 20 mm were used as part of its measuring unit.

The cold billet head 1, thermal compensator 3, the measuring element 5 (Fig. 2) and the shank cold head Billet 8 (Fig. 1) are components of the experimental device and are used to determine the forces when removing the billet from the HCCMB crystallizer. When installed on a continuous casting machine, the experimental device is mounted so that the cold billet head 1 enters the cavity of the mold 4 (Fig. 1) by 0.05–0.075 m. The shank cold head billet 8 must be clamped by two pairs of rolls of the pulling stand 9 (Fig. 1) Strain gages (not shown) are installed on the outer surface of the base of the measuring element 6 (Fig. 2).

The main objective of experimental research:

– receiving the optimal signal from load cells located based on the measuring element and its transmission to the ZetLab 410 amplifier and the ZetLab 210 analog-to-digital and digital-to-analog conversion module to the recording device;
– coordination of the cross-sectional area of the base both with the optimal deformation of the material from which the cold billet head measuring element is made, and with the magnitude of the longitudinal deformation for which the load cells are designed;

To ensure the temperature regime of the normal operation of the strain gauges when measuring the efforts to extract the billet from the mold in front of the measuring element in the body of the temperature compensator 2 (Fig. 2), four heat-insulating air layers 4 were made, designed to restrain the heat flux along the axis of the experimental device (Fig. 1) In addition, it is necessary to provide the necessary cross-section of the measuring element along with the base length L (Fig. 2). To do this, based on Hooke's law, we obtain the equation:

$$\varepsilon = P/E * F \tag{1}$$

where is $\varepsilon = \Delta l/l$ the elongation, E is the modulus of elasticity of heat-resistant steel grade St.12MX; F is the cross-sectional area along the length of the base L of the measuring element, m^2; P is the force acting on the cross-section of the base L. Given the insignificant value of the indicated area, it is expedient to carry out its circular. To do this, we perform a recess on the outer surface of the base, the value $\Delta R = 0.5 \ 10^{-2}$ m (Fig. 2), which would allow us to place resistive load cells. Given that the outer diameter of the billet is 0.03 m, the recess of the base is $0.5 \ 10^{-2}$ m, we determine the value of the internal radius, provided that $F = 5.33 \ 10^{-4} \ m^2$ according to the equation

$$d = (D - 2 * \Delta R)^2 - F/4\pi \tag{2}$$

where D, d is the outer and inner diameter of the measuring element, m. F is the cross-sectional area of the bases of the measuring element, m (Fig. 2). We assume that to determine the SFF overcoming force of 1232.4 N and at an allowable stress of 25 MPa, the deformation of the steel of which the measuring element is made will be in the elastic limit, i.e. will be no more than $2.3 \ 10^{-5}$ m. Given the above data, we obtain that the cross-sectional area of the base (F) should be $5.33 \ 10^{-4} \ m^2$.

We assume that the allowable stress in the cross-section of the base made of this grade of heat-resistant steel is 30 MPa to ensure elastic deformation of $2.3 \cdot 10^{-5}$ m. For calculations, reduce the allowable voltage to 25 MPa. The cross-section of the base L of the measuring element 6 (Fig. 2), which is subjected to tension, must meet the following requirements it is the forces acting on the experimental setup must cause elastic tensile forces in the base, which are in the area of adequate perception of the strain gauges.

As a result of experimental studies, two levels of effort in the billet were determined: efforts due to overcoming the billet of the static friction force and efforts caused by overcoming the sliding friction force. In its final form, taking into account the insignificant efforts in removing the billet from the mold, the base cross-sectional area was a ring with a cross-sectional area of $5.33 \ 10^{-4} \ m^2$.

4   Results

The test was performed on blanks with a diameter of 30 mm from Br05Ts5S5 alloy, which was cast on a horizontal continuous casting machine, with a chain determining the forces of their extraction from the mold during the cyclic movement of the billet during overcoming rest friction force (RFF) and sliding friction force (SFF).

Studies to determine the dependence of the resting friction force between the surfaces of the mandrel and the billet on various technological parameters of continuous casting are shown in Table 1.

Table 1 Experimental data on the determination of the rest and sliding friction forces during movement of a billet in an HCCMB mold at various speeds of its movement and pause duration.

№	Speed billet in the cycle, Vц 1 10-3 м/с	Duration of a pause / (movement) in a cycle, t, c	The effort to overcome the power of the rest friction force, P, N	The effort to overcome the sliding friction force, P, N
1	15.0	4.0 /(1.33)	993.4	474.0
2	15.0	5.0 /(1.67)	1011.3	474.3
3	15.0	6.0 /(2.0)	1100.1	474.1
4	18.75	5.0 /(1.67)	1232.4	529,5
5	15.0	5.0 /(1.67)	1066.7	474.1
6	12.5	5.0 /(1.67)	975.3	455.4

1. From the Table 1, it follows that the force to overcome the RFF depends on the duration of the pause since, during the stop, adhesive bonds are formed in the crystallization temperature range with the relatively cold crystallized wall. So, with a pause duration of tp - 6.0 s, the force to overcome the RFF was 1100.1 N, and with tp - 4.0 s it was 993.4 H. With a 1.5-fold increase in the pause duration, efforts to overcome SFF was 1.11 times.
2. The increase in the speed of movement of the billet leads to an increase in efforts to overcome the sliding friction force. So, at the billet movement speed in the cycle, $V_c = 0.01875$ m/s, the force to overcome the SFF was = 529.5 N, and at $V_c = 0.0125$ m/s – 455.4 N. Thus, with an increase in the speed of 1.5 times the effort to overcome the SFF increased by 1.16 times.

From Fig. 4, it follows that the cycle duration is 8.0 s. Moreover, the ratio of the period of the movement to the duration of the pause is 1: 3. The force to overcome RFF at a speed of movement of the billet in the mold of 0.01875 m/s, (pos. 1) is 1232.4 N, and the force to overcome RFF (pos. 2) is 529.5 N. Thus, for of these conditions (line 4 of Table 1), the effort to overcome SFF is 2.33 times higher than the attempt to overcome RFF.

Pos. Figures 3 and 4 in this figure represent the dependencies of the temperature on the measuring element on the number of the billet movement cycle. The distance from the mold to the rolls of the pulling stand 6 is 1.35 m. With the step of movement of the billet in a cycle equal to 0.04 m, we find that during testing, the billet can perform 33 cycles of movement. In Fig. 4 shows the dependence of temperature changes in the 10th and 25th cycle.

The area of the cross-sectional base, F, 10^{-4} m
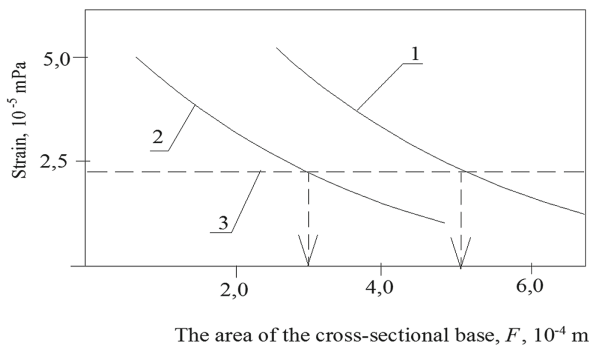
Fig. 3. Determination of the cross-sectional area of the base for the forces arising in the base of the measuring element during overcoming the rest friction force and sliding friction force: 1, 2 - Dependence of elastic deformation on the cross-sectional area of the base of the measuring element with a force of 1232 acting on it 43 N and 529.5 N; 3 - The value of permissible elastic deformation for strain gauges.

Thus, the results of experimental studies allow us to conclude that the parameters of the continuous casting process have a significant effect on the effort to extract the billet from the mold, which in turn determines the mechanical properties of the billet.
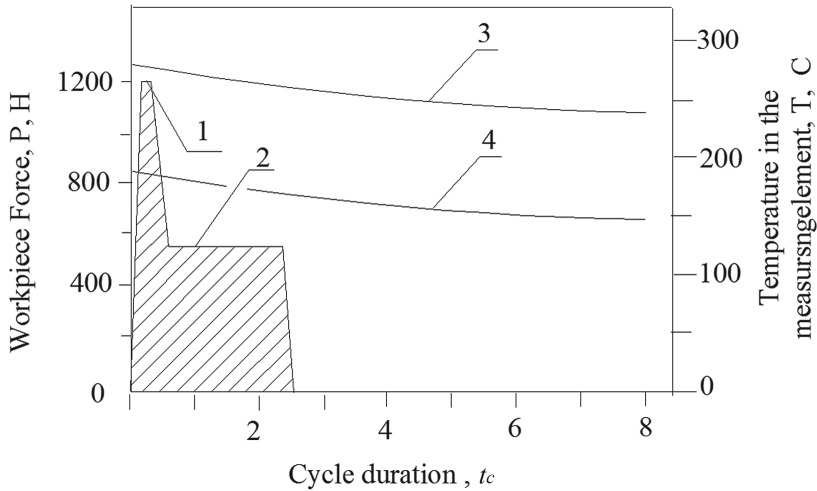
Fig. 4. Registration of efforts in the billet during its movement in the cycle with a speed of 0.01875 m/s: 1 - a force to overcome the rest friction force, N; 2 - an effort to overcome the sliding friction force in a pair: "bronze – graphite", P, N; 3, 4 - curves of temperature changes in the measuring element at the 10th and 25th measurement step.

5   Conclusions

Based on experimental studies, the following work was carried out:

1. To determine the efforts to extract the billet from the mold, a composite experimental cold billet head with force measuring element was developed using strain gauges.
2. Due to the fact that the cold billet head had contact with the melt:

   – the design of the meter provided for three heat-insulating layers that delay the heat flux along the axis of the measuring element to the base;
   – when calibrating for each of the loads 500, 1000 and 1500 N, the signal level was tested at temperatures in the range 150–350 °C.

3. It is proved that to ensure the given accuracy in determining the efforts to extract the billets, it is necessary:

   – make a cross-section of the base of the measuring element with an area equal to $5.33 \; 10^{-4}$ m^2;
   – to create the specified cross-sectional area of the base of the measuring element, it must be performed in the form of a ring.

4. As a result of experimental studies, two efforts were recorded that arose during the movement of the billet in the cycle:

- the force to overcome the static friction force, which is a surge in the billet, arising from the destruction of the adhesion forces formed between the billet and the graphite mold sleeve;
- the force to overcome the sliding friction force in pair 6 "graphite mold sleeve – billet";
- it is shown that the force to overcome the static friction force over the force to overcome the SFF under the conditions presented in Table 1, are in the range of 2.1–2.3 times.

References

1. Statistical yearbook for the production of continuously cast steel, pp. 9–12. World Steel Association, Brussels, Belgium (2018)
2. The global market for non-ferrous metals in 2016. http://www.metalresearch.ru/world_non-ferrous_2017.html. Accessed 19 Sept 2019
3. Khoroshylov, O., Kurylyak, V., Podolyak, O., Antonenko, N.: Study of the processes of shaping the hollow billets from antifriction alloys by the centrifugal and continuous casting methods. Usp. Fiz. Met. **20**(3), 367–395 (2019)
4. Lee, J., Yeo, T., Kyu Hwan, O., Yoon, J., Yoon, U.: Prediction of cracks in continuously cast steel beam blank through fully coupled analysis of fluid flow, heat transfer, and deformation behavior of a solidifying shell. Metall. Mater. Trans, 225–237 (2000)
5. Xu, H., Wen, G., Sun, W., Wang, K., Yan, B.: Analysis of thermal behavior for beam blank continuous casting mold. J. Iron Steel Res, 17–22 (2010)
6. Salazar-Campoy, M., Morales, R., Najera-Bastida, A., Calderon-Ramos, I., Cedillo-Hernandez, V., Delgado-Pureco, J.: A physical model to study the effects of nozzle design on dispersed two-phase flows in a slab mold casting ultra-low-carbon steels. Metall. Mater. Trans **49B**, 812–830 (2018)
7. Jin, X., Chen, D., Zhang, D., Xie, X.: Water model study on fluid flow in slab continuous casting mould with solidified shell. Ironmak. Steelmak, 155–159 (2011)
8. Yang, G., Sie, H., Jan, V., Ji, P., Jan, F., Ren, Z., He, J., Hu, Z., Zhao, B.: Choosing a variety of industrial control computers first of all, depending on the production conditions, the continuously cast steel billet that needs to be manufactured, and the generation of the liquid level in the mold and the desired path curve. Chinese patent: CN110102730-A (2019)
9. Li, C.: The spray positioning device of the continuous casting machine has a spray manifold that communicates with the distributor towards the center of the distributor, and positioning holes that are located on the base, and a seat that is located on the distributor. Chinese patent: CN206732081-U (2017)
10. Toishi, K., Miki, Y., Kikuchi, N.: Simulation of crack initiation on the slab in continuous casting machine by FEM. ISIJ Internat, 865–871 (2019)
11. Marita, Yo.: Analysis of deformations causing internal cracking in continuously cast billets, 271–282 (1983)
12. Lei, Z., Su, W., Hou, B., Gao, Q.: Stiffness analysis and experimental verification of segment frame of continuous casting machine. In: International Conference on Materials Science and Manufacturing Engineering, Paris, France (2019)

13. Khoroshilov, O.N., Kipensky, A.V., Lysenko, V.V., Marakhovsky, M.B., Trokhin, M.V., Kulischenko, V.V., Babischeva, I.I.: Horizontal continuous casting machine with an automatic gearless electric drive with a rolling rotor. Col. scientific papers. Bulletin of NTU « KhPI » 30(1), 175–178 (2008)
14. Khoroshilov, O.M., Kipensky, A.V., Lysenko, V.V., Marakhovsky, M.B., Trokhin, M.V.: Continuous casting machine. Declaration patent of Ukraine for utility model 28346 (2007)
15. Lei Z., Houfa S., Tianyou H., Baicheng L.: Analysis of heat transfer and thermal stress in continuous casting with mechanical reduction, pp. 355–359 (2016)

Analysis of the Initial Corrosion Stage
of a Steel Disk Under the Influence of Stress

Vladimir Klimenko, Iryna Shuda [ID], and Tetyana Zhylenko[(✉)] [ID]

Sumy State University, 2, Rymskogo-Korsakova Street, Sumy 40007, Ukraine
t.zhylenko@phe.sumdu.edu.ua

Abstract. As known, there are many types of metals corrosion, which in turn leads to the appearance of cracks, which bring the details of mechanical engineering out of operation. The work investigates the corrosion of an isotropic stress disk. To analyze the effect of corrosion on the disk operation, the method of singular integral equations is used. We conducted a literature review of this topic. We showed the solution of singular integral equations. The asymptotic stress values of an isotropic medium with a corrosion crack in the field of centrifugal forces are obtained. The analysis of the stress state of an isotropic steel disk was carried out depending on the shape, size, and location of the damage. The problem of a fixed disk with a crack, which shores are loaded with normal pressure, is considered. We built graphical illustrations that confirm the dependence of cracks appearing on the load, and also prove the compensation of load by increasing the number of cracks.

Keywords: Corrosion · Steel · Stress intensity

1 Introduction

As it is well known, metals and their alloys play a crucial role in the process of human life. They tend to destruction due to chemical or electrochemical exposure.

One of the important problems of modern science, technology, and economics is metals corrosion. The active fight against metal corrosion began in the 1950s [1] and it continues noa aiming at creating complex anti-corrosion alloys and materials preventing this process.

Many issues of the industry can be solved by finding a solution to the problem of metals corrosion.

There are the following types of corrosion as chemical, electrochemical (electrolytic, atmospheric, soil, aeration, marine, bio-corrosion, and electro-corrosion) [1]. We are considering the last one.

We know that the economic losses of the gross domestic product of countries due to the material's corrosion are of great importance. The introduction of high-strength materials in the modern industry makes this topic relevant.

Corrosion is a major problem in shipbuilding, the maritime industry, the aircraft industry because its effect is harmful to ships, airplanes, as well as to the personnel that serves them and passengers.

The effect of corrosion on steel structures reduces their functionality due to reduced tightness, strength, electrical and thermal conductivity, ductility.

Investigation of the corrosion process and the development of anti-corrosive materials and coatings can solve a number of problems: they can help reduce the metal consumption of industrial objects, increase the period of their operation, and reduce their cost.

The main purpose of the article is to study the destruction process of load-bearing structures and machine parts associated with corrosion and stresses arising from their operation. Analysis of structural conditions using a mathematical model based on the methods of integral equations can eliminate or even prevent destruction.

2   Literature Review

Investigation of the corrosion process and the development of anti-corrosive materials and coatings can solve a number of problems: they can help reduce the metal consumption of industrial objects, increase the period of their operation, and reduce their cost.

Nowadays, a lot of research is devoted to the use of composite materials [2], the analysis of the influence of heat treatment of malleable cast iron in sulfur [3], the analysis of the basic surface properties and methods for determining corrosion [4], the comparative analysis of corrosion in inorganic and organic materials [5], the assessment of corrosion inhibition efficiency [6], the corrosion mapping of several associated metal alloys [7], the corrosion analysis of electrolytic-plasma metal processing [8].

In addition, research and numerical modeling of the cracks themselves and the stresses that give rise to them are carried out: the adhesion zone and stress states of the crack tip are analyzed [9]; the growth of viscous cracks [10] and plastic cracks [11] are modeled, and the strength paradox of thick plates is revealed [10].

Singular equations were used only for the analysis of cracks in thin plates with holes [13]. The regularity of the periodicity of holes appearance was established [14]. An analysis of the growth of crack fatigue, as well as the effects of its restriction, was carried out [15, 16]. We suggest considering edge cracks and their radian stresses as they are the most destructive.

3   Research Methodology

To select the material, taking into account its exposure to workloads and the time of cracking in the early stages, we have analyzed the process of formation of a corrosion crack (Fig. 1) and its impact on the work under stress (Fig. 2).

In real solids, there are a large number of different micro defects, which under the action of various loading lead to metal destruction. In this case, it is enough to mention such universally recognized and ubiquitous defects as dislocations, grain boundaries, and the release of a new phase. Their interaction in the field of external loads essentially determines the structure of the material and, as a consequence, its strength characteristics.
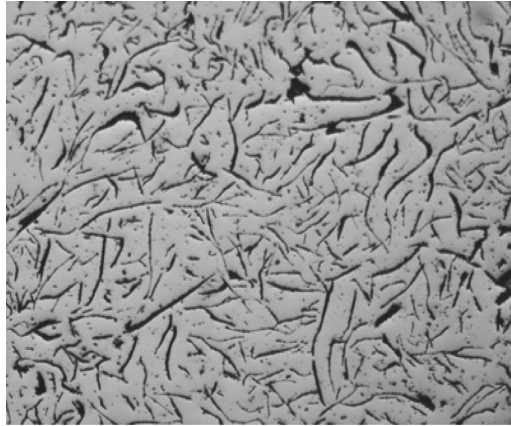
Fig. 1. One section $1 \times 1 \times 0.25$ in. ($25 \times 25 \times 6$ mm) or smaller cut of an iron casting [9].
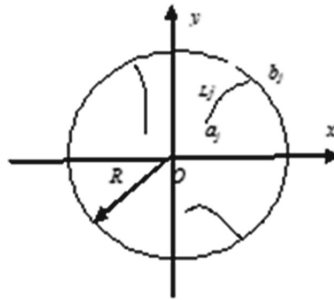
Fig. 2. Disk crack pattern.

The study of various cracks in metal plates and disks has been the subject of many researches [11–13]. Singular integral equations for finding the features of stresses on the tops of cracks were used in the works. [14–17].

Let a circular isotropic cylinder with radius R is weakened in the next tunnel by the curved cracks $L_j(j = \overline{1, n})$.

Suppose that the boundary region is free from forces and stress state in the cylinder due to the presence of a stationary temperature field.

Equation of stationary heat conduction, in this case, takes the form (1).

$$\Delta T - Q\lambda = 0, \tag{1}$$

where T - temperature; Q - intensity of heat; λ - thermal conductivity.

Hooke's law for the isotropic medium can be written as (2)

$$\varepsilon_x = \frac{1}{E}\left[\sigma_x - v\sigma_y\right] + \alpha T,$$

$$\varepsilon_y = \frac{1}{E}\left[\sigma_y - v\sigma_x\right] + \alpha T, \tag{2}$$

$$\gamma_{xy} = \frac{1}{G}\tau_{xy},$$

where α is the coefficient of thermal expansion; v - is the Poisson's ratio; E - is the modulus of elasticity; G - is the shear modulus.

We introduce the voltage function as follows (3):

$$\sigma_y = \frac{\partial^2 F}{\partial y^2}, \sigma_{yx} = \frac{\partial^2 F}{\partial x^2}, \tau_{xy} = \frac{\partial^2 F}{\partial x \partial y} \tag{3}$$

Substituting (2) in the compatibility condition for the strains, taking into account (3), we obtain a differential equation for the stress function:

$$\Delta\Delta F + \frac{E\alpha}{1-v}\Delta T = 0. \tag{4}$$

Общее решение уравнения (4) имеет вид The general solution of the Eq. (4) has the form

$$F = \mathrm{Re}[\bar{z} \cdot \varphi(z) + \chi(z)] + \frac{A}{64}z^2 \cdot z^{-2}, \tag{5}$$

$$A = \frac{E\alpha Q}{(1-v)}; z = x + iy.$$

Where $\varphi(z)$ and $\chi(z)$ are arbitrary analytic functions. The stress components are determined by the formulas (6)

$$\sigma_x + \sigma_y = 4Re\varphi(z) + \frac{A}{4}z \cdot \bar{z},$$

$$\sigma_x - \sigma_y = 2i\tau_{xy} = 2\left[\bar{z}\varphi''(z) + \chi''(z) + \frac{A}{16}z^{-2}\right]. \tag{6}$$

Assuming that the thermal field in the body is known, we represent the analytical functions $\varphi'(z)\ \chi'(z)$ in the form (7)

$$\phi'(z) = \phi_1(z) + \phi_2(z) + \chi''(z) = \psi(z) = \psi_1(z) = \psi_2(z), \tag{7}$$

where

$$\phi_1(z) = -\frac{1}{2\pi i}\int_L q(t)\frac{dt}{t-z}, \quad \phi_1(z) = \sum_{m=0}^{\infty} a_m z^m,$$

$$\psi_1(z) = \frac{1}{2\pi i}\int_L q(t)\frac{\bar{t}dt}{(t-z)^2} + \frac{1}{2\pi i}\int_L \overline{q(t)}\frac{dt}{t-z} +, \quad \psi_2(z) = \sum_{m=0}^{\infty} b_m z^m,$$

$t \in L = \cup_{j=1}^{n} L_j,$

$\phi_1(z)$ and $\psi_1(z)$ - functions taking into account the effect of the crack on the stress state (3); $\phi_2(z)$ and $\psi_2(z)$ - functions taking into account the influence of the circular boundary.

The coefficients a_m and b_m are determined using the condition of the absence of stresses on the circular boundary G.

Assuming that the crack faces are free of forces, the boundary condition is written as

$$\phi^{\pm}(t_0) + \overline{\phi^{\pm}(t_0)} - e^{i\psi}\left[\bar{t}\cdot\phi'^{\pm}(t_0) + \psi(t_0)\right] = Y,$$

$$Y(t_0) = \frac{E\alpha Q}{8\lambda(1-v)}\left(-t_0\cdot\bar{t}_0 + \frac{1}{2}\bar{t}_0^2\cdot e^{2i\psi_0}\right). \tag{8}$$

Here ψ the angle between the normal to the left bank of the section and Ox axis, the upper sign refers to the left bank of the section when moving from beginning a_j to end b_j.

Substituting the limit values of functions (7) in the boundary condition (8), we receive the singular integral Eq. (9):

$$\frac{1}{\pi i}\int_L \frac{q(t)dt}{t-t_0} + \frac{1}{2\pi i}\int_L q(t)\cdot K(t,t_0) + \overline{q(t)}\cdot K_*(t,t_0)dS = N(t), \tag{9}$$

$$N(t_0) = -\frac{E\alpha Q}{16\lambda(1-v)}\left(R^2 - 2t_0\cdot\bar{t}_0 + t_0^2\cdot e^{2i\psi_0}\right),$$

$$K(t,t_0) = \frac{d}{dS}\ln\frac{\bar{t}-\bar{t_0}}{t-t_0} + \frac{e^{2i(\psi-\psi_0)}-1}{\bar{t}-\bar{t_0}}\cdot\frac{d\bar{t}}{dS} + \frac{dt}{dS}\left[-\frac{\bar{t}}{R^2} - \frac{\bar{t_0}\cdot t\cdot\bar{t}(2R^2+\bar{t_0}\cdot t)}{R^2\cdot b^2}\right.$$
$$+ \frac{\bar{t_0}(2R^2-\bar{t_0}\cdot t)}{b^2} - \frac{t_0\cdot\bar{t}^2}{R^2\cdot b^2} + \frac{2R^2\cdot t_0\cdot t\cdot\bar{t}}{e^{2i\psi_0}\cdot b^3} - \frac{4R^2\cdot t_0}{e^{2i\psi_0}\cdot b^3}$$
$$\left.+ \frac{t}{e^{2i\psi_0}\cdot b} - \frac{t^2\cdot\bar{t}(3R^2-\bar{t_0}\cdot t)}{e^{2i\psi_0}\cdot b^3} + \frac{R^2\cdot t(3R^2-\bar{t_0}\cdot t)}{e^{2i\psi_0}\cdot b^3}\right],$$

$$K_*(t,t_0) = \frac{e^{2i(\psi-\psi_0)}-1}{\bar{t}-\bar{t_0}}\cdot\frac{d\bar{t}}{dS} - 2ie^{-2i\psi_0}\frac{Im\left[(t-t_0)\frac{d\bar{t}}{dS}\right]}{(\bar{t}-\bar{t_0})^2}$$
$$+ \frac{d\bar{t}}{dS}\left[\frac{t}{R^2} + \frac{t_0\cdot t\cdot\bar{t}(2R^2-t_0\cdot\bar{t})}{R^2\cdot\bar{b}^2} - \frac{t_0(2R^2-t_0\cdot\bar{t})}{\bar{b}^2}\right.$$
$$\left.+ \frac{t^2\cdot\bar{t_0}}{R^2 b} - \frac{t^2\cdot\bar{t_0}}{e^{2i\psi_0}\cdot b^2} + \frac{t^3}{e^{i\psi_0}\cdot b^2}\right],$$

$$b = R^2 - \bar{t_0}\cdot t; t, t_0 \in L; \psi_0 = \psi_0(t).$$

In the case of an isotropic cylinder with cracks not extending to the boundary G, we also find the solution of Eq. (9) for the class of functions having a discontinuity at the ends of the integration line

$$q(t) = \frac{q_0(t)}{\sqrt{(t-a)(t-b)}}. \tag{10}$$

According to (8), the solution of Eq. (10) is found up to an arbitrary constant. To fix the solution, it is necessary to use an additional condition to (9). Such a condition is the condition of movements uniqueness, which has the form:

- in the case of heat-conducting cracks $\int_L q(t)dt = 0$;
- in the case of insulated cracks

$$(\chi+1)\int_L q(t)dt = -\frac{a\cdot E}{2}\int_L \frac{t\cdot\omega(t)}{e^{i\psi}}dt, \chi = \frac{(\lambda+3\mu)}{(\lambda+\mu)}. \tag{11}$$

Where λ and μ are the Lama coefficients; the density $\omega(t)$ appearing on the right-hand side of (10) is determined from the integral equation of the thermal conductivity problem.

Let the cracks go to the cylinder boundary with vertex b.

In this case, we seek a solution to Eq. (8) in the class of functions bounded at one end (vertex b) and unlimited at the other (vertex a):

$$q(t) = q_0(t)\cdot\sqrt{\frac{t-b}{t-a}}. \tag{12}$$

Asymptotic stress values in the vicinity of their cracks (not reaching the boundary) were obtained in (5).

For the case of a boundary crack, the asymptotic values of the stresses of normal discontinuity σ_n and longitudinal shear τ_{ns} in the vicinity of the vertex are determined according to (9) by the formula

$$\lim_{\rho \to 0}\left[(\sigma_n - i\tau_{ns})\sqrt{\rho}\right] = -\frac{i}{2\sqrt{2}}\sqrt{S'(-1)} \cdot \left\{\Omega_0(-1)\left[\mu^3 - \bar{\mu}\right] + 2\overline{\Omega_0(-1)}\left[\mu^3 - \bar{\mu}\right]\right\},$$

$$(-1) = \frac{dS}{d\beta}\bigg|_{\beta=-1}; -1 \le \beta \le 1; q(t) = \Omega(\beta) = \Omega_0(\beta)\sqrt{\frac{1-\beta}{1+\beta}}, \qquad (13)$$

$$\mu = exp\left[i\frac{\delta - \theta}{2}\right]; t = t(\beta); a = t(-1).$$

Here $t = t(\beta)$ is the parametric representation of the section; ρ and θ - the polar radius and the angle of the point in the coordinate system with the center at the vertex a, respectively; δ - the angle between Ox axis and the vertex tangent to the crack a.

The corresponding relative stress intensity factors $\langle \sigma_n \rangle$ and $\langle \tau_{ns} \rangle$, i.e., the asymptotic values of the stresses along the crack extension beyond the apex, are obtained from (13) in the case $\theta = \delta$:

$$\sigma_n - i\tau_{ns} = -2i\sqrt{\frac{S'(-1)}{2\rho}} \cdot \overline{\Omega_0(-1)}, \qquad (14)$$

$$\langle \sigma_n \rangle = \sigma_n\sqrt{\frac{2\rho}{l}}; \langle \tau_{ns} \rangle = \tau_{ns}\sqrt{\frac{2\rho}{l}}.$$

Let us consider an isotropic cylinder with a rectilinear tunnel crack edge. The temperature at the outer boundary G is considered to be constant. The parametric equation of the cut has the form

$$t = R + l(\beta - 1)e^{i\varphi},$$

$$-1 \le \beta \le 1,$$

where R is the cylinder radius; l - half the arc length; φ - the angle of crack inclination.

4   Results

The calculations are performed for materials with the characteristics:

- elastic modulus $E = 0.8 \cdot 10^9$ kg/m^2;
- coefficient of thermal expansion $\alpha = 0.6 \cdot 10^{-5}$ 1/$^\circ$;
- coefficient of thermal conductivity $\lambda = 5.23$ V/m$^\circ$;
- Poisson's ratio $\nu = 0.15$;
- Heat dissipation rate $Q = 35000$ V/m^2.
- The radius of the cylinder was taken equal $R = 0.2$ m.

The integral Eq. (8) was solved numerically. When solving, the work procedure (10) was applied (the crack contour was divided into 25 parts; a further increase in the number of split points did not change the results).

Figure 3 and Fig. 4 illustrate the dependence $\langle \sigma_n \rangle, \langle \tau_{ns} \rangle$ on the length of a rectilinear crack at different angles of rotation. The parameter $\lambda = \frac{2l}{R}$ characterizes the relative length of the crack. It can be seen that the maximum values $\langle \sigma_n \rangle$ will take place with the crack radial orientation. In this case $\langle \tau_{ns} \rangle = 0$.
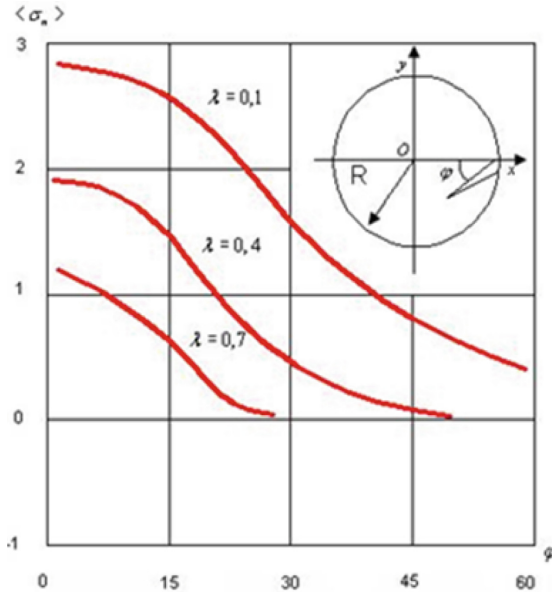
Fig. 3. The dependence of the stress intensity factor $\langle \sigma_n \rangle$ on the orientation of cracks (angle φ).
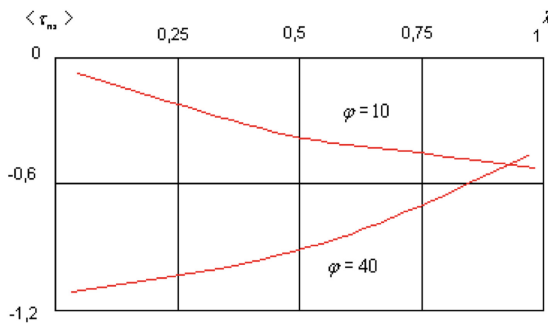
Fig. 4. The dependence of the stress intensity factor $\langle \tau_{ns} \rangle$ on the value λ.

As the crack length increases, a $\langle\sigma_n\rangle$, the decrease occurs i.e., unloading in the vicinity of the crack tip. Short edge cracks are more dangerous and tend to develop in the radial direction.

The graphs in Fig. 5 and 6 give a dependence $\langle\sigma_n\rangle$ $\langle\tau_{ns}\rangle$ on the angle of crack inclination φ for various crack lengths. The analysis of the curves suggests the same conclusion: for radial cracks of short length, we have a greater value of the intensity coefficient $\langle\sigma_n\rangle$.
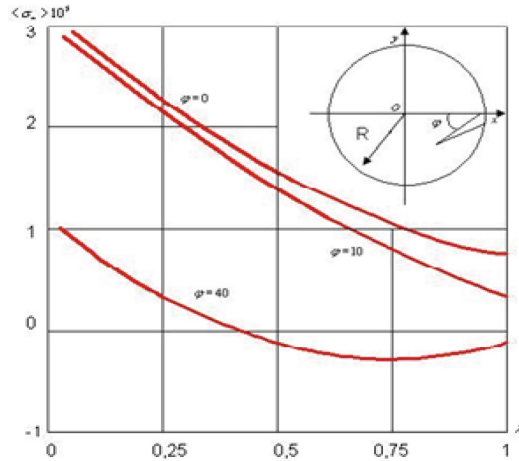
Fig. 5. The dependence of the stress intensity factor $\langle\sigma_n\rangle$ on the value λ.
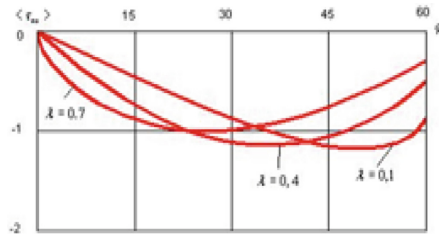
Fig. 6. The dependence of the stress intensity factor $\langle\tau_{ns}\rangle$ on the orientation of cracks (angle φ).

5   Conclusions

The obtained calculations allow us to draw the following conclusions. As the crack length increases, the stress $\langle\sigma_n\rangle$ decreases (Fig. 3). Thus, unloading occurs in the vicinity of the crack tip. Short edge cracks are more dangerous and tend to develop in the radial direction.

Analysis of the dependence $\langle \sigma_n \rangle$ and $\langle \tau_{ns} \rangle$ on the relative length of the crack $\lambda = \frac{2l}{R}$ allows us to conclude that $\langle \sigma_n \rangle$ has a maximum at the radial orientation of the crack ($\varphi = 0$). In this case, the stress intensity factor of the longitudinal shear $\langle \tau_{ns} \rangle = 0$.

The graphs show the critical stress, which contributes to crack development. After numerical calculating the possible options for the appearance of the crack, we can create a structure that will be used for a long time.

The results can be used in calculating the strength and durability of structures, as well as in the calculation of fuel elements, where stresses arise from field temperature, for example, in rods during nuclear reactions and also in mechanisms with rotating elements – turbines. Further research of composite materials modelling to eliminate cracks is planned.

References

1. Sedriks, A.J.: Corrosion of Stainless Steels. Wiley-Interscience, New York (1996)
2. Afifi, M.A.: Corrosion behavior of zinc-graphite metal matrix composite in 1 M of HCl. Hindawi Publishing Corporation ISRN Corrosion **3**, 1–8 (2014)
3. Mohamed, T.F.H., El Rehim, S.S., Ibrahim, M.A.M.: Improving the corrosion behavior of ductile cast iron in sulphuric acid by heat treatment. Der Chemica Sinica **8**(6), 513–523 (2017)
4. Dwivedi, D., Lepková, K., Becker, T.: Carbon steel corrosion: a review of key surface properties and characterization methods. RSC Adv. **7**, 4580–4610 (2017)
5. Ekemini, B.I., Uwemedimo E.U.: Phytochemical profile, adsorptive and Inhibitive behaviour of Costus afer extracts on aluminium corrosion in hydrochloric acid. Der Chemica Sinica, **3**(6), 1394–1405 (2012)
6. Guo, L., Ren, X., Zhou, Y., Shenying, X., Gong, Y., Zhang, S.: Theoretical evaluation of the corrosion inhibition performance of 1,3-thiazole and its amino derivatives. Arab. J. Chemistry **10**, 121–130 (2017)
7. Ju, H., Duan, J.Z., Yang, Y., Cao, N., Li, Y.: Mapping the galvanic corrosion of three coupled metal alloys using coupled multi electrode array: influence of chloride ion concentration. Materials, **2**(4), 634 (2018)
8. Zhylenko, T., Shuda, I.: Mathematical methods for analysis of electrolytic-plasma processing of metals and their corrosion. In: Proceedings of the 2018 IEEE 8th International Conference on Nanomaterials: Applications and Properties, vol. 4, no. 4, pp. 04NNS27 (2018)
9. Chen, C., Kolednik, O.: Comparison of cohesive zone parameters and crack tip stress states between two different specimen types. Mater. Sci. **132**, 135–152 (2005)
10. Kotousov, A.: Effect of plate thickness on stress state at sharp notches and the strength paradox of thick plates. Int. J. Solids Struct. **47**, 1916–1923 (2010)
11. Mathur, K., Needleman, A., Tvergaard, V.: Three dimensional analysis of dynamic ductile crack growth in a thin plate. Mater. Sci. **443**, 439–464 (1996)
12. Chen, C.R., Kolednik, O., Heerens, J., Fischer, F.D.: Three-dimensional modeling of ductile crack growth: cohesive zone parameters and crack tip triaxility. Eng. Fract. Mech. **72**, 2072–2094 (2005)
13. Minavarб, V.: Mir-Salimzade: Mminimization on the stressed state of a stringer plate with a hole and rectilinear cracks. J. Mech. Eng. **22**(2), 59–68 (2019)

14. Vigdergauz, S.: Simply and doubly periodic arrangements of the equi stress holes in a perforated elastic plane: the single-layer potential approach. Math. Mech. Solids **23**(5), 805–819 (2018)
15. Moresco, R., Bittencourt, E.: Numerical study of fatigue crack growth considering an elastic–plastic layer in mixed-mode loading. Int. J. Fract. **1**, 1–9 (2019)
16. Wang, B., Siegmund, T.: A numerical analysis of constraint effects in fatigue crack growth by use of an irreversible cohesive zone model. Int. J. Fract. **132**(2), 175–196 (2005)
17. Wang, B., Siegmund, T.: Numerical simulation of constraint effects in fatigue crack growth. Int. J. Fatigue **27**, 1328–1334 (2005)

Research on the Energy State of the Surface of Alloys for Gas-Turbine Engine Blades

Stephan Loskutov [iD], Dmytro Pavlenko[(✉)] [iD], Dmytro Stepanov [iD], Natalia Honchar [iD], and Olena Khavkina [iD]

National University "Zaporizhzhia Polytechnic", 64б Zhukovs'koho Street, Zaporizhzhia 69063, Ukraine
dvpl977dvp@gmail.com

Abstract. The work concerns the research on patterns of the electron work function (EWF) distribution over the sample surface, depending on the fatigue tests. When studying samples made of high-temperature alloy EP866 used for highly loaded parts of gas turbine engine (GTE) compressors, we determined a stage of reversible structural rearrangements when the EWF value for a given surface point decreases and increases periodically fluctuating around a particular average amount. At the initial stages of testing, the EWF oscillates near a specific value, which indicates the reversibility of the process of accumulation of fatigue damage and the change in the hardening processes – relaxation at these stages. Then a stage of irreversible structural changes in the material of the surface layer is observed when the EWF decreases monotonously until the sample is destructed. It was found that in the process of cyclic deformation, the material areas experiencing the same mechanical stresses correspond to the surface areas with the similar EWF values. The deformation processes preparing the formation of a fatigue crack to cause the creation of a "deformation" dip on all the EWF distribution curves, and, accordingly, the contact potential difference (CPD). It can be assumed that the maximum change in EWF in the dip corresponds to the most intensive flow of deformation processes. The EWF distribution over the sample surface makes it possible to predict the place of fatigue cracks initiation at the early testing stages.

Keywords: Electron work function · Compressor blades · Fatigue testing · Deformation processes

1 Introduction

The most crucial area of research in modern physics of metals is the study of deformation processes in the surface coatings of metallic materials. The development of ideas about the physical nature of deformation and destruction of real metal bodies and the need to take into account the features of strain in the surface area determine the tasks of studying the mechanisms of the formation and evolution of crystalline and defective structures, the mutual influence of surface and volume deformations, patterns of interaction among surface, the volume, and medium. To understand the physical

nature of the deformation processes in metals, it is necessary to investigate self-consistent processes in the electron-ion structure. One of the ways to solve this problem is to trace the experimental and theoretical dependences of the electron characteristics on the structure parameters and stress-strain state of metals.

2   Literature Review

So far, a lot of experimental data have been accumulated to illustrate the effect of the surface on the mechanical properties of metals [1, 2]. The previous work described, for example, [3], those experimental data are showing the variation of the mechanical properties of the surface layer of a nickel-based EK79-ID alloy depending on the degree of surface straining. However, a reliable method for the prediction of surface layer damage without its crash has not been found yet.

It is well known that a surface layer is significant for the detail strength. It is one of the critical factors for the details working at the periodical loadings like compressor blades of gas turbine engines [4, 5]. There are a lot of different criteria for the estimation of a surface layer quality [6]. However, most of them are used for quality estimation during manufacturing. The most widely used of them are residual stress and micro-hardness distributions [7, 8]. These types of evaluations are reliable and significant, but they cannot be used for the most details without damaging them. Furthermore, the dynamics of such changing during the life of parts have not been studied yet. So, to predict the part's life, a new parameter of the surface layer condition must be found.

It is also known that alternating mechanical stresses applied to a sample or a part cause-specific structural changes in them being localized in the surface layer [3]. In a loaded crystal, the energy can be stored not only in an elastically deformed, but also in an electronic subsystem. Mechanical energy is directly transformed into an atomic one, which excites the crystal lattice. Deformational excitation occurs in a wide range of energies, and it is with a breakdown of interatomic bonds and the formation of lattice defects. The emergence of defects causes an imbalance in the electron density due to a change in the interatomic distances. As a result, the electron work function (EWF) changes in the areas where the defects come to the surface [9, 10].

In previous works, it was discovered that EWF depends upon plastic strain, as well as upon cyclic stresses [11, 12]. The works [13, 14] are devoted to the study of the EWF structural sensitivity at various types of mechanical loading of samples made of technical aluminum and GTE blades made of titanium alloys. By the nature of the EWF distribution over the surface of metals, it is possible to determine the localization of plastic deformations [15] and predict the initiation of fatigue cracks. However, the EWF studies were conducted mainly on titanium alloys, copper, and aluminum [16, 17]. There is a lack of such research for heat-resistant alloys and super-alloys.

Such a method of diagnostic of the aviation details showed its efficiency since the studies on EWF distribution over the surface of metals have been started. The main aim of this study was to suggest a reliable method to predict the fatigue failure of heat-resistant alloys, which is used for compressor blades of GTE. According to it, the study to develop physical ideas about the energy component of deformation processes in metals and alloys, as well as the practical relevance of the problem of predicting the

fatigue failure of heat-resistant alloys, was implemented. The task to study the patterns of distribution and evolution of EWF on the surface of alloy EP866 was set in the work. This alloy (decoding – 15Cr16Co5Ni2MoWVNNb) has been used for blades of the compressor for a long time. However, there is not enough information about its EWF so far. Whereas it is a representative type of alloys for aviation engines, it is unusual for such research.

3   Research Methodology

In the experiment, the contact potential difference (CPD) was measured, i.e. the potential difference (U) that occurs between two metals when they are in direct contact. To measure it, the Kelvin's vibrating capacitor method was used. The surface of the test sample and the oscillating electrode of a known material form an adjustable capacitor. When an external circuit closes the plates of the vibrating capacitor (VC), an alternating current appears in it, which is proportional to the CPD.

Connecting in series the VC and an external constant-voltage source makes it possible to compensate the CPD - when the CPD and the voltage of the external source are equal, the current disappears. The compensation voltage is equal to the CPD between the test sample and the reference electrode. Based on these data, the EWF of the metal (Φ_{Me}) can be calculated, as the EWF of the reference standard (φ_{St}) is known.

$$\Phi_{Me} = \varphi_{St} - U \qquad (1)$$

In our case, a gold electrode with φ_{St} = 4.30 meV was used.

Since the work function of the sample is higher than the work function of the standard, the contact potential difference is negative. It can be seen from the equations that the less EWF of the studied material is the higher the CPD is and vice versa.

EWF measurements were carried out together with fatigue tests with constant fixation of the sample in the clamps of the shake table head and relative to the scanning electrode. The device includes a compact piezoelectric shake table and a set of measuring equipment. To control the measurement process and data processing, a personal computer (PC) is used.

To increase in the information content of the data obtained, EWF measurements were performed before and after fatigue tests. To establish the EWF structural sensitivity, the samples (see Fig. 1) were subjected to experiments with various operating times. The initial distribution of the CPD over the sample surface was measured, then fatigue tests were performed to a specified number of N_i cycles, and then the measurements were repeated. EP866 heat-resistant alloy is the sample material.

Scanning during the measuring EWF was performed along with the sample (along the x-axis) with a step of 1 mm, and then the standard was shifted 1 mm across the sample (along the y-axis). As a result, up to 7 lines were measured for each sample.

Sample preparation consisted of hardening in oil at temperature 1040 °C, tempering at 650 °C in air, mechanical polishing with diamond paste, and finishing annealing in vacuum at 10^{-3} Pa (10^{-5} mm of mercury) at 580 °C for 4 h followed by cooling in a vacuum. Samples were fixed overhung and tested for alternating bending. The cyclic

load was performed at the resonant frequency close to the resonant frequency of compressor blades of GTE.

The tools and equipment are described in detail in [18].
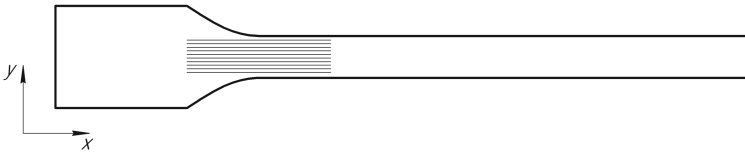
Fig. 1. Sample and its area of measuring EWF.

Since the measured EWF values are largely influenced by the environment, a detailed analysis of the structurally sensitive dependence of EWF in the case of fatigue was carried out with the background subtracted. The procedure of subtracting the background due to exposure of EWF to the environment is based on the regularities of the influence of ultraviolet radiation (UVR) of the metal surface in the process of measuring the CPD. It was found that there is a parallel shift of the CPD distribution curves during the UVR. The explanation for this phenomenon is that the UVR shifts the energy levels of atoms adsorbed on the metal surface by a certain amount and causes desorption of weakly bound adatoms. As a result, the UVR (taking into account the uniformity of illumination of the surface), the EWF changes by a constant value for all the surface points. Measuring the EWF distribution was also carried out on the surface of the same sample, which was not subjected to mechanical stress for a long time. Experimental data indicate a uniform increment of EWF caused by exposure to atmospheric changes over the entire surface. Thus, it becomes possible to find a sample area not subject to deformations, and then subtract the EWF changes in this area from the EWF values in the deformation area during the fatigue tests.

4 Results

The critical parameters of fatigue tests are as follow. The measurement number is n from 0 to 22, the cycling operating of the test is in a range of 0–$2 \cdot 10^6$, the total cyclic operation is in a range of 0–$20.4 \cdot 10^6$ and the additional conditions are varying as "after rest" (without next cycling operating), "frequency drop", and "sample destruction" (at the end of the experiment).

Detailed studies of the CPD values were taken with periodic stops for measuring the energy state and small breaks in the tests for rest. Already after $2 \cdot 10^5$ cycles in the area of the points indicated on the graph at a distance l 12 and 13 mm (see Fig. 2), a dip is formed on the curves. Negative values of the CPD are plotted on the ordinate axis.

Further testing leads to a characteristic evolution of the charge-relief distribution curves. The formation of internal discontinuity in the material causes the formation of a characteristic "deformation" dip on all distribution curves. The formation and development of fatigue micro cracks on different samples occurred in different ways.

Usually, a crack had a curved shape with 1 mm deviations from a straight-line; the crack crossed almost the entire surface of the sample forming branches in some places. Small cracks associated with the main crack are also characteristic.

Good repeatability of the main characteristics of the surface energy relief geometry is observed. The formation of the main crack is associated with a significant deformation of the energy distribution curves. The reduction of the EWF occurs at a distance of 7 mm from the crack line. A similar pattern of EWF distribution is formed with the uniaxial tension of metals in the "neck" area. Hence, it can be concluded that fatigue failure is associated with the development of processes of active plastic deformation on a significant sample surface area.
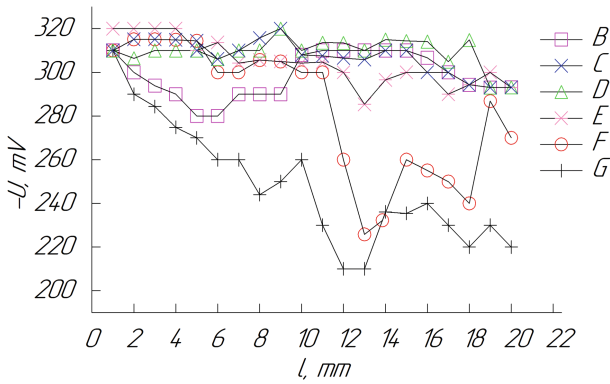
Fig. 2. Distribution of CPD values over the surface of the sample from EP866 alloy after 2·105 cycles. Measurements were carried out along six lines (B-G) parallel to the sample axis.

The average EWF change on the crack line is about 40 meV (see Fig. 3).
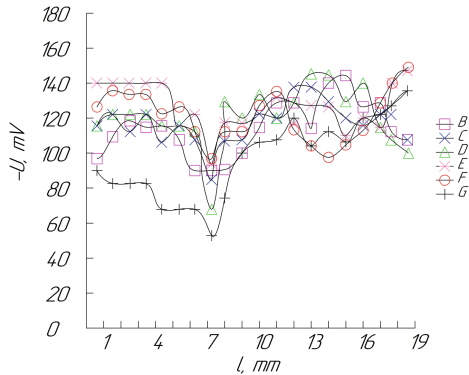
Fig. 3. CPD distribution over the surface of the sample made of EP866 alloy.

Pre-destruction tests changed the material structure throughout the sample working area to varying degrees. These changes were local. And only at a particular test point, a significant area was covered with simultaneous plastic deformation. The material lost the possibility of passing the deformation processes from one area to another one.

Figure 4 presents characteristic graphs obtained from measurements of EWF along with one of the lines of the sample working area. The bandwidth of the chart indicates the scatter of the EWF values. Two areas characterize the dependence of EWF on the number of cycles: 1 – the interval from $N = 0$ to $N = 7 \cdot 10^6$ (n from 0 to 13); 2 – from $N = 7 \cdot 10^6$ to destruction (n from 13 to 22). In the first area, the variations in the EWF oscillate around a certain average value, which varies slightly from point to point. It can be assumed that there is an equilibrium EWF value, which is characteristic of all the points on the surface. The result of a specific development is a certain change in EWF, which relaxes over time or subsequent development. The most characteristic manifestation of such relaxation is a part of the curve from $N = 1.5 \cdot 10^6$ to $N = 5 \cdot 10^6$ (n from 5 to 10), which repeats on other lines. With a total operating time of $1.5 \cdot 10^6$ cycles ($n = 5$), the EWF decreases by approximately 30 meV dramatically. Then, as a result of subsequent loading, the EWF increases, reaching its maximum at the point of $2 \cdot 10^6$ cycles ($n = 6$), and at the point $4 \cdot 10^6$ cycles ($n = 9$), it comes back to the initial value.
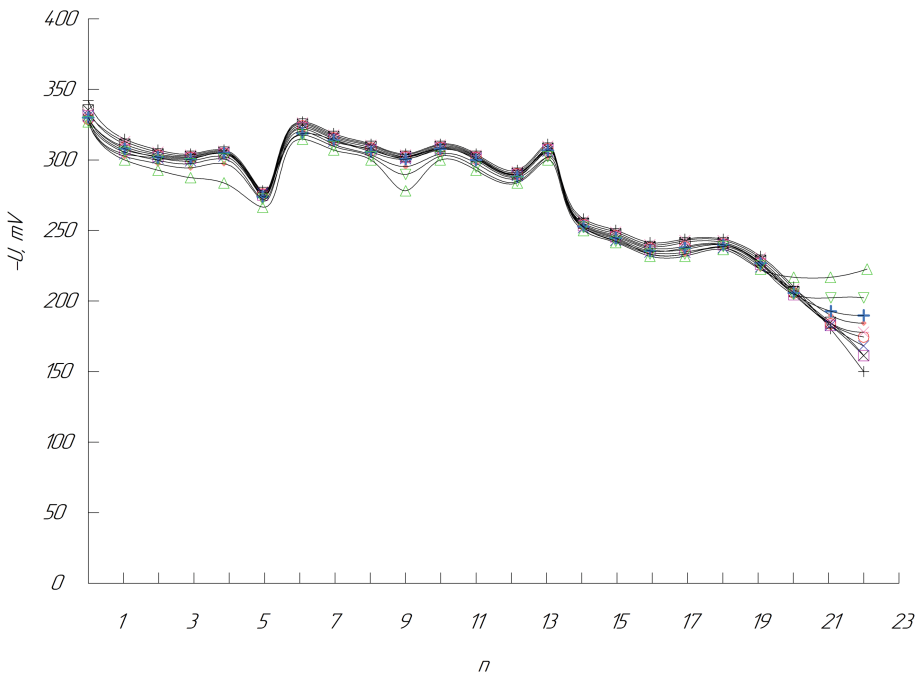
Fig. 4. Dependence of changes in the distribution of CPD over the surface of a sample made from EP866 alloy on the cyclic operating time: 10 points in the "neck" area of sample correspond to each specific operating time - the measurement number n from 0 to 22.

It is known that structural rearrangement begins in surface layer material earlier than in the volume. The analyzed feature may be associated with the surface deformation (a decrease in EWF corresponds to the plastic deformation), covering the entire sample working area. A kind of coming to the limit of cyclic fatigue of a thin surface layer occurred. Since the test was carried out at a constant cyclic load, and the supply of energy to the surface layer did not exceed the critical value (it was insufficient for new active structural rearrangements). The processes of "healing" of surface defects (diffusion of vacancies, adsorption phenomena, smoothing of dislocation steps on the surface) took place.

The second area of the dependence of EWF on the operating time differs from the first one in the tendency to monotonous EWF decrease over the entire working surface. With a total operating time of about $7 \cdot 10^6$ cycles, active defect formation in the subsurface layer or such a stage of fatigue structural processes, in which relaxation phenomena on the surface do not play a significant role, starts. Thus, the second area describes the actual fatigue deformation of materials before destruction.

When testing fatigue, the length of the lines measured was chosen in such a way as to obtain the distribution of EWF over the surface of the sample not exposed to mechanical stress too. Experimental data indicate a uniform increment of EWF over the entire surface caused by exposure to atmospheric changes. Thus it becomes possible to find an area on the sample that is not subjected to deformation and then subtract the EWF changes in this area from the EWF values in the deformation area during the fatigue test. The dependence of the changes in the distribution of CPD over the surface of the sample made of EP866 alloy on the number of operating cycles, taking into account the procedure of background subtraction, is presented in Fig. 4b. In the process of testing for fatigue, EWF changes are cyclical. The amplitude of the EWF change along one measurement line at a particular time does not exceed 20 meV.

5   Conclusions

We have suggested that the minima of the potential relief on the curves of EWF distribution over the surface of the samples tested for fatigue are due to the appearance on the surface of a large number of atomic steps carrying an electric charge. In their turn, the levels appear as a result of deforming dislocations reaching the surface, which are generated and move under the influence of alternating mechanical stresses. Thus, the picture of the metal potential relief has predictive capabilities, since it is formed by factors preceding the destruction. The non-destructive and non-contact method of measuring EWF values on the surface of metallic materials allows predicting the formation of fatigue micro-cracks in advance.

Thus, the release of dislocations to the free surface is accompanied by an increase in the atomic surface roughness (an increase in the density of charged dislocation steps), which leads to a decrease in EWF. When the density of surface steps reaches a particular value (which is related to the number of working planes of dislocation glide), the EWF change ceases. It was found that the surface covered with the dislocation corresponds to almost the entire sample working area.

Under the action of cyclic stress as a result of local plastic deformation, strain hardening occurs, and at a certain number of cycles, it becomes saturated. In this case, vacancies accumulate monotonously until the moment of destruction. As the cyclic operating time increases, the density of mobile dislocations increases. Under the cyclic loading, a significant number of point defects coming to the free surface is generated.

At a high density of dislocations, their interaction is enhanced, and the fixation occurs, which makes it difficult for new locations and the point defects accompanying them to come to the metal surface (saturation of EWF). The increase in EWF, which takes place in certain parts of the sample that is subjected to further fatigue testing, may be due to submicroscopic discontinuities of the material formed on the metal surface. In the last period, preceding fatigue failure is associated with the growth of surface micro cracks and with their penetration into adjacent areas. This process determines the localization of plastic deformation and corresponds to a local decrease in EWF on the distribution curve.

The task of studying the patterns of distribution and evolution of EWF on the surface of the heat-resistant alloy EP866, which is used for the GTE blades, was solved. Our study allows us to make an essential and new conclusion about the existence of two main kinetic stages of structural changes in the metal surface layer with fatigue:

- the stage of reversible structural changes, when the EWF value for a given surface point decreases periodically, then increases, fluctuating near a particular average value;
- the stage of irreversible structural changes in the material of the surface layer, when the EWF at this point decreases monotonously until the sample is destructed.

In general, the EWF on the crack line decreases by about 110 meV. In this way, this method makes it possible to predict the fatigue failure of details made from heat-resistant alloy reliably.

References

1. Bagherifard, S., Mario Guagliano, A.: Fatigue behavior of a low-alloy steel with nano structured surface obtained by severe shot peening. Eng. Fract. Mech. **81**, 56–68 (2012)
2. Mousokhranov, M., Kalmykov, V., Malyshev, E.: Experimental research of variability of surface energy value of Fe37-3FN, C45 and 41Cr4 steels. Int. J. Appl. Eng. Res. **12**(17), 6428–6433 (2017)
3. Pavlenko, D., Loskutov, S., Yatsenko, V., Gonchar, N.: Structural changes in the surface layers of an EK79-ID alloy upon hardening treatments. Tech. Phys. **29**(4), 345–346 (2003)
4. Novovic, D., Aspinwall, D., Dewes, R., Bowenc, P., Griffiths, B.: The effect of surface and subsurface condition on the fatigue life of Ti-25 V-15Cr-2Al-0.2C %wt alloy. CIRP Annals **65**(1), 523−528 (2016)
5. Fusen, Y., Liu, C., Gu, H., Han, F., Zhang, Y., Ali, M., Lia, G.: Geping, Lia: Effects of mechanical polishing treatments on high cycle fatigue behavior of Ti-6Al-2Sn-4Zr-2Mo alloy. Int. J. Fatigue **121**, 55–62 (2019)
6. Wu, D., Yao, C., Zhang, D.: Surface characterization and fatigue evaluation in GH4169 superalloy: comparing results after finish turning; shot peening and surface polishing treatments. Int. J. Fatigue **113**, 222–235 (2018)

7. Fleury, R.M.N., Salvati, E., Nowell, D., Korsunsky, A., Tai, Y.: The effect of surface damage and residual stresses on the fatigue life of nickel superalloys at high temperature. Int. J. Fatigue **119**, 34–42 (2019)
8. Sun, G., Wei, X., Niu, J., Shang, D., Chen, S., Sun, G.: Influence of residual stress on fatigue weak areas and simulation analysis on fatigue properties based on continuous performance of FSW joints. Metals, **9**, 284−297 (2019)
9. Stepanov, E., Gurov, K., Alekhin, V.: The dislocation structure of metals under cyclic loading. Metals **3**, 163–165 (1992)
10. Zharin, A.: Contact potential difference techniques as probing tools in tribology and surface mapping. In: Bhushan, B. (ed.) Scanning Probe Microscopy in Nanoscience and Nanotechnology. NanoScience and Technology, pp. 687 − 720. Springer, Heidelberg (2010)
11. Bhushan, B., Goldade, A.: Measurements and analysis of surface potential change during wear of single-crystal silicon (100) at ultralow loads using Kelvin probe microscopy. Appl. Surf. Sci. **157**, 373–381 (2000)
12. Levitin, V., Loskutov, S., Pravda, M., Serpetsky, B.: Work function for fatigue tested metals. Nondestruct. Test. Eval. **17**(2), 79–89 (2001)
13. Levitin, V., Garin, O., Yatsenko, V., Loskutov, S.: On structural sensibility of work function. Vacuum **63**(1–2), 367–370 (2001)
14. Zharin, A., Gusev, O., Svistun, A., Tiavlovskii, A.: Friction surface monitoring using a contact potential difference technique. Bull. TulGU – Techn. Sci. **2**, 286–295 (2011)
15. Panteleyev, K., Svistun, A., Zharin, A.: Methods for local changes in the plastic deformation diagnostics on the work function. Instrum. Method. Measurement **1**(10), 56–63 (2015)
16. Li, W., Li, D.: Effects of elastic and plastic deformations on the electron work function of metals during bending tests. Phil. Mag. **84**(35), 3717–3727 (2004)
17. Ahmed, J., Roberts, S.G., Wilkinson, A.: Characterising dislocation structure evolution during cyclic deformation using electron channelling contrast imaging. Philosophical Magazine, Taylor and Francis, **86**(29–31), 4965−4981 (2006)
18. Loskutov, S., Pavlenko, D., Honchar, N., Stepanov, D., Shhetynina, M., Dvirnyk, Y.: Influence of fatigue and restoring heat treatment on the energy relief of the surface of GTE details. Engine Build. Bull. **1**, 96−106 (2019)

Topology Optimization Procedure of Aircraft Mechanical Components Based on Computer-Aided Design, Multibody Dynamics, and Finite Element Analysis

Adriano Gabriel Manca[1] and Carmine Maria Pappalardo[2(✉)]

[1] MEID4 Academic Spin-Off of the University of Salerno, Fisciano, Italy
[2] University of Salerno, 132, Via Giovanni Paolo II,
84084 Fisciano, Salerno, Italy
cpappalardo@unisa.it

Abstract. In mechanical engineering, the optimization process is time-consuming because of the lack of communication between design, simulation, and analysis software. In the case of single productions or small quantities, this possibility is not taken into account. In the case of serial productions, on the other hand, the optimization of the design time is of paramount importance due to the large amount of money that can be saved. To address these challenges, this investigation proposes a topological optimization procedure for mechanical parts that have complex geometric shapes using the integration of CAD, MBD, and FEA software. The theory of linear elastodynamics is the basic approach used for the integration process carried out in this paper. In particular, the components analyzed in this work belong to the closing system of the ATR 42/72 cargo door. To explain the software integration procedure devised in the paper using SOLIDWORKS, MSC ADAMS, and ANSYS, a slider-crank mechanism is employed first as a demonstrative example. Subsequently, this computational procedure is applied to a flexible component of the latching system of the door whose loading conditions were previously obtained considering the entire opening mechanism modeled as a rigid multibody system. Finally, the topological optimization of the mechanical part is carried out and a consequential reduction in the amount of material to use is performed. The results obtained are considered significant since they led to considerable advantages in the door opening and closing system as well as a reduction of the total weight of the entire airplane.

Keywords: Topology optimization · Computer-Aided Design (CAD) · Multi-Body Dynamics (MBD) · Finite Element Analysis (FEA) · Aircraft components · ATR 42/72 cargo door · Integration of Computer-Aided Design and Analysis (I-CAD-A)

1 Introduction

In general, an engineer tries to transform his ideas in reality to obtain the optimal solution to a problem. To this end, the conceptual design, the virtual simulation, and the analysis of the results are essential actions to optimize the material of a mechanical part

and to make a component more profitable [1]. When designing a mechanical component, the optimization of the amount of material to be used is essential since it is directly related to saving money and time spent on manufacturing. Recently, the advent and implementation of powerful computer programs have drawn a great interest since they allow different branches of engineering, in particular mechanical and industrial engineering, to conduct studies of the dynamic behavior of various mechanical systems subjected to external forces usually described by a nonlinear structure [2–10]. In particular, the integration of Computer-Aided Design (CAD), Multi-Body Dynamics (MBD), and Finite Element Analysis (FEA) codes [11–15], which is the object of the present study, is essential to achieve this objective. Today, these three important fields are not fully compatible. For example, this inconsistency generates expenses greater than 600 million dollars a year only for the US automotive industry [16]. Therefore, many studies were devoted to the main objective of proposing an integrated procedure to address this challenging problem [17]. The method based on the linear theory of elastodynamics, on the other hand, is the fundamental approach employed in this investigation.

2   Literature Review

The connection between design, simulation, and analysis is essential to reduce calculation time and computational loads [18]. Major problems occur due to the lack of compatibility between the design (CAD) and the structural analysis environment (FEM) [19]. Because of the integration of computer-aided design and analysis, some solutions are presented to break down the existing barriers [20]. For example, Louhichi et al. proposed a method to update the CAD geometry from the mesh deformation obtained in a finite element analysis (FEM) [21]. Also, several commercial multibody systems use the floating frame of reference formulation and the results of the analysis depend largely on them [22]. The importance of communication between design, simulation, and analysis of programs covers areas of diverse nature. Computational tools have been introduced to support the designer in choosing the shape of the part, the material to be used, and the mode of production of the component with the minimum possible environmental impact [23]. In particular, to reduce the computational loads in geometric optimization studies, there are proposals for the integration of the multibody approach and finite element analysis [24]. For example, because of a CAD-MBD-FEM integration, programs such as SOLIDWORKS, MSC ADAMS, ANSYS, and MATLAB/SIMULINK are used for machine tool analysis or the kinetic analysis of an ankle rehabilitator [25]. On the other hand, structural analysis is widely used in the field of civil engineering and mechanical engineering [26]. Examples of the latter may be the mechanical behavior of plain bearings and the analysis of the stiffness of the structure of two aircraft fuselages [27]. Marusich et al. developed a finite element model to predict distortions in structural machines due to residual stresses [28]. In literature, one can find a unified view of the techniques and theory for the analysis and prediction of the reliability of structures using the probability theory [29]. Focused on the aerospace industry, Kienzler and Herrmann present as fully as possible the mechanics applied in this area (or configurational mechanics), and exhibit their usefulness in the mechanics

of defects and fractures [30]. Hansen et al. proposed improvements in evaluation capabilities in the case of BWB aircraft [31]. When talking about optimization, one can find techniques for optimizing the weight and cost of structures and different approaches to carry it out, such as working with precise and high-fidelity models or changing the limit where the stress is generated [32]. Recently, various systems based on model dimensions have been presented to classify the complexity of optimization [33]. Gradient-based methods and even a general and flexible topological optimization method called the asymptote movement method, which is compared to the existing ones, are employed [34]. A framework for optimization and environmental design of aircraft was also proposed, extending to optimize aircraft configurations for various environmental metrics [35]. In the market, there are also several computer tools used to perform a topological optimization [36]. On the other hand, this paper fits the reference research framework based on multibody dynamics [37–42], nonlinear control [43–47], and state-space system identification of mechanical systems [48–52].

3   Research Methodology

The discussion of the methodology adopted in the paper begins with the index-one differential-algebraic equations of motion of a rigid multibody system:

$$
\begin{cases}
M\ddot{q} = Q_v + Q_e - C_q^T \lambda \\
C_q \ddot{q} = Q_d
\end{cases}
\tag{1}
$$

where q represents the generalized coordinate vector of the multibody system. In Eq. (1), M is the system mass matrix, Q_v identifies the inertia quadratic velocity vector, and Q_e represents the external generalized force vector. Also, λ denotes the vector of Lagrange multipliers, C is the constraint vector, C_q identifies the Jacobian matrix of the constraint equations, and Q_d represents the constraint quadratic velocity vector. On the other hand, the equations of motion of a flexible multibody system resulting from the use of the finite element approach can be written as follows:

$$
M_f \ddot{q}_f + D_f \dot{q}_f + K_f q_f = Q_f
\tag{2}
$$

where q_f is the vector of nodal coordinates. In Eq. (2), M_f is the system mass matrix, D_f represents the system damping matrix, K_f identifies the system stiffness matrix, and Q_f denotes the external generalized force vector applied to the material nodes. These equations are the fundamental mathematical tools on which the first part of the research methodology is based. One of the most consolidated theories for simulating the dynamic behavior of rigid-flexible multibody systems is the technique known as the linear theory of electrodynamics, which represents the fundamental method used to develop the computed-aided integration procedure devised in this research work. This computational approach involves the treatment of the multibody system composed only of rigid bodies to calculate the forces of inertia and the constraint reactions due to the movement of the system. The forces obtained as a result of the rigid body dynamic analysis are then applied to flexible bodies to assess the effect of deformations. To

understand the fundamental aspect of the proposed integration method, the study of a slider-crank mechanism is used as a demonstrative example. The proposed approach is based on the following four steps: 1) MBD model development starting from the CAD model; 2) realization of the rigid dynamic analysis; 3) FEM model development starting from the CAD model; 4) realization of flexible dynamic analysis. Each part of the system under study is designed in a SOLIDWORKS environment. Once the material of each part is defined, the assembly is carried out, while the joints between the components and the acting forces are imposed. After this phase, the multibody simu-lation is developed. To this end, SOLIDWORKS has a direct connection with MSC ADAMS, which is a computer software widely used for dynamic multibody simulation. The multibody model obtained is shown in Fig. 1a. The mechanical joints considered are three revolute joints in the points A, B, and C around the Z-axis, and a translational joint in point D, thus the piston can slide along the Z-axis.
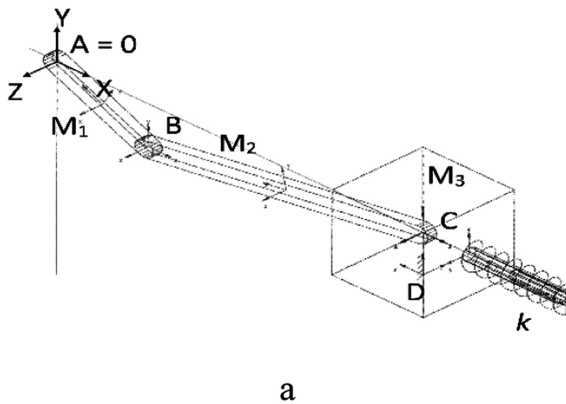
a
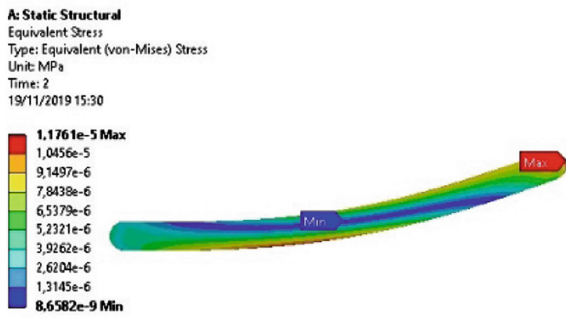
b

Fig. 1. Demonstrative example: (a) slider-crank mechanism, (b) distribution of von Mises equivalent stress on the Body 2.

First, a kinematic analysis was performed. The law of motion imposed on Body 1 is shown in Fig. 2a. The dynamical simulations gave the movement of all multibody system components in the form of explicit functions of time and allowed going ahead to the next step. To perform the finite element analysis, the angular velocity resulting from the previous analysis was imposed at the center of mass of the Body 2 and is shown in Fig. 2b. For this purpose, Body 2 was considered deformable to execute a dynamic structural analysis, as shown in Fig. 1b.

a   b
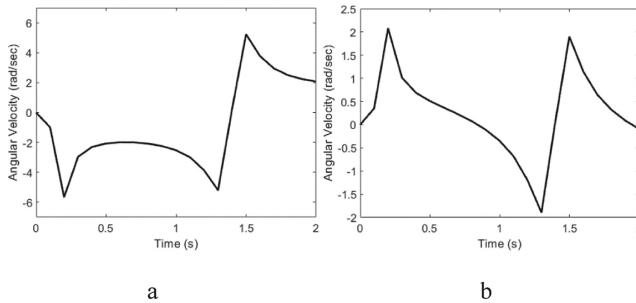
Fig. 2. Angular velocities. From left to right: (a) Body 1 angular velocity, (b) Body 2 angular velocity.

4   Results

To investigate the performance of the case study of interest, the proposed integration method is used to optimize the design of one of the components of the cargo door of the ATR 42/72 aircraft. For CAD modelling, we consider the door shown in Fig. 3a. This airplane door features an opening upwards and is employed in loading and unloading activities. Its main subsystems are a lifting subsystem, an interlocking subsystem represented in Fig. 3b, and a blocking subsystem. This work focuses on the topological optimization of one of the blocking components and proposes a new interlocking subsystem, which is employed to lock the door. This subsystem has three latches, which are considered the most fundamental components. These are also three hooks that are articulated to the bottom of the door structure, which performs a synchronized rotation in virtue of their connection elements. Once the CAD model is constructed in the SOLIDWORKS environment, considering the assignment of the material to each component, the establishment of the mechanical joints and the force field was performed and the multibody model was exported to the MSC ADAMS environment. It should be noted that the number of rigid bodies taken into account during the dynamic analysis was minimized to reduce the computational burden.

a   b
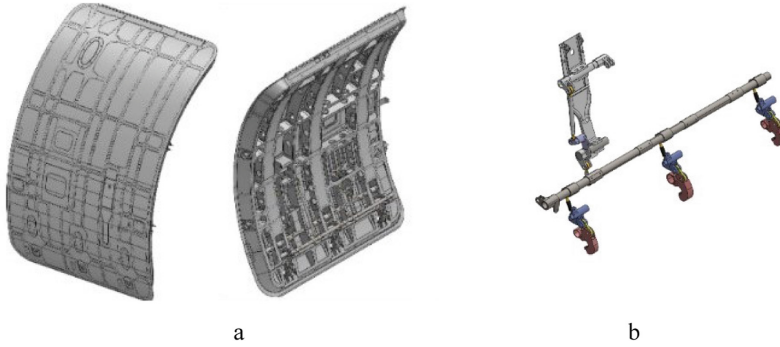
Fig. 3. Case study: (a) CAD model of the cargo door, (b) MBD scheme of an example of the latch mechanism.

By imposing a law of movement to the handle, the motion of the mechanism concerning the angular velocity of the latches was found. The material used for manufacturing all components of the interlocking mechanism was 15-5PH steel with elastic module E equal to 206 GPa, Poisson Coefficient v equal to 0.3, and maximum yield strength σ_s equal to 940 MPa. In the process of finite element analysis, static analysis was performed on the latch. The mesh used contained 6242 tetrahedral elements. In phase C, single compression support was imposed to represent the contact with the lock, and in B, a fixed point of the junction was imposed. At point A, an external force was applied, whose components are $F_x = 14566\ N$, $F_y = -14584\ N$, and $F_z = 0\ N$, as shown in Fig. 5a. These values are obtained at the end of the previous multibody dynamic analysis in the mechanical joint collocated on the latch. As a final phase of this work, a topological optimization of the latch component is carried out. For this purpose, ANSYS has a specific tool to perform this operation. The flowchart of the optimization procedure followed in the paper is shown in Fig. 4.
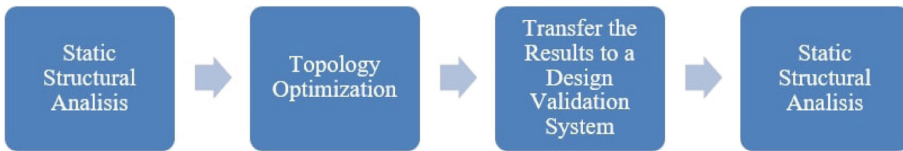
Fig. 4. Topology optimization procedure.

Through the Topology Optimization tool, and imposing 70% of the mass to be retained, the numerical simulations are performed and the results are analyzed. The Topology Optimization tool does not allow for the use of the single compression support. To solve this issue, a reaction force is calculated in the multibody model as a constraint force and this value is applied as an external force in the coupling surface of the finite element model. The results obtained from the computer simulations are shown in Fig. 5b.
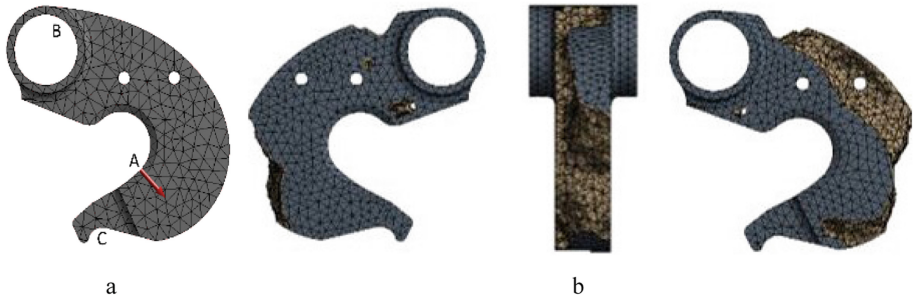
Fig. 5. Latch component: (a) finite element mesh of the original latch, (b) results of the topology optimization.

As it is apparent, this shape cannot be manufactured. Therefore, we proceed to redesign it obtaining a new component shown in Fig. 6b. As the last step, a structural analysis is performed on the mechanical component with its new configuration to evaluate its structural resistance. The numerical results arising from the static analysis obtained before and after topology optimization of the latch can be respectively observed in Figs. 6a and b. These changes led to a weight reduction of around 24.82%, with a change of around 21.78% in the maximum von Mises stress.
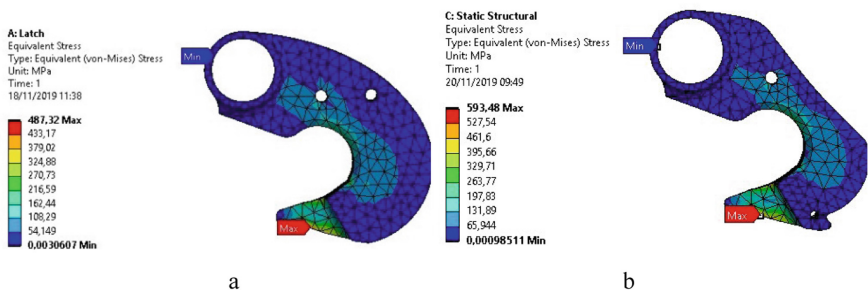
Fig. 6. Distribution of the von Mises equivalent stresses on the (a) original (left) and (b) redesigned (right) latch.

5   Conclusions

This paper focuses on a structural optimization procedure suitable for aircraft components. In particular, the central goal of this work is the process of topological optimization of one of the fundamental components of the interlocking mechanism of the ATR 42/72 cargo door. For this purpose, the integration between CAD, MBD, and FEM frameworks was used. For the computer-aided design, SOLIDWORKS was used, while for the dynamic analysis of rigid multibody systems MSC ADAMS was used. On the other hand, ANSYS was used to implement the finite element analysis of the latch.

The CAD model of the door was simplified to aid the subsequent dynamic analysis performed in a multibody software to determine the appropriate loading conditions of the consequential finite element analysis. Once the rigid dynamic analysis has been carried out, the external forces and moments acting on the latches were taken to perform a static structural analysis with the help of a finite element model developed in ANSYS. Through the ANSYS Topology Optimization tool, an optimization of component topology was carried out. After a new static structural analysis, a redesign of the component of interest was made to transform it into a mechanical part that can be conveniently manufactured. The numerical results found in this investigation showed that the new design of the aircraft component of interest has considerably improved its performance.

References

1. Li, G., Huang, Z., Wang, X.: The FEM simulation on end mill of plastic doors and windows corner cleaning based on deform-3D. In: IOP Conference Series: Materials Science and Engineering, vol. 272, no. 1, p. 012009 (2017)
2. Villecco, F.: On the evaluation of errors in the virtual design of mechanical systems. Machines **6**(3), 36 (2018)
3. Formato, A., Ianniello, D., Romano, R., Pellegrino, A., Villecco, F.: Design and development of a new press for grape marc. Machines **7**(3), 51 (2019)
4. Formato, G., Romano, R., Formato, A., Sorvari, J., Koiranen, T., Pellegrino, A., Villecco, F.: Fluid-structure interaction modeling applied to peristaltic pump flow simulations. Machines **7**(3), 50 (2019)
5. Formato, A., Ianniello, D., Pellegrino, A., Villecco, F.: Vibration-based experimental identification of the elastic moduli using plate specimens of the olive tree. Machines **7**(2), 46 (2019)
6. Naviglio, D., Formato, A., Scaglione, G., Montesano, D., Pellegrino, A., Villecco, F., Gallo, M.: Study of the grape cryo-maceration process at different temperatures. Foods **7**(7), 107 (2018)
7. Sena, P., Attianese, P., Pappalardo, M., Villecco, F.: FIDELITY: fuzzy inferential diagnostic engine for online support to physicians. In: Toi, V., Toan, N., Dang Khoa, T., Lien Phuong, T. (eds.) 4th International Conference on Biomedical Engineering in Vietnam, IFMBE Proceedings, vol. 49, pp. 396–400. Springer, Berlin, Heidelberg (2013)
8. Sena, P., d'Amore, M., Pappalardo, M., Pellegrino, A., Fiorentino, A., Villecco, F.: Studying the influence of cognitive load on driver's performances by a fuzzy analysis of lane keeping in a drive simulation. IFAC Proc. Vol. **46**(21), 151–156 (2013)
9. Sena, P., Attianese, P., Carbone, F., Pellegrino, A., Pinto, A., Villecco, F.: A fuzzy model to interpret data of drive performances from patients with sleep deprivation. Comput. Math. Methods Med. **2012**, 868410 (2012)
10. Zhang, Y., Li, Z., Gao, J., Hong, J., Villecco, F., Li, Y.: A method for designing assembly tolerance networks of mechanical assemblies. Math. Probl. Eng. **2012** (2012). https://doi.org/10.1155/2012/513958. Article ID 513958
11. Villecco, F., Pellegrino, A.: Evaluation of uncertainties in the design process of complex mechanical systems. Entropy **19**(9), 475 (2017)

12. Patel, M.D., Pappalardo, C.M., Wang, G., Shabana, A.A.: Integration of geometry and small and large deformation analysis for vehicle modelling: chassis, and airless and pneumatic tyre flexibility. Int. J. Veh. Perform. **5**(1), 90–127 (2019)

13. Kulkarni, S., Pappalardo, C.M., Shabana, A.A.: Pantograph/catenary contact formulations. J. Vibr. Acoust. **139**(1), 011010 (2017)

14. Pappalardo, C.M., Patel, M.D., Tinsley, B., Shabana, A.A.: Contact force control in multibody pantograph/catenary systems. Proc. Inst. Mech. Eng. Part K: J. Multi-Body Dyn. **230**(4), 307–328 (2016)

15. Pappalardo, C.M., Patel, M., Tinsley, B., Shabana, A.A.: Pantograph/catenary contact force control. In: ASME 2015 International Design Engineering Technical Conferences and Computers and Information in Engineering Conference. American Society of Mechanical Engineers Digital Collection (2015)

16. Braccesi, C., Landi, L., Scaletta, R.: New dual meshless flexible body methodology for multi-body dynamics: simulation of generalized moving loads. Proc. Inst. Mech. Eng. Part K: J. Multi-Body Dyn. **218**(1), 51–62 (2004)

17. Al-Jelawy, H., Kaczmarczyk, S., Cross, M., Lewis, R., Singh, N., Alkhafaji, D.: Computational analysis of the fluid-structure interaction occurring in a model of two vehicles overtaking each other. J. Phys: Conf. Ser. **1106**(1), 012009 (2018)

18. Foucault, G., Cuillière, J.-C., François, V., Léon, J.-C., Maranzana, R.: Adaptation of CAD model topology for finite element analysis. Comput.-Aided Des. **40**(2), 176–196 (2008)

19. Li, C., Fan, S., Shi, M.: Preparation of CAD model for finite element analysis. In: 2010 International Conference on Computer, Mechatronics, Control and Electronic Engineering, pp. 491–494. IEEE (2010)

20. Hamed, A.M., Jayakumar, P., Letherwood, M.D., Gorsich, D.J., Recuero, A.M., Shabana, A. A.: Ideal compliant joints and integration of computer aided design and analysis. J. Comput. Nonlinear Dyn. **10**(2), 021015 (2015)

21. Louhichi, B., Abenhaim, G.N., Tahan, A.S.: CAD/CAE integration: updating the CAD model after a FEM analysis. Int. J. Adv. Manuf. Technol. **76**(1–4), 391–400 (2015)

22. Shabana, A.A., Wang, G.: Durability analysis and implementation of the floating frame of reference formulation. Proc. Inst. Mech. Eng. Part K: J. Multi-Body Dyn. **232**(3), 295–313 (2018)

23. Russo, D., Rizzi, C.: Structural optimization strategies to design green products. Comput. Ind. **65**(3), 470–479 (2014)

24. Calì, M., Oliveri, S.M., Evangelos Biancolini, M., Sequenzia, G.: An integrated approach for shape optimization with mesh-morphing. In: Lecture Notes in Mechanical Engineering, pp. 311–322. Springer International Publishing (2019)

25. Bayas, M.P., Andrade, G.N., Arroba, S.M.A., Carrión, J.G.: Kinetic analysis of an ankle rehabilitator composed of two parallel delta robots. In: Memorias de Congresos UTP, pp. 89–97 (2018)

26. Ghali, A., Neville, A.: Structural Analysis a Unified Classical and Matrix Approach. CRC Press, Boca Raton (2017)

27. Buehrle, R.D., Fleming, G.A., Pappa, R.S., Grosveld, F.W.: Finite element model development for aircraft fuselage structures. S V Sound Vib. **35**(1), 32–38 (2001)

28. Marusich, T.D., Usui, S., Marusich, K.J.: Finite element modeling of part distortion. In: Lecture Notes in Computer Science (including subseries Lecture Notes in Artificial Intelligence and Lecture Notes in Bioinformatics), pp. 329–338. Springer, Heidelberg (2008)

29. Melchers, R.E., Beck, A.T.: Structural Reliability Analysis and Prediction. Wiley, Hoboken (2018)

30. Kienzler, R., Herrmann, G.: Mechanics in Material Space: With Applications to Defect and Fracture Mechanics. Springer, Berlin (2012)

31. Hansen, L.U., Heinze, W., Horst, P.: Blended wing body structures in multidisciplinary pre-design. Struct. Multidiscip. Optim. **36**(1), 93–106 (2008)
32. Haftka, R.T., Gürdal, Z.: Elements of Structural Optimization. Springer, Berlin (2012)
33. Venkataraman, S., Haftka, R.T.: Structural optimization complexity: what has Moore's law done for us? Struct. Multidiscip. Optim. **28**(6), 375–387 (2004)
34. Fanni, M., Shabara, M.N., Alkalla, M.G.: A comparison between different topology optimization methods (2014)
35. Henderson, R.P., Martins, J.R.R.A., Perez, R.E.: Aircraft conceptual design for optimal environmental performance. Aeronaut. J. **116**(1175), 1–22 (2012)
36. Rao, J.S., Kiran, S., Kamesh, J.V., Padmanabhan, M.A., Chandra, S.: Topology optimization of aircraft wing. J. Aerosp. Sci. Technol. **61**(3), 402 (2009)
37. Colucci, F., De Simone, M.C., Guida, D.: TLD design and development for vibration mitigation in structures. In: Karabegović, I. (ed.) New Technologies, Development and Application II. NT 2019. Lecture Notes in Networks and Systems, vol. 76, pp. 59–72. Springer, Cham (2019)
38. Guida, R., De Simone, M.C., Dašić, P., Guida, D.: Modeling techniques for kinematic analysis of a six-axis robotic arm. In: IOP Conference Series: Materials Science and Engineering, vol. 568, no. 1, p. 12115 (2019)
39. Rivera, Z.B., De Simone, M.C., Guida, D.: Unmanned ground vehicle modelling in Gazebo/ROS-based environments. Machines **7**(2), 42 (2019)
40. De Simone, M.C., Rivera, Z., Guida, D.: Obstacle avoidance system for unmanned ground vehicles by using ultrasonic sensors. Machines **6**(2), 18 (2018)
41. De Simone, M.C., Guida, D.: Identification and control of an unmanned ground vehicle by using Arduino. UPB Sci. Bull. Ser. D **80**, 141–154 (2018)
42. De Simone, M.C., Guida, D.: Control design for an under-actuated UAV model. FME Trans. **46**(4), 443–452 (2018)
43. De Simone, M.C., Guida, D.: Modal coupling in presence of dry friction. Machines **6**(1), 8 (2018)
44. De Simone, M.C., Rivera, Z.B., Guida, D.: Finite element analysis on squeal-noise in railway applications. FME Trans. **46**(1), 93–100 (2018)
45. Concilio, A., De Simone, M.C., Rivera, Z.B., Guida, D.: A new semi-active suspension system for racing vehicles. FME Trans. **45**(4), 578–584 (2017)
46. Quatrano, A., De Simone, M.C., Rivera, Z.B., Guida, D.: Development and implementation of a control system for a retrofitted CNC machine by using Arduino. FME Trans. **45**(4), 565–571 (2017)
47. Pappalardo, C.M.: A natural absolute coordinate formulation for the kinematic and dynamic analysis of rigid multibody systems. Nonlinear Dyn. **81**(4), 1841–1869 (2015)
48. Pappalardo, C.M., Zhang, Z., Shabana, A.A.: Use of independent volume parameters in the development of new large displacement ANCF triangular plate/shell elements. Nonlinear Dyn. **91**(4), 2171–2202 (2018)
49. Pappalardo, C.M., Wang, T., Shabana, A.A.: Development of ANCF tetrahedral finite elements for the nonlinear dynamics of flexible structures. Nonlinear Dyn. **89**(4), 2905–2932 (2017)
50. Pappalardo, C.M., Wang, T., Shabana, A.A.: On the formulation of the planar ANCF triangular finite elements. Nonlinear Dyn. **89**(2), 1019–1045 (2017)
51. Pappalardo, C.M., Wallin, M., Shabana, A.A.: A new ANCF/CRBF fully parameterized plate finite element. J. Comput. Nonlinear Dyn. **12**(3), 031008 (2017)
52. Pappalardo, C.M., Yu, Z., Zhang, X., Shabana, A.A.: Rational ANCF thin plate finite element. J. Comput. Nonlinear Dyn. **11**(5), 051009 (2016)

Numerical Simulation of Compression and Detonation Strokes in a Pulse Compression Detonation System

Brian Maxwell[1] , Konstyantyn Korytchenko[2],
and Olga Shypul[3(✉)]

[1] Case Western Reserve University,
10900, Euclid Avenue, Cleveland, OH 44106, USA
[2] National Technical University "Kharkiv Polytechnical Institute",
2, Kyrpychova Street, Kharkiv 61002, Ukraine
[3] National Aerospace University "Kharkiv Aviation Institute",
17, Chkalova Street, Kharkiv 61070, Ukraine
`o.shipul@khai.edu`

Abstract. At the National Technical University "Kharkiv Polytechnical Institute", an experimental pulse compression detonation (PCD) system was developed to operate on propane-air mixtures while addressing potential issues with regards to efficiency, ignitability of the gas, and the critical tube diameter for detonation. In this PCD system, the reactive gas was pre-compressed within the detonation tube, before ignition. The resulting mixture was found easier to ignite, and the transition to detonation within the tube was much more reliable and consistent. To gain further insight, and to investigate the effect of pressure gradient on the strength/velocity of outflow products and the overall thermodynamic cycle, a two-stage modelling procedure was adopted. First, a 3D inert simulation of the compression process of the PCD system was conducted using ANSYS. The resulting pressure and density profiles within the detonation tube were then prescribed as initial conditions for a 2D detonation stroke and outflow simulation. For this stage, the Compressible Linear Eddy Model for Large Eddy Simulation (CLEM-LES) framework adopted. For the PCD system, it was found that higher peak pressures were obtained at the outflow location of the tube when compared to a detonation tube filled initially at constant pressure equal to the ambient condition. As a result, the higher thermal efficiency of the detonation cycle may be achieved. However, it was found that the outflow products were under expanded, which may adversely affect the generated impulse. Therefore, the use of nozzles should be investigated in future work as part of the PCD system proposed here.

Keywords: Gas compression · Detonation initiation · Pressure and density profiles

1   Introduction

At the National Technical University "Kharkiv Polytechnical Institute", Ukraine, an experimental pulse compression detonation (PCD) system was developed to operate on propane-air mixtures while addressing potential issues with regards to efficiency, ignitability of the gas, and the critical tube diameter for detonation. In this PCD system, the reactive gas was pre-compressed within the detonation tube, before ignition, using the piston-cylinder arrangement shown in Fig. 1. Similar to the design of the US-Air Force [1], the current design offers an advantage by allowing pre-compression of the gas within the tube while remaining open to the external environment.
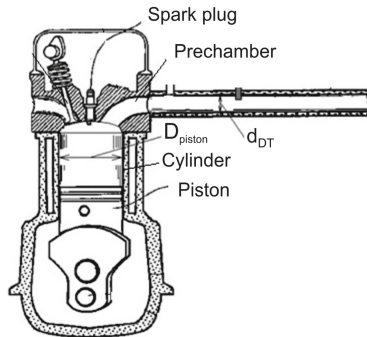
Fig. 1. Diagram of the PCD-system [3].

By pre-compressing the reactive mixture to a state of higher pressure, smaller characteristic cell size may have been achieved [2]. As a result, the mixture was easier to ignite, and the transition to detonation within the tube has been demonstrated to be much more reliable and consistent [3]. Although this experimental system has proved useful to demonstrate these advantages, in concept, the flow diagnostics are limited to pressure sensors mounted at fixed locations and flow visualization was lacking. Therefore, numerical simulations are useful to provide insight into the combustion process within the tube, the external flow field, and also the cycle efficiency.

2   Literature Review

Extensive work has already been performed on modelling detonation tube performance [4–9], such models have been limited to either application of Euler methods or gas-dynamic analysis. Moreover, the effect of viscous friction and heat loss has generally been neglected, except for Radulescu and Hanson [10], who determined that heat loss through tube walls can adversely influence performance. In addition to this past work, Perkins [11] also investigated the influence of the initial concentration gradient in the tube. However, the impact of viscous friction within the tube, and the influence of pressure/density gradients remains to be investigated, both of which are considered in the current study.

To investigate the effect of pressure gradient on the strength/velocity of outflow products and the overall thermodynamic cycle while considering tube friction, on the detonation outflow process and cycle efficiency, a two-stage modelling procedure was adopted. First, a 3D inert simulation of the compression process of the experimental PCD system [3] was modelled using a commercial CFD software (ANSYS). The resulting pressure and density profiles within the detonation tube were then prescribed as initial conditions for a 2D detonation stroke and outflow simulation. For this stage, a grid-within-a-grid approach was adopted using the Compressible Linear Eddy Model for Large Eddy Simulation (CLEM-LES) framework [12].

3 Research Methodology

Two-Stage Numerical Approach was applied as a research methodology. The compression stroke was modelled first, using ANSYS, to determine the initial pressure and density distribution within the tube before detonation initiation. The detonation and outflow process was then modelled separately using the CLEM-LES strategy, a relatively new approach to modelling highly compressible and reactive flows [12]. Justification for this approach was based on the principal assumption that time scales associated with the detonation process ($\sim 5.6 \times 10^{-4}$ s) were much shorter compared to the compression process ($\sim 1 \times 10^{-2}$ s) by at least an order of magnitude.

The compression stroke simulation was a three-dimension solution of the Navier-Stokes equations, supplemented by the SST turbulence model, using a resolution of 15 μm. The numerical domain was constructed to scale with the experimental setup and is sketched in Fig. 2a.
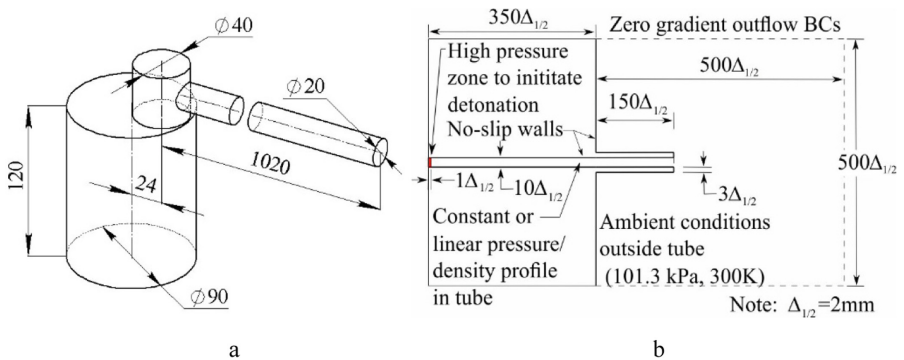
Fig. 2. Numerical domains for a) the compression stroke (in mm) and b) the detonation and outflow process.

The working fluid considered was stoichiometric propane-air, and the piston was treated as a moving wall boundary with a prescribed sinusoidal motion,

$$v_p = 18.85 \sin(\pi t/0.01), \, [\text{m/s}] \tag{1}$$

The sinusoidal dependence approximately corresponds to a transformation of a rotate motion of the crank-shaft into the linear motion of the piston. A rotation frequency of the crank-shaft and a maximum of the piston velocity were chosen in such a manner that there is a gas compression into the detonation tube. The action of the piston, once the tube was filled with the propane-air mixture, was found to generate a linear pressure distribution within the tube, with a maximum pressure of approximately ~4 atm at the closed end.

The linear pressure distribution obtained from the compression simulation was the initial condition for the detonation stroke and outflow process simulation. A two-dimensional simulation using the CLEM-LES approach was adopted, using physical scales comparable to the compression simulation and experiment. The corresponding numerical domain is sketched in Fig. 2b, which contains no-slip boundary conditions within the tube. The pressure and density distributions in the tube:

$$p(x) = 4p_0 - 3p_0(x/L) \text{ and } \rho(x) = (p(x)/p_0)^{\frac{1}{7}} \tag{2}$$

where isentropic compression was assumed. Here, $p_0 = 1$ atm and L/x represented the normalized length along the tube from the closed end, where $l = 1$ m. We note, however, that experimental evidence suggests the tube is never able to fill, resulting in concentration gradients near the open end of the tube [13]. This is currently not addressed. To initiate the detonation, sufficient energy in the form of pressure, $p = 400p_0$, was deposited within the first half-reaction length ($\Delta_{1/2}$) from the closed end of the tube. We note, however, that the actual initial flame acceleration and transition to detonation process, not modelled here, is a much more complex phenomenon originating from within the cylinder, and would likely have some impact on the cycle and performance.

Although specific details of the CLEM-LES procedure are published elsewhere [12], the chemical parameters in this study ($Q = 15$, $E_a = 60$, $A = 33.000$, and $\gamma = 1.37$) were calibrated to reproduce the correct detonation velocity of $M_{CJ} = 5.3$

CLEM-LES:
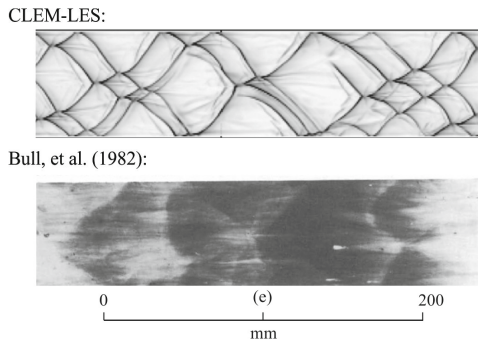
Bull, et al. (1982):

Fig. 3. To scale comparisons of sootfoils obtained using the CLEM-LES and from experiments of Bull et al. [14], for detonation propagation in stoichiometric propane-air at 1 atm.

(1807.1 m/s), half-reaction length ($\Delta_{1/2} = 2.1$ mm), post-shock laminar flame speed ($S_L = 6.64$ m/s at $M_D = 0.7 M_{CJ}$), and cell size ($\lambda \approx 50$ mm) for stoichiometric propane-air at atmospheric conditions. A resolution of $\Delta' = \Delta_{1/2}/8$ with 64 subgrid elements within each LES cell, providing an effective resolution of $\Delta'_{eff} = \Delta_{1/2}/512$, was found sufficient to resolve both the post-shock laminar flame speed and experimentally observed cellular patterns [14] (see Fig. 3).

4   Results

A typical flow field for the outflow process of the PCD system, with initially linear pressure distribution profile, is shown in Fig. 4. Here, the outflowing hot product gases have been found to expand rapidly while driving a strong incident shockwave. Within the expanding jet, internal shock structures followed by rapid expansions were found to form, with a diamond-like pattern. This is a characteristic of typical underexpanded jet bevaviour when there exists a high pressure at the jet exit, followed by the same diamond pattern of rapid expansions and shocks [15] as the outflowing gas attempts to equilibrate with the surroundings.
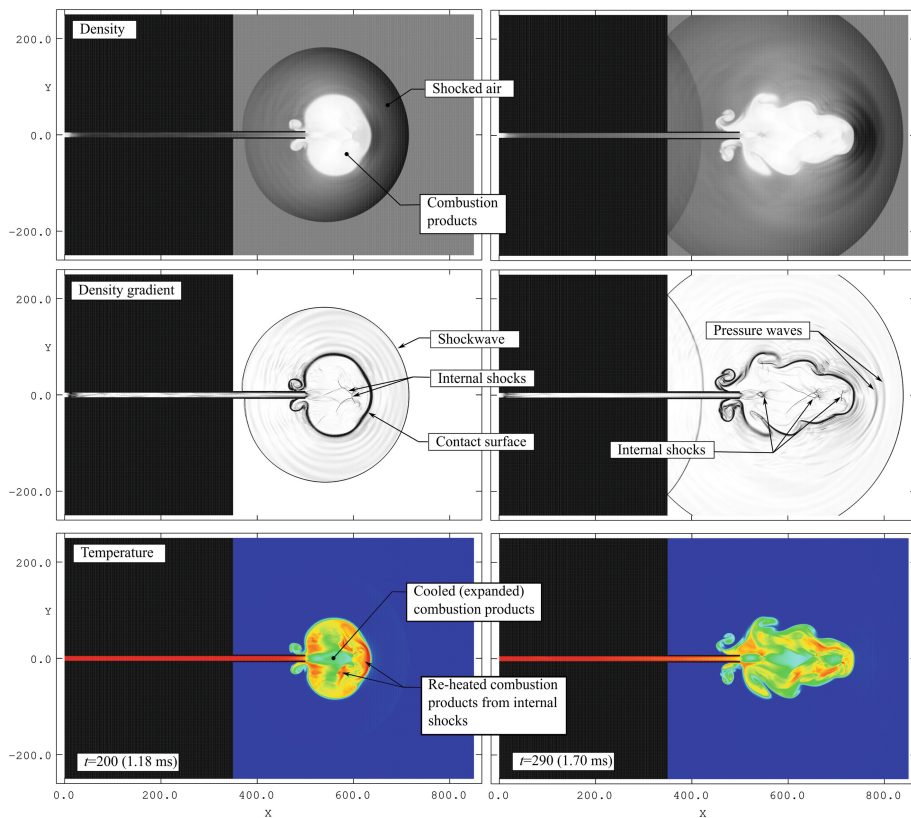
Fig. 4. Flow fields of density, density gradient, and temperature for two instances in time.

This outflow behaviour was also observed in previous investigations of pulse detonation tubes [5, 7], and is generally undesirable and leads to loss of performance. This cyclic expansion (cooling) of product gases, followed by shock-induced re-heating of the jet gas resulted in zones of varying temperature gas within the jet, with hotter regions near the jet head and outer edges of the jet outside the core regions. This behaviour is further analyzed by examining pressure and density evolutions along the centreline, $y = 0$, at several instances in time, as shown in Fig. 5. Here we first note the continual decay of the incident shockwave as the flow jets out of the tube. We expect the rapid expansion of the wave since there is no confinement outside the tube. We also note the development of inward-facing shocks, as labelled in the figure, which acts to continually shock the outflowing gas.
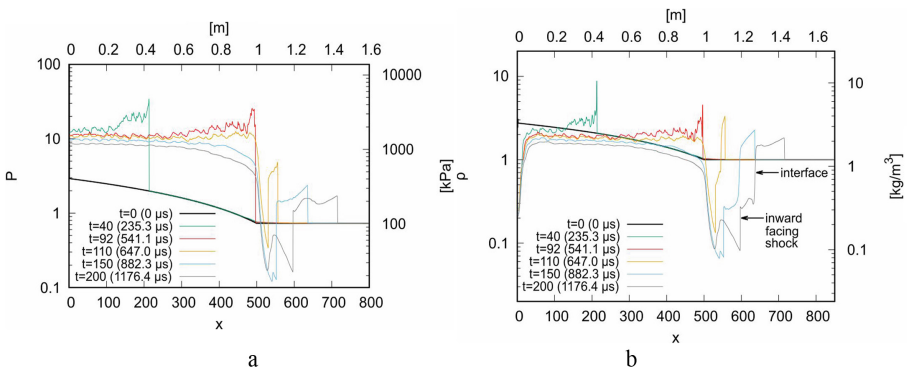
Fig. 5. Evolution of a) pressure and b) density, along the tube centreline (y = 0).

Behind each inward-facing shock, the gas always expands to lower than ambient pressures and therefore requires the formation of further shocking downstream as the jet further develops. It has previously been shown that such behaviour can adversely affect the specific impulse and thrust of the pulse detonation tube, owing to outflow pressures below ambient and entropy generation through the shocking process. As such, the use of nozzles has been suggested for promoting the expansion of the gases sufficiently before outflow into ambient to further boost efficiency [5, 7, 16, 17]. We obtained the velocity history of the wave front measured along the centreline ($y = 0$) to assess the performance of the PCD system. It is shown in Fig. 6.

For comparison, the PCD wave velocity was compared against a case where the tube pressure was not pre-compressed, also using the CLEM-LES. In this comparative case, the tube pressure was initialized with $p(x) = p_0$. Also, for both cases (linear and constant p), results are compared against Euler simulations. Here, wave velocities obtained for the initially linear pressure distribution profile were always found to accelerate toward the tube end, at velocities above the CJ-speed. This observation was found, in part, to be influenced by the forward motion of the unreacted gas resulting from the pressure gradient, ahead of the wave, as the pressure attempts to equilibrate with its surroundings. The detonation wave was therefore advected forward, to some
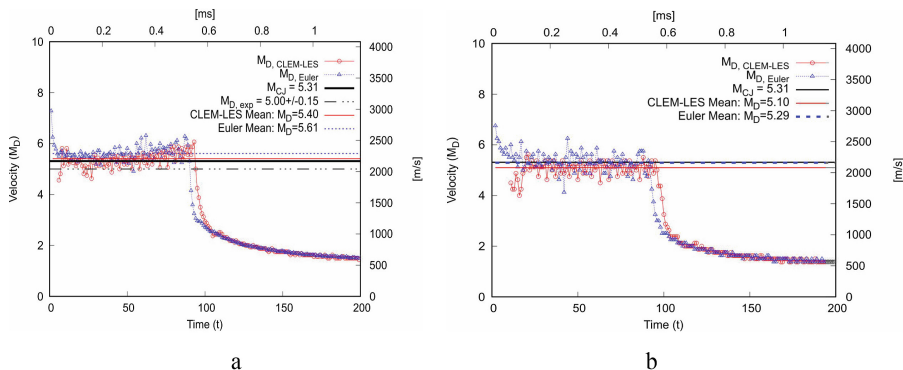
Fig. 6. Wave velocity histories for the cases: a) linear pressure distribution, b) constant pressure.

extent inside the tube, leading to faster-observed wave propagation. However, the flow velocity ahead of the wave was found to be on the order of $u \sim 0.3$, at most, inside the tube. Therefore, we attribute the overdriven wave velocity to the increased pressure behind the wave as the detonation evolved in the tube.

Next, the average wave velocities obtained from the CLEM-LES, inside the tube, were found to be lower than their counterpart Euler simulations by roughly 5%. We attribute this discrepancy to boundary layer development at the tube walls. Flow divergence due to boundary layer formation behind detonations has previously been shown to produce significant velocity deficits for flows within comparatively thin channels and tubes [18–22]. We acknowledge, however, that the recorded experimental velocity was 10% lower compared to the Euler simulation, which does not account for such losses. We also note that while a 5% deficit was observed in the CLEM-LES compared to the Euler case, there are several factors not accounted for. First, the simulations were two-dimensional and did not capture the actual boundary layer development of a three-dimensional pipe. Moreover, heat loss through the pipe walls, which has not been accounted for here, may also contribute to a slower wave, and consequently a loss of specific impulse [10]. Finally, we note difficulties in ensuring perfectly stoichiometric mixtures in the experimental PCD system, which also contribute to velocity deficits.

To further investigate the performance of the PCD system, $p-v$ diagrams were constructed in Fig. 7 for the detonation cycles of both the initially linear and constant pressure distributions, using the CLEM-LES. To construct the $p-v$ diagrams, the pressure and specific volumes were obtained at $(x, y) = (500.0)$ for several time steps over the outflow process, which corresponds to the centre of the open end of the pipe. Also shown in the figure is the theoretical detonation-cycle for a wave corresponding to the perfect gas ZND-structure associated with the CJ-detonation for the parameters for Q and γ used in the numerical model. We first note that the peak pressure is never attained in the simulations. Since the cellular structure is larger than the tube, peak pressures always occur at the tube walls and not along the centre. As a result, the peak pressure along the tube centreline is always lower than the von-Neumann pressure

associated with the detonation. Despite this, we note that the simulation starting with the linear pressure distribution can achieve a higher peak pressure compared to the case where the tube is initially at ambient pressure by roughly $\sim 10\%$.
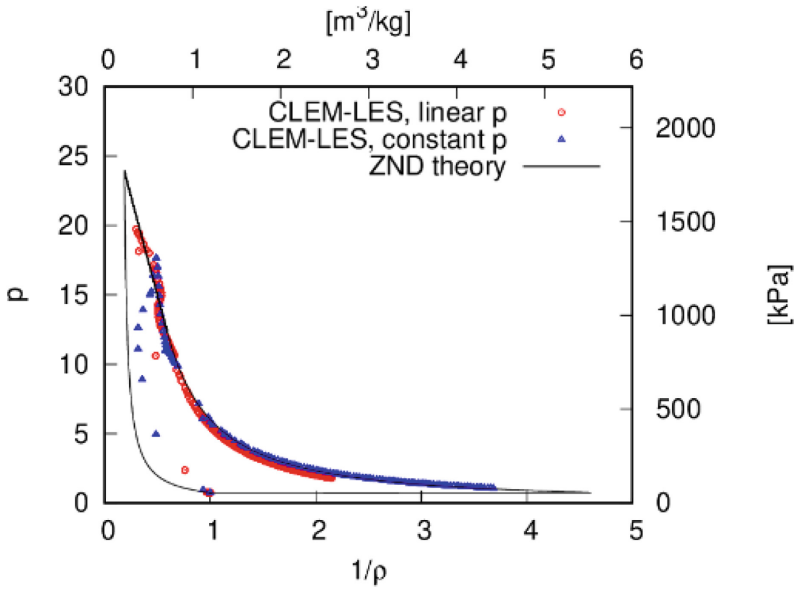
Fig. 7. *p-v* diagram for the detonation cycle.

As a result, the higher thermal efficiency of the cycle is realized by pre-compressing the gas in the tube using the PCD system. This is consistent with theoretical predictions of Wintenberger et al. [8], who found that the impulse per unit volume of the tube was directly proportional to the initial pressure, or mass of reactant in the detonation tube, i.e. $I \propto m$. In this case, the linear distribution of pressure in the tube resulted from an increase of reactant mass in the tube by a factor of 1.93 from the case where the pressure in the tube was kept constant at atmospheric conditions. In theory, the PCD system under investigation should result in nearly twice as much impulse as the constant pressure case. However, regarding thermal efficiency, a full analysis of the PCD system power input and output would be required to determine the actual useful efficiency gain of the system for practical applications.

5   Conclusion

In this work, a two-stage digital strategy was applied to model a pulsed compression detonation system. In general, the compression-detonation device allowed to permit better control the distribution of pressure, temperature and concentration of reactive gas before detonation initiation. The linear pressure profile case had M_D = 5.5 (1875 m/s),

the constant pressure case had M_D = 5.1 (1739 m/s), lower than CJ (M_CJ = 5.3, 1807 m/s) due to no-slip condition in the tube walls. From this, we can conclude that the pressure gradient results in an 8% increase in wave velocity over the constant pressure case. As a result, controlled gradients of pressure in the detonation tube were realized. This was found to give rise to higher peak pressures, obtained at the outflow location of the tube when compared to a detonation tube filled initially at constant pressure equal to the ambient condition. As a result, we may conclude that a higher thermal efficiency of the detonation cycle may be achieved. However, further detailed analysis is required. Finally, it was found that the outflow products were under expanded, which contained complex gas dynamic features such as repeating inward-facing shocks and rapid expansions of the outflowing gas. It is believed that such features may adversely affect the generated impulse owing to the presence of below ambient pressures and entropy generation in the jet gas. To remedy this issue, the use of nozzles have proved useful [5, 7, 17, 23] and should be investigated in future work as part of the PCD system proposed here.

References

1. Schauer, F., Stutrud, J., Bradley, R.: Detonation initiation studies and performance results for pulsed detonation engine applications. In: 39th Aerospace Sciences Meeting and Exhibit, Paper AIAA 2001-1129. AIAA, Reno (2001). https://doi.org/10.2514/6.2001-1129
2. Stevens, C.A., Hoke, J.L., Schauer, F.R.: Propane/air cell size correlation to temperature and pressure. In: 54th AIAA Aerospace Sciences Meeting, Paper AIAA 2016-1400. AIAA, San Diego (2016). https://doi.org/10.2514/6.2016-1400
3. Korytchenko, K., Kysternyy, Y., Sakun, O.: Propane and air mixture-based short-barrel detonation gun. In: Proceedings of the 26th International Colloquium on the Dynamics of Explosions and Reactive Systems, Paper 4332. ICDERS, Boston (2017)
4. Kailasanath, K., Patnaik, G.: Performance estimates of pulsed detonation engines. Proc. Combust. Inst. **28**(1), 595–601 (2000). https://doi.org/10.1016/S0082-0784(00)80259-3
5. Ma, F., Choi, J.-Y., Yang, V.: Thrust chamber dynamics and propulsive performance of single-tube pulse detonation engines. J. Propuls. Power **21**(3), 512–526 (2005). https://doi.org/10.2514/1.7393
6. Ma, F., Choi, J.-Y., Yang, V.: Internal flow dynamics in a valveless airbreathing pulse detonation engine. J. Propuls. Power **24**(3), 479–490 (2008). https://doi.org/10.2514/1.29957
7. Cooper, M., Shepherd, J.E.: The effect of transient nozzle flow on detonation tube impulse. In: 40th AIAA/ASME/SAE/ASEE Joint Propulsion Conference and Exhibit, Paper AIAA 2004-3914. AIAA, Fort Lauderdale (2004). https://doi.org/10.2514/6.2004-3914
8. Wintenberger, E., Austin, J.M., Cooper, M., et al.: Analytical model for the impulse of single-cycle pulse detonation tube. J. Propuls. Power **19**(1), 22–38 (2003). https://doi.org/10.2514/2.6099
9. Zheng, F., Kuznetsov, A.V., Roberts, W.L.: Numerical study of a pulsejet-driven ejector. In: 45th AIAA/ASME/SAE/ASEE Joint Propulsion Conference and Exhibit, Paper AIAA 2009-5185. AIAA, Denver (2009). https://doi.org/10.2514/6.2009-5185
10. Radulescu, M.I., Hanson, R.K.: Effect of heat loss on pulse-detonation-engine flow fields and performance. J. Propuls. Power **21**(2), 274–285 (2005). https://doi.org/10.2514/1.10286

11. Perkins, H.D.: Effects of fuel distribution on detonation tube performance. NASA Technical Memorandum NASA/TM-2002-211712 (2002)
12. Maxwell, B.M., Bhattacharjee, R.R., Lau-Chapdelaine, S.S., et al.: Influence of turbulent fluctuations on detonation propagation. J. Fluid Mech. **818**, 646–696 (2017). https://doi.org/10.1017/jfm.2017.145
13. Tangirala, V.E., Dean, A.J., Tsuboi, N., Hayashi, A.K.: Performance on a pulse detonation engine under subsonic and supersonic flight conditions. In: 45th AIAA Aerospace Sciences Meeting and Exhibit, Paper AIAA 2007-1245. AIAA, Reno (2007). https://doi.org/10.2514/6.2007-1245
14. Bull, D.C., Elsworth, J.E., Shuff, P.J., Metcalfe, E.: Detonation cell structures in fuel/air mixtures. Combust. Flame **45**, 7–22 (1982). https://doi.org/10.1016/0010-2180(82)90028-1
15. Franquet, E., Perrier, V., Gibout, S., Bruel, P.: Free underexpanded jets in a quiescent medium: a review. Prog. Aerosp. Sci. **77**, 25–53 (2015). https://doi.org/10.1016/j.paerosci.2015.06.006
16. Cambier, J.-L., Tegnér, J.K.: Strategies for pulsed detonation engine performance optimization. J. Propuls. Power **14**(4), 489–498 (1998). https://doi.org/10.2514/2.5305
17. Daniau, E., Zitoun, R., Couquet, C., Desbordes, D.: Effects of nozzles of different length and shape on the propulsion performance of pulsed detonation engines. In: Roy, G.D., Frolov, S. M., Netzer, D.W., Borisov, A.A. (eds.) High-Speed Deflagration and Detonation: Fundamentals and Control, pp. 251–262. ELEX-KM Publishers, Moscow (2001)
18. Fay, J.A.: Two-dimensional gaseous detonations: velocity deficit. Phys. Fluids **2**(3), 283–289 (1959). https://doi.org/10.1063/1.1705924
19. Chao, J., Ng, H.D., Lee, J.H.S.: Detonability limits in thin annular channels. Proc. Combust. Inst. **32**(2), 2349–2354 (2009). https://doi.org/10.1016/j.proci.2008.05.090
20. Camargo, A., Ng, H.D., Chao, J., Lee, J.H.S.: Propagation of near-limit gaseous detonations in small diameter tubes. Shock Waves **20**(6), 499–508 (2010). https://doi.org/10.1007/s00193-010-0253-3
21. Ishii, K., Monwar, M.: Detonation propagation with velocity deficits in narrow channels. Proc. Combust. Inst. **33**(2), 2359–2366 (2011). https://doi.org/10.1016/j.proci.2010.07.051
22. Wu, M.H., Wang, C.Y.: Reaction propagation modes in millimeter-scale tubes for ethylene/oxygen mixtures. Proc. Combust. Inst. **33**(2), 2287–2293 (2011). https://doi.org/10.1016/j.proci.2010.07.081
23. Eidelman, S., Yang, X.: Analysis of the pulse detonation engine efficiency. In: 34th AIAA/ASME/SAE/ASEE Joint Propulsion Conference and Exhibit, Paper 3877. AIAA, Cleveland (1998). https://doi.org/10.2514/6.1998-3877

Simulation of Bird Collision with Aircraft Laminated Glazing

Natalia Smetankina[1(✉)] , Igor Kravchenko[2] ,
Vyacheslav Merculov[2] , and Dmitry Ivchenko[2]

[1] A. Pidgorny Institute of Mechanical Engineering Problems
of the National Academy of Sciences of Ukraine,
2/10, Pozhars'koho Street, Kharkiv 61000, Ukraine
nsmetankina@ukr.net
[2] SE Ivchenko-Progress, 2, Ivanova Street, Zaporizhzhia 69061, Ukraine

Abstract. Aircraft collisions with birds are a severe safety problem. The purpose of this paper is to create a closed-form mathematical collision model that estimates the response of a laminated airplane glazing to bird impact and provides a risk score that can be utilized to underpin decisions made by engineers and designers. The collision model includes a bird impulse model, and a method for analyzing the stress-strained state of laminated airplane glazing at different operational factors is presented. The technique consists of a method for strength analysis of the laminated airplane glazing at bird impact and a method for analyzing superfluous pressure. The laminated glazing model is based on the refined theory accounting for transverse shear strains, thickness reduction, and normal element rotation inertia of each layer. The mathematical model of pressure impulse authentically reproducing bird impact is based on experimental research. Theoretical results are in good agreement with experimental data, allowing recommending the method for developing new airplane glazing elements.

Keywords: Bird strike · Laminated windshield · Safety

1 Introduction

One of the significant hazards to flight safety today is a collision with birds. Many external aircraft components of an aircraft, such as windshield, engine, and fuselage, are susceptible to collisions with birds [1, 2]. According to statistical data from the Federal Aviation Administration, the number of bird strike accidents annually has increased six times from 1,795 cases to 10,856 cases from 1990 to 2013, respectively, with the total number of accidents 138,257 at last fourteen years. Such intensive bird strike accidents have caused huge fatalities; namely, at least 103 aircraft and 262 lives were lost in civil aviation in 1912–2008, with annual property losses increasing from 614 million to 1.28 billion US dollars [3, 4].

Aircraft windshields are especially vulnerable to damage [5]. Airworthiness standards require that these critical components should be capable of withstanding bird strikes at critical flight speeds to a certain degree [6]. All windshields are designed to be safe and durable in order to withstand the bird ingestion.

Aviation standards in force require that the aircraft construction would allow the crew to conclude the flight safely after the collision with a 1.81-kg bird [7]. Besides, reliable protection from pressurization, namely a static loading, which arises through the pressure difference outside and inside the aircraft cockpit, is critical for ensuring a normal flight.

2 Literature Review

The certification of new aircraft parts by empirical tests is an expensive process as several tests may be required to evaluate windshield effectiveness [6, 7]. If computer simulations replace expensive empirical verifications, the windshield design can be optimized before an actual test is carried out. This will lower the costs and expedite design and certification processes.

It is stated that the behavior of birds impacting a rigid target is described with the hydrodynamic model. At high-speed impact, a bird behaves like a fluid with insignificant viscosity [8]. A bird strike can be considered as a soft body impact problem [9].

With the advent of highly effective FEM-based software packages, further consideration was given to the problem of the joint deformation of the bird and target. In doing so, the focus was on the accuracy of describing the process of bird damage. Lagrangian, Arbitrary Lagrangian–Eulerian (ALE), and Smooth Particle Hydrodynamics (SPH) formulations have found full application [10].

In paper [11], a bird strike to a typical helicopter windshield is investigated using SPH and the finite element method. Five types of windshield lay-ups are considered, and, in each case, the thickness that prevents the bird from perforating the windshield is calculated. Simulations showed that among the five cases presented, glass with a polyvinyl butyral interlayer could be the best choice for being used in a windshield against the bird strike. Another conclusion is that for the same initial velocity, the impact angle can cause more damage to the windshield than a direct impact.

Guida et al. [12] found that the Lagrangian-SPH combination provided the best results in terms of impact visualization and a right prediction of the deceleration of the projectile, as compared to the test results.

Paper [13] is devoted to the investigation of parameters that influence the shock regime, based on the findings of several SPH simulations and an experimental test campaign. A zoom on the numerically obtained shock pressure pulse is made, which shows that the impact pressure and duration correspond very well with the theory. The analytical values and numerical results are compared to a series of experimental impact pressure measurements with real and gelatin birds.

The windshield is an essential element of an aircraft, and certain basic features depend on its quality. The critical quality characteristics of a windshield are visibility through the canopy, the structure rigidity and reliability, and the bird impact resistance. The most widely used materials for an aircraft windshield are glass and polymers.

Yang et al. [14] elaborated an experimental and FEM of a windshield subjected to the high-speed bird impact. Authors of [15] and [16] focused on analyzing an effective numerical method to simulate bird impact aircraft windshield events, using the SPH

approach and the explicit finite element program PAM-CRASH. Salehi et al. [5] investigated the effect of the bird strike on different aircraft windows, both numerically and experimentally.

The purpose of this study is to devise the method of calculating the stress-strained state parameters for laminated aircraft windshields at bird impact and operating static load based on an immersion method.

3   Research Methodology

3.1   Mathematical Model of a Bird Impulse

Since the bird tissue is mostly composed of water, a bird has been characterized with a water-like hydrodynamic response. This fact has been confirmed through experimental studies carried out by Wilbeck and Rand [8]. Based on this argument, a hydrodynamic model of a bird impulse is proposed.

The target is a laminated glass with constant thickness subjected to impulse loads simulating impact action. The glass has a complex form in plan, and it is considered in the Cartesian system of coordinates related to its outer surface subjected to a bird strike (Fig. 1). A bird with mass M collides with the glass with velocity V. The bird trajectory of motion is at an angle α to the glass.
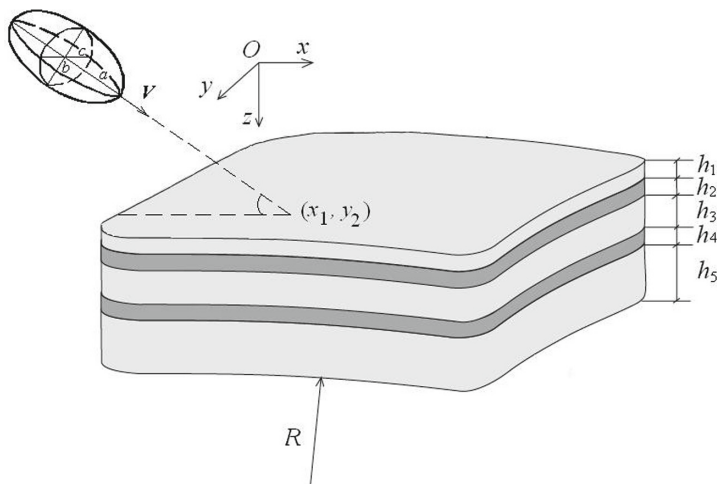
Fig. 1. The bird collision with laminated glass.

The components of the vector of the external load $\mathbf{P} = \{p_j(x, y, t)\}$ $(j = \overline{3I + 3})$ acting on the glass during a strike are represented as follows:

$$p_1 = p_2 = 0, i = \overline{1, I}; p_3 = \frac{1}{2}[1 + \text{sign}(\tau_b - t)]F(t), \tag{1}$$

where t is time; I is the number of layers; τ_b is time of the bird-and-glass interaction; $\tau_b = \frac{2\sqrt{a^2 + k^2 b^2}}{V}$; $k = ctg\alpha$; $p_3 = \frac{1}{2}P_0[1 + \text{sign}(\tau_p - t)]F$ is a function of the contact pressure over the load area;

$$F = \left[1 - \frac{(x - x_1 - \delta)^2}{a^2} - \frac{(y - y_1)^2}{b^2}\right]^{1/2};$$

u_b and v_b are lengths of semi-axes of the elliptical load area; x_1 and y_1 are coordinates indicating the point where the trajectory of motion of the bird center of mass intersects the glass.

The impact force of the bird and glass relates to the load intensity as follows:

$$P_b(t) = \iint_{\Omega(t)} p_3 d\Omega = \frac{2}{3}P_0\pi u_b v_b. \tag{2}$$

where $P_b(t)$ is contact force; $\Omega(t)$ is the area of bird and glass contact.

According to the hydrodynamic theory suggested, the first approximation of the contact interaction force $P_b(t)$ is assumed represented by the value obtained from the hydrodynamic theory. It takes the form

$$P_b(t) = \rho_b V^2 \sin^2 \alpha \pi u_b v_b, \tag{3}$$

where ρ_b is bird tissue density; $\rho_b = \frac{3M}{4\pi abc}$.

3.2   Mathematical Model of Non-stationary Vibrations of a Laminated Glass

We examine the laminated glass as an open-ended laminated cylindrical shell with a radius R. It comprises isotropic layers with the constant thickness h_i (Fig. 1). The behavior of a laminated shell is described by the first-order theory accounting for the transverse shear strain, a thickness reduction and a normal element rotation inertia in each layer

$$u_k^i = u_k + \sum_{j=1}^{i-1} h_j u_{3 + I(k-1) + j} + (z - \delta_{i-1})u_{3 + I(k-1) + i}, \, k = 1, 2, 3, \, i = \overline{1, I},$$

where $\delta_i = \sum_{j=1}^{i} h_j$, $\delta_{i-1} \le z \le \delta_i$; $u_k = u_k(x, y, t)$ $(k = 1, 2, 3)$ are displacements of coordinate surface points to coordinate axes; $u_{3+I(k-1)+i} = u_{3+I(k-1)+i}(x, y, t)$ $(k = 1, 2)$ are angles of rotation of the common element in the i-th layer about the coordinate axes; $u_{3+2I+i} = u_{3+2I+i}(x, y, t)$ is typical element reduction within the ith layer; t is time.

The equations of motion of a laminated shell affected by the impact load, as well as the respective boundary conditions on the boundary Γ, are derived using Hamilton's variational principle

$$[\Omega]\overline{U}_{,tt} - [\Lambda]\overline{U} = \overline{Q}, \tag{4}$$

$$\mathbf{B}^{\Gamma}\mathbf{U} = \mathbf{P}^{\Gamma}, (x, y) \in \Gamma, \tag{5}$$

where $\mathbf{\Omega}^{\rho}$ and $\mathbf{\Lambda}$ are symmetric matrices; $\mathbf{U} = \{u_j(x, y, t)\}$; $\mathbf{P} = \{p_j(x, y, t)\}$; $j = \overline{1, 3I + 3}$.

The problem of investigating non-stationary vibrations of a laminated shell subjected to bird impact is reduced to integrating a system of motion Eqs. (4) with an account of boundary conditions (5). The laminated shell in the plan view occupies a complex-shape domain. The domain boundary is described by equations of straight lines and arcs of circles.

The analytical solution of the problem is obtained by the immersion method [17]. According to this method, a non-closed cylindrical laminated shell is immersed into an auxiliary enveloping cylindrical shell with the same composition of layers. It is loaded within a domain Ω similar to that for the primary shell. An extra shell is the one in which contour shape and boundary conditions yield a simple analytical solution. In this case, the auxiliary shell is a simply supported non-closed cylindrical laminated with rectangular plan-view shape, allowing finding the problem solution as a trigonometric series.

To satisfy actual boundary conditions, additional distributed compensating loads $\mathbf{Q}^{\text{comp}} = \{q_j^{\text{comp}}(x, y, t)\}$ $(j = \overline{1, 3I+3})$, the intensity of which are to be found, are applied to the auxiliary shell over the boundary Γ. The compensating loads appear in the motion equations as the curvilinear distributions $\mathbf{P}^{\text{comp}} = \{p_j^{\text{comp}}(x, y, t)\}$,

$$p_j^{\text{comp}}(x, y, t) = \oint_{\Gamma} q_j^{\text{comp}}(s, t) \, \delta(x - x_{\Gamma}, y - y_{\Gamma}) \, ds, \, j = \overline{1, 3I+3},$$

where $\delta(x - x_{\Gamma}, y - y_{\Gamma})$ is a two-dimensional δ-function.

Based on the condition of satisfying boundary conditions on the boundary Γ (5), we form a system of integral equations for determining the intensities of compensating loads

$$[B^L]\overline{U} = 0, \ x, y \ \in \ L. \tag{6}$$

Displacements and loads (1) are expanded in the auxiliary shell domain into trigonometric series for functions satisfying simply supported conditions. The compensating loads are expanded into a series along boundary Γ

$$q_j^{\text{comp}}(s,t) = \sum_{\alpha=1,2} \sum_{\mu=0}^{\infty} q_{j\alpha\mu}(t)\, b_{\alpha\mu}(s), \ j = \overline{1, \ 3I+3}, \tag{7}$$

where

$$b_{1\mu} = \sin[\mu\gamma(s)], \ b_{2\mu} = \cos[\mu\gamma(s)], \ \gamma(s) = 2\pi \int_0^s d\tilde{s} \bigg/ \oint_\Gamma d\tilde{s}, \ 0 \le \gamma(s) \le 2\pi, \ \mu = \overline{0, \mu^*}\,.$$

Hence, the system of integral Eqs. (6) is transformed into a system of algebraic equations with respect to the expansion coefficients of the compensating loads (7). The system of motion Eqs. (4) is integrated by expanding the solution into the Taylor series.

4   Results

Numerical results, demonstrating the theoretical approach, were obtained for the windshield of an AN-148 aircraft (Fig. 2) under the bird strike. Figure 3 shows the computational model (layout) of the glass.

The windshield is treated as a seven-layer elastic supported glass with radius $R = 1.34$ m and dimensions $l_1 = 0.62$ m, $l_2 = 0.68$ m, $l_3 = 0.604$ m, $l_4 = 0.75$ m, $r_1 = 0.05$ m, $r_2 = 0.03$ m, $r_3 = 0.04$ m, $r_4 = 0.045$ m (Fig. 3). Layers of the windshield are made of silicate glass (layers 1, 3, 5 and 7) and polymer material (layers 2, 4, 6). Data for the glass layers are as follows: $E_i = 6.12 \times 10^4$ MPa, $\nu_i = 0.22$ and $\rho_i = 2.5 \times 10^3$ kg/m^3 for $i = 1, 3, 5, 7$; $E_i = 2.8 \times 10^2$ MPa, $\nu_i = 0.38$ and $\rho_i = 1.2 \times 10^3$ kg/m^3 for $i = 2, 4, 6$; $h_1 = h_5 = h_7 = 5$ mm, $h_3 = 12$ mm   and $h_4 = 2$ mm. Here E_i is Young's modulus for the material, ν_i is Poisson's ratio, and ρ_i is the density of the i-th layer material.

Computational results were compared with experimental data obtained with dynamic wide-band strain gauging. The strike was made in the middle of the external windshield surface parallel to the aircraft fuselage axis. During the experiment, bird bodies were launched against the laminated glass (Fig. 2). Since the experimental research was not the goal of the study, a detailed description of the method and equipment is given in [18]. Strains were measured. A rosette of strain gauges was affixed with an adhesive to the glass back surface (the point C on Fig. 3).

Fig. 2. A laminated windshield.
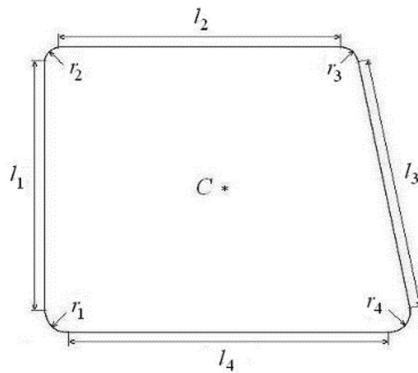
Fig. 3. Glass computational model.

Figure 4 shows the pneumatic gun for launching birds. Figure 5 shows the glass after testing. One can see that the glass is intact, and the bird's impact is like that of a fluid stream.

Fig. 4. Pneumatic gun.

Fig. 5. Laminated glass after the strike.

Figure 6 shows the theoretical and experimental results for strain ε_1^7 vs. time during the collision with a bird having a mass of 1.81 kg at the collision velocity of 157 m/s and an impact angle of $\alpha = 40°$ in the point C.
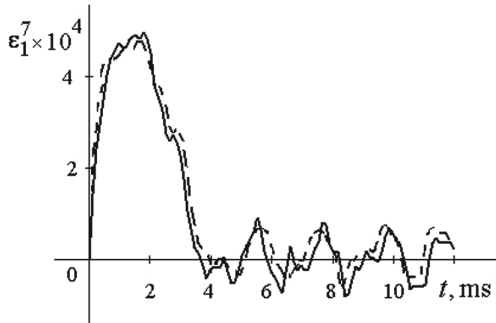
Fig. 6. Strain vs. time in point C.

The solid line is the theoretical curve, and the dashed line denotes experimental data. A good match of theoretical and experimental results confirms the feasibility and effectiveness of the method for evaluating the stress-strained stresses of aircraft glasses. Such a result confirms the adequacy of the model of impact with a bird, which was built using the hydrodynamic theory.

In accordance with international requirements, the cockpit windows should stand a maximum operating excessive pressure (pressurization) of $P_{op} = 0.0618$ MPa and the design one of $P_d = 0.247$ MPa. Thus, instead of dynamic loading (1), we consider the uniform distributed static pressure. The maximum normal tensile stresses under operating and design pressures are 9.3 MPa and 36.5 MPa, respectively. Stresses in the windshield induced by the cockpit pressurization were within feasible limits. Thus, the windshield meets the operating requirements.

5   Conclusions

Based on the hydrodynamics theory, a model of the loading impulse arising from the collision of laminated windshields with a bird is constructed. The model adequately describes the entire impact process qualitatively and quantitatively. The model's advantage is the absence of bird discretization, i.e. the strike impulse model is derived as a formula.

A method of evaluating the stress-strained state of laminated aircraft windshield is devised, which is based on the refined windshield model accounting for the effect of different operating factors. The method includes the procedure of strength calculations for laminated aircraft cockpit windows with the bird strike and the cockpit pressurization. The method is based on the technique of immersion of the initial complex-shape domain into an auxiliary simple-shape domain. It yields a simple analytical solution. The problem solution has been obtained in the form of a trigonometric series.

The advantage of the method as compared to existing approaches is as follows. The technique allows computing the sought for functions in any point of a complex-shape domain without discretizing the domain and its boundaries. This fact yields a significant reduction in the order of the resolving system of equations. It also increases computational accuracy, reduces computation time, and simplifies data preparation when solving problems encountered in practice.

The impact model and the model of unsteady vibrations of laminated glazing were implemented as a program complex in the Fortran programming language.

The stress-strained state of the laminated windshield of modern aircraft was investigated under real operating loads. The stresses were found to be within feasible limits. The comparison of calculation results and experimental data demonstrate their good agreement.

The advanced approach and calculation results can reduce the cost and time required for calculations, the pre-design, and full-scale tests of laminated aircraft windshields.

References

1. Dolbeer, R.A.: Birds and aircraft – fighting for airspace in ever more crowded skies. Hum.-Wildl. Confl. **3**(2), 165–166 (2009)
2. Heimbs, S.: Computational methods for bird strike simulations: a review. Comput. Struct. **89** (23–24), 2093–2112 (2011)
3. Dolbeer, R.A., Wright, S.E., Weller, J.R., Begier, M.J.: Wildlife strikes to civil aircraft in the United States, 1990–2009. U.S. Department of Transportation, Federal Aviation Administration, Office of Airport Safety and Standards, Serial Report No. 16, Washington, D.C., USA (2011)
4. El-Sayed, A.F.: Bird Strike in Aviation: Statistics, Analysis and Management. Wiley, New Jersey (2019)
5. Salehi, H., Ziaei-Rad, S., Vaziri-Zanjani, M.-A.: Bird impact effects on different types of aircraft bubble windows using numerical and experimental methods. Int. J. Crashworthiness **15**(1), 93–106 (2010)

6. Georgiadis, S., Gunnion, A.J., Thomson, R.S., Cartwright, B.K.: Birdstrike simulation for certification of the Boeing 787 composite moveable trailing edge. Compos. Struct. **86**(1–3), 258–268 (2008)

7. Standard Airworthiness Certification Regulations. Part 25. Airworthiness Standards: Transport Category Airplanes/U.S. Federal Aviation Administration Homepage. https://www.faa.gov/aircraft/air_cert/airworthiness_certification/std_awcert/std_awcert_regs/regs/. Accessed 15 Nov 2018

8. Wilbeck, J.S., Rand, J.L.: The development of a substitute bird model. ASME J. Eng. Power **103**(4), 725–730 (1981)

9. Abrate, S.: Soft impacts on aerospace structures. Prog. Aerosp. Sci. **81**(2), 1–17 (2016)

10. Riccio, A., Cristiano, R., Saputo, S.: A brief introduction to the bird strike numerical simulation. Am. J. Eng. Appl. Sci. **9**(4), 946–950 (2016)

11. Hedayati, R., Ziaei-Rad, S., Eyvazian, A., Hamouda, A.M.: Bird strike analysis on a typical helicopter windshield with different lay-ups. J. Mech. Sci. Technol. **28**(4), 1381–1392 (2014)

12. Guida, M., Marulo, F., Meo, M., Grimaldi, A., Olivares, G.: SPH–Lagrangian study of bird impact on leading edge wing. Compos. Struct. **93**(3), 1060–1071 (2011)

13. Allaeys, F., Luyckx, G., Paepegem, W.V., Degrieck, J.: Numerical and experimental investigation of the shock and steady state pressures in the bird material during bird strike. Int. J. Impact Eng **107**, 12–22 (2017)

14. Yang, J., Cai, X., Wu, C.: Experimental and FEM study of windshield subjected to high speed bird impact. Acta. Mech. Sin. **19**(6), 543–550 (2003)

15. Liu, J., Li, Y., Xu, F.: The numerical simulation of a bird-impact on an aircraft windshield by using the SPH method. Adv. Mater. Res. **33**(3), 851–856 (2008)

16. Li, Z.-Q., Han, Q., Yang, J.-L., Yao, X.: SPH–based numerical simulation of aircraft windshield under bird impact. J. South China Univ. Technol. (Nat. Sci.) **37**(12), 146–151 (2009)

17. Rodichev, Y.M., Smetankina, N.V., Shupikov, O.M., Ugrimov, S.V.: Stress-strain assessment for laminated aircraft cockpit windows at static and dynamic load. Strength Mater. **50**(6), 868–873 (2018)

18. Smetankina, N.V.: Non-Stationary Deformation, Thermal Elasticity and Optimisation of Laminated Plates and Cylindrical Shells. Miskdruk Publishers, Kharkiv (2011)

Chemical Process Technology

Ultrasonic Technology of Impregnation and Dosing Application of Liquid Epoxy Binders on Fabric Fiber Fillers

Aleksandr Kolosov^(✉) , Aleksandr Gondlyakh ,
Elena Kolosova , Dmitro Sidorov , and Irina Kazak

National Technical University of Ukraine "Igor Sikorsky
Kyiv Polytechnic Institute", 37, Peremohy Avenue, Kiev 03056, Ukraine
a-kolosov@ukr.net

Abstract. The developed US technology of impregnation and dosed application of liquid epoxy binders on fabric fibrous fillers using rectangular radiating plates is described. According to the developed technology, US vibrations propagate uniformly along the width of the emitting plates, and according to the command of applying a voltage to the excitation windings along the length of the emitting plates. In this case, an analogy of the physical effect is achieved in the form of the peristaltic movement of liquid and pasty media relative to the fabric filler. Also, air inclusions are squeezed out of the interfiber space and uniformity of saturation of the impregnated material is achieved. Varying the content of the polymer binder, the uniformity of its distribution in the fabric material and the removal of the excess binder are controlled by the tilt angles and dosage of the pressing force of the pairs of emitting plates to the surface of the processed material, as well as by a change in the power supplied to the transducers of the emitting plates. It is also possible to use highly viscous and highly concentrated impregnating polymeric compositions, as well as compositions with short-fiber filler.

Keywords: Ultrasound · Process · Device · Impregnation · Dosing · Application · Woven · Epoxy · Polymer

1 Introduction

Reactoplastic polymer composite materials (PCMs) are widely used in industry, sports, medicine, agriculture, as well as in strategic sectors of modern technics and technology [1]. The use of PCMs based on glass, polymer, carbon and other types of fibers is currently directly related to progress in rocket science, aviation, automotive, shipbuilding, mechanical engineering, construction, sports industry, electronics, agriculture, biomedicine [2], military industry [3] and in a number of other industries.

It should be noted that the creation of PCMs with a specific, predetermined set of properties, as well as the design of the technology for their manufacture, remains an urgent task to date [4–7]. Of particular importance is the development of the scientific and practical foundations of processes and equipment for the production of PCMs in connection with the growth in the production of thermosetting PCMs. This places high

demands on improving the existing processes for their production and realizing technological equipment while reducing energy intensity and achieving resource conservation, as well as improving productivity upon their receipt [8–11].

The greatest interest for practical use as liquid matrices for the manufacture of thermoplastic fibrous PCMs is inexpensive, high-strength, usually hard-hardened epoxy polymers (EPs) based on liquid epoxy compositions (ECs), in particular, epoxy oligomers (EOs) and epoxy binders (EBs) based on them [12]. As for the PCM's reinforcing component, namely, oriented fibrous filler (FF), it should be noted the widespread use of fiberglass in modern laminated plastics, despite the emergence of new types of fillers [13–15]. Such PCMs, as a rule, are obtained on impregnation-drying machines containing, in particular, impregnation and subsequent dosage units for the content of polymer binder (PBs) in impregnated FF.

In its turn, the use of mechanical vibrations in the ultrasonic (US) range, or US vibrations (USV) in the cavitation mode, is one of the most promising means of physical action on liquid or solid components, which are used in chemical technology to intensify a number of technological processes [16–20]. The aforementioned determines the relevance of developing an advanced US technology for impregnation and dosed application of liquid EC to fabric FF during producing laminated plastics.

2   Literature Review

It is known that the type and structure of equipment for the impregnation of rolled FF depend on the properties of FF, which are used as the basis of the canvas of fabric, impregnating polymer compositions, as well as on the quality requirements of the material obtained [21–23]. When forming epoxy laminated plastics, it is important to consider the issues of adhesion strength, since the operational properties of the final product directly depend on its strength [24–26]. Equally important is the consideration of aspects of effective physical modification of liquid EPs [27] and surface modification of reinforcing FFs [28].

One of the directions for the implementation of these modifications is the use of the US. In the technology of capillary impregnation of oriented FFs with liquid PBs [29–34] under the action of US, various physical effects that play an important role, in particular, the sound-capillary effect [35, 36], which intensifies the process of capillary impregnation of FFs with PBs.

When sonicating liquids EC at optimum, an improvement in the wettability of FF by liquid EC is achieved [37, 38], which also contributes to an increase in the adhesion strength of the cured PCM. Studies show the effectiveness of the use of the US in the production of thermoplastic PCMs, both unreinforced [39] and reinforced [40, 41]. In this case, the optimal parameters of US treatment are determined experimentally. These include the frequency range [42], operating pressure [43], as well as the amplitude, time, temperature. When simulating the flow of highly viscous polymer melts [44], the effectiveness of the use of the US should also be taken into account [45, 46].

And in the synthesis of new nanomodified PCMs, the use of the US is one of the most effective methods [47]. The intensification of PCMs molding processes with the

use of the US was considered in studies [48, 49], and the procedure for calculating the emitting US of a rectangular plate of a dosing device as described in work [50].

The above works served as the basis for the development of an advanced US technology for the impregnation and dosed application of liquid EC on constructional fabric FF in the production technology of epoxy laminated fiberglass.

3 Research Methodology

For fiberglass impregnation, EDT-10 grade "hot" curing EC was used consisting of: epoxy oligomer ED-20 (100 w.p.) + plasticizer diethylene glycol DEG-1 (10 w. p.) + hardener triethanolamine titanate TEAT-1 (16 w.p.). Structural fiberglass brand T-10-80 was used as FF. A US generator (USG) of the USG 3-4 brand was used as a source of US testing, which powered the TMS 15A-18 magnetostrictive transducer with an output power of 4 kW. Alternatively, piezoceramic transducers were used. Each TMS 15A-18 transducer was connected to its rectangular radiating plate.

The frequency f kHz, the intensity I, and the amplitude A of the USV generated by the external surface of the radiating rectangular plate into the environment were chosen as the controlled parameters of US testing. The determination of the EC content in the impregnated fiberglass fabric was carried out by the gravimetric method. The coefficient of structural homogeneity k_o of the hardened laminated fiberglass was also determined by the results of statistical analysis.

The number of parallel measurements (number of tests) per variable parameter under investigation was $N^o = 7-10$ with the reliability of $P = 95\%$.

4 Results

4.1 Features of the Developed Technology and Equipment

Figure 1 shows the general scheme of an experimental impregnating and dosing device with which the developed technology was implemented. After winding material 4 from reel 5, it is unilaterally preliminarily impregnated with liquid EC 2 on one side using an alluvial roll 17 rotating in container 18 with previously sonicated liquid EC 2. After this, US activation of the surface and degassing of the structure of the previously impregnated fabric material with US intensity I_3 and I_4 (Fig. 2) and dosed pressing force F_3 and F_4 are performed.

This is carried out using a pair of working tools 14 and 15, having individual drives from the USG 16 and in contact with previously impregnated material 4 over the entire surface of the radiating plates. In the dosing device, each dosing transducer 11, 12, 14, 15 consists of packages of magnetostrictive (permendure) or piezoelectric material, welded or attached with a threaded connection perpendicular to the non-working side of the emitting plate, and having individual excitation windings.
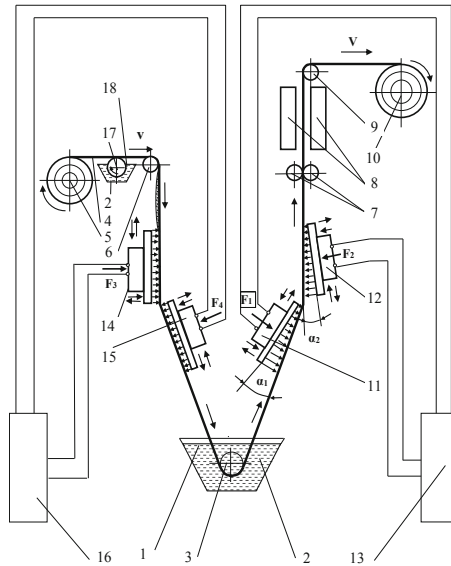
Fig. 1. Scheme of an experimental device for the impregnation and dosed application of EC on longitudinal FF using US: *1* – impregnation bath; *2, 18* – tanks with sonicated EC; *3* – submersible roll; *4* – woven material (fabric FF); *5* – winding reel; *6, 9* – envelope rolls; *7* – squeezing rolls; *8* – drying (or drying and polymerization) chamber; *10* – receiving reel; *11, 12* and *14, 15* – pairs of working US instruments; *13* – USG; *17* – alluvial roll; *V* – the speed of pulling of the material *4*; F_1 and F_2 – dosed pressing force of instruments *11* and *12*; F_3 and F_4 – dosed pressing force of instruments *14* and *15*; α_1 and α_2 – inclination angles of instruments *11* and *12* to the plane of the material *4*.

The phase voltage offset of the plates *11* and *12* is adjustable within (0–180)°. At a 180° offset, the upper *11* and lower *12* plates work on the principle of an asynchronous drive, when the antinode on one symmetrically located plate coincides with the depression on the second plate *12*, and vice versa. Oscillations propagate uniformly along the width of the emitting plates *11* and *12*, and along the length according to the command of supplying voltage to the field windings.

The frequency and amplitude of longitudinal vibrations depend on both the fabric tension force *N* of and the characteristics of the emitting surface of the working elements. Due to the phase shift of the USV, affecting one of the sides of the fabric material, relative to the US examination, directed to the other side of the material, air inclusions are squeezed out from the interfiber space and the saturation uniformity of the impregnated fabric material is achieved.

Figure 2 a shows a detailed arrangement scheme of emitting plates located in an impregnation bath; Fig. 2 b shows the arrangement scheme of the emitting plates parallel to the surface of the processed fabric material and at a variable distance from it; Fig. 2, *c*, shows an asymmetric arrangement scheme of a pair of radiating plates located between the impregnation bath and the squeezing means; Fig. 2, *d*, shows a scheme of the symmetric arrangement of the emitting plates.
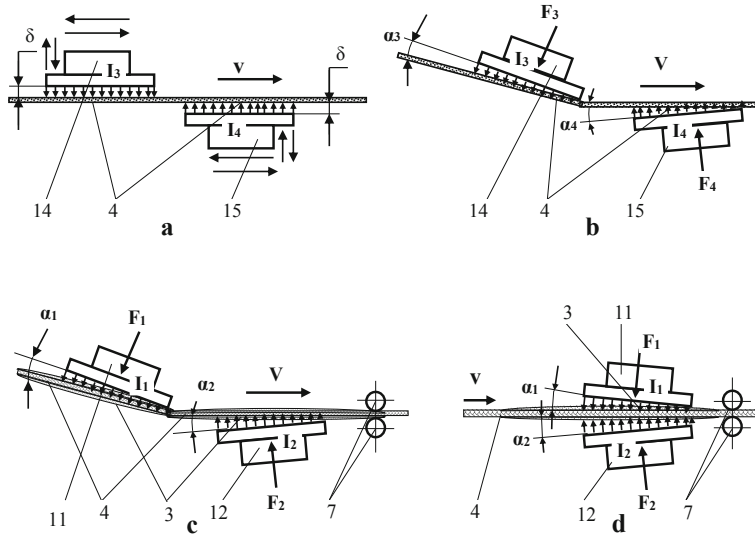
Fig. 2. Possible placement options (*a–d*) of the plates of the dosing device relative to the impregnated fabric FF: α_3 and α_4 – inclination angles of instruments *14* and *15* to the plane of the material *4*; I_1 and I_2 – US intensity of radiating plates *11* and *12*; I_3 and I_4 – US intensity of radiating plates *14* and *15*; δ – variable distance from fabric material *4*. The remaining designations are the same as in Fig. 1.

Working tools *14* and *15* (see Fig. 1) can also be located parallel to the surface of the processed and non-impregnated fabric material *4* and at a variable distance δ from it (value δ, as a rule, does not exceed the thickness of the impregnated material – Fig. 2, *a*). When using fabric materials with a small thickness and a sparse structure, the inclination angles α_3 and α_4 of the working tools *14* and *15* to the plane of the processed material *4* are in the range (0–5)°. In this case, the working elements *14* and *15* are in contact with the edge of the radiating plate, which is not impregnated and processed by fabric material *4* (Fig. 2, *b*).

When plates *11* and *12* are installed (see Fig. 1), one above the other on both sides of the impregnated material *4* (see Fig. 2, *c*), the excitation voltage is applied to magnetostrictive packets with a phase shift and in a certain sequence. Due to this, the movement of the antinode (amplitude) of the US wave from the contacting edge to the opposite direction of movement of the material of the radiating plate face is achieved. Another embodiment of the device is the location of working tools located before the means for applying EC, parallel to the surface of the treated FF and at a variable distance from it to prevent injury to both the surface of the fibers and the fabric structure.

For the same purpose, it is possible to install the working tools of the device, located up to the means for applying EC, and with angles of inclination to the plane of the processed fabric material within (0–5)°. In this case, the working elements are in

contact with the edge of the radiating plate being processed by the FF edge. Varying the content of the binder, the uniformity of its distribution in the material and removing excess binder is carried out by adjusting the angle of inclination α_1 and α_2 of the emitting plate to the surface of the fabric material *4*, changing the power (intensity I_1 and I_2) supplied to the magnetostrictive transducers, as well as the dosage of the pressing force of the emitting plates F_1 и and F_2.

The final pressing of the binder is carried out by pressing the impregnated fabric material, made in the form of two squeeze rolls *7*. After that, the impregnated and pressed material enters the drying chamber *8*, in which the sections for preliminary and final drying are located (sections not shown in Fig. 1), and after drying wound on the receiving reel *10*. An advantage of the developed technology is the increase in the upper limit of the tension of the fabric material while removing excess PB from its surface, as well as the absence of dependence of the amount of PB on a certain range of speed of the impregnated fabric material.

In the known technologies [21–23], at high speeds of pulling in the process of impregnation of the material when it enters the impregnation bath and in contact with the PB, atmospheric air enters between the PB and the material. In this case, under using low-viscosity PBs, air bubbles burst, forming shells. If highly viscous compositions are used, some of the bubbles also remain in the PB layer deposited on the fabric material. When using highly viscous PBs, the angle of oscillation α, as well as intensity I USV, increases, and vice versa. The effective variable parameters of the US treatment process (processing time t_{us}, amplitude A, frequency f, the intensity I, temperature T) are determined experimentally in each specific case, for example, using experimental and statistical modeling methods.

4.2   Results of Experimental Studies

Contact action on the surface of the fabric material with EC applied in advance was carried out at an oscillation frequency of (18–22) kHz, amplitude (3–5) μm, intensity (2–5) W/cm^2 for (0.5–5) s with a clamping force (5–15) N with varying the angle of supply of USVs to the surface of the fabric material (5–30)° and their phase shift (0–90)°. Preliminary sonicating of EC *2* was carried out for 30 min at the above parameters of US treatment, namely frequency, amplitude, intensity, but at a temperature of $T = (60–70)$ °C. The temperature of EB in the impregnation bath *1* and in the area of action of a pair of working US tools *11*, *12* (i.e., at the beginning of US treatment of the impregnated fiberglass fabric) was $T = 30$ °C.

It was investigated that the specified application of the binder $C = 35\%$ in known technologies [21–23] was achieved at a drawing speed of $V = 0.012$ m/s with a coefficient of variation of application $k_{va} = 18\%$, while in the developed technology, at a pulling speed of $V = (0.030 − 0.035)$ m/s and application variation coefficient $k_{va} = 4–5\%$ (Fig. 3).
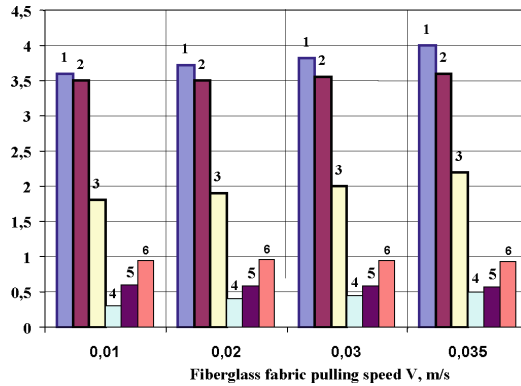
Fig. 3. The dependence of the amount of binder application C,%, the coefficient of variation of the application of the binder in the fabric material k_{va} and the uniformity coefficient of the impregnated fabric material k_o on the pulling speed of the fabric filler V according to traditional technologies [21–23] and according to the developed technology of a three-stage contact US treatment: 1 – the amount of binder application $C·0.1$, %, in the fabric material according to traditional technologies; 2 – the amount of binder in the fabric material $C·0.1$,%, according to the developed technology; 3 – coefficient of variation of the application of a binder in the fabric material $k_{va} · 0,1$,%, according to traditional technologies; 4 – coefficient of variation of the application of a binder in the fabric material $k_{va} · 0,1$,%, according to the developed technology; 5 – structural homogeneity coefficient of the impregnated fabric material $k_o · 0,1$,%, according to traditional technologies; 6 – structural homogeneity coefficient of the impregnated fabric material $k_o · 0.1$,%, according to the developed technology.

From the analysis of Fig. 3 it follows that when using the developed technology of the three-stage US treatment, the uniformity of the distribution of EC over the fabric material after removal of excess binder (structural homogeneity coefficient) increased by (1.5–2) times in comparison with the known technologies [21–23]. The viscosity value of the compositions used increased by (1.2–1.3) times at the same speed of pulling V and the pressing force F as the known technologies [21–23].

For the same viscosity values, the pulling speed V increased (1.2–1.5) times, while the structural homogeneity coefficient increased by 1.2 times and the application variation coefficient decreased (1.2–1.5) times. In this case, there is also an increase in the rate of removal of excess PB due to an increase in the speed of pulling V, which provides a given application of EC. The value of the viscosity of the impregnating compositions increased by at least (10–15)% at the same speed of pulling ($V = 0.01$ m/s) and pressing force ($F = 10$ N) with the known technologies [21–23].

Thus, the combined US processing of fiberglass (Fig. 2) leads to the following:

1. removal of the lubricant layer from the surface of the FF (fabric) immediately before its "free" impregnation with liquid EC;
2. loosening the surface of the FF fibers (which also helps to increase the specific surface area, as well as improving the wettability of the previously impregnated FF), and the removal of air inclusions;

3. EC degassing and the peristaltic nature of the motion of the binder both on the surface and in the cross-section of the impregnated FF;
4. it is possible to use highly viscous and highly concentrated impregnating polymeric compounds, as well as compositions with short-fiber fillers.

5   Conclusions

Experimental research technology and equipment for FF impregnation and dosed application of EC using US treatment has been developed. The technology and equipment that implements it can be considered as an effective tool that helps to obtain a constant and predetermined content of EC in the impregnated FF with varying the speed of the filler in the impregnation bath. By varying the intensity and angle of supply of US testing to the surface of the impregnated material, the possibility of selective exposure to each side of the processed material is achieved. The productivity of the process also increases (the speed of pulling the material in the impregnating bath and the rate of removal of excess binder) upon receipt of a uniform impregnated fabric material at the entrance to the drying and polymerization chamber.

References

1. Kar, K.K. (ed.): Composite Materials. Processing, Applications, Characterizations. Springer, Heidelberg (2017)
2. Grumezescu, V., Grumezescu, A. (eds.): Materials for Biomedical Engineering: Thermoset and Thermoplastic Polymers. Elsevier, Amsterdam (2019)
3. Benzait, Z., Trabzon, L.: A review of recent research on materials used in polymer-matrix composites for body armor application. J. Compos. Mater. (2018). https://doi.org/10.1177/0021998318764002
4. Chawla, K.K.: Composite Materials. Science and Engineering. Springer, New York (2012)
5. Yi, X.-S., Du, S., Zhang, L. (eds.): Composite Materials Engineering, vol. 1. Fundamentals of Composite Materials. Springer, Singapore (2018)
6. Yi, X.-S., Du, S., Zhang, L. (eds.): Composite Materials Engineering, vol. 2. Different Types of Composite Materials. Springer, Singapore (2018)
7. Vasiliev, V.V., Morozov, E.V.: Advanced Mechanics of Composite Materials and Structures, 4th edn. Elsevier, Amsterdam (2018)
8. Subramanian, M.N.: Basics of Troubleshooting in Plastics Processing: An Introductory Practical Guide. Handbook of Plastics Testing and Failure Analysis, 3rd edn. Wiley, Hoboken (2011)
9. Bratukhin, A.G., Bogolyubov, V.S.: Composite Manufacturing Technology. Springer, Berlin (2012)
10. Shalin, R.E.: Polymer Matrix Composites. Springer, Berlin (2012)
11. Mallick, P.K.: Processing of Polymer Matrix Composites, 1st edn. CRC Press, Boca Raton (2017)
12. Pascault, J.-P., Williams, R.J. (eds.): Epoxy Polymers: New Materials and Innovations. Wiley VCH, Weinheim (2009)

13. Wallenberger, F.T., Bingham, P.A. (eds.): Fiberglass and Glass Technology. Energy-Friendly Compositions and Applications. Springer, US (2010)
14. Bunsell, A.R.: Fundamentals of Fibre Reinforced Composite Materials, 1st edn. CRC Press, Boca Raton (2005)
15. Sathishkumar, T.P., Satheeshkumar, S., Naveen, J.: Glass fiber-reinforced polymer composites – a review. J. Reinf. Plast. Compos. **33**(13), 1258–1275 (2014). https://doi.org/10.1177/0731684414530790
16. Gallego-Juárez, J.A., Graff, K.F.: Power Ultrasonics: Applications of High-Intersity Ultrasound. Elsevier, Amsterdam (2014)
17. Suslick, K.S.: Sonochemistry. In: Kirk-Othmer Encyclopedia of Chemical Technology, 4th edn., vol. 26, pp. 516–541. Wiley, New York (1998)
18. Fedotkin, I.M., Gulyi, I.S.: Cavitation, Cavitation Engineering and Technology, Their Use in Industry, Part II. OKO, Kiev (2000). (in Russian)
19. Leighton, T.G.: The Acoustic Bubble. Academic Press, London (1994)
20. HIELSCHER Homepage. http://www.hielscher.com/sonochem. Accessed 02 Sep 2018
21. Tsyplakov, O.G.: Scientific Fundamentals of the Technology of Fibrous Composite Materials. In: Two Parts. Part 1. Perm (1974). (in Russian)
22. Shalun, G.B., Surzjenko, E.M.: Laminated Plastics. Khimiya, Leningrad (1978)
23. Vinogradov, V.M., Golovkin, G.S., Gorokhovich, A.I., Grechishkin, V.A., Tikhonov, A.I.: Technology for prepreg production of semifinished products of polymeric composite materials. In: Bratukhin, A.G., Bogolyubov, V.S. (eds.) Composite Manufacturing Technology. Soviet Advanced Composites Technology Series. Springer, Dordrecht, no. 1, pp. 29–76 (1995). https://doi.org/10.1007/978-94-011-1268-0_2
24. Crutchley, E.B.: Innovation Trends in Plastics Decoration and Surface Treatment. Smithers Rapra, Akron (2014)
25. Pestov, A.V., Kuznetsov, V.A., Mekhaev, A.V., Gorbunova, T.I., Saloutin, V.I., Smirnov, S.V., Vichuzhanin, D.I., Matafono, P.P.: Designing new adhesive materials based on epoxy oligomers filled with organic compounds. Polym. Sci. Ser. D **8**(2), 149–152 (2015). https://doi.org/10.1134/S1995421215020136
26. Banea, M.D., da Silva, L.F.M.: Adhesively bonded joints in composite materials: an overview. Rev. Pap. 1 Proc. Inst. Mech. Eng. Part L J. Mater. Des. Appl. **223**(1), 1–18 (2008). https://doi.org/10.1243/14644207JMDA219
27. Baronin, G.S., Zavrazhin, D.G., Kobzev, D.E.: The intensification of solid-phase forming process of polymers and composites with electrophysical effects of microwave and ultrasonic fields. In: Scientific Proceedings IX International Congress "Machines, Technologies, Materials", Varna, Bulgaria, pp. 16–18 (2012)
28. Mozetič, M.: Surface modification to improve properties of materials. Materials (12), 441 (2019). https://doi.org/10.3390/ma12030441
29. Kolosov, A.E.: Impregnation of fibrous fillers with polymer binders. 1. Kinetic equations of longitudinal and transverse impregnation. Mech. Compos. Mater. **23**(5), 625–633 (1988). https://doi.org/10.1007/bf00605688
30. Konovalov, V.I., Kudra, T., Gatapova, N.T.: Modern issues of transport theory during drying. Bull. Tambov State Tech. Univ. **14**(3), 538–559 (2008)
31. Trong, D.-V., Hupka, J.: Characterization of porous materials by capillary rise method. Physicochem. Prob. Miner. Process. **39**, 47–65 (2005)
32. Blunt, M.J.: Multiphase Flow in Permeable Media: A Pore-Scale Perspective. Cambridge University Press, Cambridge (2017)
33. Luikov, A.V.: Heat and Mass Transfer in Capillary-Porous Bodies. Elsevier, Amsterdam (2014)

34. Uriev, N.B.: Technology of Dispersed Systems and Materials: Physicochemical Dynamics of Structure Formation and Rheology. Wiley, Hoboken (2016)
35. Prokhorenko, P.P., Dezhkunov, N.V., Konovalov, G.E.: Ultrasonic capillary effect. Tekhnika, Minsk, Belorussia (1981). (in Russian)
36. Lanin, V.L.: Physical effects of ultrasound in liquid media and their use in engineering. Technol. Electron. Ind. **2**, 11–15 (2013)
37. Mouritz, A.P.: Ultrasonic and interlaminar properties of highly porous composites. J. Compos. Mater. **3**(34), 218–239 (2000)
38. Liu, L., Huang, Y.D., Zhang, Z.Q., Yang, X.B.: Effect of ultrasound on wettability between aramid fibers and epoxy resin. J. Appl. Polym. Sci. **99**(6), 3172–3177 (2006)
39. Kolosov, A.E.: Low-frequency ultrasonic treatment as an effective method for modifying liquid reactoplastic media. Chem. Pet. Eng. **50**(1–2), 79–83 (2014). https://doi.org/10.1007/s10556-014-9859-0
40. Kolosov, A.E.: Effect of low-frequency ultrasonic treatment regimes on reactoplastic polymer composite material operating properties. Chem. Pet. Eng. **50**(3–4), 150–155 (2014). https://doi.org/10.1007/s10556-014-9871-4
41. Kolosov, A.E., Sakharov, A.S., Sivetskii, V.I., Sidorov, D.E., Sokolskii, A.L.: Substantiation of the efficiency of using ultrasonic modification as a basis of a production cycle for preparing reinforced objects of epoxy polymer composition. Chem. Pet. Eng. **48**(5–6), 391–397 (2012). https://doi.org/10.1007/s10556-012-9629-9
42. Kolosov, A.E.: Efficiency of liquid reactoplastic composite heterofrequency ultrasonic treatment. Chem. Pet. Eng. **50**(3–4), 268–272 (2014). https://doi.org/10.1007/s10556-014-9893-y
43. Kolosov, A.E.: Low-frequency ultrasonic treatment of liquid reactoplastic media with pressure variation. Chem. Pet. Eng. **50**(5–6), 339–342 (2014). https://doi.org/10.1007/s10556-014-9904-z
44. Sakharov, A.S., Kolosov, A.E., Sivetskii, V.I., Sokolskii, A.L.: Modeling of polymer melting processes in screw extruder channels. Chem. Pet. Eng. **49**(5–6), 357–363 (2013). https://doi.org/10.1007/s10556-013-9755-z
45. Ávila-Orta, C., Espinoza-González, C., Martínez-Colunga, G., Bueno-Baqués, D., Maffezzoli, A., Lionetto, F.: An overview of progress and current challenges in ultrasonic treatment of polymer melts. Adv. Polym. Technol. **32**(S1), E582–E602 (2013). https://doi.org/10.1002/adv.21303
46. Liu, J., Chen, X., Diao, S.: Ultrasonic technology for the injection molding of polymer microstructure. Microsyst. Technol. **24**, 2253–2264 (2018)
47. Bang, J.H., Suslick, K.S.: Applications of ultrasound to the synthesis of nanostructured materials. Adv. Mater. **22**, 1039–1059 (2010). https://doi.org/10.1002/adma.200904093
48. Kolosov, A.E.: Prerequisites for using ultrasonic treatment for intensifying production of polymer composite materials. Chem. Pet. Eng. **50**(1–2), 11–17 (2014). https://doi.org/10.1007/s10556-014-9846-5
49. Kolosov, A.E., Virchenko, G.A., Kolosova, E.P., Virchenko, G.I.: Structural and technological design of ways for preparing reactoplastic composite fiber materials based on structural parametric modeling. Chem. Pet. Eng. **51**(7–8), 493–500 (2015). https://doi.org/10.1007/s10556-015-0075-3
50. Kolosov, A.E., Sivetskii, V.I., Kolosova, E.P., Lugovskaya, E.A.: Procedure for analysis of ultrasonic cavitator with radiative plate. Chem. Pet. Eng. **48**(11–12), 662–672 (2013). https://doi.org/10.1007/s10556-013-9677-9

Parameter Identification of the Capillary Rising Process in Nanomaterials for Evaporative Cooling Applications

Dmytro Levchenko[1], Ivan Pavlenko[2(✉)] , Anton Shulumei[2],
Marek Ochowiak[3], and Andrii Manzharov[2]

[1] Innovative Ideas LLC, 36, Prokof'jeva Street, Sumy 40024, Ukraine
[2] Sumy State University, 2, Rymskogo-Korsakova Street, Sumy 40007, Ukraine
i.pavlenko@omdm.sumdu.edu.ua
[3] Poznan University of Technology, 5, M. Sklodowska-Curie Avenue,
60-965 Poznan, Poland

Abstract. The article is devoted to the study of fluid lift dynamics due to the capillary effect, as well as the development of the reliable mathematical model of capillary rising process based on parameter identification considering the experimental results data. The results of the research are applicable in evaporative cooling technologies, inertial-filtering separation, and filtration processes. Additionally, they can be applied in the fields of air conditioning, heat recovery, and electricity generation cycles. The practical significance of the obtained data is in relatively high performance (absorbency, thermal resistance, and liquid transportation capacity) of studied material samples for use in heat and mass transfer equipment. The experimental research consists of four stages for five samples of paper-like porous nanomaterial. The achieved results are used to evaluate the height of the liquid rising along capillary-porous material in time of the process. According to the results of analytical and experimental studies, the mathematical model was developed for the aim of estimating the parameters of the liquid's movement. Particularly, the proposed approaches based on both quasi- and nonlinear, single- and multiparameter regression analyses, the rising-rate parameter and the maximum height of the liquid's rise along the capillary plate were identified. Carrying out the validation of the proposed mathematical models with experimental results allows concluding that the two-parameter estimation of the operating parameters with the relatively high value of the r-Pearson correlation coefficient allows clarifying the proposed reliable mathematical model of liquid's lifting process in capillary-porous media with enough accuracy.

Keywords: Evaporative cooling · Maisotsenko cycle · Porous materials · Capillary effect · Regression approach

1   Introduction

Increased interest in evaporative cooling technologies, particularly to the Maisotsenko cycle (M-cycle) [1] in different applications (e.g. air conditioning, heat recovery, and power generation cycles) induces the necessity of heat and mass exchanger improvement. The M-cycle heat exchanger's performance depends on the operating characteristics of its dry and wet channels. The dry channel enhancement process is a balance between hydraulic efficiency (i.e. minimal air pressure loss) and efficient heat-exchange area to intensify a heat transfer. Thermodynamic processes which occur in a dry channel are much simpler in comparison with ones in a wet one. The complexity of the process in the wet channel relates to the following phenomena: presence both heat and mass exchanges, evaporating on a porous surface, as well as complex two-phase flow.

There is a direct relation between M-cycle heat exchanger's performance [2] and evaporating cooling efficiency which is directly affected by factors such as the type of wet surface material, surface area, mass flowrates of air, moisture evaporation rate from the wet surface, pad efficiency, dryness of the air and relative humidity of air passing through the wet channels and volume of water used. Hence selection of wet surface media requires careful attention.

A higher wicking ability and evaporation rate can greatly increase the performance of an evaporative cooler. The problem of material properties for evaporative cooling technologies applications was considered by Zhao X. and other works were devoted to the experimental study of material properties [3].

A wide range of materials have been commonly used as the heat/mass exchanging medium and may be classified as metal, fiber, plastic, ceramic, zeolite and carbon types [4, 5]. However, it is almost impossible to choose one all-mode material for various M-cycle heat exchanger applications. For example, it is recommended to use plastic or fabric materials for low-temperature processes as air conditioning systems and water distillation and desalination systems (maximum operating temperature is about 50 °C). On the other hand, it is rational to use metallic or ceramic materials for high temperatures processes as the recuperators and regenerators for the M-Cycle Power systems and engines with high temperatures and high pressure (maximum temperature about 1150 °C). However, the mentioned above materials have a bad hydrophilic and capillary properties, which impede the porous surface effective replenishing. That is why research activities aimed at investigation, prediction, and intensification of capillary flow through a porous material in wet channels become very important. Moreover, the ability of wet channel surface to retain a water film is crucial at the transition from small to large scale M-cycle heat exchangers.

2   Literature Review

It is known the mathematical model of capillary rise of liquids in partially soluble particle beds [6] where Dissolution-Modified Washburn Model consistency was confirmed for evaluating the wettability of materials without significant dissolution of the particle bed. However, the model provides a better fit to the height versus time data of capillary rise. Other mathematical models of capillary rise effect in porous materials

were proposed by Paulo J.M. et al. [7] where the main hypothesis is based on assumption that the permeability of the material substantially depends on the pressure gradient. Therefore, the model suits better for evaluation capillary rising effects in rocks or porous media that affected by significant pressure. Also, capillary rising effect in porous media coated by ZnO and wicking mechanism of the ZnO coated microwick structure were investigated by Choi C.-H. [8]. It was found that the gravity effect and viscous force [9] plays an important role in wicking the rise of the coated wick structure [10]. The general approach for ensuring the technological equipment in the related fields is presented within the study [11], as well as the corresponding quality management systems [12] are mentioned in the papers [13, 14].

Additionally, a lot of research works are aimed at increasing the efficiency of the heat and mass exchange equipment [15]. Particularly, the performance of shell-and-tube heat exchangers [16] with different designs of baffles was investigated within the research [17]. The methodology of numerical simulation of the separation process in separation equipment [18] and ways for increasing its efficiency by the intensification of technological processes are proposed in the paper [19]. The achieved results demonstrate the possibility of increasing the heat transfer performance with a lower friction factor [20]. Moreover, the mathematical model proposed below can ensure the possibility of increasing the efficiency of the hydrodynamic processes [21], regeneration of industrial sorbents [22], and inertial-filtering modular separation equipment [23, 24] using porous nanomaterials [25, 26]. Thus, there is a lack of information for the mathematical description of the capillary rising effect that corresponds to operating conditions a porous media as heat and mass exchange and separation processes. Also, the mathematical approach for determining the reliability by simulating changes in a technical state of the equipment was developed [27]. The ways of improvement of the output characteristics of planetary hydraulic machines were proposed in the research [28].

Due to the abovementioned, the article is aimed at developing the clarified mathematical model of the capillary rising process in nanomaterials for evaporative cooling applications. The reliability of the proposed model is proved by the identification of its parameters based on the experimental research data.

3 Research Methodology

3.1 The Design Scheme of the Experimental Stand

Plates of various capillary-porous paper-like nanomaterials of constant width b and thickness δ are dipped alternately into a vessel with water (Fig. 1). The liquid in the capillary porous media and in the reservoir is affected by atmospheric pressure.

The fluid in the capillary media is wetting, and the surface tension forces raise it along the plate. The rise will be carried out until the surface tension force is balanced by the pressure force of the raised fluid column. It is necessary to evaluate experimentally the dynamics and height of the rise of the fluid in the capillary plate. Also, it is necessary to develop the mathematical model for describing the capillary rising process [29] and the prediction of capillary properties for paper-like nanomaterials [30]. This model clarifies the previous models presented in the paper [31].

This experimental stand consists of support fastening the capillary-porous material and ruler for measuring the height of liquid rise. The lower end of the capillary-porous material is dipped into a container with liquid. Measuring the height of the rise of the liquid through the capillary is carried out using a measuring ruler and horizontal movable level fixed close to the material equally to a height of raised water.
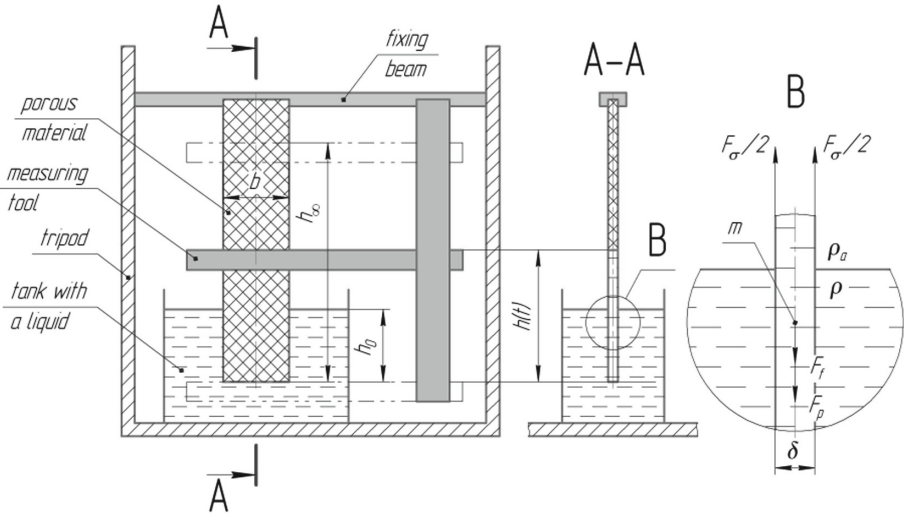
Fig. 1. The design scheme of the experimental stand and upward movement of a liquid's row.

Modeling of the capillary rising process is required to develop a profound mathematical model of heat and mass exchange processes in M-cycle apparatuses. Thus, the natural wetting of sheets caused by capillary effect for such apparatuses gives significant advantage due to reduced work of a pump and establishing preferable conditions for evaporation in wet channels (no liquid excess that makes a thin film on a heat exchange surface). Moreover, exploiting the mathematical model capillary will facilitate to predict properties and behavior of new capillary porous materials as heat and mass exchange surface apparatuses. Therefore, within the consideration of the problem, the following assumptions are accepted: a distilled is considered as test liquid rising through the capillary porous plate; the liquid in the plate is incompressible, the continuity equation is performed; thermodynamic and thermophysical parameters of the liquid (temperature, thermal conductivity, heat capacity, kinematic viscosity, and density ρ) are assumed to be constant; the dynamics of the liquid level drop in the tank is not considered in this problem; plate material is wettable (contact angle θ is in a range from 0 to $\pi/4$); the heat transfer from the air to the water in the tank and from the air to the capillary, as well as the thermal resistance of the capillary plate are neglected.

3.2 The Clarified Mathematical Model of the Capillary Rising Process

The dynamics of the capillary liquid can be studied using the 2nd Newton's law [32], and the differential equation of the liquid's upward movement (Fig. 1) is

$$\frac{d}{dt}[m(t) \cdot V(t)] = F_\sigma - F_p(t) - F_f(t), \tag{1}$$

where $V(t) = dh(t)/dt$ – velocity, m/s; $h(t)$ – the height of a liquid rising in time t; $m(t) = \rho S \cdot h(t)$ – a mass of a liquid column; $S = b \cdot \delta$ – cross-section area.

Surface tension force F_σ, pressure force $F_p(t)$ as a difference between the gravity force $m(t) \cdot g = \rho g S \cdot h(t)$ and Archimedes force $\rho_a g S \cdot h(t)$, as well as the friction force $F_f(t)$ are determined by the following dependencies:

$$F_\sigma = \sigma \Pi cos\theta; F_p(t) = (\rho - \rho_a)gh(t)S; F_f(t) = \zeta \frac{\rho}{2}\left[\frac{dh(t)}{dt}\right]^2 S \cdot sign\left[\frac{dh(t)}{dt}\right], \tag{2}$$

where $\Pi = 2(b + \delta)$ – the perimeter of the wet contour; ρ_a – air density; g – acceleration of gravity; ζ – dimensionless coefficient of the Darcy–Weisbach equation [33]:

$$\zeta = \zeta_0 + \lambda\frac{h(t)}{D} \tag{3}$$

with the following parameters: ζ_0 – coefficient of inlet losses; $\lambda = C/Re$ – coefficient of hydraulic friction depending on the dimensionless parameter C and Reynolds number $Re = dh(t)/dt \cdot D/v$, where $D = 4S/\Pi$ – hydraulic diameter; v – kinematic viscosity.

Considering all the abovementioned dependences, Eq. (1) after identity transformations can be rewritten in the following form:

$$h\frac{d^2h}{dt^2} + \left(\frac{dh}{dt}\right)^2\left[1 + \frac{1}{2}\left(\zeta_0 + \frac{Cv\,h}{D^2\frac{dh}{dt}}\right)sign\left(\frac{dh}{dt}\right)\right] = \frac{4\sigma}{\rho D}cos\theta - \left(1 - \frac{\rho_a}{\rho}\right)gh. \tag{4}$$

This formulation corresponds to the Cauchy problem for a second-order system of nonlinear differential equation with the following initial conditions: $h(0) = h_0$, and $V(0) = V_0$, where h_0 – the initial level of a liquid located above the reference plane (Fig. 1); V_0 – initial velocity. Even though Eq. (4) cannot be solved analytically, the reliability of the proposed mathematical model can be proved by the evaluating of the height h_∞. Considering the stationary mode ($t \rightarrow \infty$), the 1st and 2nd derivatives of $h(t)$ with respect to time t are equal to 0. Consequently, Eq. (4) takes the form:

$$0 = \frac{4\sigma}{\rho D}cos\theta - \left(1 - \frac{\rho_a}{\rho}\right)gh_\infty. \tag{5}$$

Particularly, in the case of thin materials ($\delta \ll b$), the hydraulic diameter $D = 4b\delta/[2(b + \delta)]$ is simplified to $D \approx 2\delta$. Consequently, it can be obtained:

$$h_\infty = \frac{2\sigma cos\theta}{(\rho - \rho_a)g\delta}.$$ (6)

It should be noted that in the case of capillary tubes with the radius equal to $D/2$, the solution of the stationary Eq. (5) is equal to the Jurin–Borelli law [34].

4   Results

To estimate the parameters of the nonlinear Eq. (4), the theory of identification by experimental research data [35, 36] is applied. In this case, the methodology of carrying out experimental research is stated below.

The lower end of the capillary-porous material is dipping into the water by 0.01 m. The influence of the velocity and depth of immersion of the material into the water is neglected. Having fixed the moment of immersion of material in water in time, velocities of water raising are calculated by the height of rising for the unit of time. Measuring the height of liquid rise on the plate should be not on its submerged end and the surface of the water. Positions of the liquid level h are measured with the step 5 min. The height of the liquid lift is measured by a ruler with an error of not more than 0.5 mm.

Experimental research includes four stages for five samples of paper-like nano-materials (Fig. 2). Change of the sample width within the investigation of the effect of capillary capacity is considered. The results are summarized in Tables 1, 2, 3 and 4.

a   b   c   d   e
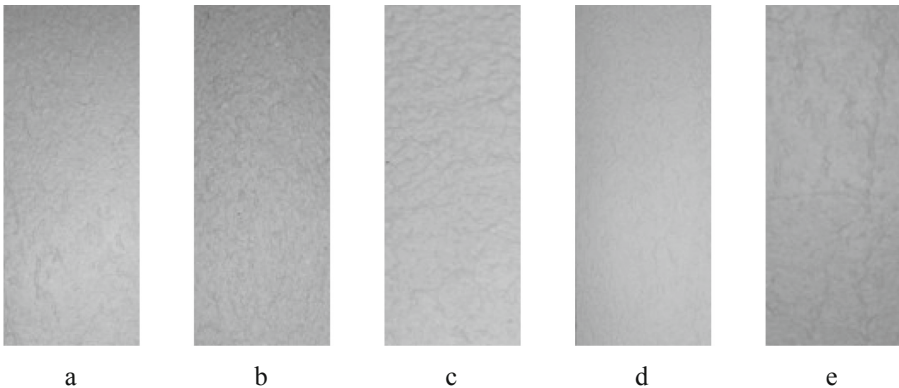
Fig. 2. Samples of capillary-porous material No. 1 (a), 2 (b), 3 (c), 4 (d), and 5 (e).

Table 1. The experimental research results for the different samples of width 0.015 m.

Time t, min	Lift height h, m				
	No. 1	No. 2	No. 3	No. 4	No. 5
5	0.107	0.088	0.086	0.093	0.098
10	0.141	0.119	0.110	0.120	0.119
15	0.169	0.144	0.136	0.141	0.152
20	0.188	0.161	0.159	0.158	0.173
25	0.209	0.173	0.168	0.172	0.189
30	0.225	0.184	0.187	0.189	0.204
35	–	0.192	0.197	0.201	0.217
40	–	0.206	–	0.213	0.238
45	–	–	–	0.225	0.244
50	–	–	–	–	0.253
55	–	–	–	–	0.259
60	–	–	–	–	0.266

Table 2. The experimental research results for the different samples of width 0.030 m.

Time t, min	Lift height h, m				
	No. 1	No. 2	No. 3	No. 4	No. 5
5	0.111	0.089	0.081	0.093	0.104
10	0.148	0.121	0.113	0.120	0.131
15	0.175	0.141	0.140	0.144	0.156
20	0.197	0.161	0.153	0.160	0.178
25	0.214	0.175	0.170	0.174	0.196
30	0.233	0.188	0.188	0.192	0.216
35	–	0.197	0.198	0.206	0.226
40	–	0.209	–	0.218	0.243
45	–	–	–	0.231	0.251
50	–	–	–	–	0.260
55	–	–	–	–	0.266
60	–	–	–	–	0.277

Table 3. The experimental research results for the different samples of width 0.045 m.

Time t, min	Lift height h, m				
	No. 1	No. 2	No. 3	No. 4	No. 5
5	0.111	0.091	0.084	0.093	0.104
10	0.148	0.123	0.114	0.120	0.131
15	0.175	0.145	0.133	0.144	0.156
20	0.197	0.164	0.151	0.160	0.178
25	0.214	0.179	0.170	0.174	0.196

(continued)

Table 3. (*continued*)

Time t, min	Lift height h, m				
	No. 1	No. 2	No. 3	No. 4	No. 5
30	0.234	0.190	0.188	0.192	0.211
35	–	0.204	0.198	0.206	0.223
40	–	0.214	–	0.218	0.240
45	–	–	–	0.231	0.249
50	–	–	–	–	0.258
55	–	–	–	–	0.266
60	–	–	–	–	0.274

Table 4. The experimental research results for the different samples of width 0.060 m.

Time t, min	Lift height h, m				
	No. 1	No. 2	No. 3	No. 4	No. 5
5	0.102	0.092	0.078	0.096	0.096
10	0.139	0.124	0.103	0.122	0.128
15	0.164	0.147	0.127	0.143	0.155
20	0.187	0.159	0.149	0.159	0.177
25	0.210	0.178	0.160	0.176	0.194
30	0.223	0.193	0.174	0.191	0.207
35	–	0.205	0.192	0.204	0.225
40	–	–	–	0.216	0.236
45	–	–	–	0.233	0.249
50	–	–	–	–	0.260
55	–	–	–	–	0.269
60	–	–	–	–	0.280

Validation of experimental results and a mathematical model allows identifying parameters of the mathematical model. Particularly, in the case of nonlinear single-parameter identification [37], based on the experimental points obtained as a result of a physical experiment, it is assumed to consider the simplified theoretical curve of the liquid rise in the following form:

$$h(t) = h_\infty \left(1 - e^{-kt}\right), \tag{7}$$

where k – rising-rate parameter.

This dependence reflects all the physical peculiarities of the process. Particularly, all the abovementioned initial conditions are satisfied. Additionally, the dependence (7) asymptotically approaches the maximum lifting height: $h(t \to \infty) = h_\infty$. It should be noted that the rising-rate parameter corresponds to the initial velocity as $k = V_0/h_\infty$.

One of the ways to determine the rising-rate parameter is to use the integral least square method [38] by minimizing the functional obtaining from Eq. (4):

$$R_S = \int_0^\infty \left\{ h\frac{d^2 h}{dt^2} + \left(\frac{dh}{dt}\right)^2 \left[1 + \frac{1}{2}\left(\zeta_0 + \frac{Cv\, h}{D^2 \frac{dh}{dt}}\right)\frac{\frac{dh}{dt}}{\left|\frac{dh}{dt}\right|}\right] - \frac{4\sigma}{\rho D}\cos\theta + \left(1 - \frac{\rho_a}{\rho}\right)gh \right\}^2 dt.$$

(8)

The substitution of the regression dependence (7) and identity (5) to Eq. (8), as well as the introduction of the following parameters

$$\alpha = \frac{\left(2 + \frac{\zeta}{2}\right)k^2}{1 + \left(1 - \frac{\rho_a}{\rho}\right)\frac{g}{k^2 h}} \approx \left(2 + \frac{\zeta}{2}\right)\frac{h}{g}$$

(9)

allows determining the functional of the integral least square method in the case of constant pressure losses ζ:

$$R_S(k) = 3\alpha^2 k^4 - 8\alpha k^2 + 6,$$

(10)

and evaluating the nontrivial value of k from the condition $dR_S(k)/dk = 0$ as follows:

$$k = \sqrt{\frac{2g/h}{3(1 + 0.25\zeta)}}.$$

(11)

The appliance of this formula for evaluation of the rising-rate parameter is highly complicated due to the unknown coefficient of hydraulic losses. In this case, the quasilinear single-parameter identification [39] can be successfully implemented using the available experimental data (Tables 1, 2, 3 and 4). Particularly, for experimentally measured height h_∞, minimization of the total square error function

$$R(k) = \sum_{i=1}^n \left[h_\infty\left(1 - e^{-kt_i}\right) - h_i\right]^2$$

(12)

from the condition $\partial R/\partial k = 0$ using the modified error function

$$R_m = \sum_{i=1}^n \left[kt_i + \ln\left(1 - \frac{h_i}{h_\infty}\right)\right]^2$$

(13)

allows evaluating the rising-rate parameter:

$$k = -\frac{\sum_{i=1}^n t_i \ln\left(1 - \frac{h_i}{h_\infty}\right)}{\sum_{i=1}^n t_i^2},$$

(14)

where h_i – the i-th experimental height at time t_i; n – number of experimental points.

The regression dependence (13) allows determining the rising-rate parameter k for the case of relatively long samples when the experimentally measured height h_∞ is less than the length of a sample. However, in the case of relatively short samples of porous material, the quasilinear multiparameter regression procedure should be applied [40] for identification both the rising-rate parameter k and maximum height h_∞. This approach based on supplementing the regression dependence (14) by the condition $\partial R_m/\partial h_\infty = 0$ allows one to obtain the missing equation:

$$h_\infty = \frac{\sum_{i=1}^{n} h_i[1 - exp(-kt_i)]}{\sum_{i=1}^{n}[1 - exp(-kt_i)]^2}. \tag{15}$$

Thus, the system of Eqs. (14) and (15) allows identifying both the parameters k and h_∞ using the numerical algorithm presented in Fig. 3 (j – iteration index; N – permissible number of iterations; ε – maximum relative error).
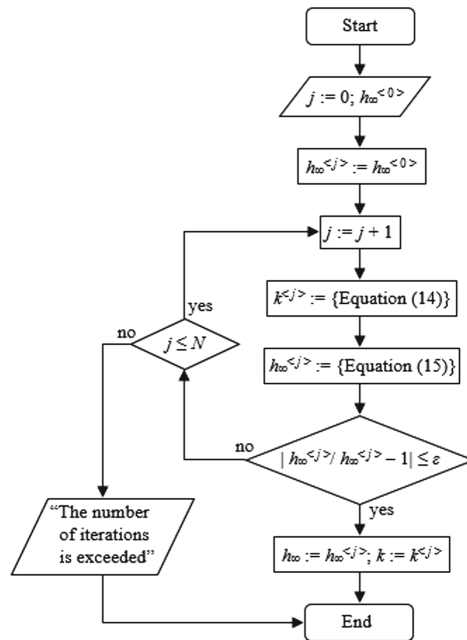
Fig. 3. Block-scheme of the algorithm for evaluating the parameters of the dependence (7).

As a result of using the abovementioned numerical calculation approaches, the regression dependences of the lift height h in time t are obtained and presented in Fig. 4. The numerical results of the regression analysis are summarized in Table 5.

It should be noted that the r-Pearson correlation coefficients in a range of 0.92–0.95 proves the significant reliability of the regression dependence (7) of the proposed mathematical model. Additionally, curves in Fig. 2 and data in Table 5 shows that the

maximum lift height and rising-rate parameters do not practically depend on the width of a sample. In this case, the average values of the evaluating data for the maximum lift height, rising-rate parameter, and initial velocity as a result of quasilinear multiparameter identification are summarized in Table 6.

As a result of experimental research and numerical calculations, it should be concluded that all the samples of the capillary-porous material have a relatively high maximum height of liquid's rising in a range of 0.20–0.28 m. In this case, the rising-rate parameter of $(1.09–1.90) \cdot 10^{-3}$ s^{-1}. The maximum height of liquid's rising equal to 0.279 m with the initial velocity of 0.53 mm/s is achieved for the sample No. 5.
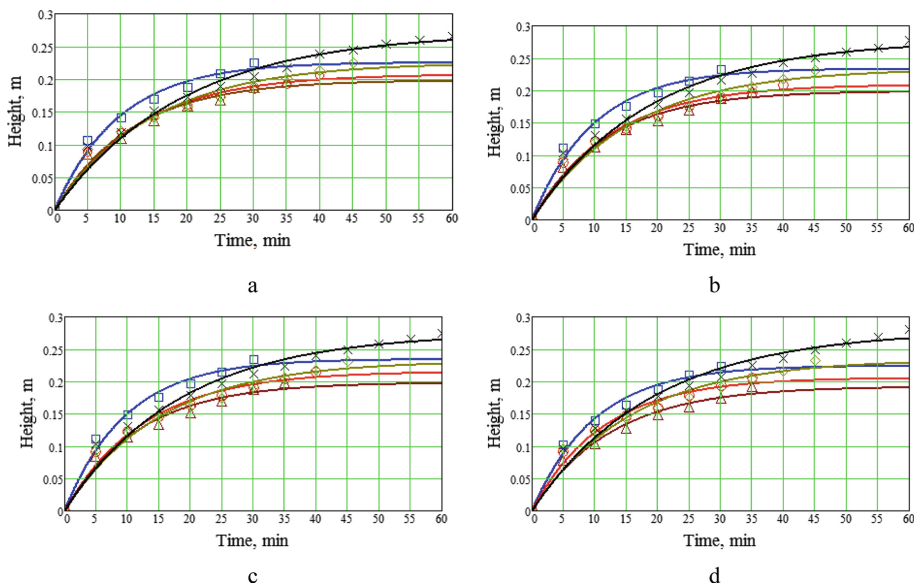
Fig. 4. The regression curves of the lift height in time for the samples 1 ($\square$), 2 ($\bigcirc$), 3 ($\triangle$), 4 ($\diamondsuit$), and 5 ($\times$) of width 0.015 m (a), 0.030 m (b), 0.045 m (c), and 0.060 m (d).

Table 5. The experimental research results for different No. of samples.

Parameter	Width $b = 0.015$ mm					Parameter	Width $b = 0.030$ mm				
	1	2	3	4	5		1	2	2	4	5
h_∞, m	0.23	0.21	0.20	0.23	0.27	h_∞, m	0.24	0.22	0.20	0.24	0.28
k, 10^{-3} s^{-1}	1.72	1.33	1.43	1.13	0.93	k, 10^{-3} s^{-1}	1.72	1.35	1.43	1.07	0.90
r	0.93	0.92	0.94	0.93	0.933	r	0.93	0.92	0.94	0.94	0.93
Parameter	Width $b = 0.015$ mm					Parameter	Width $b = 0.030$ mm				
	1	2	3	4	5		1	2	3	4	5
h_∞, m	0.24	0.22	0.20	0.24	0.279	h_∞, m	0.23	0.21	0.20	0.24	0.29
k, 10^{-3} s^{-1}	1.71	1.32	1.42	1.09	0.911	k, 10^{-3} s^{-1}	1.69	1.48	1.33	1.06	0.87
r	0.93	0.93	0.94	0.94	0.92	r	0.94	0.93	0.95	0.94	0.94

Table 6. The average parameters of the regression dependence (7) for different No. of samples.

Parameter	No. 1	No. 2	No. 3	No. 4	No. 5
h_∞, m	0.24	0.22	0.20	0.24	0.28
k, 10^{-3} s^{-1}	1.71	1.37	1.41	1.09	1.90
V_0, mm/s	0.40	0.30	0.28	0.26	0.53

5   Conclusions

Process of liquid transportation through the capillary porous media affects many aspects in engineering where capillary porous material acts as a heat and mass exchange surface for a wide range of evaporative cooling technologies including M-cycle heat and mass exchangers, recuperators and regenerators, as well as for modular inertia-filtering separation elements and filters.

As a result of the conducted theoretical and experimental research, the limiting and average values of the evaluating data for the maximum lift height and rising-rate parameters are determined based on the quasilinear multiparameter identification. It is stated that the rising-rate parameter and, correspondently, maximum lift height does not practically depend on the width of a sample in a range of 0.015–0.060 m.

The reliability of the regression dependencies is proved by the value of the r-Pearson correlation coefficient of 0.92–0.95. Thus, the developed mathematical model facilitates processes of calculation, estimation, and design of the corresponding devices and reduces the time of matching the required materials for them. Moreover, the model has a potential of development for devices where the capillary rising process intensifies by application electromagnetic or mechanical (e.g. vibration, ultrasonic) energy.

References

1. Mahmood, M.H., Sultan, M., Miyazaki, T., Koyama, S., Maisotsenko, V.S.: Overview of the Maisotsenko cycle – a way towards dew point evaporative cooling. Renew. Sustain. Energy Rev. **66**, 537–555 (2016). https://doi.org/10.1016/j.rser.2016.08.022
2. Pandelidis, D., Anisimov, S.: Numerical analysis of the heat and mass transfer processes in selected M-cycle heat exchangers for the dew point evaporative cooling. Energy Convers. Manag. **90**, 62–83 (2015)
3. Duan, Z., Zhao, X., Zhan, C., Dong, X., Chen, H.: Energy saving potential of a counter-flow regenerative evaporative cooler for various climates of China: experiment-based evaluation. Energy Build. **148**, 199–210 (2017)
4. Xu, P., Ma, X., Zhao, X., Fancey, K.S.: Experimental investigation on performance of fabrics for indirect evaporative cooling applications. Build. Environ. **110**, 104–114 (2016). https://doi.org/10.1016/j.buildenv.2016.10.003

5. Elbakian, A., Sentyakov, B., Bozek, P., Kuric, I., Sentyakov, K.: Automated separation of basalt fiber and other earth resources by the means of acoustic vibrations. Acta Montan. Slovaca **23**(3), 271–281 (2018)

6. Hammes, M.V., Heberle, E.S., da Silva, P.R., Norena, C.P.Z., Englert, A.H., Cardozo, N.S. M.: Mathematical modeling of the capillary rise of liquids in partially soluble particle beds. Powder Technol. **325**, 21–30 (2018)

7. Monteiro, P.J.M., Rycroft, C.H., Barenblatt, G.I.: A mathematical model of fluid and gas flow in nanoporous media. Proc. Natl. Acad. Sci. U. S. Am. **109**(50), 20309–20313 (2012)

8. Choi, C.-H., Krishnan, S., TeGrotenhuis, W., Chang, C.-H.: Capillary rise of nanostructured microwicks. Micromachines **9**(4), 153 (2018)

9. Sokolov, V., Krol, O., Stepanova, O.: Choice of correcting link for electrohydraulic servo drive of technological equipment. In: Ivanov, V., et al. (eds.) Advances in Design, Simulation and Manufacturing II. DSMIE 2019. Lecture Notes in Mechanical Engineering, pp. 702–710. Springer, Cham (2020). https://doi.org/10.1007/978-3-030-22365-6_70

10. Krol, O., Sokolov, V.: Modelling of spindle nodes for machining centers. J. Phys: Conf. Ser. **1084**, 012007 (2018). https://doi.org/10.1088/1742-6596/1084/1/012007

11. Antoszewski, B., Tarelnik, V.: Laser texturing of sliding surfaces of bearings and pump seals. Appl. Mech. Mater. **630**, 301–307 (2014). https://doi.org/10.4028/www.scientific.net/AMM.630.301

12. Dynnyk, O., Denysenko, Y., Zaloga, V., Ivchenko, O., Yashyna, T.: Information support for the quality management system assessment of engineering enterprises. In: Ivanov, V., et al. (eds.) Advances in Design, Simulation and Manufacturing II. DSMIE 2019. Lecture Notes in Mechanical Engineering, pp. 65–74. Springer, Cham (2020) https://doi.org/10.1007/978-3-030-22365-6_7

13. Fusko, M., Rakyta, M., Dulina, L., Sulirova, I., Edl, M.: Digitization in the technical service management system. MM Sci. J. **2018**(March), 2260–2266 (2018). https://doi.org/10.17973/mmsj.2018_03_2017105

14. Saniuk, A., Saniuk, S., Caganova, D., Kuzdowicz, P.: Key performance indicators in assessment of enterprises of metallurgical sector. In: 24th International Conference on Metallurgy and Materials, pp. 2070–2075 (2015)

15. Hoseinzadeh, S., Heyns, P.S., Chamkha, A.J., Shirkhani, A.: Thermal analysis of porous fins enclosure with the comparison of analytical and numerical methods. J. Therm. Anal. Calorim. **138**, 1–9 (2019)

16. Petinrin, M.O., Dare, A.A.: Numerical investigation of the concave-cut baffles effect in shell-and-tube heat exchanger. J. Eng. Sci. **6**(1), E1–E9 (2019). https://doi.org/10.21272/jes.2019.6(1).e1

17. Petinrin, M.O., Towoju, O.A., Ajiboye, S.A., Zebulun, O.E.: Numerical study of the effect of changing tube pitches on heat and flow characteristics from tube bundles in cross flow. J. Eng. Sci. **6**(2), E1–E10 (2019). https://doi.org/10.21272/jes.2019.6(2).e1

18. Liaposhchenko, O., Pavlenko, I., Demianenko, M., Starynskyi, O., Pitel, J.: The methodology of numerical simulations of separation process in SPR-separator. In: 2nd International Workshop on Computer Modeling and Intelligent Systems, CMIS 2019. CEUR Workshop Proceedings, vol. 2353, pp. 822–832 (2019)

19. Liaposhchenko, O., Pavlenko, I., Ivanov, V., Demianenko, M., Starynskyi, O., Kuric, I., Khukhryanskiy, O.: Improvement of parameters for the multi-functional oil-gas separator of "Heater-Treater" type. In: 2019 IEEE 6th International Conference on Industrial Engineering and Applications (ICIEA), Tokyo, Japan, pp. 66–71 (2019). https://doi.org/10.1109/iea.2019.8715203

20. Fesenko, A., Yevsiukova, F., Basova, Y., Ivanova, M., Ivanov, V.: Prospects of using hydrodynamic cavitation for enhancement of efficiency of fluid working medium preparation technologies. Period. Polytech. Mech. Eng. **62**(4), 269–276 (2018). https://doi.org/10.3311/PPme.11877

21. Fesenko, A., Basova, Y., Ivanov, V., Ivanova, M., Yevsiukova, F., Gasanov, M.: Increasing of equipment efficiency by intensification of technological processes. Period. Polytech. Mech. Eng. **63**(1), 67–73 (2019)

22. Dobrotvorskiy, S., Dobrovolska, L., Aleksenko, B., Basova, Y.: The use of waveguides with internal dissectors in the process of regeneration of industrial adsorbents by means of the energy of ultrahigh-frequency radiation. In: Advances in Design, Simulation and Manufacturing. DSMIE 2018. Lecture Notes in Mechanical Engineering, pp. 433–442. Springer, Cham (2019)

23. Sklabinskyi, V., Liaposhchenko, O., Pavlenko, I, Lytvynenko, O., Demianenko, M.: Modelling of liquid's distribution and migration in the fibrous filter layer in the process of inertial-filtering separation. In: Advances in Design, Simulation and Manufacturing. DSMIE 2018. Lecture Notes in Mechanical Engineering, pp. 489–497. Springer, Cham (2019). https://doi.org/10.1007/978-3-319-93587-4_51

24. Liaposchenko, O., Pavlenko, I., Nastenko, O.: The model of crossed movement and gas-liquid flow interaction with captured liquid film in the inertial-filtering separation. Sep. Purif. Technol. **173**, 240–243 (2017). https://doi.org/10.1016/j.seppur.2016.08.042

25. Ghasemiasl, R., Hoseinzadeh, S., Javadi, M.A.: Numerical analysis of energy storage systems using two phase-change materials with nanoparticles. J. Thermophys. Heat Transf. **32**(2), 440–448 (2018)

26. Povstyanoy, O., Zabolotnyi, O., Rud, V., Kuzmov, A., Herasymchuk, H.: Modeling of processes for creation new porous permeable materials with adjustable properties. In: Advances in Design, Simulation and Manufacturing II. DSMIE 2019. Lecture Notes in Mechanical Engineering, pp. 456–465. Springer, Cham (2020). https://doi.org/10.1007/978-3-030-22365-6_46

27. Panchenko, A., Voloshina, A., Panchenko, I., Titova, O., Pastushenko, A.: Reliability design of rotors for orbital hydraulic motors. IOP Conf. Ser.: Mater. Sci. Eng. **708**(1), 012017 (2019). https://doi.org/10.1088/1757-899X/708/1/012017

28. Voloshina, A., Panchenko, A., Panchenko, I., Titova, O., Zasiadko, A.: Improving the output characteristics of planetary hydraulic machines. IOP Conf. Ser.: Mater. Sci. Eng. **708**(1), 012038 (2019). https://doi.org/10.1088/1757-899X/708/1/012038

29. Bulgakov, V., Pilipaka, S., Adamchuk, V., Olt, J.: Theory of motion of a material point along a plane curve with a constant pressure and velocity. Agron. Res. **12**(3), 937–948 (2014)

30. Pylypaka, S., Nesvidomin, V., Zaharova, T., Pavlenko, O., Klendiy, M.: The investigation of particle movement on a helical surface. In: Ivanov, V., et al. (eds.) Advances in Design, Simulation and Manufacturing II. DSMIE 2019. Lecture Notes in Mechanical Engineering, pp. 671–681. Springer, Cham (2020). https://doi.org/10.1007/978-3-030-22365-6_67

31. Lukashov, V.K., Kostiuchenko, Y.V., Timofeev, S.V.: Hydrodynamics of a liquid film downflow on a flat surface in evaporation conditions into a flow of neutral gas. J. Eng. Sci. **6**(1), F19–F24 (2019). https://doi.org/10.21272/jes.2019.6(1).f4

32. Boyev, Y., Safyants, S., Kachkovsky, A.: Numerical study of the dynamics of the capillary rising of liquid. Metall. Energy **2011**, 1–13 (2011)

33. Kalinichenko, P., Gusak, O., Khovanskyy, S., Krutas, Y.: Substantiation and development of the procedure for calculating a hydraulic balancing device under condition of minimal energy losses. East.-Eur. J. Enterp. Technol. **2**(7–86), 36–41 (2017)

34. Liu, S., Li, S., Liu, J.: Jurin's law revisited: exact meniscus shape and column height. Eur. Phys. J. E **41**(3), 46 (2018)
35. Pavlenko, I., Liaposhchenko, A., Ochowiak, M., Demyanenko, M.: Solving the stationary hydroaeroelasticity problem for dynamic deflection elements of separation devices. Vibr. Phys. Syst. **29**, 2018026 (2018)
36. Ostroha, R., Yukhymenko, M., Lytvynenko, A., Bocko, J., Pavlenko, I.: Granulation process of the organic suspension: fluidized bed temperature influence on the kinetics of the granule formation. In: Ivanov, V., et al. (eds.) Advances in Design, Simulation and Manufacturing. DSMIE 2018. Lecture Notes in Mechanical Engineering, pp. 463–471. Springer, Cham (2019). https://doi.org/10.1007/978-3-319-93587-4_48
37. Egger, H., Pietschmann, J., Schlottbom, M.: Identification of nonlinear heat conduction laws. J. Inverse Ill-Posed Probl. **23**(5), 429–437 (2014)
38. Kaplan, M., Nicholls, D.P.: A nonlinear least squares framework for periodic grating identification with a high–order perturbation of surfaces implementation. Appl. Numer. Math. **143**, 20–34 (2019)
39. Jukic, D.: A simple proof of the existence of the best estimator in a quasilinear regression model. J. Optim. Theory Appl. **162**(1), 293–302 (2014). https://doi.org/10.1007/s10957-013-0434-1
40. Song, X., Zheng, G.-H., Jiang, L.: Identification of the reaction coefficient in time fractional diffusion equations. J. Comput. Appl. Math. **345**, 295–309 (2019). https://doi.org/10.1016/j.cam.2018.06.047

Hydrodynamics of Two-Phase Upflow in a Pneumatic Classifier with the Variable Cross-Section

Andrii Lytvynenko[1] , Ivan Pavlenko[1(✉)] ,
Mykola Yukhymenko[1] , Ruslan Ostroha[1] , and Jan Pitel[2]

[1] Sumy State University,
2, Rymskogo-Korsakova Street, Sumy 40007, Ukraine
`i.pavlenko@omdm.sumdu.edu.ua`
[2] Technical University of Kosice, 1, Bayerova Street,
080 01 Presov, Slovak Republic

Abstract. This paper is aimed at the investigation of the two-phase upflow hydrodynamics in prismatic-shape apparatuses with the variable cross-section. To reach this aim, the mathematical model of the gas flow was developed based on the averaged in time and space velocities of the turbulent flow. This model is supplemented by the research of the solid particle movement in this flow. The research novelty of the proposed research is in the obtained dependencies for determining the velocity field of solid particles in a pneumatic classifier, as well as for estimating the friction coefficient. Additionally, equations for determining the velocity field of a gas phase were developed by velocity components of the two-dimensional gas flow. As a result, related graphical characteristics of the gas flow in the pneumatic classifier were built, and trajectories of solid particles were defined with respect to the apparatus width and height. The approach for evaluating empirical parameters was proposed based on the quasi-linear regression analysis. Moreover, the conducted regression analysis allows identifying the parameters of the mathematical model by the results of numerical simulations. The proposed approach will allow optimizing the technological and operating parameters of the pneumatic classification process and design of the related separation equipment.

Keywords: Separation process · Gas-dispersed flow · Turbulent mode · Velocity field · Regression analysis

1 Introduction

n the industry, devices for hydromechanical and heat treatment of granular materials are widely used, such as pneumatic classifiers, heaters, coolers, dryers, and granulators. These apparatuses traditionally have cylindrical, conical, and prismatic body shape or their combination. In the case of the variable cross-section, the following apparatuses are commonly used: pneumatic separators for dedusting gas flows in vertical sections in gas-transportation pipes [1]; pneumatic classifiers for separation of granular materials [2] for obtaining organic mineral fertilizers [3]; separation channels in fluidized bed granulators

to prevent the removal of fine particles from into cyclones [4]. In this regard, the flow structure in technological equipment significantly impacts on the thermal and hydromechanical processes in them. Additionally, the efficiency of the abovementioned devices is determined by the velocity field of gas flow, since it determines the temperature distribution and concentration of the solid phase in a two-phase flow. Moreover, considering the hydrodynamic parameters of the gas flow is also important to determine analytical dependencies of its interaction with the solid phase. This approach allows determining velocities of particles and time of their stay in the working space of the apparatus that is necessary to evaluate the operating parameters, design and technical characteristics of the separation equipment.

It should be noted that hydrodynamic features are significantly complicated if the technological processes are realized in the apparatus with the variable cross-section. In this case, despite the presence of the obtained empirical dependencies for conical apparatuses [5], these models do not allow explaining the hydrodynamic features of two-phase flow and, consequently, realizing the reliable mathematical models.

Due to the abovementioned, developing the mathematical model of the hydrodynamics of a single-phase and two-phase flow is an urgent problem that allows obtaining the analytical and regression dependencies to identify the kinematic and dynamic characteristics of the gas-dispersed flow and the solid phase in a pneumatic classifier with the variable cross-section. As a result, further optimization of the design and technical parameters of the pneumatic classification process will be possible.

2 Literature Review

Recent publications are aimed at developing the methodologies for investigating two-phase flows. Particularly, the research works [5, 6] dials with the Lagrangian model to simulate trajectories of liquid particles in two-phase flows using the different turbulence models [7]. As a result, the vortex method is implemented based on the Lagrangian approach for solving the hydrodynamics of a liquid phase. The reliability of the obtained results is ensured by the experimental results data. The methodology for combined using an analytical approach and FEM analysis for solving the applied problems in the field of mechanical engineering is proposed in the research [8].

In the paper [9], the process of the pneumatic classification of solid particles is discussed. A mathematical model is developed to optimize operating conditions and to reach the maximum yield of the final product. As a result, it is shown that the optimum choice of the separation limits of the equipment allows obtaining particles with the standard granulometric composition. The research [10] presents the kinetics of droplets formation in a spray tower for ensuring the process efficiency and performance of the mass transfer equipment.

The research [11] is devoted to determining the efficiency of polydisperse materials classification in gravitational pneumatic classifiers with a cascade of inclined continuous shelves. As a result, the hydrodynamic characteristics of the operating process are obtained. Moreover, it is shown that local formations with high concentration of particles are formed periodically in the near-wall region.

The research work [12] is aimed at developing a new method of vibration-inertial gas-dynamic separation of gas-condensate mixtures. The formation of the gas flow and disperse particles in the curvilinear convergent-divergent channels are investigated, as well as the optimizing hydrodynamic profiling of curvilinear separation channels, is obtained. As a result, the efficiency of the inertial gas-dynamic separation of the gas-liquid mixture in separation channels is assessed for improving the reliability of the compressor equipment. Additionally, in the research work [13], a mathematical model is proposed for determining the distribution and migration of captured liquid from the separation channel during the inertial-filtering separation process.

An experimental approach for studying the separation process in pneumatic classifiers is proposed in the paper [14]. As a result, ways for improving the efficiency of separators by reducing specific load through the preliminary separation of the initial mixture are proposed. Additionally, an experimental method of spectroscopy is proposed in the research [15] to detect the presence of a liquid phase in a mixture in airstreams. In the research paper [16], a new type of centrifugal pneumatic classifier is developed based on the analysis of the principle of the pneumatic classification for powder materials. As a result, a new technological process of classification is experimentally investigated and proposed for industrial applications [17]. Ways for modeling the processes for obtaining porous materials with adjustable properties [18] using energy-saving technologies are proposed within the research work [19].

A pneumatic type of ultra fine powder separator-classifier is developed within the research work [20]. As a result, the relationships between the performance and flow conditions are investigated by the flow visualization method. Finally, it was proved that the new classifier has a comparatively large swirling flow velocity which can accurately classify ultra-fine particles of the gas-dispersed mixture. Moreover, modeling the aerodynamics of a two-phase vortex turbulent flow in the separation channel of a pneumatic centrifugal classifier is presented in the paper [21]. The velocity field of a gas phase vortex flow is determined based on the Reynolds equations. As a result, the effect of the turbulent diffusion of particles due to the pulsating motion of a gas phase is predicted based on the proposed semi-empirical probabilistic model.

In the paper [22], a pneumatic classifier without mechanical moving parts is developed, and related theoretical analysis and experimental research are carried out. As a result, the oversized ratio in fine powder is reduced to 5% [23]. In the research work [24], mathematical models of ensuring the reliability of the technological equipment are proposed, and transfer functions are adapted. The research works [25] present up-to-date trends in quality assurance [26] of the related technological equipment [27].

In the research [28], the analytical approach and the regression procedure for solving the stationary hydroaeroelasticity problem for dynamic deflection elements of separation devices are developed. The research work [29] is aimed at using a coupled computational fluid dynamics and discrete element method simulation of the horizontal pneumatic classifying of spherical and cylindrical particles. The related experimental results are carried out using the laser Doppler anemometry. As a result, gas and particle velocities are obtained. As a result, the discrepancies between simulation and experimental results attributing to the selected drag model, mesh size and mesh interpolation are analyzed.

A new method for predicting the cut size of a turbo air classifier using artificial neural networks is proposed in the paper [30]. The verification of the results by the experimental research data indicates the reliability of the proposed approach. The paper [31] deals with the experimental research on the impact of the contact elements' design parameters on the efficiency of the pneumatic classification process for the case of granular materials. As a result, the procedure for obtaining structural parameters of pneumatic classifiers is proposed.

In the research work [32], studying the influence of feed moisture on the separation efficiency is realized. Experiments were carried out for particles with sizes in a range from 45 to 110 µm. The quality of classification is proved using split factor and separation efficiency. In the paper [33], a centrifugal air classifier is developed to improve the classification efficiency and to extend a range of operating parameters, especially for the particle size less than 10 µm.

However, despite the presence of a large number of papers presented above and corresponding analytical, numerical and experimental approaches, there is still no unified methodology for studying the pneumatic classification process allowing to create simplified but reliable mathematical models of the operating process. Moreover, there is a need to develop regression procedures for determining the parameters of analytical models based on the experimental results data. Due to the abovementioned, the main aim of the research is to develop a mathematical model of the hydrodynamics of two-phase flow in the diffuser channel of a pneumatic classifier (Fig. 1).
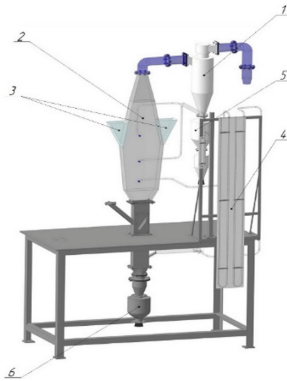
Fig. 1. The design scheme of the gas-dispersed flow in a plane channel with the variable cross-section: 1 – cyclone; 2 – pneumatic classifier; 3 – tank for initial material; 4 – manometers; 5 – tank for a fine fraction; 6 – tank for a coarse fraction.

There are the following research objectives: mathematical modeling of the flow features for the gas upflow in the vertical pneumatic classifier; mathematical modeling of single solid particle motion in the diffuser channel of the apparatus; verification of the reliability of the proposed models using numerical simulation.

3 Research Methodology

3.1 Single-Phase Gas Flow

The movement of the gas flow in a plane vertical diffuser channel is considered (Fig. 2) using the following differential equation [34]:

$$\rho_p W_Z \frac{dW_Z}{dZ} = -\frac{\lambda}{D} \frac{\rho_p W_Z^2}{2}, \tag{1}$$

where ρ_p – density of a solid particle, kg/m^3; Z – vertical coordinate, m; W_Z – vertical component of gas flow velocity, m/s; D – hydraulic diameter, m; $\lambda = C/\text{Re}^n$ – Darcy's coefficient of friction; $\text{Re} = D \cdot W_Z/v$ – Reynolds number; v – kinematic viscosity, m^2/s; C, n – dimensionless empirical parameters needed to be evaluated using the experimental results data.
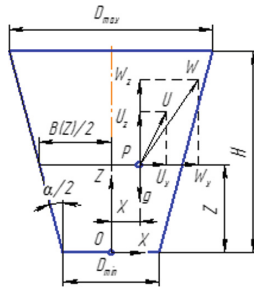
Fig. 2. The design scheme of the gas-dispersed flow in a plane channel with the variable cross-section.

In Eq. (1), since air temperatures inside and outside the apparatus are the same, mass forces acting on the gas flow are balanced by the Archimedes force. Consequently, the influence of mass forces is negligible.

According to the least square method [35, 36], the quantitative evaluation of the empirical parameters C and n is realized by minimizing the following error function:

$$R = \sum_{k=1}^{N} \left\{ \left[(W_Z^{<0>})^n - \frac{Cv^n}{2\theta} \left(\frac{1}{D_0^n} - \frac{1}{D_k^n} \right) \right]^{\frac{1}{n}} - (W_Z^{<k>})^n \right\}^2 \to min, \tag{2}$$

where $W_Z^{<0>}$, $W_Z^{<k>}$ – vertical component of gas flow velocities in the initial and current cross-sections with diameters D_0 and D_k respectively; k – number of the cross-section; N – total number of cross-sections; α – incline angle, rad.

Particularly, in the case of the self-similar area of the turbulent flow ($n = 0$), the least square method for determining the parameters C, n can be presented in the form:

$$R(C) = \sum_{k=1}^{N} \left\{ W_Z^{<0>} \left(\frac{D_k}{D_0} \right)^{-\frac{C}{2\alpha}} - W_Z^{<k>} \right\}^2 \to min, \tag{3}$$

and the condition of minimizing the error function allows determining the quasi-linear regression dependence for the dimensionless parameter C:

$$C = \alpha \frac{\sum_{k=1}^{N} ln \frac{D_0}{D_k} ln \frac{W_Z^{<k>}}{W_Z^{<0>}}}{\sum_{k=1}^{N} ln \frac{D_0}{D_k}}. \tag{4}$$

A range of the parameters C, n is determined by the flow mode (laminar or turbulent) and can be evaluated using the proposed regression procedure based on Eq. (4).

As a result, gas velocity in a cross-section k can be determined by the formula:

$$W_Z^{<k>} = W_Z^{<0>} \left(\frac{D_k}{D_0} \right)^{-\frac{C}{2\alpha}}. \tag{5}$$

Under the turbulent hydrodynamic mode, due to the chaotic motion of microparticles in the flow, the equalization of the velocity field occurs, as well as particle distribution in cross-sections of the apparatus is characterized by the flatter curve in comparison with the typical parabolic distribution. In this case, the transversal component of gas velocity can be determined using the following dependency:

$$W_X = W_Z \left[\frac{2X}{B} \left(1 - \frac{2X}{B} \right) \right]^{\frac{1}{m}}, \tag{6}$$

where X – horizontal coordinate, m; B – channel width, m; m – dimensionless empirical parameter depending on Reynolds number and determined by the following formula:

$$m = \frac{\sum_{p=1}^{P} ln \left[\frac{2X_p}{B_p} \left(1 - \frac{2X_p}{B_p} \right) \right] ln \frac{W_X^{<p>}}{W_X^{<0>}}}{2 \sum_{p=1}^{P} ln \frac{W_X^{<p>}}{W_X^{<0>}}}. \tag{7}$$

In Eq. (7), the following parameters are introduced: $W_X^{<0>}$, $W_X^{<p>}$ – vertical component of gas flow velocities in the initial and current point in X-direction with width B_p;

p – number of the measuring point; P – total number of experimental points. Moreover, it should be noted that the proposed dependence satisfies the following kinematic boundary conditions: $W_X(0, Z) = W_Z (0, Z) = 0$, and $W_X(B/2, Z) = W_Z(B/2, Z) = 0$. Additionally, the parameter m determines the shape of the velocity field. It is evaluated as a result of the implementation of the least square method for minimizing the deviations between theoretical velocities and their experimental values.

3.2   Movement of a Single Particle in the Gas Flow

Hydrodynamics of the upflow is considered for the case of a single solid particle of a gas-dispersed flow in a channel with the variable cross-section (Fig. 2). It is assumed that the change of velocity in a transverse direction does not occur. Consequently, forces of particle collision between each other and wall, friction and inertia forces are not considered due to their insignificant concentration in a gas flow in a range of 0.005–0.010 m^3/m^3. In this case, the particle movement [37, 38] is described by the following differential equation (Fig. 2):

$$\begin{cases} U_X \frac{dU_X}{dX} = \frac{3}{4} \zeta \frac{\rho}{\rho_p} \frac{(W_X - U_X)^2}{d_p^2}; \\ U_Z \frac{dU_Z}{dZ} = -g + \frac{3}{4} \zeta \frac{\rho_m}{\rho_p} \frac{(W_Z - U_Z)^2}{d_p^2}, \end{cases} \tag{8}$$

where g – gravitational acceleration, m/s^2; ρ_m – density of a gas-dispersed mixture, kg/m^3; d_p – equivalent diameter of a single particle, m; U_X, U_Z – horizontal and vertical components of the velocity, m/s; $\zeta = 0.44$ – coefficient of the hydrodynamic resistance as a function of Reynolds number in a range 800–1000 for the two-phase flow.

4   Results

As a result of numerical calculations using the 4th order Runge–Kutta method, Fig. 3 a presents the dependencies of the vertical and horizontal components of particle and flow velocities on the vertical coordinate. The resulting streamlines of the gas flow, as well as trajectories of particles, are presented in Fig. 3 b.

The presented trajectories allow concluding that solid particles in the lower part of the apparatus have an approximately zero velocity, which gradually accelerates in the Z-axis under the influence of the gas flow. Additionally, the vertical velocity component is greater than the horizontal velocity, which moves particles to the walls.
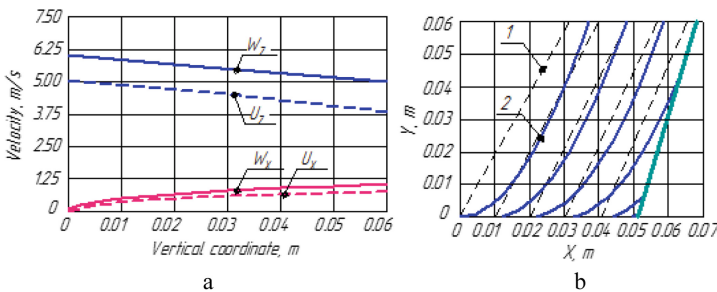
Fig. 3. The dependencies of the vertical and horizontal velocities (a) and trajectories of the gas flow 1 and particles 2.

Evaluating the trajectories particles, it can be concluded that the influence of the gas flow on a single particle is significant. It should be additionally noted that the volume concentration range of the solid phase impacts on the gas-dispersed flow motion. This fact indicates the need for a numerical experiment.

The numerical simulation results for modeling the gas-dispersed flow in a plane channel with the variable cross-section using the ANSYS software are presented in Fig. 4. In the lower diffuser part, the flow rate decreases, and the maximum velocity is in the cross-section center. Vice versa, the flow rate is reduced near the walls. The input data of the numerical model includes input flow rate, output pressure, flow mode, etc.

In the upper confuser part as an accelerating zone, flow velocity should be increased. As a result, at the outlet, the gas-dispersed flow has the same velocities both in the cross-section center and near walls. Consequently, this part of the apparatus needs to be studied separately.
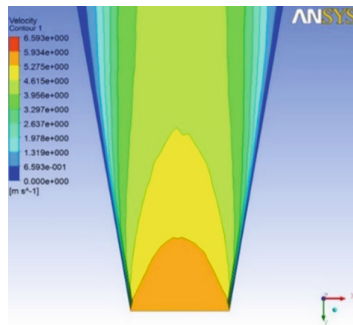
Fig. 4. The numerical simulation results of modeling.

Under the abovementioned flow velocity distribution in the apparatus, the concentration of particles in the lower part is much greater than in the upper part, because a significant value of the material is concentrated as a weighted layer. In the upper part of the apparatus, the concentration of particles is negligible, and it is mainly a fine fraction that is removed by the gas flow.

The obtained solutions of the presented equations allow determining the flow rate of a gas-dispersed flow, a single solid particle velocity field in this flow, as well as trajectories of a particle in an operating volume of the pneumatic classifier. This is important for choosing the rational hydrodynamic parameters [39, 40] to ensure technological processes in the abovementioned device.

Additionally, the achieved results allow evaluating a velocity field of solid particles in two-phase gas-dispersed flow, as well as determining changes in particle velocity in height and width of the apparatus depending on the influence of the gas flow.

Overall, the mathematical model confirms the data obtained during the experiment carried out previously, with the relative error not exceeding 4%.

5   Conclusions

Firstly, the mathematical model of the single-phase upflow hydrodynamics in a vertical diffuser channel is improved. A feature of this model is the proposed method for determining analytically the friction coefficient of gas flow. Secondly, the mathematical modeling of the two-phase gas-dispersed flow in the vertical pneumatic classifier is developed. A feature of this model is in determining the consideration of the impact of the solid phase and walls on the velocity field of the gas-dispersed flow.

The movement of a single solid particle in a vertical diffuser channel for the case of low volume concentration less than 0.005–0.010 m^3/m^3 is carried out for proposing the mathematical modeling of single solid particle motion in the diffuser channel of the apparatus. As a result, the reliability of the developed models and related research methodology is verified quantitatively and qualitatively by the numerical simulation results. Particularly, it is proved that forces of particle collision and friction forces near the apparatus walls cannot be considered.

The importance of this research is proved by its applications in the pneumatic classification of gas-dispersed mixtures, separation of mechanical mixtures and gas-liquid flows in diffuser and confuser channels for providing the efficiency of separation and purification equipment in the fields of mechanical and chemical engineering.

References

1. Yukhymenko, M., Ostroha, R., Litvinenko, A., Bocko, J.: Estimation of gas flow dustiness in the main pipelines of booster compressor stations. In: IOP Conference Series: Materials Science and Engineering, vol. 233, p. 012026 (2017). https://doi.org/10.1088/1757-899x/233/1/012026

2. Ostroha, R., Yukhymenko, M., Lytvynenko, A., Bocko, J., Pavlenko, I.: Granulation process of the organic suspension: fluidized bed temperature influence on the kinetics of the granule formation. In: International Conference on Design, Simulation, Manufacturing: The Innovation Exchange. DSMIE-2018. Lecture Notes in Mechanical Engineering, F2, pp. 463–471 (2019). https://doi.org/10.1007/978-3-319-93587-4_48

3. Ostroha, R., Yukhymenko, M., Yakushko, S., Artyukhov, A.: Investigation of the kinetic laws affecting the organic suspension granulation in the fluidized bed. East.-Eur. J. Enterp. Technol. **1**(88), 4–10 (2017). https://doi.org/10.15587/1729-4061.2017.107169

4. Li, Z., Kind, M., Gruenewald, G.: Modeling fluid dynamics and growth kinetics in fluidized bed spray granulation. J. Comput. Multiph. Flows **2**(4), 235–248 (2010). https://doi.org/10.1260/1757-482X.2.4.235

5. Shvab, A.V., Evseev, N.S.: Modeling the process of particle fractionation in a pneumatic centrifugal apparatus. J. Eng. Phys. Thermophys. **89**(4), 829–839 (2016). https://doi.org/10.1007/s10891-016-1443-3

6. Shademan, M., Nouri, M.: A Lagrangian-Lagrangian model for two-phase bubbly flow around circular cylinder. J. Comput. Multiph. Flows **6**(2), 151–167 (2014). https://doi.org/10.1260/1757-482X.6.2.151

7. Shvab, A.V., Zatikov, P.N., Sadretdinov, S.R., Chepel, A.G.: Simulation of the fractional separation of particles in an air centrifugal classifier. Theor. Found. Chem. Eng. **44**(6), 859–868 (2010). https://doi.org/10.1134/S0040579510060059

8. Pavlenko, I.V., Simonovskiy, V.I., Demianenko, M.M.: Dynamic analysis of centrifugal machine rotors supported on ball bearings by combined using 3D and beam finite element models. In: IOP Conference Series: Materials Science and Engineering, vol. 233, p. 012053 (2017). https://doi.org/10.1088/1757-899x/233/1/012053

9. Shishkin, S.F., Dzyuzer, V.Ya., Shishkin, A.S.: Pneumatic classification of sands for glass industry. Steklo i Keramika **11**, 5–8 (2001)

10. Ochowiak, M., Wlodarczak, S., Pavlenko, I., Janecki, D., Krupinska, A., Markowska, M.: Study on interfacial surface in modified spray tower. Processes **7**(8), 532 (2019). https://doi.org/10.3390/pr7080532

11. Kirsanov, V.A., Kirsanov, M.V.: Hydrodynamic characteristics of classification process in pneumatic classifier with continuous shelves. Chem. Pet. Eng. **54**(1–2), 71–74 (2018). https://doi.org/10.1007/s10556-018-0441-z

12. Liaposhchenko, O.O., Sklabinskyi, V.I., Zavialov, V.L., Pavlenko, I.V., Nastenko, O.V., Demianenko, M.M.: Appliance of inertial gas-dynamic separation of gas dispersion flaws in the curvilinear convergent-divergent channels for compressor equipment reliability improvement. In: IOP Conference Series: Materials Science and Engineering, vol. 233, p. 012025 (2017). https://doi.org/10.1088/1757-899x/233/1/012025

13. Sklabinskyi, V., Liaposhchenko, O., Pavlenko, I., Lytvynenko, O., Demianenko, M.: Modelling of liquid's distribution and migration in the fibrous filter layer in the process of inertial-filtering separation. In: International Conference on Design, Simulation, Manufacturing: The Innovation Exchange. DSMIE-2018. Lecture Notes in Mechanical Engineering, F2, pp. 489–497 (2019). https://doi.org/10.1007/978-3-319-93587-4_51

14. Phenow, E.A., Mezenov, A.A., Gigoolo, Y.Y.: Experimental study of parameters of grain milling product separation in pneumatic screw classifier. Biosci., Biotechnol. Res. Asia **13**(2), 669–680 (2016). https://doi.org/10.13005/bbra/2083

15. Kshetri, S., Steward, B.L., Birrell, S.J.: Dielectric spectroscopic sensing of fine liquid droplets in an airstream. Int. J. Fluid Power **19**(1), 42–48 (2018)

16. Wang, J., Dong, L., Jing, S., Jin, Y.: Development of a new centrifugal pneumatic classifier for powder materials. Chem. Eng. **29**(2), 43–45 (2001)

17. Povstyanoy, O., Zabolotnyi, O., Rud, V., Kuzmov, A., Herasymchuk, H.: Modeling of processes for creation new porous permeable materials with adjustable properties. In: Ivanov, V., et al. (eds.) Advances in Design, Simulation and Manufacturing II. DSMIE 2019. Lecture Notes in Mechanical Engineering, pp. 456–465. Springer, Cham (2020). https://doi.org/10.1007/978-3-030-22365-6_46

18. Hoseinzadeh, S., Moafi, A., Shirkhani, A., Chamkha, A.J.: Numerical validation heat transfer of rectangular cross-section porous fins. J. Thermophys. Heat Transf. **33**(3), 698–704 (2019). https://doi.org/10.2514/1.T5583

19. Povstyanoi, O.Y., Rud', V.D., Samchuk, L.M., Zubovets'ka, N.T.: Production of porous materials with the use of energy-saving technologies. Mater. Sci. **51**(6), 847–853 (2016). https://doi.org/10.1007/s11003-016-9912-6

20. Morimoto, H., Shakouchi, T.: Classification of ultra fine powder by a new pneumatic type classifier. Powder Technol. **131**(1), 71–79 (2003)

21. Shvab, A.V., Evseev, N.S.: Studying the separation of particles in a turbulent vortex flow. Theor. Found. Chem. Eng. **49**(2), 191–199 (2015). https://doi.org/10.1134/S0040579515020128

22. Ma, R., Chang, J., Shi, C., Zhang, X.: Theoretical and experimental study on pneumatic classification of fine-metal-powder. Adv. Mater. Res. **554–556**, 546–550 (2012). https://doi.org/10.4028/www.scientific.net/AMR.554-556.546

23. Sokolov, V., Krol, O.: Determination of transfer functions for electrohydraulic servo drive of technological equipment. In.: Advances in Design, Simulation and Manufacturing. DSMIE 2018. Lecture Notes in Mechanical Engineering, pp. 364–373. Springer, Cham (2019). https://doi.org/10.1007/978-3-319-93587-4_38

24. Fesenko, A., Basova, Y., Ivanov, V., Ivanova, M., Yevsiukova, F., Gasanov, M.: Increasing of equipment efficiency by intensification of technological processes. Period. Polytech. Mech. Eng. **63**(1), 67–73 (2019). https://doi.org/10.3311/PPme.13198

25. Dynnyk, O., Denysenko, Y., Zaloga, V., Ivchenko, O., Yashyna, T.: Information support for the quality management system assessment of engineering enterprises. In: Ivanov, V., et al. (eds.) Advances in Design, Simulation and Manufacturing II. DSMIE 2019. Lecture Notes in Mechanical Engineering, pp. 65–74. Springer, Cham (2020). https://doi.org/10.1007/978-3-030-22365-6_7

26. Tarelnik, V., Belous, A., Antoszewski, B., Zukov, A.: Problems and criteria of quality improvement in end face mechanical seal rings through technological methods. In: IOP Conference Series: Materials Science and Engineering, vol. 233, p. 012037 (2017). https://doi.org/10.1088/1757-899x/233/1/012037

27. Saniuk, S., Saniuk, A., Caganova, D.: Cyber industry networks as an environment of the industry 4.0 implementation. Wirel. Netw. 1–7 (2019). https://doi.org/10.1007/s11276-019-02079-3

28. Pavlenko, I., Liaposhchenko, A., Ochowiak, M., Demyanenko, M.: Solving the stationary hydroaeroelasticity problem for dynamic deflection elements of separation devices. Vibr. Phys. Syst. **29**, 2018026 (2018)

29. Ebrahimi, M., Crapper, M., Ooi, J.Y.: Numerical and experimental study of horizontal pneumatic transportation of spherical and low-aspect-ratio cylindrical particles. Powder Technol. **293**, 48–59 (2015). https://doi.org/10.1016/j.powtec.2015.12.019

30. Wu, S., Liu, J., Yu, Y.: Prediction of cut size for pneumatic classification based on a back propagation (BP) neural network. ZKG Int. **6**(11), 64–71 (2016)

31. Kirsanov, V.A., Kirsanov, P.V.: Effect of structural parameters of cascade elements on effectiveness of pneumatic classification. Chem. Pet. Eng. **49**(11–12), 707–711 (2014). https://doi.org/10.1007/s10556-014-9823-z

32. Kretschmar, G., Mutze, T., van der Meer, F.: Influence of feed moisture on the efficiency of dynamic air classifiers. In: 28th International Mineral Processing Congress (IMPC 2016), p. 135047 (2016)

33. Zyatikov, P., Roslyak, A.: Peculiarities of solid particles separation in an unsteady turbulent flow of a pneumatic centrifugal classifier. In: EPJ Web of Conferences, vol. 76, p. 01013 (2014). https://doi.org/10.1051/epjconf/20147601013

34. Panchenko, A., Voloshina, A., Kiurchev, S., Titova, O., Onopreychuk, D., Stefanov, V., Safoniuk, I., Pashchenko, V., Radionov, H., Golubok, M.: Development of the universal model of mechatronic system with a hydraulic drive. East.-Eur. J. Enterp. Technol. **4**(7(94)), 51–60 (2018). https://doi.org/10.15587/1729-4061.2018.139577

35. Altaf, S., Mehmood, M.S., Imran, M.: Implementation of efficient artificial neural network data fusion classification technique for induction motor fault detection. J. Eng. Sci. **5**(2), E16–E21 (2018). https://doi.org/10.21272/jes.2018.5(2).e4

36. Bilous, O.A., Hovorun, T.P., Berladir, K.V., Vorobiov, S.I., Simkulet, V.V.: Mathematical modeling of the mechanical characteristic of the activated PTFE-matrix using the method of planning the experiment. J. Eng. Sci. **5**(1), C1–C5 (2018). https://doi.org/10.21272/jes.2018.5(1).c1

37. Pylypaka, S., Nesvidomin, V., Zaharova, T., Pavlenko, O., Klendiy, M.: The investigation of particle movement on a helical surface. In: Ivanov, V., et al. (eds.) Advances in Design, Simulation and Manufacturing II. DSMIE 2019. Lecture Notes in Mechanical Engineering, pp. 671–681. Springer, Cham (2020). https://doi.org/10.1007/978-3-030-22365-6_67

38. Pylypaka, S., Klendiy, M., Zaharova, T.: Movement of the particle on the external surface of the cylinder, which makes the translational oscillations in horizontal planes. In: Ivanov, V., et al. (eds.) Advances in Design, Simulation and Manufacturing. DSMIE 2018. Lecture Notes in Mechanical Engineering, pp. 336–345. Springer, Cham (2019). https://doi.org/10.1007/978-3-319-93587-4_35

39. Voloshina, A., Panchenko, A., Boltyansky, O., Panchenko, I., Titova, O.: Justification of the kinematic diagrams for the distribution system of a planetary hydraulic motor. Int. J. Eng. Technol. **7**(4.3), 6–11 (2018). https://doi.org/10.14419/ijet.v7i4.3.19544

40. Kuric, I.: New methods and trends in product development and process planning. Acad. J. Manuf. Eng. **9**(1), 83–88 (2011)

Effect of Hydrodynamic Parameters
on Membrane Electrolysis Enhancement

Vasyl Serdiuk[1]([✉]) [ID], Vsevolod Sklabinskyi[1] [ID],
Svetlana Bolshanina[1] [ID], Alexey Ableyev[2], and Tetiana Dychenko[1] [ID]

[1] Sumy State University, 2, Rymskogo-Korsakova Street, Sumy 40007, Ukraine
`mikishasumy@gmail.com`
[2] Kusum Pharm LLC, 54, Skryabina Street, Sumy 40022, Ukraine

Abstract. The work studies the process of Cd^{2+} and Zn^{2+} cations transfer from an electrolyte to a near-membrane zone and through a cation-exchange membrane RALEX®CM-PES 11-66 at a two-chamber electrolyzer and the cations reduction as metals. The electrolyte of an anode chamber imitated possible composition of the industrial passivating baths for cadmium and zinc electroplating and contained 50 g/L sodium dichromate, 10 g/L sulfuric acid and 3 g/L Cd^{2+} or 1.755 g/L Zn^{2+}. A catholyte was presented by 1% aqueous sulfuric acid. A titanium plate (VT0 standard) was taken as a cathode, and lead (C2 grade) was taken as an anode. Various hydrodynamic conditions were studied as to their effect on the regularity of mass-transfer of impurity ions at the near-membrane zone with and without forced mixing of anolytes. Transfer of the impurity ions of Cd^{2+}, Zn^{2+} through the cation-exchange membrane with cadmium and zinc reduction at the cathode was studied at various current densities and various hydrodynamic conditions. Enhancement patterns of metallic cadmium and zinc are studied as a function of the current density increased and the forced mixing applied.

Keywords: Cation-exchange membrane · Current density · Similarity parameters · Forced mixing

1 Introduction

Hexavalent chromium compounds in the production of conversion films at electroplated coatings are required to protect the coating and to extend operation life both of a part, a machine and a mechanism as a whole. However, its notorious effect on living organisms is well-known [6]. Hence the Cr^{6+} compounds have toxic, mutagenic, cancerogenic and teratogenic properties, therefore they are not allowed in the sewage water of industry and nature [3]. The primary sources of contamination might be both the technological and washing electroplating tanks.

For technological processes, the passivating bath has the 50–200 g/L sodium dichromate and the 8–12 g/L sulfuric acid. The volume of the bath was about 100–150 L. During the experiments with this passivating solution, the solution becomes exhausted and the impurity metals appear:

$$3Zn \ + \ Na_2Cr_2O_7 + \ 7H_2SO_4 \ \rightarrow \ 3ZnSO_4 + Cr_2(SO_4)_3 + \ Na_2SO_4 + 7H_2O \quad (1)$$

$$3Cd \ + Na_2Cr_2O_7 + 7H_2SO_4 \ \rightarrow \ 3CdSO_4 + Cr_2(SO_4)_3 + Na_2SO_4 + 7H_2O \quad (2)$$
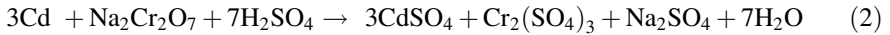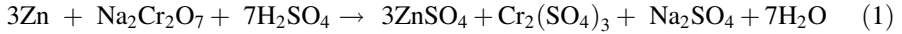
No decent chromating membrane on the zinc [8] or cadmium surface is produced as a trace amount of acid and a considerable amount of impurity ions are present in the solution, fresh portions of the reagents are therefore required into the bath after a while. The specific functionality of the passivating solution is 0.5–1.0 m^2/L, removal of electrolyte with the parts is 0.48 L/m^2. Thus, in some days of operation, these solutions become unusable and are disposed to a deacidification station to be further neutralized. These releases are instantaneous and require a considerable quantity of the reagents for neutralization. Another technique to recover the passivating bath functions is a regular addition of fresh portions of the reagents to correct the bath composition. These procedures, as a rule, increase the concentration of sodium dichromate and accumulate impurity Cd^{2+}, Zn^{2+} and Cr^{3+} ions [5, 9] in the passivating bath.

From the chemical Eqs. 1 and 2 without removal of the electrolyte considered and with the full reaction of sulfuric acid, about 0.02 mol/L Cd^{2+} or Zn^{2+} is obtained, depending on the technological process. Whatever the coating metal transfers into the solution, Cr^{3+} ions with molar concentration about 0.014 mol/L are always formed (reactions 1 and 2). As the reagents are gradually added into the passivating bath, the Cd^{2+} and Zn^{2+} concentration is ≥ 15 g/L, the Cr^{3+} concentration can be 3–7 g/L, the sodium dichromate concentration is about 200 g/L. The high concentration of $Na_2Cr_2O_7$ at the passivating bath and of the impurity metal ions promotes their concentration growth in a reclaim rinse, the washing tanks and eventually in the deacidification stations.

2 Literature Review

Energy costs and costs for neutralization of hexavalent chromium ions can only be reduced with the method of chromic solution recovery, which involves electrochemical units with ion-exchange membranes [4] to recycle the valuable components as market products [3].

Recovery is performed at the electrolyzers of direct and alternate interaction with the membranes of well-known brands (MK-40, MA-40) [5, 6]. Working solutions of the technological or washing tanks and solutions of sulfuric acid are used as catholytes and anolytes, depending on the type and purpose of the electrolyzer. In a cation-exchange electrolyzer due to its chamber separated from the main tank by a cation-exchange membrane, under direct current at a cathode and in the cathode chamber, the impurity contaminant metals are accumulated [1, 2]. With a lead anode in the main tank, there is an oxidation of hexavalent chromium from the trivalent chromium.

To study regularities in the impurity ions transfer through the cation-exchange membrane RALEX®CM-PES 11-66 should be manufactured by the well-known company Mega, Prague, Czech Republic. This membrane is heterogeneous, contains an ion-exchange group R - SO^{3-}, has a selectivity of 0.5/0.1 M KCl >90% and a transfer number $t_m > 0.95$, respectively. This work considers the effect of the forced mixing at

the near-membrane anolyte zone of the passivating test solutions with the same initial concentrations of Cd^{2+} and Zn^{2+} on their reduction as metals at the cathode.

The subject of the work is to study the hydrodynamic parameters of the impurity ions transfer from the electrolyte to the cation-exchange membrane and to find the regularity of their transfer through the membrane, to determine the effect of the current density with the constant initial concentration of the impurity Cd^{2+} and Zn^{2+} ions and the forced mixing on the electromembrane process.

3   Research Methods

The test solutions to simulate the passivating baths for cadmium and zinc electroplating were prepared to study regularities of the Cd^{2+} and Zn^{2+} mass-transfer through the cation-exchange membrane during the electromembrane process. The test solutions contained 50 g/L $Na_2Cr_2O_7$, 10 g/L H_2SO_4 and 3 g/L Cd^{2+} or 1.755 g/L Zn^{2+} to comply with their molar concentrations of 0.027 mol/L.

The concentrations of the impurity ions were taken on the basis that the electrolyte is removed by the parts and that the bath composition is corrected 1–2 times in an industrial environment. These test solutions served as anolytes at the laboratory electrochemical membrane units. A catholyte was presented by a 1% aqueous sulfuric acid. The main criterion of this study was the reduction of cadmium and zinc as elements at the cathode at the constant initial concentration of Cd^{2+} and Zn^{2+} in the test anolyte solutions with or without forced mixing of the near-membrane anolyte zone at various current densities. The catholyte pH value was maintained within 1–2 by a repetitive correction with sulfuric acid. The diagram of the membrane electrochemical process is depicted in Fig. 1.
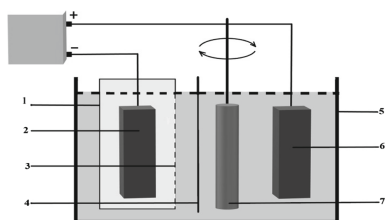
Fig. 1. Diagram of a membrane electrolyzer with an external anode and a mechanical vertical two-bladed stirrer. 1 is a cathode chamber case; 2 is an internal electrode - cathode; 3 is a cation-exchange membrane; 4 is a filter cloth; 5 is a chamber with a chromic solution; 6 is an external electrode - anode; 7 is a mechanical vertical two-bladed stirrer (side view).

To study the effect of the forced mixing, the anolyte solutions were prepared with initial Cd2+ and Zn2+ concentrations of 0.027 mol/L (Table 1).

Table 1. The concentration of the basic components and impurities in the test passivating solutions of the electroplated coatings.

Solution Nº	Forced Mixing	Concentration of $Na_2Cr_2O_7$ g/L	Concentration of H_2SO_4, g/L	Concentration of Cd^{2+}, mol/L	Concentration of Cd^{2+}, g/L	Concentration of Zn^{2+}, mol/L	Concentration of Zn^{2+}, g/L
1	−	50	10	0.027	3.0	0	0
1a	+	50	10	0.027	3.0	0	0
2	−	50	10	0	0	0.027	1.755
2a	+	50	10	0	0	0.027	1.755

A 1.5 A direct electric current was used in the experiments. The operating area of the membrane was 5 × 5 cm that is 25 cm^2, and the current density at the membrane was 0,06 A/cm^2.

The mechanical vertical two-bladed stirrer with LWH 20 × 1 × 60 mm and rotation frequency of n = 2.7 rot/s was applied for mixing the anolyte solutions.

Flow rate $\vartheta 1$ calculated from the Eq. (3) is 54 mm/s:

$$\vartheta_1 = n \cdot d \tag{3}$$

where the hydrodynamic diameter of d = 0.02 m (width of the stirrer) is schematically depicted in Fig. 2.

Fig. 2. Scheme of the electrolyte flow near an anode with the mechanical mixing applied: 1 is the direction of the current, 2 are whirls formed in an electrolyte under the influence of the electric current, 3 is an anode, 4 is a cation-exchange membrane, 5 is a mechanical vertical two-bladed stirrer.

As direct current passes between the anode and the cation-exchange membrane, the hydrodynamic channel where the mixing processes take place is formed. The mixing is caused by the anode oxygen release accompanied by a liquid-gas mixture and by electroconvection [7, 10] accompanied by the whirls formation (Fig. 2). The whirls result from heterogeneity of the membrane presented by a non-conducting polypropylene reinforcement and the conducting areas of the membrane. A part of the electrolyte is repulsed from the non-conductive areas, and given that there is an electric current, the whirls are formed [10]. The whirls provide mixing of the electrolyte part near the anode, the mass-exchange with the other part of the electrolyte is significantly slower basically through diffusion.

The stirrer generates the centrifugal and unidirected flow in every side of the circle with flow rate ϑ_1.

When the flow gets into the hydrodynamic channel between the membrane and the anode (Fig. 2), the whirls formed by the direct current affect the forced flow of the liquid. Before the flow enters the channel, it comes into resistance with a contradirectional whirl, thus the inlet rate is

$$\vartheta_{inlet} = \vartheta_1 - \vartheta_{whirl}; \qquad (4)$$

At the outlet of the channel, the outlet rate increases under the coincidence of a mechanical flow and the whirling flow:

$$\vartheta_{outlet} = \vartheta_1 + \vartheta_{whirl}; \qquad (5)$$

The average flow rate in this hydrodynamic channel is ϑ_1;
Experimental results are presented in Table 2.

Table 2. Rate of metal reduction at a cathode of a membrane electrochemical unit with mechanical mixing and current density of 0.06 A/cm.

Solution N°.	Metal reduction time, hours	Mass of obtained metal, g	Total mass of obtained metal, g	Rate of metal reduction, g/hour	Rate of metal reduction, mmol/hour
1	2	0.148	0.148	0.0896	0.7977
	4	0.155	0.303		
	6	0.235	0.538		
1a	2	0.286	0.286	0.1368	1.2165
	4	0.294	0.58		
	6	0.241	0.821		
2	2	0.145	0.145	0.0742	1.141
	4	0.159	0.304		
	6	0.141	0.445		
2a	2	0.143	0.143	0.0752	1.1564
	4	0.149	0.261		
	6	0.159	0.451		

From the experimental results in Table 2, it may be preliminary concluded that:

- forced mixing does not affect the transfer of Zn^{2+} with the concentration of 0.027 mol/L through the cation-exchange membrane and on zinc deposition at the cathode at a current density of 0.06 A/cm^2;
- transfer of Cd^{2+} ions with a concentration of 0.027 mol/L and resulting metal cadmium deposition increases by 52.6% during mechanical mixing of the anolyte at a current density of 0.06 A/cm^2;

4   Results

In the course of the experiments, metallic cadmium and zinc were reduced at the cathode in the cathode chamber at the constant current, at constant concentrations of the main components of the test solution and of impurity ions, at the constant cathode and anode current density, and the small pH range maintained within 1–2. Hydrodynamic parameters were variable in the anolyte: the experiments were performed with or without mechanical mixing at Cd^{2+} and Zn^{2+} concentration of 0.027 mol/L each.

To study hydrodynamical regularities of mass-transfer of Cd^{2+} and Zn^{2+} to the cation-exchange membrane, densities and dynamic viscosity of the anolyte solutions which contained these ions were experimentally defined. The solution density was defined by a set of the densimeters as per GOST 18995.1-73 standard. The dynamic viscosity was measured by a capillary viscometer VPZh-1 GOST 10028-62, with a capillary dia of 1.16 mm at the solution temperature of 16 °C.

For the test anolyte solutions which have a composition similar to the passivating bath for cadmium and zinc electroplating, the dynamic viscosity was measured at the solution temperature of 16 °C by the capillary viscometer VPZh-1 GOST 10028-62 with a capillary dia of 1.16 mm. The composition of two test solutions is presented in Table 3. The values for μ_0 and ρ_0 are tabular and correspond to $1.111 \cdot 10^{-3}$ mPa·s and 999 kg/m, respectively, at the given temperature. The density values of these solutions ρ_{Zn}^{2+} and ρ_{Cd}^{2+} are found by the set of the densimeters and equal 1038 kg/m^3 and 1048 kg/m^3, respectively.

Using a densimeter VPZh-1, t0 and t is found for each solution as follows:

$t_0 = 11.636$ s, $t_{Zn^{2+}} = 10.10$ s, $t_{Cd^{2+}} = 10.44$ s

The dynamic viscosity of the solutions is

$\mu_{Zn^{2+}} = 0{,}9189 \cdot 10^{-3}$ mPa·s; $\mu_{Cd^{2+}} = 0{,}9502 \cdot 10^{-3}$ mPa·s

K-value ν is a ratio of the dynamic viscosity to its density, hence

$\nu_{Zn^{2+}} = 0{,}8853 \cdot 10^{-6}$ m2/s; $\nu_{Cd^{2+}} = 0{,}9067 \cdot 10^{-6}$ m2/s;

With the kinematic viscosity and tabular values for the diffusion constant D of Zn^{2+} and Cd^{2+} known, and these values are respectively:

$D_{Zn^{2+}} = 0.72 \cdot 10^{-7}$ m^2/s; $D_{Cd^{2+}} = 0.70 \cdot 10^{-7}$ m^2/s;

The Schmidt numbers are therefore:

$Sc_{Zn^{2+}} = 12.296$; $Sc_{Zn^{2+}} = 12.953$;

Reynold's number is a ratio of the inertial forces to the viscosity forces and is described in Table 3. For a rectangular tube, the module with an H × W window and the lead anode mounted at 4–5 mm corresponds to, the hydrodynamic parameter [10] is $d_h = 2HW/(H+W)$; where H = 0.05 m, W = 0.05 m, thus $d_h = 0.05$ m.

Let us consider the electrolyte self-mixing due to electroconvection here. The flow rate υ is the rate of passing the solution between the anode and the cation-exchange membrane. Since the electric current passes through the ion-exchange areas and is reflected from the non-conducting areas of the polypropylene reinforcement due to the heterogeneity of the membrane, the excess pressure pushing the solution out occurs. When in motion, the pushed part of the solution encounters the inertial resistance of the unforced layers of the electrolyte and the membrane surface. It changes the direction of the solution, i.e. the solution is repulsed from the membrane surface [10] and two multidirectional whirls are formed (Fig. 3). These whirls cause electrolyte mixing near

the membrane. It results in a decrease of the concentration polarization at the membrane surface and enhances the mass-transfer of the cations through the membrane. Due to the heterogeneity of the membrane and the whirls formation, the hydrodynamic parameter d_h equals the whirl diameter. The flow rate equals the electrolyte motion rate in the whirl. For example, in the experiment, the whirl diameter was measured to be 45 mm, and the time for the solution to take a circle was 17.67 s, thus, since the circle length is πd and the electrolyte rate is 8 mm/s, Reynold's number is $Re_{Zn^{2+}}$ = 406.64; $Re_{Cd^{2+}}$ = 397.044.

When the forced mixing of the anolyte solutions is performed by the mechanical vertical two-bladed stirrer, for example, the hydrodynamic parameter is d_h = 0.05 m, the flow rate of the solution between the membranes is $\vartheta_1 = \vartheta_{av.}$ = 0,054 m/s, and Reynold's numbers for the solutions are respectively $Re_{Zn^{2+}\,(mix)}$ = 3049.81; $Re_{Cd^{2+}\,(mix)}$ = 2977.83.

Rate of mass-transfer in the electrolyte solution is found with the Sherwood number, which is a ratio of the convective transfer to the diffusion:

$$Sh = \frac{k \cdot d_k}{D} = a \cdot Re^b \cdot Sc^c \tag{6}$$

where k is a mass-transfer coefficient, a, b and c are the constants. Since the found Reynold's numbers correspond to the laminary flow in the channel, the ratio is written as:

$$Sh = 1.85(Re \cdot Sc \cdot d_h/L)^{0.33}, \text{ when } Re < 2300 \text{ and} \tag{7}$$

$$Sh = 0.23\,Re^{0.8} \cdot Sc^{0.33}, \text{ when } Re > 2300 \tag{8}$$

where L is the length of an active electrode and is 0.05 m. Calculations of the Sherwood numbers, the mass-transfer coefficients, and the thickness of the boundary layers are presented in Table 3.

Table 3. Calculations of some hydrodynamic parameters of the mass-transfer processes in the test analyte solutions with Cd^{2+} and Zn^{2+}.

Hydrodynamic parameter or characteristics	Presence of mechanical mixing	Ratio to be calculated	Anolyte solution with Zn^{2+}	Anolyte solution with Cd^{2+}
Reynold's numbers, Re	−	$Re = \frac{dh \cdot \upsilon}{\nu}$	406.64	397.044
	+		3049.81	2977.83
Sherwood number, Sh	−	$Sh = 1.85(Re \cdot Sc \cdot d_h/L)^{0.33}$	30.749	31.036
	+	$Sh = 0.23Re^{0.8} \cdot Sc^{0.33}$	322.677	322.055
Mass-transfer coefficient, k, m/c	−	$k = \frac{Sh \cdot D}{d_h}$	$4.92 \cdot 10^{-5}$	$4.83 \cdot 10^{-5}$
	+		$46.465 \cdot 10^{-5}$	$45.087 \cdot 10^{-5}$
The thickness of a boundary layer at the external membrane surface, δ, m	−	$k = \frac{D}{\delta}$	$1.463 \cdot 10^{-3}$	$1.449 \cdot 10^{-3}$
	+	$\delta = \frac{D}{k}$	$0.1549 \cdot 10^{-3}$	$0.1552 \cdot 10^{-3}$

Upon the electrolysis, the cation-exchange membrane transfers only the cations and retards the anions and the solvent molecules in full or in part, it enhances the accumulation of the molecules on the surface that are incapable of crossing the membrane [8]. Thus, the obtained boundary layer exhibits resistance to the cation mass-transfer through the membrane. As the voltage difference grows, the current density and the cation flux through the membrane increase and the cation concentration decreases at the boundary layer. Under the limiting current I_{lim}, the metal ion concentration at the external surface of the membrane approaches to zero and Cd^{2+} and Zn^{2+} ion transfer through the membrane becomes impossible:

$$I_{lim} = \frac{zDFC_b}{\delta\left(t_m - t_{bl}\right)} \approx \frac{zDFC_b}{\delta} \tag{9}$$

where I_{lim} is the limiting current density at the membrane surface, A/cm^2; z is the cation valence; D is the cation diffusion coefficient, cm^2/s; F is the Faraday constant, 96485 C $\cdot$ mol^{-1}; C_b is the concentration of the metal ion in the anolyte, mol/cm^3; δ is the thickness of the boundary layer at the membrane surface, cm; t_m and t_{bl} are the transference numbers of the cations in the membrane and the boundary layer, respectively.

An index related to the ion transfer through the membrane, or the transference number, is crucial for the evaluation of the membrane unit. It is defined as a part of an electric current that passes through an electrolyte solution and is transferred by this type of ions, i.e. the transference number is the ratio of electric current transferred by this type of ions to the total electric current passing through the electrolyte. Since Cd^{2+} and Zn^{2+} are deposited at the cathode in full as metals and their deposition rate υ is known, the current efficiency η that is the pure and simple mass-transfer number for the respective ion through the membrane is found as:

$$\eta = \frac{\upsilon}{q} \tag{10}$$

where η is the current efficiency; q is electrochemical equivalent, g/A hour; υ is the metal reduction rate, g/A hour. The current efficiency is calculated with the well-known Faraday laws.

Table 4 presents the data which do not consider some partial current spent on hydrogen reduction.

Table 4. Data for calculating the current efficiency of electrochemical reduction at a cathode and the limiting current density.

Impurity ion	Hydrodynamic conditions	The initial concentration of metal, mol/L	Electrochemical equivalent, q	Average rate g/hour	Current efficiency, %	Limiting current density I_{lim}, A/cm^2
Cd^{2+}	Without mixing	0.027	2.46	0.090	3.66	0.070735
Cd^{2+}	Forced mixing	0.027	2.46	0.137	5.57	0.43395
Zn^{2+}	Without mixing	0.027	1.21	0.074	6.12	0.040734
Zn^{2+}	Forced mixing	0.027	1.21	0.075	6.2	0.37976

From the data in Table 4, it may be inferred that the average deposition rate and the current efficiency were obtained in the experiment where the current density on the membrane was 0.06 A/cm^2 and the limited current density was calculated with the Eq. (9). The forced mixing and thinning of the boundary layer increase the limiting current density to be used in membrane electrolysis. As is known from the laws of electrolysis, chemical yield proportionally increases as the current density grows, that advanced the process significantly. It can be argued that without the forced mixing, the current density ranged up to the limiting one for the Cd^{2+} containing anolyte and was by the third greater than for the Zn^{2+} containing anolyte. Thus it becomes obvious that the current in the zinc-containing anolyte (without the forced mixing) was inefficiently used and its third part was wasted in the experiment since the Zn^{2+} ion concentration became zero and was refilled by the diffusion from the electrolyte.

Additional experiments were performed to confirm the abovementioned calculations. The anolyte solutions of initial impurity concentration equal to 0.027 mol/L were electrolyzed without the forced mixing at current of 0.5A, 1.0A, 1.5A, 2.0A, 2.5A that corresponded to the current density at the membrane of 0.02A/cm^2, 0.04A/cm^2, 0.06A/cm^2, 0.08A/cm^2, 0.1A/cm^2. The electrolysis lasted 6 h, for each value of the current density and each impurity ion, just as in the previous experiments. The average metal reduction rates were found (Fig. 3).

As is seen in Fig. 3, the metal deposition rates and their current efficiencies increase regularly as the current density grows. However, the processes become stable as the current ranges up to the limiting one. Slight increase of cadmium at the cathode may be explained by the higher Schmidt number as compared to zinc that is typical for mass-transfer by diffusion. At current density over 0.04 A/cm^2, which is a limiting one, the zinc reduction process is completely stable.
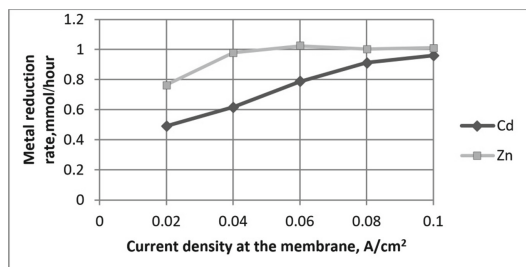

Fig. 3. Metal reduction at the cathode as a function of current density at the membrane: plot of Cd cadmium reduction; Zn plot of zinc reduction.

With forced mixing applied to the anolyte solutions of initial impurity concentration equal to 0.027 mol/L, the electrolysis was performed at 1.0A, 1.5A, 2.0A, 2.5A, 3.0A current with energy consumption considered. Current density at the membrane was 0.04A/cm^2, 0.06A/cm^2, 0.08A/cm^2, 0.1A/cm^2 and 0.12A/cm^2, respectively. The electrolysis was performed for 6 h as in the previous experiments. The experimental results indicate the enhancement in the mass-transfer of the impurity ions through the membrane (Table 5).

Table 5. Metal reduction rate at the cathodes as a function of current density and constant impurity concentration and with forced mixing applied.

Impurity ion, 0.027 mol/L	Current density at the membrane, A/cm^2	Electrochemical equivalent, q	Average deposition rate, g/hour	Average deposition rate, mmol/hour	Current efficiency, %
Cd^{2+}, Forced mixing	0.04	2.46	0.0776	0.6903	3.15
	0.06	2.46	0.108	0.9608	4.39
	0.08	2.46	0.1325	1.1788	5.39
	0.1	2.46	0.1578	1.4039	6.41
	0.12	2.46	0.1668	1.4839	6.78
Zn^{2+}. Forced mixing	0.04	1.21	0.0668	1.0276	5.52
	0.06	1.21	0.0755	1.1615	6.24
	0.08	1.21	0.0793	1.22	6.55
	0.1	1.21	0.0863	1.3276	7.13
	0.12	1.21	0.0918	1.4123	7.59

Through comparison of the data from Fig. 1 and Table 5, it becomes obvious that the quantity of the reduced metal increases on the cathode as the current density increases. With the forced mixing applied, the metal reduction on the cathode is enhanced and as a result, the metal quantity and the current efficiency are increased.

When comparing the data for metal reduction from Tables 2, 5, it may be argued that the forced mixing of the anolyte solution gradually enhances the cadmium reduction at the cathode from 12% at the current density of 0.04 A/cm^2 to 46% at 0.1 A/cm^2. Zinc reduction within the range also grows gradually from 5% to 31%.

5   Conclusions

The study of the electrolysis of the chromic solutions with the electrochemical units for electrolyte refinement at the constant current density and certain pH catholyte range has shown that the metallic zinc and cadmium are reduced at the cathode in the cathode chamber therewith refining the chromic electrolytes.

To study the regularities of the performance of the electrochemical unit with the mechanical mixing applied, the hydrodynamic parameters of the membrane electrolysis have been first defined and the results obtained are as follows:

- mechanical mixing of the chromic solution increases the mass-transfer coefficient for Zn^{2+} and Cd^{2+} in 9.4 and 9.3 times, respectively, and decreases the boundary layers of the membrane in the same amount. The concentration polarization shows a decrease by almost an order of magnitude at the external membrane surfaces which contributes to the enhancement of the metal ion transfer through the cation-exchange membrane;
- mechanical mixing of the anolyte solutions increases Reynold's number in 7.5 times and the Sherwood number in 10.49 and 10.38 times for the Cd^{2+} and Zn^{2+}

containing solutions, respectively, and significantly diminishes the membrane contamination. However, the metal reduction at the cathodes does not occur proportionally, as is illustrated above. It is explained by the concentration polarization; due to fast impurity ion transfer through the membrane, the ion concentration at the boundary layer declines to 0 when the limiting current is applied;

- increase of the current density gradually contributes to the mass-transfer of Cd^{2+} and Zn^{2+} through the membrane and increases their current efficiency;
- mechanical mixing of the near-membrane zone of the anolyte promotes the increase of the limiting current at the membrane and results in a decrease of the concentration polarization and considerable growth of the mass-transfer of the impurity ions through the membrane and the current efficiency, as a whole.

The performed studies allow the selection of the best performances of the electromembrane units and adjustment of the chromatic solutions to prolong their use as well as to reduce the reagent costs, the concentration of the contaminant in sewage water, and to cut the expenses for the contaminants neutralization.

References

1. Benvenuti, T., Krapf, R., Rodrigues, M., Bernardes, A., Zoppas-Ferreira, J.: Recovery of nickel and water from nickel electroplating wastewater by electrodialysis. Sep. Purif. Technol. **129**(29), 106–112 (2014)
2. Bolshanina, S., Ablieyeva, I., Kyrychenko, O., Altunina L., Klimanov O., Serdiuk, V.: Method of Electrolytic Regeneration of Chromium-Containing Solutions. Patent of Ukraine, No. 109623, MPC (2006.01) C02F 1/46 (2016)
3. Davoudi, M., Gholami, M., Naseri, S., Mahvi, A., Farzadkia, M., Esrafili, A., Alidadi, H.: Application of electrochemical reactor divided by cellulosic membrane for optimized simultaneous removal of phenols, chromium, and ammonia from tannery effluents. Toxicol. Environ. Chem. **96**(9), 1310–1332 (2014)
4. Dimitris, P., Zagklis, E., Arvaniti, V.: Sustainability analysis and benchmarking of olive mill wastewater treatment methods. J. Chem. Technol. Biotechnol. **88**, 742–750 (2013)
5. Kruglikov, S.: Application of electromembrane processes in chromium electroplating technology. Petrol. Chem. **56**(10), 969–976 (2016)
6. Kruglikov, S., Kolesnikov, V., Nekrasova, N., Gubin, A.: Regeneration of chromium electroplating electrolytes by the application of electromembrane processes. Theoret. Found. Chem. Eng. **52**(5), 800–805 (2018)
7. Serdiuk, V., Sklabinskyi, V., Bolshanina, S., Ivchenko, V., Qasim, M., Zaytseva, K.: Membrane processes during the regeneration of galvanic solution. J. Eng. Sci. **5**(2), F1–F6 (2018)
8. Sistatc, P., Cretinc, M., Nikonenko, V.: Impact of ion exchange membrane surface charge and hydrophobicity on electroconvection at underlimiting and overlimiting currents. J. Membr. Sci. **523**, 36–44 (2017)
9. Qian, Y., Huang, L., Pan, Y., Quan, H., Lian, H., Yang, J.: Dependency of migration and reduction of mixed $Cr2O7^{2-}$, Cu^{2+} and Cd^{2+} on electric field, ion exchange membrane and metal concentration in microbial fuel cells. Sep. Purif. Technol. **192**, 78–87 (2018)
10. Zabolotsky, V., Novak, L., Kovalenko, A., Nikonenko, V., Urtenov, M., Lebedev, K., But, A.: Electroconvection in systems with heterogeneous ion-exchange membranes. Pet. Chem. **57**(9), 779–789 (2017)

Numerical Simulation of the Mass-Transfer Process Between Ammonia and Water in the Absorption Chiller

Michal Volf[1] , Maryna Demianenko[2(✉)] ,
Oleksandr Starynskyi[2] , Oleksandr Liaposhchenko[2] ,
and Alireza Mahdavi Nejad[3]

[1] University of West Bohemia, 22, Univerzitni Street, 32600 Pilsen,
Czech Republic
[2] Sumy State University, 2, Rymskogo-Korsakova Street, Sumy 40007, Ukraine
m.demianenko@omdm.sumdu.edu.ua
[3] Wentworth Institute of Technology, 550, Huntington Avenue, Boston,
MA 02115, USA

Abstract. This paper describes the absorption process of gaseous ammonia into liquid water in the plate heat exchanger, which is considered to be the crucial part of an absorption cooling system. Two approaches are utilized to numerically simulate this absorption process. In the first approach, the dissolution of gaseous ammonia into liquid water, as well as the following chemical reaction between the dissolved liquid ammonia and liquid water, are modeled. In the second approach, only the dissolution of ammonia into water is considered. The Henry's Law with Van't Hoff correlation is used for the simulation of the ammonia absorption process, namely the calculation of the concentration of ammonia in gas and in liquid. The Henry's law is utilized since its line has the best correlation with the ammonia-water equilibrium line for the concentrations, which is taken into account in the numerical simulations. The ammonia mass flux from gas to liquid phase and its concentration at the outlet of the computational domain is determined as a result of the simulations.

Keywords: Refrigerators machines · Chillers · Ammonia absorption · CFD · Eulerian model · Henry's law · Van't Hoff correlation

1 Introduction

One of the essential improvements in absorption chillers is increasing their efficiency and intensity of the absorption process [1]. Absorbers are the critical components of the refrigeration machines. The productivity, size, and energy usage of the entire refrigeration machine is determined by the efficiency and intensity of the used absorber [2]. At the same time, it is necessary to point out that the effectiveness of the absorber is obtained by its design and the properties of the working fluid. Ammonia solution ($NH_3 \cdot H_2O$) is widely used working fluid in refrigerator machines [3] because it is considered as an environmentally friendly fluid and also the refrigeration machines with such a working fluid are works on a thermal drive. Therefore, a significant number

of theoretical and experimental research is aimed at studying the processes in the absorption chillers, namely the intensity increasing and design optimizing.

In [4], the mathematical models of the absorption processes in the counter-current absorber and in the vertical tubular absorber of refrigerating machines [5] were presented. The parametric analysis aimed at the determination of the inlet parameters influence at the absorption chillers performance was carried out, and the correlation equations for the absorber height and Nu, Sh numbers were proposed.

In [6], the theoretical and experimental study of the falling film absorber [7] in an ammonia-water absorption chiller [8] were presented. In that study the mathematical model for obtaining the heat and the mass transfer coefficients of the absorption process was proposed. Moreover, the mathematical model allows determining the heat and mass transfer coefficients of the absorber plates and on the interface between the gas and liquid phase. Also, experimental studies of the refrigeration machine to determine the real absorption process parameters and making the parametric analysis were presented.

In [9], the experimental studies of the desorption and absorption of an ammonia solution in the plate heat exchangers [10] were presented. As in the above-mentioned theoretical studies, the input parameters influence, namely the coolant temperature, the mass flow rate, and the ammonia concentration on the heat and mass transfer coefficients of those processes were determined.

In the massive amount of the research works, the plate heat exchanger is considered as an absorber because it allows creating large interphase between gas and liquid with small apparatus design. The authors of the abovementioned studies admit that it's difficult to assess the single parameter effect on a local or some global characteristics of the absorption process. One of the ways to evaluate the influence of input parameters on the output parameters, and they optimization [11], is the artificial neural networks using [12]. It should be noted that the CFD allows studying the local phenomena occurring in absorbers, which cannot be obtained by experimental or global research [13]. Computational fluid dynamics make it possible to optimize the absorbers' design and make a comprehensive parametric analysis to determine the input parameters' influence on the absorption process and observe some local phenomena in absorbers. In this case, the actual and promising goal is the numerical research of ammonia-water absorption processes in plate heat exchangers of the refrigeration machines using CFD methods.

2   Literature Review

The significant amount of the scientific works is dedicated to the study of the absorption process in chillers and other absorption equipment (CO_2 dissolving into the water using the packing layer). It should be noted that different mass transfer models can be used for each type of absorption processes.

The numerical simulation [14] of the CO_2 absorption process [15] from flue gases by solid (K_2CO_3) [16] or liquid (MEA) sorbent [17] are presented in [18]. The simulations were carried out in the ANSYS software package, namely its Fluent and CFX modules. The Eulerian-Eulerian model was chosen in the above studies as the multiphase flow model. The chemical reaction between the absorbed component and the sorbent was taken into account in the simulations. It should be noted that the multiphase system features are considered in each of the above researches, and the individual approaches were used to model mass transfer and chemical reaction. Attention should be paid to work [19], in which the process of CO_2 absorption by the MEA solution in the packing layer was simulated. In this case, two mixtures components (gas and liquid) were considered with specific laws for determining the physical and thermodynamic properties:

- gaseous phase: density – incompressible ideal gas; viscosity – mixing law; specific heat and thermal conductivity – mass weight mixing law; diffusivity – kinetic theory;
- liquid phase: density – constant value; viscosity – constant value; specific heat and thermal conductivity – mass weight mixing law; diffusivity – kinetic theory.

The research work [20] presents the results of the numerical simulation of the SO_2 absorption process. Eulerian-Eulerian multiphase flow model was used for this purpose. The [21] includes the simulation of the LiBr-water solution obtaining process in a membrane absorber by using CFD methods. The equations of continuity, energy, and diffusion were solved like steady state. The flow has been considered like Laminar.

It should be noted that different methods for the determination of the equilibrium concentration (Henry's law, Raoult's law, UDF) were used in the simulations. This is due to the modeled multiphase system features, namely the initial concentration of the target component. In the abovementioned research, the chemical reactions were simulated by UDF using, which taking into account the reaction type and rate. Therefore, it is necessary to develop a simulation methodology for each absorption process. Based on the above-said, it is required to create a particular method for numerical simulations of the ammonia-water absorption process in the plate heat exchanger.

3 Research Methodology

Based on a literature review, two approaches were proposed for modeling the absorption of ammonia by water, which is based on the theoretical process description. The first approach is the simulation of the process of the ammonia dissolving into water and a chemical reaction in a liquid between ammonia molecules and water molecules, namely the ionization ($NH_3 + H_2O \rightarrow NH_4^+ + OH^-$). In the second method, the chemical reaction has not been considered in the simulation. The ANSYS software package was chosen for simulations, namely its Fluent module. The computational domain is the volume between the two plates of the heat exchanger (Fig. 1).

The polyhedral mesh was used in this case. In both case process considered transient. The gravitational acceleration was directed from inlet to outlet. Simulation of the mixture movement was done using the Eulerian model [22], which gives good agreement with experiments [23] in case of the necessity for accounting phases interacting [24]. The additional settings were also made: Multi-Fluid VOF model – Implicit; Interface Modeling Type – Sharp. The k-ω SST model (per phase) was chosen as the turbulence model. Two mixtures were created for simulation gas-liquid flow: a gas mixture – gaseous ammonia and water vapor; a liquid mixture – water, gaseous ammonia, ammonia liquid (for the first approach) and water, ammonia liquid (for the second approach) The gas mixture was chosen as the main phase.

The Heat Transfer Coefficient - Nusselt Number equal to 3.8 was selected for calculation of the heat transfers between the phases. Mass transfer between phases was implemented by using Species Transport, Reaction - Volumetric. Turbulence-Chemistry Interaction - Finite Rate\Eddy Dissipation was selected for the chemical reaction rate. The Surface Tension coefficient is selected equal to 0.054 N/m.
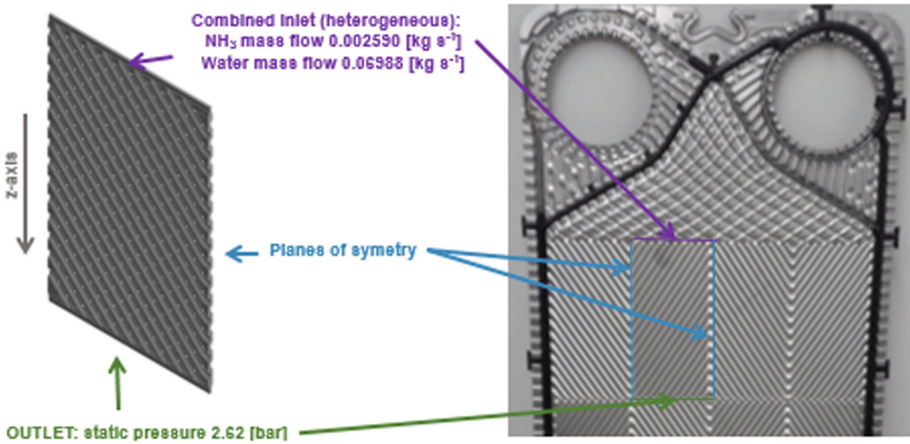

Fig. 1. The computational domain of the plate heat exchanger.

Mass transfer settings were configured separately for each absorption simulation approach:

– the first approach: from phase - vapor (species NH3 <Gas>) to phase - liquid (species NH3 <Gas>), mechanism – Species mass transfer. Model options: Equilibrium Ratio (Molar Concentration) – Molar concentration equilibrium ratio = 0.99, Interphase mass transfer coefficient – Hugmark correlation per phase (Table 1);

– the second approach: from Phase - vapor (species NH_3 <Gas>) to phase - liquid (species NH_3 <Liquid>), mechanism – Species mass transfer. Equilibrium Ratio (Molar Concentration) – Henry's Law with Van't Hoff correlation (Reference Henry's constant 0.0169; Temperature dependence 4200). Interphase mass transfer coefficient – Hugmark correlation per phase.

Table 1. The physical properties of the vapor and liquid mixture.

Vapor mixture		Liquid mixture	
Ammonia gaseous + water vapor		1-st app.: ammonia "g" + water "l" + NH$_4$OH; 2-nd app.: ammonia "l" + water "l"	
Density	Ideal gas (kg/m^3)	Density	Volume weighted mixing law (kg/m^3)
Specific heat	Mixing law (j/kg-k)	Specific heat	Mixing law (j/kg-k)
Thermal conductivity	Mass weighted mixing law (w/m-k)	Thermal conductivity	Mass weighted mixing law (w/m-k)
Viscosity	Mass weighted mixing law (kg/m-s)	Viscosity	Mass weighted mixing law (kg/m-s)
Mass Diffusivity	From NH$_3$ to H$_2$O – $1\cdot10^{-9}$ m^2/s	Mass Diffusivity	From NH$_3$ to H2O – $1\cdot10^{-9}$ m^2/s

It should be noted that the reaction rate can be described only by the Arrhenius equation, but nowadays, for ionization reaction uses another dependence (Table 2).

It should be noted that in the ANSYS database, there is no standard enthalpy for liquid ammonia. Therefore this value was added manually. Also, the molar mass of liquid ammonia was changed to 17, since the molar mass value of 28 is indicated in the

Table 2. Boundary conditions for simulations.

Material	Inlet parameters	Value
Mixture	Supersonic/initial gauge pressure	0 Pa
Vapor	Mass flow rate	0.0026 kg/s
	Total temperature	294.65 K
	Species mass fractions H$_2$O	0.003
Liquid	Mass flow rate	0.0699
	Slip velocity specification method – volume fraction	0.0221
	Total temperature	312.65
	Species mass fractions H$_2$O	0.634
	Species mass fractions NH$_4$OH (only for the first approach)	0.366
Material	Outlet parameters	Value
Mixture	Supersonic/initial gauge pressure	0 Pa
Vapor	Total temperature	300.00 K
	Species mass fractions H$_2$O	0.003
Liquid	Slip velocity specification method – volume fraction	0.0221
	Total temperature	312.65
	Species mass fractions H$_2$O	0.63
	Species mass fractions NH$_4$OH (only for the first approach)	0.37
Material	Parameters on the wall	Value
Mixture	Wall Adhesion (contact angle)	45°
	Sand-grain roughness: roughness height	0 m
	Roughness constant	0.5

ANSYS database. Hybrid initialization was used for calculations. The problem was solved by the Method-Velocity Coupling - Coupled method with the following Spatial Discretization parameters: Density – Second-Order Upwind, Momentum – First Order Upwind, Volume Fraction – Modified HRIC; Turbulent Kinetic Energy – Second-Order Upwind; Energy – First Order Upwind; Transient Formulation – First Order Implicit. The selected time step for the description of the mass transfer between two phases and reaction in the liquid phase is 1 ms; min and max iterations are 1 and 25, respectively.

4 Results

The ammonia mass flux from gas to liquid and the ammonia mass fraction at the domain outlet was presented as a numerical simulation result for two proposed approaches. The isolines of the liquid volume fraction and ammonia mass fraction are shown in Fig. 3 a, b, and Fig. 4 a, b for the first and second approaches, respectively. The liquid quantity in the domain lower part is increasing; as shown in Fig. 2 a, it means that the ammonia mass fraction reached to equilibrium ratio, and the ammonia mass flux becomes equal to zero. Those phenomena can be observed in Fig. 3 a. In Fig. 3 b, the liquid is uniformly distributed in the domain, and only in the domain lower part the liquid quantity is increasing, it means that the ammonia mass transfer from the gas phase to the liquid phase occurs in the domain. This fact indicates that ammonia is not fully absorbed after passing the domain: it is also confirmed in Fig. 4 b. The simulation results are presented in Table 3.
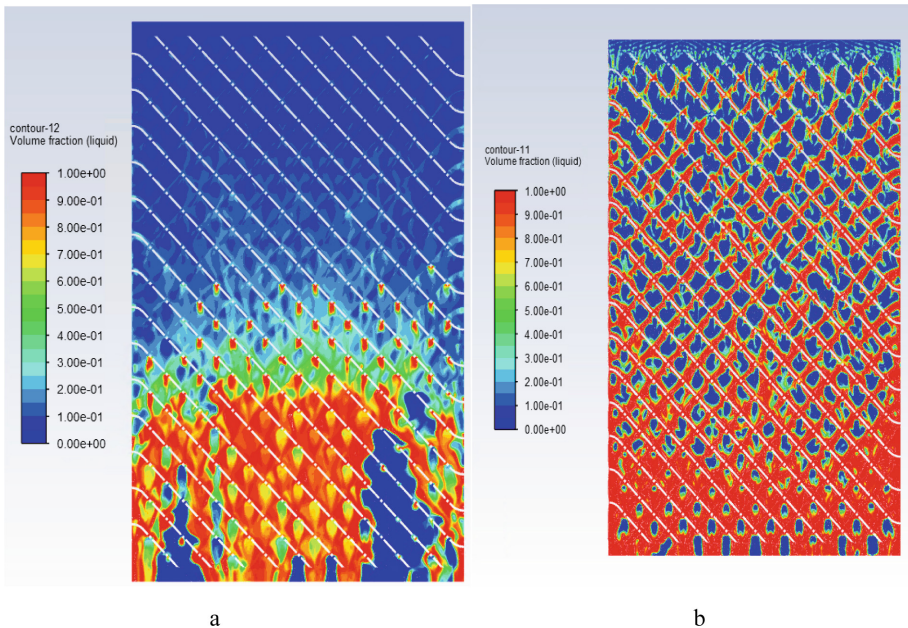

a   b

Fig. 2. The volume fraction of fluid: the first (a) and the second (b) approaches.
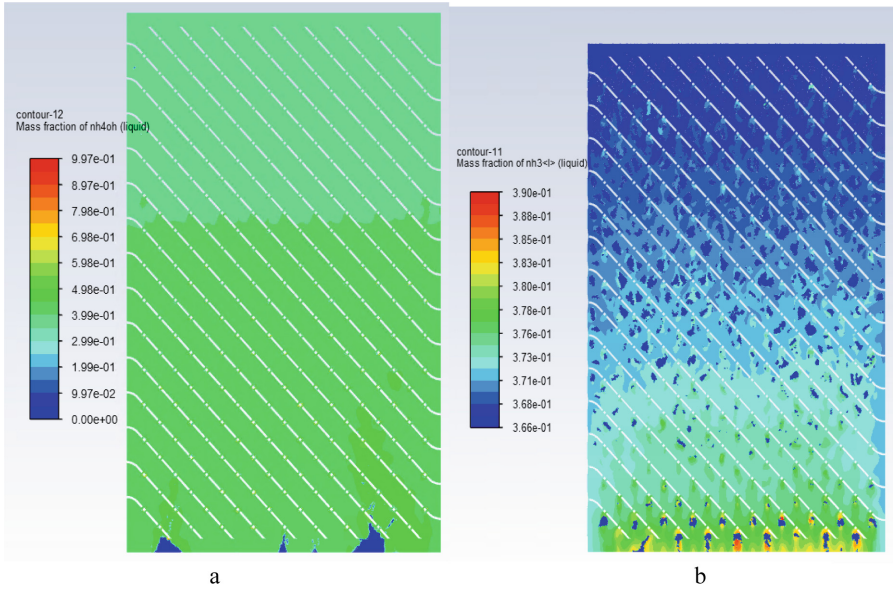
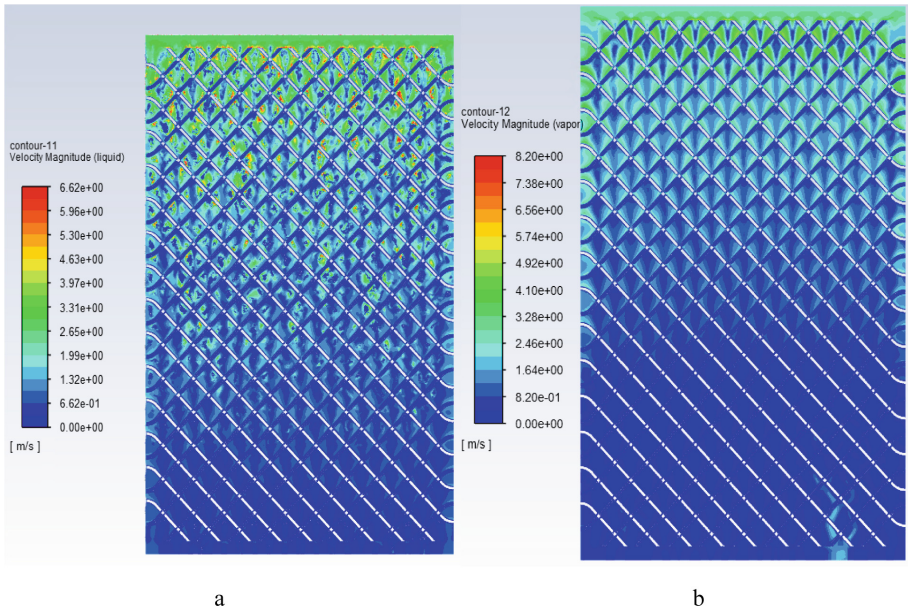**Fig. 3.** Mass fraction: NH$_4$OH (a); NH$_3$ liquid (b).

Fig. 4. Vapor velocity magnitude: a – the first approach (mass-weighted average velocity magnitude: inlet 2.505 m/s; outlet 0.579 m/s); b – the second approach (mass-weighted average velocity magnitude: inlet 2.53 m/s; outlet 0.8 m/s).

Table 3. The results of the ammonia – water absorption processes simulations

First approach			Second approach		
Mass Flow Rate (kg/s)					
Mixture	Inlet	0.0725	Mixture	Inlet	0.0725
	Outlet	0.094		Outlet	0.115
Vapor	Inlet	0.0026	Vapor	Inlet	0.0026
	Outlet	$5.7 \cdot 10^{-5}$		Outlet	$4.61 \cdot 10^{-6}$
Liquid	Inlet	0.0699	Liquid	Inlet	0.0699
	Outlet	0.0941		Outlet	0.115
Mass-weighted average mass (kg/kg)					
Ammonia solution (NH_4OH)			Ammonia liquid (NH_3)		
Inlet	0.366	Outlet 0.438	Inlet	0.366	Outlet 0.378

5 Conclusions

The two approaches were proposed for the numerical simulation ammonia-water absorption process in the plate heat exchangers. The first approach takes into account the process of ammonia mass transfer from the gas phase to the liquid and the chemical reaction between the absorbed component and the water; the second approach is only the process of the ammonia dissolving.

The mass flux from gas to liquid and ammonia mass fraction was obtained as a simulation result. Henry's law with Van't Hoff correlation was used for getting the ammonia equilibrium value in gas and liquid phase. Based on those results, it was determined that the laws proposed in ANSYS for calculating the equilibrium concentration are poorly correlated with the ammonia concentration in equilibrium. In further research, for more precise results of the ammonia-water absorption, the simulation is planned to develop the UDF.

References

1. Srikhirin, P., Aphornratana, S., Chungpaibulpatana, S.: A review of absorption refrigeration technologies. Renew. Sustain. Energy Rev. **5**, 343–372 (2000). https://doi.org/10.1016/S1364-0321(01)00003-X

2. Ibarra-Bahena, J., Romero, R.J.: Performance of different experimental absorber designs in absorption heat pump cycle technologies: a review. Energies **7**, 751–766 (2014). https://doi.org/10.3390/en7020751

3. Crepinsek, Z., Goricanec, D., Krope, J.: Comparison of the performances of absorption refrigeration cycles. WSEAS Trans. Heat Mass Transf. **4**, 65–76 (2009)

4. Goel, N., Goswami, D.Y.: Analysis of a counter-current vapor flow absorber. Int. J. Heat Mass Transf. **48**, 1283–1292 (2005). https://doi.org/10.1016/j.ijheatmasstransfer.2004.10.009

5. Jiang, M., Xu, S., Wu, X.: Numerical simulation and experiment for R124-DMAC bubble absorption process in a vertical tubular absorber. Int. J. Therm. Sci. **138**, 124–133 (2019). https://doi.org/10.1016/j.ijthermalsci.2018.12.051

6. Boudehenn, F., Bonnot, S., Demasles, H., et al.: Development and performances overview of ammonia-water absorption chillers with cooling capacities from 5 to 100 kW. Energy Procedia **91**, 707–716 (2016). https://doi.org/10.1016/j.egypro.2016.06.234

7. Triche, D., Bonnot, S., Perier-Muzet, M., et al.: Modeling and experimental study of an ammonia-water falling film absorber. Energy Procedia **91**, 857–867 (2016). https://doi.org/10.1016/j.egypro.2016.06.252

8. Triche, D., Bonnot, S., Perier-Muzet, M., Boudehenn, F.: Experimental and numerical study of a falling film absorber in an ammonia-water absorption chiller. Int. J. Heat Mass Trans. **111**, 374–385 (2017). https://doi.org/10.1016/j.ijheatmasstransfer.2017.04.008

9. Taboas, F., Valles, M., Bourouis, M., Coronas, A.: Flow boiling heat transfer of ammonia/water mixture in a plate heat exchanger. Int. J. Refrig **33**, 695–705 (2010). https://doi.org/10.1016/j.ijrefrig.2009.12.005

10. Cerezo, J., Bourouis, M., Valles, M., et al.: Experimental study of an ammonia-water bubble absorber using a plate heat exchanger for absorption refrigeration machines. Appl. Therm. Eng. **29**, 1005–1011 (2009). https://doi.org/10.1016/j.applthermaleng.2008.05.012

11. Pavlenko, I., Ivanov, V., Kuric, I., Gusak, O., Liaposhchenko, O.: Ensuring vibration reliability of turbopump units using artificial neural networks. In: Trojanowska, J., Ciszak, O., Machado, J., Pavlenko, I. (eds.) Advances in Manufacturing II. MANUFACTURING 2019. LNME, pp. 165–175. Springer, Cham (2019). https://doi.org/10.1007/978-3-030-18715-6_14

12. Liaposhchenko, O., Pavlenko, I., Demianenko, M., Starynskyi, O., Pitel, J.: The methodology of numerical simulations of separation process in SPR-separator. In: 2nd International Workshop on Computer Modeling and Intelligent Systems. CMIS 2019. CEUR Workshop Proceedings, vol. 2353, pp. 822–832 (2019)

13. Lima, A.A.S., Ochoa, A.A.V., Da Costa, J.A.P., Henriquez, J.R.: CFD simulation of heat and mass transfer in an absorber that uses the pair ammonia/water as a working fluid. Int. J. Refrig **98**, 514–525 (2018)

14. Ryan, E.M., Xu, W., De Croix, D., et al.: Multi-phase CFD modeling of a solid sorbent carbon capture system. Am. Soc. Mech. Eng. Fluids Eng. Div. FEDSM **1**, 653–661 (2012). https://doi.org/10.1115/FEDSM2012-72298

15. Chalermsinsuwan, B., Piumsomboon, P., Gidaspow, D.: A computational fluid dynamics design of a carbon dioxide sorption circulating fluidized bed. Part. Technol. Fluid. AlChE **56** (11), 2805–2824 (2010)

16. Asendrych, D., Niegodajew, P., Drobniak, S.: CFD modelling of CO2 capture in a packed bed. Chem. Process Eng. **34**(2), 269–282 (2013). https://doi.org/10.2478/cpe-2013-0022

17. Niegodajew, P., Asendrych, D.: Amine based CO2 capture – CFD simulation of absorber performance. Appl. Math. Model. **40**(23–24), 10222–10237 (2016). https://doi.org/10.1016/j.apm.2016.07.003

18. Plyatsuk, L.D., Ablieieva, I.Yu., Vaskin, R.A., Yeskendirov, M., Hurets, L.L.: Mathematical modeling of gas-cleaning equipment with a highly developed phase contact surface. J. Eng. Sci. **5**(2), F19–F24 (2018). https://doi.org/10.21272/jes.2018.5(2).f4

19. Lu, X., Xie, P., Ingham, D.B., et al.: Modelling of CO2 absorption in a rotating packed bed using an Eulerian porous media approach. Chem. Eng. Sci. **199**, 302–318 (2019). https://doi.org/10.1016/j.ces.2019.01.029

20. Qin, M., Dong, Y., Cui, L., et al.: Chemical engineering research and design pilot-scale experiment and simulation optimization of dual-loop wet flue gas desulfurization spray scrubbers. Chem. Eng. Res. Des. **148**, 280–290 (2019). https://doi.org/10.1016/j.cherd.2019.06.011

21. Asfand, F., Stiriba, Y., Bourouis, M.: CFD simulation to investigate heat and mass transfer processes in a membrane-based absorber for water-LiBr absorption cooling systems. Energy **91**, 517–530 (2015). https://doi.org/10.1016/j.energy.2015.08.018

22. Liaposhchenko, O., Pavlenko, I., Monkova, K., Demianenko, M., Starynskyi, O.: Numerical simulation of aeroelastic interaction between gas-liquid flow and deformable elements in modular separation devices. In: Ivanov, V., et al. (eds.) Advances in Design, Simulation and Manufacturing II. DSMIE 2019. LNME, pp. 765–774. Springer, Cham (2020). https://doi.org/10.1007/978-3-030-22365-6_76

23. Liaposhchenko, O., Pavlenko, I., Ivanov, V., Demianenko, M., Starynskyi, O., Kuric, I., Khukhryanskiy, O.: Improvement of parameters for the multi-functional oil-gas separator of "Heater-Treater" type. In: 2019 IEEE 6th International Conference on Industrial Engineering and Applications (ICIEA), Tokyo, Japan, pp. 66–71 (2019). https://doi.org/10.1109/iea.2019.8715203

24. Lukashov, V.K., Kostiuchenko, Y.V., Timofeev, S.V.: Hydrodynamics of a liquid film downflow on a flat surface in evaporation conditions into a flow of neutral gas. J. Eng. Sci. **6**(1), F19–F24 (2019). https://doi.org/10.21272/jes.2019.6(1).f4

Cooling Process Intensification for Granular Mineral Fertilizers in a Multistage Fluidized Bed Device

Mykola Yukhymenko[1] , Ruslan Ostroha[1(✉)] ,
Andrii Lytvynenko[1] , Yakov Mikhajlovskiy[1] ,
and Jozef Bocko[2]

[1] Sumy State University, 2, Rymskogo-Korsakova Street, Sumy 40007, Ukraine
r.ostroga@pohnp.sumdu.edu.ua
[2] Technical University of Kosice, 1/9, Letna Street,
040 01 Kosice, Slovak Republic

Abstract. The design of a multistage cooler with several inclined perforated shelves for cooling granular fertilizers is presented and explained in the article. It is proved that such device has certain technical and energy advantages compared with typical designs of coolers. For this purpose, physical modeling of the hydrodynamic structure of the fluidized bed in the shelf apparatus was carried out. The formation of hydrodynamic regimes that differ in their hydrodynamic structure depending on the design parameters of the shelf contact elements is justified. A mathematical model of the kinetics of cooling granules in a fluidized bed is developed, which makes it possible to determine the cooling time of granules and calculate the temperature profile in a suspended layer. The optimal design parameters of the shelf cooler were experimentally determined, at which the granules are intensively cooled to the technologically required temperature. The results of experimental studies are presented, which confirm the efficiency of granular fertilizers cooling in multistage shelf apparatus with less energy consumption.

Keywords: Shelf cooler · Inclined perforated shelves · Active hydrodynamic mode · Coefficient · Time · Temperature profile

1 Introduction

At present chemical companies cool the granules of mineral fertilizers that have passed the granulation and drying stages to eliminate side reactions that lead to cracking and destruction of particles.

During cooling, the granule liquid content decreases due to evaporation of residual moisture and it causes physical and chemical changes inside the granules. As a result, granules acquire the necessary strength, humidity, and temperature, i.e. they meet quality characteristics.

The production of granular phosphate fertilizers is one of the energy-intensive branches of the chemical industry. From the viewpoint of exergy analysis, the cooling

stage has up to 70% of exergy losses from the total heat supply and rather a low energy efficiency equal to 20–25%. Energy losses are due to the imperfection of heat transfer at different finite temperatures of the process flows at the inlet and outlet of the apparatus. Due to this, current fluidized bed coolers operate at high energy costs for pumping cooling air, the amount of which is 1.5–2.0 m^3 per 1 kg of cooled product. Therefore, it is urgent to develop energy-saving fluidized bed coolers in which sufficient efficiency will be combined with minimal costs for the process.

2 Literature Review

Cooling of granules is a very common technological operation and there are used various types of coolers, often convective ones [1]. Rotary coolers with one [2, 3] or two drums with parallel loading [4] have cumbersome design and provide insufficient heat transfer. For cooling and simultaneous transportation of granular materials pneumatic tube coolers are used [5, 6], however, they require increased air consumption and cooling of the product is insufficiently deep.

Fluidized bed apparatus in the technology of mineral fertilizers are most commonly used as granular material coolers [7–9]. Despite the sufficient efficiency of heat exchange processes in the fluidized bed, these devices are characterized by increased specific consumption of cooling air. In [10], it is proposed to use a vertical apparatus with the fluidized bed of granules and vibrating blades for cooling the granules. It is indicated that synchronous oscillations of the blades and the fluidization regime affect the final temperature and humidity of the granules during cooling. However, damping springs and vibration units inside the device make the design too complex and operationally unreliable.

Mine-type apparatuses with a gravitationally lowering layer can be also used for cooling granular materials [11]. Louver-type contact elements of various configurations make it possible to increase contact time and separating effect both in gas-dispersed flows [12] and gas-liquid flows [13, 14].

Apparatuses with gravitationally lowering layer include a cooler with inclined perforated shelves installed along the height of the apparatus with various design parameters. These devices have proven themselves efficient in the pneumatic classification of granular materials [15] and multistage granulation [16].

In the shelf apparatus, active hydrodynamic regimes for fluidization of granules take place at each contact stage. These regimes and necessary conditions can be easily changed over a wide range of gas flow velocities without changing the design of the apparatus. Due to the active contact of gas flows with material particles, shelf units are very effective for cooling granules of mineral fertilizers.

3 Research Methodology

Correct and more accurate determination of the kinetic parameters of particle convective cooling in the fluidized bed of material (rate and cooling time, temperature profile) is possible only using mathematical modeling in the logical path "a single particle (first level) – an ensemble of particles (second level) – fluidized bed (third level)".

When considering the heat transfer process at the first level, it becomes necessary to calculate the temperature in the center of the solid particle t_c (maximum in the entire volume of the particle) during its heat exchange with the environment. One accepts: a spherical particle of radius R is a homogeneous and isotropic medium, characterized by certain values of heat conductivity (a_h), heat capacity (c_h) and density (ρ_h). The ambient temperature t_a and the heat transfer coefficient α remain constant throughout the entire cooling process τ.

The heat transfer process is described by the differential heat equation:

$$\frac{\partial t}{\partial \tau} = a_h \left(\frac{\partial^2 t}{\partial r^2} + \frac{2}{r} \frac{\partial t}{\partial r} \right). \tag{1}$$

The solution of Eq. (1) by the method of separation of variables under boundary conditions of the third kind is presented in the general form:

$$\frac{t(r,t) - t_\alpha}{t_i - t_\alpha} = \sum_{n=1}^{\infty} B_n \sqrt{\mu_n^2 + (Bi - 1)^2} \frac{sin\mu_n \frac{r}{R}}{\mu_n \frac{r}{R}} exp\left(-\mu_n^2 Fo\right). \tag{2}$$

Where constant

$$B_n = (-1)^{n+1} \frac{2Bi}{\mu_n^2 + Bi^2 - Bi}. \tag{3}$$

Since the cooling process is quite long, the Fourier criterion is Fo ≥ 0.3, the infinite series (2) converges quickly, and one can restrict itself to only the first member of the series (n = 1). It is assumed R→0 (center of the particle) in Eq. (2). Then:

$$\frac{sin\mu_n \frac{r}{R}}{\mu_n \frac{r}{R}} \to 1$$

and Eq. (2) takes the form:

$$\frac{t_c - t_\alpha}{t_i - t_\alpha} = B_1 \sqrt{\mu_1^2 + (Bi - 1)^2} exp\left(-\mu_1^2 Fo\right). \tag{4}$$

The temperature at the center of the particle is:

$$t_c = (t_i - t_\alpha) B_1 \sqrt{\mu_1^2 + (Bi - 1)^2} exp\left(-\mu_1^2 Fo\right) + t_\alpha. \tag{5}$$

The root μ_1^2 in the Eq. (5) is equal to

$$\mu_1^2 = \frac{2Bi}{B_1} - Bi^2 + Bi. \tag{6}$$

The expression for determining the particle cooling time is obtained by solving Eq. (4) with respect to τ (included in the criterion Fo):

$$\tau_{cool} = \frac{R^2}{a_h\mu_1^2}ln\left[\frac{B_1\sqrt{\mu_1^2 + (Bi-1)^2}}{\frac{t_c-t_\alpha}{t_i-t_\alpha}}\right]. \tag{7}$$

The constant B_1 is determined from the regression equations for various ranges of values of the Bio criterion:

$$B_1 = 0,290(Bi) + 1,0, \text{ at } 0,1 < Bi < 1,0; \tag{8}$$

$$B_1 = 0,183(Bi) + 1,1, \text{ at } 1,0 \le Bi \le 2,0; \tag{9}$$

$$B_1 = 0,130(Bi) + 1,22, \text{ at } 2,0 < Bi \le 4,0. \tag{10}$$

The range $0,1 < Bi \le 4,0$ is typical for suspended (fluidized) systems. The differential heat balance equation for the allocated volume V (second level) is written as the sum of the constituent amounts of heat entering and leaving the elementary volume of solid particles and removed from the surface of solid particles due to convection. After the transformations described in [17], the equation takes the form:

$$G_fc_h\rho_h\frac{\partial t(\tau)}{\partial\tau} = G_fc_h\rho_h\frac{\partial t(\Delta x,\tau)}{\partial x} - F_{lay}\alpha(R,w)[t(R,\tau) - t_\alpha(\tau)]. \tag{11}$$

If one assumes $\partial t(\tau)/\partial\tau = 0$ in Eq. (11) for the mode of ideal displacement of the solid material flow along the surface of an inclined shelf, then one obtains:

$$t(\Delta x) = t(x)exp\left[-\frac{\alpha 6(1-\varepsilon)}{G_fc_h\rho_hd}\right]\frac{x}{u_{sp}}. \tag{12}$$

For the mode of ideal mixing of particles, in the zone above the unloading space, in Eq. (11) one assumes $\partial t(\Delta x,\tau)/\partial x = 0$. Then it is obtained:

$$t(\Delta\tau) = t(\tau)exp\left[-\frac{\alpha 6(1-\varepsilon)}{G_fc_h\rho_hd}\right]\tau_r. \tag{13}$$

Here G_f is the relative flow rate, as the ratio of the product and airflow rate, kg/kg; ε – porosity of the layer; d – average diameter of a particle in the layer, m; u_{sp} – solid particles velocity along the x-axis, m/s; τ_r – residence time of particles in the layer, s.

The final temperature of cooled granules is determined from the expression characterizing the combined model of "ideal displacement – perfect mixing" for the working section above the shelf (third level):

$$t_f = t_\alpha + (t_i - t_\alpha)exp\left[-\frac{\alpha 6(1-\varepsilon)}{G_f c_h \rho_h d}\left(\frac{x}{u_{sp}} + \tau_r\right)\right]. \tag{14}$$

The developed mathematical model made it possible to draw up an engineering method for calculating coolers with a fluidized bed that has two main stages: 1) one determines the time for cooling particles to the technologically necessary temperature t_f^* using Eqs. (6)–(10); 2) with Eq. (14), the final material temperature t_f is determined based on the conditions: $t_f \leq t_f^*$, $\tau_{cool} \leq \tau_{heat}$, $\tau_{cool} \leq (x/u_{sp})$.

Experimental studies on the cooling of granular superphosphate were carried out in devices with a cross-section of 50×100 mm and 150×300 mm. The polydisperse mixture consisted of granules 0.1–5 mm in size with a form factor of 0.85.

The source material, heated to a temperature of 90–95 °C, was fed to the upper shelf by a belt feeder. A high-pressure fan sucked in air through the apparatus. A small fraction of the material carried out by the ascending air flow was trapped in the cyclone filter. To establish the mechanism and characteristics of the gas-dispersed flow motion, one used filming under stroboscopic illumination at a frequency of 32 frames per second through the transparent walls of the apparatus. The temperature regime in the working volume of the apparatus was controlled by chromel and copel thermocouples with open junctions using a self-recording potentiometer with an accuracy of 0.5 °C.

As a criterion for assessing the cooling degree of the product in the cooler, a cooling coefficient was used, which is the ratio of the removed heat to the amount of heat that is removed when the material is completely cooled to the initial temperature of the cooling air:

$$K_{cool} = \frac{Q_{act}}{Q_{ful}} = \frac{t_{gi} - t_{gf}}{t_{gi} - t_{ai}}, \tag{15}$$

where t_{gi}, t_{gf}, t_{ai} – respectively, the initial, final temperature of the granules and the initial temperature of the cooling air, °C.

4 Results

Shelf contact elements differ from the gas distribution grids of apparatuses with a fluidized bed by the presence of unloading space between the side of the perforated shelf and the apparatus wall (Fig. 1 a). The unloading space width is expressed by the ratio l/B, where l is the distance between the shelf side and the apparatus wall, and B is the length of the apparatus side section. By varying the l/B ratio from 0.5 to 0.15 and a total area of the openings in the shelf from 5% to 30%, it is possible to influence the nature of the airflow distribution between the unloading space and the openings of the shelf, and therefore the fluidizing conditions of granules on a perforated shelf.

At $l/B = 0.5$ granules move along the surface of the inclined shelf in the form of a rapidly slipping layer at a speed of 0.2–0.3 m/s. Airflow aerodynamic forces do not provide sufficient resistance to the movement of particles and so the bulk of the material moves in the form of a thin layer on the surface of the shelf. Further its motion stops at the wall of the apparatus and the product is removed from the layer through the

unloading space due to gravitational forces. Therefore, this way of particle movement was called the regime of the "gravitationally falling layer". The porosity of such a layer reaches 0.8–0.9, and the concentration of material particles in it is 20–30 kg/m^3.

When the ratio decreases to $l/B = 0.3$ the aerodynamic force of the air flow passing through the unloading space increases and the fluidization process of the particles starts. The porosity of this layer decreases to 0.7–0.75, and the concentration of material particles, respectively, increases to 80–100 kg/m^3. At $l/B = 0.2$, a fluidized bed begins its formation.

At $l/B = 0.15$, the hydrodynamic regime of the "fluidized bed" fulfills itself. At the same time, the granules move along the surface of the inclined shelf in the form of a dense layer blown by the air flow, and in the zone above the unloading space, in the form of a suspended, intensively circulating layer. In this case, the concentration of solid particles increases to 160–280 kg/m^3, the porosity of the layer is 0.6–0.65; the velocity of particles moving on the surface of the shelf reaches 0.05–0.15 m/s.

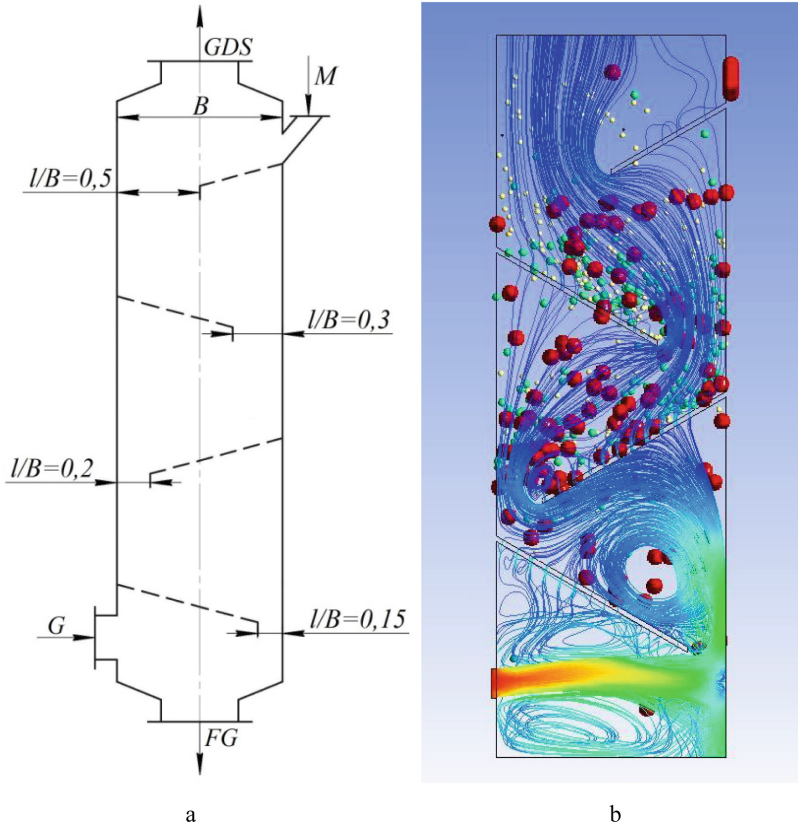a   b

Fig. 1. Multistage shelf cooler circuit (a) and visualization of flows in the shelf apparatus (b): *M* – raw material (mineral fertilizer granules); *G* – gas; *GDS* – gas-dispersed substance; *FG* – finished granules.

Figure 1, b presents a visual picture of the flows in the shelf apparatus, implemented in the software product "Ansys CFX". Flow modeling confirms the real picture of motion hydrodynamics of the gas-dispersed flow, namely, the turbulence intensity of the fluidized bed increases from the upper to the lower shelf. On the two upper shelves, the main fraction is removed into the separation space (shown in Fig. 1, b by yellow dots). On the third and fourth shelves, granules of the commercial size are fluidized (it is shown in Fig. 1, b by green and red dots).

Cooling process efficiency of granular fertilizers was studied by installing inclined shelf at 25° in the apparatus with a live section from 5% to 30% with a change in the l/B ratio ranging from $l/B = 1$ (there is no shelf as in a pneumatic tube type apparatus) up to $l/B = 0$ (the shelf covers the section of the apparatus completely as in the apparatus with the fluidized bed).

As it follows from the curves presented in Fig. 2, with a decrease in the width of the unloading space, the cooling coefficient increases to $l/B = 0.5$ at first, then its growth slows down and remains almost unchanged at $l/B = 0.3–0.5$.
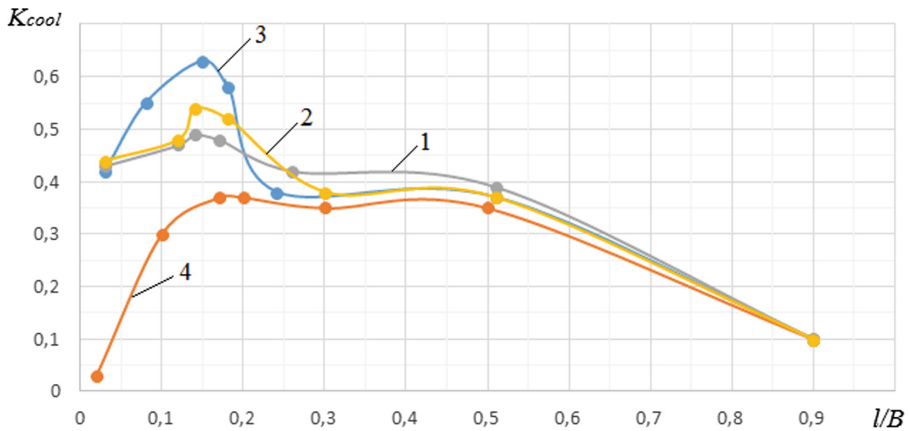

Fig. 2. Dependence of the cooling degree on the width of the unloading space: 1–4 – live section of the shelf, 5%, 10%, 15%, and 30% respectively. The used material is a polydisperse mixture of superphosphate.

With a further decrease in the width of the unloading space, the cooling degree of the material on a shelf with a live section of 15% increases significantly and reaches a maximum at $l/B = 0.15$. At the indicated design parameters, the hydrodynamic regime of the fluidized bed fulfills itself, wherein the granules are intensively cooled to a temperature of 40–45 °C.

Test results of superphosphate cooling are presented in Table 1.

A shelf cooler provides the same cooling coefficient value as the typical cooler of the fluidized bed but it operates at a specific cooling airflow rate that is 30–50% lower.

Table 1. Test results of cooling granular superphosphate.

Apparatus type	Cooling coefficient, K_{cool}	Air velocity, m/s	Airflow rate, m³/kg	Hydraulic resistance, kPa	Granule temperature t_{gi}, °C	Granule temperature t_{gf}, °C
Shelf type (one shelf)	0.4–0.5	3.5–3.7	0.6	0.1	90	55–65
Shelf type (two shelves)	0.6–0.65	3.3	0.55	0.25	90	45–48
Shelf type (three shelves)	0.7–0.75	2.7	0.45	0.4–0.45	90	38–40
Pneumatic tube	0.4	3.7	0.62	0.15	90	60
Fluidized bed	0.72	1.3	1.1	1.8–2.1	65	35

5   Conclusions

Promising the design of a multistage shelf cooler and its advantages are justified. Using physical modeling it is proved that various hydrodynamic regimes of suspended granules are implemented on the perforated inclined shelves along the height of the apparatus, namely, the "gravitationally falling layer" regime on the upper shelf and the "fluidized bed" mode on the lower one.

It is shown that, along with partial cooling, a fine fraction is carried out by the air flow on the upper shelf, and a commercial granule is completely cooled on the lower ones. A mathematical model of the cooling granules kinetics in a fluidized bed has been developed, which makes it possible to optimize calculations of the cooling process efficiency. Experimental studies have proved the effectiveness of a shelf cooler, which allows cooling mineral fertilizer granules to a temperature of 40–45 °C with specific cooling air consumption of 0.45–0.6 m³/kg.

References

1. Fruchtbaum, J.: Bulk Materials Handling Handbook. Springer, USA (2013)
2. Gongora-Leyva, E., Ruiz-Chavarria, G., Columbie-Navarro, A., Retirado-Mediacejas, Y.: The cooling of a granular material in a rotating horizontal cylinder. In: Experimental and Computational Fluid Mechanics, pp. 197–205. Springer, Switzerland (2014)

3. Tasaki, T., Urakawa, N., Amada, K., Mukawa, S., Kudo, K.: Development of a cooling technology for LD-ORP slag at nagoya works. Nippon Steel Sumitomo Metal Tech. Rep. **109**, 155–159 (2015)
4. Hlosta, J., Žurovec, D., Rozbroj, J., Ramírez-Gómez, A., Necas, J., Zegzulka, J.: Analysis and optimization of material flow inside the system of rotary coolers and intake pipeline via discrete element method modelling. Energies **11**(18), 1849 (2018)
5. Watson, R.J., Thorpe, R.B., Davidson, J.F.: Vertical plug-flow pneumatic conveying from a fluidized bed. Powder Technol. **224**, 155–161 (2012)
6. Hall, S.M.: Pneumatic conveying. In: Rules of Thumb for Chemical Engineers (Sixth Edition), pp. 173–185. Elsevier (2018)
7. Singh, R.I., Ghule, K.: Design, development, experimental and CFD analysis of a prototype fluidized bed stripper ash cooler. Appl. Therm. Eng. **107**, 1077–1090 (2016)
8. Zbigniew, R., Kolasinski, P., Zbigniew, G.: Effect of operating conditions on performance of silica gel-water air-fluidized desiccant cooler. In: International Conference on Advances in Energy Systems and Environmental Engineering (ASEE), E3S Web of Conferences, vol. 22, 1017, UNSP 00146 (2019)
9. Zbigniew, R., Kolasinski, P., Przemyslaw, B.: The influence of operating parameters on adsorption/desorption characteristics and performance of the fluidized desiccant cooler. Energies **11**(7), 1597 (2018)
10. Katz, V., Katz, S.: Cooling of granules in vibrating, suspended bed: engineering simulation. Modern Mech. Eng. **6**, 76–90 (2016)
11. Yang, L., Zhan, W.: New concept for ADS spallation target: gravity-driven dense granular flow target. Technol. Sci. **58**(10), 1705–1711 (2015)
12. Yukhymenko, M., Ostroha, R., Litvinenko, A., Bocko, J.: Estimation of gas flow dustiness in the main pipelines of booster compressor stations. IOP Conf. Ser. Mater. Sci. Eng. **233**, 012026 (2017)
13. Liaposchenko, O., Pavlenko, I., Nastenko, O.: The model of crossed movement and gas-liquid flow interaction with captured liquid film in the inertial-filtering separation channels. Sep. Purif. Technol. **173**, 240–243 (2017). https://doi.org/10.1016/j.seppur.2016.08.042
14. Pavlenko, I., Liaposhchenko, A., Ochowiak, M., Demyanenko, M.: Solving the stationary hydroaeroelasticity problem for dynamic deflection elements of separation devices. Vibrat. Phys. Syst. **29**, 2018026 (2018)
15. Kirsanov, V.A., Kirsanov, P.V.: Effect of structural parameters of cascade elements on effectiveness of pneumatic classification. Chem. Pet. Eng. **49**(11–12), 707–711 (2014)
16. Yukhymenko, M., Ostroha, R., Artyukhov, A.: Hydrodynamic and kinetic processes of the mineral fertilizer granules encapsulating in the multistage device with suspended layer. Eastern-Euro. J. Enterprise Technol. **6**(84), 22–28 (2016)
17. Ostroha, R., Yukhymenko, M., Lytvynenko, A., Bocko, J., Pavlenko, I.: Granulation process of the organic suspension: fluidized bed temperature influence on the kinetics of the granule formation. Lect. Notes Mech. Eng. **F2**, 463–471 (2019). https://doi.org/10.1007/978-3-319-93587-4_48

Substantiation of Energy Parameters
of a Continuous-Action Vibroextractor
for a Solid-Liquid System

Volodymyr Zavialov[(✉)] , Taras Mysiura , Nataliia Popova ,
Yuliia Zaporozhets , and Valentyn Chornyi

National University of Food Technologies of Ukraine, 68, Volodymyrska Street,
Kiev 01601, Ukraine
zavialov@nuft.edu.ua

Abstract. The results of studies on energy consumption for the process of extracting target components with continuous vibration extraction in a solid-liquid system with a small difference in phase densities are presented. The influence of low-frequency mechanical oscillations on energy consumption is substantiated and regularities of their change from the mode parameters of the process are established. It is established that the power required to perform vibration mixing is determined by the fictitious force in the oscillatory motion and the resistance created by the viscous friction of the mixing device in the working environment. Taking into account the fictitious component of the vibrating mixing system, the equation of total energy consumption for the continuous vibration extraction process is obtained. For the interpretation of the obtained experimental dependencies, the energy consumption by the vibration mixing devices was calculated. It has been shown that vibration mixing allows for the efficient use of the energy invested in a unit of work volume, evenly distributing it in the cross-section of the apparatus.

Keywords: Vibroextraction · Mathematical model · Hydrodynamics · Mass transfer · Diffusion · Pulsating flow

1 Introduction

Development of a new high-efficiency solid-phase extraction apparatus for systems with a small difference in phase densities fully reflects one of the main topical directions of improving the production base of processing industries and orientates to the search for new energy-saving methods for the intensification of technological processes. This is especially true of the problem of the most complete extraction of the target components from plant raw materials, including waste recycling. Thus, apparatus that use the traditional principles of the organization of the counterflow phase for the processing of small fractional raw materials in the food, pharmaceutical, and chemical industries were not workable or ineffective due to the effect of shielding particles between themselves, resulting from the low porosity of the compressed layer of the solid phase by working transport devices. For these purposes, the most promising was

the apparatus based on the use of low-frequency mechanical oscillations with the new principle of counterflow phase separation with the help of vibration transport plates of special design, which do not cause compression and provide proper porosity of the raw material layer, regardless of the fraction of solids [1–6].

At the same time, vibration extraction is a relatively new technological process. The widespread industrial use of this type of apparatus is hampered by a number of unexplained important issues related to the theory and practice of the process, including the insufficient study of energy consumption in the process.

Thus, despite the advantages and interest of industry in vibration extraction technologies for solid-liquid systems with small phase density differences, purposeful design and optimization of the vibration extractor mode parameters are impossible without deepening the fundamental ideas about their energy-consuming characteristics. Therefore, the task was to substantiate the influence of low-frequency mechanical oscillations generated by the drive system on the energy consumption in the conditions of vibration extraction of raw materials and to establish the regularities of its change depending on the design and mode parameters of the apparatus.

2   Literature Review

Regarding the comparison of the energy consumption of the process by mixing in other ways, such as those used in traditional extractors - mechanical rotation method, the following should be noted. Many years of experience in the application and research of pulsation and vibration mass transfer equipment in the chemical industry by scientists S.M. Karpacheva, I.Ya. Gorodetsky, A.A. Vasin, V.M. Olevsky [1] and their employees proved that the energy consumption of pulsation and vibration of the working environment per unit of production are than other devices with additional power supply or close to them [2]. This is explained by the fact that the pulsator or vibrator motor consumes 0.25–1 kW and is not noticeable for large devices [7]. In addition, in this case, a continuous vibration extraction uses a balanced vibration system with a relatively small amplitude and oscillation frequency. Consequently, the continuous extraction equipment created as a result of the conducted research is competitive in comparison with other, similarly used equipment, in all indicators of its work [1].

3   Research Methodology

Research methods include experimental and analytical modeling. The calculated equations of energy consumption during vibration extraction were obtained by methods based on classical provisions of the theory of mathematical modeling.

The rotation speed of the motor shaft and the oscillations of the vibration transport system within 10 Hz were carried out by an autotransformer. The power required to perform work during vibration mixing was determined by the electrical method by the difference of power in the conditions of working (with the working environment) and

idle (without working environment) movements of the vibrating system and taking into account the losses on the active resistance of the motor drive by the equation

$$N = N_w - N_i - \left(I_w^2 - I_i^2\right)R, \tag{1}$$

where N—total power required to perform mixing work, W; I_w, N_w—respectively the electric current and power required to perform the work during the work movements, A, W; I_i, N_i—respectively the electric current and power required to perform idle motions, A, W; R—active resistance of the drive motor of the apparatus, Ohm.

Changing the oscillation parameters of the vibrating mixing system, the dependence of the specific power during vibroextraction on the Reynolds criterion was established.

Experimental data processing and calculations were performed with the use of modern integrated systems MathCAD, OriginPro 8.6 and others.

4   Results

The advantages of vibration mixing in combination with vibration transportation are achieved by the improved realization of pulsating flows of the working environment in the flow speed form around the contact surface of the phases. In particular, vibration mixing can increase the capacity that effectively fits into the unit of the mixing volume, evenly distributing it in the cross-section of the apparatus of interest in creating a compact high-power single extraction apparatus. Therefore, determining the efficiency of process-intensifying devices needs to compare the process acceleration with the energy consumption of that intensification. It is known that mixing energy is expended on overcoming the fictitious forces arising from the reciprocating movement of moving parts; for lifting plates and rods, parts and moving parts crank rod mechanism, etc.

4.1   Design Features of the Continuous Vibroextractor

The studies were performed on a pilot vibration extractor of continuous action, made according to the scheme in Fig. 1. [3, 4]. The oscillation amplitude varied within $(5\ldots 15)\cdot 10^{-3}$ m, frequency – $(1\ldots 10)$ Hz. The apparatus has a vertical housing 1 with a diameter of 0.3 m, a height of 1.5 m, with devices for input and output of phases. In the working volume of the device, there is a mechanical balanced system of two vertical rods 2 with fixed vibrating plates 3 attached to them. The oscillatory counter-motion of this vibration system with a given frequency and amplitude is provided by vibration drive 5. The type of plates installed in the extractor depends on the type of raw material.

As an example, in Fig. 2. a transport-separation plate is presented [3, 4]. The function of the plate is realized by the difference of hydraulic resistances of the working environment flow through the conical multi-directional transport elements 1 included in the nozzles, as shown in Fig. 2 [8].

The optimum ratio of the geometrical parameters of the transport 1 and filter 2 elements creates the porosity of the solid phase layer, the proper flow rate of the surface of the extractant with a low level of longitudinal mixing in the apparatus.

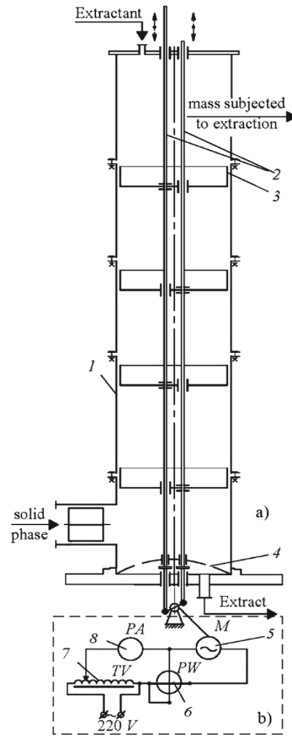**Fig. 1.** a) scheme of a continuous vibration extractor; b) scheme of energy consumption measurements: (1) apparatus body; (2) rods; (3) vibratory transport plate; (4) filter; (5) vibratory drive; (6) wattmeter; (7) autotransformer; (8) ammeter.
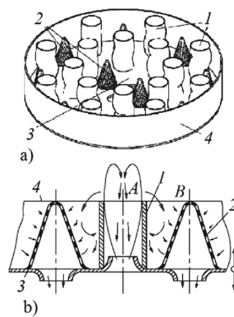

Fig. 2. Transport-separation plate: a) general view of the plate; b) phase separation scheme: (1) pipes; (2) filter elements; (3) plate; (4) board.

The fine fractional solid phase is fed into the apparatus under the last lower plate and in the form of a meal is discharged from the apparatus at the level of the upper one. The extractant is fed to the first top plate and in the extract, the form is removed through filter 2. The oscillation energy of the driven system with controlled frequencies and amplitudes through the vibration transport devices is realized in the working volume of the apparatus.

4.2 Mathematical Description of Energy Consumption During Vibroextraction

It should be assumed that energy is spent on vibration extraction to overcome the fictitious forces arising from the reciprocating movement of the moving parts of the apparatus, to move the vibration transport system up and down and to overcome the resistance of its friction forces to the working environment. Assuming that the vibration transport system is a fixed set of hydraulic resistance through which the flow of the working environment moves alternately in one direction and the other, the total energy consumption for the process can be determined by the equation:

$$N = n(N' + N'')/2 + nN_g + N_I, \tag{2}$$

where n — the number of vibratory plates; N′, N″, Ng, NI—accordingly the energy consumption for overcoming hydraulic resistance when moving the working medium up and down through the transport and filter elements of the plates, through the lateral gap between the plate and the apparatus body and to compensate for the fictitious forces of the moving structural elements of the apparatus. It should be noted that the vibration transport system (a system of two rods with the alternate fixing of plates on them) leads to movement in the counter-phase level by mass of the subsystem, and therefore - provides minimal energy consumption for the movement of these masses.

Appropriate equations can be used to calculate a certain component of energy consumption, taking into account the design and operating parameters of the apparatus [9–11]. For example, to determine the energy consumption to overcome the hydraulic resistance of a plate when it moves up N′ — down N″:

$$N' = n_1 N'_1 + n_2 N'_2, \tag{3}$$

$$N'' = n_1 N''_1 + n_2 N''_2, \tag{4}$$

where n_1, n_2 — respectively, the number of transport and filter elements on one plate; N'_1, N'_2, N''_1, N''_2—respectively, the energy consumption to overcome the hydraulic resistance of one transport and one filter element when moving the plate up and down.

That is, a generalized form of the equation for the calculation of these components will look like:

$$N_1^{'('')} = Q_1^{'('')} \cdot \Delta p_1^{'('')} = w_0 \cdot \Delta p_1^{'('')} \cdot \pi d_{e_i}^2 \Big/ 4, \tag{5}$$

where $\Delta p_i'^{(\prime\prime)} = \rho w_0^2 \left(\lambda_i H_i / d_{e_i} \xi_{in_i} + \xi_{p_i} + \xi_{out_i} \right) / 2$—pressure drop on both sides of the plate; $\xi_{in_i}, \xi_{p_i}, \xi_{out_i}$—coefficients of local hydraulic resistance, respectively, at the inlet of the mixture flow into the plate elements, at its instantaneous expansion and the outlet of the plate elements; $w_0 = 2Af(1-\varepsilon)/\varepsilon$—the initial middle integral velocity of pulsating flows during the period of oscillations generated by the plate elements, which ensure the transportation of the working environment through a certain plate element; A, f—respectively, the amplitude and frequency of oscillation; ε—relative total free cross-section of the plate; $Q_1'^{(\prime\prime)}$—volumetric flow rate of the working environment through the plate element; H, de—respectively, the length of the friction surface of the element through which the working mixture moves and the equivalent diameter of the plate element; λ—the coefficient of friction between the environment and the surface of the plate element.

In Eq. (5), due to the small value of the ratio $\lambda_i H_i / d_{e_i}$, it will be logical to consider it only in the case of calculating the energy consumption when flowing the working environment through a transport element with a branch pipe height H_p and energy consumption for overcoming hydraulic resistance when moving the working environment through the peripheral gap between the plate with the board height H_b and the apparatus body.

Therefore, to account for the inertial component, let us consider the driving system of the vibroextractor, whose kinematic scheme is shown in Fig. 3. Note that the widespread use of connecting rod electromechanical drive mechanisms has been obtained to create vibrating oscillations of the nozzles. In such a drive the connecting rod is the link between the crank and the rod [12–15].
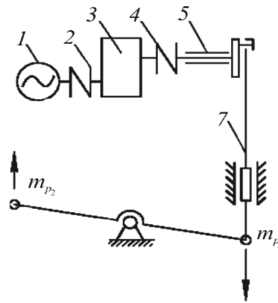

Fig. 3. Scheme of electromechanical crank drive: (1) electric motor; (2), (4) couplings; (3) reducer; (5) eccentric; (6) connecting rod; (7) rod; $mp_1 = mp_2$—respectively, the mass of vibration transport systems moving in counter-phase

The energy consumed by the drive of the vibrating apparatus can be represented in the form of components: static power spent on lifting the moving parts of the plates (nozzles, rods, parts of the crank mechanism, fasteners); the energy expended to overcome fictitious forces arising from the reciprocating movement of moving parts; the energy consumed to overcome the friction forces of the working devices (plates) by interaction with the working environment in the apparatus, and the friction forces in the

elements of the drive parts. Respectively, the force consisting of similar components acts on the apparatus stock. Knowledge of the required power and force acting on the stock is necessary for the correct selection of energy equipment and to calculate the strength of the elements of extraction equipment with oscillating effects in the working volume of the apparatus [1].

So, by analogy [1] the fictitious force of the vibrating mixing system, that is, the inertial component of the energy consumption N_I, must take into account the mass of the plate, stock, the corresponding fasteners of the plates and pushing force from the environment acting on the system immersed in the work environment:

$$P_I = \frac{m_s + m_l}{g \cdot \rho_s} (\rho_s - \rho_l) \cdot \frac{d^2 S}{dt^2}, \tag{6}$$

where ρ_s—density of structural materials, kg/m³; ρ_l—density of the working environment, kg/m³; $d^2 S/dt^2 = -2\pi^2 f^2 A \sin \beta$—acceleration of the moving system of the crank mechanism, moving at an angular speed $dS/dt = \pi A \cos \beta$ (see kinematic scheme in Fig. 3).

Then

$$P_I = \frac{m_s + m_l}{g \cdot \rho_s} (\rho_s - \rho_l) \cdot 2\pi^2 f^2 A \sin \beta. \tag{7}$$

Finally, given the above, we will have:

$$N = \frac{w_0 \pi d^2 n}{8} \cdot \sum P_1'^{(")} + N_g + \frac{m_s + m_l}{g \cdot \rho_s} (\rho_s - \rho_l) \cdot 2\pi^2 f^2 A \sin \beta. \tag{8}$$

where m_s, m_l—respectively, the mass of structural materials and the working environment moving the plate, kg; β—the angle of rotation of the crank mechanism, °; g—free-fall acceleration, m/s².

It should be noted that, for the vibration extractor of continuous action, the requirement of constructive execution of the vibration transport plate is to manufacture and install it in the apparatus body with a minimum gap around the periphery. Therefore, when calculating the energy consumption for such apparatus, it is possible to disregard the component N_g, the energy consumption for overcoming hydraulic resistance when moving the working environment up and down through the lateral gap at the periphery of the plate.

4.3   Investigation of the Influence of Regime Parameters of the Device on Energy Consumption

Investigation of energy consumption for continuous process in the system of kapron crumb – water was performed on the model of the vibrating extractor shown in Fig. 1-a according to the schematic diagram of electrical measurements Fig. 1-b. At the same time, the ratio of liquid and solid phases at a temperature of 293 °K varied from

0.25 to 0.85. The oscillation frequency of the vibration transport system varied within 1–10 Hz; the oscillation amplitude was fixed at values $(5, 10, 15) \cdot 10^{-3}$ m.

For interpretation of the obtained experimental data, the energy consumption by working devices for vibration mixing was calculated.

The results of the experiments were summarized in the form of dependencies of the specific consumption of consumed electricity on the process at different mode parameters of the apparatus operation from the Reynolds pulsation criterion in the coordinates $N/Q = \varphi(\text{Re})$, where Q—volumetric performance of the apparatus in the solid phase, m^3/s (Fig. 4).
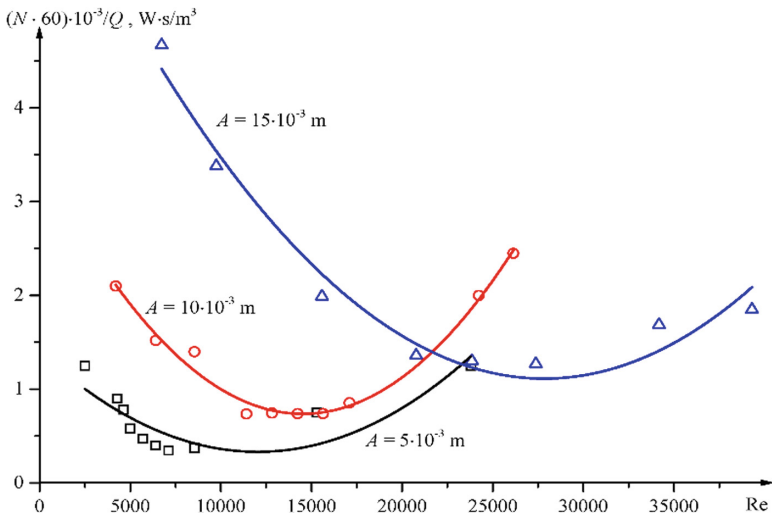

Fig. 4. The dependence of the specific electricity consumption on the oscillation intensity of the vibration transport system in the continuous process of vibration extraction.

The Reynolds pulsation criterion $\text{Re}_p = w_0 d/v$ was calculated by the value of the initial middle integral and average cross-section of the transport element (nozzle) of the pulsating flow rate $w_0 = 2Af(1-\varepsilon)/\varepsilon$, where ε—the total cross-section, which is the ratio of the area of the plate holes and the gap along the periphery (in the area of the plate installation) to the cross-sectional area of the apparatus; A, f—respectively, the amplitude and frequency of vibration of the vibration transport system. That is $\text{Re}_p = 4A^2 f(1-\varepsilon)/(v\varepsilon)$.

It is established that the oscillation amplitude of the vibration system has the most significant influence on energy consumption during transportation and phase separation. Also, the nature of the curves leads to the conclusion that the process can be optimized.

In other words, of the three given oscillation amplitudes, the most favorable is the amplitude $10 \cdot 10^{-3}$ m. Also, the minimum energy consumption for all three graphs also determines the optimal oscillation frequency.

Thus, for amplitude $5 \cdot 10^{-3}$ m, the optimal oscillation intensity is 40 m/s, which corresponds to a frequency of 8 Hz; for amplitude $10 \cdot 10^{-3}$ m, the optimal oscillation intensity is—30 m/s at a frequency of 3 Hz; for amplitude $15 \cdot 10^{-3}$ m, the intensity is – 43 m/s at a frequency of 2.7 Hz.

The results of the experiments confirm that continuous counterflow vibration phase separation provides an increase in the amount of energy that is effectively invested in a unit of working volume - due to its uniform distribution in the cross-section of the apparatus.

5 Conclusions

The advantage of the vibration mixing method in the conditions of the process of solid-phase extraction in comparison with mixing by the currently most promising turbine stirrer is achieved due to the best mass transfer and energy realization of pulsating flows of the working environment.

The vibration mixing and the pulsating flows of the working environment generated in the holes of the transport elements create optimal hydrodynamic conditions for intensive mass transfer and contribute to the efficient investment of energy in the unit of the mixing volume, evenly distributing it in the cross-section of the apparatus of interest in the creation of a compact mass transfer apparatus of a single high power.

The power required to perform vibration mixing is determined by the fictitious force of the oscillating motion and the resistance created by the viscous friction of the mixing device in the viscous work environment.

The optimal mode parameters for a continuous process that ensure proper phase separation with low energy consumption are the amplitude of oscillations from $10 \cdot 10^{-3}$ to $15 \cdot 10^{-3}$ m at a frequency of up to 4 Hz, depending on the properties of the solid phase.

The realization of the obtained results makes it possible to develop a method of engineering calculation of the energy characteristics of continuous vibration extraction in a solid-liquid system with a small difference of phase densities for the design of appropriate industrial equipment in the pharmaceutical, food and chemical industries.

References

1. Gorodeckij, I., Vasin, A., Olevskij, V., Lupanov, P.: Vibratory Mass Transfer Apparatus. Chemistry, Moscow (1980). [in Russian]
2. Beloglazov, I.: Solid Phase Extractors. Chemistry, Leningrad (1985). [in Russian]
3. Zavialov, V., Misyura, T., Popova, N., Zaporozhets, Y., Dekanskiy, V.: Investigation of hydrodynamics during continuous vibroextraction in a liquid–solid body system. In: Ivanov, V., et al. (eds.) Advances in Design, Simulation and Manufacturing. DSMIE-2018. LNME, pp. 524–535 (2019). https://doi.org/10.1007/978-3-319-93587-4_55
4. Zavialov, V., Mysiura, T., Popova, N., Sukmanov, V., Chornyi, V.: Regularities of solid-phase continuous vibration extraction and prospects for its industrial use. In: Ivanov, V., et al. (eds.) Advances in Design, Simulation and Manufacturing II. DSMIE-2019. LNME, pp. 920–930 (2020). https://doi.org/10.1007/978-3-030-22365-6_92

5. Dyachok, V., Dyachok, R., Gaiduchok, O., Ilkiv, N.: Mathematical model of mass transfer from lamina of the leaf into extractant. Chem. Chem. Technol. **9**(1), 107–110 (2015)
6. Cvetković, An.-M., Jurina, T., Valinger, D., et al.: The estimation of kinetic parameters of the solid-liquid extraction process of the lavender flower (Lavandula x hybrida L.) Croatian J. Food Sci. Technol. **10**(1), 64–72 (2018)
7. Karpacheva, S., Raginskiy, L., Horhorina, L.: The use of pulsation technology for the intensification of chemical production. J. Appl. Chem. **9** (1986). (in Russian)
8. Popova, N., Zavialov, V., Misyura, T., et al.: Development of mathematical models of external mass exchange under conditions of vibroextraction from vegetable raw materials. Chem. Chem. Technol. **9**(3), 367–374 (2015)
9. Promtov, M., Stepanov, A., Aleshin, A., Kolesnikova, M.: Intensification of hemic acid extraction by pulse flow of vermicompost and sapropel slurries. Chem. Eng. Res. Des. **108**, 217–221 (2016)
10. Brunet, L., Prat, L., Wongkittipong, R., Gourdon, C., Casamatta, G., Damronglerd, S.: A new pulsation policy in a disk and doughnut pulsed column applied to solid-liquid extraction of andrographolide from plants. Chem. Eng. Technol. **28**(1), 110–118 (2005)
11. Rakotondramasy-Rabesiaka, L., Havet, J.L., Porte, C., Fauduet, H.: Solid–liquid extraction of protopine from Fumaria officinalis L.–kinetic modelling of influential parameters. Ind. Crops Prod. **29**(2/3), 516–523 (2009)
12. Joshi, M.: Performance Monitoring System for Electromagnetic Vibrating Feeders of Coal Handling Plant. Plant Maintenance Resource Center, M-News Edition 27 (2002)
13. Despotovic, Z.: Mathematical model of electromagnetic vibratory actuator. In: Proceedings of the XII International Symposium of the Power Electronics 2003 N. Sad 5-7, XI vol. 3, no. 2, pp 1–5 (2003)
14. Nguyen, V., Nguye, Ph, Hoang, M.: Parametric torsional vibration of mechanical drive systems with non-uniform transmission mechanisms. Technische mechanik **28**(3–4), 310–323 (2007)
15. Dimitrov, K., Pradal, D., Vauchel, P., Nikov, I., Dhulster, P.: Modeling and optimization of extraction and energy consumption during ultrasound-assisted extraction of antioxidant polyphenols from pomegranate peels. Environ. Prog. Sustain. Energy **38**(1) (2019)

Heat and Mass Transfer

Development of the Typical Design
of the High-Pressure Stage of a Steam Turbine

Olena Avdieieva(✉) , Oleksandr Usatyi , and Oleksii Vodka

National Technical University "Kharkiv Polytechnic Institute",
2, Kyrpychova Street, Kharkiv 61002, Ukraine
o.avdieieva@gmail.com

Abstract. The article describes the creation of a methodology for the optimal high-efficiency flowing parts of the first compartments of powerful steam turbines, which consists of typical stages. The use of typical stages when creating the flow part of a high-pressure cylinder can significantly reduce the cost of manufacturing a steam turbine cylinder. A method for the formulation of the optimization problem is proposed. It ensures the finding of profiles for the nozzle and, accordingly, rotor blades of the same shape with minimal losses on the example of a 310 MW turbine. As a result of the optimization of the first compartment of the high-pressure cylinder, the optimal flow part of the compartment was obtained. Based on which the plan of the numerical experiment was constructed with 6 variable profile parameters. The calculations were carried out using 3D modeling of the working medium flow. Based on the calculation results, the optimal profile was obtained, the profile loss of which is 2.35% less than that of the base one.

Keywords: Steam turbine · High-pressure cylinder · Optimization · CFD · AxStream · Plan of the numerical experiment

1 Introduction

The technological progress in the energy sector at the present stage of development leads to the fact that the moral aging of the operating equipment is ahead of its physical aging. In addition, modern requirements for the operation of turbines, especially their maneuverability, have significantly changed. The assembly units and parts of the turbines were designed 25–30 years ago and their designs don't meet modern operation and production requirements. In order to reduce the cost and increase the competitiveness of new turbine models and modernized turbines, the construction of their structures should be based on the use of unified assembly units with optimal efficiency parameters and with the possibility of their operation in both pure condensation and heating modes. One of the basic assembly units is the turbine stage. In cylinders of high pressure (CHP), it is a common practice to have constant profile along the height of blades of nozzles. It allows setting the task of creating a typical turbine power with optimal performance characteristics.

2   Literature Review

Designing turbine elements at the modern level requires complex mathematical models. Such models have been constructed in [1–10]. Many works use methods of computational hydrodynamics to build models of the flow of the working medium [1, 2, 7]. Other works are based on the idea of optimizing parameters using simplified flow models [3–6, 8–10]. Despite the difference in approaches and projected objects, an unambiguous method for designing optimal high-pressure cylinders has not yet been developed [11–14]. Therefore, the ideas and methods presented in this work are relevant. The task of creating an optimal design of a typical stage, especially for the first compartment of the flow path (FP), is quite relevant not only in terms of lowering the cost of construction, but also taking into account the fact that the first compartment of the CHP has a very significant contribution to the total power of the turbine. The maximum (optional) value of the steam consumption that flows through the first compartment requires the most efficient use of this potential, which is possible only with typical turbine stages with the highest efficiency.

3   Research Methodology

It is well-known that the internal dissipation of energy in the FP axial turbine consists of energy loss in nozzles and blades, loss with the initial velocity of the working medium and various additional losses. The values of the energy loss coefficients in the nozzle and blade cascades are used to estimate the actual flow rates of the working fluid at the exit from the corresponding cascades. Total losses in the nozzle and blade cascades consist of profile and secondary losses, which respectively represent functions of a number of geometric characteristics of turbine profiles and cascades, as well as gas-dynamic parameters of the flow of the working fluid. For example, the coefficient of profile losses ζ_{pr} in the general form can be expressed as follows:

$$\zeta_{pr} = \zeta\big(\beta_{1g}, \beta_1, \beta_{2e}, M_{w_{2t}}, \bar{t}, \mathrm{Re}, C_{\max}, \delta, \chi, Y, E\big), \tag{1}$$

Here β_{1g} is the geometric (skeletal, metallic) angle of the nozzle entrance and blade profiles; β_1 is the angle of the steam flow to the grid; β_{2e} is the effective angle of the nozzle and blade cascades output; $M_{W_{2t}}$ – the theoretical Mach number at the exit from the nozzle and blade cascades; $\bar{t}$ – the relative step of the grid; Re – the number of Reynolds flow of the working medium; $C_{\max}$ – maximum thickness of the profile; δ – the thickness of the initial edge of the profile; χ – degree of uneven flow at the entrance to the grid; Y – the degree of non-stationary flow flowing on the grid; E – initial degree of turbulence of the flow. Thus, it is obvious that to create typical turbine stages with optimal efficiency indicators it is necessary to have not only the optimal unified form of the profiles of the turbine nozzle and blade cascades but also the optimal value of the parameters that characterize the meridional circuits of the FP of the first compartment of the CHP, as well as the corresponding characteristics of the nozzle and blade profiles and the working medium at the entrance and exit of the cascades. Therefore, before

solving the problem of finding the optimal unified form of the profile, it is necessary to obtain optimal values of the meridional contours FP of the first compartment of the CHP, as well as the parameters of the turbine nozzle and blade cascades and the parameters of the working medium and methods for the optimal design of multi-stage before and behind the cascade. The latter problem can be solved with the use of methodologies FP [11].

4 Results

4.1 Evaluation of the Efficiency of the FP Prototype and Optimization of the First Compartment of the CHP

For a comparative estimation of the FP efficiency of the CHP prototype and its optimal variant in the first stage of work, it is necessary to determine the efficiency of the prototype compartment. For this purpose, in the first place, the design studies of its characteristics using TOP (TurboOptProject) [11] software have been carried out.

As the initial data for calculating the prototype compartment and its subsequent optimization, the following characteristics have been used. Parameters at the inlet to the compartment (total pressure $P_0^* = 18{,}75$ MPa, total enthalpy and $i_0^* = 3290{,}71$ kJ/kg); steam parameter at the output from the compartment (pressure $P_2 = 6{,}054$ MPa); steam flow rate through the compartment $G_t = 274{,}03$ kg/s; geometry, which characterizes the meridional circuits of the FP of the prototype compartment, the average diameters of the nozzles and blades, as well as the height of their blades, respectively (D_n, D_b, l_n, l_b); the geometric angles of the input and effective angles of the output of nozzles and blades, respectively $(\alpha_{0g}, \beta_{1g}, \alpha_{1e}, \beta_{2e})$; microgeometry of the stages of the compartment (different purpose of the slit, overlap, projections, sealing characteristics, etc.). An analysis of the source data of the prototype compartment showed that it consists of the stages in which the root diameters, the number of nozzles and blades, the geometric (metallic) angles of the input of nozzle and blade profiles, and the effective angles of the outlet of the nozzle and blade cascades, chords and the shape of the profiles in the root are identical for all stages in the compartment. It is known that these features are typical for turbine stages. So, it is being dealt with a compartment consisting of typical turbine stages. The results of the computational study of its effectiveness are given below: the power of the compartment Nc = 71.17 MW; work on the rim of the wheel Luc = 270.862 kJ/kg; the stage heat drop of the compartment $H_{0c} = 322.227$ kJ/kg; internal relative efficiency $\eta_{oi} = 0.8263$;

The analysis of integral performance indicators of the prototype compartment showed that it has a fairly high level of efficiency, taking into account the existence of significant constraints in the form of mandatory use of a typical design of turbine stages. To develop a more efficient (optimal) compartment, which should consist of optimal standard stages, which in turn should be formed from the same high-efficiency nozzle and, accordingly, blades, recruited from profiles that have the optimal aerodynamic shape of the circles, it is necessary to correctly formulate an optimization problem setting. At the same time, the characteristics inherent in the typical steps should be taken into account:

1. the geometric angles of the input (α_{0g}, β_{1g}) and the effective angles of the output (α_{1e}, β_{2e}) at the root of the nozzle and, correspondingly, the blades should be the same at the steps of the compartment;
2. identical nozzle and corresponding blades profiles for all stages, both at the root diameter and throughout the length of the blades.

Optimization of the first compartment, which consists of typical turbine degrees, was carried out in the TOP software. The formation of the optimization problem has been performed in accordance with Fig. 1.
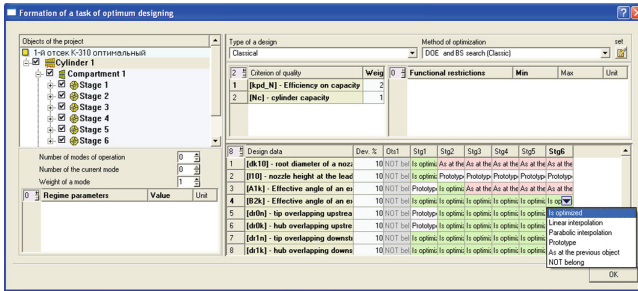

Fig. 1. The dialog for forming the optimization task.

Figure 1 shows that during optimization conditions for the simultaneous unification of the design of 6 pressure stages is set. The statement of the optimization problem provided the determination of optimal values of root diameters, effective angles of nozzle output α_{1e}, and, respectively, blades β_{2e}, nozzle and blade heights, whose values have been automatically calculated using an algorithm of the overkill value, the height of the first stage blade along the input edge and the nozzle root diameter of the first compartment.

For example, in order to find the optimal FP variant of the first compartment to provide identical root diameters at the entrance to the nozzle cascade (NC) for all compartment steps, the following conditions have been set: the root diameter of the first stage has been selected as the base size, with the automatic forming of the flow path, and for the remaining stages of the first compartment, this parameter has been taken equal to the value in the previous stage. So, for the second stage, the root diameter at the entrance to the NC is set equal to the root diameter of the NC of the first stage. For the third stage, the root diameter of the NC is set equal to the root diameter of the NC of the second stage, which is equal to the root diameter of the first stage. Thus, by passing successively all the steps of the compartment and fulfilling this condition, we obtain for each FP structure of the first compartment that is automatically generated the equality of the root diameters at the input to the NC for all stages of the first compartment. To control the change of effective exit angles to the root for the NC α_{1e} as the optimized basic parameter has been chosen α_{1e} in the second stage (Fig. 1). The effective nozzle exit angle of the first stage of pressure is used to ensure the equality of the vapor flow through the compartment for all FP variants that are generated during the search for the

optimal design of the FP compartment. Thus, the value α_{1e} of the algorithm in the process of finding the optimal solution for the stages of the first compartment is given the same starting from the second stage of pressure. In the process of controlling the effective angles of the exit at the root (β_{2e}) for all blades cascades (BC) in the process of forming the geometry of various variants of the first-phase FP, a similar algorithm have been used, starting with the first stage of pressure, which ensured the equality of these parameters for all stages of the FP of the first compartment. Thus, by changing the value β_{2e} of the first stage in the process of optimization it is automatically assigned this value to all BC of the first compartment. Taking into account that in the process of optimization a one-dimensional mathematical model has been used "by the mean radius", all values of the effective angles at the root $(\alpha_{1e}, \beta_{2e})$ have been calculated for each stage on the mean radius, taking into account the law of twist $C_u r =$ const. To find the optimal meridional contours of the FP of the first compartment, appropriate values of the overlaps at the root and periphery between all adjacent shoulder blades of the FP compartment is used. It varied in the process of optimization along with the values of the first stage nozzle height along the input edge. In addition, in the process of evaluating the efficiency of the blades, internal optimization of the input geometric (metallic, skeletal) angle of the blades profiles on the mean radius of the turbine stages has been used. As a result of the optimization of the first compartment of a high-power steam turbine, an efficiency increase of 0.56% to 83.19% and a power on 0.57 MW to 71.74 MW have been achieved. A comparison of the basic parameters that provided greater efficiency of the optimal version of the compartment, consisting of typical turbine stages, is given in Table 1.

Table 1. Comparison of the basic design parameters.

№	Var	D_n, m	D_b, mm	I_n, mm	I_b, mm	α_{1e}, deg.	β_{2e}, deg.	β_{1g} deg.
1	Prot	1.004	1.005	22.0	25.0	13.44	21.18	33.61
	Opt	0.989	0.989	22.0	25.5	14.51	21.28	35.76
2	Prot	1.008	1.008	25.5	28.5	13.69	21.23	33.62
	Opt	0.993	0.993	25.5	28.5	13.30	21.22	33.06
3	Prot	1.012	1.012	29.5	32.5	13.76	21.28	33.61
	Opt	0.996	0.996	30.0	33.5	13.36	21.12	33.44
4	Prot	1.016	1.017	34.0	37.0	13.81	21.35	33.61
	Opt	1.001	1.002	34.5	37.0	13.42	21.05	33.31
5	Prot	1.024	1.025	41.5	44.5	13.81	21.35	33.62
	Opt	1.008	1.008	42.0	45.5	13.52	20.89	34.46
6	Prot	1.03	1.031	48.0	51.0	13.81	21.35	33.62
	Opt	1.014	1.015	49.0	52.5	13.61	20.76	34.79

Some important indicators of the typical turbine stages of the prototype compartment and the optimal compartment option are shown in Figs. 2, 3, 4, 5, 6, 7, 8 and 9. The data from Table 1 and the following figures will be analyzed to identify the reasons for the improvement in the efficiency indicators of the optimal FP variant of the

first compartment. In both versions of the compartments, all turbine stages are pulsed (active), in which most of the existing thermal transition of the stages are triggered in the nozzle cascade. Therefore, in the optimum variant of the FP compartment, the first stage of the pressure has a lower available heat loss compared to the prototype compartment (Fig. 2) and larger squares of the nozzle velocity coefficients (φ^2) (Fig. 6) and the blades (ψ^2) (Fig. 7). In spite of this, the stages have less efficiency and power (Figs. 3, 4). This suggests that there are quite good reasons that led to a drop in the efficiency and power of the first stage of the optimal compartment option. In the first place, the decrease in efficiency has been influenced by a significant increase in losses from leakages in the radial over bandgap (Fig. 8) and in the root gaps (Fig. 9). The aforementioned increase in the leakage of steam in the gap is due to the growth of the reactivity stages of the first stage of the optimal variant compared with the prototype compartment. If in the prototype compartment the levels of reactivity near the root at the medium radius and periphery are respectively 0.6%, 4.5%, and 8.5%, and due to an increase in the effective angle of the nozzle grid near the root to 14.20°. (in the prototype of 13.16°), and the levels of reactivity in the corresponding radii increased to 4.2% at the root, up to 8.0% in the mean radius and up to 8.5% in the periphery. Despite the deterioration in the efficiency of the first stage of the optimal version of the FP, this also has its rationale. First, this deterioration refers to the smallest available heat dissipation in comparison with other stages (Fig. 2), and thus negatively affects a smaller part of the energy supplied. Secondly, given that the first stage is located after a controlling stage that affects the structure of the steam flow that flows from it rather negatively, then causing additional losses due to the flow of the first stage pressure nozzle. By reducing the existing heat dissipation of the first stage, the results are related to the deteriorated conditions of the steam to the lesser part of the energy, which leads to a decrease in the level of total losses of the entire compartment. It should be noted that practically all performance indicators from the second to the sixth stage, except the efficiency of the blades (ψ^2) (Fig. 7), have better values in comparison with the stages of the prototype compartment (Figs. 3, 4, 6, 8, 9). Taking into account that the levels of reactivity from the second to the sixth stage of the optimal variant of the compartment are smaller, and hence the lower levels of heat fluctuations that are triggered in these blades, the levels of the negative influence of the decrease, translated into absolute values of energy losses, practically do not increase in comparison with losses in the blades prototype compartment. Thus, the overall balance of various kinds of losses has led to higher integral performance indicators of the optimal version of the FP compartment compared with the prototype compartment; a positive result has been achieved on the background of a very efficient prototype compartment. Conducted calculations for obtaining optimal geometrical characteristics of the FP compartment, which consist of typical turbine stages, are a mandatory preparatory step before the creation of typical nozzles and blades. Further research in this direction will not touch the nozzle cascades, as today they have achieved a very high level of efficiency. A fairly large number of recent studies in this direction have not found solutions that would significantly improve their effectiveness. Therefore, further research will be devoted to the development of highly efficient standard blades based on a new turbine profile with a highly efficient aerodynamic form.
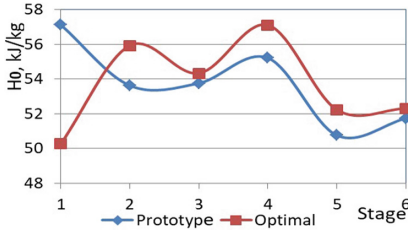
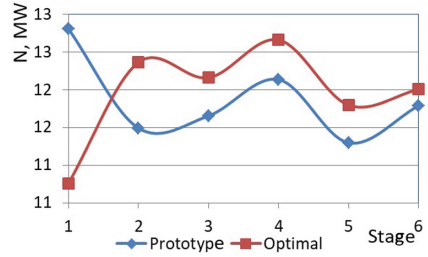**Fig. 2.** Distribution of available heat distances between stages of compartments.

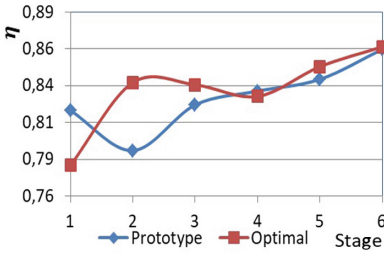**Fig. 3.** Distribution of capacities between stages of compartments.

Fig. 4. Effectiveness of the stages of compartments.
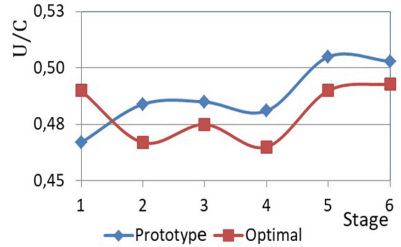

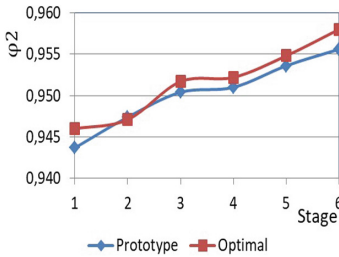**Fig. 5.** The ratio of compartment velocities.

Fig. 6. Squares of velocity coefficients of nozzle cascade compartments.
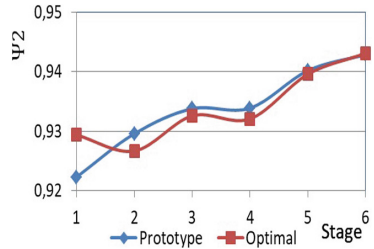

Fig. 7. Squares of velocity coefficients working grids of compartments.
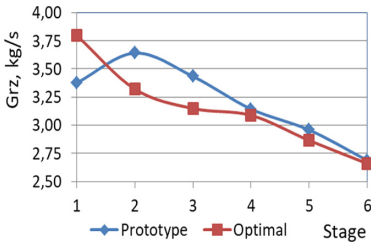
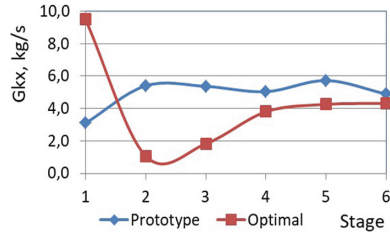**Fig. 8.** Steam leakage in radial over-seal seals.

Fig. 9. Leakage of steam in the root gaps.

4.2   Development of a Typical High-Performance Blade Profile

To create a working blade profile for a typical turbine stage, the following actions have been performed:

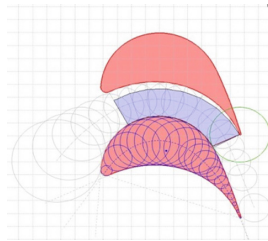1. A base profile and, on its basis, a base blades cascade have been created (Fig. 10).

Fig. 10. Blade based on the basic profile of the blade.

2. Using 3D modeling (ANSYS CFX), the core losses rate of the basic cascade has been determined.
3. To improve the performance of the basic cascade, computational studies have been carried out to optimize the aerodynamic shape of a typical profile, taking the base profile as the initial approximation point. Using the 6-factor Rechtschaffner plan, the plan of the calculated experiment has been formed. For the experiment plan, the following independent parameters have been selected as parameters affecting the efficiency of the turbine nozzle and blade cascades: geometric input angle of the nozzle and blade profile (β_{1g}) geometric output angle of the nozzle and blade profile (β_{2g}) angle of taper of the input edge of the profile (β_{ust}) angle of taper of the original edge (γ_1) angle deflection of the original edge (γ_2) angle of the profile (γ_{otg}). The ranges of changes of these parameters in the process of the numerical experiment in accordance with the plan are given in Table 2. According to each line of the plan, working profiles have been constructed at the root, and then they have

been transferred to conditions that corresponded to the mean radius of one of the steps. In this case, it was the 4th stage of the compartment.

4. Using 3D modeling, the profile losses of all blades have been determined, which have been constructed in accordance with the design of the experiment plan.

The construction of the aerodynamic shape of turbine profiles has been performed in the AxStream software. Based on the base profile, a blade has been created (Table 2). To minimize the amount of CFD calculations during the study, the theory of planning the experiment of the Rechtschaffner has been used with formal macromodels (FMM) (1) method for increasing the accuracy of the created dependencies. In this case, the vector of the observation plan of the numerical experiment has been formed from the squares of the coefficients of the nozzle and blade cascade velocity (ψ^2). The use of the rich six-factor plan of the Rechtschaffner and an additional plan for increasing the accuracy and adequacy of the analytical dependence (FMM) of the form required the conduct of 41 calculations of the efficiency of the blades profiles, which shape has been created in accordance with the plan of the numerical experiment. The research method is based on the numerical simulation of flow processes in turbomachines. For this purpose, a grid of finite element (FE) model is constructed. The FE mesh has been structured. The end elements have the shape of a hexahedron. Its boundaries have been oriented parallel or perpendicular to the lines of flow.

Table 2. The ranges of parameter change in a numerical experiment

Parameter	Min	Prototype	Max
Input geometric profile angle β_{1g}, degree	30.28	34.28	37.28
The original geometric angle of the profile β_{2g}, degree	17.22	18.29	19.22
Profile installation angle β_{inst}, degree	14.0	19	19.0
The sharpening angle of the input edge of the profile γ_1, degree	52.25	55	57.75
The sharpening angle of the output edge of the profile γ_2, degree	5.7	6	6.3
Bending angle of the output edge of the profile γ_b, degree	15.2	16	16.8

All calculations have been performed in two-dimensional CFD formulation. Under the two-dimensional CFD, the formulation is meant a three-dimensional viscous calculation with a mesh grid height in one element. At the same time, the condition of "symmetry" has been set on the upper and lower limits of the calculated area. It models the effect of an infinitely long blade. Such approach allows excluding the influence of endwall losses on the flow profile. At the boundaries of the profile created a thickening of the mesh model. The statement of the optimization problem and methods for its solution are described in detail in [11]. According to the results of the calculations, a working profile has been found, which aerodynamic form has the maximum efficiency ($\psi^2 = 96.758$).To determine the efficiency of the blade, the CFX I-S diagram has been built. The evaluation of the required parameters used to determine the efficiency is performed at a distance of one throat from the original edge. In general, by the nature of

the distribution of the coefficient of profile losses, it is evident that they are 5.59% for the base profile and 3.24% for the optimal. That is, the use of a profile with data geometric characteristics leads to a decrease in losses of 2.35%.

5   Conclusions

The methodology of creating the optimal high-performance FP of the first compartments of power steam turbines, consisting of typical turbine stages, has been developed. The method of formation of an optimization problem setting, which provides finding profiles for the nozzle and correspondingly blades cascades of the same shape, is required for the creation of high-performance typical turbine stages. As a result of the optimization of the first chamber compartment of a high-power steam turbine, an increase in its efficiency has been achieved by 0.56% to 83.19% and power by 0.57 MW to 71.74 MW.

References

1. Yuan, X., Tanuma, T., Zhu, X., Lin, Z., Nomura, D.: A CFD approach to fluid dynamic optimum design of steam turbine stages with stator and rotor blades. Turbomachinery **7**(Parts A, B, and C), 2209–2218 (2010)
2. Verstraete, T., Prinsier, J., Di Sante, A., Della Gatta, S., Cosi, L.: Design optimization of a low pressure steam turbine radial diffuser using an evolutionary algorithm and 3D CFD. In: Proceedings of the ASME Turbo Expo 2012: Turbine Technical Conference and Exposition, Copenhagen, Denmark, pp. 603–613 (2012)
3. Bellucci, J., Rubechini, F., Arnone, A., Arcangeli, L., Maceli, N., Dossena, V.: Optimization of a high-pressure steam turbine stage for a wide flow coefficient range. In: Proceedings of the ASME Turbo Expo 2012: Turbine Technical Conference and Exposition, Copenhagen, Denmark, pp. 615–625 (2012)
4. Zachary, J.: Steam turbine design considerations for ultrasupercritical cycles. In: Proceedings of the ASME Turbo Expo 2010: Power for Land, Sea, and Air, Glasgow, UK, pp. 2171–2179 (2010)
5. Tanuma, T.: Design and analysis for aerodynamic efficiency enhancement of steam turbines. In: Advanced Steam Turbines Modern Power Plants, pp. 109–126. Teikyo University, Tokyo (2017)
6. Tanuma, T.: Development of last-stage long blades for steam turbines. In: Advanced Steam Turbines Modern Power Plants, pp. 279–305. Teikyo University, Tokyo (2017)
7. Jang, H.J., Kang, S.Y., Lee, J.J., Kim, T.S., Park, S.J.: Performance analysis of a multistage ultrasupercritical steam turbine using computational fluid dynamics. Appl. Therm. Eng. **87**, 352–361 (2015)
8. Weidtmann, K., Bühler, P., Braining, E., Haj Ayed, A., Lin, G.: High efficient steam turbine design based on automated design space exploration and optimization techniques. www.euroturbo.eu. Accessed 25 Sep 2019
9. Manassaldi, J.I., Arias, A.M., Scenna, N.J., Mussati, M.C., Mussati, S.F.: A discrete and continuous mathematical model for the optimal synthesis and design of dual pressure heat recovery steam generators coupled to two steam turbines. Energy **103**, 807–823 (2016)

10. Usatyi, O., Avdieieva, O., Maksiuta, D., Tuan, P.: Experience in applying DOE methods to create formal macromodels of characteristics of elements of the flowing part of steam turbines. In: AIP Conference Proceedings, vol. 2047, 020025 (2018)
11. Zhang, C.-W., Li, L.-Y., Zheng, Z.-H.: Numerical simulation of forging process for steam turbine blade. Int. J. Mech. Mechatron. Eng. **17**(3), 48–52 (2017)
12. McBean, I., Havakechian, S., Masserey, P.-A.: The development of long last stage steam Turbine Blades. In. ASME Turbo Expo 2010: Power for Land, Sea and Air, Glasgow, UK, pp. 2245–2256 (2010)
13. Baran, Jolanta: Redesign of steam turbine rotor blades and rotor packages – environmental analysis within systematic eco-design approach. Energy Conv. Manag. **116**, 18–31 (2016)
14. Barbarelli, S., Florio, G., Scornaienchi, N.M.: Developing of a small power turbine recovering energy from low enthalpy steams or waste gases: Design, building and experimental measurements. Thermal Sci. Eng. Prog. **6**, 346–354 (2018)
15. Boiko, A., Govorushchenko, Yu., Usaty, A.: Optimization of the Axial Turbines Flow Paths, Science Publishing Group, New York (2016)

Improvement of the Heat Substation Design for District Heating Supply Systems

Tetiana Babak[1] , Alexey Demirskyy[1] , Gennadii Khavin[1(✉)] ,
and Viktoria Nevludova[2]

[1] National Technical University "KhPI",
2, Kyrpychova Street, Kharkiv 61002, Ukraine
gennadii.khavin@gmail.com
[2] National University of Radioelectronics,
14, Nauky Avenue, Kharkiv 61000, Ukraine

Abstract. New requirements and trends for the design and retrofit of heat substations of the central heating system are formulated. The main differences in the design of the central and individual heat substations are considered. The classification of heat substations for heating and hot water supply depending on the equipment included is given. The strategy of computer-aided design of the central heat substations under conditions of a new tariff policy is presented. The basis of the design is the simulation of the equipment selection that has not only technical compliance but also ensures the economic efficiency of implementation, which guarantees the reliability and operability of the substation during its operation. A model of operation of the substation in various conditions (time of year, the day of the week, day time) is presented. Mathematical models are implemented as a computer-aided design system, which allows us to calculate new heat substations and to make a high-efficiency retrofit, and does not require special training of personnel.

Keywords: Heat substation · CAD system · Retrofit of heating system · Modeling software

1 Introduction

A retrofit and modernization of the current heat substations are determined by the following reasons. Firstly, the task of replacing the shell-and-tube heat exchangers to plate ones is still relevant. Secondly, the undertaken substitution of shell-and-tube heat exchangers to plate units was conducted mostly by project data exclusively, regardless of real needs and without taking into consideration new subscribers' connection. Thirdly, equipment selection was made not considering the differences and intensity in heat transfer, hydraulic characteristics, and features of the plate heat exchanger operation, especially when designing a two-level hot water supply (HWS) system. Fourth, energy saving in buildings (insulation) decreases the heat load while non-uniformity in HWS load distribution during the day grows. This last feature is particularly apparent in summer and less in spring and autumn when citizens move out of the city.

The basis of the heat substations (HS) within the centralized heat supply consists of heat exchangers, pumps and control systems. Nowadays the retrofit, i.e. the replacement of the shell-and-tube heat exchangers to plate ones of central and district HSs is getting over. There is a tendency of the retrofit and modernizing of the HS installed in the '90s and 2000s. On the other hand, the needs in individual heat modules (IHM) of small capacity for wide application in different buildings have increased. At the same time, heat supplying companies set the new requirement at HS to prove HSs' efficiency for a non-peak-load period, to ensure their efficiency and reliability during the peak-load period (retaining working functions despite of the soiling of heat exchanging surface), interchangeability of separate units and appliances of HSs supplied by different manufacturers. Apart from that, a necessary component at this period is an economic justification with the calculation of the cost of new equipment or retrofit of the existing ones, as well as feasibility study and exploitation of the results. On the other hand, there is a tendency to perform HSs' retrofit and equipment supply directly from manufacturers.

Therefore, in the face of increased requirements for saving thermal energy consumption, ensuring the reliability of equipment operation and rapid modernization of existing HSs, the task of creating and implementing instrumental support (software) for the design of heat substations and analyzing their work, becomes more relevant than ever.

2 Literature Review

At present, HS production is organized in all countries having centralized heat supply and HWS. HSs are produced in batches according to standard dimensions and by individual design. Schematic outlays, element composition, and control systems' operation have been worked out and tested in practice [1, 2]. All companies producing currently plate heat exchangers (PHE) possess their own HS designs for various types and dimensions of PHE [3, 4]. Besides, in the Commonwealth of Independent States (CIS) many countries, many companies have an HS production for any type of plate heat exchangers and control systems.

It should be noted that there is a qualitative difference in the nomenclature of HS produced in the western countries, CIS and China. Historically, centralized heat supply systems have relied on central or group heat points that served more than a dozen living and public buildings. These HSs were placed in separate buildings and were equipped by shell-and-tube heat exchangers. The piping system of the supply and return heat carrier (HWS was not provided in China) ensured heat supply and HWS to buildings proper that the equipment was located in a separate structure. In the western countries using a centralized heat supply, the HS installation was made in the building itself [5]. Such a structural scheme required a large number of HSs of small capacity, which corresponds to high standards of quiet operation, the absence of vibrations, and high reliability of control and monitoring of cost data collection, and maintenance.

These are completely different approaches. In the first case, it is necessary to perform the design or retrofit of each HS by capacity, their distance from the heat supply network, the number of the served consumers, the character of heat load, while in the second case is the standard HSs of the same capacity and design.

The main tendency in CIS countries is observed as moving of HSs into the buildings. In practice, it allows saving heat supply service payments despite the high investment cost [6]. Apart from that, it is observed an intensive development of hybrid heat supply systems, especially in small towns and settlements [7], and the combined use of HSs for heating and air conditioning [8].

Thus, all the mentioned problems and growth of tariffs make it necessary to develop the methods and mathematical models of automatic design systems enabling them to perform a high-quality design or retrofit of heat points. So in [9] the problem of reducing the temperature of the return network heat carrier for various schemes of connecting the hot water preparation system (parallel, two-stage and two-stage mixed) was considered. An economic assessment of the schemes is presented and the concept of a critical or consumer heat demand is introduced. It is suggested that before modernization, it is necessary to determine the critical demand value based on actual operating data, and, depending on this, implement a parallel or two-stage connection scheme hot water heat exchangers. The problem of controlling the operation HS from increasing the temperature difference of the external (network) heat carrier and its temperature at the outlet of the HS (return temperature) was considered in [10]. This difference determines the flow rate of the network heat carrier, and therefore, the cost of heating, as this value is measured by the heat energy meter. An HS operation control is proposed, which uses the technology of a wireless sensor and an actuator together with a service-oriented architecture. This technology allows you to analyze the operation of heat exchangers, circulation pumps and a control valve, which improves the ability to control.

The purpose of the work is to create a universal tool (software) for multivariant and quick design of group and individual HSs, as well as modernization and rational control of their work in off-design conditions.

To achieve this goal and create a software product, the following tasks were formulated:

- to develop a classification of group and individual HSs according to the type of connections to heating networks and the preparation of hot water;
- to create software for the calculation of plate heat exchangers and the selection of pumping equipment of various manufacturing companies;
- to propose and justify the criteria for evaluating the performance of HS in an off-design period and formulate measures for the rational operation of the HS control system;
- to provide for changes and upgrades when connecting new subscribers and disconnecting old ones;
- to substantiate the guaranteed operation of the HS throughout the entire period of operation, taking into account the appearance of fouling the heat transfer surface of heat exchangers;
- to provide the possibility of monitoring the operation of the HS depending on the temperature of the network heat carrier, season, day of the week, time of day;
- to realize the possibility of external (by fronts) and internal control temperature of the heat carrier;

– to provide mathematical modeling of the operation of the HS in the emergency period (a sharp decrease in temperature and (or) the flow rate of the network heat carrier);
– to provide easiness of using the software and the possibility of its use directly by the organizations operating HS.

3   Research Methodology

For local and individual HSs in the case of independent heating and hot water supply system, the most efficient is the connection of the heating system via the heat exchanger of the heating system and the two-stage mixed scheme of HWS (see Fig. 1). Central or individual HSs (module heat units) with the capacity of 10 kW to 10 MW shown in Fig. 1 are used as HSs for residential or industrial buildings as well as when retrofitting of central HSs heat distribution stations and boiler houses.
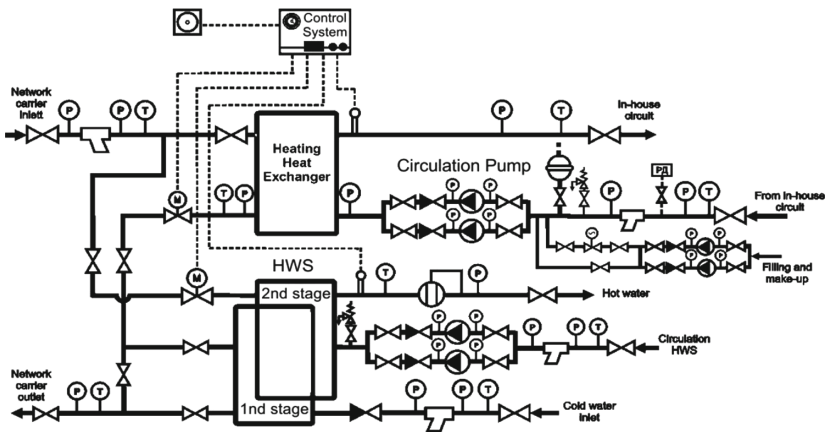

Fig. 1. A basic circuit of heat substation with a two-stage mixed scheme connection of HWS to district heating network.

HSs are based on plate heat exchangers of gasketed and brazed type and are equipped with pump equipment, automation and other regulation equipment [11]. In standard configuration, an HS consists of two modules: the heating system, and the HWS system.

The classification according to the installed equipment of the heating substation with the independent heating system connection can provide the following options for the substation layout.

Classification according to the feeding line:

• the scheme of heating substation system with the pump unit on the feeding line;
• the scheme of heating substation system with the return valve on the feeding line;
• the scheme of heating substation systems without an automatic recharge.

Classification according to the installed equipment on the network line:

- the scheme of heating substation system with an electrically operated valve on the network heat carrier supply pipeline;
- the scheme of heating substation system with an electrically operated valve in the return pipeline of the network heat carrier;
- the scheme of heating substation system with a three-way valve in the return pipeline of the network heat carrier (with constant flow rate).

Classification according to the installed equipment in the heating circuit:

- the scheme of heating substation system with circulation pump unit in the return pipeline of the internal heating circuit;
- the scheme of heating substation systems with a circulation pump unit on the flow line of the internal heating circuit.

Thus, the number of installation schemes of the heat substation is limited and, consequently, the substation's equipment has a rather limited number of items. It allows the standard production of the manufactured equipment and such heat substations.

One of the main criteria when choosing connections of water heating units of hot water supply (HWS heat exchangers) to the centralized networks is the minimum of the total cost on heating pipes and heat substations. At equal conditions of heat loads of HWS and heating; equal rated water temperatures in heat supply networks for the closed system of centralized water supply the simplest is the parallel scheme. It is characterized by the smallest heating surface of heat exchangers and the largest consumption of network water at an HS. The series two-stage scheme and the mixed scheme with the limit of maximum consumption of network water are characterized by the smallest rate network water consumption at an HS but the maximum area of HWS heat exchangers. The two-stage mixed scheme on estimated network water consumption and the heating surface of the HWS water heater occupies an intermediate position. As the main schemes to connect HWS water heaters to heat supply networks are currently considered the two-level combined and parallel scheme.

The two-staged connection circuit of HWS heat exchangers with the absence of the storage tank has the advantages over other connecting schemes in a wide range of $0.2 \leq k_{max} \leq 1$ that is relevant to the majority of residential buildings, where k_{max} is the ratio of the maximum heat load of hot water supply to the maximum load of the radiator heating system. In case if k_{max} ratio is outside of the range then the application of a parallel circuit is applied. For small k_{max} values in comparison with the parallel schemes, the additional complexity of the designed schemes are not regulated by the decrease in circuit water consumption, and for big k_{max} values, the heat transfer surface of HWS heat exchangers increases dramatically.

For the closed heating supply systems from Combined Heat and Power system (CHP), as well as for the boiler with a capacity of more than 35 MW, the following connection circuit schemes are usually applied to obtain the target high-temperature estimation on the central control unit of the combined radiator heating and hot water supply flow rates:

- the mixed connecting circuit with the limitation of the maximum flow rate of circulated water on the heat station or two-stage serial connecting circuit for the central heating station of individual heat substation, if the constraints mentioned above are absent, the value k_{max} is between $0.2 \leq k_{max} \leq 1$ and without storage tank for hot water supply system;
- a mixed connecting scheme when individual heat substation goes with elevator;
- a mixed connecting scheme for central heat station and individual heating substation if k_{max} values are between $0.2 \leq k_{max} \leq 1$ and available storage tank for HWS system;
- the parallel connecting circuit for central heat station and individual heating substation if k_{max} values are in the ranges of $k_{max} < 0.2$ and $k_{max} > 1$ and intermittent duty of water consumption.

For the closed heat supply systems of boiler houses with the capacity equal to 35 MW or less for all heat stations, the parallel circuit is always selected. According to the range of loads relations of k_{max} for which the HWS heat exchangers are calculated in closed connecting circuit systems, the standard design of central heat stations can be used in a wide range of ambient air temperatures for the radiator heating.

Making a classification according to the installed equipment of the HWS heat substation, the following options for the substation layout can be outlined. The classification according to the installed equipment on the network supply chain is the following:

- the scheme of heat substation for HWS system equipped by an electrically operated valve on the network heat carrier supply pipeline;
- the scheme of heat substation for HWS system equipped by an electrically operated valve in the network heat carrier return pipeline;
- the scheme of heat substation for the radiator heating system with the three-way valve installed in the network heat carrier return pipeline (with constant flow rate).

Classification according to the installed equipment in the circuit of cold heat carrier of HWS system (presence or absence of step-up pump):

- the scheme of heat substation for the HWS system without a step-up pump unit;
- the scheme of heat substation for the HWS system with a step-up pump unit installed on the pipeline, which supplies cold water;
- the scheme of heat substation for the HWS system with a step-up pump unit installed in the pipeline, which supplies hot water.

The number of versions of the hot water supply substation has a rather limited number of items for the heating points of the heating system makes it possible to substantially unify the production of such heat substations.

4   Results

Considering the HS design with the independent scheme of heat system connection with the circulation and the make-up pump and the two-stage mixed HWS scheme is shown in Fig. 1.

In an independent heating system, the feed of the water to the system is accomplished through the return pipe of the heat network mains (sometimes from the feeding one). This enables a considerable decrease of the soiling in the heat exchanger's heat transfer surface. The independent heating system is installed with a water expansion tank and it operates under pressure from this tank. It is common for systems designed for the work with a temperature gradient of 105–70 $^{\circ}$C to have the tank installed at 2.5–3 m up than the upper points of the system to avoid water boiling in those points. This feature is not provisioned for in the systems with low water intake. At modern heat points with plate heat exchangers the membrane, water expansion tanks are installed. The main function is to prevent the growth of static pressure in the heating system on account of thermal water expansion, as well as compensation of heat carrier losses and protecting equipment from the corrosion and pressure rising. At an individual heat substation, membrane tanks are connected to the back-pipe of the inner circuit.

For this scheme, the additional feeding is made through the make-up pump. Feeding automation is accomplished using an electromagnetic valve installed in the pump block on the signal from the electric-contact pressure gauge. There is also provided the alarm signal sending if the regulated pressure is out of preset parameters. The application of such scheme is usually realized when the following conditions are satisfied: the absence of immediate water-taking from the heating network; the pressure in front of the regulator's working part is always higher than the regulated pressure; the hourly consumption of the feed water G (kg/h) does not exceed the value calculated by the formula $G \leq 1.4 \sqrt{\Delta p}$ [6], where Δp is the pressure difference in front of and behind the regulator, kPa.

The local regulation of heat supply in the heating system is made by the heating regulator (electric valve) that maintains a constant temperature in the supply main of a building's heating system (after the heat exchanger of the heating system). The needed temperature in the feed main is determined and constantly adjusted by the readings of the ambient air temperature sensor. The adjustment by the ambient air temperature sensor's data is maintained for heating semi-systems connected with buildings' facades. This approach ensures heat carrier differentiated distribution considering the influence of solar energy, wind, and the building's orientation, heat needs of the premises located at opposite facades. In this case, heat supply at IHM is regulated separately by facades' heating semi-systems.

One of the most urgent tasks at the HS design is the choice of HWS heat exchangers connection scheme to the centralized networks and calculation of the HWS system. In this connection, the most important task is the possibility of rapid multi-variant calculations of HS's heat exchangers and other equipment for various schemes determining the capital investments in the HS and the consequent operating cost. The latter circumstance enables us to choose the optimal variant that is out of the ratio of capital investments to operating costs for various combinations of heat loads of HWS and heating system at the design stage and to model an HS operation in working modes and emergencies.

Considering the hot water supply schedule is sharply non-uniform, the obligatory condition of the HWS heat exchangers connection is equipping them with hot water temperature regulators. The parallel and two-stage schemes are applied in case of independent regulation of the heating and HWS loads.

The calculation of heat exchangers for hot water supply is made for the maximum hourly water consumption on HWS. The determination of this consumption includes the maximum HWS load, heat losses of the piping system and the cost of heat for circulation water heating. HWS heat exchangers are calculated for the minimum temperature of water of the feeding pipe of the heating network. The value of the minimal water temperature is determined by the presence of HWS systems as heat consumers in the centralized heat supply.

In real water supply schemes, especially in large residential areas the low pressure of cold water coming is observed into a heat exchanger warmed up. In this case, it is impossible to supply hot water due to hydraulic resistance within the heat exchanger and the building. To overcome this situation, the booster pump is installed, mostly on the cold water supply pipe.

In the developed automatic design it is currently realized some schemes of all heat substations given in the classification. For these schemes, it is common to install the electricity-driven valve on the supply pipe of the network heat carrier and of the circulation pump unit on the return pipe of the heating system's internal circuit. Also, the application of a membrane expansion water expansion tank, safety valve, filters, and other additional equipment is supposed. To ensure the operation of the heat point a control system of one of the two types is installed for the heating system module or heating module plus HWS.

Cost optimization of the heat point is designed according to the minimum cost criterion, i.e. as equipment of HS, equipment of those manufacturers with minimum cost is offered. The nomenclature can be changed according to the agreement with the customer.

The optimal calculation of plate heat exchangers is made by the criterion of reduced costs by taking into the decline in their operation while exploiting them due to soil of heat transfer area.

At the final stage of the design, the value of the capital and operation cost are calculated along with the economic efficiency of the introduction of a new heat point or retrofit of the existing one and the payback period (Fig. 2 and 3), following the documentation package for the completed project is formed.
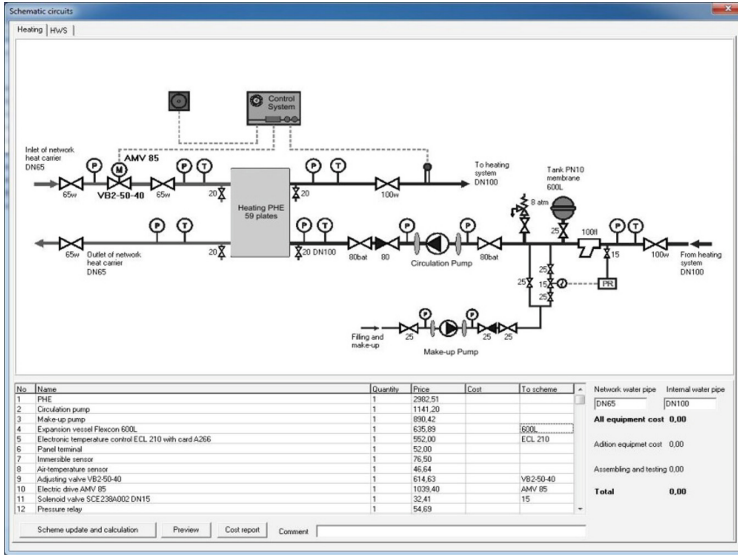
Fig. 2. General view of the concept and nomenclature of installed equipment for the heating system.
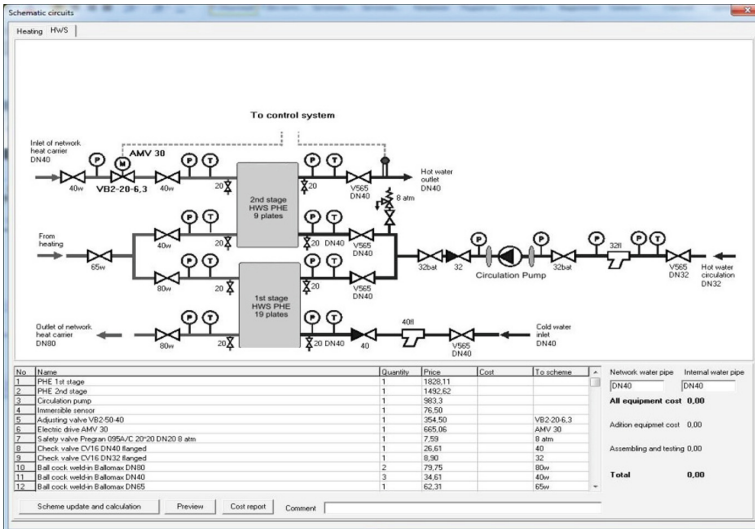

Fig. 3. General view of the schematic diagram and the range of installed equipment for the HWS system.

5 Conclusions

Based on the developed classification of group and individual HSs according to the type of connections to heating networks and the preparation of hot water, mathematical software has been developed which allows designing and upgrading HSs. Heat exchangers of the various model are selected according to the criterion of reduced costs, taking into account the fouling appearance during operation and the possibility of increasing capacity. The choice of auxiliary equipment is selected according to the criterion at the minimum cost. Modeling of HS operation includes rational control during an off-design period and the ability to monitor HS operation depending on the temperature of the network heat carrier, time of year, day of the week, and time of day. For individual HS, in addition to the control of the outside temperature, there is a possibility of external (by fronts) and internal control. Separately, for the designed TP, the calculation is provided in the peak and emergency load mode.

References

1. Guidelines for District Heating Substations Approved by the Euroheat & Power Board Prepared by Task Force Customer Installations (2008)
2. Guidelines for District Heating Substation/ Charter 1. https://www.scribd.com//District-Heating-Substation-Guide (2008)
3. Efficient heat transfer substations for district heating/. www.lsta.lt/files/events/ 2011-05-09-10…/12_Danfoss.pdf. Accessed 18 Sept 2019
4. Lillqwist, R.: Energy efficient design of district heating substations degree, Thesis Distributed energy systems (2017)
5. Sipilä, K., Nuorkivi, J.: The Building Level Substation – The Innovation of District Heating System. Pietiläinen, Juvenes Print, Tampere (2015)
6. District heating of buildings Regulations and guidelines, Publication K1/2013 Finnish Energy Publication, District Heating Substation Group (2014)
7. Mikulandric, R., Krajačić, G., Duić, N., Khavin, G., Lund, H., Vad, B., Mathiesen, P.: Ostergaard performance analysis of a hybrid district heating system: a case study of a small town in Croatia. J. Sustain. Dev. Energy, Water Environ. Syst. **3**(3), 282–302 (2015)
8. Babak, T., Duić, N., Khavin, G., Boldyryev, S., Krajačić, G.: Possibility of heat pump use in hot water supply systems. J. Sustain. Dev. Energy, Water Environment Syst. **4**(3), 203–215 (2016)
9. Zsebik, A., Sitka, G.y.: Heat exchanger's connection – a tool of decreasing return temperature in district heating networks. Energy Eng. **98**(5), 20–31 (2001)
10. Gustafsson, J.: Distributed wireless control strategies for district heating substations, Licentiate thesis, Luleå University of Technology, Sweden (2009)
11. Bohm, B.: Production and distribution of domestic hot water in selected Danish apartment buildings and institutions. Energy Convers. Manag. **67**, 152–159 (2013)

Experimental Research of the Excessive Water Injection Effect on Resistances in the Flow Part of a Low-Flow Aerothermopressor

Dmytro Konovalov[1](✉) , Halina Kobalava[1] ,
Vitaliy Maksymov[1] , Roman Radchenko[1] , and Mykola Avdeev[2]

[1] Admiral Makarov National University of Shipbuilding,
9, Heroes of Ukraine Avenue, Mykolayiv 54025, Ukraine
dimitriyko79@gmail.com
[2] Kherson Shipbuilding Company, 32b Torhova Street, Kherson 73009, Ukraine

Abstract. Water injection to the compressor channel is one of the effective ways to increase the power and efficiency of gas turbine plants. A promising method of water spraying is to use a jet apparatus – an aerothermopressor. Experimental studies of the excessive water injection effect on resistances in the flow part of a low-flow aerothermopressor are presented in this paper. To conduct an experimental study, an experimental setup was developed. An analysis of the obtained experimental data was carried out. A decrease in pressure losses by 15–20% relative to pressure losses in a "dry" aerothermo-pressor is stated. Checking the calculated equation for adequacy with experimental data is shown in a discrepancy in a range from 40% to −20%. An empirical equation is obtained to determine the pressure losses for the low-flow aerothermopressor (checking the calculated empirical equation for adequacy with experimental data is shown a discrepancy in a range from +15% to −15%). It was found that the pressure loss becomes equal to or exceeds the losses for the dry aerothermopressor when the flow rate water amounts more than 0.2 (20%).

Keywords: Thermogasdynamic compression · Injection · Relative pressure losses

1 Introduction

Complex schemes with cyclic air cooling are usually used in modern gas turbine plants (GTP) to increase fuel and energy efficiency. They are used to bring the process of compressing the working fluid in gas turbine compressors closer to isothermal. It leads to an increase in the thermal efficiency of the cycle and a decrease in specific fuel consumption [1–3].

One of the promising areas is the contact cooling of cyclic air by using a two-phase jet apparatus – an aerothermopressor. This device provides efficient evaporative cooling of the gas turbine without loss of total pressure. Pressure losses due to the friction are reduced with the rational organization of work processes and the corresponding development of the apparatus flow part design. By increasing the total air pressure at the outlet, the efficiency of the aerothermopressor is increased up to 30% [4, 5].

2   Literature Review

One of the most common ways to increase the efficiency of gas turbines is to use the cyclic air intercooling in the compression process. Thus, the compressor efficiency increase is achieved by approximating the final compression temperature to the initial temperature (the compression process becomes close to isothermal) [3, 6]. The water injection to the compressor channel is one of the effective ways to increase the power and efficiency of gas turbine plants [3, 7, 8]. The water injection fulfills two functions: it removes the heat from the airflow and returns the heat to the gas turbine cycle.

One of the current directions in increasing the efficiency of power plants is to use the aerothermopressor as a means of efficient water spraying while increasing the mass flow rate of the working fluid in the gas turbine plant [5]. Due to evaporative cooling in the aerothermopressor, an effect of the thermodynamic compression takes place – gas pressure is increased in the process of instantaneous evaporation of water injected into the gas (air) flow accelerated to a speed close to sound [9]. This apparatus combines two working processes: contact cooling of cyclic air and cyclic air pressure increase [4, 9, 10]. The difference of this cooling cyclic air method is that due to the intensive heat and mass transfer processes and a high flow rate, sufficient liquid thin atomization occurs. When injecting more water than is necessary for a complete evaporation, an additional evaporation of the remaining droplets in the airflow compressed in the gas turbine compressor is done. Due to this, the necessary conditions are created to ensure the process of an isothermal compression.

A significant influence on the working processes in the aerothermopressor is carried out by design factors. These factors affect energy consumption to overcome the friction forces and local resistance in the aerothermopressor flow part. To ensure a positive increase in pressure, the gas velocity in the aerothermopressor evaporation chamber should be near the speed of sound. The relative velocity, in this case, is in the range $M = 0.5$–0.9 Mach number. However, at such gas velocities, the aerodynamic resistance of the aerothermopressor [4, 10] is significantly increased.

The positive effect of using the aerothermopressor is greater the smaller the pressure loss through aerodynamic resistance [5] is. One of the ways to increase the efficiency of the aerothermopressor (relative increase in pressure) is to inject water into the flow part in an amount greater than necessary. This method ensures a dispersed mode of flow along the entire length of the aerothermopressor [11]. To determine the aerodynamic resistance losses in the low-flow aerothermopressor, it is necessary to clarify the methodology for determining the total aerodynamic resistance.

3   Research Methodology

The main objective of the research is to study the effect of the water injection (in excess of the amount necessary for evaporation) into the aerothermopressor flow part on the pressure losses due to aerodynamic resistance and to determine the dependences for calculating such losses.

The calculation model developed by the authors was used considering the calculation features: of gas turbine cycles with the cyclic air intercooler; of the thermodynamic compression effect; of contact cooling processes of moist air. Based on the computational model, a software complex has been developed. It allows determining parameters at the characteristic points of the cycle, GTP efficiency parameters (efficiency, power, specific fuel consumption, etc.), working process parameters in the aerothermopressor, and its geometric characteristics.

The calculation of GTP cycles was carried out according to well-known methods [6, 12] considering the features of processes in moist air [13]. The effect of thermodynamic compression was calculated considering the dependences [4, 9, 10]. The calculation of the evaporation of finely dispersed water was carried out considering contact heat transfer in gas turbine and combined-cycle plants [8, 14, 15].

The reliability of the work results is ensured by the tasks correct formulation of the theoretical and experimental research, the confirmation of the adequacy of the mathematical model with satisfactory agreement between the calculated and experimental data, using modern methods of experimental study and analytical modeling.

To conduct an experimental study, an experimental setup was developed (Fig. 1). The experimental setup is designed to simulate the aerothermopressor operation in the conditions of GTP cyclic air cooling.

The experimental aerothermopressor consists of the following elements: a receiving chamber with a nozzle for injecting water into the flow; a confuser; an evaporation chamber; a diffuser; nozzles for installing temperature and pressure sensors. All elements of the aerothermopressor are removable allowing carrying out studies for the different geometric characteristics: a confuser – inlet diameter $D_{c1} = 65$ mm; a convergent angle $\alpha = 30°$; an evaporation chamber – diameter $D_{ch} = 25$ mm; length $L_{ch} = 125; 175$ mm; a diffuser – length $L_{ch} = 192$ mm; a divergence angle $\beta = 6°$; a nozzle – the distance between the water exit point to the receiving chamber inlet $L_f = 5; 65; 125$ mm.

In the course of the study, the airflow rate was 6.0 m^3/h, at the pressure of 0.32 MPa, with the velocity in the evaporation chamber of 0.4–0.9 M.

All temperature, pressure, and airflow sensors were connected to a developed computerized monitoring system. The parameters were measured with an interval $\tau = 1$ s. To record the readings of measuring instruments, eight-channel meters I8-TS (temperature measurement) and I8-AT (pressure measurement) were used by RegMik. To collect and organize the information about the data, a PI485/USB RS485, a communication interface converter was used.

The error of the experimental results was determined by the error of the measuring instruments, methodological, and systematic errors.

The gas expansion process occurs adiabatically in the aerothermopressor subsonic nozzle. A liquid is supplied to the receiving chamber located up to the confuser, which is mechanically finely atomized with a special nozzle. In the evaporation section, these flows interact, and, as a result, droplets are accelerated, crushed, heated, and evaporated, and gas is also cooled [4]. There are three main operating modes of the aerothermopressor [4]:

1) the influence of the water droplets resistance prevails over the positive effect of evaporation and determines the gas flow behavior. The Mach number is increased, the static pressure of the flow is decreased, and the water temperature is risen approaching the saturation temperature;

2) the water evaporation is predominated. The Mach number is decreased, and the total and static pressure is increased;

3) the surface friction (it was relatively insignificant in the first two modes) becomes the predominant factor. This mode takes place when the liquid is evaporated completely.
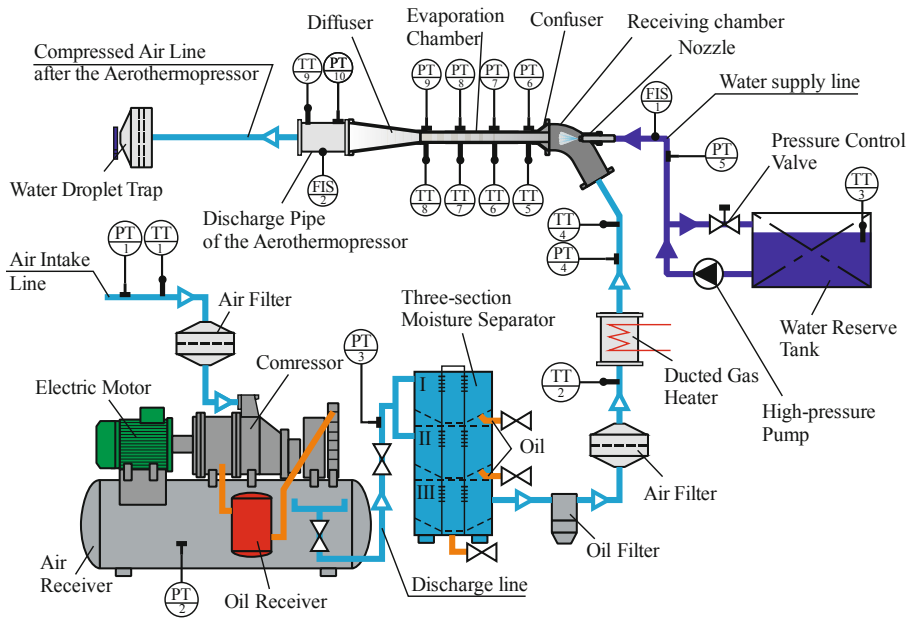

Fig. 1. The scheme of the experimental setup.

This mode takes place when the liquid evaporates completely. When providing the injection of water in an amount more than necessary for the evaporation, the third mode will be absent. This can positively affect the increase in the total pressure of the flow as a result of the thermodynamic effect.

Pressure losses due to the resistance (acceleration or deceleration of the droplet, depending on the initial velocity at the nozzle exit) can be determined by the aerodynamic resistance coefficient of the droplet in the airflow [8, 15]:

$$\zeta_d = \left(\frac{16}{Re_d} + \frac{2.2}{Re_d^{0.5}} + 0.32 \right) \cdot \left(\frac{1.5\mu_w + \mu_{air}}{\mu_w + \mu_{air}} \right), \tag{1}$$

where μ_{air}, μ_w – dynamic viscosity of air and water.

Reynolds number for a drop moving in the airflow:

$$Re_d = \frac{\delta_w \Delta w_w \rho_{air}}{\mu_{air}}, \tag{2}$$

where Δw_w – droplet velocity relative to air velocity, δ_w – water droplet diameter.

The local resistance coefficients also determine pressure losses due to aerodynamic resistance in the aerothermopressor flow part: the confuser (nozzle) – ζ_c; the working chamber (evaporation chamber) – ζ_{ch}; the diffuser – ζ_{dif}.

For a dispersed flow, an equation can be given to determine the hydrodynamic pressure loss. It is used in the phase slip model [17]. The mass flow rates occurring in the evaporation chamber of the low-flow aerothermopressor (with the diameter of the evaporation chamber $D_{ch} < 30$ mm, $G_g < 1.5$ kg/s) is (ρw) > 100 [10].

The hydraulic resistance of two-phase flow with phase slip is calculated by the Lockhart-Martinelli method [11, 16]. According to this method, the pressure loss due to the friction of a two-phase flow dP/dZ can be expressed in terms of their value for one phase:

$$\frac{dP}{dZ} = \Phi_w^2 \left(\frac{dP}{dZ}\right)_w \text{ or } \frac{dP}{dZ} = \Phi_{air}^2 \left(\frac{dP}{dZ}\right)_{air}, \tag{3}$$

where Martinelli parameter Φ [17]:

$$\Phi_w = \frac{\Phi_{air}}{X_{tt}} = X_{tt}^{-1} + 2.85 \cdot X_{tt}^{-0.48}; \Phi_{air} = 1 + 2.85 \cdot X_{tt}^{0.523}, \tag{4}$$

Martinelli-Nelson parameter X_{tt} [18]:

$$X_{tt} = \left(\frac{\mu_w}{\mu_{air}}\right)^{0,1} \left(\frac{1-x}{x}\right)^{0,9} \left(\frac{\rho_{air}}{\rho_w}\right)^{0,5}, \tag{5}$$

where $x = G_{air}/(G_{air} + G_w)$ – dryness of the vapor.

Pressure friction losses of the water phase and the gas phase:

$$\left(\frac{dP}{dZ}\right)_w = \frac{\zeta_{ch.w} \cdot (\rho_{air} w_{air})^2 (1-x)^2}{2D_{ch}\rho_w} \text{ or } \left(\frac{dP}{dZ}\right)_{air} = \frac{\zeta_{ch.air} \cdot (\rho_{air} w_{air})^2 (1-x)^2}{2D_{ch}\rho_{air}}. \tag{6}$$

The friction coefficient for turbulent flow in the evaporation chamber is found by the Blasius equation [19]:

$$\zeta_{ch} = 0.3164 \cdot Re^{-0.25}. \tag{7}$$

The phase with the determining pressure drop must be taken as the one whose pressure gradient is more significant importance for a given vapor content [11], while the total pressure loss is:

$$\Delta P_{\text{ch}} = \bar{l}_{\text{ch}} \cdot \frac{\Phi_{\text{w}}^2 \cdot \zeta_{\text{ch·w}} \cdot (\rho_{\text{air}} \cdot w_{\text{air}})^2 \cdot (1 - x)}{2 \cdot \rho_{\text{w}}},$$ (8)

$$\Delta P_{\text{ch}} = \bar{l}_{\text{ch}} \cdot \frac{\Phi_{\text{air}}^2 \cdot \zeta_{\text{ch·air}} \cdot (\rho_{\text{air}} \cdot w_{\text{air}})^2 \cdot (1 - x)}{2 \cdot \rho_{\text{air}}},$$ (9)

where $l_{\text{ch}} = (L_{\text{ch}}/D_{\text{ch}})$ – relative length of the evaporation chamber.

To calculate losses from the total resistance for the confuser ζ_c and the diffuser ζ_{dif} using the equation for the local loss coefficient [19]. For aerothermopressor calculated values: $\zeta_c = 0.005–0.010$; $\zeta_{\text{dif}} = 0.01–0.20$.

Thus, combining Eqs. (1), (7)–(9) to determine the pressure losses in the aerothermopressor flow part:

$$\Delta P_{\text{tr}} = \Delta P_{\text{ch}} + \frac{(\zeta_d(g_{\text{w}} + \Delta g_{\text{w}}) + \zeta_c + \zeta_{\text{dif}}) \cdot (a_{\text{df}} \cdot M)^2 \rho_{\text{air}}}{2},$$ (10)

where a_{df} – sound speed in the two-phase flow; g_{w} – amount of water required for complete evaporation; Δg_{w} – excess water.

Relative pressure losses in the aerothermopressor flow part:

$$\delta_{\text{tr}} = \frac{\Delta P_{\text{tr}}}{P_1} = \frac{P_1 - P_2}{P_1},$$ (11)

where P_1, P_2 – aerothermopressor inlet and outlet pressure.

4   Results

The experimental determination of pressure losses in the aerothermopressor flow part was carried out for a number of mass flow rates of water and it was compared with the values of pressure loss without water injection (dry aerothermopressor). The dependences plotted from experimental points are shown in Fig. 2.

The maximum pressure losses are made for the aerothermopressor without the water injection: at the inlet pressure $P_1 = 150–300$ kPa – $\Delta P_{\text{tr}} = 20–70$ kPa ($\delta_{\text{tr}} = 10–27\%$). At the water injection of $G_{\text{w}} = 0.0175$ kg/s (8%), pressure losses is decreased – $\Delta P_{\text{tr}} = 20–55$ kPa ($\delta_{\text{tr}} = 6–22\%$), but with an increase in the amount of the injected water, the pressure losses is increased: at $G_{\text{w}} = 0.0407$ kg/s (15%) – $\Delta P_{\text{tr}} = 20–60$ kPa ($\delta_{\text{tr}} = 7–24\%$), at $G_{\text{w}} = 0.0487$ kg/s (17%) – $\Delta P_{\text{tr}} = 20–65$ kPa ($\delta_{\text{tr}} = 9–26\%$). This is explained by the fact that, with a gradual increase in the water flow rate, the pressure losses also increase due to the droplets resistance in the flow. When the flow rate amounts are $g_{\text{w}} > 0.2$ (20%), the pressure loss becomes equal to or exceeds the losses for the dry aerothermopressor. A comparison of the experimental and calculated dependences (Fig. 3) shows that the calculated line of pressure loss at pressures $P_1 = 250–300$ kPa lies below the line constructed from the experimental data. Moreover, the calculated data are 8–12 kPa less (10–20%).

Equation checking (10) for adequacy with experimental data on the pressure loss ΔP_{tr} shows a discrepancy from $+40\%$ to -20% (Fig. 4), which can be considered satisfactory. However, the discrepancy is quite large, and it might explain the difficulty in determining the initial velocity of the droplet, and therefore underestimated pressure losses due to the droplet's aerodynamic resistance in the airflow.

To obtain more accurate values of the relative pressure losses δ_{tr} in the flow part of the low-flow aerothermopressor, it was proposed to obtain an empirical equation depending on the relative water flow rate g_w and the inlet air pressure P_1. The equation was determined by the approximation method:

$$\delta_{tr} = 0.0457 - 7.3581 \cdot 10^{-8} \cdot P_1 + 0.4682 \cdot g_w + 1.7814 \cdot 10^{-12} \cdot P_1^2 - 1.0768 \cdot g_w^2. \tag{12}$$
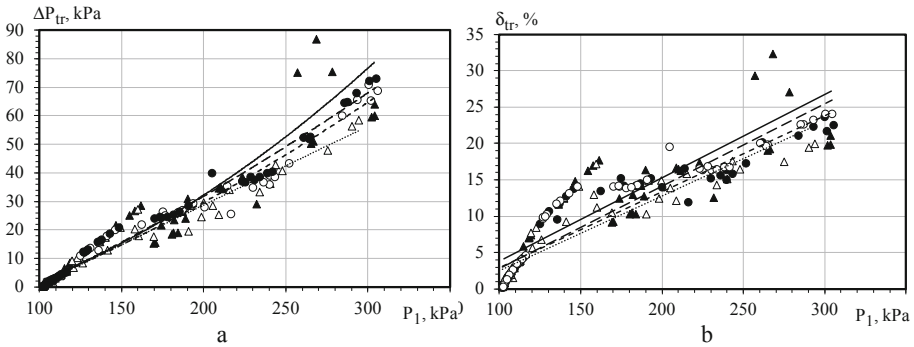

Fig. 2. The experimental data on the measurement of pressure losses ΔP_{tr} (a) and relative pressure losses δ_{tr} (b) in the aerothermopressor flow part on the air pressure at the inlet P_1 at various injected water rates G_w: ▲; _____ – 0 kg/s; Δ; ………… – 0.0175 kg/s; ○; _ _ _ _ _ _ – 0.0407 kg/s; ●; __ __ __ __ – 0.0487 kg/s.

This equation (regression coefficient R = 0.9260) was obtained for the following characteristics of the aerothermopressor: $G_{air} = 0.10–0.52$ kg/s; $M = 0.4–0.8$; $P_1 = 125–300$ kPa; $g_w = 0–0.4$; $t_1 = 50–180$ °C. The deviation of the calculated $\delta_{tr.C}$ values from the experimental $\delta_{tr.E}$ is $\pm15\%$ (Fig. 5), which is more accurate. However, such equation does not make it possible to calculate aerothermopressors with high airflow.

Thus, at the injected water in an amount greater than necessary for evaporation, the pressure losses in the aerothermopressor is decreased by 15–20% relative to the losses in the dry aerothermopressor. This makes it possible to increase the relative increase in the total pressure in the aerothermopressor $(P_2/P_1)_{atp}$. Thus, when simulating the aerothermopressor operation to cooling cyclic air of the gas turbine WR-21 (Fig. 6) from Rolls Royce ($N_e = 25250$ kW, $g_e = 0.190$ kg/(kW·h), $\eta_e = 41.2\%$) without the injection with the excess water – $(P_2/P_1)_{atp} = 1.025–1.060$; the injection of the excess water $g_w = 0.1$ (10%) – $(P_2/P_1)_{atp} = 1,045–0,080$, so the total pressure is increased by 2%.
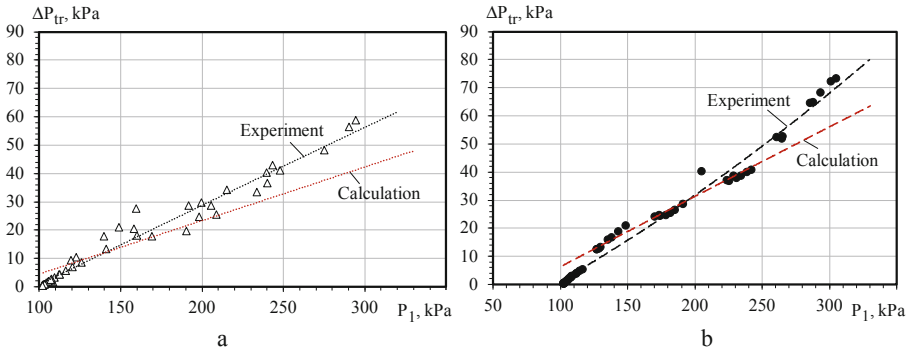
Fig. 3. Dependences of experimental and calculated data on the measurement of pressure losses ΔP_{tr} in the aerothermopressor on the air pressure at the inlet P_1 at various injected water rates G_w: a – 0.0175 kg/s; b – 0.0487 kg/s.
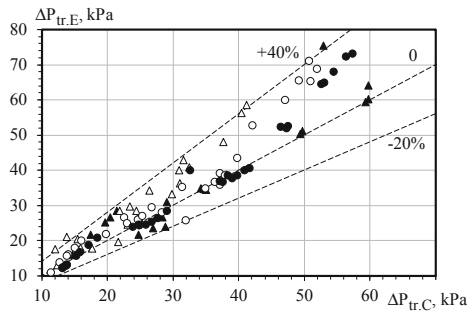

Fig. 4. Comparison of the experimental data on the measurement of pressure losses $\Delta P_{tr.E}$ in the aerothermopressor flow part with the calculated data $\Delta P_{tr.C}$ (Eq. (10)) at various injected water rates G_w: ▲ – 0 kg/s; △ – 0.0175 kg/s; ○ – 0.0407 kg/s; ● – 0.0487 kg/s.
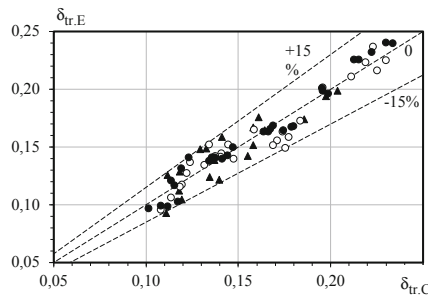

Fig. 5. Comparison of the experimental data on the relative pressure losses in the aerothermopressor flow part $\delta_{tr.E}$ with the calculated data $\delta_{tr.C}$ (Eq. (12)) at various injected water rates G_w: ▲ – 0 kg/s; △ – 0.0175 kg/s; ○ – 0.0407 kg/s; ● – 0.0487 kg/s.
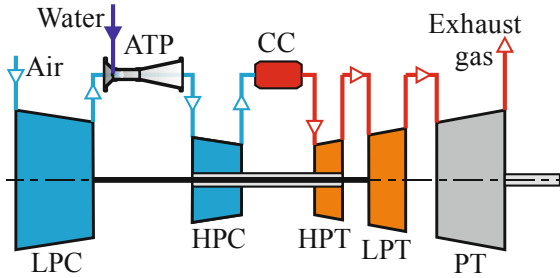
Fig. 6. The scheme of the gas turbine with cyclic air cooling by the aerothermopressor: ATP – aerothermopressor; LPC, HPC – low and high pressure compressors; CC – combustion chamber; HPT, LPT – low and high-pressure turbines; PT – power turbine.

5 Conclusions

An analysis of the obtained experimental data on pressure losses in the aerothermopressor flow part shows that the water injection in an amount g_w in excess of necessary for the evaporation provides a decrease in these losses by 15–20% relative to pressure losses in a dry aerothermopressor. A calculation equation to determine the pressure losses in the aerothermopressor flow part is presented; it takes into account the influence of the droplet aerodynamic resistance and the hydrodynamic resistance of the two-phase flow. Checking the calculated equation for adequacy with experimental data shows a discrepancy in a range from 40% to –20%.

An empirical equation is obtained to determine the pressure losses for the low-flow aerothermopressor at the airflow rate of G_{air} = 0.10–0.52 kg/s. Checking the calculated equation for adequacy with experimental data shows a discrepancy of ±15%.

The application of excessive water injection into the aerothermopressor to cooling cyclic air of the gas turbine allows increasing the relative pressure $(P_2/P_1)_{atp}$ in the aerothermopressor by 2%.

The study results can be used in the methodology of aerothermopressors rational design to determine the optimal geometric characteristics of the apparatus flow part. The finely dispersed two-phase flow obtained in the aerothermopressor can be further vaporized to the high-pressure gas turbine compressor. This fact will ensure that the compression process is close to isothermal. The application of the principle of the excess water injection in the aerothermopressor is relevant for using at the intercooling of cyclic air of gas turbine plants and the charge air cooling of internal combustion engines.

References

1. Romanovskyy, H.F., Vashchylenko, M.V., Serbin, S.I.: Theoretical Bases of the Ship Gas-Turbine Aggregates Designing. UDMTU, Mykolayiv (2003)
2. Romanovskyy, H.F., Serbin, S.I., Patlaychuk, V.M.: Modern Gas Turbine Units. NUOS, Mykolayiv (2005)

3. Jonsson, M., Yan, J.: Humidified gas turbines – a review of proposed and implemented cycles. Energy **30**, 1013–1078 (2005)
4. Stepanov, I.R., Chudinov, V.I.: Some Problems of Gas and Liquid Motion in the Channels and Pipelines of Power Plants. The Science Publisher, Leningrad (1977)
5. Konovalov, D., Kobalava, H.: Efficiency analysis of gas turbine plant cycles with water injection by the aerothermopressor. In: Ivanov, V., et al. (eds.) Advances in Design, Simulation and Manufacturing II. DSMIE 2019. LNME, pp. 581–591. Springer, Cham (2020)
6. Radchenko, A., Radchenko, M., Konovalov, A., Zubarev, A.: Increasing electrical power output and fuel efficiency of gas engines in integrated energy system by absorption chiller scavenge air cooling on the base of monitoring data treatment. In: HTRSE-2018, 6 p. E3S Web of Conferences 70, 03011 (2018)
7. Chaker, M.A., Meher-Homji, C.B., Mee III, T.: Inlet fogging of gas turbine engines: experimental and analytical investigations on impaction pin fog nozzle behavior. J. Eng. Gas Turbines Power **128**(4), 826–839 (2003)
8. Dykyy, M.O., Solomakha, A.S.: Features of the contact cooling process of cyclic air in gas turbine plants and the way of its realization. Energy: Econ. Technol. Ecol. **1**, 22–27 (2012)
9. Vulis, L.A.: Gas Flow Thermodynamics. Gosenergoizdat, Moscow (1950)
10. Fowle, A.: An Experimental Investigation of an Aerothermopressor Having a Gas Flow Capacity of 25 Pounds Per Second. Massachusetts Institute of Technology, Cambridge (1972)
11. Radchenko, N.: A concept of the design and operation of heat exchangers with change of phase. Arch. Thermodyn.: Polish Acad. Sci. **4**(25), 3–19 (2004)
12. Perelshtein, B.H.: To the entropy analysis of the thermal resistance in the combustion chamber of the gas turbine engine and the "aerothermopression effect". Aerosp. Tech. **1**, 77–80 (2003)
13. Wang, S.K.: Handbook of Air Conditioning and Refrigeration, 2nd edn. McGraw-Hill Publisher, New York (2000)
14. Dykyy, M.O.: Marine Gas and Steam Turbine Plants. Shipbuilding, Leningrad (1978)
15. Dolinsky, A.A., Ivanitsky, G.K.: Heat and Mass Transfer and Hydrodynamics in Vapor-Liquid Dispersed Flow. Naukova Dumka, Kyiv (2008)
16. Lockhart, R.W., Martinelli, R.C.: Proposed correlation of data for isothermal two-phase, two-component flow in pipes. Chem. Eng. Prog. **45**(1), 39–48 (1949)
17. Soliman, M., Schuster, J.R., Berenson, P.J.: A general heat transfer correlation for annular flow condensation. Trans. ASME: Ser. C **90**(2), 267–276 (1968)
18. Martinelli, R.C., Nelson, D.B.: Prediction of pressure drop during forced – circulation boiling of water. Trans. ASME **70**, 695–702 (1948)
19. Idelchik, I.E.: Handbook of Hydraulic Resistances. Mashinostroenie Publisher, Moscow (1992)

Characteristics of the Rotary Cup Atomizer Used as Afterburning Installation in Exhaust Gas Boiler Flue

Victoria Kornienko[1]([✉]) [iD], Roman Radchenko[2] [iD],
Dmytro Konovalov[1] [iD], Andrii Andreev[1] [iD],
and Maxim Pyrysunko[1] [iD]

[1] Kherson Branch of Admiral Makarov National University of Shipbuilding, 44,
Ushakova Avenue, Kherson 73003, Ukraine
kornienkovikal987@gmail.com

[2] Admiral Makarov National University of Shipbuilding, 9, Heroiv Stalinhradu
Avenue, Mykolayiv 54025, Ukraine

Abstract. The requirements concerning the development of the high-performance fuel combustion equipment with a low environmental impact and high flexibility have significantly increased. Therefore, a sophisticated analysis is needed for obtaining the data for designing the afterburning installation. There are few experimental and literature data on a rotary cup atomizer, but they do not allow to get criteria equations and primarily to determine the average droplet size. The research is aimed at investigating of atomization characteristics of rotary cup atomizer. Experimental studies of atomization characteristics were carried out on the experimental setup with atomized liquid of fuel oil, water, and water-fuel emulsions. For determining the droplet diameter of atomized liquid, the method of collecting droplets on glass slides coated with a layer of viscous liquid, in which the droplets of atomized liquid do not dissolve, was used. The uneven distribution of atomized liquid around the axis of atomizer was measured using a sector collector. The dependence of the effect of over the cross-section of atomizer cup on the average droplet diameter of atomized fuel, the coefficient of uneven distribution of atomized liquid around the axis of the atomizer, the atomizer root angle on air pressure and atomizer speed have been investigated by using the experimental data. Based on the experimental and theoretical data, a nozzle with atomizer diameter $d_p = 25$ mm was selected, which satisfactorily atomizes the fuel at a flow rate of 1–3 kg/h and provides the required diameter of emulsion droplets.

Keywords: Water-fuel emulsion · Exhaust gas · Rotary cup atomizer · Droplet diameter · Atomization characteristic

1 Introduction

In modern internal combustion engines (ICE) with utilizing exhaust gas heat, it is problematically to generate steam in the exhaust gas boiler (EGB) to ensure the operation of a waste heat recovery turbo-generator (RTG). This fact is caused by a decrease in exhaust gas temperature of ICE. One of the ways to increase the capacity of

RTG is to burn additional fuel in the afterburning installation in EGB flue, that gives certain advantages. Introducing afterburning increases the efficiency of cogeneration, as well as the flexibility of RTG, boiler, and afterburning installation [1].

The fuel afterburning in front of EGB influences considerably the efficiency of any waste heat recovery system including co-generative internal combustion engines [2, 3] and gas turbines [4], trigeneration plants for the generation of power, heat, and cooling (refrigeration and air conditioning) [5] with high efficient heat exchangers [6, 7].

When fuel is burnt in the exhaust flow, it is necessary to pay attention to conducting the organization of the combustion process of this fuel. As studies show, it is better to burn water-fuel emulsions (WFE) [8, 9] of a particular composition. Rather extensive experience in the practical use of emulsified fuels has been accumulated and described in detail. Water does not worsen, but improves combustion processes due to additional crushing of fuel droplets caused by micro explosions, an increase in the combustion surface of particles [10, 11], and proper mixing of fuel with air. At low fuel consumption, effective atomization is only possible with pneumatic, steam, and rotary cup atomizer. In small boilers, the preference is given to a rotary cup atomizer. Therefore, if it is necessary to burn small amounts of fuel, the use of a rotary cup atomizer may turn out to be a real solution.

The requirements concerning the development of high-performance equipment with low environmental impact and high flexibility have increased lately. Therefore, a comprehensive analysis is needed to obtain the necessary data for designing the afterburning installation.

2   Literature Review

The rotary cup atomizer is a special atomizer used for improved automotive painting [12]. A model to predict the droplet size was developed by combining two already-reported models [13, 14]. Authors [15, 16] present study investigates liquid flow patterns on the inner surface of a rotary cup atomizer and the effect of these flow patterns on the breakup patterns at the edge of the rotary cup. It also estimates the atomization characteristics based on the diameter of liquid ligaments issuing from the cup edge. In [17] behaviors of liquid films scattering from a disk-type or cup-type rotary atomizer are studied using computations based on the three-dimensional Smoothed Particle Hydrodynamics method. Experimental results obtained in [18] study put forward a clear link between the shaping air flow rate and the rotation frequency on the aerodynamics and also provide valuable leads to design the shaping airflow in modern rotary bell sprayers. Authors [19, 20] experimentally investigated the effects of operational conditions and liquid properties on the formation and breakup of ligaments from a high-speed rotary cup atomizer.

Experimental and literature data on the rotary cup atomizer are small, which does not allow obtaining criteria equations and determining the average droplet size. The research aims to investigate the atomization characteristics of the rotary cup atomizer.

The research tasks are:

– to assess the effect of the cross-section of an atomizer cup on average diameter droplets of the atomized fuel;
– to determine the coefficient of the uneven distribution of the atomized liquid around the axis of an atomizer;
– to assess the dependence of an atomizer root angle on the air pressure and on the atomizer speed.

3   Research Methodology

The rotary cup atomizer is insensitive to fuel oil viscosity since the fuel is exposed to a high temperature before atomization, washing the inner surface of the atomized cone, as a result of which the viscosity of the fuel oil is quickly brought to 2° or less. The high speed of the cup allows fuel atomization very finely. Due to this, it is possible to organize a better emulsion preparation and provide a complete fuel burning at a deficient excess of air. For ensuring the required dispersion during the atomization of fuel and WFE, sustainable combustion of fuel at a flow rate of about 1…3 kg/h, the operation of a rotary cup atomizer on experimental installation, taking into account the provisions mentioned above were studied.

A drawing of a manufactured rotary cup atomizer is presented in Fig. 1.
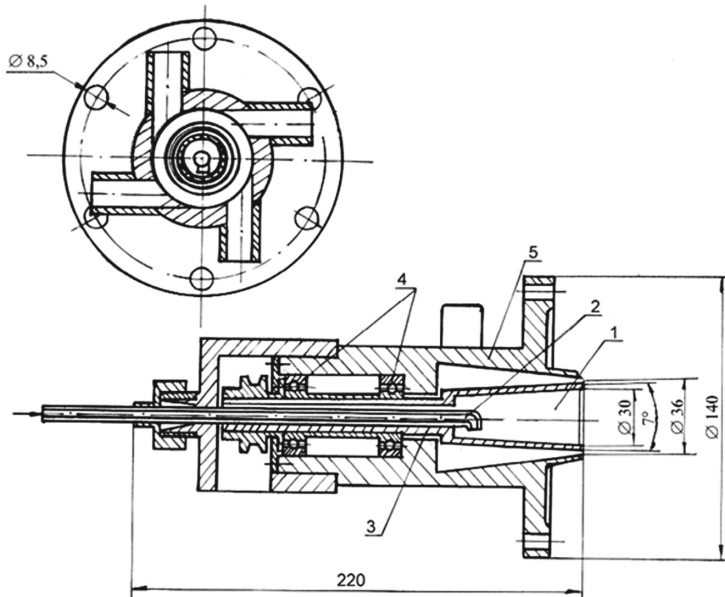

Fig. 1. Drawing of a rotary cup atomizer: 1 – spray cone; 2 – fixed tube; 3 – hollow shaft; 4 – bearings; 5 – cone.

The fuel was supplied to the spray cone *1* by means of a fixed tube *2* inserted into the hollow shaft *3* of the spray cone rotating in bearings *4* mounted in the cone *5*.

The effect of the cross-section of the atomizer cup on the average diameter of droplets of atomized fuel was studied at a particular installation. The layout of the experimental setup for studying the operation of the rotary cup atomizer is shown in Fig. 2.
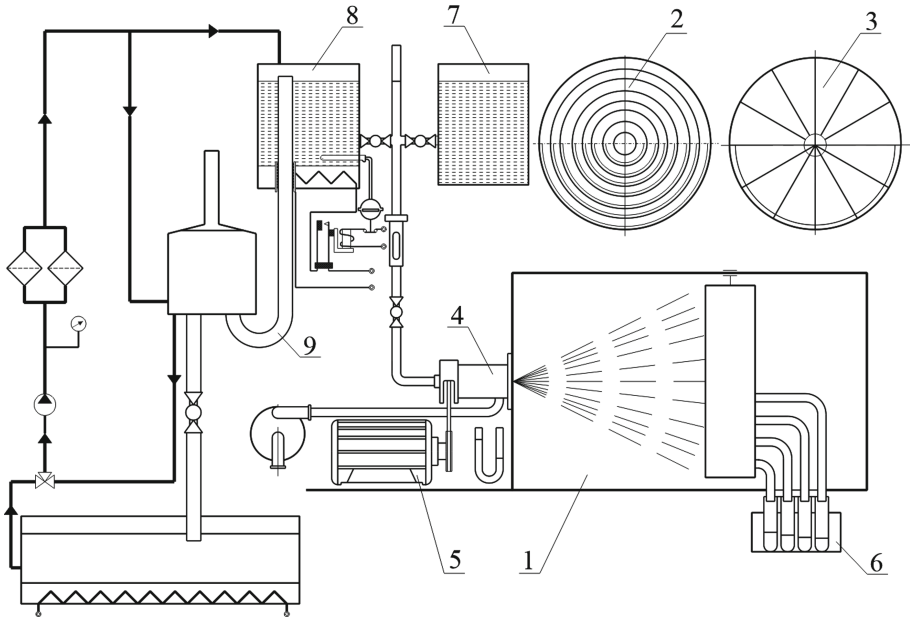

Fig. 2. Design of the experimental installation: 1 – bracket; 2 – circle collector; 3 – sector collector; 4 – rotary cup atomizer; 5 – drive motor; 6 – measuring beakers; 7 – tank of water; 8 – tank of WFE; 9 – tube.

The test fluid was supplied by gravity to the rotary cup atomizer *4*. The water was supplied from the supply tank *7*, and the fuel or WFE was supplied from reservoir *8*. The drive motor *5* rotated the rotary cup atomizer *4*. A circle collector *2* and a sector collector *3* with measuring cups *6* were installed to verify the operation of the atomizer.

For determining the droplet diameter of atomized liquid, the method of collecting droplets on glass slides coated with a layer of viscous liquid, in which the droplets of atomized liquid do not dissolve, was used. In this case, the compressor oil is used as such a liquid. When a droplet of liquid hits the surface of the plate, an imprint is obtained.

For determining the valid diameter of droplet d from its imprint d', the following empirical formula can be used

$$d'/d = 0.77 \text{ We}^{0.2} \tag{1}$$

where: d' – an imprint of a droplet; d – valid diameter of droplet; We – Weber number.

$$We = \rho v^2 / \sigma \qquad (2)$$

where: We – Weber number; ρ – liquid density of a droplet; v – droplet velocity before collision; σ – coefficient of surface tension of liquid droplet.

With regard to the layer thickness to the droplet diameter of more than 1.5, the value d'/d near to unity in the above range of Weber number ($We = 1500$).

Water, fuel oil, and WFE containing 30% water and 70% fuel oil were used as the atomized liquid. The catch plate was placed for a short period at a specific place in atomizer. Then this plate with trapped droplets was placed under a microscope with a measuring grid, the division value of which determines the interval of droplet sizes in the group. After these measurements, the number of droplets was calculated, and the average diameter of droplets was identified as the arithmetic average of droplets close in diameter.

The uneven distribution of atomized liquid around the axis of atomizer was measured using a sector collector. Moved to different distances from the atomizer so that its axis coincides with the axis of the atomizer. The number of sectors in the collector is accepted 12. Each of the sectors is connected to a volumetric beaker. The receiving holes of the beaker should have pointed edges to prevent droplets from reflecting from their edges. The uneven distribution coefficient of atomized liquid around the axis of the atomizer is defined as the ratio of the difference between the maximum Q_{max} and minimum Q_{min} fluid volumes that fall into separate sectors to the average volume Q_{av}:

$$\varepsilon = (Q_{max} - Q_{min})N / \Sigma Q_i \qquad (3)$$

where: Q_{max} – maximum fluid volume; Q_{min} – minimum fluid volume; Q_i – average fluid volume; N – the number of collector sector.

The dependences of the atomizer root angle on the air pressure and the atomizer speed are determined empirically. To determine the atomizer, root an angle photographing torch flame was used, a strong lateral light illuminated on the screen of black velvet background. The scheme of determining the value of the atomizer root angle is shown in Fig. 3.

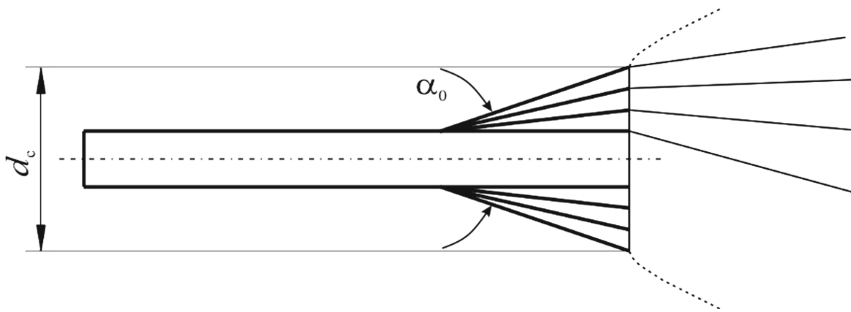**Fig. 3.** Determining the value of atomizer root angle: d_c – atomizer cup diameter; α^0 – atomizer root angle ($d_c = 30$ mm, $\alpha^0 = 7°$; $d_c = 28$ mm, $\alpha^0 = 5°$; $d_c = 26$ mm, $\alpha^0 = 20°$; $d_c = 25$ mm, $\alpha^0 = 15°$).

4   Results

Figure 4 shows the dependences of fraction diameter of atomized liquid in the cross-section of the atomizer with a change in the flow rate of atomized liquid and an atomizer speed, which show that at a low water flow rate (about 1 kg/h), the average diameter of droplets was in the range of 20–30 μm. With increasing water consumption, the average droplet diameter increases slightly and is 30–35 μm.
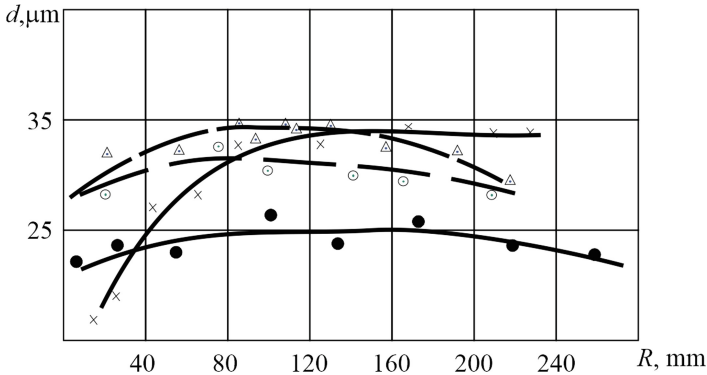

Fig. 4. Correlations for the dependence of the droplet distribution (in diameter) over the cross-section of an atomizer (atomizer diameter $d_p = 25$ mm; atomizer speed $n = 6200$ min^{-1}) ● – water consumption 1,2 kg/h; ✕ – water consumption 3,0 kg/h; ⊙ – WFE consumption 1,0 kg/h; △ – fuel oil consumption 1,0 kg/h.

The results of measurements and calculations show that with an increase in the flow rate, more uniform atomization of liquid is ensured, the coefficient of uneven ε decreases with the distance from an atomizer (Fig. 5).
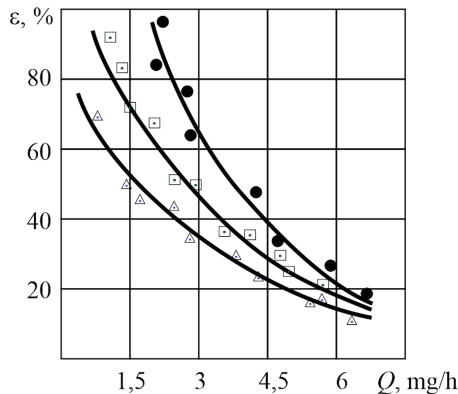

Fig. 5. Correlations for the dependence of the ratio of uneven ε the flow of atomized liquid from changes in flow at various distances l from the cutoff of an atomizer cup: ● – $l = 150$ mm; ▫ – $l = 250$ mm; △ – $l = 350$ mm

The test results empirically determined as the atomizer root angle dependences of air pressure and atomizer speed are shown in Figs. 6, 7 and 8. The presented curves show that the atomizer root angle of the atomized liquid largely depends on the air pressure. By changing the air pressure, you can adjust the atomizer root angle.
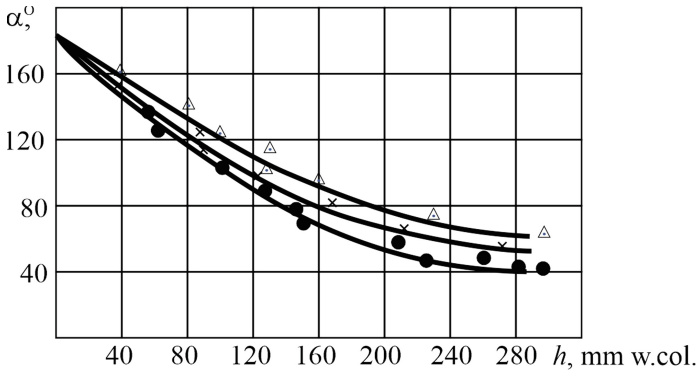
Fig. 6. Correlations for the dependence of the atomizer root angle values from air pressure (atomizer speed $n = 5500$ min^{-1}, water consumption 4 kg/h) for different atomizer diameter: $\bullet$ – $d_p = 25$ mm; $\times$ – $d_p = 26$ mm; $\triangle$ – $d_p = 28$ mm

The study of the effect of atomizer diameter on the magnitude of atomizer root angle showed a proportional increase in the value of atomizer root angle with increasing atomizer diameter.

Changing of atomizer speed also contributes to changing the atomizer root angle, but to a much lesser extent (Fig. 8).

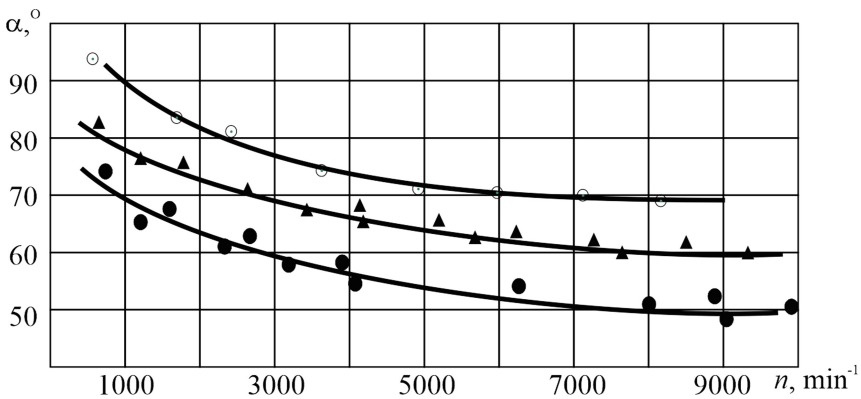**Fig. 7.** Correlations for the dependence of the atomizer root angle values from atomizer speed (air pressure $h = 250$ mm w. col., water consumption 4,0 kg/h): $\bullet$ – $d_p = 25$ mm; $\blacktriangle$ – $d_p = 26$ mm; $\odot$ – $d_p = 28$ mm
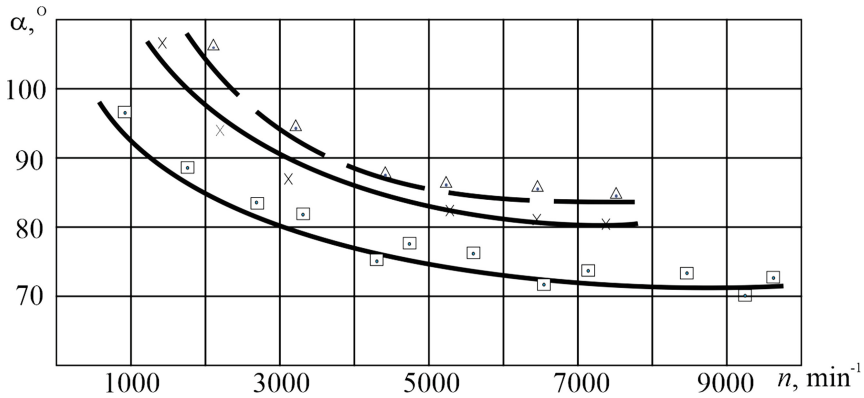
Fig. 8. Correlations for dependence of atomizer root angle values from atomizer speed (air pressure $h = 250$ mm w.col., $d_p = 26$ mm): ⊡ – water consumption 1,0 kg/h; ✕ – WFE consumption 1,0 kg/h; △ – fuel oil consumption 1,0 kg/h

Based on the experiments and conclusions made, a nozzle with a atomizer diameter $d_p = 25$ mm was selected with an air pressure $h = 250$ mm water column and a atomizer speed 5000 min^{-1}, which satisfactorily atomizes the fuel at a flow rate of 1… 3 kg/h and provides the required diameter emulsion droplets for targeted research.

5 Conclusions

The dependence of the effect of the cross-section of an atomizer cup on the average droplet diameter of atomized fuel has been investigated to obtain criteria equations for determining the average diameter of droplets when WFE is sprayed.

The coefficient of uneven distribution of atomized liquid around the axis of atomizer, the atomizer root angle on air pressure, and on the atomizer speed have been investigated to select atomizer diameter and atomizer speed.

The rotary cup atomizer was manufactured, and experimental installation was designed for study the operation characteristics of rotary cup atomizers.

Experimental researches have shown that when WFE is sprayed with a rotary cup atomizer, the diameter of the droplets remains constant throughout the torch cross-section.

Issuing from the experimental and theoretical data, a nozzle with atomizer diameter $d_p = 25$ mm was selected, which satisfactorily atomizes the fuel at a flow rate of 1– 3 kg/h and provides the required diameter of emulsion droplets for targeted research.

The work considers only one of the aspects of the issue – the investigation of rotary cup atomizer characteristics for the combustion of fuel oils and WFE based on them. The results of the research in this direction proved the prospects for the further study of regions of specific flows of the atomized liquid at different atomizer diameters, fluid flow rates, and varying distances from an atomizer.

References

1. Barbu, E., Ionescu, S., Vilag, V., Vilcu, C., Popescu, J., Ionescu, A., Petcu, R., Prisecaru, T., Pop, E., Toma, T.: Integrated analysis of afterburning in a gas turbine cogenerative power plant on gaseous fuel. WSEAS Trans. Environ. Dev. **6**, 405–416 (2010)

2. Radchenko, A., Radchenko, M., Trushliakov, E., Kantor, S., Tkachenko, V.: Statistical method to define rational heat loads on railway air conditioning system for changeable climatic conditions. In: 5th International Conference on Systems and Informatics: ICSAI 2018, Jiangsu, Nanjing, China, pp. 1308–1312 (2018)

3. Radchenko, A., Radchenko, M., Konovalov, A., Zubarev, A.: Increasing electrical power output and fuel efficiency of gas engines in integrated energy system by absorption chiller scavenge air cooling on the base of monitoring data treatment. In: HTRSE-2018, E3S Web of Conferences, vol. 70, p. 03011 (2018). 6 p.

4. Radchenko, R., Radchenko, A., Serbin, S., Kantor, S., Portnoi, B.: Gas turbine unite inlet air cooling by using an excessive refrigeration capacity of absorption-ejector chiller in booster air cooler. In: HTRSE-2018, E3S Web of Conferences, vol. 70, p. 03012 (2018). 6 p.

5. Radchenko, M., Radchenko, R., Ostapenko, O., Zubarev, A., Hrych, A.: Enhancing the utilization of gas engine module exhaust heat by two-stage chillers for combined electricity, heat and refrigeration. In: 5th International Conference on Systems and Informatics, ICSAI 2018, Jiangsu, Nanjing, China, pp. 240–244 (2019)

6. Radchenko, N.: A concept of the design and operation of heat exchangers with change of phase. Arch. Thermodyn. Pol. Acad. Sci. **4**(25), 3–19 (2004)

7. Bohdal, T., Sikora, M., Widomska, K., Radchenko, A.M.: Investigation of flow structures during HFE-7100 refrigerant condensation. Arch. Thermodyn. Pol. Acad. Sci. **4**(36), 25–34 (2015)

8. Baskar, P., Kumar, S.A.: Experimental investigation on performance characteristics of a diesel engine using diesel-water emulsion with oxygen enriched air. Alexandria Eng. J. **56**(1), 37–146 (2017)

9. Patel, K.R., Dhiman, V.: Research study of water-diesel emulsion as alternative fuel in diesel engine – an overview. Int. J. Latest Eng. Res. Appl. **2**(9), 37–41 (2017)

10. Radchenko, M., Radchenko, R., Kornienko, V., Pyrysunko, M.: Semi-empirical correlations of pollution processes on the condensation surfaces of exhaust gas boilers with water-fuel emulsion combustion. In: Ivanov, V. (ed.) Advances in Design, Simulation and Manufacturing II, DSMIE 2019. Lecture Notes in Mechanical Engineering, pp. 853–862. Springer, Cham (2020)

11. Kornienko, V., Radchenko, R., Stachel, A., Pyrysunko, M.: Correlations for pollution on condensing surfaces of exhaust gas boilers with water-fuel emulsion combustion. In: Tonkonogyi, V. (ed.) Grabchenko's International Conference on Advanced Manufacturing Processes, InterPartner 2019. Lecture Notes in Mechanical Engineering, pp. 530–539. Springer, Cham (2020)

12. Ray, R., Henshaw, P., Biswas, N.: Characteristics of spray atomization for liquid droplets formed using a rotary bell atomizer. J. Fluids Eng. **141**(8), 081303 (2019). 7 p.

13. Ray, R.: Evaporation of spray from a rotary bell atomizer. Electronic theses and dissertations, p. 5704 (2015).

14. Guettler, N., Paustian, S., Ye, Q., Tiedje, O.: Numerical and experimental investigations on rotary bell atomizers with predominant air flow rates. In: 28th European Conference on Liquid Atomization and Spray Systems, ILASS 2017, Valencia, Spain (2017).

15. Ogasawara, S., Daikoku, M., Shirota, M., Inamura, T., Saito, Y., Yasumura, K., Shol, M., Aoki, H., Miura, T.: Liquid atomization using a rotary bell cup atomizer. J. Fluid Sci. Tech. **5**(3), 464–474 (2010)
16. Petrone, G., Cammarata, G., Caggia, S., Anastasi, M.: Reacting flows in industrial duct-burners of a heat recovery steam generator. In: Excerpt from the Proceedings of the COMSOL Conference, Hannover (2008). 7 p.
17. Izawa, S., Iso, T., Nishio, Y., Fukunishi, Y.: Ligament formation and droplet breakup on disk-type and cup-type rotary atomizers. Trans. JSME **84**(862), 18 (2018)
18. Stevenin, C., Béreaux, Y., Charmeau, J.Y., Balcaen, J.: Shaping air flow characteristics of a high-speed rotary-bell sprayer for automotive painting processes. J. Fluids Eng. **137**(11), 111304 (2015). 8 p.
19. Hatayama, Y., Haneda, T., Shirota, M., Inamura, T., Daikoku, M., Soma, T., Saito, Y., Aoki, H.: Formation and breakup of ligaments from a high speed rotary bell cup atomizer (Part 1: observation and quantitative evaluation of formation and breakup of ligaments). Trans. Jap. Soc. Mech. Eng. Ser. B **79**(802), 1081–1094 (2013)
20. Soma, T., Katayama, T., Tanimoto, J., Saito, Y., Matsushita, Y., et al.: Liquid film flow on a high speed rotary bell-cup atomizer. Int. J. Multiph. Flow **70**, 96–103 (2015)

Possibility of Using Liquid-Metals for Gas Turbine Cooling System

Oksana Lytvynenko[(✉)] , Oleksandr Tarasov ,
Iryna Mykhailova , and Olena Avdieieva

National Technical University "Kharkiv Polytechnic Institute",
2, Kyrpychova Street, Kharkiv 61002, Ukraine
lytvynenko.oksana2016@gmail.com

Abstract. The possibility of using heat pipes to cool elements of a gas turbine is considered. The temperature of the parts gas turbine should be approximately equal to 850–950 °C to ensure its safe operation. This temperature range is suitable for a special type of heat pipes with a liquid metal coolant. It is proposed to reduce the temperature gradients on the turbine blade by mounting porous reservoirs with a liquid metal coolant on the inner surface of the blade body. In a closed porous reservoir, a two-phase state of the coolant is maintained, and heat is transferred by the mutually opposite movement of steam and liquid due to diffusion. The solution to the problem of modeling the processes of motion and phase transition in a porous medium filled with coolant is presented. The problem of thermal conductivity of a multilayer system consisting of a heated shell of a blade and a porous reservoir filled with a liquid metal coolant is formulated, and a numerical solution is proposed. As a practical example of the use of high-temperature heat pipes, a new type of aircraft engine nozzle cooling system has been developed. The example consists of two parts. The first part showed a decreasing temperature gradient in the leading edge of the gas turbine nozzle. The second part concerns the development of the cooling system of the nozzle as the whole.

Keywords: Gas turbine · Cooling system · Two-phase model · Porous reservoir · Liquid-metal heat carrier · Nozzle vane · Gas turbine blade

1 Introduction

Currently, an important direction in the development of energy gas turbine engineering is the creation of large unit capacity installations and their inclusion in combined-cycle plants. The tasks of improving stationary and transport gas turbine installations and gas turbine engines of all types are solved by mastering ever higher gas temperatures (T_g). Since the rates of increasing the heat resistance of alloys for gas turbines are significantly behind the growth of T_g, the only real way to increase T_g shortly is to use cooling of the most heated and most loaded parts of gas turbines, primarily nozzle and rotor blades. Therefore, the study and development of the problems of mastering high gas temperatures in gas turbine installations through the use of highly efficient cooling of

turbine parts are one of the most relevant directions in the development of modern gas turbine engineering [1].

2 Literature Review

Despite the fact that there is a lot of experience of design organizations and firms in the development of various methods of cooling gas turbine parts, in particular, convective, film, porous and combined cooling systems, the creation of new, more efficient cooling methods remains relevant [2–6].

Porous heat pipes are characterized by a high value of the conditional coefficient of thermal conductivity, which makes them suitable for heat transfer of high power in almost isothermal conditions. This property is very attractive for using heat pipes to cool gas turbine elements. A set of R&D papers dedicated to the implementation of heat pipes or their elements in a process of high-temperature gas turbines components cooling is known. Some of them propose double-circuit cooling using thermo-siphon systems. The thermo-siphon is a special case of the heat pipe with gravitational reversing of condensate to an evaporation zone. It doesn't use a porous structure and, consequently, the capillary effect is not observed. The authors of [7] proposed a mixed version of a high-temperature cooling system for gas turbine engine blades, in which a thermo-siphon with Na or K as a cooling medium is inserted into the deflector and used together with air cooling. In this case, the blade is the evaporation zone for the thermo-siphon, and the condensation zone is discharged into the second circuit, where the heat carrier is cooled by the air coming from the fan.

The authors of [8] analyze the advantages and disadvantages of thermo-siphon cooling systems developed on the concepts of closed and open thermo-siphon and thermo-siphon with mixed convection. The same source describes liquid metals as a heat carrier and the essential blades of gas turbines cooled by liquid metal over the turbines with air cooling concerning the greater specific capacity.

Cooling elements made from porous materials are one of the perspectives and effective ways for heat exchange intensification. The physical basis of this method is an extremely high intensity of heat exchange between a porous body and flowing through its heat carrier due to a very extensive surface of contact. The analysis showed that the use of heat pipes for cooling elements of gas turbines is limited due to the variety of positions in the space of the cooling elements and, consequently, the different effects of gravitational forces on them. However, it is promising to use heat pipes to equalize the temperature field of bodies in those places where the boundary conditions change quite sharply. An example of such highly loaded elements is the leading edge of the nozzle and blades, the zone of the laminar-turbulent transition. In these cases, the heat transfer coefficient on the outer surface of the blade at a short distance varies from two to three times. Note that the starting and ending points of the transitional regime of the boundary layer are not determined reliably and may fluctuate depending on the engine mode. As it follows, the position of the maximum heat transfer coefficient in the transition zone cannot be accurately fixed. The specified uncertainty of the heat transfer coefficient from gas does not allow organizing reliable adequate heat removal from the inside of the blade to the air. In this regard, it is of interest to study the possibility of

reducing temperature gradients along the shell of the blade by installing a porous reservoir with a liquid metal coolant on the inner surface of the blade.

This way, the problem is reduced to the determination of multilayer system heat balance, which comprises a heated blade shell, porous medium filled with liquid metal heat carrier and internal separated thin wall cooled by air. Compared to ordinary heat pipes schemes, this variant assumes the system without steam catch channels, i.e. completely closed porous reservoir, in which the two-phase state of heat carrier is maintained and heat transfer is carried out by concurrent diffusion-induced motion of steam and liquid.

3   Research Methodology

The two-phase model [9, 10] has been used to describe the processes. The model allows reducing the number of governing energy conservation equations. It is quite completely described in referenced literature, therefore only the main idea and practical implementation are presented here.

The model was adapted to gas turbine conditions and numerically solved with the finite element method. The mixed two-phase model was presented as a multiphase mixture of diffusing components (phases) where the interfacial zone between components is not a negligible magnitude but occupies a whole volume of the reservoir.

The model comprises conservation equations of mass, impulse, and energy as well as boundary and initial conditions based on a suggestion of independent phase motion. Thus, the target parameters are the parameters of two-phase media (density – ρ, velocity – u, enthalpy – h, relative enthalpy – H) connected by algebraic correlations to corresponding parameters of separate phases taking into account saturation and mobility of separate phases (λ_l, λ_v):

$$\begin{aligned}
\rho &= s\rho_l + (1-s)\rho_v, \\
\rho u &= \lambda_l u_l + \lambda_v u_v, \\
\rho h &= s\rho_l h_l + (1-s)\rho_v h_v, \\
H &= \rho h - \rho_v h_v,
\end{aligned} \tag{1}$$

where, index l refers to the liquid phase, v to steam phase. Liquid and steam densities and enthalpies in these equations correspond with saturation curves for the taken value of pressure.

Phases' mobility (λ_l, λ_v) depends on steam and liquid kinematical viscosity and value of saturation. The completely closed system is under consideration, in which two-phase media remains immobile while steam and liquid mass velocities equal in absolute value and have opposite directions.

$$\lambda_l u_l + \lambda_v u_v = 0. \tag{2}$$

A driving force of separate phases is capillary pressure:

$$p_c = p_v - p_l, \tag{3}$$

that can be defined by expression as follows

$$p_c = \left(\frac{\varepsilon}{K}\right)^{1/2} \sigma J(s), \tag{4}$$

where Leverett's *J*-function is formed by the saturation only.

The energy conservation equation, with the exception of the gravity element, can be represented with respect to the conditional enthalpy of the mixture *H* as

$$\Omega \frac{\partial H}{\partial t} + \nabla \cdot (\gamma_h u H) = \nabla \cdot \left(\frac{\Gamma_h}{\rho} \nabla H\right). \tag{5}$$

Entered in (5) factors, i.e. heat capacities ratio Ω, advection correction coefficient γh, and diffusion coefficient Γ_h are determined respectively:

$$\Omega = \varepsilon + \rho_s c_s (1 - \varepsilon) \frac{dT}{dH}, \tag{6}$$

$$\gamma_h = \left[s + \frac{\rho_v}{\rho_l}(1 - s)\right] \frac{\lambda_l(s)}{s}, \tag{7}$$

$$\frac{\Gamma_h}{\rho} = D + k_{eff} \frac{dT}{dH}, \tag{8}$$

where dT/dH is a mixture enthalpy derivative of temperature; $\lambda_l(s)$ – is relative mobility of the liquid phase; k_{eff} – is an effective heat conductivity of porous material; D – is a coefficient of capillary diffusion.

The diffusion coefficient reflects cross-motion phases and varies within the region of computation dependently on the saturation value

$$D(s) = \frac{\sqrt{\varepsilon K} \sigma}{\mu_l} \frac{s(1 - s)}{\frac{v_v}{v_l} s + (1 - s)} \frac{dJ(s)}{ds} \tag{9}$$

Equations (5–9) are correct as for the two-phase zone as for steam and liquid zones are taken separately. As far as the two-phase zone is considered, it is assumed that energy transfer is carried out exclusively at the account of diffusion and there is no heat exchange between porous solid and heat carrier. As practice shows, this assumption is quite valid for liquid-metal heat carriers.

This model was adapted to the operating conditions of gas turbines and numerically solved by the finite element method (FEM).

The energy equation for a solid is usually represented relative to temperature

$$c\frac{\partial T}{\partial t} = \nabla \cdot (k\nabla T),\tag{10}$$

where c – is the volumetric heat capacity, k – is the thermal conductivity.

The solution to this equation was carried out in the framework of a single code using the FEM. The joint problem of the thermal conductivity of a porous body with a liquid metal coolant and a solid was solved by two methods: joint and separate. The first method involved solving a complete system of equations for the entire object as a whole, together with conjugation equations at similar points. The second method was based on the sequential solution of the problem for solids and porous bodies, after which boundary conditions were imposed at the mating boundaries based on the solution obtained at this iteration.

A comparison of the two methods showed greater stability of the joint method, although in most cases a separate method allows you to get a solution more quickly.

To solve the problem of the thermal state of a multilayer system, the conjugation conditions at the interface between a solid and a porous body were formulated, and a number of model problems were solved [11, 12].

4 Results

The choice of the working fluid should be carried out first of all based on the range of the operating temperatures and capability with the material of casing to provide high thermal stability. The working fluid must be able to wet a wick and the material of the casing. The edge angle must be zero-order or very little. For the providing of the high heat-transfer capability of the pipe at the lowest flow rate of working fluid and hence at the minimal drop of pressure along the pipe it is desirable to use liquid with a high value of latent heat of vaporization. Hydraulic resistance of the flow will be low if the working medium has little viscosity of the steam and liquid phases. The temperature range of the gas-turbine at which it is necessary to cool the vanes is 900–1100 °C. The high-temperature heat pipes with liquid-metal heat-carrying agents run in such a range of temperatures. The liquid-metals have the best property for this case. Among them, there is potassium, natrium, lithium. Especially satisfactory properties are found to have natrium and lithium. Lithium owns the most favorable properties regarding heat transfer among all heat-carrying agents. Natrium has slightly worse thermophysical properties. However, at the running of lithium, the casing of pipe must be manufactured from expensive chemically stable to lithium alloy while natrium can run in a pipe made from stainless steel. That is why natrium is widely used in high-temperature heat pipe [13, 14]. We also chose Na as a heat-carrying agent for the current study. Natrium at operating temperature 900 °C has thermophysical properties that are equal: hfg = 3913 kJ/kg – the latent heat of vaporization, ρ = 745,4 kg/m^3 – density, μ = 0,17·10^{-3} Pa·s – dynamic viscosity, σ = 0,113 N/m – surface tension [13, 14].

The usage of the heat pipe for the cooling of the turbine blades has some difficulties. The main one among them is the gravitation action which forces differently on

the heat pipes capacity depending on the arrangement of vanes in a guide vane assembly. That is why the choice of the porous structure is predetermined by the maximum height of the liquid lifting. In the simplest case, the design of the heat pipe maybe is presented as a vane with two times enlarged height. The vane should be made as a shell with the arranged porous structure on its interface. The boiler of such a heat pipe will be located on the working part of a vane that flowed around by hot gas. The condenser must be out of the flow-through part of the turbine and cooled for example by air.

It is known that the most effective porous material is the homogeneous low-trans wick in case of the acting of gravity. This condition is contented by copper caked powder with the radius of pores $r = 9 \cdot 10^{-6}$ m, by permeability $K = 1.74 \cdot 10^{-12}$ and by porosity $\varepsilon = 0.27$ [12]. Specific heat flux from the hot gas to the vane surface can be estimated by value q > 106 W/m^2. The vane height usually approximately can be ranged as 0.04–0.1 m. Hence, the height of the liquid phase lifting in the capillary structure must be $l = 0.08$–0.2 m. The maximum value of lifting liquid Na for given wick is $l = \frac{2r}{\rho g \sigma} = 3{,}4$ m. Therefore, this wick covers all probable requirements of lifting liquid.

Two important examples of the use of porous reservoirs in the design of a gas turbine blade cooling system are presented in this part of the paper. The first example has shown decreasing the temperature gradient in the leading edge of gas turbine nozzle vane. The second example concerns the development of the cooling system of the nozzle vane on the whole. Let us consider the design of blade leading edge (LE) to prove the effectiveness of porous element with liquid metal.

It is known that boundary conditions at the LE can be changing in a wide range. For example, the heat transfer coefficient can be about 5–6 kW/(m$^2 \cdot$K) at the stagnation point and then it decreases to a value of 2–3 kW/(m$^2 \cdot$K) at the short distance in 2–5 mm along blade surface. You can imagine a situation where the stagnation point moved along the profile of the blade relative to its initial position due to changes in working conditions. At the same time, the air cools the inner surface with the same efficiency. These conditions should cause thermal unevenness, which can be weakened by the porous element. We considered only part of LE of 2 mm in width and with a porous element of 1.5 mm in width that was fixed inside of blade. The thin of 0.2 mm cover was touched at the porous element to protect liquid metal leakage. The average pore diameter was about 0.009 mm that corresponded to the porosity of 0.6. The air of 450 °C cooled the internal surface of the system with heat transfer intensity 1250 W/m^2 K. Gas temperature was 1100 °C and its intensity was changed at the LE surface in a range of 2–6 kW/(m$^2 \cdot$K). Thermal analysis of the LE showed the appropriate temperature irregularity: the maximum temperature was about 930 °C and minimum −880 °C at the external surface (Fig. 1). So the drop in temperature was 50 °C. The temperature distribution was much more irregular when the porous element was replaced by the metal: maximum and minimum of the temperature was 1010 °C and 940 °C.
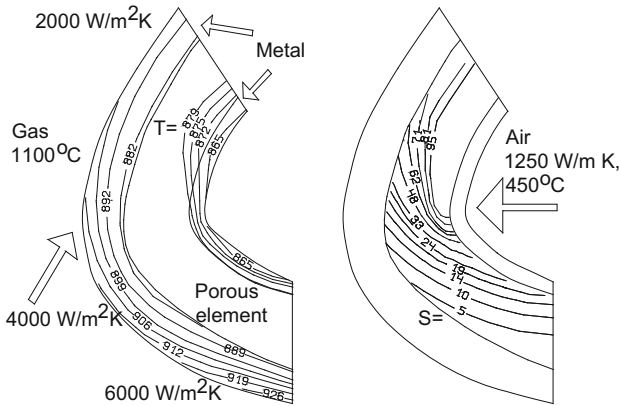
Fig. 1. Temperature (left), a saturation of porous element (right) of the LE part.

The following example concerns the efficiency of the nozzle blade cooling system of a high-temperature gas turbine as a whole (Fig. 2). The boundary conditions on the surface of the blade on the gas side were obtained using the integral method of calculating the boundary layer. The boundary conditions between the inner surface of the shell and the air were determined using hydraulic and thermal calculations of the cooling system [15].
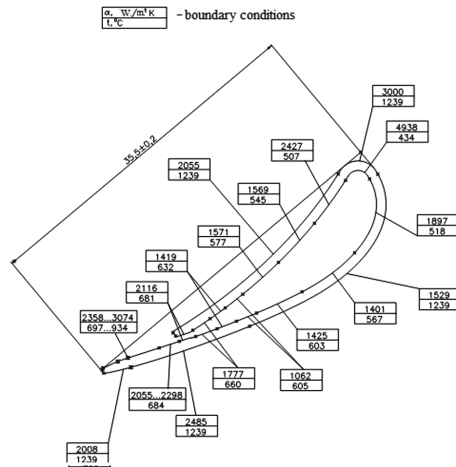

Fig. 2. Boundary conditions from gas and air.

The temperature field of the initial blade design was calculated using the developed here method and the ANSYS (Fig. 3). The calculations were performed under the same boundary conditions. A comparison of the results showed their complete identity, which indicates the reliability of the proposed method and software implementation.
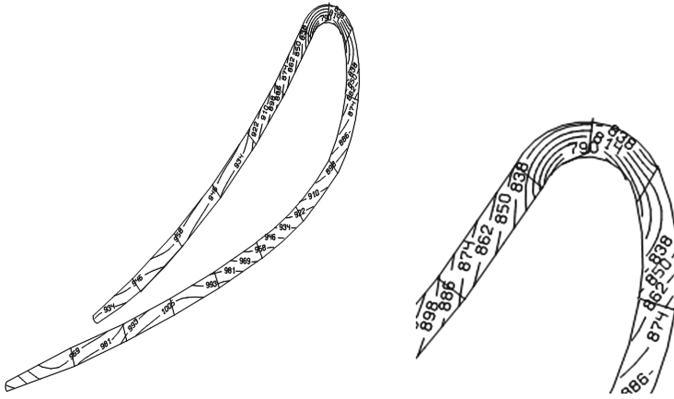
Fig. 3. The temperature field of the metal shell.

The temperature field of the shell is happened to be rather uneven. The maximum temperature is observed in the region of the outlet edge and equals to about 1020 °C. The air temperature at the inlet edge is about 838 °C. The temperature gradient along the convex and concave parts of the scapula reaches 100–150 °C.

The use of a porous reservoir saturated with a two-phase coolant at a saturation temperature of 765 °C led to a leveling of the temperature field and a decrease in the temperature of the leading and trailing edges (Fig. 4). The boundary conditions on the gas side remained the same as in the original design. The porous layer had a thickness of 3 mm, which is 2 times the thickness of the shell.

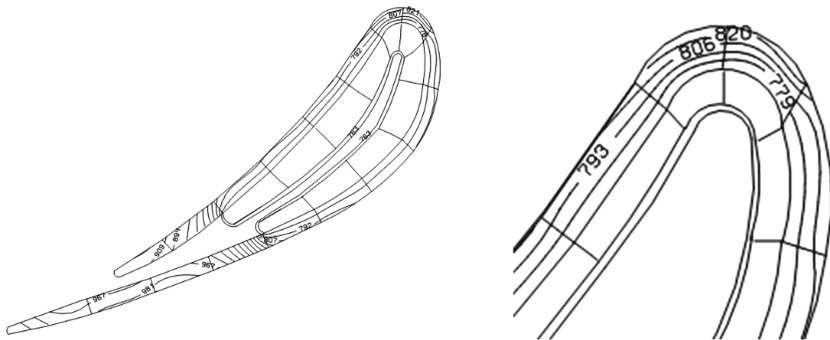**Fig. 4.** The temperature field of the blade with a porous reservoir.

The temperature of the trailing edge dropped to 970 °C and the leading edge to 820 °C. The temperature gradients on the convex and concave surfaces sharply decreased at the places of installation of the porous structure and amounted to about 13 °C. However, the trailing edge cannot be cooled effectively due to the small size,

and the porous structure cannot be placed there. The average value of the saturation in the porous structure is 47% (Fig. 5).
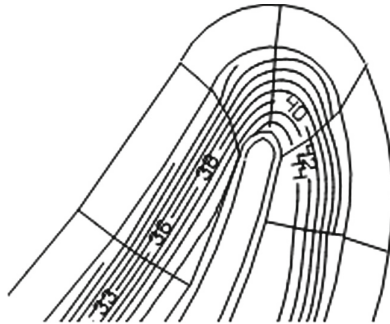

Fig. 5. Saturation lines of the blade with a porous reservoir.

In places of thinning of the porous reservoir, this value decreases. A redistribution of saturation lines is observed along the concave surface. The minimum value of saturation is 16%, where the increase in heat flux is associated with a high coefficient of heat transfer from gas (2055 W/m² K). Such a distribution of saturation lines indicates that in this section there is an intense, oppositely directed movement of vapor and liquid. The different intensities of the two-phase transfer also make it possible to achieve a uniform temperature field of the shell.

5   Conclusions

Based on the two-phase heat transfer model in a porous medium, a mathematical model of the boiling process and the dynamics of a liquid-metal coolant in a porous medium surrounded by an unevenly heated shell are developed.

This model allows the designing of efficient cooling systems for thermally loaded parts of gas turbines with help of the porous elements with a liquid metal coolant that even out the temperature field and increasing the degree of cooling.

It was proven that liquid natrium is a more suitable metal for cooling the blades of a gas turbine since it can work for a long time in a stainless steel tank without any changes in the properties and corrosion of the casing.

It was showed that processes in the porous reservoirs filled with a liquid metal coolant are an effective way for leveling the temperature even in areas with a sharp change in the intensity of heat transfer from gas to the surface of the blade. In particular, this applies to the leading and trailing edges of the blade, as evidenced by the distribution of saturation lines.

References

1. Kopelev, S.Z., Slitenko, A.F.: Designs and calculation of GTE cooling systems. Basis, Kharkiv (1994)
2. Frąckowiak, A., Wolfersdorf, J.V., Ciałkowskia, M.: Optimization of cooling of gas turbine blades with channels filled with porous material. Int. J. Therm. Sci. **136**, 370–378 (2019)
3. Fan, X., Li, L., Zou, J., Zhou, Y.: Cooling methods for gas turbine blade leading edge: comparative study on impingement cooling, vortex cooling and double vortex cooling. Transfer **100**, 133–145 (2019)
4. Wang, J., Du, C., Wu, F., Li, L., Fan, X.: Investigation of the vortex cooling flow and heat transfer behavior in variable cross-section vortex chambers for gas turbine blade leading edge. Int. Commun. Heat Mass Transf. **108**, 104301 (2019)
5. Moskalenko, A.B., Kozhevnikov, A.I.: Estimation of gas turbine blades cooling efficiency. Procedia Eng. **150**, 61–67 (2016)
6. Sciubba, E.: Air-cooled gas turbine cycles – part 1: an analytical method for the preliminary assessment of blade cooling flow rates. Energy **83**, 104–114 (2015)
7. Yoshida, T.: Cooling systems for ultra-high temperature turbines. Ann. N. Y. Acad. Sci. **934**(1), 194–205 (2006)
8. Manushin, E.A., Baryshnikova, E.S.: Turbine cooling systems for high temperature gas turbine engines. Results of Science and Technology. Series Turbine Engineering, vol. 2, Moscow (1980)
9. Chao-Yang, W., Beckermann, C.: A two-phase mixture model of liquid-gas flow and heat transfer in capillary porous media - I. Formulation. Int. J. Heat Mass Transf. **36**(11), 2747–2758 (1993)
10. Chao-Yang, W., Beckermann, C.: Numerical study of boiling and natural convection in capillary porous media using the two-phase mixture model. Numer. Heat Transf. Part A **26**, 375–398 (1994)
11. Tarasov, A.I., Lytvynenko, O.A.: The use of porous media for leveling the temperature field of gas turbine elements. Bull. Natl. Tech. Univ. "Kharkiv Polytech. Inst." Ser.: "Power Heat Eng. Process. Equip." **9**(12), 175–180 (2002)
12. Tarasov, A.I., Lytvynenko, O.A.: Use of elements with a liquid metal coolant in gas turbine cooling systems. Improv. Turbine Install. Methods Math. Model.: Sat. Sci. Proc., vol. 1, pp. 270–274 (2003)
13. Dunn, P.D., Reay, D.A.: Heat Pipes. Pergamon Press, Oxford (1976)
14. Haim, H.B., Torrance, K.E.: Boiling in low-permeability porous materials. Int. J. Heat Mass Transf. **25**(1), 45–55 (1982)
15. Avdieieva, O., Lytvynenko, O., Mykhailova, I., Tarasov, O.: Method for Determination Flow Characteristic in the Gas Turbine System. Lecture Notes in Mechanical Engineering, pp. 499–509. Springer, Cham (2019)

Analysis of the Efficiency of Engine Inlet Air Chilling Unit with Cooling Towers

Andrii Radchenko[1(✉)] , Andrzej Stachel[2] , Serhiy Forduy[3] ,
Bohdan Portnoi[1] , and Oleksandr Rizun[1]

[1] Admiral Makarov National University of Shipbuilding,
9, Heroiv Stalinhradu Avenue, Mykolayiv 54025, Ukraine
nirad50@gmail.com
[2] West Pomeranian Technical University,
17, Aleja Piastów, 70-310 Szczecin, Poland
[3] PepsiCo, Inc., 32/2, Moskovska Street, Kiev 01010, Ukraine

Abstract. The processes of cooling air at the inlet of energy installations by exhaust heat conversion chillers with heat removal from them by cooling towers of the circulating cooling system are studied on the example of a gas turbine. Two-stage air cooling is considered using combined type exhaust heat conversion chillers, which utilizes the exhaust gas heat of a gas turbine and which includes absorption lithium-bromide and refrigerant ejector chillers as stages to convert waste heat into cold. The data on current heat loads on exhaust heat conversion chillers and cooling towers in accordance with climatic conditions of operation with the different distribution of heat loads on the cooling towers according to their number was obtained on the base of the results of modeling the operation of the gas turbine cooling complex. It was shown the possibility to increase the fuel saving due to turbine inlet air cooling through decreasing the number of cooling towers and electricity consumption for driving the fans of cooling towers.

Keywords: Turbine · Climate · Thermal load · Chiller · Cooling tower · Fa

1 Introduction

With increasing an ambient air temperature t_{amb} at the inlet the fuel efficiency of combustion engines decreases [1, 2]. Thermodynamic efficiency of gas turbine units (GTU) at high ambient temperatures t_{amb} can be improved with the corresponding reduction of fuel consumption by cooling air in air coolers at the inlet of GTU by chillers (Ch), which utilize the exhaust gas heat [3, 4].

The effect of turbine inlet air cooling depends on its depth which in turn depends on the type of chiller. So, in absorption lithium-bromide chiller (ACh) it is possible to cool air to temperatures 15–20 °C [5, 6], and in refrigerant ejector chiller (ECh) to temperatures 7–10 °C and lower [7, 8]. Therefore, a combined absorption-ejector chiller (AECh) complex with ACh for cooling ambient air to a temperature $t_{a2} \approx 15$ °C in a high-temperature stage AC_{HT} and ECh for deeper air cooling to $t_{a2} \approx 10$ °C in a low-temperature stage AC_{LT} of a two-stage air cooler at the inlet of GTU has been proposed [9, 10].

Since heat is removed from AECh by cooling towers (CT) of the reverse cooling system, and their heat load, in turn, depends on the AECh thermal coefficients – coefficients of performance (COP), then we have to solve the problem of determining the rational heat loads of $Q_{0.HT}$ and $Q_{0.LT}$ by redistributing heat loads between the stages AC_{HT} and AC_{LT}, respectively between the ACh and ECh, which would provide deep cooling air at the GTU inlet with minimum design heat loads on the CT and their minimal amounts simultaneously.

The goal of the study is to increase the fuel saving due to gas turbine inlet air cooling through decreasing the number of cooling towers for removing the heat from turbine inlet air cooling complex and electricity consumption for driving the fans of cooling towers.

The tasks to be solved for achieving the goal: determining of the rational design heat load on two-stage air coolers (AC) at the inlet of GTU (rational design cooling capacity of AECh) to provide closed to maximum annual fuel saving; determining of actual current heat loads on two-stage AC at the inlet of GTU and their distribution between the AC_{HT} and AC_{LT} stages, respectively between the ACh and ECh of AECh and corresponding heat loads on cooling towers (CT) of different rated heat loads and number of CT taking into account a fuel consumption for electric fans of CT; determining the maximum fuel saving due to GTU inlet air cooling and the corresponding number of cooling towers (CT).

2 Literature Review

In combustion engines a cyclic air is an ambient air, therefore their performance is strongly affected by climatic conditions [11, 12]. With an increase in temperature at the inlet their fuel consumption increases, efficiency and effective power drops [1, 2]. The simplest and cheapest method of cooling air is spraying water directly into the cyclic air stream [13–15], but its efficiency is limited by wet bulb temperature. An enhancement of GTU fuel efficiency at high temperatures of ambient air is possible by its cooling in chillers using the exhaust gas heat [16, 17]. The available waste heat potential of engines used by ACh can be enhanced through deep utilization [18].

The ACh provides cooling GTU inlet air to the temperature of about 15 °C with the use of exhaust gas heat. ACh requires a tenth of the energy consumed by vapor compression chillers, are environmentally-friendly, noise free, and can be easily integrated within existing plants [17]. In a high efficient ACh, producing water with temperatures of around 7 °C, the cooling of air is possible to the temperature 15 °C [18], whereas in ECh – down to 10 °C, but the efficiency of heat conversion in ECh is low compared to ACh: the ECh coefficient of performance is $\zeta_E = 0.2$–0.25 versus $\zeta_A = 0.7$–0.8 for ACh [17, 18]. So it is reasonable to apply ACh for ambient air cooling to 15 °C in an AC_{HT} at the GTU inlet and further air subcooling in an AC_{LT} to 10 °C by ECh [18].

The CT of open type is the most effective for heat extraction in the circulating water supply systems and got a widespread use in air conditioning, trigeneration and combustion engines [19]. The temperature difference between CT supply water temperature and the outdoor wet-bulb temperature is about 3 °C and determines the cooling potential of the system.

3   Research Methodology

For a generalization of received results over a wide range of GTU a design cooling load, i.e. the cooling capacity of the chiller, required for cooling the ambient air to the target temperatures 10 °C and 15 °C in different climatic conditions (ambient air temperature t_{amb}, relative humidity φ_{amb}) varying during a year, is evaluated as specific cooling capacity q_0, related to the unit of air mass flow $G_a = 1$ kg/s in the AC.

The specific cooling capacity:

$$q_0 = \xi \cdot c_{ma} \cdot (t_{amb} - t_{a2}), \tag{1}$$

where: q_0 – specific cooling capacity, kJ/kg; ξ – moisture coefficient; t_{amb} – ambient air temperature, °C; t_{a2} – air temperature at the air cooler outlet, °C; c_{ma} – moist air specific heat, kJ/(kg·K).

The total project cooling capacity:

$$Q_0 = G_a \cdot q_0, \tag{2}$$

where: Q_0 – cooling capacity, kW; G_a – air mass flow, kg/s.

The GTU with two-stage cooling inlet air to 15 °C in the AC_{HT} by ACh and further subcooling air down to 10 °C in the AC_{LT} by ECh are considered for evaluation of the fuel saving due to inlet air cooling and rational design cooling capacities q_0 of chillers in different climatic conditions. The rational values of specific heat load on the AC, that is the AECh cooling capacity, required for cooling the ambient air to the temperatures 10 and 15 °C to ensure the maximum specific annular fuel saving $\Sigma\Delta b_e$ taking into account on-site climatic conditions are determined [20].

The specific annular fuel saving $\Sigma\Delta b_e$:

$$\Sigma\Delta b_e = \sum(\Delta t_a \cdot \tau) \cdot b_{et}, \tag{3}$$

where: $\Sigma\Delta b_e$ – specific annual fuel consumption economy, kg/kW; Δt_a – current air temperature drops, °C; τ – time interval, h; b_{et} – specific fuel consumption economy for 1 °C air temperature drop, kg/(kW·h).

To demonstrate the approach to the evaluation of efficiency performance of GTU inlet air chilling complex with different cooling towers the current fuel consumption reduction was calculated and summarized over a hot day (just as an example) for different rated power and number of cooling towers in various climatic regions to determine their rational values.

The resulting fuel saving due to cooling air at the GTU inlet:

$$\begin{aligned}\Sigma B_e &= \Sigma B_{e\_AC} - \Sigma B_{e\_F} \\ &= \Sigma(\Delta t_a \cdot b_{et} - \Delta P_{AC} \cdot b_{ep}) \cdot \tau \cdot N_e \cdot 10^{-3} - \Sigma(N_{eF} \cdot b_{eGTU}) \cdot \tau, \end{aligned} \tag{4}$$

where: ΣB_{e_AC} – fuel consumption reduction due to turbine inlet air cooling, kg; ΣB_{e_F} – fuel consumption to drive electrical fans of cooling towers, kg; ΔP_{AC} – air pressure drop in AC, Pa; b_{ep} – specific fuel consumption to overcome the resistance of

AC, kg/(kW·h); N_e – turbine power, kW; N_{e_F} – electrical power of cooling tower fans, kW; b_{eGTU} – specific fuel consumption of GTU, kg/(kW·h).

4   Results

The ambient air parameters change considerably during GTU operation. Changes in ambient air temperature t_{amb}, relative humidity φ_{amb} [21] and absolute humidity d_{amb} during July 2017 for compressor stations in various regions of Ukraine are presented in Fig. 1.
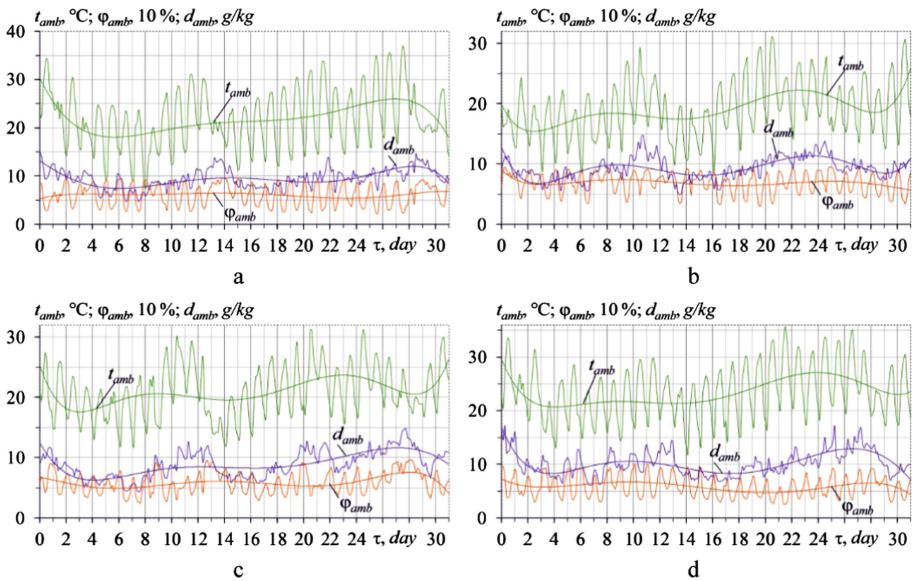
Fig. 1. Current values of ambient air temperature t_{amb}, absolute humidity d_{amb} and relative humidity φ_{amb} for July 2017: **a** – Shebelynka, Kharkov region; **b** – Ternopol region; **c** – Boyarskaya, Kiev region; **b** – Marievka, Nikolayev region.

A deeper turbine inlet air cooling to the temperature 10 °C in AECh as compared with its traditional cooling to 15 °C in ACh provides 1,75–2,25 times more annual fuel consumption increase (Fig. 2).
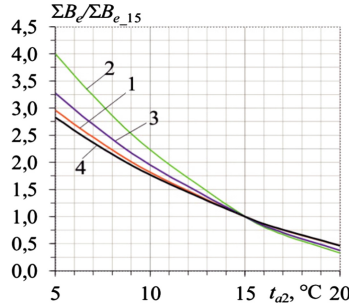
Fig. 2. The annual values of fuel consumption saving $\Sigma B_e / \Sigma B_{e\_15}$ due to cooling GTU inlet air from ambient air temperatures t_{amb} to different cooling air temperatures t_{a2} in relative values compared with cooled air in the ACh to 15 °C depending on the cooling air temperatures for different regions of Ukraine: 10 °C is in the ECh; 15–20 °C is in the ACh for the 2017 year for compressor stations: 1 – Shebelynka, Kharkiv region, 2 – Ternopil, Ternopil region, 3 – Boyarskaya, Kyiv region, 4 – Marievka, Mykolaiv region.

The scheme of GTU with two-stage inlet air cooling is shown in Fig. 3.
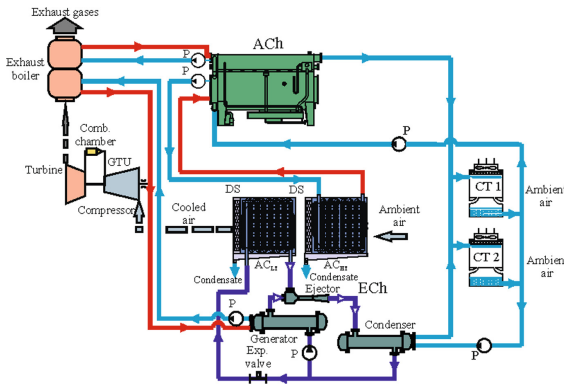
Fig. 3. The scheme of GTU with two-stage AECh inlet air cooling complex: from ambient air temperatures to 15 °C in the AC_{HT} by ACh and further air cooling to 10 °C in AC_{LT} by ECh with heat removal from the AECh in open CT with fan circulation of ambient air: DS – droplet separator; P – pump.

To determine the rational design heat load on two-stage air coolers (AC) at the inlet of GTU (rational design cooling capacity of AECh) that provides maximum annual fuel saving [20] the annual values of specific fuel saving $\Sigma \Delta b_e$ for 2017 versus a design specific cooling capacity q_0 (air flow $G_a = 1$ kg/s) at different temperatures of cooled air t_{a2} (10 °C is in AECh; 15 °C is in the ACh) for various operation climatic conditions in different regions are calculated and presented in Fig. 4.
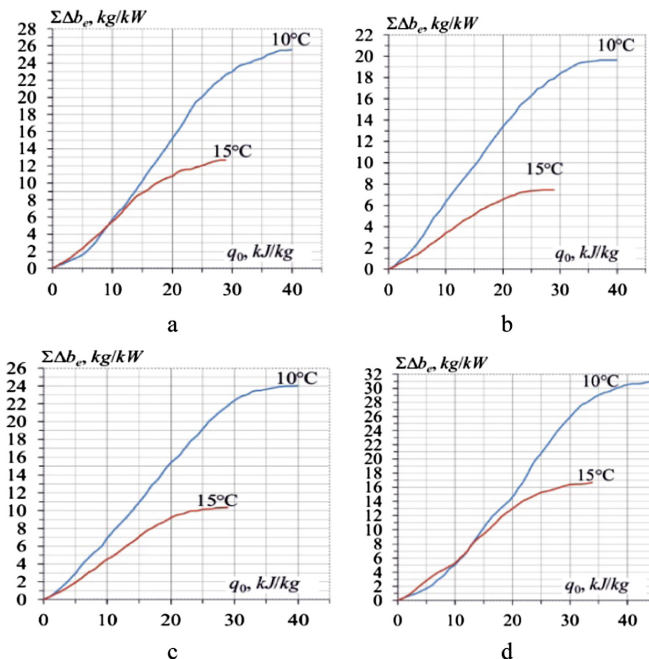
Fig. 4. The annual values of specific fuel saving $\Sigma\Delta b_e$ for 2017 versus a design specific cooling capacity q_0 (air flow G_a = 1 kg/s) at different temperatures of cooled air t_{a2}: 10 °C is in AECh; 15 °C is in the ACh; **a** – Shebelynka, Kharkov region; **b** – Ternopol; **c** –Boyarskaya, Kiev region; **d** – Marievka, Nikolayev region.

The calculations are carried out for Zorya–Mashproekt UGT 10000 (N_{eISO} = 10,5 MW), for which the air temperature reduction Δt_a by 1 °C leads to a decrease in the specific fuel consumption Δb_e by 0.7 g/(kW·h) [22]. For the GTU operation climatic conditions in different regions, 2017 year, a specific cooling capacity q_0 = 24 kJ/kg can be considered as a rational design specific cooling capacity of ACh for cooling ambient air at the GTU inlet to the temperature 15 °C at which the annual specific fuel saving $\Sigma\Delta b_e$ is closed to the maximum value at high enough rate of its increment. When ambient air is cooled in a two-stage AC by AECh to 10 °C (in the AC$_{HT}$ by ACh to 15 °C and the AC$_{LT}$ by ECh to 10 °C) the rational design of/for the specific cooling capacity of AECh is respectively q_0 = 34 kJ/kg.

The current values of thermal loads on two-stage AC and their AC$_{HT}$ and AC$_{LT}$ – stages and corresponding thermal loads on cooling towers CT during July 10, 2017 (as an example) for climatic conditions of different regions with gas turbine compressor stations are presented in Fig. 5.

The heat load on the CT was calculated as $Q_{CT} = (Q_{0.HT}/\zeta_A + Q_{0.HT}) + (Q_{0.LT}/\zeta_E + Q_{0.HT})$ in dependence on heat load $Q_{0.HT}$ on AC$_{HT}$ and $Q_{0.LT}$ on AC$_{LT}$, i.e. on the cooling capacity of ACh and ECh and on their thermal coefficients ζ_A = 0.7…0.8 and ζ_E = 0.2…0.25.
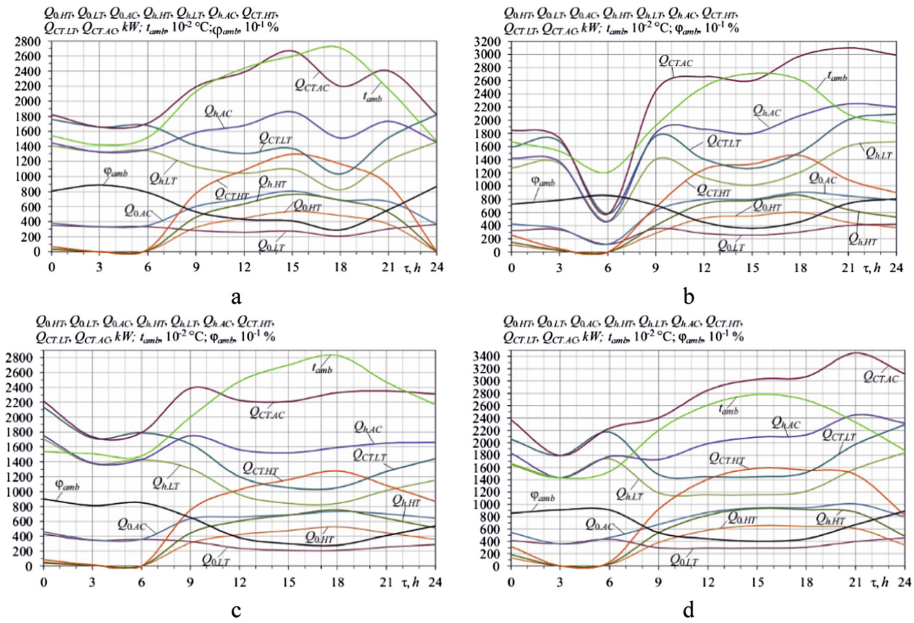
Fig. 5. Current values of t_{amb} and φ_{amb}, current heat loads $Q_{0.HT}$ and $Q_{0.LT}$ on the AC_{HT} and AC_{LT} and their sum $Q_{0.AC}$, the values of current actual heat load on ACh $Q_{h.HT}$ and ECh $Q_{h.LT}$ generator and their sum $Q_{h.AC}$, current heat load on CT, needed to remove the heat $Q_{CT.HT}$ from the ACh and $Q_{CT.LT}$ from the ECh and their sum $Q_{CT.AC}$ during July 10, 2017: **a** –Shebelynka, Kharkov region; **b** –Ternopol region; **c** – Boyarskaya, Kiev region; **d** – Marievka, Nikolayev region.

To determine a rational number of CT of different rated heat loads two options of distribution of thermal load $Q_{CT.AC}$ on two-stage AC at the inlet of GTU were simulated for different cooling complexes: 8 CT with a rated heat load 500 kW of each (overall 4000 kW) and 3 CT with a rated heat load 1500 kW of each and overall 4500 kW (Fig. 6).

The advantage of the first option is the ability to smooth control the heat loads on the CT by turning on/off the necessary units, however, a rather complicated cooling system with many CT is needed. The second option provides a simpler system, but the smoothness of power regulation is lost. The capital cost of thermal equipment (referred to 1 kW of power increment) for CT of the higher-rated heat load is usually less than for lower heat load rated equipment.

As Fig. 6 shows, the summarized fuel economy ΣB_{eF}^{3} with account fuel consumption for electric fans for the second option with 3 CT and rated heat load 1500 kW of each is a bit higher than the value ΣB_{eF}^{8} for the first option with 8 CT and rated heat load 500 kW of each. So, the option with CT with 3 CT and greater heat capacity Q_{CT}^{3} is more preferable due to less electric power N_e to drive the fans. With such a distribution, both an increase in GTU fuel economy of 2–3% per day, and the operation of the turbine inlet air cooling complex takes place and is simplified, and capital expenditures decrease.
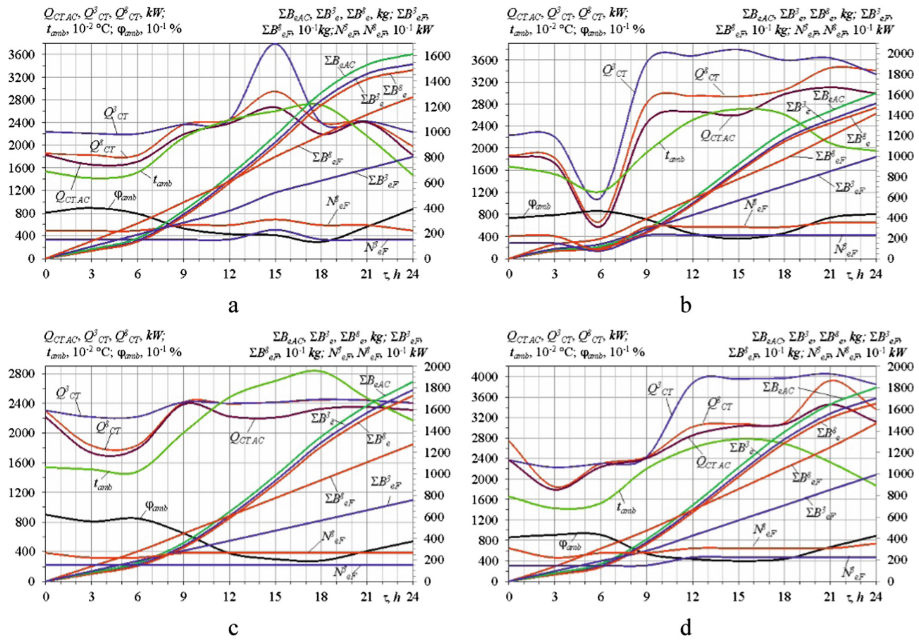
Fig. 6. Current values of t_{amb} and φ_{amb}, summarized fuel economy ΣB_{e_AC} without account fuel consumption for electric fans, ΣB_{eF}^8 and ΣB_{eF}^3 with account fuel consumption for 8 and 3 fans for the CT rated cooling capacity 500 kW (8 units, 4000 kW) and 1500 kW (3 units, 4500 kW); current heat load $Q_{CT.AC}$ on CT according to actual loading, heat loads Q_{CT}^8 and Q_{CT}^3 on 8 and 3 CT, electrical power consumption N_{eF}^8 and N_{eF}^3 during July 10, 2017: **a** –Shebelynka, Kharkov region; **b** –Ternopol; **c** – Boyarska, Kiev region; **d** –Marievka, Nikolayev region.

5 Conclusions

The data on actual current heat loads on two-stage cooling air at the inlet of GTU to the temperature about 15 °C in a high-temperature stage AC_{HT} fed by chilled water from ACh and further subcooling to 10 °C and lower in a low-temperature stage AC_{LT} fed by refrigerant from ECh and distribution of heat removed from ACh and ECh between cooling towers (CT) of different rated heat loads and the number considering a fuel consumption for electric fans of CT were obtained by modeling the operation of the gas turbine cooling complex for some regions of Ukraine with different climatic conditions.

With this, the rational design heat loads on two-stage air coolers (AC) at the inlet of GTU (rational design cooling capacity of AECh) to provide maximum annual fuel saving taking into account the current variable heat loads according to current climatic conditions were calculated using the method developed by authors.

The possibility to increase the fuel saving due to turbine inlet air cooling through decreasing the number of cooling towers and electricity consumption for driving the fans of cooling towers was shown.

The option with less number of CT and greater their heat capacity is more preferable due to less electric power to drive the fans that lead to increase in GTU fuel economy by 2–3% and simplified operation of turbine inlet air cooling complex.

References

1. Kumar, T.A., Muzaffarul, H.M., Islam, M.: Effect of ambient temperature on the performance of a combined cycle power plant. Trans. Can. Soc. Mech. Eng. **37**(4), 1177–1188 (2013)
2. Günnur, Ş.G., et al.: The effect of ambient temperature on electric power generation in natural gas combined cycle power plant-a case study. Energy Rep. **4**, 682–690 (2018)
3. Zhang, T., Liu, Z., Hao, H., Chang, L.J.: Application research of intake-air cooling technologies in gas-steam combined cycle power plants in China. Power Energy Eng. **2**, 304–311 (2014)
4. Yang, Ch., Yang, Z., Cai, R.: Analytical method for evaluation of gas turbine inlet air cooling in combined cycle power plant. Appl. Energy **86**, 848–856 (2009)
5. Elberry, M.F., et al.: Performance improvement of power plants using absorption cooling system. Alexandria Eng. J. **57**, 2679–2686 (2018)
6. Mahmoudi, S.M., Zare, V., Ranjbar, F., Farshi, L.: Energy and exergy analysis of simple and regenerative gas turbines inlet air cooling using absorption refrigeration. J. Appl. Sci. **9**(13), 2399–2407 (2009)
7. Butrymowicz, D., Gagan, J., Śmierciew, K., Łukaszuk, M., Dudar, A., Pawluczuk, A., Łapiński, A., Kuryłowicz, A.: Investigations of prototype ejection refrigeration system driven by low grade heat. In: HTRSE-2018, E3S Web of Conferences, vol. 70, 03002 (2018)
8. Elbel, S., Lawrence, N.: Review of recent developments in advanced ejector technology. Int. J. Refrig **62**, 1–18 (2016)
9. Radchenko, R., Radchenko, A., Serbin, S., Kantor, S., Portnoi, B.: Gas turbine unite inlet air cooling by using an excessive refrigeration capacity of absorption-ejector chiller in booster air cooler. In: HTRSE-2018, E3S Web of Conferences, vol. 70, 03012 (2018)
10. Forduy, S., Radchenko, A., Kuczynski, W., Zubarev, A., Konovalov, D.: Enhancing the fuel efficiency of gas engines in integrated energy system by chilling cyclic air. In: Tonkonogyi, V. et al. (eds.) Grabchenko's International Conference on Advanced Manufacturing Processes. InterPartner 2019. Lecture Notes in Mechanical Engineering, pp. 500–509. Springer, Cham (2020)
11. Popli, S., Rodgers, P., Eveloy, V.: Trigeneration scheme for energy efficiency enhancement in a natural gas processing plant through turbine exhaust gas waste heat utilization. Appl. Energy **93**, 623–636 (2012)
12. Popli, S., Rodgers, P., Eveloy, V.: Gas turbine efficiency enhancement using waste heat powered absorption chillers in the oil and gas industry. Appl. Therm. Eng. **50**, 918–931 (2013)
13. Konovalov, D., Kobalava, H.: Efficiency analysis of gas turbine plant cycles with water injection by the Aerothermopressor. In: Ivanov, V., et al. (eds.) Advances in Design, Simulation and Manufacturing II. DSMIE 2019. Lecture Notes in Mechanical Engineering, pp. 581–591. Springer, Cham (2020)
14. Konovalov, D., Trushliakov, E., Radchenko, M., Kobalava, G., Maksymov, V.: Research of the Aerothermopresor cooling system of charge air of a marine internal combustion engine under variable climatic conditions of operation. In: Tonkonogyi, V., et al. (eds.) Grabchenko's International Conference on Advanced Manufacturing Processes. InterPartner-2019. Lecture Notes in Mechanical Engineering, pp. 520–529. Springer, Cham (2020)

15. Yanga, Y., Wangd, B., Zhoue, Q.: Air conditioning system design using free cooling technology and running mode of a data center in Jinan. Procedia Eng. **205**, 3545–3549 (2017)
16. Al-Ibrahim, A.M., Varnhamm, A.: A review of inlet air-cooling technologies for enhancing the performance of combustion turbines in Saudi Arabia. Appl. Therm. Eng. **30**, 1879–1888 (2010)
17. Radchenko, A., Radchenko, M., Konovalov, A., Zubarev, A.: Increasing electrical power output and fuel efficiency of gas engines in integrated energy system by absorption chiller scavenge air cooling on the base of monitoring data treatment. In: HTRSE-2018, E3S Web of Conferences, vol. 70, 03011 (2018). 6 p
18. Radchenko, M., Radchenko, R., Ostapenko, O., Zubarev, A., Hrych, A.: Enhancing the utilization of gas engine module exhaust heat by two-stage chillers for combined electricity, heat and refrigeration. In: 5th ICSAI 2018, Jiangsu, China, pp. 240−244 (2019)
19. Mulyandasari, V.: Cooling tower selection and sizing (engineering design guideline). KLM Technology Group. Practical Engineering Guidelines for Processing Plant Solutions (2011)
20. Radchenko, A., Bohdal, L., Zongming, Y., Portnoi, B., Tkachenko, V.: Rational designing of gas turbine inlet air cooling system. In: Tonkonogyi, V., et al. (eds.) Grabchenko's International Conference on Advanced Manufacturing Processes. InterPartner-2019. Lecture Notes in Mechanical Engineering, pp. 591–599. Springer, Cham (2020)
21. Meteomanz. http://www.meteomanz.com/. Accessed 21 May 2019
22. SE SPCGTC "Zorya"–"Mashproekt", Nikolaev gas turbines of industrial application, Publ. (2004). 20 p.

Enhancement of the Operation Efficiency of the Transport Air Conditioning System

Mykola Radchenko[1](✉) , Dariusz Mikielewicz[2] ,
Veniamin Tkachenko[1] , Michał Klugmann[2] ,
and Andrii Andreev[1]

[1] Admiral Makarov National University of Shipbuilding,
9, Heroiv Stalinhradu Avenue, Mykolaiv 54025, Ukraine
`nirad50@gmail.com`
[2] Gdansk University of Technology, 11/12, Gabriela Narutowicza,
80-233 Gdańsk, Poland

Abstract. On analyzing the operation of air coolers of railway air conditioning (AC) systems, characterized by considerable variations in current heat loads according to actual climatic conditions on the route lines, the reserves to increase its efficiency by the intensification of refrigerant evaporation in air coils and to enlarge the range of deviation of refrigerant flows from their optimum values without noticeable decreasing heat flux were revealed. It has been proved that overfilling the air cooler coils by liquid refrigerant injector recirculation enables excluding the final dry-out stage of refrigerant evaporation with extremely low intensity of heat transfer and as result provides increasing the heat efficiency of air coolers (overall heat flux) by 20–30% compared with conventional air coolers with complete refrigerant evaporation and superheated vapor at the exit. Moreover, a larger deviation of current heat load on railway route lines is permitted without considerable falling air cooler heat efficiency due to refrigerant injector recirculation at available many circulations. The method to determine the rational design heat load on air coolers of railway AC systems, providing closed to maximum refrigeration output generation over the considered period, was developed.

Keywords: Railway air conditioner · Changeable heat load · Liquid refrigerant recirculation

1 Introduction

The performance of railway AC systems is characterized by considerable variations in current heat loads on their air coolers according to actual climatic conditions on the route line. So, the problem is to determine the rational design heat load on air coolers of railway conditioners, providing closed to maximum refrigeration output generation over the considered period, and develop the system of refrigerant circulation in air coolers enabling a large deviation of current heat loads from their rational design value without considerable falling air cooler heat efficiency.

The system of refrigerant circulation in air coolers by an injector that enables excluding the final dry-out stage of refrigerant evaporation with extremely low intensity of heat transfer and as result provides increasing the heat efficiency of air coolers (overall heat flux) by 20–30% compared with conventional air coolers with complete refrigerant evaporation and superheated vapor at the exit was proposed. The injector uses the potential energy of high-pressure liquid refrigerant, leaving a condenser, which is conventionally lost while it throttling to evaporation pressure in an expansion valve.

2 Literature Review

Many researches deal with improving the performance of AC systems by the intensification of heat transfer processes in evaporators [1, 2] and condensers [3], application of various refrigerant circulation contours: refrigerant flow variation [4] within part load [5] and intermittent [6] runnings, traditional [7, 8] and advanced [9] vapour ejector circulation and their two-stage combination with absorption chiller [10, 11], waste heat recovery absorption [12, 13] and thermopressor with liquid injection [14, 15] technics.

As the modern trend in AC systems, the application of Variable Refrigerant Flow (VRF) system is considered to modulate heat load by varying refrigerant feed to air coolers [16, 17]. The VRF system maintains the zone comfort by supplying an adequate amount of refrigerant to air coils to meet cooling duties. The performance evaluations showed that the VRF system reduced energy consumption by 40% to 60% compared to that of central AC systems [18]. In majority VRF investigation, the accent is made on ambient air processing in air coolers [19, 20] greatly influenced by current changeable loading. The problem of inefficient operation of air coolers caused by dry-out of inner walls at the final stage of inside tube refrigerant evaporation followed by dropping the intensity of heat transfer remains unsolved.

As the alternative approach of the heat load modulation in AC systems, the concept of incomplete refrigerant evaporation [21, 22] with overfilling air coils leads to excluding a dry-out of the inner surface of air coils is developed through liquid refrigerant recirculation by the injector (jet pump).

Considerable changes in the current heat loads q_0 on the air cooler need choosing its rational design value, providing maximum annual effect due to engine inlet air cooling [23] or maximum refrigeration output generation AC systems [24, 25].

The study is aimed at the development of the method to determine the rational design of heat load on the air coolers of railway AC systems, providing closed to maximum refrigeration capacity generation, and the system of refrigerant circulation in air coolers, that allows a considerable deviation of refrigerant flow from the optimum value, corresponding the maximum heat flux, without considerable reduction of heat flux, under changeable actual heat loads during railway routs.

3   Research Methodology

The operation of railway AC systems is characterized by considerable changes in the current heat loads Q_0 on the route lines and in corresponding specific heat loads i.e. specific cooling capacity related to the unit of air mass flow:

$$q_0 = Q_0/G_a, \tag{1}$$

where G_a is – ambient air mass flow in an air cooler, kg/s.

The specific cooling capacity is calculated as

$$q_0 = \xi \cdot c_a \cdot (t_{amb} - t_{a2}), \text{ kJ/kg}, \tag{2}$$

where ξ is a coefficient of water vapor condensation heat, determined as a ratio of the overall heat, removed from the air being cooled, including the latent heat of water vapor condensed from the wet ambient air to the removed sensible heat; t_{amb} is an ambient air temperature; t_{a2} is a target air temperature at the air cooler outlet; c_a is the specific heat of ambient air.

The current heat loads q_0 are calculated according to varying actual ambient air parameters (temperature t_{amb} and relative humidity φ_{amb}) on the route lines with using the Meteomanz program [26] or others.

So as the efficiency of AC systems and their refrigeration machine performance depends on their cooling loading (current cooling capacities) q_0 and a duration τ of their operation, the summarised refrigeration capacity $\sum(q_0 \cdot \tau)$ generated during railway routes over the hottest month, might be considered as a primary criterion for the choice of a rational design cooling load of AC system.

For this, the current refrigeration capacities $q_0 \cdot \tau$, generated by the refrigeration machine in response to the cooling duties for cooling ambient air to the target air temperature t_{a2}, taking into account the corresponding duration τ of each current values of refrigeration capacities q_0, have been summarized during railway routes over the summer month to determine the monthly refrigeration output generation $\sum(q_0 \cdot \tau)$.

The monthly refrigeration output generation $\sum(q_0 \cdot \tau)$ in the dependence of design refrigeration capacity q_0 for actual climatic conditions on the route line was used to determine the rational value of design refrigeration capacity $q_{0.rat}$, providing closed to maximum monthly refrigeration output generation.

4   Results

4.1   Heat Loads on Railway Air Conditioning System on Route Line

The current values of temperature t_{amb} and relative humidity φ_{amb} of ambient air with using the Meteomanz program [26] and temperature decrease Δt_a within cooling ambient air from current ambient temperatures t_{amb} to the temperature $t_{a2} = 15\,°C$ and corresponding current specific refrigeration capacity (specific heat load on the air cooler) q_0, kW/(kg/s), or kJ/kg (at air mass flow $G_a = 1$ kg/s), during direct route Kyiv–Kherson (K-Kh) and return route Kherson–Kyiv (Kh-K) per day for 1.08-3.08.2017 are presented in Fig. 1 and 2.
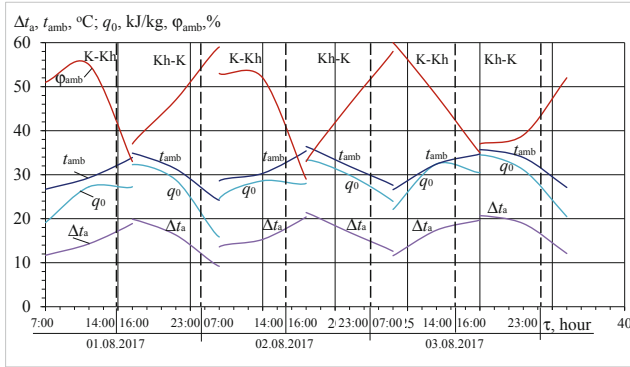
Fig. 1. Current values of temperature t_{amb} and relative humidity φ_{amb} of ambient air, temperature decrease Δt_a due to cooling ambient air to $t_{a2} = 15\ ^\circ C$ and corresponding current specific refrigeration capacity q_0 during direct routes Kyiv–Kherson (K-Kh) and return routes Kherson–Kyiv (Kh-K) for 1.08-3.08.2017.

As Fig. 1 shows the behavior of the curves corresponding to current values of specific refrigeration capacity q_0 and temperature decrease Δt_a within cooling ambient air to the temperature $t_{a2} = 15\ ^\circ C$ does not coincide because of variation in relative humidity φ_{amb} of ambient air and corresponding latent heat.

The results of summarizing the specific refrigeration capacity values $\sum(q_0 \cdot \tau)_{r1}$ (at air mass flow $G_a = 1$ kg/s) for cooling ambient air to the temperature $t_{a2} = 15\ ^\circ C$ during direct Kyiv–Kherson (K-Kh) and return Kherson–Kyiv (Kh-K) routes and their summarized value $\sum(q_0 \cdot \tau)$ for 1.08-3.08.2017 through summarizing their values $\sum(q_0 \cdot \tau)_{r1}$ for each route are presented in Fig. 2.
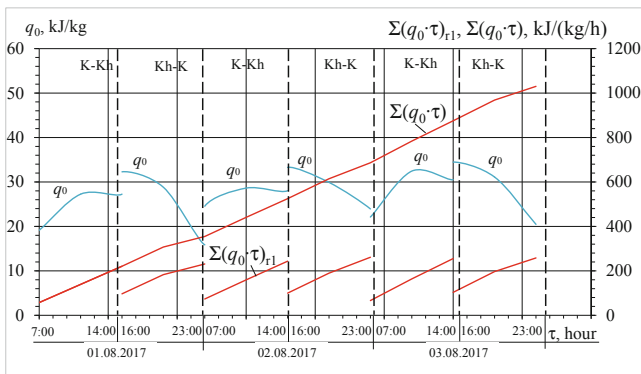
Fig. 2. Current values of specific refrigeration capacity q_0 and summarized values of specific refrigeration capacity $\sum(q_0 \cdot \tau)_{r1}$ for cooling ambient air to the temperature $t_{a2} = 15\ ^\circ C$ within each route (direct Kyiv–Kherson (K-Kh) and return Kherson–Kyiv (Kh-K) routes) and their summarized value $\sum(q_0 \cdot \tau)$ for 1.08-3.08.2017.

As Fig. 2 shows, the summarized values of specific refrigeration capacity $\sum(q_0 \cdot \tau)_{r1}$ for air conditioning in the direct (K-Kh) and return (Kh-K) routes are nearly the same that is confirmed by the monotonous rate of their increments $\sum(q_0 \cdot \tau)$ for 1.08-3.08.2017.

Considerable changes in the current heat loads q_0 on the air cooler need choosing its rational design value, providing maximum refrigeration capacity generation over the considered period. The monthly refrigeration output in relative values $\sum(q_0 \cdot \tau)$ (at air mass flow $G_a = 1$ kg/s) against the design of specific refrigeration capacity $q_0 = Q_0 / G_a$ of refrigeration machine for cooling ambient air to the temperature $t_{a2} = 15$ °C and climatic conditions on the route lines Cherson–Kyiv, and Kyiv–Cherson for July 2017 year, are presented in Fig. 3.
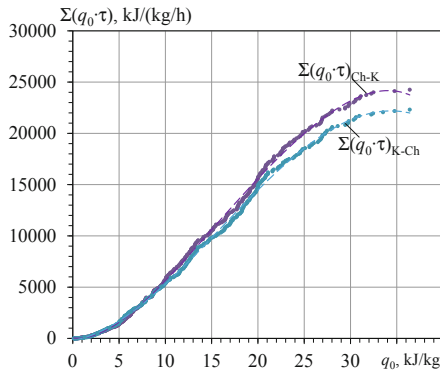
Fig. 3. The monthly refrigeration output in relative values $\sum(q_0 \cdot \tau)$ for ambient air cooling to the temperature $t_{a2} = 15$ °C against designed specific refrigeration capacity $q_0 = Q_0 / G_a$: $\sum(q_0 \cdot \tau)_{K-Kh}$ – summarized for all direct railway routes Kyiv-Kherson; $\sum(q_0 \cdot \tau)_{Kh-K}$ – summarized for all return railway routes Kherson–Kyiv, July 2017.

As Fig. 3 shows, the monthly (July) specific refrigeration output $\sum(q_0 \cdot \tau)$ for cooling ambient air to the temperature $t_{a2} = 15$ °C at specific refrigeration capacity $q_0 = 32$ kJ/kg, or kW/(kg/s), is evaluated as $\sum(q_0 \cdot \tau) \approx 22$ MJ/(kg/h) for all direct railway routes Kyiv–Kherson as well as $\sum(q_0 \cdot \tau) \approx 24$ MJ/(kg/h) for all return railway routes Kherson–Kyiv in July and achieved with the monotonous rate of their monthly increments $\sum(q_0 \cdot \tau)$ with increasing the specific refrigeration capacity q_0 up to 32 kJ/kg.

Because of the negligible rate of the monthly increments $\sum(q_0 \cdot \tau)$ the further increase in specific refrigeration capacity q_0 from 32 to 37 kJ/kg does not result in an appreciable increment in the monthly refrigeration output $\sum(q_0 \cdot \tau)$ for July but causes oversizing refrigeration machine, that leads to increasing its cost. Thus, the specific refrigeration capacity $q_0 = 32$ kJ/kg, or kW/(kg/s), is accepted as rational one to calculate a total designed refrigeration capacity Q_0 of refrigeration machine according to the total air mass flow G_a, kg/s:

$$Q_0 = G_a \cdot q_0, \text{ kW.} \tag{3}$$

4.2 A Fundamental Approach in Enhancing Heat Efficiency of Air Coolers

Convective evaporation of a refrigerant inside tubes (channels) is characterized by a sharp drop in intensity of heat transfer at the final stage of evaporation when so-called burnout takes place (Fig. 4). This occurs due to tube inner wall surface drying out with transition of annular flow to disperse (mist) flow.

In compact air coolers with finned tubes the coefficient of heat transfer to refrigerant α_a at the final stage of its evaporation is much lower than to air α_{air}. This results in a sharp decrease in overall heat transfer coefficient k and the heat flux q at burnout vapor fraction about $x_{cr} \approx 0, 9$ corresponding to drying the tube inner wall surface with the transition from annular to disperse flow (Fig. 4).
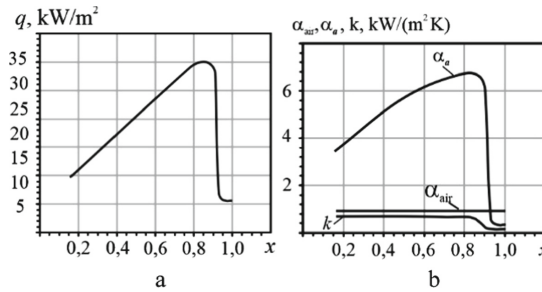
Fig. 4. Variation of heat transfer coefficients to boiling refrigerant α_a, air α_{air} and overall heat transfer coefficient k (**a**) and heat flux q with vapor mass fraction x (**b**).

Calculations were conducted for plate finned tubes of 10 and 12 mm inside and outside diameters, air temperature at the inlet $t_{air1} = 25$ °C and outlet $t_{air2} = 15$ °C, refrigerant boiling temperature at the exit $t_{02} = 0$ °C, refrigerant R142b.

Taking into account that a refrigerant vapor at the exit of conventional air cooler with the thermo-expansion valve is to be superheated by 5–10 °C, a share of the surface, corresponding to the final stage of refrigerant boiling and vapor superheating with extremely low intensity of heat transfer, is about 20–30%.

A sharp decrease in the heat transfer coefficient to refrigerant α_a with the transition from annular to disperse flow takes place for most of the refrigerants.

4.3 Enhancing Heat Efficiency of Air Coolers of Railway Conditioners in Varying Climatic Conditions

The performance of railway conditioners is characterized by considerable changes in heat loads according to current climatic conditions on the routes.

To provide intensive heat transfer on all the length of air cooler coils it is necessary to exclude their ending post dry out sections, i.e. make the air coolers operate with incomplete boiling. The unevaporated liquid should be separated from the vapor in the liquid separator and directed again by a jet pump (injector) to the air cooler for evaporation.

An injector recirculation of liquid refrigerant in air cooler can be successfully implemented in refrigeration machines of railway conditioners (Fig. 5).

The injector uses the potential energy of refrigerant pressure drop from condensing to evaporation pressure, which is conventionally lost while throttling high-pressure liquid refrigerant in the thermo-expansion valve.
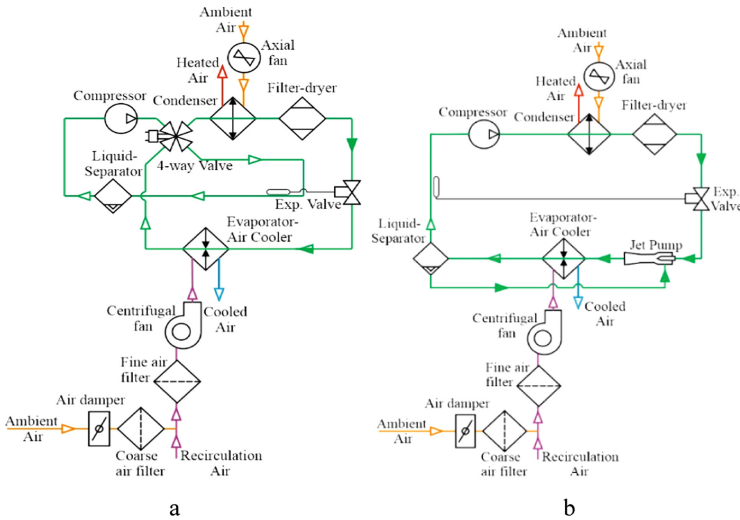
Fig. 5. The schemes of conventional (**a**) and developed railway conditioners with recirculation of liquid refrigerant in the evaporator-air cooler by the jet pump (**b**).

The highest thermal efficiency of the air cooler corresponds to the maximum value of heat flux

$$q_{max} = k\theta, \tag{4}$$

where θ is a logarithmic temperature difference; k is an overall heat transfer coefficient. The existence of maximum heat flux q_{max} is caused by the following. With an increase in the mass velocity of refrigerant ρw the heat transfer coefficient to refrigerant α_a and overall heat transfer coefficient k increases. The refrigerant pressure drop ΔP and corresponding refrigerant boiling temperature drop Δt_0 increase also. Such opposite influence of the refrigerant mass velocity ρw upon k and θ causes the existence of maximum of function $q = k\theta$ at a quite definite value of ρw. This value is considered as the optimum mass velocity of refrigerant $(\rho w)_{opt}$.

The results of thermal efficiency comparison of conventional air cooler with complete evaporation and superheated vapor at the exit and of advanced air cooler with incomplete evaporation due to liquid refrigerant recirculation by injector are shown in Fig. 6. The conditions at the air cooler outlet are the following: refrigerant boiling temperature at the evaporator exit $t_{02} = 0$ °C, there is a dry inner tube wall with a vapor

superheated in 10 °C for the conventional throttle circuit and wetted wall with $x_2 < x_{cr}$ for the injector recirculation circuit; in disperse mixture the vapor is superheated in 5 °C as compared to the boiling temperature t_{02}; refrigerant R142b; incoming air velocity $w = 6$ m/s.
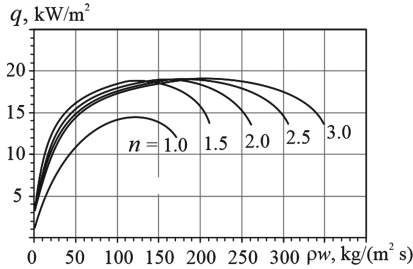
Fig. 6. Mean values of heat fluxes q against refrigerant mass velocities ρw: R142b, $t_{02} = 0$ °C; the number of circulation $n = 1.0$ – for conventional complete evaporation; $n > 1.0$ – for incomplete evaporation with liquid refrigerant recirculation by the injector.

Complete evaporation of refrigerant in the conventional air cooler is characterized by a number of its circulation $n = 1/x_2 = 1.0$, where x_2 – refrigerant mass vapor fraction at the outlet.

Figure 6 shows, that recirculation of liquid refrigerant in the air cooler by injector provides an increase in heat flux q by 20…30% compared with conventional air coolers with complete refrigerant evaporation and superheated vapor at the exit and enables a larger deviation of refrigerant mass velocities ρw from their optimum values (more than twice) without noticeable decreasing the heat flux q. This means that larger cooling load fluctuations are permitted without falling air cooler heat efficiency.

On analyzing the changes of current heat loads on air cooler of railway conditioner on route line Kyiv–Kherson–Kyiv within the range of $q_0 = 18$–34 kJ/kg (Fig. 2) taking into account of rational specific refrigeration capacity $q_{0rat} = 32$ kJ/kg (Fig. 4), their deviation is within the range $q_{0rat}/q_0 = 0.94$–1.8, whereas the available permissible deviation of refrigerant mass velocities ρw from their optimum values due to injector liquid refrigerant circulation (Fig. 6) is $\rho w/\rho w_{opt} = 0.5$–$2.0$, i.e. larger.

5   Conclusions

The method to determine the rational design heat load on air coolers of railway AC systems, matching current changeable climatic conditions and providing closed to maximum refrigeration output generation over any considered period of performance, was developed. The system of refrigerant circulation in air coolers by an injector that enables excluding the final dry-out stage of refrigerant evaporation with extremely low intensity of heat transfer and as result provides increasing the heat efficiency of air coolers (overall heat flux) by about 20% compared with conventional air coolers with complete refrigerant evaporation and superheated vapor at the exit was proposed. The

injector uses the potential energy of high-pressure liquid refrigerant, leaving a condenser, which is conventionally lost while it throttling to evaporation pressure in the expansion valve. Recirculation of liquid refrigerant in air coolers by injector enables a large deviation of refrigerant mass velocities from their optimum values (more than twice) without noticeable decreasing the heat flux, which means that larger current cooling load fluctuations on railway route lines are permitted without considerable falling air cooler heat efficiency.

So as any railway AC system includes liquid separator to collect excessive refrigerant during changeable current heat loads and to provide a safe performance of compressor (Fig. 5a), the proposed innovative refrigerant injector recirculation system does not need any considerable changes in conditioner design and addition refrigerant volume due to decreased air cooler dimensions by about 20% (Fig. 6).

References

1. Khovalyg, D.M., Baranenko, A.V.: Dynamics of two-phase flow with boiling refrigerant R134a in minichannels. J. Techn. Phys. **85**(3), 34–41 (2015). [in Russian]
2. Liu, H., Dong, H.: Refrigerant guiding pipe and heat exchanger having refrigerant guiding pipe. Patent US, 20130199764 (2013)
3. Bohdal, T., Sikora, M., Widomska, K., Radchenko, A.M.: Investigation of flow structures during HFE-7100 refrigerant condensation. Archives Thermodyn. Polish Acad. Sci. **36**(4), 25–34 (2015)
4. Goetzler, W.: Variable refrigerant flow systems. ASHRAE J. **49**(4), 24–31 (2007)
5. Im, P., Malhotra, M., Munk, J.D., Lee, J.: Cooling season full and part load performance evaluation of variable refrigerant flow (VRF) system using an occupancy simulated research building. In: Proceedings of the 16th International Refrigeration and Air Conditioning Conference at Purdue, West Lafayette, USA, 11–14 July (2016)
6. Zhang, L., Wang, Y., Meng, X.: Qualitative analysis of the cooling load in the typical room under continuous and intermittent runnings of air-conditioning. Procedia Eng. **205**, 405–409 (2017)
7. Butrymowicz, D., Gagan, J., Śmierciew, K., Łukaszuk, M., Dudar, A., Pawluczuk, A., Łapiński, A., Kuryłowicz, A. Investigations of prototype ejection refrigeration system driven by low grade heat. In: HTRSE-2018, E3S Web of Conferences, vol. 70, p. 03002, HTRSE-2018 (2018)
8. Smierciew, K., Gagan, J., Butrymowicz, D., Karwacki, J.: Experimental investigations of solar driven ejector air-conditioning system. Energy Build. **80**, 260–267 (2014)
9. Elbel, S., Lawrence, N.: Review of recent developments in advanced ejector technology. Int. J. Refrig **62**(February), 1–18 (2016)
10. Radchenko, R., Radchenko, A., Serbin, S., Kantor, S., Portnoi, B.: Gas turbine unite inlet air cooling by using an excessive refrigeration capacity of absorption-ejector chiller in booster air cooler. In: HTRSE-2018, E3S Web of Conferences, vol. 70, p. 03012 (2018)
11. Radchenko, M., Radchenko, R., Ostapenko, O., Zubarev, A., Hrych, A.: Enhancing the utilization of gas engine module exhaust heat by two-stage chillers for combined electricity, heat and refrigeration. In: 5th International Conference on Systems and Informatics, ICSAI 2018, pp. 240–244. Jiangsu (2019)

12. Radchenko, A., Radchenko, M., Konovalov, A., Zubarev, A.: Increasing electrical power output and fuel efficiency of gas engines in integrated energy system by absorption chiller scavenge air cooling on the base of monitoring data treatment. HTRSE-2018, 6 p. E3S Web of Conferences, vol. 70, p. 03011 (2018). HTRSE-2018 (2018)

13. Forduy, S., Radchenko, A., Kuczynski, W., Zubarev, A., Konovalov, D.: Enhancing the fuel efficiency of gas engines in integrated energy system by chilling cyclic air. In: Tonkonogyi, V. et al. (eds.) Grabchenko's International Conference on Advanced Manufacturing Processes. InterPartner-2019. Lecture Notes in Mechanical Engineering, pp. 500–509. Springer, Cham (2020), 10 p.

14. Konovalov, D., Kobalava, H.: Efficiency analysis of gas turbine plant cycles with water injection by the aerothermopressor. In: Ivanov, V. et al. (eds.) Advances in Design, Simulation and Manufacturing II. DSMIE 2019. Lecture Notes in Mechanical Engineering, pp. 581–591. Springer, Cham (2020)

15. Konovalov, D., Trushliakov, E., Radchenko, M., Kobalava, G., Maksymov, V.: Research of the aerothermopresor cooling system of charge air of a marine internal combustion engine under variable climatic conditions of operation. In: Tonkonogyi, V. et al. (eds.) Grabchenko's International Conference on Advanced Manufacturing Processes. InterPartner-2019. Lecture Notes in Mechanical Engineering, pp. 520–529. Springer, Cham (2020)

16. Khatri, R., Joshi, A.: Energy performance comparison of inverter based variable refrigerant flow unitary AC with constant volume unitary AC. Energy Procedia **109**, 18–26 (2017)

17. Lee, J.H., Yoon, H.J., Im, P., Song, Y.-H.: Verification of energy reduction effect through control optimization of supply air temperature in VRF-OAP system. Energies **11**(1), 1 (2018)

18. Liu, C., Zhao, T., Zhang, J.: Operational electricity consumption analyze of VRF air conditioning system and centralized air conditioning system based on building energy monitoring and management system. Procedia Engineering **121**, 1856–1863 (2015)

19. Park, D.Y., Yun, G., Kim, K.S.: Experimental evaluation and simulation of a variable refrigerant-flow (VRF) air-conditioning system with outdoor air processing unit. Energy Build. **146**, 122–140 (2017)

20. Zhu, Y., Jin, X., Du, Z., Fang, X., Fan, B.: Control and energy simulation of variable refrigerant flow air conditioning system combined with outdoor air processing unit. Appl. Therm. Eng. **64**, 385–395 (2014)

21. Radchenko, N.: A concept of the design and operation of heat exchangers with change of phase. Archives Thermodyn. Polish Acad. Sci. **25**(4), 3–19 (2004)

22. Trushliakov, E., Radchenko, M., Bohdal, T., Radchenko, R., Kantor, S.: An innovative air conditioning system for changeable heat loads. In: Tonkonogyi, V., et al. (eds.) Grabchenko's International Conference on Advanced Manufacturing Processes. InterPartner-2019. Lecture Notes in Mechanical Engineering, pp. 616–625. Springer, Cham (2020)

23. Radchenko, A., Bohdal, L., Zongming, Y., Portnoi, B., Tkachenko, V.: Rational designing of gas turbine inlet air cooling system. In: Tonkonogyi, V., et al. (eds.) Grabchenko's International Conference on Advanced Manufacturing Processes. InterPartner-2019. Lecture Notes in Mechanical Engineering, pp. 591–599. Springer, Cham (2020)

24. Radchenko, A., Radchenko, M., Trushliakov, E., Kantor, S., Tkachenko, V.: Statistical method to define rational heat loads on railway air conditioning system for changeable climatic conditions. In: 5th International Conference on Systems and Informatics: ICSAI 2018, pp. 1308–1312. Jiangsu (2018)

25. Trushliakov, E., Radchenko, M., Radchenko, A., Kantor, S., Zongming, Y.: Statistical approach to improve the efficiency of air conditioning system performance in changeable climatic conditions. In: 5th International Conference on Systems and Informatics: ICSAI 2018, pp. 1303–1307. Jiangsu, Nanjing, China (2018)
26. Meteomanz Homepage. http://www.meteomanz.com/. Accessed 21 May 2019

The Efficiency of Refrigeration Capacity Regulation in the Ambient Air Conditioning Systems

Eugeniy Trushliakov [iD], Andrii Radchenko [iD],
Mykola Radchenko$^{(\boxtimes)}$ [iD], Serhiy Kantor [iD], and Oleksii Zielikov [iD]

Admiral Makarov National University of Shipbuilding,
9, Heroiv Stalinhradu Avenue, Mykolaiv 54000, Ukraine
nirad50@gmail.com

Abstract. The operation of the ambient air conditioning systems (ACS) is characterized by considerable fluctuations of the heat load in response to the current climatic conditions. It needs the analyses of the efficiency of the application of compressors with frequency converters for refrigeration capacity regulation in actual climatic conditions. A new method and approach to analyzing the effectiveness of ACS cooling capacity adjusting by using the compressor with changing the rotational speed of the motor as an example have been developed, according to which the overall range of changeable heat loads is divided into two zones: the zone of ambient air processing with considerable fluctuations of the current heat load, that requires effective refrigeration capacity regulation by the compressor with frequency converters (from 100% rated refrigeration capacity down to about 50%) and not an adjustable zone of reduced refrigeration capacity below 50% rated refrigeration capacity of the compressor. The magnitudes of threshold refrigeration capacity between both zones are chosen according to the rational value of installed (design) refrigeration capacity on the ACS, required for cooling the ambient air to a target temperature that ensures the maximum annual refrigeration capacity production in actual current climatic conditions. The proposed method and approach to the analysis of the efficiency of the refrigeration capacity regulation of the ACS compressor by distributing the overall range of changes in current heat loads allows increasing the efficiency of utilizing the installed refrigeration capacity in prevailing climatic conditions.

Keywords: Ambient air processing · Stable heat load · Changeable heat load · Threshold refrigeration capacity · Refrigeration capacity distribution

1 Introduction

Significant fluctuations of the heat load characterize the operation of the ambient air conditioning systems (ACS) under the current ambient air temperature t_{amb} and relative humidity φ_{amb} [1, 2]. At the same time, the operation of closed type ACS (processing of indoor air) is characterized by relatively insignificant fluctuations in the heat load on the air coolers (AC), corresponding to changes in the room air temperature within a

narrow range (about 5 °C). For such closed type ACS it is advantageous to use compressors with frequency converters that provide refrigeration capacity regulation from nominal (rated) to 50% of nominal and lower.

The study aims to develop an approach to the analysis of the efficiency of regulating the refrigeration capacity of an ACS compressor with a frequency converter for actual climatic conditions.

2   Literature Review

In a number of investigations, the air conditioning is considered as one of the technologies for combined cooling, heating, and power (CCHP) [3, 4]. Some of the technical innovations and methodological approaches in waste heat recovery might be applied for traditional refrigeration technologies in air conditioning, in particular, the evaporative cooling [5], two-stage air-cooling, as well as methods to choose rational design value of refrigeration capacity to match current cooling demand [6–8].

Numerous researchers have studied the energy efficiency of the VRF system [9, 10] and proposed some practical recommendations [11, 12]. The simulation results in work [13] show that the VRF systems would save around 15–42% and 18–33% for HVAC site and source energy uses compared to the rooftop unite variable air volume systems (RTU-VAV) systems. The author [14] proposes the method of calculating the thermal load of a building. The VRF systems operate with high part-load efficiency [15, 16], which results in top daily and seasonal energy efficiency. Hence, as ACS typically spend most of their operating hours τ in the range of 40% to 80% of maximum capacity [17]. Results [18] show that ACS have great potential for energy saving, and the adjustability of VRF ACS is better than that of a centralized air conditioning system. The authors [19] study analyzes the cooling load rules of a typical room comparatively under the intermittent and continuous running of ACS.

A combination of the HVAC system with RTU used as the outdoor air processing (OAP) system in the VRF and control strategies to enhance its energy performance and thermal comfort was proposed [10, 20]. The VRF system with energy recovery ventilation (ERV) [21] and a dedicated outdoor air system (DOAS) was introduced [22]. The evaluation of indoor thermal environments and energy consumption of the VRF system [23, 24] with a heat pump desiccant (HPD) was conducted [25].

The HVAC system that processed outdoor air loads by supplying refrigerant from the outdoor unit performed simultaneously as an outdoor unit in the VRF system in contrast with the OAP, which had compressors [26]. In the VRF-OAP system, the multiple indoor units and the OAP were simultaneously connected to an outdoor unit.

The authors [27] developed a control algorithm of the supply air temperature (threshold temperature) in the outdoor air processing (OAP). A higher energy reduction compared with the conventional operation without refrigerant flow regulation, revealed when the outdoor air temperature was closer to the indoor temperature setpoint, was quite evident due to superlative applying the variable speed compressor in part-load modes. The authors [28] on the base of field test results revealed that the actual OAP capacity should be less than 30% of the design outdoor unit capacity to prevent a lack of indoor unit cooling capacities.

3   Research Methodology

In the general case, an overall heat load of any ACS comprises the unstable heat load zone, corresponding to ambient (outdoor) air processing with considerable heat load fluctuations in response to actual climatic conditions, and a comparatively stable heat load zone for subsequent air cooling (subcooling) to a target temperature.

In modern VRF systems, the load modulation is performed by varying refrigerant feed to air coolers. The COP and the specific (per unit of refrigerant mass flow) generated refrigeration capacity are stabilized due to a change in the rotational speed of the piston compressor while reducing the heat load to 50% of the nominal.

Authors developed a methodological approach to the analysis of the efficiency of regulation of the cooling capacity of ACS in actual climatic conditions, according to which the overall range of changes in current heat loads is divided into two zones: a zone of effective regulation of the refrigeration capacity without energy loss and a zone of the reduced not adjustable (unregulated) refrigeration capacity.

For the convenience of calculation for other refrigeration capacities of ACS the heat loads are represented in relative (specific) values per unit air mass flow ($G_a = 1$ kg/s) – as specific heat load, or refrigeration capacity of a refrigerating machine (RM),

$$q_0 = Q_0/G_a, \text{kJ/kg}, \tag{1}$$

where Q_0 is the total heat load (refrigeration capacity) for airflow G_a.

The rational value $q_{0.\text{rat}}$ of specific refrigeration capacity q_0 on the AC, required for cooling the ambient air to a target temperature of 10 °C, ensures the maximum specific annual refrigeration capacity production $\sum (q_0 \cdot \tau)$ taking into account the actual current climatic conditions [29]. The specific cooling capacity is calculated as follows:

$$q_0 = \xi \cdot c_{\text{ma}} \cdot (t_{\text{amb}} - t_{\text{a2}}), \text{kJ/kg}, \tag{2}$$

where: ξ – coefficient of water vapor condensation heat, calculated as a ratio of the overall heat removed from the air being cooled, including the latent heat of water vapor condensed from the ambient air to the sensible heat transferred; c_a – humid air specific heat. The specific annual refrigeration capacity production

$$\sum (q_0 \cdot \tau) = \sum (\xi \cdot c_a \cdot (t_{\text{amb}} - t_{\text{a2}}) \cdot \tau). \tag{3}$$

The specific refrigeration capacity consumption in the zone of its frequency regulation $q_{0.10/2\text{reg} > 0}$ (positive values in the area of adjustable refrigeration capacity from 100 to 50% – above threshold value $q_{0.10\text{rat}}/2$) defined as $q_{0/2\text{reg} > 0} = q_0 - q_{0.\text{rat}}/2 \geq 0$, as well as below the range of its frequency regulation $q_{0.10/2\text{reg} < 0}$ (positive values in the unregulated range of refrigeration capacity below 50% – below $q_{0.10\text{rat}}/2$): $q_{0/2\text{reg} < 0} = q_{0\text{rat}}/2 - q_0 \geq 0$. The values of the unused excess of the installed refrigeration capacity: $q_{0.10\text{rat}}/2 - q_{0.10/2\text{reg} > 0}$ in the zone of its frequency regulation (above $q_{0.10\text{rat}}/2$), its excess: $q_{0.10\text{rat}}/2 - q_{0.10/2\text{reg} < 0}$ outside the range of its control (below

$q_{0.10rat}/2$), the total expenditures of increasing consumption $\sum \left(q_{0.10/2reg > 0} \cdot \tau\right) = \sum \left[\left(q_{0.10} - q_{0.10rat}/2\right) \cdot \tau\right] \geq 0$ and excess of refrigeration capacity $\sum \left[\left(q_{0.10rat}/2 - q_{0.10/2reg > 0}\right) \cdot \tau\right] = q_{0.10} - q_{0.10rat}/2 \geq 0$ in the zone of its regulation (above $q_{0.10rat}/2$) and consumption $\sum \left(q_{0.10/2reg < 0} \cdot \tau\right) = \sum \left[\left(q_{0.10rat}/2 - q_{0.10}\right) \cdot \tau\right] \geq 0$ and excess of installed refrigeration capacity $\sum \left[\left(q_{0.10rat}/2 - q_{0.10/2reg < 0}\right) \cdot \tau\right] = \sum \left[\left(q_{0.10} - q_{0.10rat}/2\right) \cdot \tau\right] \geq 0$ below the range of its regulation (lower $q_{0.10rat}/2$).

4   Results

For the climatic conditions of the south of Ukraine, when the air is cooled to $t_{a2} = 10\ °C$, the maximum specific annual refrigeration capacity production $\sum \left(q_0 \cdot \tau\right)$ takes place at the specific refrigeration capacity $q_0 \approx 34$ kJ/kg as rational $q_{0.rat}$ [29]. Current values of t_{amb}, specific heat loads at the ACS air cooler (AC) $q_{0.10}$, consumption of the specific refrigeration capacity in the zone of its frequency regulation $q_{0.10/2reg > 0} = q_{0.10} - q_{0.10rat}/2 \geq 0$ (positive values in the area of adjustable refrigeration capacity from 100 to 50% – above threshold value $q_{0.10rat}/2$ in Fig. 1a and below the range of its frequency regulation $q_{0.10/2reg < 0} = q_{0.10rat}/2 - q_{0.10} \geq 0$ (positive values in the unregulated range of refrigeration capacity below 50% – below $q_{0.10rat}/2$ in Fig. 1b) for climatic conditions (Voznesensk, Mykolaiv region, 2015) are shown in Fig. 1.

As Fig. 1 shows, the share of cold production at 50% frequency regulation of the refrigeration capacity is $\sum \left(q_{0.10/2reg > 0} \cdot \tau\right) / \left(\sum \left(q_{0.10/2reg > 0} \cdot \tau\right) + \sum \left(q_{0.10/2reg < 0} \cdot \tau\right)\right) \approx 0,47$, i.e. about 47% of the total monthly amount of cold spent for cooling the air in the range of variation of the current heat load $q_{0.10}$ from 0 to $q_{0.10rat} = 34$ kJ/kg. However, with respect to the unused monthly excess of the installed cooling capacity over the expendable for cooling the air $\sum \left[\left(q_{0.10rat}/2 - q_{0.10/2reg > 0}\right) \cdot \tau\right] = q_{0.10} - q_{0.rat}/2 \geq 0$ in the region of 50% of its frequency regulation, the share of refrigeration capacity monthly production is $2200/(2200 + 10500) \approx 0,17$ (Fig. 1a, i.e., about 17%, and almost half as much $(2200/[2\ (2200 + 10500)] \approx 0,087)$ in the entire range of changes in the current heat load $q_{0.10}$ from 0 to $q_{0.10rat} = 34$ kJ/kg for the July.

This indicates, firstly, the presence of significant reserves to increase the efficiency of ACS by using the excess of the installed refrigeration capacity over that consumed for cooling air, in particular, by accumulating it for subsequent consumption, which provides a significant reduction in the installed refrigeration capacity, and secondly, the possibility to use other methods of regulating the refrigeration capacity in addition to changing the speed of the compressor motor, for example, by turning off the cylinders or the compressor itself in the case of several compressors, etc.

If ACS operates in June or August, the efficiency of applying the refrigeration capacity control by changing the rotational speed of the compressor electric motor will be even lower, and taking into account 3–5 times higher cost of compressors with frequency converters, their application for ACS becomes problematic.
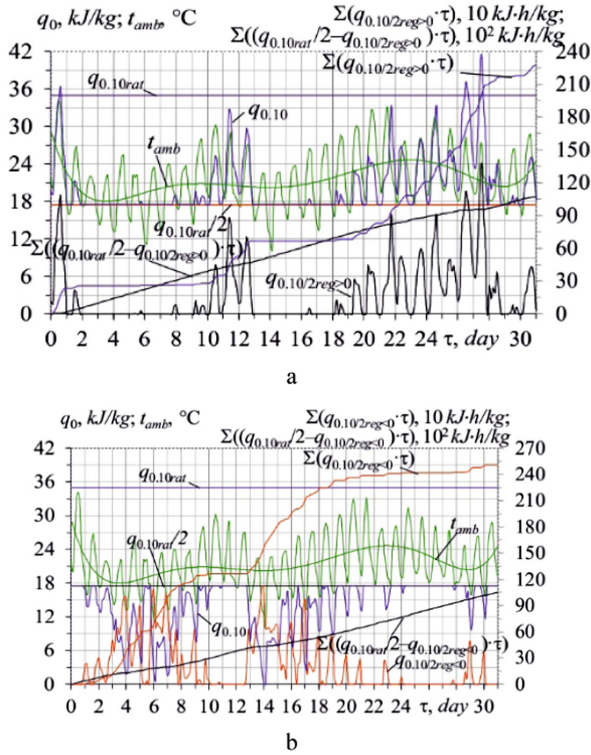
a

b

Fig. 1. Current values of t_{amb}, refrigeration capacity $q_{0.10}$, consumption $q_{0.10/2reg>0}$ and unused excess $(q_{0.10rat}/2 - q_{0.10/2reg > 0})$, total monthly consumption $\sum (q_{0.10/2reg > 0} \cdot \tau)$ and excess $\sum \left[(q_{0.10rat}/2 - q_{0.10/2reg > 0} \cdot \tau) \right]$ within frequency regulation (**a**), values of $q_{0.10/2reg < 0}$ and $(q_{0.10rat}/2 - q_{0.10/2reg < 0})$, $\sum (q_{0.10/2reg < 0} \cdot \tau)$ and $\sum \left[(q_{0.10rat}/2 - q_{0.10/2reg < 0}) \cdot \tau \right]$ below regulation (**b**): $q_{0.10/2reg > 0} = q_{0.10} - q_{0.10rat}/2 \geq 0$ (adjustable range); $q_{0.10/2reg < 0} = q_{0.10rat}/2 - q_{0.10} \geq 0$ (unregulated range); threshold value $q_{0.10rat}/2 \approx 17$ kJ/kg.

When the ambient air is being cooled from t_{amb} to the higher temperatures $t_{a2} = 15$, 17 and 20 °C, as the cooling temperature t_{a2} rises a significant proportion of the unstable heat load is replaced from its adjustable range $(q_{0/2reg > 0} = q_0 - q_{0.rat/2} \geq 0)$, which falls on the $q_0 \geq q_{0.rat}/2$, into the range of unregulated heat load $q_0 \leq q_{0.rat}/2$ (Fig. 2, 3 and 4).
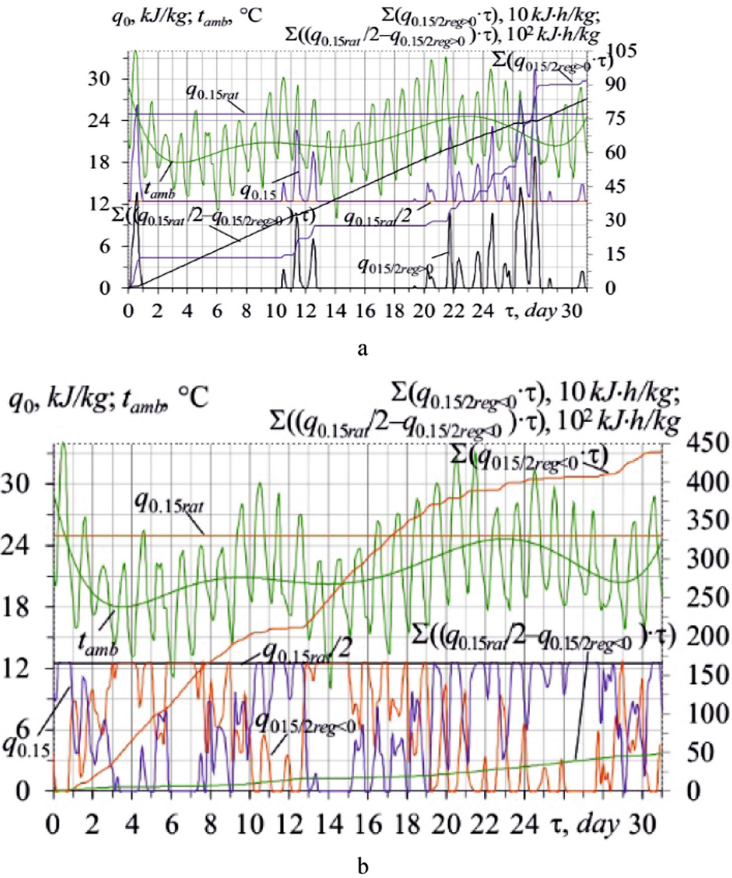
Fig. 2. Current values of t_{amb}, specific refrigeration capacity of ACS $q_{0.15}$, consumption of refrigeration capacity $q_{0.15/2reg > 0}$ and unused excess of installed refrigeration capacity ($q_{0.15rat}/2 - q_{0.15/2reg > 0}$), the total monthly consumption $\sum (q_{0.15/2reg > 0} \cdot \tau)$ and excess $\sum [(q_{0.15rat}/2 - q_{0.15/2reg > 0}) \cdot \tau]$ of refrigeration capacity within frequency regulation (**a**), values of $q_{0.15/2reg < 0}$ and $(q_{0.15rat}/2 - q_{0.15/2reg < 0})$, $\sum (q_{0.15/2reg < 0} \cdot \tau)$ and $\sum [(q_{0.15rat}/2 - q_{0.15/2reg < 0}) \cdot \tau]$ below the range of its regulation (**b**) when cooling the ambient air from t_{amb} to $t_{a2} = 15\ °C$: $q_{0.15/2reg > 0} = q_{0.15} - q_{0.15rat}/2 \geq 0$ (adjustable range); $q_{0.15/2reg < 0} = q_{0.15rat}/2 - q_{0.15} \geq 0$ (unregulated range); threshold value $q_{0.15rat}/2 \approx 12\ kJ/kg$.

As Fig. 2 shows, the share of the refrigeration capacity monthly production at 50% frequency regulation of refrigeration capacity is: $\sum (q_{0.15/2reg > 0} \cdot \tau) / (\sum (q_{0.15/2reg > 0} \cdot \tau) + \sum (q_{0.15/2reg < 0} \cdot \tau)) \approx 0,17$, i.e., about 17% of the total monthly amount of the refrigeration capacity expended for cooling the air in the range of variation of the current heat load $q_{0.15}$ from 0 to $q_{0.15rat} = 25\ kJ/kg$.
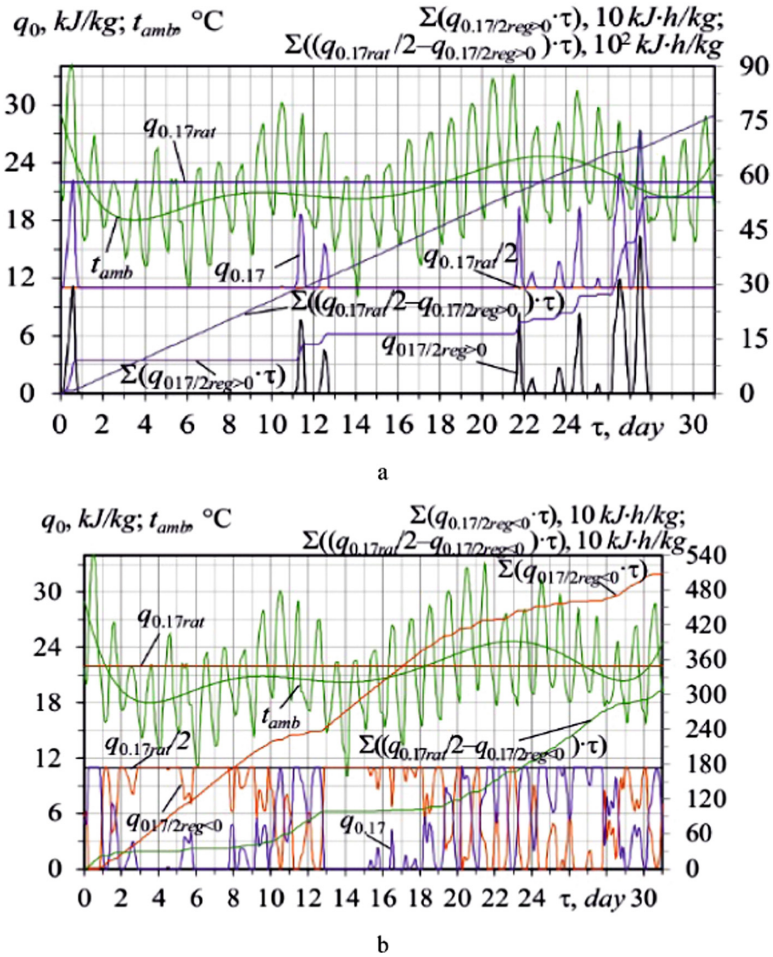
Fig. 3. Current values of t_{amb}, specific refrigeration capacity $q_{0.15}$, consumption $q_{0.17/2reg > 0}$ and unused excess of installed refrigeration capacity ($q_{0.17rat}/2 - q_{0.17/2reg > 0}$), the total monthly consumption $\sum(q_{0.20/2reg > 0} \cdot \tau)$ and excess $\sum[(q_{0.17rat}/2 - q_{0.17/2reg > 0}) \cdot \tau]$ of refrigeration capacity within frequency regulation (**a**), values of $q_{0.17/2reg < 0}$ and ($q_{0.17rat}/2 - q_{0.17/2reg < 0}$), $\sum(q_{0.17/2reg < 0} \cdot \tau)$ and $\sum[(q_{0.17rat}/2 - q_{0.17/2reg < 0}) \cdot \tau]$ below the range of its regulation (**b**) when cooling the ambient air from t_{amb} to $t_{a2} = 17\,°C$: $q_{0.17/2reg > 0} = q_{0.17} - q_{0.17rat}/2 \geq 0$ (adjustable range); $q_{0.17/2reg < 0} = q_{0.17rat}/2 - q_{0.17} \geq 0$ (unregulated range); threshold value $q_{0.17rat}/2 \approx 11$ kJ/kg.

The share of the refrigeration capacity monthly production at 50% frequency regulation of refrigeration capacity is: $\sum(q_{0.17/2reg > 0} \cdot \tau) / (\sum(q_{0.17/2reg > 0} \cdot \tau) + \sum(q_{0.17/2reg < 0} \cdot \tau)) \approx 0.093$, i.e. about 9.3% of the total monthly amount of the refrigeration capacity expended for cooling the air in the range of variation of $q_{0.17}$ from 0 to $q_{0.17rat} = 22$ kJ/kg (Fig. 3).
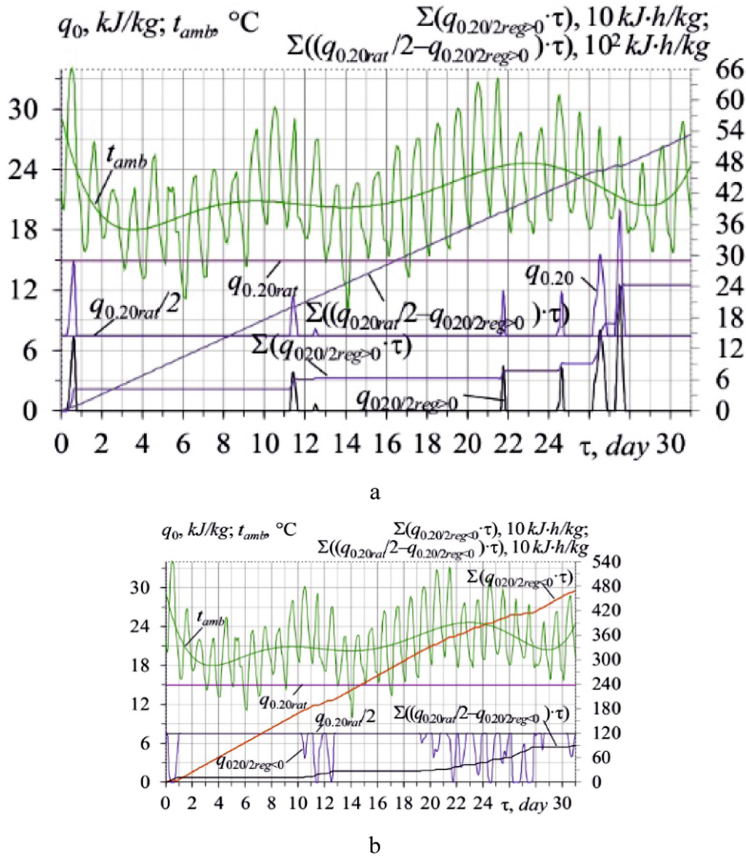
Fig. 4. Current values of t_{amb}, consumption of specific refrigeration capacity $q_{0.20/2reg\,>\,0}$ and unrealized excess of installed refrigeration capacity $(q_{0.20rat}/2 - q_{0.20/2reg\,>\,0})$, the total monthly consumption $\sum (q_{0.20/2reg\,>\,0} \cdot \tau)$ and excess $\sum [(q_{0.20rat}/2 - q_{0.20/2reg\,>\,0}) \cdot \tau]$ of refrigeration capacity within frequency regulation (**a**), values of $q_{0.20/2reg\,<\,0}$ and $(q_{0.20rat}/2 - q_{0.20/2reg\,<\,0})$, $\sum (q_{0.20/2reg\,<\,0} \cdot \tau)$ and $\sum [(q_{0.20rat}/2 - q_{0.20/2reg\,<\,0}) \cdot \tau]$ below the range of its regulation (**b**) when cooling the ambient air from t_{amb} to $t_{a2} = 20\ °C$: $q_{0.20/2reg\,>\,0} = q_{0.20} - q_{0.20rat}/2 \geq 0$ (adjustable range); $q_{0.20/2reg\,<\,0} = q_{0.20rat}/2 - q_{0.20} \geq 0$ (unregulated range); threshold value $q_{0.20rat}/2 \approx 7.5$ kJ/kg.

As Fig. 4 shows, the share of the refrigeration capacity monthly production at 50% frequency regulation of the refrigeration capacity is $\sum (q_{0.20/2reg\,>\,0} \cdot \tau)/$ $(\sum (q_{0.20/2reg\,>\,0} \cdot \tau) + \sum (q_{0.20/2reg\,<\,0} \cdot \tau)) \approx 0.05$, i.e., about 5% of the total amount of the refrigeration capacity monthly spent for cooling the air in the range of changes in the current heat load $q_{0.20}$ from 0 to $q_{0.20rat} = 15$ kJ/kg, which indicates an extremely low efficiency of regulation of ACS refrigeration capacity by the speed of rotation of the piston electric motor compressor and the need for other control methods.

5   Conclusions

A method and approach to the analysis of the efficiency of regulation of the refrigeration capacity of ACS in actual climatic conditions is proposed, according to which the entire range of changes in current heat loads is divided in two zones: a zone of ambient air processing with considerable fluctuations of the current heat load, that requires effective refrigeration capacity regulation by compressor with frequency converters (from 100% rated refrigeration capacity down to about 50%) and a not adjustable zone of the reduced refrigeration capacity below 50% rated refrigeration capacity of compressor. The magnitudes of threshold refrigeration capacity between both zones are chosen according to the rational value of the installed refrigeration capacity on the ACS, required for cooling the ambient air to a target temperature that ensures the maximum annual refrigeration capacity production in actual climatic conditions.

It is shown that for the summer month, the proportion of the refrigeration capacity monthly consumed for cooling the ambient air to the target temperature with a 50% frequency control of the refrigeration capacity is about 10% of its total amount that could be monthly produced at rated load. This fact indicates a low efficiency of regulating the refrigeration capacity of ACS by changing the rotation speed of the reciprocating compressor electric motor and the need for other control methods.

The proposed method and approach to the analysis of the efficiency of the refrigeration capacity regulation of the ACS compressor by distributing the overall range of changes in current heat loads allows revealing the reserves for increasing the efficiency of utilizing the installed refrigeration capacity in prevailing climatic conditions.

References

1. Marque, R.P., Hacon, D., Tessarollo, A., Parise, J.A.R.: Thermodynamic analysis of trigeneration systems taking into account refrigeration, heating and electricity load demands. Energy Build. **42**, 2323–2330 (2010)
2. Ortiga, J., Carles, B.J., Alberto, C.: Operational optimization of a complex trigeneration system connected to a district heating and cooling network. Appl. Therm. Eng. **50**, 1536–1542 (2013)
3. Radchenko, M., Radchenko, R., Ostapenko, O., Zubarev, A., Hrych, A.: Enhancing the utilization of gas engine module exhaust heat by two-stage chillers for combined electricity, heat and refrigeration. In: 5th International Conference on Systems and Informatics, ICSAI 2018, Jiangsu, Nanjing, China, pp. 227–231 (2018)
4. Sugiartha, N., Tassou, S.A., Chaer, I., Marriott, D.: Trigeneration in food retail: an energetic, economic and environmental evaluation for a supermarket application. Appl. Therm. Eng. **29**, 2624–2632 (2009)
5. Eidan, A.A., Alwan, K.J.: Enhancement of the performance characteristics for air-conditioning system by using direct evaporative cooling in hot climates. Energy Procedia **142**, 3998–4003 (2017)
6. Radchenko, A., Radchenko, M., Trushliakov, E., Kantor, S., Tkachenko, V.: Statistical method to define rational heat loads on railway air conditioning system for changeable climatic conditions. In: 5th International Conference on Systems and Informatics, ICSAI 2018, Jiangsu, Nanjing, China, pp. 1308–1312 (2018)

7. Radchenko, R., Radchenko, A., Serbin, S., Kantor, S., Portnoi, B.: Gas turbine unite inlet air cooling by using an excessive refrigeration capacity of absorption-ejector chiller in booster air cooler. In: HTRSE-2018, E3S Web of Conferences, vol. 70, p. 6 (2018)

8. Trushliakov, E., Radchenko, M., Radchenko, A., Kantor, S., Zongming, Y.: Statistical approach to improve the efficiency of air conditioning system performance in changeable climatic conditions. In: 5th International Conference on Systems and Informatics, ICSAI 2018, Jiangsu, Nanjing, China, pp. 1303–1307 (2018)

9. Alahmer, A., Alsaqoor, S.: Simulation and optimization of multi-split variable refrigerant flow systems. Ain Shams Eng. J. **9**, 1705–1715 (2017)

10. Chua, K.J., Chou, S.K., Yang, W.M., Yan, J.: Achieving better energy-efficient air conditioning – a review of technologies and strategies. Appl. Energy **104**, 87–104 (2013)

11. Yun, G.Y., Choi, J., Kim, J.T.: Energy performance of direct expansion air handling unit in office buildings. Energy Build. **77**, 425–431 (2014)

12. Yun, G.Y., Lee, J.H., Kim, H.J.: Development and application of the load responsive control of the evaporating temperature in a VRF system for cooling energy savings. Energy Build. **116**, 638–645 (2016)

13. Kim, D., Cox, S.J., Cho, H., Im, P.: Evaluation of energy savings potential of variable refrigerant flow (VRF) from variable air volume (VAV) in the U.S. climate locations. Energy Rep. **3**, 85–93 (2017)

14. Sait, H.H.: Estimated thermal load and selecting of suitable air-conditioning systems for a three story educational building. Procedia Comput. Sci. **19**, 636–645 (2013)

15. Ilie, A., Dumitrescu, R., Girip, A., Cublesan, V.: Study on technical and economical solutions for improving air-conditioning efficiency in building sector. Energy Procedia **112**, 537–544 (2017)

16. Li, Y., Wu, J., Shiochi, S.: Modeling and energy simulation of the variable refrigerant flow air conditioning system with water-cooled condenser under cooling conditions. Energy Build. **41**, 949–957 (2009)

17. Enteria, N., Yamaguchi, H., Miyata, M., Sawachi, T., Kuwasawa, Y.: Performance evaluation of the variable refrigerant flow (VRF) air-conditioning system subjected to partial and unbalanced thermal loadings. J. Therm. Sci. Technol. **11**(1), 1–11 (2016)

18. Liu, C., Zhao, T., Zhang, J.: Operational electricity consumption analyze of VRF air conditioning system and centralized air conditioning system based on building energy monitoring and management system. Procedia Eng. **121**, 1856–1863 (2015)

19. Zhang, L., Wang, Y., Meng, X.: Qualitative analysis of the cooling load in the typical room under continuous and intermittent runnings of air-conditioning. Procedia Eng. **205**, 405–409 (2017)

20. Zhu, Y., Jin, X., Du, Z., Fang, X., Fan, B.: Control and energy simulation of variable refrigerant flow air conditioning system combined with outdoor air processing unit. Appl. Therm. Eng. **64**, 385–395 (2014)

21. Fengxia, H., Zhongbin, Z., Hu, H., Zemin, C.: Experimental study on the all-fresh-air handling unit with exhaust air energy recovery. Energy Procedia **152**, 431–437 (2018)

22. Park, D.Y., Yun, G., Kim, K.S.: Experimental evaluation and simulation of a variable refrigerant-flow (VRF) air-conditioning system with outdoor air processing unit. Energy Build. **146**, 122–140 (2017)

23. Aynur, T.N., Hwang, Y., Radermacher, R.: Integration of variable refrigerant flow and heat pump desiccant systems for the cooling season. Appl. Therm. Eng. **30**, 917–927 (2010)

24. Aynur, T.N., Hwang, Y., Radermacher, R.: Integration of variable refrigerant flow and heat pump desiccant systems for the heating season. Energy Build. **42**, 468–476 (2010)

25. Aynur, T.N., Hwang, Y., Radermacher, R.: Simulation comparison of VAV and VRF air conditioning systems in an existing building for the cooling season. Energy Build. **41**, 1143–1150 (2009)
26. Im, P., Malhotra, M., Munk, J.D., Lee, J.: Cooling season full and part load performance evaluation of variable refrigerant flow (VRF) system using an occupancy simulated research building. In: Proceedings of the 16th International Refrigeration and Air Conditioning Conference at Purdue, West Lafayette, USA (2016)
27. Lee, J.H., Yoon, H.J., Im, P., Song, Y.-H.: Verification of energy reduction effect through control optimization of supply air temperature in VRF-OAP system. Energies **11**(1), 49 (2018)
28. Khatri, R., Joshi, A.: Energy performance comparison of inverter based variable refrigerant flow unitary AC with constant volume unitary AC. Energy Procedia **109**, 18–26 (2017)
29. Trushliakov, E., Radchenko, M., Bohdal, T., Radchenko, R., Kantor, S.: An innovative air conditioning system for changeable heat loads. In: Tonkonogyi, V., et al. (eds.) Grabchenko's International Conference on Advanced Manufacturing Processes. InterPartner-2019. LNME, pp. 616–625. Springer, Cham (2020)

Energy Efficient Technologies and Industrial Ecology

Improvement of the Model System to Develop Eco-Friendly Bio-Utilization of Phosphogypsum

Yelizaveta Chernysh[1]($\boxtimes$) and Koichi Hasegawa[2]

[1] Sumy State University, 2 Rymskogo-Korsakova Street, Sumy 40007, Ukraine
e.chernish@ssu.edu.ua
[2] Chubu University, Kasugai, 1200, Matsumoto, Aichi 487-8501, Japan

Abstract. This paper focused on the modeling of the possibility of bacteria growth under medium that different content phosphogypsum (PG) doses for environmental protection purposes with special attention to the analysis of the effect of PG features underestimation of *E. coli* growth. The culture of *E. coli* is diluted with Lysogeny broth (LB) initially without adding PG to obtain an optical density at 600 nm (OD_{600}) of 0.05. Study is carried out by adding different doses of PG (250 mg/200 mL LB; 500 mg/200 mL LB; 1000 mg/200 mL LB). The OD_{600} is measured with the use of an absorption spectrophotometer. Under modeling PG feature effluence, several factors are identified that impact on bacteria growth and the general methodological approach to assessing the biochemical activity of PG is formed. The important direction for feature study the effect of PG use as a component of the medium for *E. coli* is the assessment of mutations and adaptive biochemical mechanisms, in particular, the possibility of biofilm formation. Microorganisms in biofilms are better adapted and much more resistant to high concentrations of various groups of xenobiotics. In some cases, the matrix itself is involved in bioremediation, sorbing and retaining toxic substances from the aqueous phase.

Keywords: Environmental protection · Phosphogypsum · Modeling influence · *E. coli* · Bioremediation

1 Introduction

The sharp increase in industrial products worldwide in recent decades has flowed a large number of toxic pollutants to nature, which creates a significant burden on the biosphere. Bioremediation today is one of the promising methods for solving the problem of toxic substances [1]. The development of environmentally friendly waste transformation is a priority task for the green economy in many countries, and biotechnology greatly helps in this direction. Addressing the environmental consequences of emergencies is often a difficult environmental task. A search is constantly underway for the best way to reclaim vast land areas, restore the productivity of water bodies contaminated. Biological objects, in particular bacteria, are actively involved in the conversion of compounds of various origin, including human-made.

The use of biological products in a classic form for wastewater treatment is complicated by the lack of increased buoyancy in cultures of hydrocarbon-oxidizing

microorganisms. The buoyancy of the bio-sorbent is provided by particles of hydrophobized peat, in the pores of which bacterial cells responsible for biological activity are immobilized. Biosorbent combines the physical method of eliminating oil pollution (sorption) with its further biological degradation by microorganisms. Another advantage of the biosorbent is the ability to quickly localize pollution on the surface of the water, preventing the spread in depth and on the surface of the water body [2].

Cleaning and disinfection of domestic and industrial wastewater is an important task of effective environmental management. This problem is especially acute at production facilities with insignificant water circulation, where the construction of their treatment facilities is not economically feasible, and the remoteness of the facilities does not allow to discharge effluents to treatment facilities of settlements or larger enterprises. The use of modular wastewater treatment plants can solve this problem [2–4].

The use of various methods of environmental protection based on biological processes is the most environmentally friendly approach. The current level of knowledge of the processes occurring in living cells and the development of hardware design can significantly increase the effectiveness of biological and chemical methods [1].

Thus, the development of technology for wastewater and chemical by-products treatment is urgently required. Bioremediation, mainly using bacteria is a valid strategy. The current biological method for wastewater treatment is well studied. But since the microbial community and their metabolism are complex to optimize, then the target is changed.

2 Literature Review

Escherichia coli is used as applications for a long time to produce useful substances and develop biosensors for monitoring environments. Its low maintenance cost, rapid cell growth a simple genome structure allow us to understand whole biochemical and molecular systems of this organism [5]. E. coli has a high biosynthetic capacity and can grow well in a defined mineral medium supplemented with a carbon source. As municipal solid waste (MSW) contains naturally high carbohydrates, it can be utilized as a carbon and energy source for bacterial cultivation [5]. In the study of Majida Khanafer et al. (2017), raw domestic sewage in Kuwait City contained about 10^6 mL^{-1} colony-forming units of Enterobacter hormaechei subsp. oharae (56.6%), Klebsiella spp. (36%), and E. coli (7.4%) were detected. These coliforms isolated from the sewage grew successfully on a mineral agar medium with crude oil vapor as a sole source of carbon and energy [6]. The E. coli isolated from municipal wastewater showed characterized molecular marker patterns distinguishable from that in human and animal bodies [7].

Brewery spent grains (BSG), one of the by-products of brewery production, were used to study for hydrogen (H_2) production by *E. coli*. *E. coli* BW25113 wild type strain, hydrogenase (Hyd)-negative mutant with deletions of genes encoding key subunits Hyd 1–4 ($\Delta hyaB$, $\Delta hybC$, $\Delta hycE$, $\Delta hyfG$), or that with $\Delta hyaB$ $\Delta hybC$ double mutant were investigated with regards to growth, acidification of the medium, redox potential kinetics and H_2 production when using BSG hydrolysate. Thus, the results lead to the development of approaches for the production of H_2 simultaneously with the processing of waste [8].

Effect of e-waste on *E. coli* PQ-37 genomic integrity was evaluated by Solomon E. Owumi et al. (2014) using the SOS chromo test. Damage to *E. coli* deoxyribonucleic acid (DNA) increased proportionally to the metal concentrations [9].

Phosphogypsum is the chemical by-product of phosphate fertilizer production. Huge dumps of the phosphogypsum are left in 52 countries, totalling in 5.6–7.0 billion tons [10]. The annual increase of its accumulation in the world reaches 120–130 million tons, and the mass fraction of utilization does not exceed 10%. At this time, more than 55 million tons were accumulated on the territory of Ukraine [11, 12].

Accordingly, it is necessary to determine the directions of processing and utilization of phosphogypsum as a secondary raw material resource, provided that the toxic component is bound to sparingly soluble compounds and removed from biochemical conversion cycles elements in the biosphere.

This paper focused on the modeling of the possibility of *E. coli* growth under medium that content different phosphogypsum doses for environmental protection purpose.

To achieve this aim, the following tasks were set:

– modeling and analysis of the effect of phosphogypsum features under estimation of E. coli growth;
– developing the methodological approach of the estimation of bacteria growth under the medium that included phosphogypsum.

3 Research Methodology

3.1 Phosphogypsum Composition Analysis

The surface morphology of samples was observed by Scanning Electron Microscope (SEM) JSM-6510LA (JEOL Ltd., Japan) and the composition was analyzed by energy dispersive X-ray analysis (EDS).

3.2 Methods of Bacteria Growth Investigation

A single colony of *E. coli* was picked up, transferred into the Lysogeny broth (LB), and cultured overnight at 37 °C with constant shaking at 200 rpm. The cultured *E. coli* was diluted with fresh LB broth to obtain an optical density at 600 nm (OD_{600}) of 0.05 as an initial inoculum. LB broths with different doses of phosphogypsum (PG) (PG250 = 250 mg/200 mL LB; PG500 = 500 mg/200 mL LB; PG1000 = 1000 mg/200 mL LB, 25 mL each in 50 mL culture tube) were prepared, with added 100 µL of initial *E. coli* inoculum and cultured at 37 °C with constant stirring 200 rpm. Triplicate 100 µL aliquots were removed every hour for 5 h and after 24 h from each condition, and the OD_{600} values were measured using a multi-spectrophotometer 96-well plate reader (Synergy H1, Gen5 version 2.05) (BioTek® Instruments, Japan). Bacterial growth experiments were repeated 5 times independently to analyze the effect PG on bacterial growth.

Modeling and processing of experimental data were carried out using Microsoft Excel and bioinformation databases such as KEGG: Kyoto Encyclopedia of Genes and Genomes.

4   Results

4.1   Modeling and Analysis of the Effect of Phosphogypsum Features under Estimation of E. coli Growth

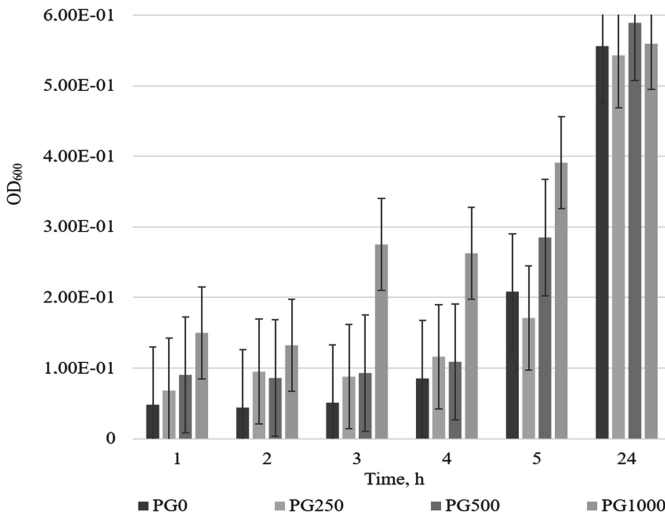Figure 1 shows the growth of *E. coli* in LB broth with different doses of PG.

Fig. 1. OD_{600} cultural suspension at different doses of Phosphogypsum.

To obtain these data, the average values of the change in the OD_{600} value in a series of experiments were found. At the beginning of the experiment, when analyzing the same sample (measuring one sample three times at different doses of PG), very different OD_{600} values were observed under the same conditions, since the precipitation of the PG components during mixing influenced the measurement readings. It was decided to take into account the primary OD_{600} of the culture medium with different PG concentrations. But in subsequent measurements, there was still a significant variation in the readings of the OD_{600} value. This was facilitated by the rapid sedimentation of particles of PG components. Therefore, in further experiments, the only supernatant was taken. During the first 5 h of *E. coli* cultivation, an OD_{600} increase was observed in samples with PG compared with the culture medium without its addition.

It's a very important task in developing the methodological approach for assessing the biochemical activity of PG with understanding influence chemical features of PG under metabolic pathways and OD_{600} measurement.

Since PG is a poorly soluble compound, its solubility in water does not exceed 1000 mg/L. Such a low solubility in water is since PG is formed from gypsum crystals, and it also has inclusions of aluminosilicates (see Fig. 2). Ca, S, Si, Al, P are the most represented elements in the PG composition (see Fig. 3).
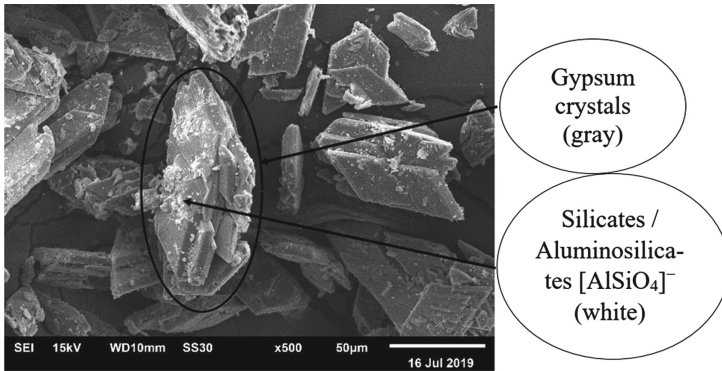

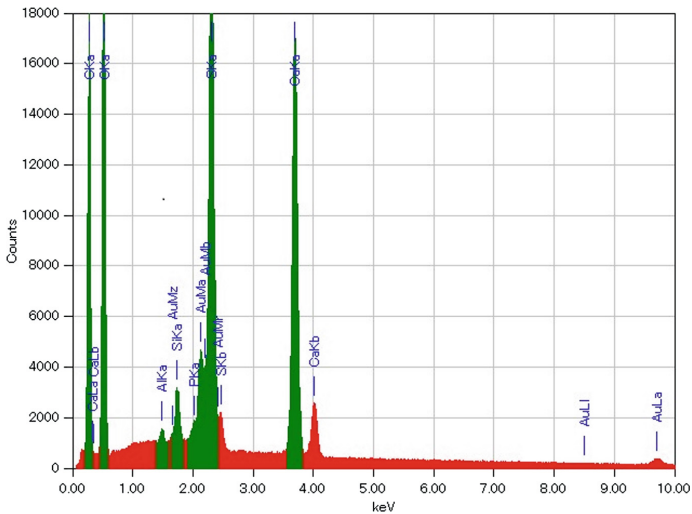**Fig. 2.** SEM images of phosphogypsum sample.

Fig. 3. EDS spectra of the field (Au is presented only under the metallization process of the sample).

But the metabolic activity of bacteria can affect the solubility of PG. Several factors influencing on the bacterial growth under this system are discussed; (i) the initial increase in the turbidity of the culture medium with different doses of PG and the rapid deposition of PG components on the bottom of the tube with a decrease in the turbidity;

(ii) partial splitting of the components of PG in the medium during the time of cultivation of *E. coli* and reducing sediment; (iii) after 24 h, tubes with culture media with PG and without it had approximately the same turbidity (see Fig. 4) and this was confirmed when evaluating the optical density (see Fig. 1).
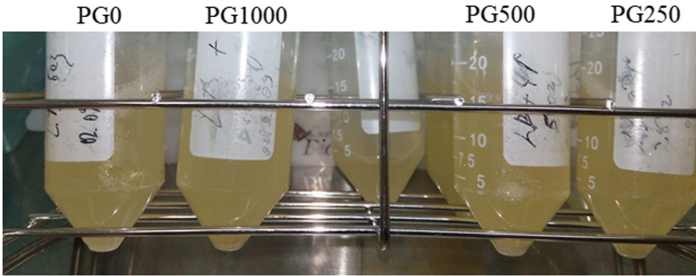

Fig. 4. Photography tubes after 24 h of *E. coli* cultivation.

Thus, the important task is the correct assessment of the effect of PG properties on a possible increase in the turbidity of the nutrient medium of some samples when raising this precipitate with stirring, which affects the evaluation of the experimental results.

Such effects of the influence of PG can be seen on the three-dimensional surface of the change in the OD_{600} of the culture suspension (Fig. 5), which indicates the need for a series of experiments taking into account the above-mentioned observed properties in the 'culture-medium- PG' system. This will allow the most objective assessment of PG effect on *E. coli* growth.
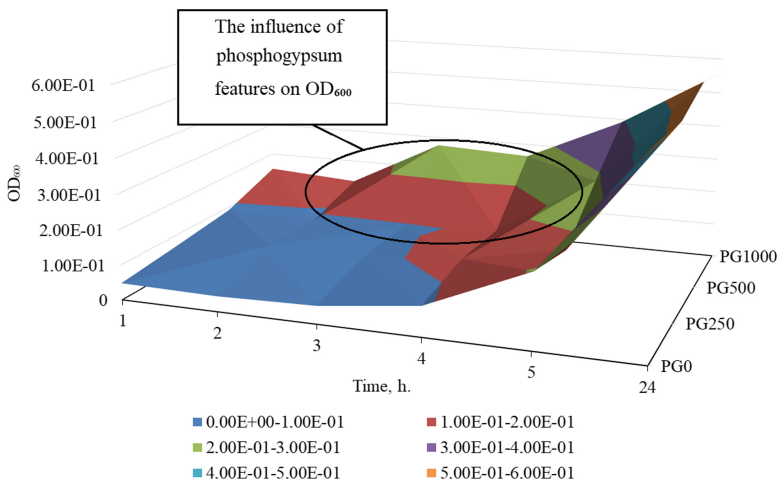

Fig. 5. 3D surface under the 'culture-medium- PG' system.

4.2 Developing Methodological Approach of Estimation Bacteria Growth Under Medium that Included Phosphogypsum

Figure 6 shows the general methodological approach for assessing the biochemical activity of PG. It is also important to evaluate the change in the solubility of PG components upon exposure to metabolites.

The methodological idea of model systems to develop eco-friendly bio-utilization of PG is as follow: (i) select biotechnologically amenable bacteria as models; (ii) check bacteria responses against PG; (iii) analyse their responses genetically and theoretically; (iv) apply these findings to the bacteria which are used in the plant of wastewater treatment.

Under this research, we use *E. coli* as a model to estimate its response against PG effluence. It should be noted that a separate study of the metabolic pathways of strict anaerobes is necessary. For example, sulfate-reducing bacteria (SRB) that use sulfate as an electron acceptor and SRB can be involved in a consortium with methanogenic bacteria during anaerobic digestion.
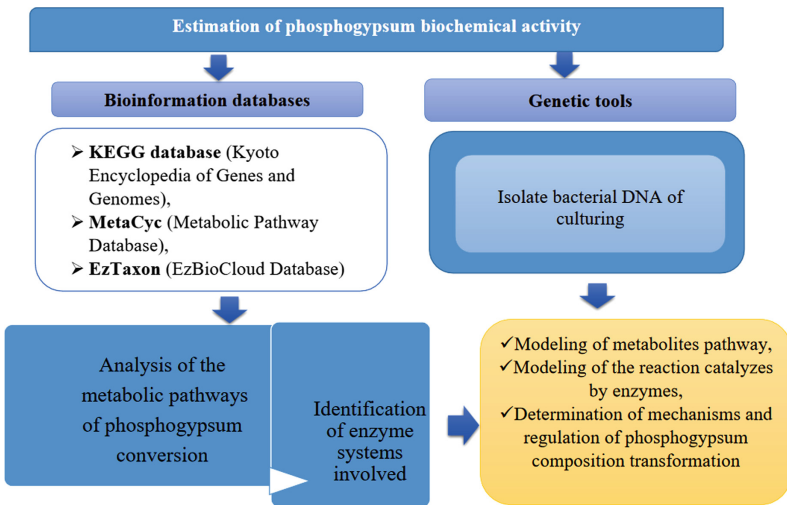

Fig. 6. The general model of estimation bacteria growth under medium that included phosphogypsum.

Thus, the important direction for assessing the possibility of using PG as a component of the medium for *E. coli* is the assessment of mutations and adaptive biochemical mechanisms, in particular, the possibility of biofilm formation (Fig. 7).
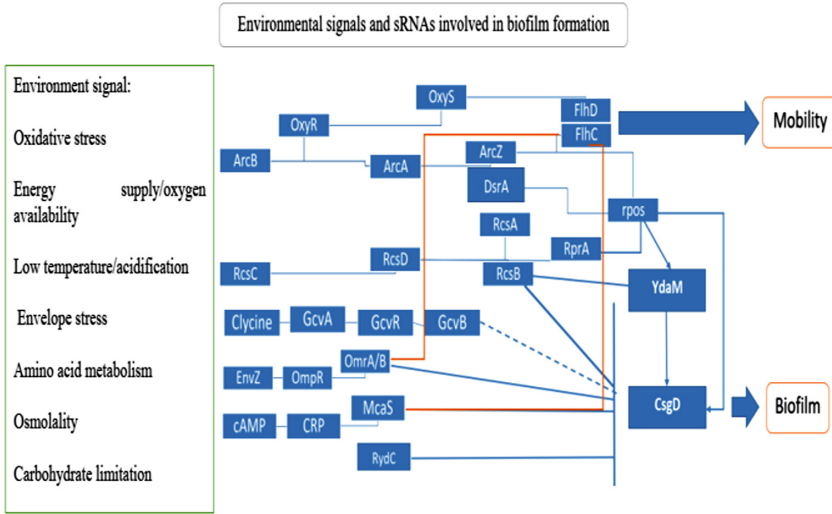
Fig. 7. Model of biofilm formation factors. Based on data from the KEGG database (https://www.kegg.jp/kegg-bin/show_pathway?ko02026+K07677).

Figure 7 shows the following notation according with KEGG database: ArcB is a two-component system, OmpR family, aerobic respiration control sensor histidine kinase; ArcA is a two-component system, OmpR family, aerobic respiration control protein; ArcZ is a small regulatory RNA; OxyR is a LysR family transcriptional regulator, hydrogen peroxide-inducible genes activator; OxyS is a small regulatory RNA; DsrA is a non-coding RNA that regulates both transcription, by overcoming transcriptional silencing by the nucleoid-associated H-NS protein, and translation, by promoting efficient translation of the stress sigma factor; small regulatory RNA; FlhD is a flagellar transcriptional activator; FlhC is a flagellar transcriptional activator; RcsC is a two-component system, NarL family, capsular synthesis sensor histidine kinase; RcsD is a two-component system, NarL family, sensor histidine kinase; RcsA is a LuxR family transcriptional regulator, capsular biosynthesis positive transcription factor; rpos is a RNA polymerase nonessential primary-like sigma factor; YdaM is a diguanylate cyclase; ScgD is a LuxR family transcriptional regulator, csgAB operon transcriptional regulatory protein; GcvA is a LysR family transcriptional regulator, glycine cleavage system transcriptional activator; GcvR is glycine cleavage system transcriptional repressor; EnvZ is a two-component system, OmpR family, osmolarity sensor histidine kinase; OmpR is a two-component system, OmpR family, phosphate regulon response regulator; OmrA/B is a small regulatory RNA; CRP is a FNR family transcriptional regulator, cyclic AMP receptor protein; McaS is a mast cell activation syndrome, small regulatory RNA; RydC is a small regulatory RNA.

E. coli showed that the type of bacterial motility is necessary for the formation of biofilms. The bacterial mobility provided by the flagella is necessary to establish a connection between the bacteria and the surface, while the mobility provided by the fimbriae is necessary for the formation of microcolonies. When establishing the initial

interaction, a stable connection between bacteria and the surface of the substrate is ensured due to specific proteins of the cell membrane, adhesins [13].

Biofilms, in this case, are more preferable than planktonic cultures, because, as mentioned earlier, this type of community is more resistant to changing environmental conditions. Microorganisms in biofilms, being protected by a layer of the extracellular matrix, are better adapted and much more resistant to high concentrations of various groups of xenobiotics, in particular, chlorine and nitrogen-containing aromatic compounds. In some cases, the matrix itself is involved in bioremediation, sorbing and retaining toxic substances from the aqueous phase.

Thus, the development of an approach to the treatment of wastewater and chemical wastes such as PG for coagulation and aggregation to achieve the effective removal of biogenic and toxic substances using multidimensional biofilms containing, in addition to hydrocarbon-oxidizing bacteria, other ecologically trophic groups, for example, *E. coli*, is one of the possible areas for further research.

5 Conclusions

1. Under modeling PG feature effluence several factors were identified that impact on bacteria growth: (i) the initial increase in the turbidity of the culture medium with different doses of PG and the rapid deposition of PG components on the bottom of the tube with the decrease in the turbidity; (ii) partial splitting of the components of PG in the medium during the time of cultivation of *E. coli* and reducing sediment; (iii) after 24 h, tubes with culture media with PG and without it had approximately the same turbidity and this was confirmed when evaluating the optical density.
2. The methodological approach was developed for assessing the biochemical activity of PG for understanding influence chemical features under metabolic pathways and OD_{600} measurement. The important direction for assessing the effect of PG use as a component of the medium for *E. coli* is the assessment of mutations and adaptive biochemical mechanisms, in particular, the possibility of biofilm formation. It is also important to evaluate the change in the solubility of PG components upon exposure to metabolites. It should be noted that a separate study of the metabolic pathways of strict anaerobes is necessary for providing a special technology model of implementation on the wastewater treatment plant.

References

1. Nozhevnikova, A.N., Bochkova, E.A., Plakunov, V.K.: Multi-species biofilms in ecology, medicine and biotechnology. Mikrobiologiya **84**(6), 623–644 (2015). (in Russian)
2. Pystina, N.B., Listov, E.L., Balakirev, I.V., Nikishova, A.S., Lipnik, S.I.: The use of modern biotechnology in solving urgent environmental problems of the oil and gas complex. Sci. Tech. Collect. News Gas Sci. **2**(13), 113–117 (2013). (in Russian)

3. Corcoran, E., Nellemann, C., Baker, E., Bos, R., Osborn, D., Savelli, H. (eds.): Sick Water? The Central Role of Waste-Water Management in Sustainable Development. A Rapid Response Assessment. United Nations Environment Programme, UN-HABITAT GRID-Arendal, Norway (2010)

4. Connor, R.: The United Nations World Water Development Report 2015: Water for a Sustainable World. UNESCO, Paris (2015)

5. Rosander, E., Svedendahl Humble, M., Veide, A.: Municipal solid waste as carbon and energy source for escherichia coli. Adv. Recycl. Waste Manag. **1**(2), 2–8 (2016). https://doi.org/10.4172/2475-7675.1000114

6. Khanafer, M., Al-Awadhi, H., Radwan, S.: Coliform Bacteria for Bioremediation of Waste Hydrocarbons. Hindawi BioMed Res. Int. (2017). https://doi.org/10.1155/2017/1838072

7. Zhi, S., Banting, G.S., Ruecker, N.J., Neumann, N.F.: Stress resistance in naturalised waste water *E. coli* strains. J. Environ. Eng. Sci. **12**(2), 42–50 (2017). https://doi.org/10.1680/jenes.16.00021

8. Poladyan, A., Trchounian, K., Vassilian, A., Trchounian, A.: Hydrogen production by Escherichia coli using brewery waste: optimal pretreatment of waste and role of different hydrogenases. Renewable Energy **115**(C), 931–936 (2018)

9. Owumi, S.E., Odunola, O.A., Gbadegesin, M.A., Ayoola, B., Onuchukwu, E.: Effect of electronic waste on *E. coli* genomic integrity: a possible role for metal induced carcinogenesis. Toxicol. Environ. Chem. **96**(10), 1581–1591 (2014). https://doi.org/10.1080/02772248.2015.1029480

10. Hermann, L., Kraus, F., Hermann, R.: Phosphorus processing – potentials for higher efficiency. Sustainability **10**, 1482 (2018)

11. Chernysh, Y., Balintova, M., Plyatsuk, L., Holub, M., Demcak, S.: The influence of phosphogypsum addition on phosphorus release in biochemical treatment of sewage sludge. Int. J. Environ. Res. Public Health **15**, 1269–1283 (2018)

12. Plyatsuk, L.D., Chernysh, Y.Y., Ablieieva, I.Y., Yakhnenko, O.M., Bataltsev, E.V., Balintova, M., Hurets, L.L.: Remediation of soil contaminated with heavy metals. J. Eng. Sci. **6**(1), H1–H8 (2019). https://doi.org/10.21272/jes.2019.6(1).h1

13. Svjetlana, M., Vrane, J.: Characteristics and significance of microbial biofilmformation. Periodicum biogorum **109**(2), 115–121 (2007). https://bib.irb.hr/datoteka/314210.9._Maric_Vranes-Periodicum.pdf

Influence of High-Octane Bioadditives on Physical and Chemical Properties of Low-Octane Gasoline

Nina Merezhko[1] , Valentyna Tkachuk[2(✉)] ,
Viktoria Romanchuk[3] , Oksana Rechun[2] ,
and Oksana Zolotariova[1]

[1] Kyiv National University of Trade and Economics,
19, Kioto Street, Kyiv 02156, Ukraine
[2] Lutsk National Technical University, 75, Lvivska Street, Lutsk 43018, Ukraine
v.tkachuk@lntu.edu.ua
[3] Lviv Polytechnic National University,
12, Bandera Street, Lviv 79013, Ukraine

Abstract. The problem of environmental safety of road transport has become an integral part of the security of Ukraine. The annual increase in vehicle emissions into the atmosphere requires the strengthening of environmental requirements for commercial fuels and exhaust gases of internal combustion engines. Modern cars require high-octane fuel with anti-knock properties, which are characterized by an experimental octane number of 92.95 and 98. For cars with gasoline engines with a compression ratio of up to 8, which are present in the fleet of Ukraine, as well as for trucks of the previous generation, there is a need for gasoline with a lower octane number. The presence of imported cars requires the production of gasoline, which would meet environmental requirements and would have a low cost. In this regard, increasing interest in the use of bioadditives, that would improve the environmental and operational properties of the fuel. World experience shows that the use of 10–15% bioadditives in the gasoline mixture does not have a negative impact on the technical and operational performance of the internal combustion engine. Therefore, the study of the influence on the physical and chemical properties of low octane gasoline is relevant.

Keywords: Gasoline · Operational properties · Quality · Ecological purity · Bioadditives

1 Introduction

The main share in the market of passenger cars in Ukraine is occupied by imports, which share in 2017 was more than 95% of capacity. For 9 months in 2018, the share of used cars has been 63% [1, 2]. According to [3] the number of new cars produced in 2017, is relatively small on the roads of Ukraine - only 150 thousand.

Modern cars require high-octane fuel with anti-knock properties, which are characterized by a research octane number of 92.95 and 98. For cars with gasoline engines with a compression ratio of up to 8, which are present in the fleet of Ukraine, as well as

for trucks of the previous generation, there is a need for gasoline with a lower octane number. The use of high-octane gasoline in cars with a compression ratio of up to 8 is the cause of a number of breakdowns: failure of the piston fingers, painting liners connecting rod and main bearings; cracking of insulation and burnout of contacts of spark plugs; burnout of the bottoms of pistons; burnout of working facets of exhaust valves and their seats; burnout of gaskets between the head and the cylinder block; burnout of piston rings and their increased wear. However, environmental safety and the low cost of such gasoline remain one of the priority requirements in the production of gasoline.

The presence of imported cars requires the production of gasoline, which would meet environmental requirements and would have a low cost. In this regard, there is growing interest in the use of bioadditives, which would improve the environmental and operational properties of the fuel. World experience shows that the use of 10–15% bioadditives in the gasoline mixture does not have a negative impact on the technical and operational performance of the internal combustion engine. In addition, the use of such fuel has more advantages, because it is more environmentally friendly, it generates less emission from combustion. Biofuels can be adapted to existing engine designs, which will be well used in all conditions. At the same time, such fuel is better for engines, it reduces the overall cost of controlling engine pollution and, therefore, its use requires fewer maintenance costs. At the same time, modern requirements for gasoline are that gasoline must provide a homogeneous fuel-air mixture of the required composition at all temperature conditions. In this case, the fuel should evaporate well, have a small surface tension, good starting properties and provide a quick warm-up of the cold engine. To do this, the fuel must have a high heat of combustion, burn completely, without detonation in all modes of operation of the engine. Modern cars require high-octane fuel with anti-knock properties characterized by motor octane 92.95 and 98. At the same time, in the fleet of Ukraine, there are cars with gasoline engines with a compression ratio of up to 8.5, as well as trucks of the previous generation, which require the use of low-octane gasoline.

2   Literature Review

World experience shows that the use of 10–15% biodiesel in a gasoline mixture does not have a negative impact on the technical and operational performance of the internal combustion engine [4]. In addition, there are more advantages in the use of such fuel, since it is a more environmentally friendly type of fuel when it is used; less emission is generated during combustion. Biofuels can be adapted to existing engine designs, which will be well used in all conditions. At the same time, such fuel is better for engines, it reduces the overall cost of controlling engine pollution and, therefore, its use requires fewer maintenance costs. At the same time, modern requirements for gasoline are that gasoline must provide a homogeneous fuel-air mixture of the required composition at all temperature conditions. In this case, the fuel should evaporate well, have a small surface tension, good starting properties, and provide a quick warm-up of the cold engine. To do this, the fuel must have a high heat of combustion, burn completely, without detonation in all modes of operation of the engine.

Many bioadditives and fuel compositions based on them have been patented and used in the world [5]. The experience of using high-octane compounds of various classes has shown that the most promising among them are oxygen-containing applications, or oxygenates [6–8]. In the previous publication, we studied the effect of ethanol on the performance properties of gasoline [9].

The problems of efficient and economical use of energy resources and expansion in the structure of the total energy consumption of renewable energy sources have been widely covered in scientific works of foreign scientists: Ajanovic A., Bentivoglio D., Rasetti M., Popp J., Lakner Z., Harangi-Rákos M., Fári M., Tyner W. and others [10–13]. Alcohol fuels have high antetonation properties, so they are used in carburetor engines with forced ignition. Also, alcoholic fuels provide a high-efficiency factor for engine workflow throughout the range of working mixtures. This reduces the specific energy consumption per unit of power. It is important to reduce the number of toxic components in exhaust gases, nitrogen oxides particularly.

3   Research Methodology

Estimation of parameters of operational properties for mixed fuels is performed using standard methods of investigation of the physical and chemical properties of fuels, which are standard for both oil and alternative fuels [14]. The processing of experimental results was carried out on the software [15].

Density, sulphur and oxygen content, molecular weight, actual resin content, refractive index, the heat of combustion and evaporation were determined in the gasoline fractions and bioadditives used for research. All these indicators were determined by standard methods. The structure-group composition of gasoline was determined by chromatographic method on the gas chromatograph Agilent-6890 with flame ionization detector, as well as by chromate mass spectrometry on the mass spectrometer LKB-2091. Octane number by research and motor methods was determined according to SSTU ISO 5164:2005. When adding additives to gasoline, their octane numbers were determined by the experimental method. Based on the results of the conducted dossier the recipe of petrol A-80 was suggested. The properties of the obtained gasoline with bioadditives were checked for compliance with the requirements of SSTU 7687:2015 according to the most important indicators, which were determined by standard methods.

4   Results

Gasoline fractions obtained at refineries at atmospheric distillation plants have low octane numbers, in the range of 65–75 according to the research method [16]. At low octane values, the use of such fuel is fraught with negative consequences for the engine due to the detonation of the fuel. Among the most common there are premature wear of valves and seats, as well as residues of carbon on the walls and surfaces. Therefore, the octane number must be suitable for a particular engine, so it is relevant to use various methods to increase the octane number of gasoline. In the traditional scheme of the

refinery, the catalytic reforming process is used to increase the octane number of straight-run gasoline, and its final product - the reformate is added to the gasoline as the main source of aromatic hydrocarbons and benzene (the aromatics content in the reformate is 60–70%, including benzene 2–7% by weight.) [17]. The reforming process itself is quite energy-intensive using expensive platinum catalysts, and the yield of the target products is 80–84% by weight. To reduce the proportion of aromatic hydrocarbons and benzene, various options for processing reformation products are offered, but they lead to additional costs. However, the requirements of the standards regulate the content of aromatic hydrocarbons in gasoline to 35%, benzene to 1% [18]. A drastic reduction of aromatic hydrocarbons, including benzene, can be achieved by reducing the proportion of reforming products and using octane-boosting components to preserve the octane number of gasoline at the required level [6]. In this regard, there is growing interest in the use of bio supplement, which would improve the environmental and operational properties of fuel and be economically feasible when adding to gasoline with a low octane number [19].

The use of bio-alcohol as a fuel or fuel additive has long been known: in 1914 it was proved that the transition from gasoline to alcohol was possible, and in 1934 in Europe, more than 2.65 million m3 of alcohol-benzine mixtures were produced [20].

The advantage of alcohol-containing fuels is reducing the amount of carbon monoxide, nitrogen oxides, and soot in the exhaust gases of engines. In addition, alcohols have high anti-knock properties and are the most effective anti-knock additive. Alcohol-gasoline mixtures are similar in motor properties to traditional petroleum fuels. Despite the lower heat of combustion, such compositions provide work on impoverished mixtures, so the increase in fuel consumption, in this case, is insignificant: the average re-consumption of fuel ethanol containing is 5%. As a result of the use of alcohol, not only carbon monoxide and hydrocarbon emissions are reduced, but also the emission of nitrogen oxides from the exhaust gases of cars.

Bioesters are promising motor fuels. In comparison with alcohols, their advantages are that the oxygen content in their molecules is two times lower. The lower heat of combustion is much higher than in alcohol. Esters are corrosive inactive or low active, almost insoluble in water, environmentally safer, and detonation resistance is inferior to alcohol. The list of oxygenates that was used is large: bioesters-methyl-tert-butyl, methyl-tert-amyl, ethyl-tert-butyl, diisopropyl and others; biospirts-methanol, ethanol and some others.

The purpose of this work is to assess the effect of bio-additives on the physical and chemical properties of gasoline fractions obtained from various oils, to determine the necessary amount of bio-additives to achieve the octane number 80.

Gasoline fractions were obtained during the distillation of oil from the Rozhniativske deposit (fr. 54–200), Styniavske deposit (fr. 49–200 C), mixtures of Western Ukrainian oil deposits and mixtures of East Ukrainian oil deposits. As for supplements methanol, ethanol, isopropanol, isobutanol, methyl tertiary butyl ether (MTBE) and ethyltretbutyl ether (ETBE) were used. Biomethanol increases the octane number of gasoline improves the combustion process of fuel and has a very high heat of evaporation. For its production, it is possible to use vegetables reducing raw materials, which can be converted into synthesis gas (biomass, biogas, agricultural and wood waste). Due to the high octane number, which allows increasing the compression ratio

to 16, methanol is used for refueling racing motorcycles and cars. The main advantage of gasoline-methanol fuels is the reduction of nitrogen oxides, carbon monoxide, and other harmful substances in the exhaust gases of cars. However, the use of methanol in many countries is prohibited due to its high toxicity, volatility, and increased hygroscopicity, which also creates a number of technical difficulties when using alcohol-gasoline mixtures [21, 22]. Bioethanol is a less hygroscopic product, which has more heat of combustion and less heat of evaporation. It is significantly less toxic than methanol. Its advantage also lies in the fact that it is made from renewable raw materials. The main producer of ethanol in the world is Brazil, the second in the volume is the United States. The use of fuels with ethanol is successfully implemented worldwide. In the USA since 1978 gasohol fuel with an ethanol content of 10% has been produced, in Brazil since 1930 fuel mixes contained 2–8% ethanol have been used. About a quarter of the modern car fleet of this country runs on alcohol-based fuel, which contains gasohol and is gasoline with 20% pure ethanol [21]. In Sweden, Finland, gasoline is operated with 85% ethanol. As of 2012, the main producers of bioethanol are the United States ($\approx$40 million t/g) mainly from corn and Brazil - from sugar cane ($\approx$15 million t/g) [21]. In Western Europe, the main producers of bioethanol are France, Sweden. Spain, Germany.

However, ethanol has a number of disadvantages: absolute ethanol is hygroscopic (although to a lesser extent than methanol); corrosive; negatively affects rubber and plastic parts. Biobutanol can completely replace gasoline in internal combustion engines. In terms of technical characteristics, biobutanol is superior to ethanol: the heat of combustion is 25% greater than that of ethanol and 10% greater than that of gasoline. It is safe to use because it evaporates 6 times less than ethanol and is 13.5 times less volatile than gasoline; it does not cause corrosion [23]. Butanol has a low saturated vapor pressure and its mixture with gasoline is not as hygroscopic. It provides a better fuel economy than gasoline-ethanol blends. Butanol will also provide lower greenhouse gas emissions into the atmosphere. However, obtaining this type of fuel is quite difficult. According to analysts, butanol can become an important part of the fuel market for transport. However, currently, its production is at the initial stage of development. Isopropanol is characterized by high maximum allowable concentration and octane rating values, has good physical stability in mixtures with gasoline, and also provides physical stability of gasoline-ethanol mixtures [24]. The addition of 6% isopropanol increases the octane number by the motor method of the straight-run fraction of gasoline by 13, and the octane number by the experimental method-by 17 points. When isopropanol is added in an amount of more than 6%, its effectiveness decreases as an antidetonator [25]. Methyl tert-butyl ether (MTBE) is widely used in the production of gasoline as a high-octane component (octane number according to the research method 115–135 units) and contributes to more complete combustion of motor fuel without the formation of solid deposits on the cylinder walls of the internal combustion engine and prevent corrosion of the metal surface. In the EU the maximum legal content of MTBE in gasoline is 15% [8]. The addition of 10–15% MTBE increases the octane number of gasoline by an average of 6–12 units [26]. Currently, the issue of environmental safety of MTBE application is very acute, in connection with which its homologues-ethyl and butyl esters of tert-butanol are considered as an alternative additive.

Ethyltretbutyl ether (ETBE) is a clear, colorless or pale yellow liquid, an organic compound with a characteristic ethereal odor, obtained from ethanol (47% vol.) and isobutylene (53% Vol.). The addition of ETBE to gasoline up to 15% is allowed by the Technical regulations. ETBE on an industrial scale was first used in 1992 in France and since that time the popularity of its use as an antidetonator has been steadily growing [27, 28]. The undoubted advantage of ETBE is its biodegradability in nature, as well as the possibility of using ethyl alcohol obtained from vegetable raw materials (bioethanol) as a raw material. Physical and chemical parameters of bio-applications to gasoline are presented in Table 1. The applications have sufficiently high calorific value, high octane numbers, low saturated vapour pressure, which will improve the combustion of the combustible mixture.

Table 1. Physical and chemical parameters of bioapplications to gasoline.

Indicators	Oxygenates					
	Methanol	Ethanol	Iso-propanol	Iso-butanol	MTBE	ETBE
Density at 20 °C, kg/m3	795	790	780	802	742	746
Evaporation combustion heat	22707	26945	33300	35690	33200	30600
kJ/kg	1104	839	666	562	–	
Flash point (in closed crucible),°C	6,5	12	13	27	−28	–
Octane number						
- by research method	122	121	117	108	115	118
- by the motor method	93	97	95	91	97	102
Saturated vapor pressure, kPa	35	17	13	9,7	53,0	34,5
Oxygen content, % vol	50,0	34,78	32,0	21,6	16,18	15,38

Physical and chemical parameters of gasoline fractions of various oils used for experiments are presented in Table 2. Gasoline fractions straight-bottomed from the Rozhniativske oil deposit (fr. 54–200), Styniavske deposit (fr. 49–200 C), mixtures of Western Ukrainian oil fields and oil mixtures of Eastern Ukrainian fields are characterized by a low sulphur content, a sufficiently high content of aromatic and naphthenic hydrocarbons.

The density of gasoline fractions of oils is 753–769 kg/m^3. Water-soluble alkalis and acids are absent. The octane number of these fractions is determined by the experimental method is not high. For a number of mini refineries that do not have production facilities to increase the octane number of gasoline fractions, it is relevant to use high-octane applications that are environmentally safe and do not contain benzene, aromatic hydrocarbons, sulphur compounds. The above-mentioned biological applications were added to straight-run gasoline in the amount reaching the octane number 80. The results are presented in Table 3.

Table 2. Physical and chemical parameters of gasoline fractions of various oils.

Name of the indicator	Rozhniativskie deposit Fraction 54–200 °C	Styniavskie deposit Fraction 49–200 °C	A mixture of West-Ukrainian oils	The mixture of Eastern-Ukraine. oils
Sulphur content, % wt.	0,021	0,017	0,016	0,014
Group composition, % mass.:				
- paraffin hydrocarbons, % wt.	53,12	51,23	38,6	36,2
- naphthenic hydrocarbons, % wt.	28,02	27,59	34,2	38,6
- olefin hydrocarbons, % wt.	0,11	0,15		
- aromatic hydrocarbons, % by weight.	18,75	21,03	27,2	25,2
Refractive index	1,4275	1,4274	1,4302	1,4316
Density, kg/m^3	763	753	769	754
Molecular weight	126,5	118		
Actual resins, mg/100 cm^3	23	27	19	21
The octane number of the experimental method	65	63	66	67

Table 3. Determination of octane numbers of mixed gasoline using straight-run gasoline of various oils and alcohols.

Addition to gasoline	Octane number	The amount of additive to reach octane number 80, %			
		Gasoline Styniava (ON = 63)	Gasoline Rozhniativ (ON = 65)	Gasoline mixture of West-Ukrainian oils (ON = 66)	Gasoline mixture of Eastern-Ukrainian oils (ON = 67)
methanol	122	28,8	26,3	25,0	23,6
ethanol	121	29,3	26,8	25,5	24,1
isopropanol	117	31,5	28,8	27,5	26,0
isobutanol	108	37,8	34,9	33,3	31,7
MTBE	118	30,9	28,3	26,9	25,5
ETBE	119	30,4	27,8	26,4	25,0

Optimal formulations of low octane gasoline with various bio-applications are proposed based on the prices of the components of such mixtures and the requirements for their quality (Table 4).

Table 4. Recommended recipe for gasoline with octane number = 80.

Compound mixtures	Octane number	% content	The octane number of the mixture	Price of the component	Price of the mixture
Straight-run gasoline	65	57	80,82	15000	20628
Reformat	95	29		27200	
isobutanol	108	4		26000	
MTBE	119	10		31500	

The lowest cost will be in a mixture of straight-run gasoline and Isobutanol, even though its content in the mixture is the highest (Table 5).

Table 5. Compliance of indicators of the received gasoline to requirements according to SSTU 7687:2015.

Name of indicator	Value of norm	Identified indicators	Research method
Octane number by the experimental method	80	80,5	SSTU ISO 5164
Crowded steam in summer, kPa	45–80	68,1	SSTU EN13016-1
Density at 15 °C, kg/m^3, within	720–775	762	SSTU EN ISO3675
Fractional composition:			
- the volumetric fraction of evaporation at 70 °C, %	20,0–50,0	32,0	According to SSTU 2177
- the volume of evaporation at 100 °C, %	46,0–71,0	64,0	
-volume of evaporation at temperature 150 °C, %	75,0	76,0	
- the boiling point is finite, °C, not higher	210	203	
- volume fraction of residual after boiling, %, not more	2	1,5	
Sulphur content, mg/kg	10	48	SSTU EN ISO 20884
Volume fraction of aromatic hydrocarbons, %	35	34	SSTU 7686
Volume fraction of benzene, %	1	0,9	SSTU EN12177
Mass fraction of oxygen, %	2,7	2,7	SSTU EN 12177
The concentration of actual resins, mg/100 cm^3	5	4	SSTU GOST 1567
Corrosion on a copper plate (3 h at 50 °C) class	1	1	SSTU EN ISO 2160

5   Conclusions

The use of octane-boosting applications such as Isobutanol and MTBE, as well as reformate, increases the octane number of straight-run gasoline, while the cost of gasoline remains competitive. Gasoline fractions obtained during the distillation of oil from the Rozhniativskie deposit (fr. 54–200 °C), Styniavskie deposit (fr. 49–200°C), mixtures of Western Ukrainian oil fields and mixtures of East Ukrainian oil fields.

Biofuels in the amount of 10 and 20% was added to straight-run gasoline.

Optimal formulations of low octane gasoline with various bio-applications are proposed based on the prices of the components of such mixtures and the requirements for their quality. The lowest cost was in a mixture of straight-run gasoline and Isobutanol despite the fact that its content in the mixture is the highest. The amount of Isobutanol in the composite mixture should be left in the amount of 4%, MTBE in the amount of 10%. Then the total oxygen content will be within acceptable norms. The content of the reformate in the mixture is set at 29%.

Having analyzed the physical and chemical parameters of the resulting gasoline mixture, we concluded that this type of fuel meets the requirements of SSTU 7687:2015, i.e. it can be used in gasoline engines of motor vehicles.

References

1. Analysis of the Ukrainian passenger car market. https://pro-consulting.ua/issledovanie-rynka/analiz-rynka-legkovyh-avtomobilej-ukrainy-2018-god. Accessed 28 Oct 2019
2. Dyma, O.: Passenger car market and prospects of its development in Ukraine. Bulletin of Lviv commercial Academy. Econ. Ser. **46**, 44–49 (2014)
3. Named the exact number of cars in Ukraine and their average age, https://auto.24tv.ua/nazvana_tochna_kilkist_avtomobiliv_v_ukraini_ta_yikh_serednii_vik_n6262. Accessed 26 Oct 2019
4. Borzaiev, B., Kerpov, S., Kapustin, V.: Multifunctional additives to automobile gasoline. Chem. Technol. Fuels Oils **2**, 18–20 (2007)
5. Chen, H., Yang, L., Zhang, P., Harrison, A.: The controversial fuel methanol strategy in China and its evaluation. Energy Strat. Rev. 28–33 (2014)
6. Nguyen, V.T.: Production of motor gasoline with improved environmental properties: in relation to the conditions of the Republic of Vietnam. Ph.D thesis, Ufa (2008)
7. Rasskazchikova, T., Kapustin, B., Karpov, S.: Ethanol as a high-octane additive to automotive gasoline. Fuel Oil Chem. Technol. **4**(524), 3–7 (2004)
8. Oparina, L.A., Kolyvanov, N.A., Gusarova, N.K., Saprygina, V.N.: Oxygenate additive to fuel based on renewable raw materials. Appl. Chem. Biotechnol. 8(1), 19−34 [in Russian]. https://doi.org/10.21285/2227-2925-2018-8-1-19-34. Proceedings of Universities
9. Tkachuk, V., Rechun, O., Merezhko, N., Bozhydarnik, T., Karavaiev, T.: Assessment of the quality of alternative fuels for gasoline engines. In: Ivanov, V., et al. (eds.) Advances in Design, Simulation and Manufacturing. DSMIE-2019. Lecture Notes in Mechanical Engineering, pp. 871 –881. Springer, Cham (2019). https://doi.org/10.1007/978-3-030-22365-6_46
10. Veloso, A., José, M., Machado, C., Márcia, Y., Pasa, D.: The effect of temperature on the properties of the NBR/PVC blend exposed to ethanolfuel and different gasolines. Fuel **113**, 679–689 (2013)

11. Ajanovic, A.: Biofuels versus food production: Does biofuels production increase food prices? Energy **36**, 2070–2076 (2011)
12. Bentivoglio, D., Rasetti, M.: Biofuel sustainability: review of implications for land use and food price. Rivista di Economia Agraria, Anno LXX, 7–31 (2015)
13. Popp, J., Lakner, Z., Harangi-Rákos, M., Fári, M.: The effect of bioenergy expansion: Food, energy, and environment. Renew. Sustain. Energy Rev. **32**, 559–578 (2014)
14. SSTU 8696:2016 Alternative fuels for gasoline engines. Specifications. Kyiv, Ukraine (2017)
15. Kuts, Yu., Povstyanoy, O.: Computer-informative software for research of the new materials of constructional application. Funct. Mat. **1**, 175–178 (2017)
16. Topilnytskyi, P., Hrynyshyn, O., Machynskyi, O.: Technology of Primary Processing of Oil and Gas: Textbook. Publisher of Lviv Polytechnic, Lviv (2014). (in Ukrainian)
17. Boichenko, S., Pushak, A., Topilnytskyi, P., Leida, K.: Motor fuels: properties and quality. Center for Educational Literature, Kyiv (2017)
18. SSTU 7687:2015 Gasoline car EURO. Technical conditions. Kyiv, Ukraine (2015)
19. Kozak, F., Melnyk, V., Prynko, I., Voitsechivska, T.: Economic efficiency of bioethanol use in internal combustion engines. Automobile transport **42**, 22–28 (2018)
20. Makarov, V., Petrykin, A., Emelianov, V., Shamonina, A., Varannik, V., Onoichenko, S.: Alcohols as additives to gasoline. Automotive industry **8**, 24 (2005)
21. Matiushyna, R., Achmetov, S., Shiriyazdanov, R., Davletshin, A., Telyashev, E., Rachimov, M.: Priorities in the production and application of biofuels at the post-oil stage of fuel energy development. Oil Refin. Petrochem. **10**, 35–38 (2012)
22. Machiela, P.: Summary of the Fire Safety Impacts of Methanol as a Transportation Fuel (2001)
23. Varfolomeev, S., Efremenko, E., Krylova, L.: Biofuel. Rus. Chem. Rev. **79**(6), 491–509 (2010). https://doi.org/10.1070/RC2010v079n06ABEH004138
24. Bohdanov, S., Lavrik, A., Terevov, A.: Influence of oxygenate additives on anti-knock properties of fuels for automobile engines with forced ignition. Bull. South Ural State Univ. **23**, 86–89 (2008)
25. Onoichenko, C., Emelianov, V., Aleksandrova, E.: The use of additives based on isopropanol in the production of gasoline. Oil Refin. Petrochem. **2**, 32–36 (2003)
26. Tsarev, A., Karpov, S.: Increase of ecological and operational characteristics of automobile gasoline by introduction of oxygenates. Chem. Technol. **8**, 324–328 (2007)
27. Yakovlev, A., Melnichenko, I., Baklaeva, N., Ivanova, A.: Efficiency of application of ethyl-tert-butyl ether (ETBE) in the production of high-octane gasoline. Economics of oil refining (2009). http://www.epn-consulting.ru/effektivnosti-primeneniya-etil-tret-butilovogo-efira-etbe-v-proizvodstve-vysokooktanovyx-avtobenzinov/. Accessed 28 Oct 2019
28. Vildanov, F., Latypova, F., Chanyshev, R., Daminev, R., Karimov, O., Mamliieva, A.: Production of ethyl tert butyl ether-a promising direction for the use of bioethanol in Russia. Bashkir Chem. J. **20**, 145–149 (2013)

Improvement of the Production Technology of Liquid Biofuel from Technical Fats and Oils

Mikhailo Mushtruk[✉], Volodymyr Vasyliv, Nataliia Slobodaniuk,
Roman Mukoid, and Olena Deviatko

National University of Life and Environmental Sciences of Ukraine,
15, Heroiv Oborony St, Kyiv 03041, Ukraine
`mixej.1984@ukr.net`

Abstract. Because of petrol energy saving, emission standards of diesel exhaust gases hazardous substances requirement toughening, as well as carbonic oxide exhaust emission control, many countries need to find how to reduce the negative influence of heat engine over the environment. The most important operation of biodiesel technical processing from fat and oil waste were studied. The importance of keeping within the mass ratio of fat, oil, and alcohol was shown. The influence of fat and oil quality stock raw materials on the composition of biodiesel were estimated. Requirements for input raw materials were developed. A determining influence of raw material moisture on the mechanism of triglycerides transesterification in fatty acids methyl ester was shown, that, according to its operational characteristics, is close to petro-diesel fuel. The raw material free fatty acids (FFA) in conjunction with water make the process ineffective. As a result of scientific research, the technology of biodiesel production from vegetable oils and animal fats has been substantiated and its equipment support is offered. Experimental - industrial tests of mobile plants showed its possible to produce a good quality product that meets the modern operational requirements for biodiesel that could be used in engines without significant redesign. As a result of scientific research, the technology of biodiesel production from vegetable oils and animal fats has been substantiated and its equipment support was offered. A hardware-processing configuration and a layout equipment plant of mobile plant for the production of biodiesel from fats and oils were developed.

Keywords: Waste · Animal fat · Vegetable oil · Alcohols · Free fatty acids · Transesterification · Bio-Fuel · Plant

1 Introduction

Dependence on the petrol import of more countries places a premium one problem of national, economic and energy security, by contrast, overuse of petroleum products poses a significant environmental hazard. This particular cause determines the need for research and development aimed at diversifying the raw material base as well as search for alternative motor fuels for cars, mechanisms, and vehicles [1, 9].

Ukrainian meat processing factories have enough resources of animal fat and fatty waste, annually accumulate in volume about 200 thousand tons. There is a technical possibility of its utilization due to the processing of environmentally friendly fuel with a high-quality rate [1–4].

Synthesized alternative fuel from vegetable oils and industrial animal fats, agricultural and restaurants wastes, seaweeds, etc., also form carbon dioxide during burning, but this gas that was previously consumed by plants from the air, and because of this the use of biomass as a fuel raw materials reduces the greenhouse effect that disturbs the Earth population [1, 16].

2   Literature Review

A diesel engine inventor - Rudolf Diesel in 1900 during the worldwide exhibition in Paris demonstrated a diesel engine that worked on vegetable peanut butter [2]. It was not until later that, thanks to the low price of petroleum fuels it began to be used in diesel engines and, with its further improvement, focused on petroleum products [3].

Technical animal fats (TAF), waste edible oils, as raw material sources of energy, are not only an alternative to reducing the cost of fossil fuels in agricultural production and transport companies, it is as well an important factor in the environmentally friendly energy supply system [1].

Vegetable and animal oils and fats (VAOF) are the future-proof raw material for the industrial production of biodiesel, because biofuels, obtained as a result of their transesterification by alcohols, have the characteristics similar with those of fuel derived from petroleum. This fuel should be used for diesel engines even with no construction modification [1].

VAOF consists of triglycerides, free fatty acids, phospholipids, stearin and often of the excess of water. VAOF usually has a lot of dirt that gives a special property for this raw material and prevents its direct consumption not only for food purposes but also for fuel production [4]. These problems could be eliminated by purification and some transformation of the chemical composition of fats and its subsequent alcohol exchange [3].

Methanol, ethanol, propanol, butanol and other alcohols can be used to fat triglycerides transesterification, and its monoesters are correspondingly called methyl, ethyl, propyl, and butyl esters. Methyl alcohol is the most commonly used [4].

The production of biofuels from fatty raw materials would reduce its cost and allowed making the best use of fat waste, as well as have a positive influence on environmental conditions in Ukrainian localities and reduce the negative motor vehicle emissions impact on the public health [5].

Consequently, trending is the search for alternative, cheaper and more environmentally friendly fuels that are meant to be biodiesel based on lipids, which could be produced directly by agricultural enterprises and the meat and dairy industries' enterprises. Increasing the VAOF's processing efficiency and production of biodiesel is an actual research issue [1].

The goal of research. Traditional industrial biodiesel processing design includes preliminary mechanical purification of raw materials (oils or fats), neutralization of its free fatty acids, that complicate processing and increase its time [6]. It's various well

known technological improvements of fatty acid esters production that improve the quality of the fuel but do not allow increasing its yield and reducing the reaction time [7]. Consequently, the improved production technology biodiesel and corresponding equipment, in particular for waste fats and oils, is a strategic technical pathway that requires a scientific and practical study, and that is the goal of the presented research.

3   Research Methodology

Experimental studies were conducted to assess the influence of the main parameters of the process of conversion of animal fats and vegetable oils to methanol with a catalyst KOH on the quantity and quality of methyl esters of fatty acids. To carry out the research, a developed and manufactured laboratory plant was used (see Fig. 1) [1].
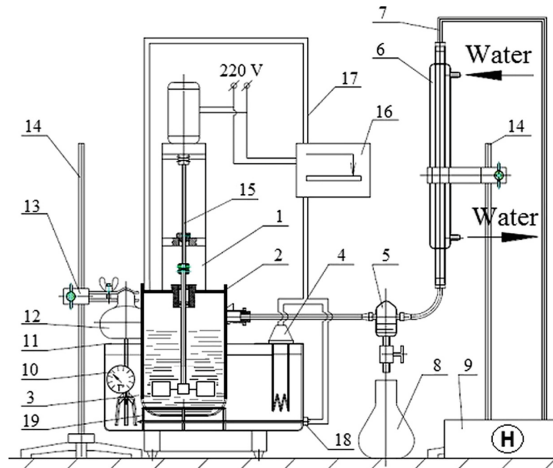
Fig. 1. Laboratory installation for biofuel research [1]: 1 – engine tripod; 2 – vial for reagent; 3 – mixer; 4 – thermostat; 5 – condensate collection; 6 – refrigerator; 7 – pipeline; 8 – flask for collecting condensate; 9 – vacuum pump; 10 – thermometer; 11 – "water bath"; 12 – capacity for the preparation of potassium methylate; 13 – clamp; 14 – tripod; 15 – shaft mixer; 16 – thermoregulatory; 18 – thermocouple installed in the body of the "water bath"; 19 – stand.

IT allows changing according to the plan of the full factor experiment of type 2^4 of the reagent composition, to regulate the speed of the mixer shaft and the temperature of the technological process. Experiments were carried out using oils and fats with an acid number of 2–5 mg KOH/g. The frequency of rotation of the shaft of the mixer varied from 10.5 to 52.4 s^{-1} at an interval of 10.5 s^{-1}; the temperature was maintained by the liquid thermostat TZh-TS-01/12 in the range from 20 °C to 70 °C in a step of 10 °C [1].

In the pilot studies, the following indicators of biodiesel quality were determined: density - with the help of pycnometers; viscosity – viscosimeter of the VLZ - 1 with a diameter of the capillary 0,54 mm; flash temperature in a closed crucible - device
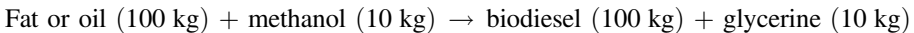
TVZ-LAB-01; acid number - titration of free fatty acids with aqueous KOH solution. Quantitative characteristics of the process of transesterification (volume of ether and glyceride phases) are established using measuring cylinders [1].

In the course of experimental studies, the effect of reagent concentration, temperature, design parameters of periodic and continuous reactors and mechanisms of mixing mechanization on the technological parameters of the process of transformation of fats into biodiesel was established [1, 6].

In the study of biodiesel production, methods of experimental-statistical simulation using the software package Mathcad 15 were used. To do this, the experiment plan 24 was used with interdependent variables. The assessment of the quality of biodiesel was carried out in accordance with DSTU 6081: 2009 and EN 14214: 2003 [13, 14].

Biodiesel can be produced from any vegetable oil or animal fat through the fatty acids esterification method. Of course, in its chemical nature, fats, for example, have a vegetable origin – it is a composition of esters of triatomic alcohol (glycerine) and many fatty acids [1, 8, 20]. Glycerine in fats can be substituted by molecules of methyl or ethyl alcohol and as well get ether, but with a lower pour point temperature and a smaller viscosity. These fatty acids methyl (ethyl) esters (esters) are exactly biodiesel. The main co-product of the reaction of oil transesterification is glycerol with some dirt. Such kind of glycerol after purification should be used in the chemical, pharmaceutical and perfumery industries.

Even a tenuous review of literature sources shows that in obtaining diesel biofuel, for example, from vegetable oils, the valid approximate ratio is the following [9, 10]:

$$\text{Fat or oil } (100 \text{ kg}) + \text{methanol } (10 \text{ kg}) \rightarrow \text{biodiesel } (100 \text{ kg}) + \text{glycerine } (10 \text{ kg})$$

This ratio is a simplified formula for the following reaction of the transesterification of triglycerides (see Fig. 2).
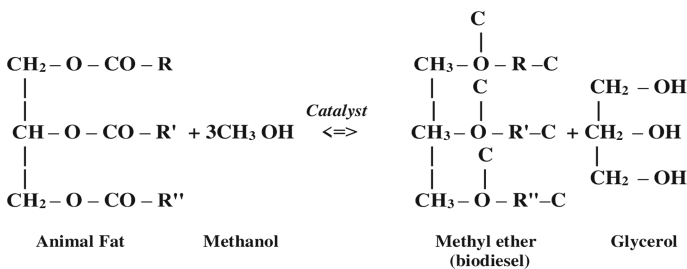

Fig. 2. Simplified formula for the reaction of the transesterification of triglycerides R, R', R'' – is a long chain of carbon and hydrogen atoms, called chain fatty acids. For example, palmitinic acid form chain $R = - (CH_2)_{14} - CH_3$, stearinic acid - $R = - (CH_2)_{16} - CH_3$, oleinic acid - $R = - (CH_2)_7 CH = CH(CH_2)_7 CH_3$, linolic acid - $R = - (CH_2)_7 CH = CH - CH_2 - CH = CH(CH_2)_4 CH_3$, linolenic acid - $R = - (CH_2)_7 CH = CH - CH_2 - CH = CH - CH_2 - CH$.

These five types of chains are oils and animal fats distinguishing that make possible production of diesel biofuel.

For clarity, we consider oils and animal fats and assume that its triglyceride consists of three acid chains of only oleinic acid.

Reacting with methanol over the KOH catalyst, such a triglyceride would yield the following resultant (see Fig. 3).
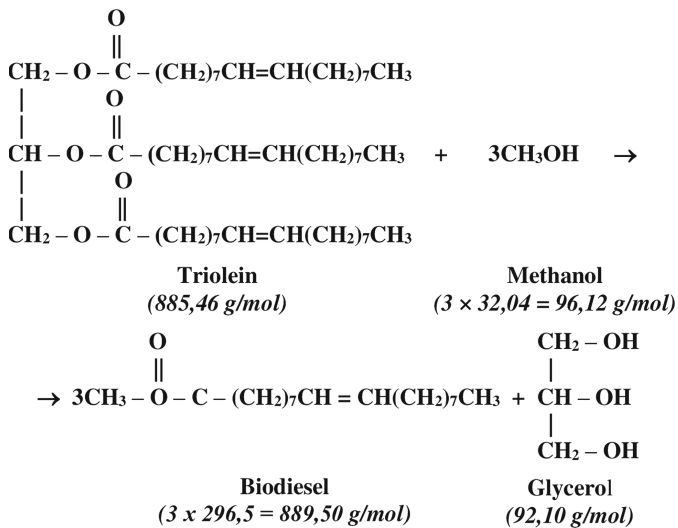
$$O$$
$$\|$$
$$CH_2 - O - C - (CH_2)_7CH=CH(CH_2)_7CH_3$$
$$|\qquad O$$
$$|\qquad \|$$
$$CH - O - C - (CH_2)_7CH=CH(CH_2)_7CH_3 \quad + \quad 3CH_3OH \quad \rightarrow$$
$$|\qquad O$$
$$|\qquad \|$$
$$CH_2 - O - C - (CH_2)_7CH=CH(CH_2)_7CH_3$$

Triolein   **Methanol**
(885,46 g/mol)   *(3 × 32,04 = 96,12 g/mol)*

$$O \qquad\qquad\qquad CH_2 - OH$$
$$\| \qquad\qquad\qquad\qquad |$$
$$\rightarrow 3CH_3 - O - C - (CH_2)_7CH = CH(CH_2)_7CH_3 \ + \ CH - OH$$
$$|$$
$$CH_2 - OH$$

Biodiesel   **Glycerol**
(3 x 296,5 = 889,50 g/mol)   *(92,10 g/mol)*

Fig. 3. Scheme of the reaction of transesterification of fats using methanol and potassium hydroxide.

The molecular mass of triolein is 889.50 g/mol, and the biodiesel fuel extracted from triolein is 885.46 g/mol.

Giving a 100% excess of methanol would ensure a reaction guaranteed to undergo. Then the reaction mass balance could be written the following way:

$$\text{Fat or oil } (100 \text{ kg}) + \text{ methanol } (21,71 \text{ kg})$$
$$\rightarrow \text{ biodiesel } (100,45 \text{ kg}) + \text{ methanol } (10,86 \text{ kg}) \tag{1}$$

For the reaction undergoing, 1% weight part of catalyst KOH comparing to oil mass is required. This mass balance can be compared to the volume of the reagent. Then the specific gravity of the reagents in the reaction (kg/l) would be distributed the following way: triolein - 0,8988; methanol - 0,7914; biodiesel - 0,8739; glycerine - 1,263.

4   Results

According to the results of laboratory tests, the obtained biodiesel was found to meet the Biofuel Standards for Transport in the EU EN 14214:2003 assumes 0,24% of glycerine in the fuel. In the case that the triglycerides compose exclusively of trioleines, the glycerine molecule would weigh 92.10 g/mol, and the triolein molecule would weigh 885.46 g/mol. Thus, trioleine contains 92.10/885.46 = 0.104, or 10.4% glycerine. This glycerine is fixed because of attachment to the triglyceride molecule. If the oil contains 10.4% of glycerine to prevent its conversion to monoglycerides and diglycerides, upon condition that biodiesel contains 0.24% of glycerol, the reaction of the transesterification of the triglyceride should be 97.7% chemical reaction:

$$\frac{10,4 - 0,24}{10,4} \cdot 100 = 97,7\% \tag{2}$$

This can not always be done, especially when the oil has excess water and free fatty acids that are present as well, usually in crude oils.

For example, free oleinuc acid interacting with a catalyst over water forms soap and the catalyst bind in forms that do not accelerate the reaction of transesterification and do not facilitate the separation of glycerine from triglycerides.

Because of this, free fatty acids and water should be present in oils in at the minimum [11, 18, 20, 22].

If the water in the oil is present in a significant amount, then in conditions of higher-temperature there could be no reaction of the transesterification, but the reaction of hydrolysis of triglycerides in diglycerides and free fatty acid [1, 17–20].

Free fatty acids over a KOH catalyst could further be converted into a quantity of soap that binds gel reagents. It would not divide into biofuel and glycerol after the reaction completion.

As a rule, for the production of biodiesel from the existing range of alcohols, methanol would be selected (R correspond to CH_3), but it is possible to use other alcohols, such as ethanol. To ensure that the reaction would proceed from left to right in the arrow direction, it should add an excess of methanol in the reactor, and reaction could be carried out properly at optimal pressure and temperature over an optimal catalyst amount, that is practically a know-how.

After conducting experimental studies, it was found that the biodiesel fuel production from fat or oil must undergo an irreversible reaction, in general terms, it could be written as (Fig. 4).

Thus, the final quality of diesel fuel depends on the following: the amount of water in the raw material, its impurity of free fatty acids, the quality of methyl alcohol, the amount of catalyst, the temperature and pressure in the reactor, the presence of a biofuels washing operation, the period of the transesterification process, the availability of a fuel purification system from foreign inclusions, etc.
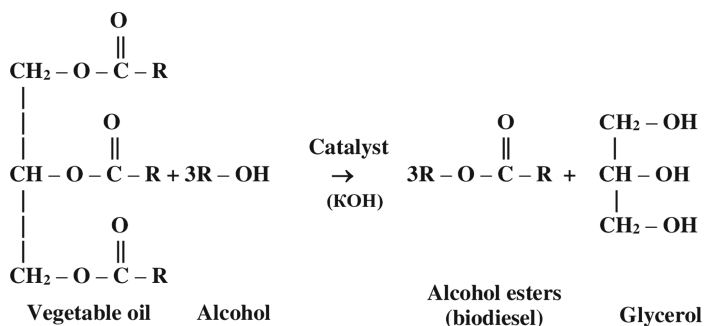
Besides triglycerides in a reagent, the mixture could be monoglycerides, excess methanol, glycerol, the catalyst that contaminate the final product. Therefore, after demixing and fractionation of reagents mixture, the raw biodiesel should be rinsed well with water with often added small amounts of sulphuric acid or edible salt. And at the

final stage of fuel production, methanol and water should be removed ("dry") in rectification tower with a special nozzle [1, 16].

Thus, the final quality of diesel fuel depends of the following: the amount of water in the raw material, its impurity of free fatty acids, the quality of methyl alcohol, the amount of catalyst, the temperature and pressure in the reactor, the presence of a biofuels washing operation, the period of the transesterification process, the availability of a fuel purification system from foreign inclusions, etc.

$$
\begin{array}{l}
\hspace{2.2cm} \overset{\displaystyle O}{\underset{\displaystyle \|}{}} \\
CH_2 - O - C - R \\
\hspace{0.3cm}| \\
\hspace{0.3cm}| \hspace{1.4cm} \overset{\displaystyle O}{\underset{\displaystyle \|}{}} \hspace{2.2cm} \text{Catalyst} \hspace{1.4cm} \overset{\displaystyle O}{\underset{\displaystyle \|}{}} \hspace{1.2cm} CH_2 - OH \\
CH - O - C - R + 3R - OH \hspace{0.6cm} \xrightarrow{\ \ \ \ } \hspace{0.6cm} 3R - O - C - R + \hspace{0.3cm} CH - OH \\
\hspace{0.3cm}| \hspace{5.2cm} \text{(KOH)} \hspace{4.2cm}| \\
\hspace{0.3cm}| \hspace{1.4cm} \overset{\displaystyle O}{\underset{\displaystyle \|}{}} \hspace{7.4cm} CH_2 - OH \\
CH_2 - O - C - R
\end{array}
$$

Vegetable oil   Alcohol   Alcohol esters
(biodiesel)   Glycerol

Fig. 4. Scheme of the irreversible reaction of biodiesel production from vegetable and animal fats.

Besides triglycerides in a reagent, the mixture could be monoglycerides, excess methanol, glycerol, the catalyst that contaminate the final product. Therefore, after demixing and fractionation of reagents mixture, the raw biodiesel should be rinsed well with water with often added small amounts of sulphuric acid or edible salt. And at the final stage of fuel production, methanol and water should be removed ("dried") in rectification tower with a special nozzle [1, 16, 21–23].

A number of technological process parameters are practically very difficult to calculate, because of this we have identified such parameters experimentally and it would compose the issue of the next publication.

All the calculations and researches made it possible to develop the equipment and technological scheme of the line for the production of diesel biofuels from food and processing wastes and to design the technology of biofuels production (see Fig. 5).

The process of production of diesel biofuels consists of several stages, which are implemented in the oil - purification and ester modules of the plant.

Pre-purified and heated to the temperature of the transesterification reaction fat is fed into the reactor.

The apparatus 40 pre-prepares an alcohol-catalytic solution (for example, methyl alcohol and caustic potassium), which is fed into the reactor 23. Under constant stirring and heating in the reactor, the formation of esters.

Upon completion of the transesterification reaction and settling of the reaction mixture from the reactor 23, the pump removes glycerol (crude glycerol). The reactor is then fed a pre-prepared washing solution (acidic or neutral) from tank 27. This solution allows the pre-selection of soap, methanol, and surfactants from the precipitate, which

is removed from the reactor and sent for further treatment to be removed from the reactor. It has some useful fractions used for the preparation of detergents and lubricants for metalworking.

The obtained esters from the reactor, using pumps, are fed to a rotary distillation unit 28 where the reaction products are separated into esters, water, and methyl vapors and by-products. Methanol and water vapors are condensed in the absorber 36. The recovered methanol is returned to the apparatus 40 and the water to special storage.
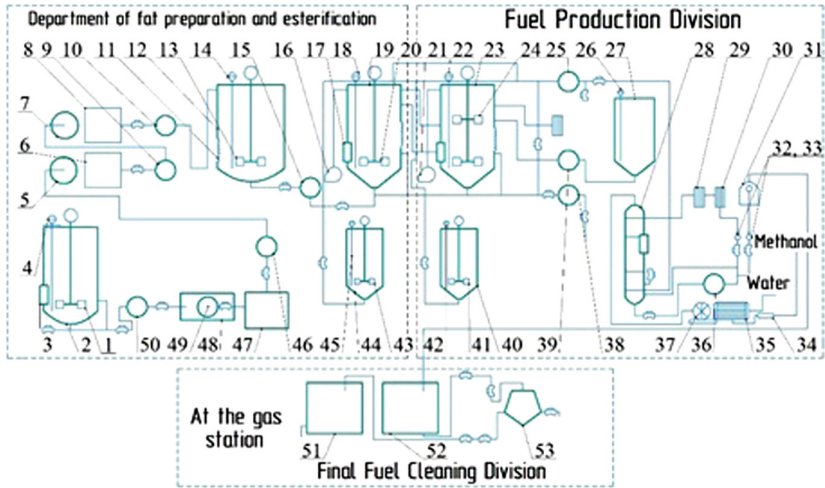
Fig. 5. Technological scheme of the line for biodiesel production from food and processing wastes.

The pre-purified water and methanol fatty esters, after passing through a system of filters 31 filled with the adsorbent "Amberlite", are further purified from water, glycerol, soap and fall into the collecting tank. Pure esters are collected into a container 51 and then pumped into a refueling column. Due to the preliminary purification of raw materials and the correction of fatty acidity, the use of a rotary distillation unit 28 and a vacuum pump 37 (Fig. 5), the filter system 31 with the adsorbent "Amberlite" and the separator 53 managed to obtain diesel fuel, which is of European quality (EN 14214) and national (DSTU 6081: 2009) [1, 11, 12] standards.

Such technology of production of biodiesel from technical animal fats can be implemented at the mobile plant located on two metal platforms with a size of 12000 × 2400 mm, which are easily transported on car trailers - long-distance.

It should be noted that to ensure the biofuels required quality, it is necessary to set strict requirements for raw materials.

The designed technological process and manufactured automatic mobile plants for the production of biodiesel are exploited at OJSC "Proskuriv" (Khmelnytsky city) and the Chyhyrynsky agrarian company, and the high quality of biological fuel is confirmed by the Ukrainian Research Institute of Forecasting and Testing of Equipment for

Agricultural Production named after Leonid Pogorilyi of Ministry of agrarian policy and food of Ukraine [1, 2, 15].

When technical animal fat or oil is used for the production of biodiesel, it must first be pre-processed:

- Melting;
- Separation of the melted fat-water-protein mixture by centrifugation on a solid precipitate and a fat-water emulsion;
- Separation of a fat-water emulsion to get free-of-liquid fat;
- Bringing the acid index to the norm.

The innovative technical solutions, used in the processing configuration, allowed to provide production of high-quality biofuels. Thus, the kinematic viscosity of fuel at a temperature of 40 °C is 4.5 mm^2/s, that meets the requirements of current standards (3.5, …, 5.0 mm^2/s), the flashpoint is 140 °C (for the euro standard, not less than 120 °C), that positively affects the operation of diesel engines. The fuel density at a temperature of 15 °C is 880 kg/m3, which is also within the norm. Methanol, water, sulfur, glycerin, mechanical dirt and soap residues in fuel are completely absent, and therefore it could be considered environmentally friendly and safe to use. The cetane number is 53 (at least 51), that ensures effective combustion in the engine, and the acid value does not exceed 0.15 mg KOH/g (by standard no more than 0.5).

5   Conclusions

To ensure the biodiesel meets requirements of the existing standards, special attention must be paid to the preparation of raw materials for processing, notably: to ensure the moisture content in fatty substances is not higher than 7%, to reduce the acid value to 2 mg KOH/g due to neutralization of free fatty acids, as well as remove mechanical dirt and use pure methanol (99.8%) and water with a neutral reaction for washing biofuels.

A strong effect on the quality of fuel exercise the temperature and pressure in the reactor, the amount of catalyst, the duration of the transesterification process, the presence in the processing fuel washing and drying.

Experimental - industrial tests of mobile plants showed its possible to produce a good quality product that meets the modern operational requirements for biodiesel that could be used in engines without significant redesign.

The quality of diesel biofuel, manufactured by the implemented mobile plants meets the requirements of DSTU 6081:2009 and EN 14214:2003.

The results of research into the conversion of fat waste into biodiesel in the future will be the basis for the design of technological equipment and optimization of its modes of operation, as this area is a relevant topic of research.

References

1. Mushtruk, M., Sukhenko, Yu., Boyko, Yu.: Deep Processing of Fats in Bioproducts. Comprint, Kyiv (2017)

2. Farooq, M., Ramli, A., Subbarao, D.: Biodiesel production from waste cooking oil using bifunctional heterogeneous solid catalysts. J. Clean. Prod. **59**, 131–140 (2013)

3. Adewale, P., Dumont, M., Ngadi, M.: Recent trends of biodiesel production from animal fat wastes and associated production techniques. Renew. Sustain. Energy Rev. **45**, 574–588 (2015)

4. Banković-Ilić, I., Stojković, I., Stamenković, O., et al.: Waste animal fats as feedstocks for biodiesel production. Renew. Sustain. Energy Rev. **32**, 238–254 (2014)

5. Sukhenko, Yu., Sukhenko, V., Mushtruk, M., et al.: Changing the quality of ground meat for sausage products in the process of grinding. East. Eur. J. Enterp. Technol. **4**(11(88)), 56–63 (2017)

6. Barnwal, K.: Prospects of biodiesel production from vegetable oils in India. Renew. Sustain. Energy Rev. **9**(4), 363–378 (2015)

7. Sukhenko, Y., Sukhenko, V., Mushtruk, M., Litvinenko, A.: Mathematical model of corrosive-mechanic wear materials in technological medium of food industry. In: Ivanov, V., et al. (eds.) DSMIE-2018. LNME, pp. 507–514. Springer, Cham (2019)

8. Nisar, J.: Enhanced biodiesel production from Jatropha oil using calcined waste animal bones as catalyst. Renew. Energy **101**, 111–119 (2017)

9. Sander, A., Košćak, M., Kosir, D., Milosavljević, N.: The influence of animal fat type and purification conditions on biodiesel quality. Renew. Energy **118**, 752–760 (2018)

10. Kirubakaran, M., Selvan, V.: A comprehensive review of low cost biodiesel production from waste chicken fat. Renew. Sustain. Energy Rev. **82**, 390–401 (2018)

11. DSTU 6081:2009.: Documentation – Presentation of these and similar documents

12. EN 14214:2003.: Documentation – Presentation of these and similar documents

13. Xiong, H., Guo, X., Xie, W.: Biodiesel remote monitoring system design based on IOT. In: LNCS, pp. 750–756 (2018)

14. Chai, M., Tu, Q., Lu, M.: Etherification pretreatment of free fatty acid in biodiesel production, from laboratory to industry. Fuel Process. Technol. **125**, 106–113 (2014)

15. Hawrot, M., Wijatkowski, A., Mikiciuk, M.: Influence of diesel and biodiesel fuel–contaminated soil on microorganisms, growth and development of plants. Plant Soil Environ. **60**(35), 189–194 (2015)

16. Issariyakul, T., Dalai, A.: Biodiesel from vegetable oils. Renew. Sustain. Energy Rev. **31**, 446–471 (2014)

17. Nielsen, P., Rancke-Madsen, A., Holm, H.: Production of biodiesel using liquid lipase formulations. J. Am. Oil Chem. Soc. **93**(7), 905–910 (2016)

18. Surendra, K., Olivier, R., Tomberlin, J., et al.: Bioconversion of organic wastes into biodiesel and animal feed via insect farming. Renewable Energy **98**, 197–202 (2016)

19. Sheiko, T., Tkachenko, S., Mushtruk, M., et al.: The studying the processing of food dye from beet juice. Potravinarstvo Slovak J. Food Sci. **13**(1), 688–694 (2019)

20. Mohadesi, M., Aghel, B., Maleki, M., Ansari, A.: Production of biodiesel from waste cooking oil using a homogeneous catalyst: Study of semi–industrial pilot of micro reactor. Renew. Energy **136**, 677–682 (2019)

21. Bentivoglio, D., Rasetti, M.: Biofuel sustainability: review of implications for land use and food price. Rivista di Economia Agraria Anno **LXX**, 7–31 (2015)

22. Pinzi, S., Leiva, D., López-García, I., et al.: Latest trends in feed stocks for biodiesel production. Biofuels, Bioprod. Biorefin. **8**(1), 126–143 (2014)

23. Mohammadshirazi, A., Akram, A., Rafiee, S., et al.: Energy and cost analyses of biodiesel production from waste cooking oil. Renew. Sustain. Energy Rev. **33**, 44–49 (2014)

Influence of the Magnetic Field Gradient on the Efficiency of Magnetic Water Treatment

Ihor Roi[1] , Iryna Vaskina[1(✉)] , Krzysztof Jozwiakowski[2] ,
Roman Vaskin[1] , and Ivan Kozii[1]

[1] Sumy State University, 2 Rymskogo-Korsakova Street, Sumy 40007, Ukraine
`i.vaskina@ecolog.sumdu.edu.ua`
[2] University of Life Sciences in Lublin,
7 Leszczynskiego Street, 20-069 Lublin, Poland

Abstract. This paper focuses on the study of the influence of a magnetic field gradient on the efficiency of the magnetic water treatment process (MWT). For this purpose, the changes in the kinetics of oxidation of organic matter with ozone were used. The methods of theoretical analysis of the geometry of the magnetic field in the equipment of water purification technologies were applied for experimental study of the influence of the inhomogeneous magnetic field on the kinetics of the oxidation reaction of organic pollution. Statistical processing of experimental results allowed approximation of the regression equation of MWT efficiency on the rate of magnetic induction change and duration of processing. The efficiency of MWT does not increase monotonically with increasing duration of the MWT process both increasing the value of magnetic induction change. The speed of the aqueous solution and the geometry of the inhomogeneous magnetic field are closely related and have been one of the main parameters that determine the MWT efficiency. These parameters can be expressed by the magnitude of the magnetic induction change. Experimentally established dependencies can find application in the development of scientific and methodological bases for the implementation of the process of magnetic treatment of polluted waters for the purification intensification in environmental protection systems.

Keywords: Magnetic water treatment · Aqueous solution · Inhomogeneous magnetic field · Magnetic induction change · Magnitude

1 Introduction

The current situation is alarming regarding great water scarcity, even in water-rich regions. It requires innovative technologies to ensure proper treatment of raw, process, and sewage waters. To solve this problem, we need to identify robust methods of purifying water at a lower cost and with less energy. At the same time, we should minimize the anthropogenic impact on the environment. Magnetic water treatment (MWT) is one of such perspective methods. This technology is not a new one, but it remains relevant.

Changes in the physicochemical properties of aqueous solutions (such as kinetics of reactions, hydration of solutes, density, viscosity and surface tension of an aqueous solution) are the basic principles of water treatment using magnetic fields. The main parameters of MWT are magnetic field characteristics. The sizes of the device and magnets themselves, their location, depend on them. These are the basic contour and mode parameters of the magnetic treatment devices. The obtained results find practical application in water treatment processes and allow choosing the optimum design and mode processing parameters.

2 Literature Review

Magnetic treatment is used with different propose for many processes. The use of magnetic processing can be widely used in environmental protection. In addition to water treatment [1], it is promising regarding leaching some ions from the soil [2].

The main problem of the magnetic water treatment implementation is the lack of studies of the mechanisms of the MWT effect. The magnetic field has an influence on chemical properties of water, scale formation and morphology [3]. It can modify the detergency and the mineral fouling [4] and the accelerated coagulation of scale-forming particles [5]. However, most studies are focused on the effect of reducing carbonate deposit during MWT application [6–9]. This fact confirms the lack of knowledge regarding the dependence efficiency of the magnetic processing on the characteristics of the magnetic field.

The results of different studies [5, 10, 11] and the practical experience of applying MWT prove that the effects of MWT have a complex dependence on MWT parameters and do not increase in proportion with the magnetic induction. The variety of MWT data, their incomprehensibility, volatility, and practical relevance have led to the emergence of different hypotheses for the MWT mechanism [12].

The lack of common approaches to the interpretation of the nature of physical and chemical effects of MWT, general principles of the process, and the criteria for selecting the optimal design parameters of MWT devices, led to the emergence of a large variety of MWT devices. They differ in several features (Fig. 1 - author's classification). MWT devices differ by the type and shape of magnets, the completeness of the magnetic field use, the scope, conditions of use and design features, etc.

The basis of all types of MWT devices is the motion of an aqueous solution in a non-uniform magnetic field (the presence of the apparatus sections with a magnetic induction drop $\Delta V \neq 0$). The geometry of the magnetic field and the inhomogeneity of the magnetic induction distribution along the pipe while passing aqueous solution are the most significant parameters. It depends on the characteristics of the magnets (polarity, magnetization method, pole shape) and their arrangement along the water trajectory [13, 14]. MWT efficiency is also influenced by the duration of treatment and physical parameters of water (temperature), mineral and dispersed composition [15–18].
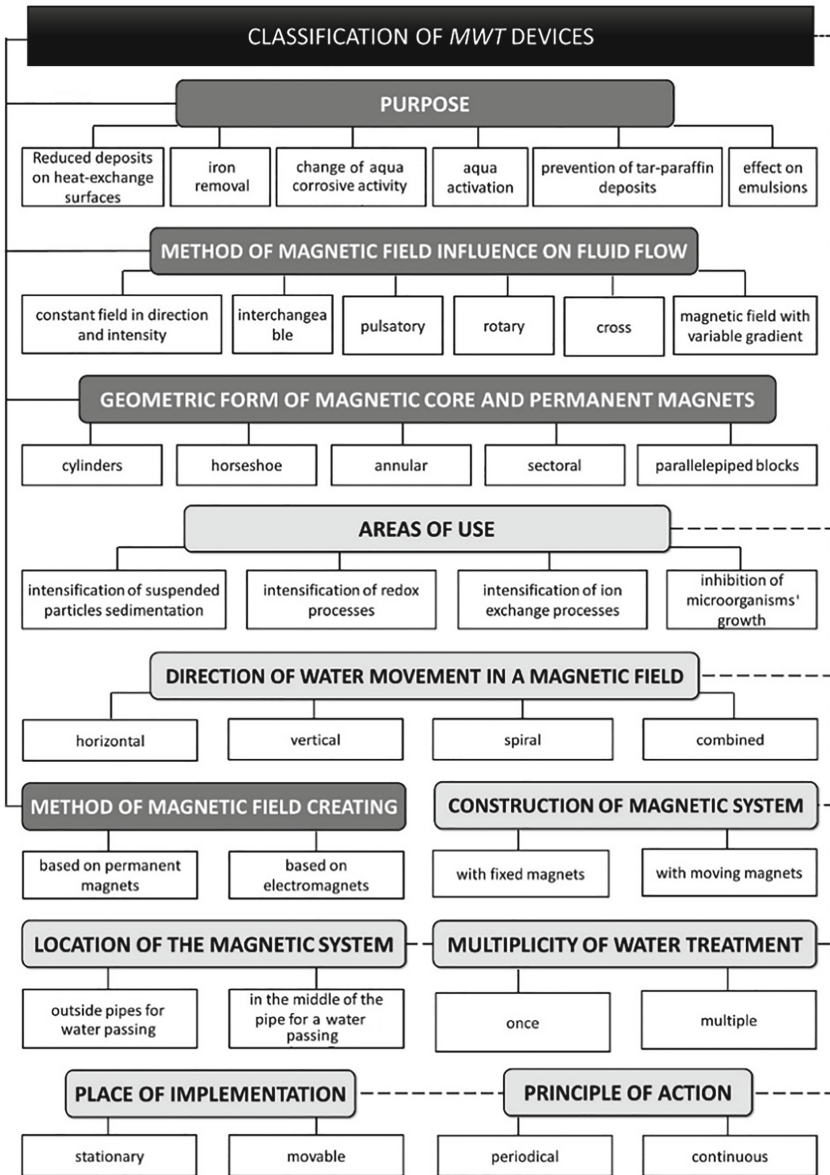
Fig. 1. Classification of MWT devices.

The gradient of the magnetic field is a more important factor than the magnetic field strength [19]. This effect was experimentally confirmed. New approaches have been proposed by [15] to explain the increased rate of water evaporation using a magnetic field.

One of the indicators of an inhomogeneous magnetic field impact on an aqueous solution and the course of subsequent processes is a change in the kinetics of chemical reactions. So, the main aim of this research is to carry out experimental studies of MWT parameters impact on the reaction kinetics of organic matter oxidation with ozone. Ozone was chosen as an indicator of changes in the physicochemical properties of an aqueous solution after MWT.

3   Research Methodology

Experimental studies of the directional influence of an inhomogeneous magnetic field on the oxidation kinetics of organic compounds with ozone were carried out using an oxalic acid solution. It is relatively slow oxidized by ozone, which made it possible to monitor the effectiveness of MWT. MWT efficiency was defined as an increase in the efficiency of oxidization of oxalic acid (%) relative to the usual conditions of oxidation.

For the experimental studies a laboratory stand was made (see Fig. 2).
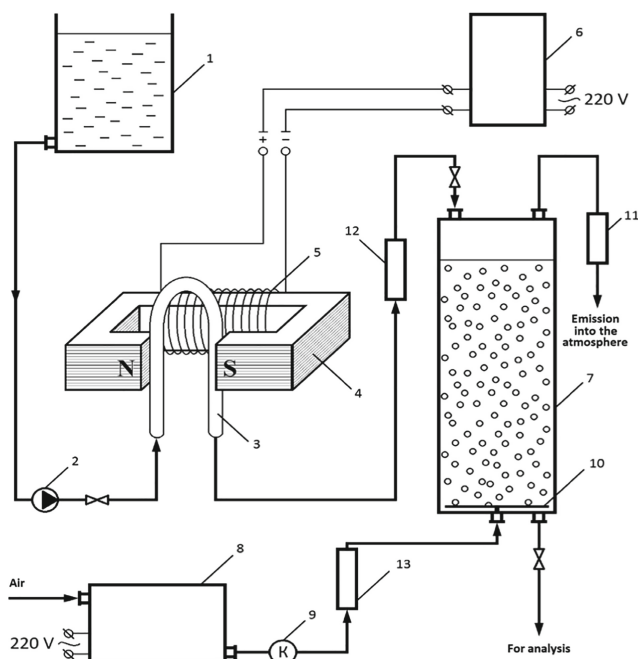
Fig. 2. Laboratory stand for studying the influence of MWT on the kinetics of oxidation reaction; 1 – tank with the working solution; 2 – pump; 3 – pipe for passing the solution in the gap between the poles of the magnets; 4 –from electrical steel core; 5 – coil; 6 – AC rectifier; 7 – bubbling reactor; 8 – ozonator; 9 – air compressor; 10 – dispersing element; 11 – activated carbon column.

The working solution (with a given concentration of oxalic acid and pH) from the tank (1) using the pump (2) was fed into a pipe (3). The pipe is made of diamagnetic material and placed in the gap of electrical steel core (4), on which the coil (5) is wound. At the same time, when passing the solution through the pipe (3), the coil (5) was fed a direct current from the rectifier (6). When passing DC through the coil (5) in the core gap (4) there is a magnetic field, the induction of which depends on the amount of direct current, which allowed regulating the magnitude of the magnetic field induction in the gap of the apparatus of magnetic processing. The magnetic field treated solution from the pipe (3), which then was fed into the bubbling reactor (7).

After filling the reactor (7) from the ozonator (8) using the compressor (9), the ozone-air mixture was fed into the reactor (7) through the dispersing element (10). The dispersing element is a ceramic plate. The ozone-air mixture, which passed the solution, was fed into the column (11) through the pipe outlet. Then the air mixture purified of ozone went to the atmosphere.

To study the influence of the regime parameters of the MWT devices, a series of experiments were carried out according to a similar process scheme - a single passage of a solution in a magnetic field and further ozonation. The effect of each of the defined mode parameters was studied independently.

The studies used experimental solutions with a constant concentration of oxalic acid $(C_2H_2O_4) - 0.1$ kg/m^3. The initial pH level was taken as 7. The solution temperature was 293 K ($\pm 0,2$). Further ozonation of solutions for all experiments was carried out under similar conditions with a constant flow rate of the ozone-air mixture of $1.67 \cdot 10^{-6}$ m^3/s and ozone concentration – 0.16 kg/m^3. Ozonation in a bubbling reactor was carried out during 1200 s.
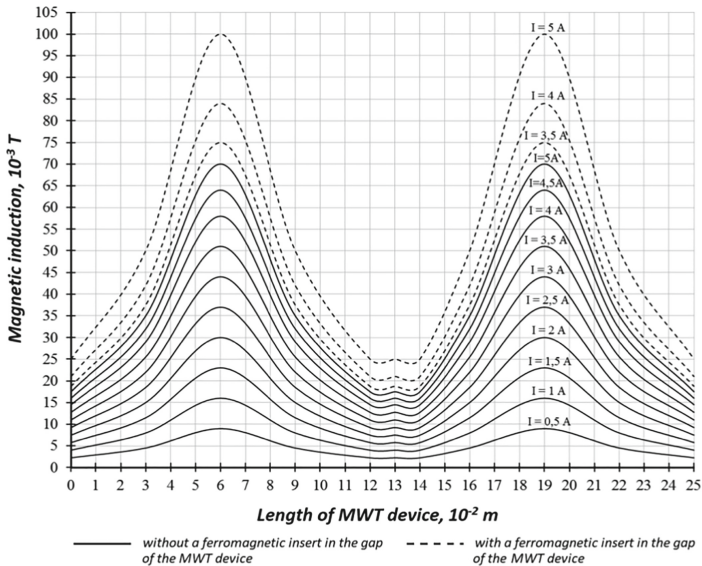
Fig. 3. The change in the magnetic induction in the gap of the MWT device along the tube for aqueous solution passing.

The inhomogeneity of the magnetic field in the MWT device in regard to the unit volume of the solution was provided by the movement of the aqueous solution in the magnetic field with the magnitude variation from 0 to B_i, along the trajectory. The differential induction of ΔB was ensured by the non-uniformity of its distribution along the pipe for aqueous solution passage (Fig. 3) At a constant length of pipe section l_i, the inhomogeneity of the magnetic field was ensured by a change in magnetic induction, from 0 to B_i, or B'_i, which allowed the inhomogeneity change of the magnetic field at other constant processing parameters.

Theoretical aspects of the work are based on physical and mathematical modeling. The methods of titrometric analysis and pH-metry were used to determine the efficiency of organic matter oxidation and control of the physicochemical parameters of MWT and ozonation processes. The experimental data were processed using regression analysis software packages.

4 Results

The long-term operation of MWT devices [11, 12, 15, 16] has proved that the obligatory condition of MWT is the movement of an aqueous solution in a non-uniform magnetic field. The speed of the aqueous solution is one of the determining parameters of MWT. The analysis of the typical frame showed that the principle of MWT devices is the movement of an aqueous solution with velocity v_S in a section of pipe with the length l, placed in a non-uniform magnetic field, where the magnetic induction varies from B_{min} to B_{max}, or vice versa. The analysis of the elementary area of any MWT device proves that at $v_S = 0$ the magnetic field will be constant for each unit of water volume for any induction drop ΔB in the section l. From a physical point of view, it is clear that the velocity v_S directly affects the magnitude of the magnetic induction drop ΔB for a solution volume unit. But the maximum magnitude of the magnetic field induction B_{max} is not so important at the value $\Delta B/\Delta t$. It coincides with [16], where the effect of MWT is observed at low induction values.

The MWT efficiency depends on the processing time and the solution speed in an inhomogeneous magnetic field. Such dependencies are complicated by the design parameters of the MWT devices (placement of magnets, the length of the MWT devices sections with the magnetic induction drops). The influence of the rate of magnetic induction change v_B (T/s) on MWT efficiency was analyzed considering all these parameters. The parameter v_B simultaneously takes into account the design parameters of MWT devices, such as the magnetic induction drop ΔB, the length of the devices section with a non-uniform magnetic field l, and one mode parameter - the speed of the aqueous solution v_S (Eq. 1):

$$v_B = \frac{\Delta B}{\Delta t} = \frac{(B_{max} - B_{min})v_s}{l} \tag{1}$$

where B_{min}, B_{max} – the minimum and maximum magnitudes of magnetic field induction at the pipe section where the magnetic induction changes, T; Δt – the time at which the aqueous solution passes the distance l, s; l – the length of the pipe section at which the

induction of the magnetic field changes from B_{min} to B_{max} or vice versa, m; v_s - the speed of aqueous solution, m/s.

The dependence of MWT efficiency on the rate of magnetic induction changes (v_B) with simultaneous consideration of the total duration of MWT (τ) was characterized by the largest increase in oxidation efficiency of oxalic acid with ozone (Fig. 4). The results of the control experiment were based on the oxidation of oxalic acid by ozone after passing the solution throughout the MWT device without switching on the magnetic field ($v_B = 0$).
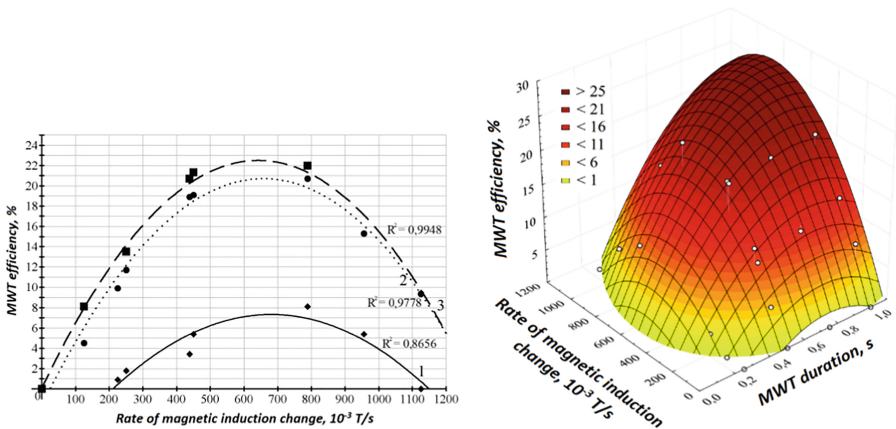
Fig. 4. Dependence of the MWT efficiency on the rate of magnetic induction change: points – experimental results; lines – mathematical modeling results 1 – MWT duration (0,25 s); 2 – MWT duration (0,5 s); 3 – MWT duration (1 s)

Statistical processing of experimental results allowed approximation of the regression equation of MWT efficiency on the rate of magnetic induction change v_B and duration of processing τ:

$$E_{MWT} = -14{,}653 + 38{,}670 v_B + 45{,}656 \tau - 35{,}975 v_B^2 - 30{,}851 \tau^2 + 22{,}845 v_B \cdot \tau,$$

where E_{MWT} – MWT efficiency, %; v_B – the rate of magnetic induction change, T/s; τ – MWT duration, s.

The efficiency of MWT at a duration of 0.5–1 s, does not increase monotonically with increasing value of v_B and reaches its maximum in the range from $400 \cdot 10^{-3}$ to $800 \cdot 10^{-3}$ T/s. Increasing the rate of magnetic induction change above $800 \cdot 10^{-3}$ T/17 s was carried out by creating a sharp drop in magnetic induction. The efficiency of MWT decreased due to higher magnitudes of magnetic induction even with other constant processing parameters. It indicates the complexity of the relationship between MWT efficiency and the magnitude of magnetic induction.

The efficiency of MWT does not increase monotonically with the increasing duration of the MWT process. Thus, at constant values of v_B, increased duration of

treatment from 0.25 to 0.5 s dramatically increases the oxidation efficiency of oxalic acid. At the processing time from 0.5 to 1 s oxidation efficiency does not increase significantly, and a further increase in the duration is technically unreasonable.

5   Conclusions

The speed of aqueous solution in an inhomogeneous magnetic field is determined by the conditions of the appearance of MWT effects, which are more than the magnitude of the induction of a magnetic field. The speed of the aqueous solution and the geometry of the inhomogeneous magnetic field are closely related and are one of the main parameters that determine the MWT efficiency. We can express these parameters using the magnitude of the magnetic induction change. It makes possible to explain the nature of the MWT effects on the processing of aqueous solutions by relatively weak magnetic fields.

The duration of the magnetic treatment has a significant effect on the intensity of MWT effects. The efficiency of MWT decreases while using higher magnitudes of magnetic induction. It indicates the complexity of the processes occurring in aqueous solutions under the influence of a non-uniform magnetic field and requires further studies.

Results will expand possibilities for using MWT in technological processes of water preparation and purification, such as scale deposition reduction on heat exchange surfaces, increasing the removal efficiency of suspended particles from contaminated water during the stages of coagulation, flotation or filtration. Increasing kinetics of chemical reactions after MWT reduces reagents' needs and increases the purification efficiency of reagent treatment of contaminated water.

References

1. Zaidi, N.S., Sohaili, J., Muda, K., Sillanpää, M.: Magnetic field application and its potential in water and wastewater treatment systems. Sep. Purif. Rev. **43**(3), 206–240 (2013)
2. Zlotopolski, V.: The Impact of magnetic water treatment on salt distribution in a large unsaturated soil column. Int. Soil Water Conserv. Res. **5**(4), 253–257 (2017)
3. Latva, M., Inkinen, J., Rämöc, J., Kaunistoa, T., Mäkinena, R., Ahonen, M., Matilainen, J., Pehkonene, S.: Studies on the magnetic water treatment in new pilot scale drinking water system and in old existing real-life water system. J. Water Proc. Eng. **9**, 215–224 (2016)
4. Lipus, L.C., Ačko, B., Neral, B.: Influence of magnetic water treatment on fabrics' characteristics. J. Clean. Prod. **52**, 374–379 (2013)
5. Lipus, L.C., Kropeb, J., Crepinseka, L.: Dispersion destabilization in magnetic water treatment. J. Colloid Interface Sci. **236**(1), 60–66 (2001)
6. Gryta, M.: The influence of magnetic water treatment on CaCO3 scale formation in membrane distillation process. Sep. Purif. Technol. **80**(2), 293–299 (2011)
7. Mehta, D., Mazumdar, S., Singh, S.K.: Magnetic adsorbents for the treatment of water/wastewater – a review. J. Water Process Eng. **7**, 244–265 (2015)
8. Mahmoud, B., Yosra, M., Nadia, A.: Effects of magnetic treatment on scaling power of hard waters. Sep. Purif. Technol. **171**, 88–92 (2016)

9. Gilart, F., Deans, D., Ferrer, D., López, P., Ribeaux, G., Castillo, J.: High flow capacity devices for anti-scale magnetic treatment of water. Chem. Eng. Process. **70**, 211–216 (2013)
10. Kobe, S., Dražić, G., McGuiness, P.J., Stražišar, J.: The influence of the magnetic field on the crystallisation form of calcium carbonate and the testing of a magnetic water-treatment device. J. Magn. Magn. Mater. **236**(1–2), 71–76 (2001)
11. Toledo, E.J.L., Ramalho, T.C., Magriotis, Z.M.: Influence of magnetic field on physical–chemical properties of the liquid water: Insights from experimental and theoretical models. J. Mol. Struct. **888**, 409–415 (2008)
12. Plyatsuk, L.D., Roy, I.O., Chernysh, Y.Y., Kozii, I.S., Hurets, L.L., Musabekov, A.A.: Clarification of the recent scientific approaches in magnetic water treatment. J. Eng. Sci. **6**(1), F12–F18 (2019)
13. Seyfi, A., Afzalzadeh, R., Hajnorouzi, A.: Increase in water evaporation rate with increase in static magnetic field perpendicular to water-air interface. Chem. Eng. Process. **120**, 195–200 (2017)
14. Al-Ogaidi, A.A.M., Wayayok, A., Rowshon, M.K., Abdullah, A.F.: The influence of magnetized water on soil water dynamics under drip irrigation systems. Agric. Water Manag. **180**, 70–77 (2017)
15. Chibowski, E., Szcześ, A.: Magnetic water treatment – a review of the latest approaches. Chemosphere **203**, 54–67 (2018)
16. Koshoridze, S.I., Levin, Y.K.: Model of scale deposition with magnetic water treatment. Formerly nanomech. Sci. Technol. Int. J. **5**(1), 51–71 (2014)
17. Kozic, V., Hamler, A., Ban, I., Lipus, L.C.: Magnetic water treatment for scale control in heating and alkaline conditions. Desalin. Water Treat. **22**(1–3), 65–71 (2010)
18. Szcześ, A., Chibowski, E., Holysz, L., Rafalski, P.: Effects of static magnetic field on water at kinetic condition. Chem. Eng. Process. **50**(1), 124–127 (2011)
19. Coey, J.M.D.: Permanent magnets: plugging the gap. Scr. Mater. **67**(6), 524–529 (2012)

Heat Exchange Characteristics of Trays for Concentrating Solutions in Direct Contact with Hot Gas Emissions

Musii Tseitlin$^{(\boxtimes)}$, Valentyna Raiko , and Oleksii Shestopalov

National Technical University "Kharkiv Polytechnic Institute",
2, Kyrpychova St., Kharkiv 61002, Ukraine
`michelzeitlin@gmail.com`

Abstract. The paper presents the comparative study results of the thermal characteristics of trays applicable for concentrating technological and waste liquids in direct contact with hot gas emissions. The dual-flow tray with large perforation, a baffle tray, similar to that of the mixing condensers, and a paset, i.e. a tray, consisting of a funnel and a cone with a smaller outer diameter, mounted above it, were tested. The enthalpy exchange coefficient was chosen as a comparison parameter since it takes into account both "dry" (due to the temperature difference) and "wet" (due to evaporation) types of heat exchange. Using this coefficient, the degree of influence of liquid temperature and hydrodynamic factors (gas velocity and irrigation density) to the kinetics of enthalpy exchange during the interaction between air and 15% sodium chloride solution was evaluated. It was found out, that according to the degree of influence on the heat exchange intensity, factors arranged in the following sequence: air velocity, related to the entire apparatus cross-section; spray density and temperature.

Moreover, the impact of temperature appeared to be, although noticeable, but negligible. Processing the experimental results mathematically, formulas are obtained to calculate the enthalpy exchange coefficients for all contact trays researched. Recommendations are also provided for their use.

Keywords: Thermal characteristics · Dual-flow tray · Baffle tray · Paset · Direct contact heat exchanger · Enthalpy exchange coefficient

1 Introduction

The waste heat resources utilization is known to face some difficulties. First of all, it is their relatively low temperature, leading, to problems in finding consumers, on the one hand, and, on the other hand, to relatively high metal consumption and the cost of heat exchange equipment. Waste gas is usually contaminated with dust, and often with aggressive components. Also, hot wastewater often contains caustic substances, solid-phase and dissolved components that can deposit sediment on heat exchange surfaces.

Considering equipment, the so-called "contact heat utilizers", in which hot gas in direct contact with the liquid heating and/or evaporating it, seem to be promising [1, 2]. The advantages of such equipment are simplicity, cheapness, high intensity of heat and

mass exchange processes, absence of a rigid surface that separates the heat exchange medium. The latter is especially important when the solution is highly corrosive or when solid sediment is observed. Anyway, the concentration of solutions in direct contact with flue gas cannot be concerned as the best method in terms of heat utilization. However, this disadvantage is relevant only if paid fuel is used to obtain the hot stream. When utilizing waste power resources, for example, flue gas, the level of heat use is minor in comparison with the mentioned advantages.

The purpose of this research is to find and compare the heat and mass exchange characteristics of trays proper to use in a heat exchange apparatus when working with both light liquid and suspensions, forming strong sediments.

2 Literature Review

2.1 Trays for Working with Waste Water

Most of the known contact heat exchangers are packed bed columns [1, 2], which are improper for working with suspensions and crystallizing liquids despite having appropriate heat and mass exchange characteristics. Therefore, only constructions of trays applicable to operate in apparatuses with step phase contact are considered below.

Apparatuses, sectionalized in height with dual-flow trays, which are disks perforated with holes from 60 to 120 mm in diameter, are of significant interest from the viewpoint of utilizing suspensions heat [3]. The study results of heat and mass exchange on these trays can be found in works [4]. Dual-flow trays are easy to manufacture and, as the experience of soda ash production has shown, they can work with deposits overgrown for a long time [3]. Nevertheless, their disadvantages are unstable hydrodynamic regime and insignificant transverse mixing [5]. The latter leads to liquid and gas bypass in case tray diameters are large [6].

Contact coolers with segment shelves (baffles tray) [7], similar in design to those used in mixing condensers, are widely used in the industry. Dusty gas can cool down without clogging inside the apparatus of this type. The baffle tray contact cooler is used for cooling coke gas, saturated with moisture from 80 to 35 °C. Such types of equipment are also used in soda ash production. In particular, data on the heat exchange properties of these apparatuses can be found in work [8].

To utilize the heat of the distillate liquid of soda ash production it is recommended in work [9] to use trays, formed by series cones and funnels overlapping 55–60% of the apparatus cross-section. In [9] this device is called a "cascading contact element." Further for brevity, we will call it "paset". As the researchers' outline, the interphase surface on such trays is formed due to the distribution of the liquid by crushing it into separate streams and drops. This method is considered to be the best one for contact heat exchangers.

In direct contact apparatuses [10, 11] of various designs, the concentration process is accomplished both with direct-flow and with countercurrent flow of the liquid and the gas [12, 13].

In most studies of the heat and mass exchange characteristics in contact heat utilizing, the common problem mentioned is their relatively low accuracy. In the

calculations based on the equations obtained by the authors of these works, errors are no less than 15%. Using the water-air system as a model can also cause difficulties in implementing the results obtained to real industrial gas and liquid systems.

2.2   Calculation Methods for Contact Heat Exchangers

Engineering calculations of contact apparatuses are diversified. That represents the complexity of the hydrodynamic and thermal conditions in the active apparatus space to a certain extent, and, in particular, the difference in the formation methods of an interphase surface and its structure [14]. When studying the heat exchange character-istics of trays in direct liquid and gas contact, the peculiarity is in the close interde-pendence of heat and mass exchange (evaporation or condensation of liquid), which cannot be studied separately except special cases. Mathematical models, taking into account this feature by simultaneously calculating heat and mass exchange (see, for example, [15, 16]), are characterized by excessive complexity, which is not always offset by the corresponding accuracy.

   Allowing both simple graphical and instrumental calculations, the methodological approach to the calculation of contact heat exchangers are considered to be of sig-nificant interest, presented in work [17]. Problems, noted above, can be overcome if heat and mass exchange processes are regarded as a single enthalpy exchange process. In this case, the driving force of the process is also calculated in units of specific enthalpy. It is believed that this approach was initially proposed by Merkel and Hirsch to calculate the first stage of the drying process. In work [18], it was adapted to calculate the processes of contact heat exchange of liquid and gas. Following the approach proposed in this work, the enthalpy of gas changes in contact with the liquid, both due to the evaporation of air (the so-called "wet" heat exchange) and due to heat exchange under different temperature (the so-called "dry" heat exchange), and it is proportional to the difference between the enthalpy of gas which is in equilibrium with liquid and the actual one. Mathematically, this can be given as follows:

$$G\frac{dH_g}{dS} = k_H\left(H_g - H^*\right). \tag{1}$$

k_H is found by the formula:

$$\frac{1}{k_H} = \frac{1}{k_g} + \frac{H^* - H_i}{\alpha_l(t_l - t_i)}, \tag{2}$$

where G is the mass gas flow rate, kg/s; S is the area of the phase interface, m²; k_H is enthalpy exchange coefficient, kg/m²s; H_g is air enthalpy, kJ/kg; H^*; H_i is the enthalpy of gas which is in equilibrium with the bulk of the solution and with the liquid on the phase interface, respectively, kJ/kg; α_l is the heat exchange coefficient from the liquid bulk to the phase interface; t_i, t_l are the temperatures of the gas-liquid interface and the liquid bulk, respectively °C; k_g is mass exchange coefficient in gas, kg/m²s.

This approach can significantly simplify the calculation of the apparatus for the heat utilization process; however, the lack of experimental data, which would allow calculating the enthalpy exchange coefficient for various trays, hinders its practical application.

3   Research Methodology

The study was carried out on a bench, which included an experimental apparatus, a set of auxiliary equipment, which made it possible in particular to heat the liquid, and a set of measuring instruments. The experimental apparatus consisted of a base with mounted pipelines for supplying air and draining the solution, three transparent shells having a diameter and height of 0.5 m, mounted on it, and a lid equipped with a pipeline for draining air and a device for distributing the liquid pouring into the apparatus. The researched trays were mounted between the shells. Three types of them were examined: dual-flow trays perforated with holes of 60 mm in diameter, the so-called paset or a tray in the form of a funnel with a cone mounted above it, and a baffle tray, similar in design to those used in mixing condensers. All of them were designed so that the area of the narrowest places for the passage of gas was at least 40% of the apparatus cross-section area.

We studied the dependence of the enthalpy exchanging coefficient (k_H) to the gas velocity (w), irrigation density (l), liquid temperature (t), and the design of the tray. The temperature of the initial liquid varied in the range from 60 to 90 °C, the irrigation density was from 0.2 to 5 dm^3/m^{2}s, and the gas velocity was from 0.2 to 3.5 m/s in most of the experiments. The experiments were carried out with a 15% solution of sodium chloride. On the one hand, this solution is close in properties to many real technological solutions, and, on the other hand, it is relatively accurate and simple to calculate the amount of evaporated mass by changing of the chloride ion concentration in solution.

During the initial processing of the experimental results, the enthalpy exchange coefficient was determined (k_H, see Eq. (1)). For this purpose, a particular computer program was developed to calculate the process in the experimental apparatus, which made it possible to select a value of k_H, at which the values of the calculated parameters of the liquid and gas coincided with those obtained as the result of the experiment.

4   Results

The estimation of the enthalpy transfer coefficient dependence on the solution temperature was initially based on the analysis of Eq. (2), which allowed us to expect that the influence of this factor will be significant. The experimental results showed that with a change in the temperature of the initial liquid in a rather wide range (of the order of 40 °C) the value of k_H decreased noticeably with increasing temperature. Still, this change turned out to be negligibly small in comparison with the impact of other factors studied. The reason for this is that, by the accepted method for calculating k_H, it was

related to the average temperature in the apparatus, and this value varied in a relatively narrow range, which depended mainly on the irrigation density. So, at $l = 0.2$ dm^3/m^{2}s, the average temperature varied in the range of 7–9 °C, and at $l = 5$ dm^3/m^{2}s – 15–20 °C.

When studying the impact of gas velocity and irrigation density on the enthalpy exchange coefficient, all three trays mentioned above, were included. In the range of gas velocities of 0.2–1.7 m/s in the absence of liquid accumulation on the plates, as expected, the dependencies of the enthalpy exchange coefficients on the gas velocity turned out to be qualitatively identical for all trays. In this range, slightly higher k_H values were observed at the dual-flow tray. This can be explained by the larger perimeter of holes for gas passing in comparison with the paset and the baffle tray.

With an increase in the gas velocity in the range of 2–2.5 m/s, the accumulation of liquid is on, caused by the entrainment of liquids from the lower trays to the upper ones and the formation of layers from sprays and jets. With increasing air velocity, the slope of the graphs of changes in k_H noticeably increases. This can be easily explained by the intensification of drop crushing in the constrictions of the trays (in the neck of the funnel and along the edge of the cone for the paset and in the space between the baffle tray and the wall of the apparatus) and their subsequent separation, i.e., the intensification of the renewal of the phase interaction surface. An increase in air velocity above 2.5 m/s slows down the growth of the enthalpy exchange coefficient.

Regarding the dual-flow tray, due to the poor representation of the experimental results typical for these trays, no changes were identified in the rising of the enthalpy exchange coefficient in the range of air velocity of 2–2.5 m/s. Therefore, at higher gas velocity, the k_H value begins to "lag" the paset and baffle tray. Moreover, this "lag" reaches up to 20%. The reason for this can be judged by a slowdown in the growth of k_H with increasing air velocity from 3 to 3.5 m/s. This behaviour of the considered dependence can be explained by the longitudinal mixing of the liquid, caused by the increase of the spraying from plate to plate at these airspeeds. In contrast to the dual-flow tray, the paset and baffle tray have spray separation zones. Therefore, such spraying is much less on them.

It should be outlined that, although in contrast to the dual-flow tray, the dependencies of k_H to the gas velocity show the obvious impact of hydrodynamic regimes change for both the paset and the baffle tray, this impact is not so significant and can be neglected in the mathematical processing of the dependence of k_H to w.

Since the heat and mass exchange characteristics of the dual-flow tray are sufficiently studied and presented in the literature [3–6], further research results are presented only for the paset and baffle tray.

Figure 1a shows the dependency graph of the enthalpy exchange coefficient to the gas velocity for a paset, and Fig. 1b – for a baffle tray.
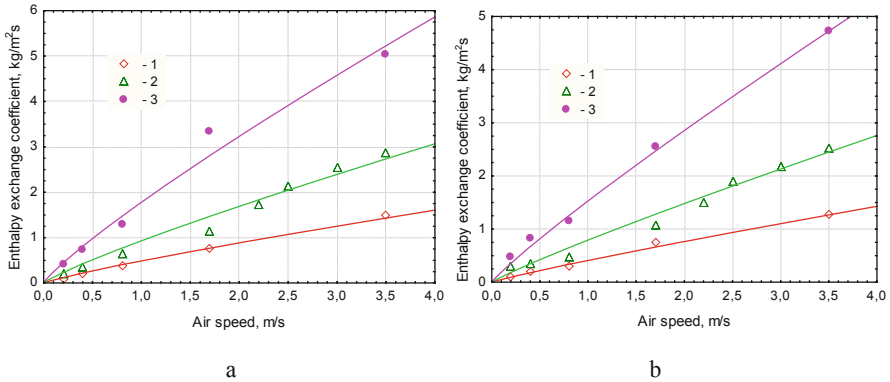
Fig. 1. The dependency graph of the enthalpy exchange coefficient to the air velocity for (a) paset and (b) a baffle tray at irrigation densities (dm^3/m^{2}s): 1–0.2; 2–1; 3–5.

The graph lines for the paset are drawn in Fig. 1 according to the equation

$$k_H = 0,931w^{0,86}l^{0,402} \tag{3}$$

and for a baffle tray according to the equation

$$k_H = 0,793w^{0,90}l^{0,41}. \tag{4}$$

In Fig. 1, the graphs show satisfactory coincidence of the experimental points with the calculation by mentioned equations; however, without representing the hydrodynamic regimes change in the range of 1.7–2.5 m/s. Nevertheless, even with this simplification, the correlation coefficient between experiment and calculation exceeds 0.98, which can be considered as a rather reliable result.

Analyzing Eqs. (3) and (4), it can be observed that the experimental data might be represented by an equation as follows:

$$k_H = b_0 \prod_{i=1}^{n} X_i^{b_i}, \tag{5}$$

where X_i is the factor influencing the kinetics of heat exchange (here, this is the air velocity in the entire apparatus cross-section and the irrigation density); b_i is the coefficient.

Also, the exponents at the air velocity in the entire apparatus cross-section and the irrigation density are very close for both: the paset and the baffle tray, which could be expected, concerning the resemblance of operation principles of these trays. However, the main difference between Eqs. (3) and (4) is the proportionality coefficient, which is 0.931 and 17% higher in Eq. (3) than in Eq. (4), i.e. the enthalpy exchange coefficient is significantly higher for a paset than for a baffle tray.

For further analysis, the level lines projection of three-dimensional graphs of Eqs. (3) and (4) are shown on a plane with coordinates of the gas velocity – irrigation density in Fig. 2. This figure can also be used to estimate the values of k_H for given w and l.

a   b
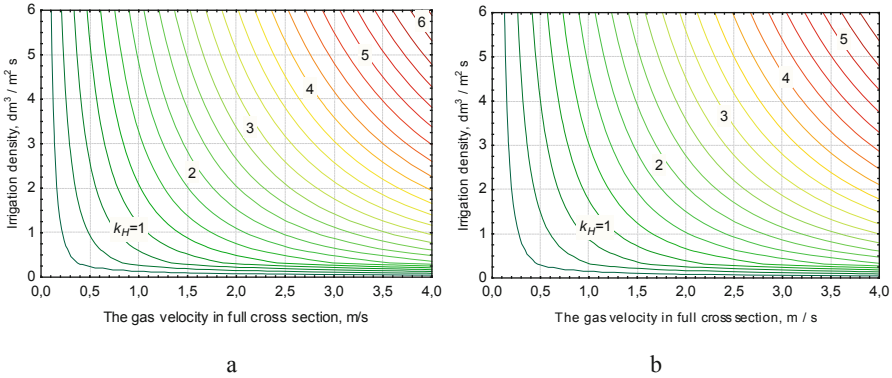
Fig. 2. The dependency graph of the enthalpy exchange coefficient on the paset (a) and on the baffle tray (b) to the air velocity in the entire apparatus cross-section and the irrigation density.

As it is shown in Fig. 2, at low air velocity, up to 0.5 m/s, the irrigation density has a somewhat slight impact on the enthalpy exchange intensity (in Fig. 2, the lines of the graphs are almost vertical in a practically applicable range of l). However, with increasing gas velocity, the impact of irrigation density increases and at the velocity of 3.0–3.5 m/s the impact of w and l on k_H becomes approximately the same.

Comparing the obtained results with the data on the dependence of the enthalpy exchange coefficient to w and l for the dual-flow tray, obtained in work [3] in the form of the equation

$$k_H = 0,678w^{0,89}l^{0,69}, \qquad (6)$$

it can be observed that the impact of the gas velocity on k_H is the same as in Eqs. (3) and (4) (w exponent is 0.89 for the dual-flow tray, and 0.86 and 0.90 are for the paset and baffle tray, respectively). Nevertheless, the impact of irrigation density on k_H is significantly higher in the dual-flow tray than in our experiments (the exponents for l are 0.69 in Eq. (5), and 0.40 and 0.41 in (3) and (4), respectively). This can be explained by separation zones in the paset and the baffle tray apparatus. Such zones appear due to the angular motion of gas and facilitate the internal circulation of the liquid, providing large liquid retardation on each tray. In contrast to the dual-flow tray, this accumulated liquid is stable on the trays. As it is shown in work [2], sprays and jets layers can arise and disappear spontaneously on a dual-flow tray under the same conditions The mentioned above circumstances neutralize the impact of irrigation density on k_H on the dual-flow tray in comparison with the paset and baffle tray.

The analysis of Eqs. (3)–(5) shows that, in general, the enthalpy exchange coefficient is lower for the dual-flow tray than for the others, which is indicated by the lower proportionality coefficient in Eq. (5). However, due to the more significant impact of irrigation density, this difference decreases with increasing irrigation density. The calculation shows that even at $l = 3$ dm^3/m^{2}s, k_H for the dual-flow tray turns out to be equal to this indicator for the baffle tray, and at high irrigation density, it exceeds that, but, in the range studied, it remains less than that for the paset.

Considering the results obtained, we can conclude that paset has the best indicators of heat exchange intensity. Moreover, its main drawback is the design complexity, which leads to difficulties in cleaning from contamination and increases metal consumption in comparison with other tray researched. The dual-flow tray does not have these drawbacks. Besides, when operating at a gas velocity of less than 2 m/s, it shows results only inferior to the paset and baffles tray. However, we should beware of liquid and gas bypasses typical for large-diameter apparatuses. The baffle tray is a compromise solution and can be used in heat exchangers working with liquids containing suspensions and forming deposits on trays.

5   Conclusions

The paper presents the comparative study results of the thermal characteristics of trays applicable for concentrating technological and wastewater in direct contact with hot gas emissions. The dual-flow tray with large perforation, a baffle tray, similar in design to the mixing condensers, and a paset, i.e. a tray consisting of a funnel and a cone with a smaller outer diameter, set above it, were tested.

The enthalpy exchange coefficient was selected as a parameter for comparison, taking into account both "dry" (due to the temperature difference) and "wet" (due to evaporation) types of heat exchange. The degree of exposure of liquid temperature and hydrodynamic factors (gas velocity and irrigation density) to the kinetics of enthalpy exchange during the interaction between air and 15% sodium chloride solution was evaluated using this coefficient.

It was found out, that according to the degree of exposure to the heat exchange intensity, the factors are arranged in the following sequence: air velocity, related to the entire apparatus cross-section; irrigation density and temperature. Moreover, the impact of temperature appeared to be negligible. Processing the experimental results mathematically, formulas are obtained to calculate the enthalpy exchange coefficients for all tray structures researched. Recommendations are also provided for their use.

References

1. Lage, P., Campos, F.B.: Advances in direct contact evaporator design. Chem. Eng. Technol. **27**(1), 91–96 (2004)
2. Pianko-Oprych, P.: Modelling of heat transfer in a packed bed column. Pol. J. Chem. Technol. **13**(4), 34–41 (2011)

3. Kolmetz, K., Ng, W.K., Faessler, P., Sloley, A., Zygula, T.: Distillation - 1: design guidelines outline solutions for reducing fouling in distillation columns. Oil Gas J. **102**(31), 60–64 (2004)
4. Domingues, T.L., Secchi, A.R., Mendes, T.F.: Overall efficiency evaluation of commercial distillation columns with valve and dualflow trays. AIChE J. **56**(9), 2323–2330 (2010)
5. Taranenko, G.V.: Calculation of the lower operating limit of dual-flow plates with different geometrical characteristics. ScienceRise **3**(2), 67–73 (2015)
6. Taranenko, G.V.: Hydrodynamic modeling of the operating regimes of dual-flow plates installed in columns of various diameter. ScienceRise **6**(35), 34–38 (2017)
7. Genić, S., Jaćimović, B., Vladić, L.: Heat transfer rate of direct-contact condensation on baffle trays. Int. J. Heat Mass Transf. **51**(25–26), 5772–5776 (2008)
8. Tseytlin, M.A., Rayko, V.F., Gareyev, A.T.: Contact cooling of compressed gases. In: Republican interdepartmental scientific and technical collection "Power engineering", vol. 55, pp. 85–87. KhGPU, Khar′kov (1996). (in Russian)
9. Tseytlyn, M., Dassuky, M.: Study of the hydrodynamic characteristics of a cascade contact device. Integr. Technol. Energy Sav. **1**, 41–47 (2009). (in Russian)
10. Lemenand, T., Durandal, C., Della Valle, D., Peerhossaini, H.: Turbulent direct contact heat transfer between two immiscible fluids. Int. J. Therm. Sci. **49**(10), 1886–1898 (2010)
11. Huang, F., Zheng, J., Baleynaud, J.M., Lu, J.: Heat recovery potentials and technologies in industrial zones. J. Energy Inst. **90**(I6), 951–961 (2017)
12. Ribeiro Jr., C.P., Lage, P.L.C.: Population balance modeling of bubble size distributions in a direct-contact evaporator using a sparger model. Chem. Eng. Sci. **59**(12), 2363–2377 (2004)
13. Chaumat, H., Billet, A.M., Delmas, H.: Hydrodynamics and mass transfer in bubble column: influence of liquid phase surface tension. Chem. Eng. Sci. **62**(24), 7378–7390 (2007)
14. Narayan, G.P., Mostafa, H.S., Steven, L., et al.: Bubble columns for condensation at high concentrations of noncondensable gas: heat-transfer model and experiments. AIChE J. **59**(5), 1780–1790 (2013)
15. Boulama, K., Galanis, N., Orfi, J.: Heat and mass transfer between gas and liquid streams in direct contact. Int. J. Heat Mass Transf. **47**, 3669–3681 (2004)
16. Zezhi, Z., Abolfazl, S., Sungtaek, Y.: Thermohydraulic characteristics of a multi-string direct-contact heat exchanger. Int. J. Heat Mass Transf. **126**(11), 536–544 (2018)
17. Qianjian, G., Xiaoni, Q., Peng, S., Pengjiang, G.: New explicit analytical solutions of equations for heat and mass transfer in a cooling tower energy system. Adv. Mech. Eng. **11**(12), 1–8 (2019)
18. Estefane, P., Rayko, V.F., Tseytlyn, M.A.: The study of heat and mass transfer during the water-evaporation concentration of brine. East.-Eur. J. Enterp. Technol. **29**(5/1), 40–44 (2007). (in Russian)

Author Index